MICROSTRUCTURE-BASED COMPUTATIONAL MODELING OF MECHANICAL BEHAVIOR OF POLYMER MICRO/NANO COMPOSITES

A Dissertation

by

ARDESHIR HEYDARKHAN TEHRANI

Submitted to the Office of Graduate and Professional Studies of
Texas A&M University
in partial fulfillment of the requirements for the degree of

DOCTOR OF PHILOSOPHY

Chair of Committee,	Stefan Hurlebaus
Co-Chair of Committee,	Mary Beth Hueste
Committee Members,	Ramesh Talreja
	Anastasia Muliana
Head of Department,	Robin Autenrieth

December 2013

Major Subject: Civil Engineering

ABSTRACT

This dissertation is devoted to the virtual investigation of the mechanical behavior of micro/nano polymer composites (MNPCs). Advanced composite materials are favored by the automotive industry and army departments for their customizable tailored properties, especially for strength and ductility compared to pure polymer matrices. Their light weight and low finished cost are additional advantages of these composite materials.

Many experimental and numerical studies have been performed to achieve the optimized behavior of MNPCs by controlling the microstructure. Experiments are costly and time consuming for micro scale. Hence, recently numerical tools are utilized to help the material scientists to customize and optimize their experiments.

Most of such numerical studies are based on characterizing the MNPCs through simple microstructures, as circular particles or straight fibers embedded in a specific polymer matrix. Although these geometries are effective in virtual modeling some types of composite material behavior, they fail to address some critical key micro-structural features, which are important for our goals. Firstly, they fail to properly address the randomness of particles. Secondly, 2D analyses have limitations and they can provide qualitative insight, rather than evaluate the quantitative response of the material behavior. Thus, in order to fill this gap, a user friendly software program, REV_Maker, is developed in this project for generating 2D and 3D RVEs (representative volume elements) to precisely represent the morphology of material in microstructural level.

In models, polymers are usually considered as viscoelastic-viscoplastic or hyperelastic-viscoplastic materials without taking into account viscodamage models. Therefore, in this work rate- and time-dependent damage (viscodamage) is separately considered to fully investigate the initiation and growth of damage inside polymer composites.

Besides, most of the common viscoelastic and viscoplastic models assumes small deformation; therefore, in this dissertation a procedure is established, which incorporates all required modifications to generalize a small strain constitutive model to its identical large deformation range. Thus, here a straightforward generalization and implementation method based on classical continuum mechanics is proposed, which due to its simplicity, can be applied to a wide range of elastoplastic constitutive models. Then, the available viscoelastic and viscoplastic models are extended to large strain framework. By applying the generalized viscous models, one may address and measure the large deformation response of MNPCs.

Numerous simulations were conducted to predict the overall responses of micro/nano composites with different morphologies (particles volume fractions, orientations, and combinations). The effect of each particle, and the combination of particles on the composite responses are compared and presented.

ACKNOWLEDGEMENTS

First, I would like to thank my former advisor Dr. Rashid K. Abu Al-Rub who got me started on this work. He supervised and provided support including discussion on the required theory, and also providing feedback on computational simulations.

Thanks also go to my chair and co-chairs from Civil Engineering Department; Dr. Stefan Hurlebaus and Dr.Mary BethHueste, for helping me finish my PhD. The value of their reviewings is highly appreciated.

Moreover, I would like to appreciate my committee members, Dr. Ramesh Talreja from Department of Aerospace Engineering, and Dr. Anastasia Muliana from Department of Mechanical Engineering. They provided me insightful comments for better understanding the behavior of polymer and polymer composites.

Thanks also go to my friends, colleagues, and the department faculty and staff for making my time at Texas A&M University a great experience. I also want to extend my gratitude to ARO (Army Research Office) for funding the majority of this research project.

Last, but not the least, I wish to acknowledge the ceaseless support and love that my parents and my wife have given me during my time at Texas A&M University.

TABLE OF CONTENTS

CHAPTER Page

CHAPTER Page

CHAPTER Page

LIST OF FIGURES

Page

Page

Page

Page

Page

Page

Page

Page

Page

Page

Page

Page

Page

Page

Page

Page

LIST OF TABLES

Page

Page

CHAPTER I

INTRODUCTION

1.1 Problem Statement

According to the invention and usage of light-weight materials in industry and in army departments for light-weight vehicular and personal protections; utilizing traditional heavy steels and alloys is not an effective and efficient approach. Therefore, Low-Density Composite Materials (LDCM) for light-weight armor packages as well as light-weight parts in auto industry, are highly desirable. There is a significant need for improving the impact loading performance, and increasing the strength of light-weight composite materials. These materials are commonly used in industry (especially in aircrafts) and also for army assets to decrease the weight and degradation, along with increasing the strength, flexibility, mobility, and fracture toughness to achieve improved resistance against impact loadings.

Varying performance can be achieved for composite materials by combining constituents with different thermo-mechanical properties. Metals and polymers have been used for the host material (matrix), which is reinforced with different types of inclusions. Since the impact damage performance and strength of composite materials can be enhanced by adding micro/nano inclusions such as different types of fibers and/or particles with various sizes and distributions, the proposed research leads to develop and apply a fundamental understanding of the key role of particle size, aspect ratios, distribution, and also interfacial effects on the strengthening (strain-hardening) and

micro-damage (strain-softening) mechanisms. These items finally guide to design better LDCMs with proper and more desirable optimized micro/nano structure that can show an improved performance while subjected to different types of loadings.

To achieve a fundamental understanding on the effects of the properties and microstructural geometries of the inclusions on the overall responses of composites, various micromechanical models have been formulated. However, most of the models have been applied to simple geometries. Therefore, a reliable relationship between material microstructure features, that specifically describes the effects of particles sizes, aspect ratios, different patterns (orientations and distributions), different inclusions mixtures, average inter-particles spacing, and also interfacial properties of the composite materials, remains elusive. Hence, the main objective of the proposed research is to develop and apply efficient computational modeling and constitutive laws that can be employed for describing and predicting a realistic response of the micro/nano structure of composite materials.

From an economic point of view (cost and time), setting various straightforward micromechanical experiments on a number of material samples including different particle shapes, sizes, and morphologies, different micromechanics (particles inter-spacing and volume factions), different constituents properties subjected to various loading conditions is not a practical task. Therefore, an effective computational modeling scheme that can provide a better understanding of the micro/nano composite structures of LDCMs is needed.

Work-hardening is one of the primary concepts for increasing both the strength and fracture toughness of materials. However, it is noteworthy to recall that any increase

in strength in general is associated with a loss in ductility. These properties can be enhanced by the second phase inclusions of different sizes. For example, Fig.1.1 shows a composite material (containing nano-ceramics) in which the particles are distributed heterogeneously (randomly), and are divided into two or three different sizes. Until now, it has been sugested that adding smaller size particles increases the strength of the composite through the strain hardening mechanism, while the larger particles lower the fracture toughness by strain softening (Hao et al., 2004).

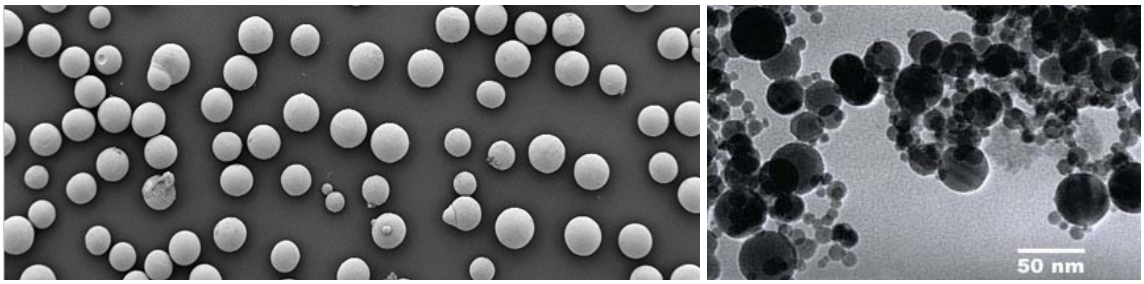

(a) **(b)**

Fig. 1.1. 2D image of: (a) Nano-ceramics granules, (b) Nano-ceramics composite. (nano-ceramics applications- http://www.plasmachem.com).

Thus, by optimizing the volume fractions, shapes, sizes, distribution, and interfacial properties, one will be able to enhance the strength and fracture toughness of a composite simultaneously. Even though currently advanced technology provides many ways to achieve either high strength or fracture toughness in materials which are conducted by some high technical processing, the challenge remains to simultaneously achieve both properties.

The size of micro-structural inclusions has an important effect on the mechanical properties of a material (Abu Al-Rub and Voyiadjis, 2004a, b). For example,

experimental works on particle-reinforced composites have revealed that an extensive increase in the macroscopic yield strength, flow stress, and fracture toughness can be achieved by reducing the size of inclusions, whereas the volume fraction is constant (Kiser et al., 1996; Kouzeli and Mortensen, 2002; Lloyd, 1994; Nan and Clarke, 1996; Niihara et al., 1993; Rhee et al., 1994a; Zhao et al., 1993; Zhu et al., 1995). Producing light-weight composites needs a systematic way for investigating and designing the proper dimensions, shape, and the quantity of the required components. To achieve this goal, the following questions have to be answered:

- What types of inclusions are needed to gain better mechanical performance of a microstructure in a Polymer Composite Material (PCM)?
- What are the optimum volume fractions and dispersion for each type of inclusion that can enhance the mechanical responses of these materials?
- Which constitutive models can better explain the characteristics behaviors of PCMs?
- How can a cost effective procedure for different microstructures be achieved?

Polymer and PCMs exhibit time and rate dependent responses, therefore in this research, unified viscoelastic, viscoplastic, and viscodamage models are employed for characterizing the polymer matrix. These unified models have been formulated on the bases of the principle of virtual power and laws of thermodynamics and utilizing large deformation frameworks. By using this model for the host material, the effects of particle shapes and sizes, aspect ratios, diverse distributions, different inclusions mixtures, average inter-particles spacing, and also interfacial properties of polymer composites are computationally investigated.

1.2 Constituents in Nanocomposites

Studying the open literature and the industeries producing micro/nano polymer composites reveals that the micro/nano inclusions for improving the mechanical properties of the composites can be listed as:

- Carbon Nano Tubes or Fibers (single-, double-, and multi-walled with high and extremely high aspect ratios).
- Nano-metals (e.g. nano Aluminum, nano Iron, nano Nickel).
- Nano-ceramics (e.g. nano Carbides, nano Nitrite, nano Titanium).
- Nano-clays (nano-clay/polymer composites are categorized as: (a) conventional composite, (b) partially intercalated, (c) fully intercalated, and (d) fully exfoliated).

Therefore, in this section the reasons and interests for utilizing these inclusions in polymer composites are described.

1.2.1 Motivation for Investigating Nano-Clay Particles

Inspired by the intresting results obtained by a group of researchers in Japan by incorporating nano-clays into nylon (Usuki et al., 1993), extensive work has been carried out over the past two decades on the addition of nano-clay particles into polymers for the purpose of greatly enhancing their properties. In these types of composites, generally the tensile modulus, tensile strength, glass transition temperature, resistance against the absorption of moisture, resistance against flammability, and fracture toughness have been investigated. Yasmin et al. (2003) added up to 10 wt% (weight fraction) of clay into epoxies, and obtained up to a 60% increase in elastic modulus, although the tensile

strength decreased. For resins such as epoxies, which are normally used as the matrix for composites in advanced composite structures, toughness is a very important parameter for evaluating the amount of enhancement. For improving the toughness of epoxies, many researchers have tried to use nano-clays. Liu et al. (2004) added 4 wt% of nano-clay into Diglycidyl-Ether of biphenyl and obtained an increase in elastic modulus, decrease in glass transition temperature, and 80% increase of stress intensity factor from about 0.5 to about $0.9\,\mathrm{MPa}\sqrt{\mathrm{m}}$. In 2004, Liu et al. (2004) at Concordia Center for Composites showed that by adding just 5 wt% of clay, the strain energy release rate (three-point bending of specimen with a notch) of an aircraft epoxy system can be enhanced from 125 to 650 $\mathrm{J/m^2}$ (420% increase). Such increase in fracture toughness of the mixture provides great encouragement for these approches.

1.2.2 Motivation for Studying Carbon Nanotubes

The recent discovery of carbon nanotubes (CNTs) has gained more interest due to providing unique properties generated by their structural perfection, small size, low density, high strength, heat conductivity, and also excellent electronic properties. Indeed, the longitudinal Young's modulus of CNTs falls between 0.4 and 4.15 TPa, while a tensile strength approaching 100 GPa (Buryachenko and Roy, 2005). Carbon nanotubes occur in three distinct forms, single-walled nanotubes (SWNT), which are composed of a graphite sheet rolled into a perfect cylinder, double-walled nanotubes (DWNT) having two concentric graphite cylinders, and multi-walled nanotubes (MWNT), which consist of multiple concentric graphite cylinders. A high aspect ratio of CNT and its extraordinary mechanical properties (strong as diamond and flexible as polymers) make

them ideal reinforcing fibers in the nano-composites field. Hence, CNTs can be utilized to produce advanced nano-composites with improved stiffness and strength. Tensile tests on composites confirm that adding only 1 wt% of nanotubes results in 40% and 30% increase in elastic modulus and strength, respectively (Qian et al., 2000). This illustrates a significant amount of load transfer across the nano tube–matrix interface. Moreover, the CNTs provide very high interfacial area while embedded in a nano-composite matrix. This can also provide a form of mixture and assemblies with unique architectures that might be constructed by interconnected CNTs. In the last decade, some researchers observed a substantial increase in the effective properties of polymer nano-composites (PNCs) (Chen et al., 2006; Gojny et al., 2006; Zhu et al., 2004). On the other hand, in spite of the promising properties of CNTs, other researchers have claimed and reported several experiments with a little enhancement of the elastic properties of the PNCs (Ajayan et al., 2000; Moisala et al., 2006; Qian et al., 2002).

The above mentioned research and results explain the motivations for studying physical properties of polymer composites containing nano-clay particles and CNTs. According to such background, investigating the properties of polymer composites with different particles necessitates an efficient systematic technique. Also, polymer composites usually contain two or three different constituents, and the micromechanical modeling is a suitable approach for investigating the effects of components in a composite. Thus, in this work, effort is focused on automatically creating various microstructures representing realistic configurations of different types of composites. The benefits of utilizing micromechanical modeling can be listed as follows

- Proper selection of the inclusions (particles, fibers, or both).
- Proper and ideal arrangements and patterns for particles and fiber-reinforcement inside the matrix (i.e. producing and inspecting different materials systems).
- Satisfying the designing requirements (mechanical/thermal).
- Leading to the evidences that facilitate the processes of fabrication.
- Minimizing the manufacture risks (cost, schedule, and technical).

1.3 Research Objectives

The macroscopic mechanical behavior of polymer composites strongly depends on their microstructure, which is highly governed by the type of inclusions and the pattern of dispersion. It is noteworthy to mention that the reinforcement forms can be listed as continuous fibers, discontinuous or chopped fibers, whiskers, particles, platelets, etc. Hence, the ultimate goal of the proposed research is studying the overall mechanical responses of polymer composite materials containing various types of embedded micro/nano inclusions such as: ceramics, clays, metal particles, as well as carbon nano tubes or carbon nano fibers. Also, composites including both nano-ceramics and CNTs or both nano-clays and CNTs, will be examined. This goal can be achieved by studying the effects of particle shapes and sizes, aspect ratios, miscellaneous distributions, different inclusions mixtures (particles-particles, particles-fibers), average inter-particles spacing, and also the properties of interfacial contact faces in a polymer composite. The specific objectives of the proposed research are listed as follows:

- Studying and applying viscous based constitutive models, to be able to evaluate the time and rate dependency behavior of polymer-based composite materials.
- Extending the small deformation constitutive models to their identical large deformation framework.
- Calibration and validation of the material parameters.
- Creating realistic complex micromechanical representative volume elements (RVEs) for different types of inclusions with in polymer composites systems.
- Investigating how the micro-structural and morphological changes can affect the total responses of these materials. Also, how they can enhance the mechanical properties of the composites. This may be accomplished by utilizing the viscoelastic, viscoplastic, and viscodamage models to investigate the following phenomena:
  - Strain localization and shear banding.
  - Initiation of damage at inclusion-matrix interfaces and boundaries.
  - Micro-damage propagation inside the matrix and around the constituent phases.
  - Energy dissipation through viscoelastic, viscoplastic, and viscodamage models.

The above mentioned objectives of the research are achieved by the following tasks.

1.3.1 Investigating Viscous Based Constitutive Models for Evaluating Time and Rate Dependency Behavior of Polymer-Based Composite Material

The most common linear viscoelastic models are convolutional integral constitutive model based on the Boltzmann superposition principle (Findley and Onaran, 1974). However, most polymers are known to exhibit non-linear viscoelastic (NVE) behavior (i.e. creep and relaxation modulus are stress and strain dependent,

respectively), especially at relatively higher stresses and/or temperature levels. This type of non-linearity can be modeled by using Schapery's single-integral NVE constitutive model (Schapery, 1969a). The NVE response of polymers and PCMs can be well-predicted by applying this model (see e.g. Christensen (1966); Schapery (1969a, 1974, 2000); Sadkin and Aboudi (1989); Haj-Ali and Muliana (2004); Muliana and Haj-Ali (2008)). Nevertheless, the Schapery model was written based on the small strain notion and since the deformation in polymer and polymer composite materials in many cases are not in the range of small deformation; hence, this model should be re-derived based on finite strain concept. This task has been accomplished and explained in Chapter 4.

In several constitutive models, the viscoplastic (unrecoverable) deformations are considered as non-linear functions of stress and time. For this purpose, Perzyna's theory (Perzyna, 1971) has been widely used for predicting the permanent deformation in polymers and polymer composites. Recently, viscoplastic constitutive models of polymers based on an overstress which has non-linear rate-dependent behaviors have been formulated (e.g. Krempl and Ho (1998); Colak (2005); Hall (2005)). Kim and Muliana (2009) employed a recursive iterative method to implement this viscoelastic–viscoplastic constitutive model. They showed that the coupling of the non-linear viscoelasticity model of Schapery and Perzyna's viscoplasticity model is reasonable for accurately predicting the nonlinear mechanical responses of polymers at different stresses. Therefore, a Perzyna-type viscoplasticity is hired and extended to large deformation framework to capture the plastic behavior of polymers. This task is discussed in Chapter 5.

After yield stress, polymer chains move (plastic flow) inside the material to find a proper stable position. During the flow procedure, polymers show a reduction in their capacity for carrying loads (strain softening). Then, after the chains are locked in the stable position, they can carry more loads (strain hardening). But, during both flowing (softening) and locking (hardening) procedures, because of expanding and opening of the molecular chains some of them and their pendent branches break and create micro/nano voids in the material (which causes these materials to experience micro-damages under various loading conditions). Also, the initial free local volume (FLV) in between the polymer chains are expanded, which increase the tiny voids. Thus, specific phenomena such as tertiary creep, post-peak softening behavior of the stress-strain response, and degradation in mechanical properties cannot be explained only by viscoelastic and viscoplastic constitutive models. Thus, to better represent the complex behavior of polymers and polymer composite materials, the combined effects of viscoelasticity, viscoplasticity and viscodamage (i.e. delayed or time-dependent damage) needs to be considered in the constitutive laws for these materials. Thus, a rate dependent damage model which was first proposed by Darabi et al. (2011) for HMA (hot mixed asphalt materials), is utilized. But, there is no need to change the viscodamage model in view of the fact that this model is not on the base of infinite strains. These models are extended based on large deformation approaches, and are implemented into the well-known commercial finite element code ABAQUS (2008) via the user material subroutine, UMAT.

1.3.2 Extending Small Strain Constitutive Models to Large Deformation Range

Constitutive relations for investigating the behavior of polymers need finite strain theory. Several models have been vastly studied; however, it is very difficult to evaluate a large strain constitutive model directly by just capturing some large deformation data sets. Actually, many elegant and practical elastoplastic models have been established and examined for different conditions and experimental tests. Therefore, one of the strategies for studying large deformation is extending the available small strain constitutive models to finite strain framework. The main core of such generalization is based on how to decompose the elastic and plastic portions of the total strain, in a way to be compatible, applicable, and identical to small deformation constitutive laws. For deriving the required relations, Lagrangian notion has been used instead of Eulerian, and all has been explained in detail in Chapter 3.

1.3.3 Calibration and Validation of Material Parameters

The full utility of proposed constitutive laws to finally model the macroscopic mechanical behavior of PMCs strongly depends on the accuracy of the input parameters. The main steps for the determination of material parameters associated with the presented constitutive models in Subsection 1.3.1 can be summarized as

- Procedure for determining the combined viscoelastic and viscoplastic model parameters in a systematic way, by using the creep-recovery test is thoroughly discussed in Chapter 5.
- Required procedure for finding the viscodamage parameter's model is also fully described in Chapter 5.

- Mechanical properties of nano-clay constituents are taken from the results determined by Sheng et al. (2004). The elastic modulus of CNTs are so scattered in open literatures, so the mechanical properties of CNTs are extracted based on the calculation of an equivalent-continuum modeling by Odegard et al. (2002).

Subsequently, these models will be used for predicting the viscoelastic, viscoplastic, and damage responses of PMMA-based nano-composites under different loading conditions.

1.3.4 Creating Realistic Micromechanical Representation for Different Types of Inclusions

There are some ways for creating micromechanical models such as: creating matrix and inclusions manually in a well-known commercial software like ABAQUS, ProE, Solidworks, and ANSYS. The other method is based on TEM or SEM images of a desired composite. Then the images should be analyzed, rendered, and purged to be processed by some CAD family software (Aviso, AutoCAD and 3d-Max) to be converted to geometrical objects. Thereafter, the geometry files have to be exported to the finite element software to mesh the entities. Both ways has some limitations. The first technique can be applied manually which is a very time consuming task and also the finite element family software usually are just able to create regular based shapes or parts (one can create complex geometry based on simple entities).

The second method, image based technique is also cumbersome, and it needs a 3D image scanner and many samples in different sizes with several types of particles and/or various weight fractions. It is obvious that creating so many samples and then converting them to numerical representation is a hardly possible task.

Therefore, to overcome this problem and also to be able to create different material systems automatically, decision was made to create software which is able to generate RVEs in both 2D and 3D, containing various types of particles and shapes. The software has been written by utilizing Borland C++ Builder compiler. This program is capable to generate and disperse different types of particles and inclusions for micro/nano composite materials.

The procedure for creating such models is that the program checks the available positions for the desired particles without intersecting other objects. Then, it automatically generates the required script files for AutoCAD to draw the geometry, and afterwards generates the related Python code to import the geometry from AutoCAD to ABAQUS. Subsequently, it applies all the necessary options and settings to the model in ABAQUS to create a complete finite element representation as a CAE file.

1.3.5 Effects of Inclusions Morphological Properties on Composites Responses

To investigate the effect of microstructural pattern the following question should be answered: How can the mixture of different inclusions enhance the mechanical properties of PCMs, through utilizing a unified viscoelastic, viscoplastic, and viscodamage constitutive model for the host material? Thus, in the micromechanical simulations, the following phenomena should be studied:

- Strain localization and shear banding.
- Initiation of damage at the inclusion-matrix interfaces.
- Energy dissipation through viscoelastic, viscoplastic, and viscodamage models.
- Micro-damage propagation inside the matrix and around the constituent phases.

1.3.5.1 Strain Localization and Shear Banding

In PMMA which is a glassy amorphous polymer, shear bands occur with no increase in volume while subjected to compressive loads. It means PMMA is governed by shear band phenomena rather than crazing in compression. Strain localized zones in a composite and their interaction with damage nucleation and propagation are considered and investigated.

1.3.5.2 Energy Dissipation Through Viscoelastic, Viscoplastic, and Viscodamage Constitutive Models

Since the inelastic work done by mechanical deformations dissipates energy which increases the temperature inside a material, this phenomenon can be considered especially when the material is subjected to high strain rate loadings. The change in temperature can be achieved by using the principle of maximum rate of energy dissipation (or the principle of maximum rate of entropy production). It states that the material dissipates energy in the easiest possible way (for more details see: Rajagopal (2000) and Abu Al-Rub and Darabi (2012)).Therefore, as presented recently by Khan (2011) and Darabi et al. (2012), a systematic thermodynamic framework for deriving the constitutive equations for the dissipative thermodynamic conjugate forces, in large deformation framework, are presented in Appendix E. In addition, the numerical implementation is done by adding subroutines in the well-known finite element software ABAQUS (2008) in the user materials subroutine UMAT.

1.3.5.3 Micro-Damage Propagation Inside Matrix and Around Constituent Phases

One of the main parts of this research is studying the effect of constituents on the pattern of micro-damage propagation inside different composites. In addition, evaluating and comparing the total damaged volumes for different types of inclusions are the key point for better understanding the damage initiation and growth. On the other hand calculating the dissipated energy due to micro-damaged regions, along with the amount of damage density inside the composites, for different inclusions and morphologies scenarios, gives a comprehensive point of view of the realistic behavior of polymer composites.

1.3.5.4 Initiation of Damage at Inclusion-Matrix Interfaces

The significant increase in the yield strength with decreasing particle size is observed in (Kiser et al., 1996; Lloyd, 1994; Rhee et al., 1994), and may be taken as a hint in this direction. The interfacial interaction between the matrix and particles may have a significant effect on the macroscopic yield response and ultimate strength of PMCs. In other words, it is expected that as the particle size decreases, the interfacial energy increases, and the effects of the boundary layer thickness (BLT) on composite strength is significant. If the BLT is comparable to other material length scales, one is able to consider an effective BLT at boundaries in continuum simulations (Gudmundson, 2004). But, if the BLT is negligible as compared to the length scales, then the associated energy to the boundaries can be used to simulate the effect of this layer. It should be noted that, the interface strengthening phenomenon can be characterized within strain gradient plasticity theory by incorporating an interfacial energy term in the internal work

that depends on the plastic strain state at the interface of the plastically deforming material (Abu Al-Rub, 2008; Abu Al-Rub and Voyiadjis, 2006b; Aifantis and Willis, 2005; Gudmundson, 2004). But studying such phenomenon is out of the scope of this work, and strain gradient plasticity theory is not studied. Here, just the initiation of continuum damage for different kinds of inclusions are investigated at the interface of inclusions and polymer matrix.

CHAPTER II

BACKGROUND AND LITERATURE REVIEW

2.1 Introduction

Composites made of thermoplastic polymers materials (as the matrix) along with nano particles and/or continuous fibers are attractive for mass production, because they combine several good features, such as the advantages of stiffness, strength and density, and are also beneficial from manufacturing and economics points of view. They have the potential for industrial and advanced engineering applications, including manufacturing of the components of the future light-weight armors, cars, and airplanes. However, these materials propose special challenges with regard to prediction of their physical properties, which arise from their evident time and rate dependency. The time and rate dependency of polymers lead to study of the viscoelasticity and viscoplasticity and damage of the matrix polymer, and its sensitivity to the thermal and mechanical history during processing.

The goal of this study is to approach the prediction of the finite deformation of thermoplastic matrix composites. The modeling is accomplished at the microscale level of analysis, which deals with a microscale representation of the constitutive models for PMMA polymer matrix containing different types of inclusions.

2.2 Factors Affecting Performance

There are several factors that can control the mechanical properties and responses of a composite, like strengthening and softening mechanisms. In composite materials,

hardening can be subdivided to direct and indirect strengthening. Beside this phenomenon, the softening mechanisms also have significant influences on mechanical performance and failure behavior of composite materials. The two most important localized deformation mechanisms in glassy thermoplastics (here: PMMA) are crazing and shear banding (Bucknall, 1977; Kinloch and Williams, 1980). These phenomena have been suggested to be the two dominant energy-dissipating mechanisms in polymers by several researchers (Bucknall, 1977; Bucknall and Partridge, 1983; Sultan and McGarry, 1973), but others have raised some doubts on these claim (Kinloch et al., 1983; Kunz-Douglass et al., 1980).

2.2.1 Strengthening and Softening Mechanisms

Some of the possible strengthening mechanisms for general composites and also polymer composites are proposed as: matrix strengthening, particle strengthening, and microstructure strengthening. When a discontinuous particle-based composite is subjected to tensile loading, the load is transferred from the surrounding matrix to the particles mainly through interfacial shear stress (Sheng et al., 2004). In other words, direct strengthening in composite materials comes from the load transferring from a softer material (host material which here is PMMA polymer) to the harder phase(s), like: nano-ceramics, nano-clays, and nano-metallic particles, or carbon nano tubes or fibers. This event is the main source of partitioning the stress and strain between different phases during deformation. Likewise, strengthening behavior of composite materials depends on the inclusions' morphologies and volume fractions. Another reason for hardening is indirect strengthening, which results from the matrix molecular structure

(e.g., heavier molecular chains, entanglement and re-orientation of chains, semi-crystallized regions). Moreover, plastic hardening can be assigned to the heterogeneous plastic deformations that are due to the plastic strain incompatibility at the interfaces of matrix and inclusions. For a polymer matrix, there are several other possible toughening mechanisms that have been proposed by several researchers:

- Crack-tip blunting mechanism (Kinloch and Williams, 1980).
- Particle deformation and crack bridging (Kunz-Douglass et al., 1980).
- Cavitation-induced shear deformation or stress-relief (Donald and Kramer, 1982).
- Crack pinning (which is a mechanism stop the progress of advancing cracks in composites proposed by Lange (1970)) (Zaiser et al., 2009).

In addition, the softening mechanisms affecting the composite materials responses can be listed as follows

- Strain localization and shear banding.
- Debonding at inclusion-matrix interfaces.
- Micro-damage in the host material (matrix).
- Adiabatic heating due to inelastic energy conversion into heat.

2.2.3 Effects of Crazing

Crazing is a phenomenon that frequently precedes fracture in some glassy thermo plastic polymers. Crazing occurs in regions of high hydrostatic tension, or in regions of highly localized yielding, which leads to the formation of interpenetrating micro-voids and small fibrils. If an applied tensile load is sufficient, these bridges elongate and break, causing the micro-voids to grow and coalesce. As micro-voids combine, cracks begin to

form and evolve. A craze is different from a crack in a way that it can continue to carry load. Furthermore, the process of craze growth prior to cracking absorbs fracture energy and effectively increases the fracture toughness of a polymer. The initial energy absorption per area in a craze region has been found to be up to several hundred times that of the un-crazed region, but quickly decreases and levels off. Crazes form at highly stressed regions associated with scratches, flaws, stress concentrations and molecular chains in-homogeneities. Crazes generally propagate perpendicular to the applied tension. Crazing occurs mostly in amorphous, brittle polymers like PS, PMMA, and PC; and it is typified by a whitening of the crazed region. One of the main differences between crazing and shear banding is that crazing occurs with an increase in volume, while shear banding does not. This means that under compression, many of these brittle, amorphous polymers will demonstrate shear banding rather than crazing, as there is a contraction of volume instead of an increase. In addition, when crazing occurs, one will typically not observe "necking" or concentration of force upon one spot in a material. Rather, crazing will occur homogeneously throughout the material.

2.2.4 Effects of Damage

Experimental observations show the main mechanisms on fracture of composite materials are attributed to the presence of micro/nano inclusions along with the localized plasticity and damage defects (Fig. 2.1). They lead to non-uniform behavior in composites such that additional load causes failure mechanism occurring near the localized zones. Nano-clay composites have shown directional crack patterns that bypass the clay

agglomerates, and the cracks take tortuous paths between the regions of high clay concentration due to toughening mechanisms such as crack tip pinning and bifurcation

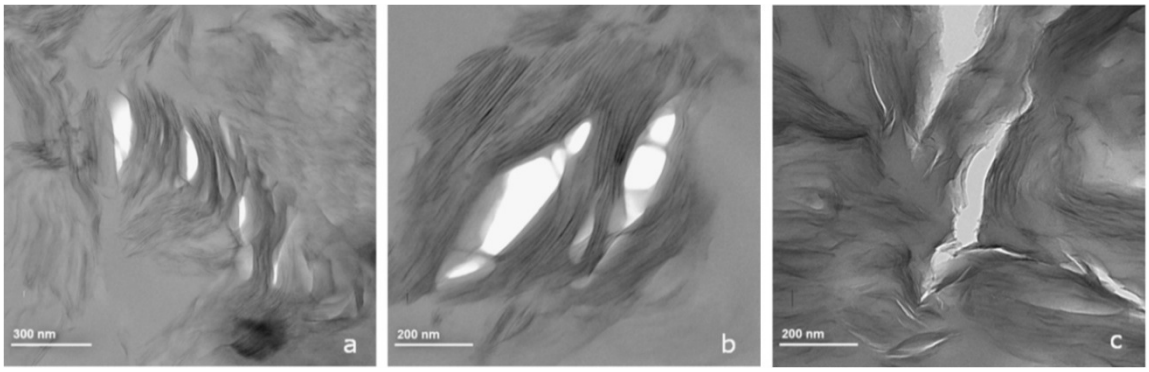

Fig. 2.1. Transmission electron micrographs showing: (a) and (b) micro-voids in clay galleries; and (c) micro-voids ahead of a major crack tip (Khan et al., 2011).

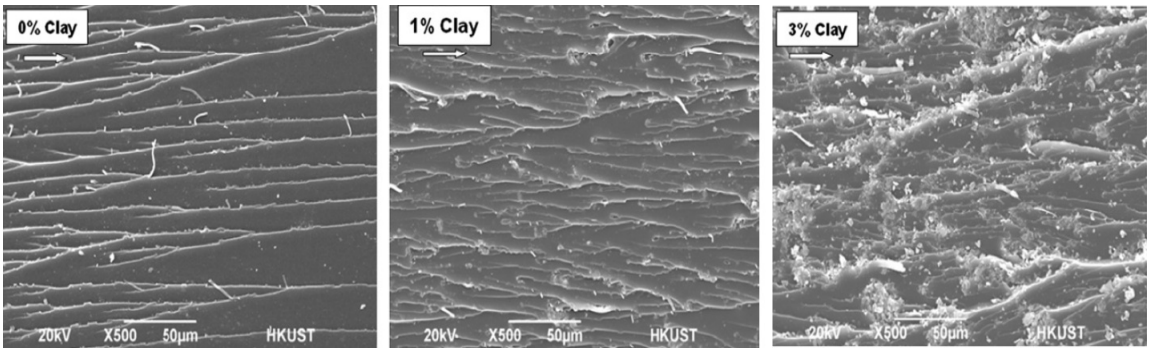

Fig. 2.2. SEM images of compact tension fracture surfaces of clay–epoxy nano-composites. Increasing clay contents shows crack initiation (Khan et al., 2011).

To illustrate the effect of clay particles on the perturbation of fracture surfaces; Fig. 2.2 shows that the neat resin exhibited a typically smooth surface with a homogenous material flow. Upon addition of clay, the fracture surfaces become rough. It can be seen that the higher the clay contents, the rougher the fracture surfaces. Moreover, nucleation of micro-voids and -cracks due to de-cohesion of embedded particles or inclusions from

the host material is another reason for fracture. Also, hard phase fracture along with the growth and coalescence of developing voids and cracks and their neighbors under favorable stress directions with the help of plastic strain and hydrostatic-stress; ultimately lead to the complete loss of macroscopic load bearing capacity of specimen. Thus, the interfaces between different phases play an important role in the total strength and fracture toughness of LDCM (Bandstra et al., 2004; Dierickx et al., 1997; Lee et al., 2005; Yuan and Misra, 2006). For this purpose, see Fig. 2.3.

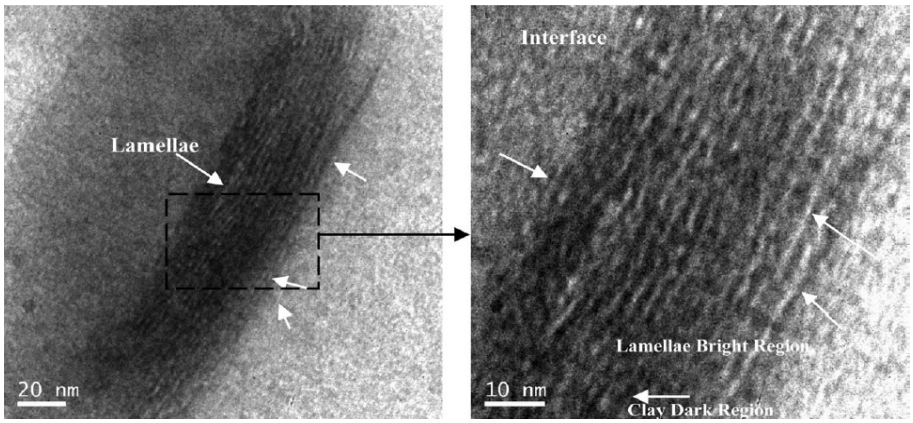

Fig. 2.3. TEM of PP, 4wt% nanoclay composites showing uniform distribution of clay and the interface between PP and clay. Black regions are clay and white regions are crystalline lamellae (Yuan and Misra, 2006).

In addition, the shear instability can be delayed by increasing the interfacial strength of the particle-matrix, which can postpone the debonding phenomenon, then micro-voids nucleation, and consequently micro-cracks propagation; hence, increasing the interfacial strength improves the total performance under various loading conditions.

Based on these mechanisms, two main approaches that are identified as micromechanical damage models and phenomenological damage models have been

proposed to model the non-linear material degradation behavior due to damage. The phenomenological model stem from the concept of Kachanov (1958) who was a pioneer in continuum damage mechanics. Different forms of his approach have been applied for modeling the damage behavior of different materials (Bažant and Oh, 1983; Carol et al., 1994; Murakami and Kamiya, 1997). The former model shows strong coupling between plasticity and damage as one smooth generalized yield surface that has been defined and an associated flow rule for both plasticity and damage will be utilized. However, Abu Al-Rub and Voyiadjis (2003) showed this model has some limitations.

2.3 Large Deformation Generalization

The elastoplastic or viscoelastic-viscoplastic constitutive relations for large deformation need finite strain theory. Such models have been vastly studied and also very significant results have been obtained (Cuitino and Ortiz, 1992; Green and Naghdi, 1971; Hasan and Boyce, 1995; Kröner, 1960; Lubliner, 1986; Rajagopal and Srinivasa, 1998; Simo and Ortiz, 1985; Weber and Anand, 1990). However, it is very difficult to evaluate a large strain constitutive model directly by only capturing some large deformation data sets. Actually, many elegant and practical elastoplastic models have been established and examined for different conditions and experimental tests. Nevertheless, the existing sophisticated and complex elastoplastic or viscoelastic-viscoplastic constitutive laws for small strain conditions for materials such as: concrete and geotextiles (which are pressure-sensitive dilatant), asphaltic material (Darabi et al., 2011), and polymer and polymer composites (Kim and Muliana, 2009), have been developed based on additive decomposition of strain (or strain rate) to elastic and plastic

parts. Furthermore, it would be difficult to convert them to a multiplicative decomposition based model. Besides, it is shown that an additively separation procedure, especially for Green-Lagrange strain measure tensor is possible, but some other considerations should be applied (Bažant, 1996). Bažant also proposed a transformation of Green-Lagrange finite strain tensor whose parameters almost show that the degrees of freedom can equivalently replace the small strain measure to other strain measures. He showed if the dependency of higher order terms of deviatoric strain tensor on the volumetric strain is taken into account, the strain tensor will be allowed to additively decomposed. However, here it is derived and shown that there exist several other items that should be applied to convert a small-strain based model to a finite strain one.

Moreover, the calculations for large deformation problems are noticeably more complex than for small strain problems. Therefore, another possible strategy could be generalizing the existing constitutive laws that have been developed based on the infinite deformation concept to finite strain. This task can be accomplished by introducing some material parameters and/or applying some modifications to the models to provide the capability for capturing large deformation behavior. The first option has some disadvantages, since additional material parameters for generalizing a small-strain to large-strain model needs to be calibrated by some large deformation experimental tests (and also accepting the non-uniformity of the strain field).

In the established well-known theorem for studying infinite deformation, the structure of elastoplasticity response of materials is conventionally built on introducing elastic and plastic strains and their rates. In this case, it is assumed that the infinitesimal strain may be additively separated to reversible (elastic) and irreversible (plastic)

components. By the advantage of incremental manner of elastoplastic behavior, the following rate form has been extensively introduced and reported (see: Bruhns (2009))

$$\dot{\varepsilon} = \dot{\varepsilon}^{\mathrm{e}} + \dot{\varepsilon}^{\mathrm{p}} \tag{2.1}$$

in which, ε is the total strain in a body, ε^{e} and ε^{p} are the elastic and plastic portions of strain tensors, respectively. For large elastoplastic deformations, the total deformation rate for characterizing the flow-like behavior of a material is the rate of deformation or stretching tensor, D, which is the symmetric part of the velocity gradient tensor (Lubliner, 1990). Then, a direct extension of the separation in Eq. (2.1) is

$$D = D^{\mathrm{e}} + D^{\mathrm{p}} \tag{2.2}$$

where, D^{e} and D^{p} are the elastic and plastic stretching tensors, respectively. For the case of finite deformation, there generally exist different approachs for appropriately decomposing and deriving formulas for such constitutive laws (Naghdi, 1990; Xiao et al., 2006). As a result of this discussion, Bruhns (2009) categorized three different ways for describing a physically reasonable decomposition of finite elastoplasticity behavior, which are concisely explained in the following:

1) The classical set of additively partitioning of the rate of deformation tensor, D, for describing finite deformation [see Eq. (2.2)].
2) The multiplicative separation of the deformation gradient to elastic and plastic components, which is commonly used in most descriptions of finite inelastic deformations (Rajagopal and Srinivasa, 1998)

$$F = F^{\mathrm{e}} F^{\mathrm{p}} \tag{2.3}$$

where F is the total deformation gradient of a distorted domain, F^{e} and F^{p} are the elastic and plastic deformation gradient, correspondingly.

3) Based on the Lagrangian description, plastic strain E^{p} is introduced as an ascent primitive variable (Green and Naghdi, 1965), and the Lagrangian strain is additively split-up to elastic and plastic parts, as

$$E = E^{e} + E^{p} \tag{2.4}$$

Here, similar to the previous equations, E is the total Green-Lagrange strain in a body, E^{e} and E^{p} are the elastic and plastic portions of the Lagrangian strain tensors, respectively. For utilizing each one of the above approaches, there are some issues for decomposing the elastic and plastic portions of the response of material:

1) In simulations of simple shear problems fictitious fluctuations were observed for some of the rates (Bruhns et al., 2001), and as a consequence of these deficiencies, the decomposition is believed not to be satisfactory describe finite elastoplasticity.
2) It is shown that multiplicatively separating the deformation gradient tensor, along with the logarithmic rate and the Hencky strain is able to consistently combine both settings (Hibbitt et al., 2008). But unfortunately, the logarithmic strain is fundamentally complex in converting its work-conjugate stress tensor to either the second Piola-Kirchhoff (II-PK) or Cauchy stresses.
3) In the third approach, nonetheless E^{e} is the elastic portion of strain, it is accurate only in the case of infinitesimal elastic deformation. It means such separation is acceptable when the elastic fraction of deformation is in small range. Thus, the part that here is so-called elastic component is introduced by the difference of E and E^{p}.

Here, the reasons why Eulerian concept has not been selected for generalizing small to large deformation are explained. The Eulerian formulation problems of finite elastoplasticy are concerned with different objective rates that appear in different constitutive laws, and their dependency should be investigated, or such rates must be presented in a uniform method. On the other hand, because the Green-Lagrange strain is invariant in rotation; hence, it is proper to be hired for discretized (incremental) numerical analysis (Rolph, 1983). In Lagrangian type models, the material time derivative can be applied directly to the consistency condition, $\dot{f} = 0$, (f is the yield surface) for the elastoplastic models, and the derivative via chain rule can also be applied to the tensors and tensor products that exist in this function. But, for the Eulerian relations this derivation cannot be directly applied, since integration and derivation on an unknown volume (current configuration) is not applicable (Bathe et al., 1975).

Another similar question arises: "What should be done with Eulerian quantities? Which objective time derivative should be taken, and what would be the criterion to answer this question?" (Bruhns, 2009). Also, Simo and Hughes (1998) noted that in the Eulerian formulations framework, the objectivity principle implies that each constitutive relation is isotropic (i.e. the constitutive functions are invariant under orthogonal groups of rotations). Therefore, the constitutive models based on Eulerian formulation concept may be applicable only to isotropic materials, and if there is any sort of anisotropy like orthotropy or transverse isotropy, their functionality cannot be guaranteed.

The other reason for selecting Lagrangian rather than Eulerian concept is that the Lagrangian strain measure and its work-conjugate stress pair (second Piola-Kirchhoff

stress) are frame indifferent, and the response does not change by observer. But, if any stress or strain in the current configuration is chosen, then the constitutive models should be derived along with stress and strain rates. For the sake of conciseness of this chapter it is not proved here, but the reader is referred to Johnson and Bammann (1984) for more details. Also, several researchers have shown that finite strain problems with constitutive models written in rate forms can lead to apparently unrealistic results (Cassenti and Annigeri, 1989). For example, Johnson and Bammann (1984) proved for simple shear problems in large strain range that oscillations in the shear stress is observable if kinematic hardening is used but will not occur if isotropic hardening is assumed. They showed these fluctuations are caused mainly by the use of the Jaumann rate of stress.

An important key role to formulate the internal energy of deformable bodies is the energy conjugacy between stress and strain tensors. In some standard commercial finite element software such as ANSYS and ABAQUS, the incremental finite strain formulation that is not fully work-conjugate to the stress is being used (Ji et al., 2010). This means that the energy produced by stress increments on its strain increments pair does not provide the second-order accuracy for expressing the work-done in a body. In these softwares, specifically the stress increments are based on the Jaumann rate of Kirchhoff stress that is energy-conjugate with the increments of the natural (Hencky or logarithmic) strain tensor (note that the Kirchhoff stress itself is energy-conjugate with the rate of deformation tensor). However, in these finite element programs the stress increments correspond to the increments of Green-Lagrange strain tensor. Although this problem was emphasized (Bažant, 1971), demonstration of its significance in realistic

conditions has been lacking. Wooseok et al. (2010a) showed in buckling of a highly orthotropic columns and also sandwich columns in compression, which are very soft in shear, utilizing non-conjugate stress and strain measures can cause large error ($\approx 100\%$) of the critical load, even though the strains were in small range. Also, employing Eulerian strain needs a proper definition for stress measure which should be work-conjugate to it. As discussed by Norris (2008), finding a proper work conjugate stress for Eulerian strain needs unique co-rotational form. Besides, using non-conjugate stress and strain tensors may be admissible for some materials. But, the elastic parts of strains as well as the total volumetric strains must be in the small range. Thus, the algorithm used should guarantee that the energy dissipation by large inelastic strains is nonnegative (Bažant et al., 2000). Using work conjugate strain and stress tensors is appropriate because the strain will be holonomic (path-dependent), and strain components can be characterized as meaningful deformation measures (Ji et al., 2010). Under these conditions, Lagrangian based models appear to be more reasonable and practical.

It should be noted that employing these stress and strain measures has an important advantage, because constitutive models in large deformation range should take into account the objectivity concept. While deriving the constitutive laws for investigating large deformation, the rate of stress should be defined to be frame-indifferent. Thus, different corotational rates have been defined (Johnson and Bammann, 1984; Nagtegaal and De Jong, 1982) to guarantee that the quantity of stress is independent of the observer. However, each of the corotational rates is proper for certain types of materials and one cannot pick them arbitrarily. Moreover, using the corotational

rates result in some computational issues such as the Jaumann rate creates peculiar oscillations in shear stress response, and the Green-Naghdi and other rates have been reported to result in residual stress (Meyers et al., 2003; Zhou and Tamma, 2003). One way to handle this issue is hiring the stresses and strains that are defined in the natural state (material configuration), because such stress and strain fields are quantified in the same way by different observers. Henceforth, to ensure the objectivity of the material response, the constitutive laws can be expressed in terms of the II-PK stress and its energy conjugate strain pair (Green-Lagrange strain). This is one advantage of using Lagrangian framework.

2.4 Large Deformation Viscoelastic Model

Polymers have shown a wide range of interesting and desirable properties. The remarkable mechanical properties of polymers and polymer composites are due to the arrangement and inter-linking of their chains (Painter and Coleman, 1997). As the use of polymeric materials increases, a comprehensive understanding of these materials becomes necessary to perform better economical designs. Extensive attempts have been devoted to develop mathematical relations for the small deformation regime (Christensen, 2003). The presented models for finite strain viscoelasticity all rely on assumptions that have been debatable (Boyce et al., 1988; Ehlers and Markert, 2003; Haupt et al., 2000; Makradi et al., 2005; Mott et al., 1993; Reese, 2003). From a continuum point of view, much less emphasis has been made for multiaxial finite deformation subjected to a wide range of strain rates and temperature (Khan et al., 2006). Ogden (1997) noted that the polymers have displayed very complicated

properties rather than elastic and viscous behavior, and moreover continuum mechanics method does not consider the molecular nature of polymers and simply treats them in terms of elasticity rules for solid parts, and as fluid for viscous features. With the purpose of making qualitative predictions for the behavior of a body through using a constitutive model, the description of stress as a function of deformation history or vice versa, should be considered in a way that is convenient for both mathematical and experimental aspects.

The theory of classical linear viscoelasticity modeling has been primerily presented in two main systems: differential forms and hereditary integrals. Both can be derived and formulated to take hereditary effects into account from irreversible thermodynamics starting point. Lockett (1972) stated that the hereditary integrals are more general in comparison to the other approach, even though the differential forms have some advantages as

1) Utilizing the stress/strain or stress/strain rates parameters is more appealing than the creep and relaxation kernel functions.
2) The parameters in differential forms can be related directly to the spring and dashpots in the rheological model.

On the other hand, the reports by Rooijackers (1988) and Morman (1985) indicate that the integral models are preferred, because the most differential models are difficult to apply. In the literature, different types of integral models are identified. It is possible to develop Multiple Integral Models (MIM) from functional theories, and usually these derivations are based on thermodynamics in systematic methods. Nonetheless, these

models are generally too complex to be practical, because determination of the large amount of material parameters in such models is not reasonable in practice, and furthermore, the numerical calculations are too expensive for practical applications.

Several non-linear theories for viscoelastic materials have been developed, and most of them have similar structures. In these models as a whole, the same as in linear cases, the stress field depends on the strain history or conversely. Some of these models are established based on physical concepts and some are prepared and purely built on just capturing experimental data. These developed models can be categorized in three main groups (Khan et al., 2006), as the differential relations, single integrals, and MIM. The main disadvantage of MIM is that the polynomial expression can be continued to higher orders and leads to many material parameters, and determination of such functions is practically impossible. For instance, in the MIM proposed by Green and Rivlin (1957) the behavior was assumed to be isotropic, which forces some complexity to the model in that level. Also, the material functions in the MIM technique depend on many integrand variables. Although MIM offers a realistic non-linear viscoelastic model because each function and parameter has a physical meaning, for determining these variables in these models unreasonable number of experimental data is required.

A number of single integral models for viscoelasticity can be found, and most of them are only capable for describing linear viscoelasticity. Such models are generally developed based on empirical or semi-empirical considerations (Caruthers et al., 2004; Lockett, 1972; Morman, 1985). Coleman and Noll (1961) derived one model using a single integral constitutive equation to characterize the behavior of isotropic non-linear

incompressible solid, which is based on a the theory of linear viscoelasticity in large strain range through the concept of fading memory. O'Dowd and Knauss (1995) also proposed a single integral model in which the stress is II-PK and Boit is the strain measure. In this model, the non-linear behavior is considered in the model by a function depending on the three invariants of the Boit strain tensor. The model is easy to implement, but the relaxation function has more variables comparing to other single integral models.

Pipkins and Rogers (1968) constructed a model based on an assumed non-linear behavior of a material to a series of step strain inputs. The proposed integral series formulation was derived for detecting the non-linear response of an arbitrary stress or strain history. In their method, each term has a definite intrinsic meaning that is independent of the choice of strain measure. Also, the first term in their equation is a single integral with a non-linear integrand that can be determined by a single step creep or relaxation test. Moreover, Pipkins and Rogers (1968) showed that the experiments in most cases agree with the single integral approximation, which is given by just the first integral term alone. To generalize their model to a finite strain range, they proposed to replace the Cauchy stress, σ, with its Kirchhoff transformed quantity as $F^{-1}\sigma F^{-T}$ (the same as the II-PK stress measure without considering the effect of volume change mapping scalar, J), and also exchanging the small strain, ε, with the right Cauchy-Green tensor ($C = F^{T}F$). Moreover, the initial strain conditions from $\varepsilon = 0$ should be changed by $C = I$. One of the advantages of Pipkins and Rogers constitutive equation is that it involves fewer relaxation functions, and has the following general form

$$\sigma_{ij}^{t} = -\rho\delta_{ij} + F_{ik}^{t}\left[R_{kl}\left(C^{t};0\right) + \int_{0}^{t} \frac{\mathrm{d}R_{kl}\left(C^{\tau};t-\tau\right)}{\mathrm{d}\tau}\mathrm{d}\tau \right] F_{jl}^{t} \tag{2.5}$$

where ρ is an unknown scalar, F is the deformation gradient tensor, and $R\left(C;t\right)$ is the strain dependent relaxation function brought by a single step strain input (Wineman, 1972). In addition, Pipkins and Rogers (1968) stated the role of stress and strain can be interchanged to obtain the creep response instead of stress-relaxation. Also, it was noted that the choice of the strain tensor can be fairly arbitrary with any other permissible strain measure. However, the strain and stress measures must be work conjugate to make the model stable and prevent of any undesired fluctuations and errors in the results.

Furthermore, Schapery (1964, 1966) presented a single integral model based on Gibbs energy for non-linear viscoelastic materials, that has been widely used. From the literature, it can be understood that the model performs reasonably well for many material cases, and especially polymers. This model is able to take into account the anisotropy and internal dissipation (Rooijackers, 1988).

It is evident that the macroscopic response of a system (body) depends on a wide number of quantities that each relate to an individual phenomenon. In addition, all systems interact with their surroundings that cause inevitable fluctuations of those quantities. If only the internal energy (from all the quantities) is allowed to fluctuate, and the other ones are kept constant, then the temperature of the system is meaningful and measurable. Afterwards, the system's properties can be described appropriately using the Helmholtz free energy as the thermodynamic potential (when the volume of the system is constant). In the other case, if both the internal energy and the macroscopic volume of

the system fluctuate; the Gibbs energy will be used, in which the system's properties are determined by temperature and pressure.

2.5 Unified Viscoelastic, Viscoplastic and Viscodamage Model

Numerous experimental observations and studies have shown that the responses of both pure polymers and polymer composites are in the class of materials with time-, temperature-, rate-, and pressure-dependency that exhibit both recoverable (viscoelastic) and irrecoverable (viscoplastic) deformations, even under relatively low stress levels. As the stress increases, the dependent responses become more pronounced (Kim and Muliana, 2009). For example, creep tests on high-density polyethylene (HDPE) (Lai and Bakker, 1995), polycarbonate (Frank and Brockman, 2001), and aramid and polyester fibers (Chailleux and Davies, 2003, 2005) show a combination of both viscoelastic and viscoplastic responses even at the room temperature and for short loading times. It has been observed in many types of polymers (Crissman and Zapas, 1985; Lai and Bakker, 1995; Zapas and Crissman, 1984) and polymer composites (Megnis and Varna, 2003; Pasricha et al., 1995; Ségard et al., 2002; Tuttle and Brinson, 1986) that creep strains are not entirely recovered even after sufficiently long recovery periods. These permanent strains are attributed to the changes in polymers mulecular structure during deformation, plastic flow localization, expanding and opening of the molecular chains (rearrangement of polymer chains), that all cause micro-cracks and micro-voids in pure polymers. For polymer composites, particle-matrix debonding and also interactions between particles and matrix during the loading time (when the applied loads transfer to inclusions) have been observed as the source of permanent deformation (Bocchieri, 2001; Megnis and

Varna, 2003). Thus, to better represent the complex behavior of polymers and polymer composite materials (PCMs), the combined effects of viscoelasticity, viscoplasticity, and viscodamage (i.e. delay or time-dependent damage) have to be included in the constitutive modeling of these materials. Therefore, viscoelastic, viscoplastic, and continuum damage mechanics models are generally the most successful for this goal.

At relatively low stress levels, creep in polymeric materials can be generally described using linear viscoelastic models. The most common linear viscoelastic models are the integral-based models that are built on the Boltzmann superposition principle (Findley and Onaran, 1974). But, most polymers are known to exhibit non-linear viscoelastic behavior (i.e. creep and relaxation moduli are stress and strain dependent, respectively), especially at relatively higher stresses and/or temperature levels. This type of non-linearity can be modeled by using Schapery's non-linear single integral viscoelastic constitutive model (Schapery, 1969b). Although finding proper values or functions for its non-linear parameters for this model in some cases may be difficult, the non-linear viscoelastic response of polymers and PCMs can be well-predicted by applying Schapery-type non-linear viscoelastic models (Christensen (1966); Schapery (1969b, 1974, 2000); Sadkin and Aboudi (1989); Haj-Ali and Muliana (2004).

In several constitutive models, the viscoplastic (unrecoverable) deformations are considered as non-linear functions of stress and time. For this purpose, Perzyna theory (Perzyna, 1971) has been widely used for predicting the permanent deformations in polymers and polymer composites. Chailleux and Davies (2003, 2005) have shown that Perzyna's viscoplastic model is able to explain the viscoplastic responses of aramid and

polyester fibers. Recently, viscoplastic constitutive models of polymers based on an overstress that has non-linear rate-dependent behaviors have been formulated (Colak, 2005; Hall, 2005; Krempl and Ho, 1998). Some reviews on currently developed constitutive viscoplastic models for polymers can be found in Colak (2005).

In addition, a non-linear viscoelastic and viscoplastic constitutive model derived from thermodynamics framework was proposed by Schapery (1997), and was employed and modified by Kim and Muliana (2009) through applying a recursive iterative method to implement this viscoelastic-viscoplastic constitutive model. They showed that the coupling of the non-linear viscoelastic model of Schapery and Perzyna's viscoplasticity model is reasonable for accurately predicting the non-linear mechanical response of polymers at different stress and temperature levels. However, the changes in materials microstructure during deformation (such as expanding, opening, and breaking of the molecular chains of polymers) cause these materials to experience a significant amount of micro-damage (micro-cracks and micro-voids) under various loading conditions, where specific phenomena such as tertiary creep, post-peak softening behavior of the stress-strain response, and degradation in mechanical properties cannot be explained only by viscoelastic and viscoplastic constitutive models. Also, the effect of loading history on polymers is the outcome of the evolution of the microstructure state of material which has been experimentally revealed to depend on: (1) Internal energy (Hasan and Boyce, 1993; Oleynik et al., 1990), (2) Free local volume (Hasan and Boyce, 1995), and (3) Bi-refringence (Arruda and Boyce, 1993).

While exploring the polymers behavior, because the deformation is in the range of large strain, the associated volume changes are also no longer small; thus, taking in to

account the FLVs have a pronounce effect on the material response (O'Dowd and Knauss, 1995). For incorporating the effect of the free volumes, O'Dowd and Knauss introduced this phenomenon as a function to modify the time of relaxation. They also showed that there is almost no recovery of strain when the material is unloaded to zero stress state, which is mostly induced by the changes in the free volume. The other reason for considering the effect of FLVs is tha, in reality the yielding phenomenon in polymers occurs as the result of highly inhomogeneous deformations. Therefore, the effects of free volume have a key role in addressing the time dependent description of polymers.

Hasan and Boyce (1995) phenomenologically illustrated the mechanisms and effects of the free volumes on amorphous polymer behavior. Briefly, they considered an initial configuration with no transformation strain energy, such that polymer in this state has a number of sites with possible meaningful transformation. During the initial stages of deformation (at low stress levels) only the regions containing high FLV can transform loads at meaningful rates, and the related transformation strain energy is stored elastically in the relatively rigid surroundings (lower FLV). By increasing the stress, the regions with lower FLV will be appropriate and reachable for carrying load, and the response becomes highly non-linear. Now, further energy is stored in the material by the creation of new defects (more free volume sites). The creation of these new soft sites reduces the macroscopic capacity for carrying loads. Throughout such strain softening, the material state shows the evolution of a steady state flow condition that is the outcome of numerous FLV sites that leads to continuous flowing. In their model, they assumed the changes of the free volume are a function of pressure, time, and temperature.

In order to incorporate the effects of the FLVs, in another approach, Anand and coworkers introduced a scalar parameter as the internal state variable, φ, into the Helmholtz free energy to characterize the FLV (Anand and Ames, 2006; Anand and Gurtin, 2003). This variable enables the model to capture the highly non-linear stress-strain behavior that leads the yield-peak and gives rise to post-yield strain softening (since the local free-volumes associate with certain meta-stable states) (Gearing and Anand, 2004).

To date, less emphasis has been placed on predicting the damage evolution in polymers. Schapery (1975) developed a damaged-viscoelastic-viscoplastic model according to the laws of thermodynamics. His model is based on these concepts: (i) the elastic-viscoelastic correspondence principle to model the linear viscoelastic behavior of the material; (ii) the continuum damage mechanics for modeling damage evolution; and (iii) the principle of time-temperature superposition for including time, rate, and temperature effects. Items one and two are characterized through the pseudo strain concept. But, Schapery's viscoelastic-viscoplastic-damage model has some limitations, as it can be used only for predicting viscoplasticity and damage evolution in tensile stresses. In addition, it behaves as a linear viscoelastic model, without considering the temperature and stress levels, for the small strain range.

Seidel et al. (2005) introduced a model for predicting the evolution of damage in viscoelastic particle-reinforced composites in which the damage parameters correspond to the time-varying area fraction of the growing voids with respect to the cross-sectional area of the representative volume, which was seen as an improvement to Yoon and

Allen's model (1999). This model is developed for cohesive zones, without considering the viscoplastic response. Also, Zhang and Ellyin (2004) took into account the damage evolution for investigating the non-linear viscoelastic behavior of fiber-reinforced polymer laminates, but this model did not consider the effects of viscoplastic behavior. Moreover, this damage evolution law acts upon smeared cracking, and it does not have the capability to distinguish between time, rate, and temperature dependent behaviors.

The main goal and focus of this work is to introduce a viscodamage model and to couple it to the non-linear viscoelastic and viscoplastic constitutive models for predicting the highly non-linear response of polymers in the softening region after post peak yield. Surprisingly although there are several damage models for polymers, to the author's best knowledge, few studies have been focused on coupling of non-linear-viscoelasticity, viscoplasticity, and viscodamage to predict the thermo-mechanical behavior of polymers and PCMs. It is notable that there are only a few coupled viscoelastic, viscoplastic, and rate dependent damage models that can be used to predict the mechanical responses of polymers and PCMs at different temperatures, stress levels, and strain rates.

One of the challenges in the modeling of polymers and PCMs is that the damage nucleation and growth depend on rate of loading, temperature, and the history of deformation. Therefore, a combination of non-linear thermo-viscoelasticity, thermo-viscoplasticity effects, and a rate- and temperature-dependent damage model (thermo-viscodamage) seems unavoidable. The terms "thermo" and "visco" are used in here to respectively address the temperature- and time- and rate-dependent behavior of polymers. Thereby, as mentioned above, this study attempts to bridge the gap and propose a general, single, accurate, reliable, and practical constitutive model to

overcome the limitations of the current models for predicting the macroscopic behavior and evolution of damage in polymers. The damage model which was first proposed by Darabi et al. (2011) for HMA (Hot mixed asphalt) materials is utilized in this work.

2.6 Representative Volume Element for Microstructure

One of the main objectives of the mechanics of heterogeneous materials is to gain their effective properties from the knowledge of the constitutive models and spatial distribution of their components (Kanit et al., 2003). For the purpose of solving this issue, several homogenization methods have been established. These research studies have reached a high level of complexity and efficiency (Kanit et al., 2003), especially in linear elasticity and thermal conductivity. These techniques can be found in literature (e.g. Sanchez-Palencia and Zaoui (1987), Nemat-Nasser et al. (1993)). Besson et al. (2001) and Jeulin and Ostoja-Starzewski (2002) have also extended the methods for some certain nonlinear properties. Severe limitations for the macroscopic linear properties of composites exist, such as those noted by Kanit et al. (2003):

- In some works, the well-known Voigt and Reuss bounds is hired. These models take into account only the volume fraction of the constituents.
- Incorporating the notion of isotropic distribution of phases has been considered by Hashin and Shtrikman (1963).
- In the case of random particles in a media, the third order bounds were achieved in a general case by Beran (1965). Later, the case of two-phase materials was probed by Miller (1969) and Milton (1982).

- The incorporation of more statistical information on the heterogeneous distribution (random) of inclusions in a host material leads to a hierarchy of bounds, as suggested by the systematic theory of Kröner (1980), and also in Torquato and Stell (1982), Torquato and Lado (1986) and Torquato (1991).

Several remarkable methods for predicting the constitutive behavior of the FRCs (fiber reinforced composites) have been introduced. Among them, the analytical homogenization approach based on the Eshelby's strain concentration tensor (Eshelby, 1957) (in which the fibers are considered as a second phase inclusion) is greatly supported and widely used. Besides, significant success has been achieved by employing some techniques based on the Mori-Tanaka's mean field method (Mori and Tanaka, 1973; Pan et al., 2008). These methods are developed and employed to determine the material properties for unidirectional composites as a function of fiber volume fraction and aspect ratio. These methods have limitations and fail for studying FRCs with different aspect ratios and/or curvy-linear shape (waviness) of fibers. It should be noted that some of the restrictions are optimal in the sense that a definite microstructures could be designed and give the exact value of the bound as the effective property of the composite.

Due to the computational efficiency of homogenization techniques, they can be employed in zooming-window analyses for statistically evaluating the sample size effects on the simulated response of the materials; nevertheless, these methods do not yield any information for stress–strain response on the micromechanical level (Pan et al., 2008). Actually, predicting the complicated behavior of composite materials that contain inclusions with complex geometries and distributions by utilizing the homogenization

methods is almost impossible. However, investigating and modeling of their thermo-mechanical and fracture properties are still fields of current research.

These analytical models are limited for predicting the effective response of even simple composites let alone when complex microstructural geometries are required to be studied. The micromechanical models based on representative volume element (RVE) have been widely used to predict the effective inelastic and non-linear characteristics of composites with complex geometry of microstructures. For a microstructure containing several properties, the bounds are too much to give a useful approximation of the effective properties. On the other hand, estimations like self-consistent models can give a practical sensible prediction, but are aproperiate for a very specific morphology of constituents (Kanit et al., 2003). These reasons lead to numerical methods such that the next available approach is enabled through using the powerful computers and advanced commercial finite element software, like NASTRAN, PATRAN, PRO-E, ABAQUS, and ANSYS. Indeed, it is possible to virtually test (simulate) the material behavior directly using 3D finite element method (FEM) on a number of statistically representative geometric entities, referred to as RVEs (Duschlbauer et al., 2006; Gusev, 1997; Kari et al., 2007; Meraghni et al., 2002). The notion of optimal designing materials based on the virtual testing (numerical simulations) of microstructures can be conducted, if a large quantity of numerical-geometrical experiments for different types of materials and microstructures can be carried out in an automatic systematic way.

The next stage after developing a robust matrix constitutive model in the micromechanical modeling approach is the creation of an RVE for virtually testing the composite materials. One of the fundamental key points of the FEM study is the

recognition and generation of proper RVEs, through which the effective homogeneous material properties of the composite may be derived. In definition, an RVE is a statistical representation of material (Hill, 1963); in another word, an RVE is assumed to represent the physical property of a composite material within a certain framework. Fig. 2.1 depicts this concept. Thus, according to this background, one RVE must be large enough such that it contains a number of inclusions in a heterogeneous material, and the effective homogenized properties that can be derived from the RVE represent the true material characteristics in the macroscopic scale.

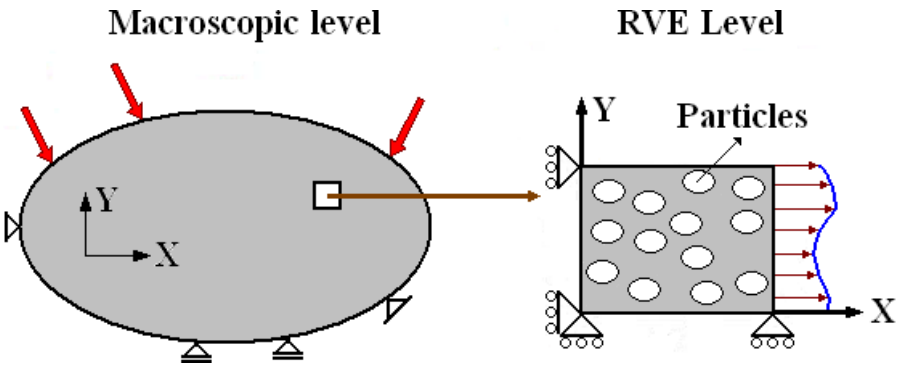

Fig. 2.4. Graphically illustrating the definition of an RVE that represents a domain.

The essential question is how can the geometry of a desired RVE at the micro-level (on which FEM is performed) be identified and generated numerically. Obviously, it depends on the morphological geometry of the microstructure of the composite material. Henceforth, vast efforts have been dedicated to model simple geometries such as a unit cell containing one sphere or one fiber in 3D. Besides, many researchers have generated 3D unidirectional fibers in 3D RVEs domains. However, for the case of

composites containing fibers, the identification of an RVE directly relates to the woven fibers (Ivanov and Tabiei, 2001; Quek et al., 2004), and also fibers in laminates configuration (repeatable architecture composites) (Caiazzo and Costanzo, 2000). Several researchers mentioned that for composite materials containing random inclusion arrangements, numerically constructing an RVE is not straightforward (Böhm et al., 2002; Duschlbauer et al., 2006; Gusev et al., 2002; Tu et al., 2005). But in this work, in Chapter 6, it is shown and explained how to solve this issue.

Some researchers have developed special codes for automatically generating RVEs (Mishnaevsky, 2007; Wang et al., 2011), based on creating multi-particle unit cells for nano composites. For instance, Meso3DFiber was developed by Mishnaevsky. It provides straight fibers as shown in Fig. 2.5. The reader is referred to Chapter 6 of this dissertation to compare the complexity of the generated models by the developed RVE_Maker software by the auther and the RVEs generated by Meso3DFiber software.

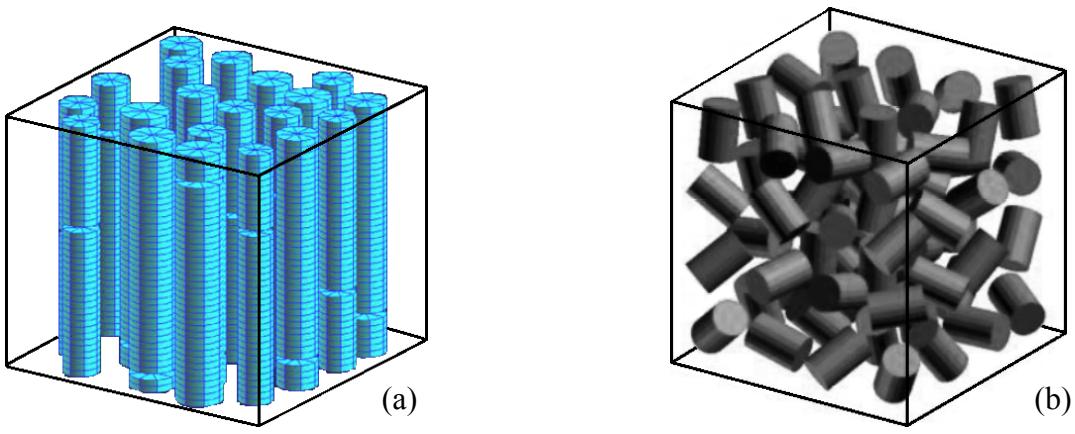

Fig. 2.5. 3D unit cell: (a) with 20 straight fibers, and (b) small chopped fibers in random orientation, generated by Meso3DFiber software (Mishnaevsky, 2012; Mishnaevsky and Brondsted, 2009).

CHAPTER III

LARGE DEFORMATION GENERALIZATION OF INFINITE VISCOELASTIC AND VISCOPLASTIC MODELS BASED ON GREEN-LAGRANGE STRAIN

3.1 Introduction

Investigating large deformation behavior needs constitutive models developed based on finite strain theory, and for this purpose several models for polymeric materials have been proposed. However, assessing a large strain model directly by large deformation data is difficult, because the strain and stress fields are non-uniform in the large deformation range. Because, there are many well-established elastoplastic models that have been proposed and examined by various research groups for a significant time; thus, one approach for studying large deformation behavior is extending the available models that are built on small strain concept to the finite deformation framework.

The purpose of this chapter is providing and introducing a method to extend a small strain constitutive model to an identical large deformation model. Hence, the overall items and derivations that should be considered for such generalization are explained. The total Lagrangian strain is additively partitioned into its elastic and plastic components, which is based on the multiplicative decomposition of deformation gradient. This separation technique, when is applied, can operate at the kinematics level. Therefore, this procedure can be utilized for generalizing a wide class of independent infinite elastoplastic constitutive models (that are developed according to additive

decomposition of elastic and plastic portions of deformation) to their equivalent finite models in the finite deformation range (which is controlled by the framework of the additive/multiplicative decomposition of deformation gradient). The recommended numerical algorithm is developed in such a way that the extension from standard small-strain formula to large-strain context is straightforward.

3.2 Stress and Strain Energy Conjugacy

There are various measures for stress and strain that describe a domain subjected to external loads. Any type of stress can be hired to formulate the internal energy in the domain. On the other hand, when a certain strain measure is used for explaining the deformation then the counterpart stress variable, which should be combined with the strain, cannot be selected arbitrarily. The ideas of the concepts and definitions of stress and strain are interweaved, no matter of the existence of a strain energy function (Başar and Weichert, 2000). At the most basic levels, the stresses and strains are related through the mechanical power; thus the rate of work-done per unit current volume of a body can be mathematically expressed as (Norris, 2008)

$$\mathrm{tr}(\sigma L) = \mathrm{tr}(\sigma D) = \dot{w} \tag{3.1}$$

where σ is the Cauchy stress, L is the velocity gradient, and D is the rate of deformation (stretching) tensor (symmetric part of L). Even though it can be useful to introduce a reference configuration, this concept for work-conjugacy is independent of the notion of configuration. Now, let's define T and E be the stress and strain associated with the reference configurations, respectively; then T and E are mutually work-conjugate if they satisfy

$$\mathrm{tr}(T\dot{E}) = \dot{w}\det(F) \qquad \Rightarrow \qquad \frac{1}{J}\mathrm{tr}(T\dot{E}) = \dot{w} \tag{3.2}$$

where F is the deformation gradient between the current and reference descriptions, and the scalar factor $\det(F)$ shows the change in volume between the current and reference states. Eq. (3.2) is usually used as the starting point for defining a stress measure. For developing a constitutive model, the choice of the strain, E, is not unique and it depends on the physics of the material that is being modeled. However, selecting the strain measure fixes the definition of stress with respect to the work-conjugacy relationship in Eq. (3.2). It is surprising but true that the same simple connection is not applicable to the relation between Eulerian strain and the Cauchy stress or Kirchhoff stress (that both are in the current configuration). Actually, the problem is the definition of a strain such that $\dot{\varepsilon} = D$. But, since the Eulerian strain is in the current configuration, a particular corotational rate for strain measure tensor is needed to be sought, in such a way that the strain rate gives the deformation rate, as: $\overset{\nabla}{\varepsilon} = D$.

Xiao et al. (1998) proved that there exists a unique solution according to the Hencky strain $\mathrm{Ln}(V)$ (V is the left Cauchy stretch tensor in polar decomposition) combined with the logarithmic rate. The fundamental relation for Eulerian conjugate stress is based on the conclusions of Xiao et al. (1997) work that states

$$\overset{\nabla \log}{\mathrm{Ln}(V)} = D \tag{3.3}$$

where $\nabla \log$ is the objective corotational rate defined by the logarithmic spin. But deriving and implementing the natural strain and its rates is burdensome.

The major difference between Lagrangian and Eulerian work-conjugacy is that the Eulerian requires the consideration of the corotational rate, which is quite arbitrary, but each of the rates can be approperiate for modeling certain types of materials. On the other hand, since Lagrangian strain is in the reference configuration, there is no need to concern about the corotational rate. Norris (2008) has shown that every acceptable Eulerian strain measure, $f(V)$, with respect to the definition of the function f, is associated with a unique corotational rate, so-called the *f*-rate, where the skew-symmetric matrix Ω^f is called the *f*-spin or *f*-rate and introduced as

$$\Omega^f = \omega + \mathbb{P} D \tag{3.4}$$

in which ω is the vorticity or spin tensor (the skew-symmetric part of velocity gradient), and the fourth order projection tensor, $\mathbb{P}$, is explained based on stretch and identity tensors, as

$$\mathbb{P} = \left(V \otimes I - I \otimes V\right)^* \left[\Delta f(V) - \left(V \otimes I + I \otimes V\right)^{-1} \left(V^2 \otimes I + I \otimes V^2\right)\right] \tag{3.5}$$

The $(\cdot)^*$ symbolizes the pseudo-inverse operator of the tensor, and from now on, I is the identity tensor. The logarithmic rate ($\nabla \log$) is a special case of the *f*-rate (Ω^f) which corresponds $\mathrm{Ln}(V)$ to the stretching tensor, D. This fundamental result (Xiao et al., 1997) for the logarithmic rate is generalized to arbitrary Eulerian strain measures, $e = f(V)$, through

$$\overset{\nabla \log}{e} = \left(\nabla f(V)\right)\left(\Delta \mathrm{Ln}(V)\right) D \tag{3.6}$$

Now, for investigating the work-conjugacy, Eqs. (3.1) and (3.2) are revisited, such that

$$\mathrm{tr}(\tau \overset{\nabla \log}{e}) = \mathrm{tr}(\sigma D) \tag{3.7}$$

Considering $\nabla f(V)$ and $\Delta \mathrm{Ln}(V)$ are invertable and also they can commute (i.e. $AB = BA$), and since the above equation should be valid for all D; therefore, the stress conjugate to the general Eulerian strain measures, $\varepsilon = f(V)$, is

$$\tau = \left(\Delta f(V)\right)\left(\nabla \mathrm{Ln}(V)\right)\sigma \qquad \text{(for logarithmic spin)} \tag{3.8}$$

Or in a straightforward formula, Eq. (3.8) can be expressed in spectral decomposition form as

$$\tau = \sigma^f + \sum_{i=1}^{n}\sum_{j=1}^{n}\left(\frac{\mathrm{Ln}(\lambda_i) - \mathrm{Ln}(\lambda_j)}{f(\lambda_i) - f(\lambda_j)} - 1\right) V_i \otimes V_j \sigma \qquad \text{(for logarithmic spin)} \tag{3.9}$$

The conjugate stress that can be found through using the *f*-rate is optimal in the sense that it is the closest conceivable stress to the Cauchy stress. In other words, this strain rate can get the actual stretching tensor, D. Also, the optimal modified stress, σ^f, is defined by the arbitrary function *f* through the following equation

$$\sigma^f = \sigma + \sum_{i=1}^{n}\left[\frac{1}{\lambda_i f(\lambda_i)} - 1\right] V_i \otimes V_i \sigma \tag{3.10}$$

Xiao also showed the modified stress, σ^f, can also be reduced to the Cauchy stress, if and only if: $f(V) = \mathrm{Ln}(V)$. Hence, this uniqueness is valid only for the logarithmic rate, and shows how the conjugate stress in that case is related to the modified stress, σ^f. This achievement supports the results obtained by Xiao et al. (1997) for the logarithmic rate and the natural (Hencky) strain measure, when the idea of the logarithmic rate to arbitrary strain functions is generalized through the strain dependent spin Ω^f.

In the following, it is shown that the II-PK stress and the GL strain are work conjugate. Afterwards the work conjugacy of Kirchhoff stress and the Euler-Almansi strain will be studied.

3.2.1 Second Piola-Kirchhoff Stress and Green-Lagrange Strain Work Conjugacy

The II-PK stress and the GL strain in continuum mechanics are frequently used, and are defined as

$$T = J F^{-1}\sigma F^{-\mathrm{T}} \qquad \text{and} \qquad E = \frac{1}{2}\left(C - I\right) \tag{3.11}$$

where $C = F^{\mathrm{T}}F$ is the right Green-Cauchy tensor. The time derivative of Green-Lagrange strain can be derived as

$$\dot{E} = \frac{1}{2}\left(\dot{C}\right) = \frac{1}{2}\left(\dot{F}^{\mathrm{T}}F + F^{\mathrm{T}}\dot{F}\right) \tag{3.12}$$

Also, the work-done per unit reference volume of material in Eq. (3.1) is $\mathrm{tr}(T\dot{E}) = \mathrm{tr}(T_{ij}\dot{E}_{jk}) = T_{ij}\dot{E}_{ji}$. Therefore, one can say

$$T\dot{E} = \frac{J}{2}F^{-1}\sigma F^{-\mathrm{T}}\left(\dot{F}^{\mathrm{T}}F + F^{\mathrm{T}}\dot{F}\right) \tag{3.13}$$

In indicial notation, the trace of $T\dot{E}$ can be shown as

$$T_{ir}\dot{E}_{ri} = \frac{J}{2}F^{-1}_{ik}\sigma_{kl}F^{-\mathrm{T}}_{lr}\left(\dot{F}^{\mathrm{T}}_{rm}F_{mj} + F^{\mathrm{T}}_{m}\dot{F}_{ni}\right) = \frac{J}{2}\left(\underbrace{F^{-1}_{ik}\sigma_{kl}F^{-\mathrm{T}}_{lr}\dot{F}^{\mathrm{T}}_{rm}F_{mi}}_{\mathrm{Part}\,(1)} + \underbrace{F^{-1}_{ik}\sigma_{kl}F^{-\mathrm{T}}_{lr}F^{\mathrm{T}}_{m}\dot{F}_{ni}}_{\mathrm{Part}\,(2)}\right) \tag{3.14}$$

Now, the terms in parts 1 and 2 can be simplified as follows

$$\begin{aligned}\mathrm{Part}\,(1):\ F^{-1}_{ik}\sigma_{kl}F^{-\mathrm{T}}_{lr}\dot{F}^{\mathrm{T}}_{rm}F_{mi} &= \sigma_{kl}\left(F^{-\mathrm{T}}_{lr}\dot{F}^{\mathrm{T}}_{rm}\right)\left(F_{mi}F^{-1}_{ik}\right) = \sigma_{kl}\left(\dot{F}_{mr}F^{-1}_{rl}\right)^{\mathrm{T}}\left(F_{mi}F^{-1}_{ik}\right)\\ &= \sigma_{kl}\left(L_{ml}\right)^{\mathrm{T}}\left(\delta_{mk}\right) = \left(\sigma_{kl}L_{lm}\right)\left(\delta_{mk}\right) = \left(\sigma_{kl}D_{lm}\right)\left(\delta_{mk}\right) = \sigma_{kl}D_{lk}\end{aligned} \tag{3.15}$$

The same as Part 1, one can come up with Part 2, as: $F_{ik}^{-1}\sigma_{kl}F_{lr}^{-\mathrm{T}}F_{m}^{\mathrm{T}}\dot{F}_{ni}=\sigma_{kl}D_{lk}$. Therefore, the trace of energy increment can be written as

$$\mathrm{tr}(T\dot{E})=T_{ir}\dot{E}_{ri}=\frac{J}{2}\left[\sigma_{kl}D_{lk}+\sigma_{kl}D_{lk}\right]=J\sigma_{kl}D_{lk} \tag{3.16}$$

Thus, the simplified expression for the work-done shows

$$\dot{w}=\frac{1}{J}\mathrm{tr}(T\dot{E})=\frac{1}{J}\left(J\sigma_{kl}D_{lk}\right)=\sigma_{kl}D_{lk} \tag{3.17}$$

Hence, Eq. (3.17) along with the above derivations demonstrations that the II-PK stress and the GL strain are work conjugate.

3.2.2 Kirchhoff Stress and Euler-Almansi Strain Work Conjugacy

The Kirchhoff stress and the Euler-Almansi strain in continuum mechanics are defined as

$$T=J\sigma \qquad \text{and} \qquad e=\frac{1}{2}\left(I-B^{-1}\right) \tag{3.18}$$

where $B=FF^{\mathrm{T}}$ is the left Green-Cauchy tensor. The time derivative of Euler-Almansi strain is

$$\dot{e}=\frac{1}{2}B^{-1}\left(\dot{B}\right)B^{-1}=\frac{1}{2}B^{-1}\left(\dot{F}F^{\mathrm{T}}+F\dot{F}^{\mathrm{T}}\right)B^{-1} \tag{3.19}$$

By replacing $B^{-1}=(FF^{\mathrm{T}})^{-1}=F^{-\mathrm{T}}F^{-1}$ into the recent equation, one can get

$$\dot{e}=\frac{1}{2}F^{-\mathrm{T}}F^{-1}\left(\dot{F}F^{\mathrm{T}}+F\dot{F}^{\mathrm{T}}\right)F^{-\mathrm{T}}F^{-1}=\frac{1}{2}\left(F^{-\mathrm{T}}F^{-1}\dot{F}F^{-1}+F^{-\mathrm{T}}\dot{F}^{\mathrm{T}}F^{-\mathrm{T}}F^{-1}\right) \tag{3.20}$$

Eq. (3.20) may be rearranged as

$$\dot{e}=\frac{1}{2}\left((FF^{\mathrm{T}})^{-1}(\dot{F}F^{-1})+(\dot{F}F^{-1})^{\mathrm{T}}(FF^{\mathrm{T}})^{-\mathrm{T}}\right)=\frac{1}{2}\left(B^{-1}L+L^{\mathrm{T}}B^{-1}\right) \tag{3.21}$$

Since, B is symmetric and $L = D + \omega$ (D is symmetric, and ω is skew-symmetric), therefore

$$B^{-1}L = B^{-1}D \tag{3.22}$$

Thus, the rate of Eulerian strain $\dot{e}$ may be rewritten as

$$\dot{e} = \frac{1}{2}\left(B^{-1}D + DB^{-1}\right) \tag{3.23}$$

Now, for exploring the work conjugacy, one has to show the following equivalency

$$\frac{1}{J}\mathrm{tr}(T\,\dot{e}) \overset{?}{=} \dot{w} \tag{3.24}$$

By substituting Eq. (3.18) and (3.23) into Eq. (3.24), the following relation has to be studied

$$\frac{1}{2}\mathrm{tr}\left(\sigma\left[B^{-1}D + DB^{-1}\right]\right) \overset{?}{=} \dot{w} \tag{3.25}$$

In indicial form, it can be expressed as

$$T_{ir}\,\dot{e}_{rj} = \frac{J}{2}\sigma_{ik}\left(B^{-1}_{km}D_{mj} + D_{kn}B^{-1}_{nj}\right) \tag{3.26}$$

With respect to Eq. (3.26), one can write

$$\mathrm{tr}(T\,\dot{e}) = \frac{J}{2}\left(\mathrm{tr}\left(\sigma_{ik}\,B^{-1}_{km}\,D_{mj}\right) + \mathrm{tr}\left(\sigma_{ik}\,D_{kn}\,B^{-1}_{nj}\right)\right) = \frac{J}{2}\left(\underbrace{\sigma_{ik}\,B^{-1}_{km}\,D_{mi}}_{\text{Part 1}} + \underbrace{\sigma_{ik}\,D_{kn}\,B^{-1}_{ni}}_{\text{Part 2}}\right) \tag{3.27}$$

Now, in order to simplifying Parts 1 and 2, it should be recalled that: $B^{-1}D = B^{-1}L$; therefore, these parts may be expanded as

$$\begin{aligned}
&\text{Part 1:}\quad \sigma_{ik}B^{-1}_{km}D_{mi} = \sigma_{ik}B^{-1}_{km}L_{mi} = \sigma_{ik}\left(F_{kp}F^{\mathrm{T}}_{pm}\right)^{-1}\left(\dot{F}_{mq}F^{-1}_{qi}\right) = \sigma_{ik}F^{-\mathrm{T}}_{rm}F^{-1}_{kr}\dot{F}_{mn}F^{-1}_{ni} \\
&\text{Part 2:}\quad \sigma_{ik}D_{kn}B^{-1}_{ni} = \sigma_{ik}B^{-1}_{kn}L_{ni} = \sigma_{ik}\left(F_{kp}F^{\mathrm{T}}_{pn}\right)^{-1}\left(\dot{F}_{nq}F^{-1}_{qi}\right) = \sigma_{ik}F^{-\mathrm{T}}_{pm}F^{-1}_{kp}\dot{F}_{nq}F^{-1}_{qi}
\end{aligned} \tag{3.28}$$

These formulations could not be simplified anymore, because unlike GL strain which contains the deformation gradient, F, in the derivations, there is no F in the Eulerian form of the energy increments. Therefore, Kirchhoff stress and the Euler-Almansi strain are not work conjugate

$$\frac{1}{J}\mathrm{tr}(T\dot{E}) \neq \mathrm{tr}(TD) = \dot{w} \tag{3.29}$$

It is evident that work-conjugacy is simpler for the reference or Lagrangian stress and strain than for their counterparts in the current or Eulerian configuration.

3.2.3 Work Conjugate Stresses and Strains

As mentioned in continuum mechanics text books (Bower, 2009; Dill, 2007), Cauchy stress is the best actual measure for describing the internal forces (force per unit area) acting inside a deformed object. The other stress measures are work-conjugate (or energy-conjugate) to other specific strains or rate of deformation measures. It means that the multiplication of stress by the time derivative of the related strain (or rate of deformation) measure, gives the rate of work-done by the forces (Dvorkin, 2010). The rate of work done by stresses acting on a small material element with volume in the undeformed solid (and volume in the deformed solid) can be expressed and computed as (Bower, 2009)

$$\dot{W} = D_{ij}\,\sigma_{ij}\,\mathrm{d}v = D_{ij}\,\tau_{ij}\,\mathrm{d}v_o = \dot{F}_{ij}\,P_{ij}\,\mathrm{d}v_o = \dot{E}_{ij}\,S_{ij}\,\mathrm{d}v_o \tag{3.30}$$

where D is the stretch rate tensor, $\dot{F}$ is the deformation gradient change rate, and $\dot{E}$ is the GL strain change rate tensor. Also $\mathrm{d}v$ and $\mathrm{d}v_o$ are the infinitesimal volume element in the current and reference configurations, respectively. Here, it is noteworthy to

mention that Cauchy stress, σ, and also Kirchhoff stress, τ, are not conjugate to any appropriate strain measure. That is the reason why the nominal and material stresses should be defined. The first Piola-Kirchhoff stress (nominal stress) is conjugate to the rate of deformation gradient, and the II-PK stress (material stress) is conjugate to the Lagrange strain tensor. All of the equalities in Eq. (3.30) can be easily derived based on Eqs. (3.1) and (3.2).

3.3 Standard Forms of Small and Large Deformation Constitutive Relations

Here, it is required to recall the general computational form of mathematical relation of small deformation elastic-plastic models that are desired to be extended to the finite deformation one. As is widely known, the small strain models have been constructed on the essence of incremental analysis of a solid domain. In the following, the general form of governing equations for computing the small deformation behavior are concisely listed

$$\varepsilon_{t+\Delta t} = \varepsilon^{\mathrm{e}}_{t+\Delta t} + \varepsilon^{\mathrm{p}}_{t+\Delta t} \tag{3.31}$$

$$\varepsilon^{\mathrm{p}}_{t+\Delta t} = \varepsilon^{\mathrm{p}}_{t} + \Delta\varepsilon^{\mathrm{p}}_{t+\Delta t} \tag{3.32}$$

$$\dot{\varepsilon}^{\mathrm{p}}_{t+\Delta t} = \dot{\lambda}\left.\frac{\partial f}{\partial \sigma}\right|_{t+\Delta t} \tag{3.33}$$

where ε, ε^{e}, and ε^{p} are total strain, elastic strain, and plastic strain, respectively; $\dot{\varepsilon}^{\mathrm{p}}$ is the rate of plastic strain, $\dot{\lambda}$ is the plastic multiplier, and for the case of viscoplasticity this scalar is also a function of viscosity, f is a favorite yield surface function, σ is the Cauchy stress, and $\dfrac{\partial f}{\partial \sigma}$ is the direction of expansion of the yield surface. Since non-

linear numerical models are solved iteratively, the quantity of stress field should be updated by a linearization technique. Therefore in Eq. (3.34), the stress tensor will be updated through a defined function, and *K* is an appropriate consistent tangent stiffness.

$$\sigma_{t+\Delta t} = \hat{\sigma}(\varepsilon_{t+\Delta t}) \qquad , \qquad K_{t+\Delta t} = \left.\frac{\partial \Delta\hat{\sigma}}{\partial \Delta\varepsilon}\right|_{t+\Delta t} \tag{3.34}$$

Now, one standard form for finite deformation elastoplastic model should be selected. The basics and historical details of the theory of finite deformation can be studied in Moran et al. (1990). The following general incremental equations are presented

$$F_{t+\Delta t} = F^{\mathrm{e}}_{t+\Delta t}\, F^{\mathrm{p}}_{t+\Delta t} \tag{3.35}$$

$$L^{\mathrm{p}}_{t+\Delta t} = \dot{F}^{\mathrm{p}}_{t+\Delta t} \left(F^{\mathrm{p}}_{t+\Delta t}\right)^{-1} = \dot{\lambda}\, \left.\frac{\partial f}{\partial S}\right|_{t+\Delta t} \tag{3.36}$$

$$S_{t+\Delta t} = \hat{S}(F_{t+\Delta t}) \tag{3.37}$$

$$K_{t+\Delta t} = \left.\frac{\partial \Delta\hat{S}}{\partial \Delta E}\right|_{t+\Delta t} \tag{3.38}$$

The flow rule contains the magnitude of the plastic flow, λ, and the flow direction as $\frac{\partial f}{\partial \sigma}$, the same as Eq. (3.33), and S is the II-PK tensor. Notice that the discretization method for the plastic flowing rule and finding the deformation gradient of plastic portion of the deformation is the essential part of the generalization. From Eq. (3.36) the $F^{\mathrm{p}}_{t+\Delta t}$ may be found in two ways. The first way is built on the previous deformation gradient tensor, F^{p}_{t}, which reduces the equation to a system of linear algebraic equations, but this method gives an approximation and computationally is a time consuming task.

The next approach is exponential solution. If the rigid body rotation lumped to the elastic part, finding the solution for $F^{\mathrm{p}}_{t+\Delta t}$ is easier, but updating $F^{\mathrm{e}}_{t+\Delta t}$ will face some problems. However, if the rotation is lumped to the plastic portion, the solution needs more mathematical manipulation, which is fully discussed in Section 3.5. It is also crucial to recall that since the flow rule in plasticity is defined in the intermediate configuration (plastic or unloaded configuration) the frame indifference concept has been consistently satisfied (Ortiz and Martin, 1989).

3.4 Kinematics

3.4.1 Fundamental Kinematics Formulation

From continuum mechanics, one may recall the general form for motion of a particle is defined as

$$x = x(X, t) \tag{3.39}$$

where X is the position of a material particle in the initial or reference configuration, and x is the spatial position in the current configuration. The deformation gradient F describes the motion of the body

$$F = \frac{\partial x}{\partial X} \quad , \quad \det(F) > 0 \tag{3.40}$$

From continuum mechanics, the particle velocity v and the velocity gradient L are defined by

$$v = \dot{x} \quad , \quad L = \frac{\partial v}{\partial x} = \dot{F}F^{-1} \tag{3.41}$$

Here, and from now on, $(\dot{\cdot})$ denotes the material time derivative. The deformation gradient, F, may be multiplicatively decomposed into orthogonal rigid body rotation,

and symmetric positive-definite pure stretch deformation tensors, well-known as polar decomposition, that is

$$F = RU = VR \quad , \quad R^{-1} = R^{\mathrm{T}} \tag{3.42}$$

The symmetric stretch tensors V and U are known as left and right stretch tensors. The velocity gradient is decomposed to symmetric (or objective) deformation rates D, and skew-symmetric spin rate (or vorticity tensor) ω, as

$$L = D + \omega \quad , \quad D = \frac{1}{2}\left(L + L^{\mathrm{T}}\right) \quad , \quad \omega = \frac{1}{2}\left(L - L^{\mathrm{T}}\right) \tag{3.43}$$

3.4.2 Green-Lagrange Strain Partitioning

Consider one elastoplastic deformed configuration of a material domain as $\Re$, and its initial configuration as $\Re^o$. Also, the deformation gradient F maps the material particle position from the initial or reference configuration to the spatial position in the current configuration, Fig. 3.1. As can be seen in this figure the presence of the plastic part for the deformation gradient field introduces another configuration $\tilde{\Re}$, which is called intermediate configuration.

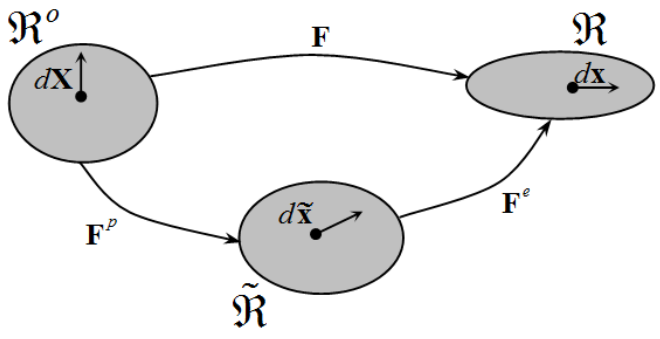

Fig. 3.1. Illustration of deformation gradient mapping tensor, and multiplicative decomposition into elastic and plastic components.

Here, the intermediate configuration is introduced, even though it is not physically attainable. It is defined and considered as a set of all unloaded configurations.

In the second type of large deformation formulation, Eq. (2.3), the deformation gradient has been multiplicatively decomposed to the elastic and plastic components. By considering Eq. (2.3) and Eq. (3.41), one can expand the velocity gradient in terms of viscoelastic and viscoplastic deformation tensors, as

$$\begin{aligned} L &= (\overline{\dot{F}^{\mathrm{ve}} F^{\mathrm{vp}}}) \left(F^{\mathrm{ve}} F^{\mathrm{vp}} \right)^{-1} \\ &= \left(\dot{F}^{\mathrm{ve}} F^{\mathrm{vp}} + F^{\mathrm{ve}} \dot{F}^{\mathrm{vp}} \right) \left(F^{\mathrm{vp}\,-1} F^{\mathrm{ve}\,-1} \right) = \left(\dot{F}^{\mathrm{ve}} F^{\mathrm{ve}\,-1} \right) + F^{\mathrm{ve}} \left(\dot{F}^{\mathrm{vp}} F^{\mathrm{vp}\,-1} \right) F^{\mathrm{ve}\,-1} \end{aligned} \tag{3.44}$$

The velocity gradient of viscoelasticity is defined as $L^{\mathrm{ve}} = \dot{F}^{\mathrm{ve}} F^{\mathrm{ve}\,-1}$, and velocity gradient of viscoplasticity, $L^{\mathrm{vp}} = F^{\mathrm{ve}} \tilde{L}^{\mathrm{vp}} F^{\mathrm{ve}\,-1}$ where $\tilde{L}^{\mathrm{vp}} = \dot{F}^{\mathrm{vp}} F^{\mathrm{vp}\,-1}$, one can obtain the decoupled velocity gradient as

$$L = L^{\mathrm{ve}} + L^{\mathrm{vp}} \tag{3.45}$$

Small deformation models have been usually written based on additively decomposing elastic and plastic strains or strain rates. Such decomposing is also possible for the large deformation concept, for both Eulerian and Lagrangian strains. From now on, GL strain quantity that shows how much right Green-Cauchy deformation tensor, $C = F^{\mathrm{T}} F$, differs from the unity tensor, I, is considered. At this time, in order to discretize the GL strain to its viscoelastic and viscoplastic parts, the definition of GL strain needs to be recalled, for the total elastic and plastic strain portions.

$$E = \frac{1}{2}\left(C - I\right) = \frac{1}{2}\left(F^{\mathrm{T}} F - I\right) \tag{3.46}$$

$$E^{ve} = \frac{1}{2}\left(F^{ve\,T} F^{ve} - I\right) \tag{3.47}$$

$$E^{vp} = \frac{1}{2}\left(F^{vp\,T} F^{vp} - I\right) \tag{3.48}$$

From Eq. (2.3), the right Cauchy-Green deformation tensor can be written as

$$C = F^{T}F = \left(F^{ve}F^{vp}\right)^{T}\left(F^{ve}F^{vp}\right) = F^{vp\,T}\left(F^{ve\,T} F^{ve}\right)F^{vp} \tag{3.49}$$

Since $E \neq E^{ve} + E^{vp}$; thus, in order to additively decompose GL strain to viscoelastic strain, E^{ve}, and viscoplastic strain, E^{vp}, the difference of total GL strain and the elastic and plastic portions should be found. Hence, substituting Eqs. (3.46), (3.47) and Eq. (2.3) into $E - E^{vp}$, and after some straightforward manipulations, one can get

$$E - E^{vp} = F^{vp\,T}\frac{1}{2}\left(F^{vp\,T} F^{ve} - I\right)F^{vp} = F^{vp\,T}\left(E^{ve}\right)F^{vp} \tag{3.50}$$

which finally leads to the viscoelastic and viscoplastic partitioning in the next expression

$$E = F^{vp\,T}\left(E^{ve}\right)F^{vp} + E^{vp} \tag{3.51}$$

Eq. (3.51) shows the total Green-Lagrange strain can be additively decomposed to viscoelastic and viscoplastic components, in such a way that the elastic portion should be mapped to the plastic configuration. Moreover, since plastic and/or viscoplastic models have been usually written based on strain rates, the time derivative of Lagrangian strain is required. Thus, by applying material time derivation on Eq. (3.51), one can get

$$\dot{E} = \dot{F}^{vp\,T}\left(E^{ve}\right)F^{vp} + F^{vp\,T}\left(\dot{E}^{ve}\right)F^{vp} + F^{vp\,T}\left(E^{ve}\right)\dot{F}^{vp} + \dot{E}^{vp} \tag{3.52}$$

And by factorizing the deformation gradient and its transpose from the viscoelastic terms, one may come up with the following expression for the total strain rate

$$\dot{E} = F^{\text{vp}^{\text{T}}}\left[\left(\dot{F}^{\text{vp}}F^{\text{vp}^{-1}}\right)^{\text{T}}E^{\text{ve}} + \dot{E}^{\text{ve}} + E^{\text{ve}}\left(\dot{F}^{\text{vp}}F^{\text{vp}^{-1}}\right)\right]F^{\text{vp}} + \dot{E}^{\text{vp}} \tag{3.53}$$

Finally, the time derivative of GL strain can be decoupled into the viscoelastic and viscoplastic components as the following simplified form

$$\dot{E} = F^{\text{vp}^{\text{T}}}\left[\dot{E}^{\text{ve}} + 2\,\text{symm}\left(E^{\text{ve}}\dot{F}^{\text{vp}}F^{\text{vp}^{-1}}\right)\right]F^{\text{vp}} + \dot{E}^{\text{vp}} \tag{3.54}$$

In Eq. (3.54), the viscoplastic strain rate is independent of elastic part. On the other hand, the viscoelastic strain rate is dependent to the rate of viscoelastic strain in the current time increment, $\dot{E}^{\text{ve}}$, and to the total amount of viscoelastic, E^{ve}, viscoplastic deformation gradient, F^{vp}. Similar to Eq. (3.51) the total viscoelastic strain rate should be transformed from its own configuration (intermediate) to the viscoplastic configuration (or final configuration). The recent equation for the GL strain rate can also be rewritten in the following form

$$\dot{E} = F^{\text{vp}^{\text{T}}}\left[\dot{E}^{\text{ve}} + \mathbb{Z}^{\text{T}}\dot{E}^{\text{vp}}\mathbb{Z}\right]F^{\text{vp}} \qquad , \qquad \mathbb{Z} = F^{\text{vp}^{-1}}F^{\text{ve}} \tag{3.55}$$

Both Eq. (3.54) and (3.55) are applicable, and their usage depends on how the other formulations are derived. Furthermore, based on Eq. (3.46), the general form of the material time derivative of GL strain tensor has the next expression

$$\dot{E} = \frac{1}{2}\left[\dot{F}^{T}F + F^{T}\dot{F}\right] \tag{3.56}$$

By factorizing the deformation gradient from the right and its transpose from the left side, Eq. (3.56) will be explained as

$$\dot{E} = \frac{1}{2}F^{\text{T}}\left[\left(\dot{F}F^{\text{-1}}\right) + \left(\dot{F}F^{\text{-1}}\right)^{\text{T}}\right]F \tag{3.57}$$

Recalling the rate of deformation tensor from Eq. (3.43); hence, the general form for GL strain time derivative is

$$\dot{E} = F^{\mathrm{T}} D F \tag{3.58}$$

3.4.3 Equivalency of Current and Conventional Methods

Since in the first type of finite deformation models, the additively decomposition of velocity gradient, L, or its symmetric part, D, is used; therefore, it needs to be proved that Eq. (3.45) and the derivations which leads to Eq. (3.54) are equivalent. Hence, for this purpose, by substituting Eq. (3.58) into viscoplastic part of Eq. (3.54), and recalling $L = \dot{F} F^{-1}$, one can rewrite Eq. (3.54) as

$$\dot{E} = F^{\mathrm{vp}\,\mathrm{T}} \left[\dot{E}^{\mathrm{ve}} + E^{\mathrm{ve}} \tilde{L}^{\mathrm{vp}} + \tilde{L}^{\mathrm{vp}\,\mathrm{T}} E^{\mathrm{ve}} \right] F^{\mathrm{vp}} + F^{\mathrm{vp}\,\mathrm{T}} D^{\mathrm{vp}} F^{\mathrm{vp}} \tag{3.59}$$

After some mathematical manipulation, the strain rate will be written as

$$\dot{E} = F^{\mathrm{vp}\,\mathrm{T}} \left[\dot{E}^{\mathrm{ve}} + \left(E^{\mathrm{ve}} + \frac{1}{2} I \right) \tilde{L}^{\mathrm{vp}} + \tilde{L}^{\mathrm{vp}\,\mathrm{T}} \left(E^{\mathrm{ve}} + \frac{1}{2} I \right) \right] F^{\mathrm{vp}} \tag{3.60}$$

Now, multiplying both sides of Eq. (3.60), from right side by F^{-1} and from left side by $F^{-\mathrm{T}}$, one can come up with

$$F^{-\mathrm{T}} \dot{E} F^{-1} = F^{-\mathrm{T}} F^{\mathrm{vp}\,\mathrm{T}} \left[\dot{E}^{\mathrm{ve}} + \left(E^{\mathrm{ve}} + \frac{1}{2} I \right) \tilde{L}^{\mathrm{vp}} + \tilde{L}^{\mathrm{vp}\,\mathrm{T}} \left(E^{\mathrm{ve}} + \frac{1}{2} I \right) \right] F^{\mathrm{vp}} F^{-1} \tag{3.61}$$

From Eq. (3.47), $E^{\mathrm{ve}} + \frac{1}{2} I = \frac{1}{2} F^{\mathrm{ve}\,\mathrm{T}} F^{\mathrm{ve}}$ is achieved, and the inverse form of Eq. (3.58) can be expressed as $D = F^{-\mathrm{T}} \dot{E} F^{-1}$. Therefore, by replacing these achievements and also Eq. (2.3) into Eq. (3.61), it can be modified as

$$F^{-\mathrm{T}}\dot{E}F^{-1}=\left(F^{\mathrm{ve}}F^{\mathrm{vp}}\right)^{-\mathrm{T}}F^{\mathrm{vp}\,\mathrm{T}}\left[\dot{E}^{\mathrm{ve}}+\frac{1}{2}F^{\mathrm{ve}\,\mathrm{T}}F^{\mathrm{ve}}L^{\mathrm{vp}}+\frac{1}{2}L^{\mathrm{vp}\,\mathrm{T}}F^{\mathrm{ve}\,\mathrm{T}}F^{\mathrm{ve}}\right]F^{\mathrm{vp}}\left(F^{\mathrm{ve}}F^{\mathrm{vp}}\right)^{-1} \tag{3.62}$$

And after some mathematical simplification, the total stretching rate tensor will be expressed as

$$D=D^{\mathrm{ve}}+\frac{1}{2}\left[\left(F^{\mathrm{ve}}\tilde{L}^{\mathrm{vp}}F^{\mathrm{ve}\,-1}\right)+\left(F^{\mathrm{ve}}\tilde{L}^{\mathrm{vp}}F^{\mathrm{ve}\,-1}\right)^{\mathrm{T}}\right] \tag{3.63}$$

Recalling: $D=\frac{1}{2}\left(L+L^{\mathrm{T}}\right)$, Eq. (3.63) can be revised as

$$\frac{1}{2}\left(L+L^{\mathrm{T}}\right)=\frac{1}{2}\left(L^{\mathrm{ve}}+L^{\mathrm{ve}\,\mathrm{T}}\right)+\frac{1}{2}\left[\left(F^{\mathrm{ve}}\tilde{L}^{\mathrm{vp}}F^{\mathrm{ve}\,-1}\right)+\left(F^{\mathrm{ve}}\tilde{L}^{\mathrm{vp}}F^{\mathrm{ve}\,-1}\right)^{\mathrm{T}}\right] \tag{3.64}$$

The recent relation can be cut down to the following equation

$$L+L^{\mathrm{T}}=\left[L^{\mathrm{ve}}+\left(F^{\mathrm{ve}}\tilde{L}^{\mathrm{vp}}F^{\mathrm{ve}\,-1}\right)\right]+\left[L^{\mathrm{ve}}+\left(F^{\mathrm{ve}}\tilde{L}^{\mathrm{vp}}F^{\mathrm{ve}\,-1}\right)\right]^{\mathrm{T}} \tag{3.65}$$

Removing the transpose terms, leads to the decoupling of the velocity gradient to viscoelastic and viscoplastic terms

$$L=L^{\mathrm{ve}}+F^{\mathrm{ve}}\tilde{L}^{\mathrm{vp}}F^{\mathrm{ve}\,-1} \tag{3.66}$$

The derivations from Eq. (3.59) to Eq. (3.66) generally confirms that Eq. (2.3) which is usually employed in the second type of finite deformation models is exactly equivalent to Eq. (3.54) which is derived based on additively decomposing the elastic and plastic (or viscoelastic and viscoplastic) portions of the total GL strain. Indeed, Eq. (3.54) admits a multiplicative decomposition of elastic and plastic parts of total deformation, and can be utilized for generalizing infinite deformation models to large deformation range.

3.5 Computations of Green-Lagrange Strain and Strain Rates

3.5.1 Rigid Body Rotation

The concept of polar decomposition in Section 3.1 for the deformation gradient for both elastic and plastic projections, with respect to Eq. (2.3), gives two stretches and two rotations for either elastic or plastic portions. Therefore, when identifying the response of each elastic or plastic deformation, two different components should be investigated: stretch and rotation. Hence, the solution for decomposing the whole deformation will totally face to four tensor ingredients.

Decomposing and finding viscoelastic and viscoplastic rotations separately need more considerations. It is worthy to mention that decoupling elastic and plastic rotations leads to an indeterminate problem. Therefore, it is assumed that the elastic deformations are not affected by plastic flow, which means that the elastic deformation is independent of the history of plastic deformation. This assumption is also physically argumentative, especially for large plastic flow (Nemat-Nasser, 1982), but the influence of plastic on elastic distortion is not considered here.

Moreover, based on Lee (1969) and later Fardshisheh and Onat (1974), it is also assumed that the local rotation does not affect the elastic response. Hence, without loss of generality, all the rotations can be lumped to just the viscoplastic component. Lumped the rotations to the plastic part, the elastic rotation will vanish ($R^{ve} = I$); thus, the elastic deformation gradients will be reduced to just pure stretching. Eq. (3.67) explains the above discussion in mathematical form

$$F = F^{ve}F^{vp} = V^{ve}R^{ve}V^{vp}R^{vp} = \left(V^{ve}V^{vp}\right)R^{vp} = VR \quad , \quad R^{vp} = I \quad , \quad R^{vp} = R^{total} \qquad (3.67)$$

Fig. 3.2 schematically shows the effects of mapping the initial configuration of a domain, through the components of deformation as pure elastic stretching, pure plastic stretching, and total rotation; which all are equivalent to the effect of the total deformation gradient.

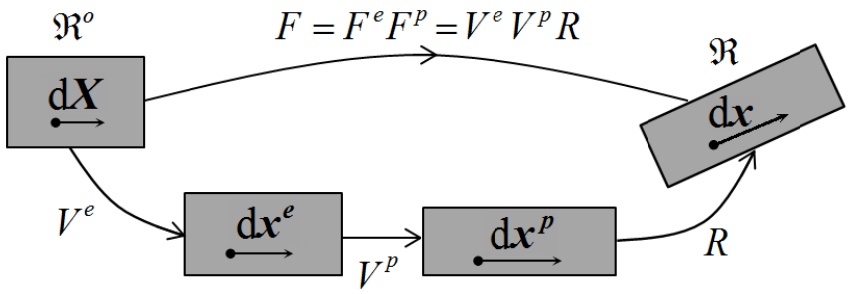

Fig. 3.2. Elastic and plastic stretch and total rigid body rotation on initial configuration of an object compared to total deformation gradient mapping.

Based on continuum mechanics for polar decomposition, the total rotation (that contains both elastic and plastic rotations) can be calculated independent of elastic and plastic deformations, through the following procedure. At first, Left Cauchy-Green deformation tensor ($B = FF^{\mathrm{T}}$), should be obtained

$$B = FF^{\mathrm{T}} = (VR)(VR)^{\mathrm{T}} = VRR^{\mathrm{T}}V = V^2 \qquad \Rightarrow \qquad V = \sqrt{FF^{\mathrm{T}}} \tag{3.68}$$

After calculating the total left stretch tensor, V, the total rotation can be computed as

$$R = V^{-1}F = B^{-1/2}F \tag{3.69}$$

Eq. (3.69) can be straightforwardly computed using the spectral decomposition method for tensor B. The spectral decomposition of the second-order tensor B is

$$B = v\,\lambda v^{\mathrm{T}} \tag{3.70}$$

in which v is a matrix containing the eigenvectors, and λ is a diagonal matrix containing the eigenvalues, with respect to the arrangement of eigenvectors in v. Hereafter, the square root of tensor B will be computed as

$$B^{-1/2} = \left(v\ \lambda v^{\mathrm{T}}\right)^{-1/2} = v\ (\lambda)^{-1/2}\ v^{\mathrm{T}} = v \begin{bmatrix} \lambda_1^{-1/2} & 0 & 0 \\ 0 & \lambda_2^{-1/2} & 0 \\ 0 & 0 & \lambda_3^{-1/2} \end{bmatrix} v^{\mathrm{T}} \tag{3.71}$$

The rotation tensor is exactly and directly calculated based on the polar decomposition concept. Thus, there is no need to compute the increments of rotations through the numerical integration of the rate equations in each analysis time interval. In this work, the total rigid body rotation has been assumed to be constant throughout an increment and its value is equal to the final rotation in that increment, $R_{t+\Delta t}$.

3.5.2 Computing Incremental Strain

Here, the required equations for calculating the increment of GL strain at the current analysis time $(t+\Delta t)$ based on the deformation gradient quantities at the previous and the current time increments, is explained. In small deformation problems, additively upgrading the stresses and strains components is satisfactory, since in small strain case there is not any non-linear term in the strain measure; so, the linear terms can be added or deducted. Furthermore, because the original configuration and all the other incremental configurations are considered as the same; therefore, the additive updating for the stress components is also acceptable. Conversely, in Lagrangian and Eulerian strain tensors, because of the presence of non-linear terms in the definition of these strain measures (the multiplicative terms in the next relations) additive updating is impossible.

$$
\begin{aligned}
E_{IJ} &= \frac{1}{2}\left(\frac{\partial U_I}{\partial X_J}+\frac{\partial U_J}{\partial X_I}\right)+\frac{1}{2}\left(\frac{\partial U_K}{\partial X_I}\frac{\partial U_K}{\partial X_J}\right) \qquad \text{(Lagrangian)} \\
e_{ij} &= \frac{1}{2}\left(\frac{\partial U_i}{\partial x_j}+\frac{\partial U_j}{\partial x_i}\right)-\frac{1}{2}\left(\frac{\partial U_k}{\partial x_i}\frac{\partial U_k}{\partial x_j}\right) \qquad \text{(Eulerian)}
\end{aligned}
\tag{3.72}
$$

Additive updating can be acceptable if and only if the time increment of analysis is very small, where in the multiplication of deformation terms will be practically zero. However, in mathematical form

$$
E_{t+\Delta t} \neq E_t + \Delta E_{t+\Delta t} \quad \text{(Lagrangian)} \qquad , \qquad e_{t+\Delta t} \neq e_t + \Delta e_{t+\Delta t} \quad \text{(Eulerian)} \tag{3.73}
$$

Henceforth, one can track the following technique for computing and/or updating the GL strain at the current time increment. From Eq. (3.46) and Eq. (3.56) the total Lagrangian strain and its time derivative are available as $E_{t+\Delta t}=\frac{1}{2}\left(F_{t+\Delta t}^{\mathrm{T}}F_{t+\Delta t}-I\right)$ and $\dot{E}_{t+\Delta t}=\frac{1}{2}\left[\dot{F}_{t+\Delta t}^{\mathrm{T}}F_{t+\Delta t}+F_{t+\Delta t}^{\mathrm{T}}\dot{F}_{t+\Delta t}\right]$, respectively. Moreover, because the deformation gradient is a mapping tensor, the following sequential multiplicative form for updating the deformation gradient emerges from its definition

$$
F_{t+\Delta t}=\Delta F_{t+\Delta t}\,F_t \qquad \Rightarrow \qquad \dot{F}_{t+\Delta t}=\frac{1}{\Delta t}\left(F_{t+\Delta t}\right)\left(F_t\right)^{-1} \tag{3.74}
$$

Thus, if increment is used rather than rate, the term $\dot{F}^{\mathrm{T}}F$ in this expression can be rewritten as

$$
\dot{F}_{t+\Delta t}^{\mathrm{T}}\,F_{t+\Delta t}=\frac{1}{\Delta t}\left(F_t\right)^{-\mathrm{T}}\left(F_{t+\Delta t}\right)^{\mathrm{T}}\left(F_{t+\Delta t}\right)=\frac{1}{\Delta t}\left(F_t\right)^{-\mathrm{T}}C_{t+\Delta t} \tag{3.75}
$$

Considering the transpose of the recent equation, and $\dot{F}^{\mathrm{T}}F=\left(F^{\mathrm{T}}\dot{F}\right)^{\mathrm{T}}$; hence, one can simply revise the GL strain rate to achieve the increment of Lagrangian strain, as

$$\Delta E_{t+\Delta t} = \frac{1}{2}\left[\left(F_t\right)^{-\mathrm{T}} C_{t+\Delta t} + C_{t+\Delta t} \left(F_t\right)^{-1} \right] \tag{3.76}$$

Therefore, one should find the current right Cauchy-Green tensor, $C_{t+\Delta t} = F_{t+\Delta t}^{\mathrm{T}} F_{t+\Delta t}$, and the inverse of the deformation gradient tensor in the previous time increment to be able to determine the amount of the increment of GL strain from time t to $t+\Delta t$.

The other technique for computing the Lagrangian incremental strain is discussed as next. In this approach, the incremental strain will be found out through the equation of the strains in the current and previous increment and the definition of incremental strain, all according to the deformation gradient and the increment of deformation gradient, as

$$E_{t+\Delta t} = \frac{1}{2}\left(F_{t+\Delta t}^{\mathrm{T}} F_{t+\Delta t} - I\right) \;,\; E_t = \frac{1}{2}\left(F_t^{\mathrm{T}} F_t - I\right) \;,\; \Delta E_{t+\Delta t} = \frac{1}{2}\left(\Delta F_{t+\Delta t}^{\mathrm{T}} \Delta F_{t+\Delta t} - I\right) \tag{3.77}$$

Therefore, one can expand the difference of the current and previous GL strain as

$$E_{t+\Delta t} - E_t = \frac{1}{2}\left(F_{t+\Delta t}^{\mathrm{T}} F_{t+\Delta t} - F_t^{\mathrm{T}} F_t\right) = \frac{1}{2}\left(F_t^{\mathrm{T}} \Delta F_{t+\Delta t}^{\mathrm{T}} \Delta F_{t+\Delta t} F_t - F_t^{\mathrm{T}} F_t\right) \tag{3.78}$$

The recent equation finally delivers the next equality for computing the incremental GL strain (which is utilized in this dissertation)

$$\Delta E_{t+\Delta t} = F_t^{-\mathrm{T}} \left(E_{t+\Delta t} - E_t\right) F_t^{-1} \tag{3.79}$$

This equation means that the incremental GL strain is the defference of the current and previous strain which is transformed backward to the previous converged state. Thus, when F_t and $F_{t+\Delta t}$ are given by FEM software or computed through constitutive equations like $F_{t+\Delta t} = F_{t+\Delta t}^{\mathrm{ve}} F_{t+\Delta t}^{\mathrm{vp}}$, the incremental strain can be found through Eqs. (3.76), (3.77), or (3.79).

3.5.3 Plastic Strain Rate

In this section a relationship for the viscoplastic strain rate, $\dot{E}^{vp}$ is carried out. In small deformation the rate of expansion of the yield surface is written as mentioned in Eq. (3.33). But in finite deformation, the rate of deformation is co-directional with the outward normal to the local smooth yield surface (Hill and Rice, 1973; Lubarda and Benson, 2001), and generally has the following form (similar to Eq. (3.36)

$$D^{vp} = \dot{\lambda}^{vp} \frac{\partial g}{\partial S} \quad , \quad D^{vp} = \frac{1}{2}\left(L^{vp} + L^{vp\,T}\right) = \frac{1}{2}\left[\left(\dot{F}^{vp} F^{vp\,-1}\right) + \left(\dot{F}^{vp} F^{vp\,-1}\right)^{T}\right] \tag{3.80}$$

After finding the rate of stretching tensor, D^{vp}, calculating the viscoplastic deformation gradient, F^{vp}, is required, that the next numerical technique should be followed. Here, it is recalled that: $F^{vp} = V^{vp} R = R U^{vp}$; thus, the general form of the velocity gradient based on its stretch and rotation components is

$$L = \dot{F} F^{-1} = (\dot{R}\dot{U})(RU)^{-1} = (\dot{R}U + R\dot{U})(U^{-1}R^{-1}) \tag{3.81}$$

The velocity gradient and its transpose are simplified and written in the succeeding form

$$L = \dot{R}R^{T} + R\left(\dot{U}U^{-1}\right)R^{T} \quad , \quad L^{T} = R\dot{R}^{T} + R\left(U^{-1}\dot{U}\right)R^{T} \tag{3.82}$$

Therefore, by substituting Eq. (3.82) into Eq. (3.80), the mathematical relation for the rate of deformation tensor may be furnished as

$$2D^{vp} = \left[\dot{R}R^{T} + \left(\dot{R}R^{T}\right)^{T}\right] + R\left(\dot{U}U^{-1} + U^{-1}\dot{U}\right)R^{T} \tag{3.83}$$

Since R is an orthotropic tensor; thus, $\dot{R}R^{T}$ is a skew-symmetric tensor; therefore, the summation in the first bracket will vanish, because

$$RR^{T} = I \quad \Rightarrow \quad (\dot{R}\dot{R}^{T}) = 0 \quad \Rightarrow \quad \dot{R}R^{T} + R\dot{R}^{T} = 0 \tag{3.84}$$

Henceforth, Eq. (3.80) is reduced to

$$2D^{\text{vp}} = R\left(\dot{U}U^{-1} + U^{-1}\dot{U}\right)R^{\text{T}} \tag{3.85}$$

In Eq. (3.83), D^{vp} and the total rotation are known. Thus, in order to calculate the right Cauchy-Green stretch tensor, U^{vp}, a suitable relation for explaining the rate of stretch which depends on the previous and current stretch quantities, has to be found. There exist two ways to solve this equation; one is based on exact integration, and the other one is based on numerical iterative method. For the first solution attempt, it is assumed that in each analysis time increment the multiplication of the incremental stretch and the inverse of stretch (also called pullback stretch) can commute with each other, i.e.

$$\Delta U U^{-1} = U^{-1}\Delta U \tag{3.86}$$

Because a chosen constitutive law is being solved in the essence of discretized incremental approach, the ΔU which maps the previous configuration to the current configuration (just in stretching point of view and not rotation), the ΔU is almost very close to the identity tensor. Based on this assumption, and by replacing Eq. (3.86) into Eq. (3.85) and multiplying both sides to the time increment, the next relation can be achieved

$$2\left(R_{t+\Delta t}\right)\left(\frac{\mathrm{d}U^{\text{vp}}}{U^{\text{vp}}}\right)\left(R_{t+\Delta t}\right)^{\text{T}} = 2D^{\text{vp}}_{t+\Delta t}\,\mathrm{d}t \tag{3.87}$$

Multiplying both sides of Eq. (3.87) to the current rotation and its transpose, the required equation for computing the viscoplastic stretch is obtained

$$\frac{\mathrm{d}U^{\text{vp}}}{U^{\text{vp}}} = \left(R_{t+\Delta t}\right)^{\text{T}}\left(D^{\text{vp}}_{t+\Delta t}\,\mathrm{d}t\right)\left(R_{t+\Delta t}\right) \tag{3.88}$$

At this point, the total current rotation, $R_{t+\Delta t}$, which was calculated by Eq. (3.69) is known, and also D^{vp} has been computed through the chosen plastic constitutive model in Eq. (3.80). Therefore, the quantity of the right hand side of the recent equation is known. Subsequently, in order to calculate the viscoplastic stretch, U^{vp}, one can solve the above tensorial differential equation through the following procedure. For simplicity, in the rest of this section, the RHS of Eq. (3.88) is represented by $\mathbb{X}\,\mathrm{d}t$, which means

$$\mathbb{X}\,\mathrm{d}t = \left[\left(R_{t+\Delta t} \right)^{\mathrm{T}} D^{\text{vp}}_{t+\Delta t} \left(R_{t+\Delta t} \right) \right] \mathrm{d}t \tag{3.89}$$

Integrating both sides of Eq. (3.89), leads to

$$\int_{I}^{U^{\text{vp}}_{t+\Delta t}} \frac{\mathrm{d}U^{\text{vp}}}{U^{\text{vp}}} = \int_{0}^{t+\Delta t} \mathbb{X}\,\mathrm{d}t \quad \Rightarrow \quad \mathrm{Ln}\left(U^{\text{vp}}_{t+\Delta t} \right) - \mathrm{Ln}\left(I \right) = \int_{0}^{t+\Delta t} \mathbb{X}\,\mathrm{d}t \quad \Rightarrow \quad \mathrm{Ln}(U^{\text{vp}}_{t+\Delta t}) = \int_{0}^{t+\Delta t} \mathbb{X}\,\mathrm{d}t$$

$$U^{\text{vp}}_{t+\Delta t} = \exp\left(\int_{0}^{t+\Delta t} \mathbb{X}\,\mathrm{d}t \right) \tag{3.90}$$

By utilizing the recent equation, and splitting up the integral inside the exponential operator, the total stretch tensor, U^{vp}, in the current time increment can be numerically decoupled as

$$U^{\text{vp}}_{t+\Delta t} = \exp\left(\int_{0}^{t} \mathbb{X}\,\mathrm{d}t + \int_{t}^{t+\Delta t} \mathbb{X}\,\mathrm{d}t \right) = \exp\left(\int_{0}^{t} \mathbb{X}\,\mathrm{d}t \right) \cdot \exp\left(\int_{t}^{t+\Delta t} \mathbb{X}\,\mathrm{d}t \right) \tag{3.91}$$

which gives the successive multiplicative updating form as

$$U^{\text{vp}}_{t+\Delta t} = \Delta U^{\text{vp}}_{t+\Delta t}\; U^{\text{vp}}_{t} \tag{3.92}$$

To calculate and update the new viscoplastic stretch tensor, sequential multiplicative method ought to be used

$$U_{t+\Delta t}^{\text{vp}} = \Delta U_{t+\Delta t}^{\text{vp}}\ U_{t}^{\text{vp}} \qquad \text{or} \qquad U_{t+\Delta t}^{\text{vp}} = \Delta U_{t+\Delta t}^{\text{vp}}\ \Delta U_{t}^{\text{vp}} \ldots \Delta U_{\Delta t}^{\text{vp}} \tag{3.93}$$

Therefore, the current viscoplastic stretch tensor is

$$U_{t+\Delta t}^{\text{vp}} = \exp(\mathbb{X}\,\Delta t)\, U_{t}^{\text{vp}} \tag{3.94}$$

Here, the exponent of a second-order tensor must be found out. For this issue, the exponent of a tensor can be computed through the spectral decomposition of a matrix the same as in Eq. (3.70) and (3.71). Thus, the exponent of tensor $\mathbb{X}\,\Delta t$ will be computed as

$$\exp(\mathbb{X}\,\Delta t) = \exp(v\ \lambda v^{\text{T}}) = v\ \exp(\lambda)\, v^{\text{T}} = v \begin{bmatrix} \exp(\lambda_1) & 0 & 0 \\ 0 & \exp(\lambda_2) & 0 \\ 0 & 0 & \exp(\lambda_3) \end{bmatrix} v^{\text{T}} \tag{3.95}$$

On the other hand, the second solution technique for computing the viscoplastic stretch tensor is described here. If the ΔU and U^{-1} cannot commute, then both sides of Eq. (3.85) can be multiplied by the time increment as

$$2\Delta t\, D^{\text{vp}} = R\left(\Delta U^{\text{vp}} U^{\text{vp}\,-1} + U^{\text{vp}\,-1} \Delta U^{\text{vp}}\right) R^{\text{T}} \tag{3.96}$$

Multiplying both sides of Eq. (3.96) by rotation tensors, modifies it as

$$\Delta U^{\text{vp}} U^{\text{vp}\,-1} + U^{\text{vp}\,-1} \Delta U^{\text{vp}} = \mathbb{Y} \qquad , \qquad \mathbb{Y} = 2\Delta t\ \left(R_{t+\Delta t}\right)^{\text{T}} D_{t+\Delta t}^{\text{vp}} \left(R_{t+\Delta t}\right) \tag{3.97}$$

The recent equation can be solved iteratively, because the RHS is computed and known, and by introducing an initial plastic stretch tensor for U^{vp}, the ΔU^{vp} can be calculated through a linear system of equation as

$$\Delta U_{t,\text{k}}^{\text{vp}}\ U_{t,\text{k}}^{\text{vp}\,-1} + U_{t,\text{k}}^{\text{vp}\,-1} \Delta U_{t,\text{k}}^{\text{vp}} = \mathbb{Y} \tag{3.98}$$

where $\mathbf{k}$ is the number of iterations. In the first increment of plasticity, the $U_{t,\mathbf{k}}^{\mathbf{vp}}$ is the identity tensor, and a proper initial value for the plastic stretch tensor in other increments

can be the value of converged stretch tensor in the previous analysis time, i.e. $U^{vp}_{t,0} = U^{vp}_{t-\Delta t}$. The linear algebraic equation for solving Eq. (3.98) is explained in Appendix A. Afterwards, the plastic stretch tensor can be upgraded through one of the following updating procedure

$$U^{vp}_{k+1} = \Delta U^{vp}_{k+1}\, U^{vp}_{k} \tag{3.99}$$

In several papers (Bardenhagen and Kober, 2004; Simo et al., 1985; Voyiadjis et al., 2006), for updating the deformation gradient or stretch tensors, additive correction has been employed (i.e. $F^{vp}_{k+1} = \Delta F^{vp}_{k+1} + F^{vp}_{k}$ or $U^{vp}_{k+1} = \Delta U^{vp}_{k+1} + U^{vp}_{k}$). Additive correction just relates to the incremental motion concept as: $x = X + \nabla u \cdot X$, and is mistakenly used for updating these tensors. In order to upgrade the mapping tensors such as: F, R, and U the sequential multiplicative updating scheme should be used. Nevertheless, additive correction for the mapping tensors is mathematically admissible (since it is the first order approximation of the expansion series) only when the amount of time increment is very small, but small time increment makes the simulations very time costly.

It is obvious that from the algebraic equation system, Eq. (3.98), $\Delta U^{vp}_{t,k}$ can be found and after updating the stretch tensor through Eq. (3.99), for the next iteration, $U^{vp}_{t,k}$ must be inversed. Once the viscoplastic stretch tensor is calculated, the viscoplastic deformation gradient can be easily found by polar decomposition formula: $F^{vp} = RU^{vp}$. Subsequently, utilizing Eq. (3.58) delivers the viscoplastic strain rate.

3.5.4 Elastic Strain Rate

In order to use Eq. (3.54) for finding the total strain rate, one needs to find the viscoelastic strain rate, $\dot{E}^{\text{ve}}$, as well. By using Eq. (3.47), and recalling that the elastic rotation has been lumped to the plastic part; the viscoelastic strain rate can be derived in the following form

$$E^{\text{ve}} = \frac{1}{2}\left(F^{\text{ve T}} F^{\text{ve}} - I\right) = \frac{1}{2}\left(U^{\text{ve}\,2} - I\right) \quad \text{and} \quad F^{\text{ve}} = R^{\text{ve}} U^{\text{ve}} = U^{\text{ve}} \;,\; R^{\text{ve}} = I \tag{3.100}$$

Thus, the total viscoelastic stretch is driven by

$$U^{\text{ve}}_{t+\Delta t} = \sqrt{I + 2E^{\text{ve}}_{t+\Delta t}} \tag{3.101}$$

Now, the material time derivation can be simply applied to the total elastic strain in Eq. (3.100), which delivers

$$\dot{E}^{\text{ve}} = \frac{1}{2}\left[\left(U^{\text{ve}}\dot{U}^{\text{ve}}\right) + \left(U^{\text{ve}}\dot{U}^{\text{ve}}\right)^{T}\right] \tag{3.102}$$

Thus, $\dot{U}^{\text{ve}}$ should be found by utilizing the successive multiplication updating method, which provides the rate of mapping tensor (here rate of stretch) through projecting backward by the previous tensor and then projecting forward by the current tensor

$$\dot{U}_{t+\Delta t} = \frac{1}{\Delta t} U_{t+\Delta t}\, U_t^{-1} \tag{3.103}$$

From Eq. (3.102) and (3.103), it may be concluded that

$$\dot{E}^{\text{ve}} = \frac{1}{2\Delta t}\left[\left(U^{2}_{t+\Delta t}\, U_t^{-1}\right) + \left(U^{2}_{t+\Delta t}\, U_t^{-1}\right)^{T}\right] = \frac{1}{\Delta t}\,\text{symm}\left[U^{2}_{t+\Delta t}\, U_t^{-1}\right] \tag{3.104}$$

Since E^{ve}, $\dot{E}^{\text{ve}}$, $\dot{E}^{\text{vp}}$, F^{vp}, and $\dot{F}^{\text{vp}}$ have been found; the rate of total GL strains can be calculated based on Eq. (3.54).

3.5.5 Upgrading Lagrangian Strain

As mentioned in Section 3.5, the Lagrangian or Eulerian strains cannot be updated by additive corrections. Here, the required equations for updating the GL strain at the current time, $t+\Delta t$, based on the increment of the GL strain at the current time, and the deformation gradient at the previous time, t, is described. Recalling Eq. (3.76), since $\Delta E_{t+\Delta t}$ has been calculated by a selected constitutive model, and also the deformation gradient in the previous time increment is known (previous converged configuration); therefore, Eq. (3.76) is reduced to a system of linear equations and can be solved for computing $C_{t+\Delta t}$. The right Cauchy-Green deformation tensor is symmetric and has six independent components, thus a sparse algebraic equation system is preferred to solve it. In the following the solution for the sparse system is presented. For computing $C_{t+\Delta t}$, the off diagonal components C_{12}, C_{13}, and C_{23} can be calculated at first by using Eq. (3.105) and Eq. (3.106):

$$\begin{bmatrix} A_{11} & A_{12} & A_{13} \\ A_{21} & A_{22} & A_{23} \\ A_{31} & A_{32} & A_{33} \end{bmatrix} \begin{bmatrix} C_{12} \\ C_{13} \\ C_{23} \end{bmatrix} = \begin{bmatrix} 2f_{11}f_{22}\Delta E_{21} - f_{12}f_{22}\Delta E_{11} - f_{21}f_{11}\Delta E_{22} \\ 2f_{11}f_{33}\Delta E_{31} - f_{13}f_{33}\Delta E_{11} - f_{31}f_{11}\Delta E_{33} \\ 2f_{22}f_{33}\Delta E_{32} - f_{23}f_{33}\Delta E_{22} - f_{32}f_{22}\Delta E_{33} \end{bmatrix} \tag{3.105}$$

$$\begin{aligned} &A_{11} = (f_{11}+f_{22})(f_{11}f_{22}-f_{12}f_{21}) \qquad A_{12} = f_{22}(f_{11}f_{32}-f_{31}f_{12}) \qquad A_{13} = f_{11}(f_{31}f_{22}-f_{32}f_{21}) \\ &A_{21} = f_{33}(f_{11}f_{23}-f_{21}f_{13}) \qquad A_{22} = (f_{11}+f_{33})(f_{11}f_{33}-f_{13}f_{31}) \qquad A_{23} = f_{11}(f_{21}f_{33}-f_{23}f_{31}) \\ &A_{31} = f_{33}(f_{13}f_{22}-f_{12}f_{23}) \qquad A_{32} = f_{22}(f_{12}f_{33}-f_{13}f_{32}) \qquad A_{33} = (f_{22}+f_{33})(f_{22}f_{33}-f_{32}f_{23}) \end{aligned} \tag{3.106}$$

where for the sake of simplicity f_{ij} are the components of the second order tensor F_t^{-1}. Secondly, the three diagonal components of the right Cauchy-Green deformation tensor can be found as

$$
\begin{aligned}
C_{11} &= \left[\Delta E_{11} - C_{12} f_{21} - C_{13} f_{31}\right] / f_{11} \\
C_{22} &= \left[\Delta E_{22} - C_{12} f_{12} - C_{23} f_{32}\right] / f_{22} \\
C_{33} &= \left[\Delta E_{33} - C_{13} f_{13} - C_{23} f_{23}\right] / f_{33}
\end{aligned}
\tag{3.107}
$$

After computing $C_{t+\Delta t}$, through Eq. (3.46) the GL strain can be easily calculated. This method can be used when the time increment is very small. Otherwise the second method should be used.

The second technique for computing GL strain at the current time ($t+\Delta t$), is explained here. Integrating both sides of Eq. (3.76) (in the rate form) leads to find the increment of strain for a typical time, t, as

$$
2 \int_{t}^{t+\Delta t} \dot{E}_t \, \mathrm{d}t = \int_{t}^{t+\Delta t} \dot{F}_t^{\mathrm{T}} F_t + F_t^{\mathrm{T}} \dot{F}_t \, \mathrm{d}t \tag{3.108}
$$

In order to compute the integration over the rate of deformation, $\dot{F}_t$, iterative scheme should be hired, since the integration cannot be applied to only the rate of tensors

$$
2 \int_{t}^{t+\Delta t} \dot{E}_\tau \, \mathrm{d}\tau \neq \int_{t}^{t+\Delta t} \dot{F}_\tau^{\mathrm{T}} \mathrm{d}\tau \; F_\tau + F_\tau^{\mathrm{T}} \int_{t}^{t+\Delta t} \dot{F}_\tau \, \mathrm{d}\tau \quad \text{or} \quad 2\Delta E_t \neq \Delta F_t^{\mathrm{T}} F_t + F_t^{\mathrm{T}} \Delta F_t \tag{3.109}
$$

In large deformation concept, contrary to small deformation, converting a rate to its identical increment is not achievable by multiplying the time increment to the rate. Actually, the rate must be integrated over the chosen time span to provide the increment of the desired quantity. Thus, to compute the deformation gradient increment, the integration should be discretized as

$$
\Delta F_{t+\Delta t} = \int_{t}^{t+\Delta t} \dot{F}_{t+\Delta t} \, \mathrm{d}t \approx \sum_{\mathrm{k}=1}^{N} \dot{F}_{t+\Delta t}^{(\mathrm{k})} \, \Delta t_{\mathrm{k}} \tag{3.110}
$$

where the subscript k is the iterations for updating $F_{t+\Delta t}$. Butr, Eq. (3.110) can be used just when the time increment is very small. Fig. 3.3 graphically illustrates this iterative method for updating the deformation gradient based on its rate. The solid lines have physical meanings that are the converged updated configurations, whereas the dotted ones represent the non-equilibrated configurations, which only have numerical existence.

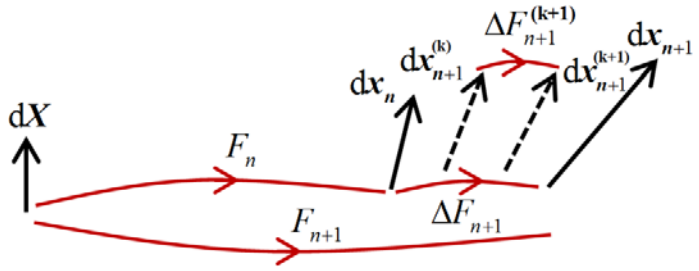

Fig. 3.3. Graphical depiction for iteratively updating deformation gradient tensor.

Therefore, the following discretization for computing the integral form is considered:

$$\int_{t}^{t+\Delta t} \dot{F}_t^{\mathrm{T}} F_t \, \mathrm{d}t \approx \sum_{\mathrm{k}=1}^{N} \dot{F}_{t+\Delta t}^{(\mathrm{k})^{\mathrm{T}}} F_{t+\Delta t}^{(\mathrm{k})} \, \Delta t_{\mathrm{k}} \tag{3.111}$$

where $N = \big((t+\Delta t)-t\big)/\Delta t_{\mathbf{k}}$ is the number of time span divisions between t and $t+\Delta t$. Also, $F_{t+\Delta t}^{(\mathbf{0})} = F_t$ and $F_{t+\Delta t}^{(\mathbf{N})} = F_{t+\Delta t}$; thus, Eq. (3.108) may be written in discretized form

$$2\Delta E_{t+\Delta t} = \sum_{\mathbf{k=1}}^{\mathbf{N}} \dot{F}_{t+\Delta t}^{(\mathbf{k})^{\mathbf{T}}} F_{t+\Delta t}^{(\mathbf{k})} \, \Delta t_{\mathbf{k}} + \sum_{\mathbf{k=1}}^{\mathbf{N}} F_{t+\Delta t}^{(\mathbf{k})^{\mathbf{T}}} \dot{F}_{t+\Delta t}^{(\mathbf{k})} \, \Delta t_{\mathbf{k}} \tag{3.112}$$

The rate of deformation gradient in each time span is defined as

$$\dot{F}_{t+\Delta t}^{(\mathbf{k})} = \frac{1}{\Delta t_{\mathbf{k}}} \Delta F_{t+\Delta t}^{(\mathbf{k})} = \frac{1}{\Delta t_{\mathbf{k}}} F_{t+\Delta t}^{(\mathbf{k})} \, F_{t+\Delta t}^{(\mathbf{k}\text{-}\mathbf{1})^{-1}} \tag{3.113}$$

For simplifying Eq. (3.112), one can modify the second term of this equation by considering the result of Eq. (3.113) as

$$F_{t+\Delta t}^{(k)^T}\dot{F}_{t+\Delta t}^{(k)}\ \Delta t_k = F_{t+\Delta t}^{(k)^T}\Delta F_{t+\Delta t}^{(k)} = F_{t+\Delta t}^{(k)^T}F_{t+\Delta t}^{(k)}\ F_{t+\Delta t}^{(k-1)^{-1}} = C_{t+\Delta t}^{(k)}\ F_{t+\Delta t}^{(k-1)^{-1}} \tag{3.114}$$

Moreover, since the two summation terms in Eq. (3.112) are the transpose of each other, this equation can be rewritten as

$$2\Delta E_{t+\Delta t} = \sum_{k=1}^{N}\left(F_{t+\Delta t}^{(k-1)^{-T}} C_{t+\Delta t}^{(k)} + C_{t+\Delta t}^{(k)}\ F_{t+\Delta t}^{(k-1)^{-1}}\right) \quad \text{or} \quad \Delta E_{t+\Delta t} = \text{symm}\sum_{k=1}^{N} F_{t+\Delta t}^{(k-1)^{-T}} C_{t+\Delta t}^{(k)} \tag{3.115}$$

The required steps for iteratively computing $C_{t+\Delta t}$ and updating the GL strain is demonstrated as a flow chart in Fig. 3.4.

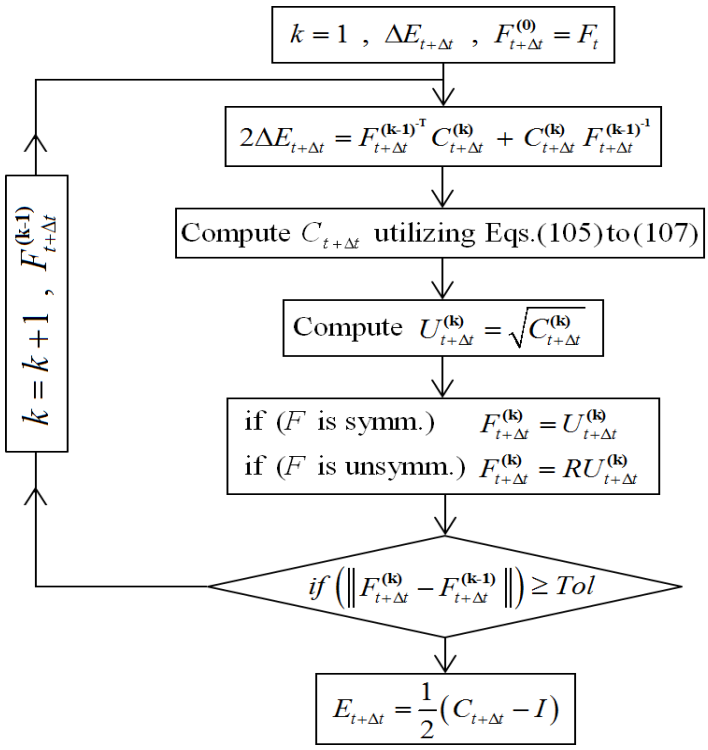

Fig. 3.4. Iterative procedure for updating GL strain, based on the quantity of GL strain increment and the previous deformation gradient.

The third approach for computing the GL strain at the current time is also elaborated here. Dissimilar to Eqs. (3.112) to (3.115), here the components of the rate of deformation gradient are not substituted in the formula. Hence, by following the same iterative procedure for calculating the deformation gradient in Eq. (3.115), one can get

$$2\Delta E_{t+\Delta t} = \sum_{\mathbf{k=1}}^{\mathbf{N}} \left(\Delta F_{t+\Delta t}^{\mathbf{T}} \, F_{t+\Delta t}^{(\mathbf{k})} + F_{t+\Delta t}^{(\mathbf{k})^{\mathbf{T}}} \, \Delta F_{t+\Delta t} \right) \tag{3.116}$$

where the superscript $\mathbf{k}$ is the number of iterations. Similar to Eq. (3.76), Eq. (3.116) will be reduced to a linear system of equations and can be solved for $\Delta F_{t+\Delta t}$. To solve the recent algebraic equation, the same procedure as explained in Eqs. (3.105) to (3.107) can be utilized by just switching the two variables; tensor C should be interchanged by ΔF and also $F_{t+\Delta t}^{(\mathbf{k})}$ by f. The initial value for $F_{t+\Delta t}$ is the deformation gradient tensor in the last converged increment: $F_{t+\Delta t}^{(\mathbf{0})} = F_t$. Now, after computing $\Delta F_{t+\Delta t}$ based on $\Delta E_{t+\Delta t}$ and $F_{t+\Delta t}^{(\mathbf{k})}$, for the next iteration the deformation gradient, $F_{t+\Delta t}^{(\mathbf{k+1})}$, needs to be updated as

$$F_{t+\Delta t}^{(\mathbf{k+1})} = \Delta F_{t+\Delta t} \, F_{t+\Delta t}^{(\mathbf{k})} \tag{3.117}$$

Once more, similar to Eq. (3.99), both additive and multiplicative upgrading for tensor F is possible, and the additive one is acceptable just when the time increment is very small. By repeating the iterations the deformation gradient tensor will be upgraded, and eventually the total Lagrangian strain can be found by Eq. (3.46).

The third method looks to be capable to find and update the deformation gradient if this tensor, F, is symmetric. In other words, it should be just pure stretch, because the $\Delta F_{t+\Delta t}$ tensor has nine independent components and $\Delta E_{t+\Delta t}$ is symmetric and gives six

independent linear equations. But, this system of equation gives a symmetric $\Delta F_{t+\Delta t}$ in all iterations, and then the deformation gradient will be updated through

$$F_{t+\Delta t} = \left(\prod_{\mathbf{k=1}}^{\mathbf{N}} \Delta F_{t+\Delta t}^{(\mathbf{k})} \right) F_t = \left(\Delta F_{t+\Delta t}^{(\mathbf{N})} \; \Delta F_{t+\Delta t}^{(\mathbf{N-1})} \cdots \Delta F_{t+\Delta t}^{(\mathbf{1})} \right) F_t \tag{3.118}$$

Even though each $\Delta F_{t+\Delta t}^{(\mathbf{k})}$ is symmetric, the multiplications of these symmetric tensors, in general, are non-symmetric. Moreover, if the outcome of these multiplications is symmetric the multiplication by F_t may be again symmetric or non-symmetric. The symmetry concept of F_t comes from the geometrical change of deformation.

However, the forth and easiest technique is similar to Eq. (3.79) (which is for computing incremental GL strain). According to Eq. (3.79) the GL strain at the current time is found by transforming the current incremental strain to the previous converged state and then is added to the previous strain tensor. It means strains should in the same deformation state, in order to be summable.

$$\Delta E_{t+\Delta t} = F_t^{-\mathrm{T}} \left(E_{t+\Delta t} - E_t \right) F_t^{-1} \qquad \Rightarrow \qquad E_{t+\Delta t} = F_t^{\mathrm{T}} \left(\Delta E_{t+\Delta t} \right) F_t + E_t \tag{3.119}$$

3.5.6 Decomposing Finite Volumetric and Deviatoric Strains

In order to generalize a small strain constitutive model to a large deformation one, there exist some other concerns that should be taken into account. In many small strain constitutive relations, the strains and stresses are conventionally separated to volumetric and deviatoric quantities. In finite deformation context, the volumetric and deviatoric separation of strains and stresses are also required, but they do not obey the same relation in small strain. Actually in finite strain concept, the volumetric measure is

a tensor and not scalar, and volumetric and deviatoric tensors should be multiplicatively decomposed. Converting and utilizing multiplicative form for volumetric and deviatoric strains make some difficulties in mathematical formulations. Thus, it is more convenient to preserve the additive form even for generalizing small to large deformation models.

From continuum mechanics (Flory, 1961; Lubliner, 1986; Sidoroff, 1974; Simo and Ortiz, 1985), and according to the Hu-Washizu variational principal, the stretch tensor in polar decomposition can be multiplicatively split-up to deviatoric stretch, U_D, (volume preserving), and volumetric stretches, U_V (dilatational). These components are explained in Eq. (3.120) and schematically illustrated in Fig. 3.5. Here, the deviatoric deformation is also called isochoric, which means deformation at constant volume.

$$F = RU = RU_{\mathrm{D}}U_{\mathrm{V}} \tag{3.120}$$

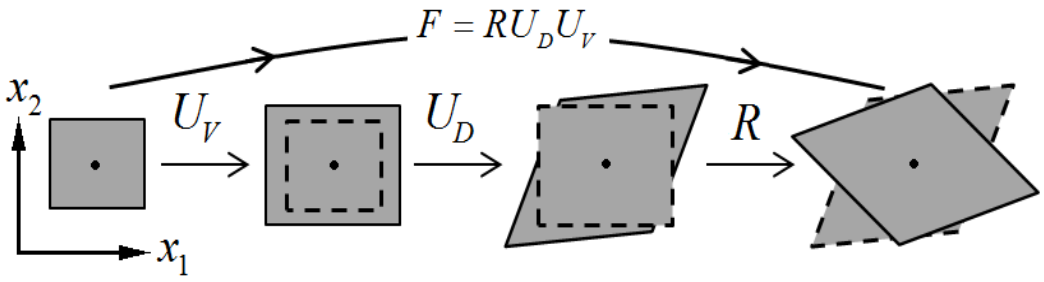

Fig. 3.5. Illustration the components of total deformation gradient projection: volumetric expansion, deviatoric deformation, and rigid body rotation on a rectangular sample.

Here, the same as Eq. (3.42), R is the total rigid body rotation. Based on the recent equation, the right Green-Cauchy tensor will have the following form

$$F^{\mathrm{T}}F = \left(RU_{\mathrm{D}}U_{\mathrm{V}}\right)^{\mathrm{T}}\left(RU_{\mathrm{D}}U_{\mathrm{V}}\right) = U_{\mathrm{V}}U_{\mathrm{D}}\left(R^{\mathrm{T}}R\right)U_{\mathrm{D}}U_{\mathrm{V}} = U_{\mathrm{V}}U_{\mathrm{D}}^{2}U_{\mathrm{V}} \tag{3.121}$$

Thus, Eq. (3.46) can be used to find the volumetric and deviatoric parts of GL strain, as

$$E_{\mathrm{V}} = \frac{1}{2}\left(U_{\mathrm{V}}^{2} - I\right) \qquad , \qquad E_{\mathrm{D}} = \frac{1}{2}\left(U_{\mathrm{D}}^{2} - I\right) \tag{3.122}$$

Now, in order to find the relation between volumetric and deviatoric quantities of Lagrangian strain, the same procedure from Eqs. (3.50) to (3.55) can be used:

$$E - E_{\mathrm{V}} = \frac{1}{2}\left(U_{\mathrm{V}} U_{\mathrm{D}}^{2} U_{\mathrm{V}} - I\right) - \frac{1}{2}\left(U_{\mathrm{V}}^{2} - I\right) \tag{3.123}$$

Utilizing Eq. (3.122) and (3.123), one can obtain the following decomposition for volumetric and deviatoric Lagrangian strains

$$E = U_{\mathrm{V}}\left(E_{\mathrm{D}}\right)U_{\mathrm{V}} + E_{\mathrm{V}} \tag{3.124}$$

Based on the current derivations, some other useful equations are presented that are proper to be hired in incremental techniques for computing the GL strain from its volumetric and deviatoric components. For this case, the time derivation of the total Lagrangian strain in Eq. (3.124) in comparison to Eq. (3.51), leads to an equivalent relation similar to Eq. (3.54) and (3.55). Hence, the same route as mentioned in Eqs. (3.51) to (3.55) is followed to find the decomposition of the incremental GL strain based on the increment of volumetric and deviatoric parts; and can be formulated as

$$\Delta E = U_{\mathrm{D}}\left[\Delta E_{\mathrm{V}} + 2\,\mathrm{symm}\left(E_{\mathrm{V}} \Delta U_{\mathrm{D}} U_{\mathrm{D}}^{-1}\right)\right]U_{\mathrm{D}} + \Delta E_{\mathrm{D}} \tag{3.125}$$

Or in the other form, it may be expressed as

$$\Delta E = U_{\mathrm{D}}\left[\Delta E_{\mathrm{V}} + \left(U_{\mathrm{D}}^{-1} U_{\mathrm{V}}\right)^{\mathrm{T}} \Delta E_{\mathrm{D}} \left(U_{\mathrm{D}}^{-1} U_{\mathrm{V}}\right)\right]U_{\mathrm{D}} \tag{3.126}$$

Moreover, if volumetric stretch has a spherical form like: $U_{\mathrm{V}} = v\, I$, where the variable v is the value of volumetric change; then, one can simplify Eq. (3.126) as following

$$\Delta E = U_{\mathrm{D}}\left(\Delta E_{\mathrm{V}}\right)U_{\mathrm{D}} + \left(\Delta E_{\mathrm{D}}\right)v^{2} \tag{3.127}$$

These equations are correct just when the time increment is small enough for converting rate to increment. While generalizing a small-strain model to finite deformation, the above decoupling approach in Eqs. (3.125) and (3.126) can be employed, but they are computationally very expensive; therefore, it is recommended to avoid using them through generalization (if possible). However, pure additive decomposition is also possible, provided that the volumetric strain is small enough not to affect the pure distortional deformation (Bažant, 1996). Additively partitioning the strain can greatly simplify the finite-strain generalization for a selected small-strain model. GL strain is a special case of a general formula set for Lagrangian strain tensors (Fu and Ogden, 2001; Hill, 1968):

$$E^{(m)} = \frac{1}{2m}\left(U^{(2m)} - I\right) \tag{3.128}$$

which is also a subset of a more general case of finite strain measure, called Doyle-Ericksen tensors (Bažant and Cedolin, 2010; Doyle and Ericksen, 1956):

$$\text{when } m \neq 0: \quad \varepsilon^{(m)} = m^{-1}\left(U^{m} - I\right) \quad , \quad \text{when } m = 0: \quad \varepsilon^{(m)} = \mathrm{Ln}(U) \tag{3.129}$$

To split-up the volumetric and deviatoric strains, Eq. (3.120) should be substituted into the right Cauchy-Green deformation tensor, $C = F^{\mathrm{T}}F$. Thus, tensor C is written as

$$F^{\mathrm{T}}F = \left(U_{\mathrm{V}}^{\mathrm{T}}U_{\mathrm{D}}^{\mathrm{T}}R^{\mathrm{T}}\right)\left(R\,U_{\mathrm{D}}U_{\mathrm{V}}\right) = J^{2/3}U_{\mathrm{D}}^{2} \quad , \quad U_{\mathrm{V}} = \sqrt[3]{J}\,I \tag{3.130}$$

Henceforth, the general formula of Lagrangian strain tensor can be modified as

$$\varepsilon^{(m)} = m^{-1}\left[\left(J^{2/3}U_{\mathrm{D}}^{2}\right)^{m/2} - I\right] = m^{-1}\left[J^{m/3}U_{\mathrm{D}}^{m} - I\right] \tag{3.131}$$

This equation can be simply factorized, and the finite strain tensor is additively decomposed to volumetric and deviatoric (isochoric) tensors, as

$$\varepsilon^{(m)} = \varepsilon_{\mathrm{V}}^{(m)} + \varepsilon_{\mathrm{D}}^{(m)} \quad , \quad \varepsilon_{\mathrm{V}}^{(m)} = m^{-1}\left(J^{m/3} - 1\right)I \quad , \quad \varepsilon_{\mathrm{D}}^{(m)} = m^{-1}J^{m/3}\left(U_{\mathrm{D}}^{m} - I\right) \tag{3.132}$$

The $\varepsilon_{\mathrm{D}}^{(m)}$ is more appropriate to be called isochoric, since its trace is not equal to zero. It is noteworthy to mention that additive decomposition in Eq. (3.132) (the third relation) is still affected by volumetric changes, since it depends on the value of J. Additive partitioning of large strain is proper and applicable; however, it is limited to moderately large strains (up to about 10%) (Bažant et al., 2000).

Up to this point, the decomposition of volumetric and deviatoric GL strain has been discussed. However, during implementation, one should be able to systematically compute the volumetric and deviatoric incremental strains in each time span. In this case Eqs. (3.77) or (3.79) should be followed, and the key point is at first computing the volumetric incremental strain. Hence, based on Eq. (3.79), it can be found as

$$\Delta E_{t+\Delta t}^{\mathrm{vol}} = F_t^{\mathrm{vol}\,-\mathrm{T}}\left(E_{t+\Delta t}^{\mathrm{vol}} - E_t^{\mathrm{vol}}\right)F_t^{\mathrm{vol}\,-1} \tag{3.133}$$

Also, based on Eq. (3.130), the GL volumetric strain is

$$F_t^{\mathrm{vol}} = U_t^{\mathrm{vol}} = J_t^{1/3}I \quad , \quad C_t^{\mathrm{vol}} = J_t^{2/3}I \quad \Rightarrow \quad E_t^{\mathrm{vol}} = \frac{1}{2}\left(J_t^{2/3} - 1\right)I \tag{3.134}$$

In this case, it is assumed that the volumetric deformation does not contain the rigid body rotation ($F^{\mathrm{vol}} = U^{\mathrm{vol}}$). Now, substituting the recent equation into Eq. (3.133) provides the increment of volumetric GL strain, as

$$\Delta E_{t+\Delta t}^{\mathrm{vol}} = \frac{1}{2}\left(J_{t+\Delta t}^{2/3} - J_t^{2/3}\right)\left(F_t^{\mathrm{vol}}F_t^{\mathrm{vol}^{\mathrm{T}}}\right)^{-1} = \frac{1}{2}\left(\left(J_t^{-1}J_{t+\Delta t}\right)^{2/3} - 1\right)I \tag{3.135}$$

Then, the deviatoric portion of the incremental strain can be found through its exact definition as

$$\Delta E^{\text{dev}}_{t+\Delta t} = F_t^{\text{dev}\,-\mathrm{T}} \left(E^{\text{dev}}_{t+\Delta t} - E^{\text{dev}}_{t} \right) F_t^{\text{dev}\,-1} \tag{3.136}$$

The distortional part of the deformation gradient is $F^{\text{dev}} = F\, F^{\text{vol}\,-1}$; thus, according to Eq. (3.136) and the increment of deformation gradient ($\Delta F_{t+\Delta t} = F_{t+\Delta t}\, F_t^{\,-1}$), one can get

$$\Delta E^{\text{dev}}_{t+\Delta t} = \frac{1}{2}\left[\Delta J^{-2/3}_{t+\Delta t} \left(\Delta F^{\mathrm{T}}_{t+\Delta t} \Delta F_{t+\Delta t} \right) - I \right] \tag{3.137}$$

After rephrasing the terms in this equation, the incremental deviatoric strain will be achieved as

$$\Delta E^{\text{dev}}_{t+\Delta t} = \Delta J^{-2/3}_{t+\Delta t} \left[\Delta E_{t+\Delta t} - \Delta E^{\text{vol}}_{t+\Delta t} \right] \tag{3.138}$$

The next flowchart (Fig. 3.6) explains the procedure for calculating the incremental volumetric and deviatoric strains.

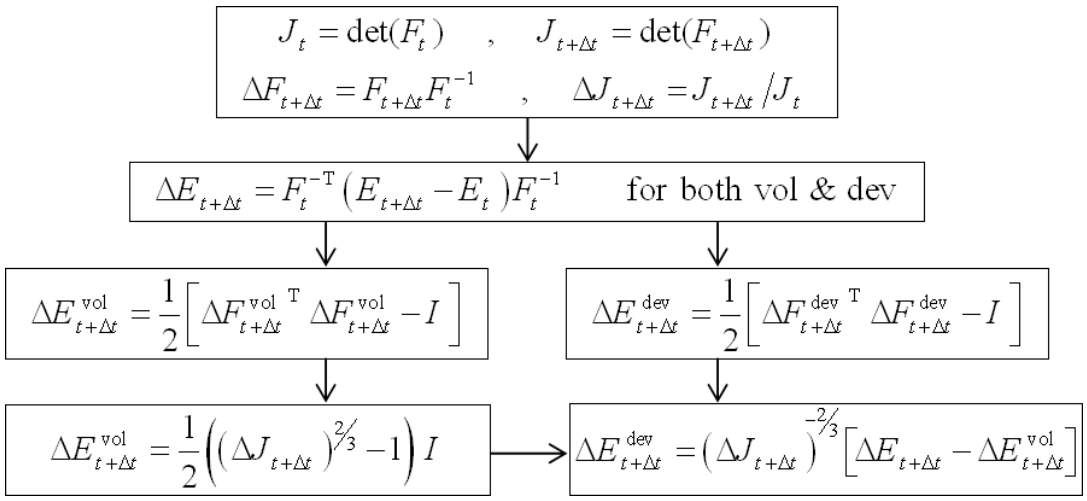

Fig. 3.6. Sequences for computing the incremental portions of volumetric and deviatoric GL strain based on the quantity of previous and current deformation gradient tensors.

3.6 Second Piola-Kirchhoff Stress Calculations

3.6.1 Decomposition to Volumetric and Deviatoric Portions

In many applications (e.g. soil mechanics and biomechanics) the hydrostatic pressure and distortional components of Cauchy stress are split up. Similar decomposition, with the purpose of decoupling the volumetric and deviatoric (isochoric) quantities of second Piola-Kirchhoff stress, in large deformation generalization is required, as well. From continuum mechanics (Holzapfel et al., 2000; Liefeith and Kolling, 2007) the II-PK stress can be written as

$$S = JF^{-1}\sigma F^{-\mathrm{T}} = JF^{-1}\sigma F^{-\mathrm{T}}\mathbb{P} + J\rho C^{-1} \quad , \quad \mathbb{P} = \mathbb{I} - \frac{1}{3}C \otimes C^{-1} \quad , \quad S = S^{\mathrm{iso}} + S^{\mathrm{vol}} \qquad (3.139)$$

where $\{\mathbb{I}\}_{ijkl} = \left[\delta_{ik}\delta_{jl} + \delta_{il}\delta_{jk}\right]/2$ is the fourth-order identity tensor, and $\mathbb{P}$ is the fourth-order projection tensor that provides the deviatoric operand in the reference state. $\rho = \mathrm{d}U/\mathrm{d}J$, and function U is a purely volumetric contribution in the Helmholtz free energy, and $J = \det(F)$. It comes from Coleman's method, that the II-PK stress is derived from the free energy function according to (Holzapfel, 2000)

$$S = \frac{\partial \psi}{\partial E} = 2\frac{\partial \psi}{\partial C} = 2\partial_C\left(\psi^{\mathrm{iso}} + \psi^{\mathrm{vol}}\right) = S^{\mathrm{iso}} + S^{\mathrm{vol}} \qquad (3.140)$$

where: $S^{\mathrm{vol}} = \rho J C^{-1}$, $S^{\mathrm{iso}} = J^{-2/3}\,\mathrm{DEV}\left(\frac{\partial \psi}{\partial E}\right)$, $\mathrm{DEV}(X) = X - \frac{1}{3}[X : C]C^{-1}$. Here ρ is a Lagrange multiplier that enforces the isochoric motion (Baek et al., 2007). Altenbach and Altenbach (1995) mentioned the easiest way to extend the linear elastic response of a material from infinitesimal to large deformation is exchanging the small strain ε_{ij}, by GL strain tensor E_{ij} in the corresponding (isothermal) strain-energy density

$$w(\varepsilon_{ij}) = \frac{\lambda}{2}\left(\varepsilon_{kk}\right)^2 + \mu\ \varepsilon_{ij}\varepsilon_{ji} \qquad \rightarrow \qquad w(E_{ij}) = \frac{\lambda}{2}\left(E_{kk}\right)^2 + \mu\ E_{ij}E_{ji} \tag{3.141}$$

where λ and μ are Lame constants. This strain-energy density is known as Saint Venant-Kirchhoff. Such strain-energy density is a postulated scalar-valued function on one tensorial variable. Therefore, the definition of the II-PK stress (beside volumetric and deviatoric quantities) and its relation with GL strain is

$$S_{ij} = \frac{\partial w}{\partial E_{ij}} = 2\frac{\partial w}{\partial C_{ij}} \qquad , \qquad S_{ij} = \lambda E_{kk}\delta_{ij} + 2\mu E_{ij} \tag{3.142}$$

Another illustration of an elastic constitutive relation for isotropic materials in finite strain range may be written as (Bažant et al., 2000)

$$S_{ij} = 3KE_{ij}^{\mathrm{V}} + 2\mu E_{ij}^{\mathrm{D}} \qquad , \qquad K = \lambda + 2\mu \tag{3.143}$$

Note that here, the material constant K is formally comparable to the bulk modulus, but does not have the same physical meaning, since in large deformation the trace of GL strain is not equal to the change of volume. Moreover, if there is not defined any strain-energy density, through substituting the decoupled Cauchy stress into the definition of II-PK stress, one can come up with the next decoupling

$$S = JF^{-1}\left(\sigma^{\mathrm{dev}} + \sigma^{\mathrm{vol}}\right)F^{-T} = S^{\mathrm{dev}} + J\rho C^{-1} \tag{3.144}$$

It is noteworthy to mention although $\mathrm{tr}(\sigma^{\mathrm{dev}}) = 0$, the trace of S^{dev} is not zero because of the inverse and inverse-transpose of deformation gradient tensors (Bonet and Wood, 1997). But, the trace operator may be converted to double contractions with respect to $\mathrm{tr}(A^{\mathrm{T}}B) = A:B$; thus, the following relation is achieved: $S^{\mathrm{dev}}:C = 0$. This result

enables the hydrostatic pressure portion to be calculated, and the decoupling of II-PK stress has the following form

$$S = JF^{-1}\sigma_{\mathrm{Dev}}F^{-\mathrm{T}} + \frac{1}{3}(S:C)C^{-1} \tag{3.145}$$

3.6.2 Updating Stress Measure

As mentioned in continuum mechanics (Bower, 2009), Cauchy stress is the best actual measure of internal forces (force per unit area) acting inside a deformed object. Other stress measures are work-conjugate (or energy-conjugate) to other strain or rate of deformation, meaning that the multiplication of stress by the time derivative of the related strain (or rate of deformation) measure, gives the rate of work-done by the forces (Bower, 2009; Dvorkin, 2010). Also, because GL strain is naturally work-conjugate to the II-PK stress, and they have been widely used in the constitutive models based on finite deformation concepts; therefore, in this section, updating the II-PK in a general form is explained. Governing equations generally should be linearized and solved by incrementally iterative methods, because the tangent stiffness matrix is non-linear with respect to displacement components. To derive linearized incremental equations, in small-strain notion, the Cauchy stress is updated by accumulating the current stress increment to the previous converged stress, which is well-known as

$$\sigma_{t+\Delta t} = \sigma_t + \Delta\sigma_{t+\Delta t} \tag{3.146}$$

When a constitutive model is written based on large strain and its stress pair, in all computational iterations the stress tensor should be upgraded, as well. Bathe et al. (1975) mentioned that for updating II-PK stress (in total Lagrangian formulation) only the

incremental tensor of stress (and even GL strain) must be added to the previous coverged stress state. But, mathematically it is not possible. In this section, it is basically shown that such additive updating is not exact and even truthful to update the II-PK stress similar to small deformation (like Eq. (3.146)), it means that: $S_{t+\Delta t} \neq S_t + \Delta S_{t+\Delta t}$. Thus for this issue, the definition of the II-PK stress in continuum mechanics should be revisited

$$S_{t+\Delta t} = J_{t+\Delta t}\, F^{-1}_{t+\Delta t} \sigma_{t+\Delta t} F^{-\mathrm{T}}_{t+\Delta t} \tag{3.147}$$

By replacing the updated Cauchy stress, from Eq. (3.146), which is in the current configuration into Eq. (3.147), the II-PK stress for the current analysis time span, can be expanded as

$$S_{t+\Delta t} = J_{t+\Delta t}\, F^{-1}_{t+\Delta t} \left(\sigma_t\right) F^{-\mathrm{T}}_{t+\Delta t} + J_{t+\Delta t}\, F^{-1}_{t+\Delta t} \left(\Delta\sigma_{t+\Delta t}\right) F^{-\mathrm{T}}_{t+\Delta t} \tag{3.148}$$

Here, the second term is equal to the increment of II-PK stress, $\Delta S_{t+\Delta t}$, at the current time. But the first term is not equivalent to the II-PK stress at the previous time step. In fact, the converged II-PK stress in the previous time is equal to

$$S_t = J_t\, F^{-1}_t \left(\sigma_t\right) F^{-\mathrm{T}}_t \tag{3.149}$$

The first term of the summation in Eq. (3.148) is the value of the previous Cauchy stress tensor which is mapped backward to the initial configuration by the current deformation tensor. Moreover, if the analysis time is small enough (very small), the difference of deformation gradient tensor in the previous and current time will be negligible, such that: $F_{t+\Delta t} \approx F_t$, and one can update the II-PK stress by just simply adding the stress increment to the previous II-PK stress. On the other hand, it ought to be recalled that reducing the amount of the analysis time increment makes the simulations

computationally very costly. Also, more computations and increments cause more rounds off problems. Consequently, the total II-PK stress for the current time increment, (which in constitutive models implementations is usually stored and used for the next time increment) can be updated by considering the proper definition of the II-PK stress increment, which is the Kirchhoff transformation of the incremental Cauchy stress with respect to the incremental deformation gradient, which may be expressed as

$$\Delta S_{t+\Delta t} = \Delta J_{t+\Delta t}\, \Delta F^{-1}_{t+\Delta t} \left(\Delta \sigma_t\right) \Delta F^{-\mathrm{T}}_{t+\Delta t} \tag{3.150}$$

To find $\Delta S_{t+\Delta t}$ inside the decomposed form of II-PK stress as shown in Eq. (3.148), one needs to consider the incremental deformation gradient as $\Delta F_{t+\Delta t} = F_{t+\Delta t} F_t^{-1}$ and the incremental change of volume as $\Delta J_{t+\Delta t} = J_{t+\Delta t} / J_t$. Thus, Eq. (3.148) is modified to

$$S_{t+\Delta t} = J_{t+\Delta t}\, F^{-1}_{t+\Delta t} \left(\sigma_t\right) F^{-\mathrm{T}}_{t+\Delta t} + J_t F_t^{-1} \left(\Delta S_{t+\Delta t}\right) F_t^{-\mathrm{T}} \tag{3.151}$$

This equation means that, in order to upgrade the II-PK stress the previous converged Cauchy stress should be transformed backward to the current Kirchhoff configuration. Also, the new II-PK stress increment ($\Delta S_{t+\Delta t}$) should be transformed backward to the previous Kirchhoff configuration. This sets both stress tensors in the same configuration (initial state). Now the two transformed stress tensors can be added to each other to provide the updated II-PK stress. The recent equation may be written in another form as

$$S_{t+\Delta t} = J_t\, F_t^{-1} \left[\Delta J_{t+\Delta t}\, \Delta F^{-1}_{t+\Delta t} \left(\sigma_t\right) \Delta F^{-\mathrm{T}}_{t+\Delta t} + \Delta S_{t+\Delta t} \right] F_t^{-\mathrm{T}} \tag{3.152}$$

The recent equation means that the previous converged Cauchy stress state, σ_t , should be transformed backward according to the current incremental Kirchhoff configuration,

$\Delta F_{t+\Delta t}$. In fact, it puts σ_t in the same state as $\Delta S_{t+\Delta t}$, thus they are allowed to be added. Then the result of the summation should be transformed backward with respect to the previous Kirchhoff configuration (F_t) to provide the new II-PK stress.

3.6.3 Finite Deformation Consistent Tangent for GL Strain and II-PK Stress

Hiring the consistent modulus is essential in stabilizing the asymptotic rate of quadratic convergence in the Newton-Raphson technique for global finite element approach. If a constitutive model considers large volume changes and non-linear geometry, the exact definition of the consistent tangent stiffness (Jacobian) should be used to confirm and guarantee a rapid convergence. These conditions usually come across when the models consider either large elastic strains or pressure-dependent plasticity (ABAQUS, 2008). In the former case, the total-form of constitutive equations relate the Cauchy stress to the deformation gradient; and in the latter case, rate-form constitutive laws are commonly employed. For the total-form constitutive laws, the exact consistent tangent is defined through the variation in Kirchhoff stress with respect to the rate of deformation, as

$$\delta(J\sigma_{ij}) = J \cdot K_{ij} : D_{ij}\, \mathrm{d}t \qquad \text{or} \qquad K_{ij} = \frac{1}{J}\frac{\delta(J\sigma_{ij})}{D_{ij}\, \mathrm{d}t} \tag{3.153}$$

In an infinite deformation circumstance, for the rate-form constitutive laws, the Jacobian matrix can be modified to the following equation

$$K_{ij} = \frac{1}{J}\frac{\partial(\Delta J\sigma_{ij})}{\partial(\Delta\varepsilon_{ij})} \qquad \text{or} \qquad K_{ij} = \frac{\partial(\Delta\sigma_{ij})}{\partial(\Delta\varepsilon_{ij})} \tag{3.154}$$

One of the advantages of using GL strain and II-PK stress is that the complicated objective derivations is rather simplified and reduced to the time derivations (in the reference configuration). Therefore, finding the consistent tangent modulus is not faced to the corotational complexities. Bathe et al. (1975) mentioned that with the aim of linearizing the equilibrium equations for both total Lagrangian and Updated Lagrangian (UL) formulation, the incremental II-PK stresse are related to the incremental GL strains, using the following constitutive tensor

$$\Delta S_{ij} = C_{ijkl}\, \Delta E_{kl} \tag{3.155}$$

where the forth order tensor C_{ijkl} is the tangent modulus and is a function of material state and the geometry. However, in the constitutive laws for finite deformation, the tangent stiffness according to GL strain and II-PK stress can be adjusted to the next expressions

$$\delta(S_{ij}) = K_{ij} : \delta(\dot{E}_{ij}\, \mathrm{d}t) \qquad \text{or} \qquad K_{ij} = \frac{\partial(\Delta S_{ij})}{\partial(\Delta E_{ij})} \tag{3.156}$$

These relations show the consistent elastoplastic (or viscoelastic-viscoplastic) tangent is identical to its small strain counterparts. In Appendix B, the derivation of the stiffness tangent via the discretization of the principal of virtual work is concisely presented.

3.7 Infinite to Finite Extension Technique

The required steps for basically generalizing an infinite constitutive relation to an identical finite strain model are presented here. The key point is finding a proper logical connection between the finite and infinite deformation formulation counterparts. A well-organized scheme for solving a chosen governing equation is built on an elastic estimator and plastic corrector procedure. This method has been regularly employed in

infinitesimal deformation problems (Lubliner, 1990). In this work, it is assumed that the finite strain is a displacement-driven problem. Thus, the deformation gradient tensor is supposed to be known at the end of each analysis time increment; and besides, it is constant in the time step. Also, in all iterations inside an increment, the total rigid body rotation is assumed to be constant. The generalization steps are explained as following:

1) The incremental Lagrangian strain tensor for the current time increment should be computed through the given and previous deformation gradient tensors, the same as Eqs. (3.76), (3.77), or (3.79).
2) The total rigid body rotation, R, may be calculated by Eqs. (3.69) to (3.71).
3) Based on the chosen constitutive model, a "trial stress" should be defined, and the yielding condition should be checked regatding this trial stress. If the trial stress state does not violate the yield condition, then no plasticity occurred and $F^{p} = I$.
4) If the trial stress satisfies the yield condition, then the plastic corrector should be activated. The strain rate, $\dot{\varepsilon}^{p}$, in the flowing rule for plasticity/viscoplasticity in infinite models should be replaced by the rate of deformation tensor, D^{p}, as introduced in Eq. (3.80).
5) Utilizing Eqs. (3.89) and (3.95) or Eqs. (3.98) and (3.99), gives the plastic stretch tensor, U^{vp}, in the current time increment, according to the estimated trial stress. Then, the plastic deformation gradient tensor and the plastic strain rate will be computed by: $F^{vp} = RU^{vp}$ and Eq. (3.58), respectively.
6) For the elastic part, there exist two situations:

- If the selected small strain constitutive model has a specific relation for assessing the elastic response; then, based on the procedure in Appendix A, the total Lagrangian elastic strain tensor should be calculated. Then by using Eqs. (3.101) and (3.103) the elastic stretch tensor, U^{ve} and its time derivative, $\dot{U}^{ve}$, will be found. Afterwards, the computed incremental Lagrangian strain tensor in step (1), should be checked with Eq. (3.54) or Eq. (3.55). Then the convergence, based on the increment of strains, must be checked. The tangent stiffness matrix is subsequently computed through Eq. (3.156). The II-PK stress will be updated by Eq. (3.151). If the convergence was not satisfied, then the procedure from step (4) should be repeated.
- If there is no criteria in the selected constitutive model for the elastic portion of the total response, and also if the elastic part is in the small deformation range; then like the type-3 of large deformation approach (Eq. (2.3)), the elastic strain can be calculated by subtracting the plastic strain from the total stain as: $E^{e} = E - E^{p}$. Otherwise, the elastic response is deduced from the total deformation gradient, by $F^{e} = FF^{p^{-1}}$, and then the updated plastic deformation gradient, through Eq. (3.47).

A consequence of these correspondences is that the explained procedure identically converts a combined elastoplastic (or viscoelastic-viscoplastic) constitutive model which is based on small strain concept to those in large strain formulation.

3.8 Summary

This study, which presents in detail the large-strain formulation, proposes a generalization procedure for converting a standard relation of small-strain constitutive law to an arbitrarily large strain model. The approached method for generalization is accomplished with the demand that the large-strain model is obtainable by some simple modification and generalization of an existing small-strain constitutive model.

The steps described for the generalization are purely kinematic based; and therefore, the above procedures are applicable to different types of materials within the framework of additive/multiplicative decomposition of elastic and plastic strains. Because no restriction is considered in the extension method; hence, the elastic and plastic responses can be selected independently and arbitrarily (e.g. anisotropy). Moreover, because the rigid body rotation is taken into account in the plastic deformation gradient; therefore, contrary to other finite deformation models, in this approach the plastic spin is not zero.

The extension method in this work can simplify the implementation of finite deformation models through incremental updates. Also, the proposed generalization technique indicates that the consistent tangent modulus can be formulated equivalently the same as in the small strain concept, but regarding the utilized stress and strain measures.

CHAPTER IV

GENERALIZING SCHAPERY VISCOELASTIC MODEL TO MULTIAXIAL LARGE DEFORMATION FRAMEWORK

4.1 Introduction

In this chapter, a numerical integration algorithm for the non-linear viscoelastic behavior of materials has been derived according to Schapery's approach which is built on the Gibbs complementary energy. In this model, the II-PK stress is used as the stress quantity and GL as the strain measure, for analyzing the viscoelastic behavior in finite deformation range.

One of the most important advantages of using II-PK stress and its energy conjugate strain pair (GL strain) is that the material time derivative can be applied directly without considering any special corotational derivation to the stress state, and/or Lie derivative to the strain measure; because, these stress and strain quantities have been defined in material (initial) configuration. In fact, the corotational rates such as Jaumann and Green-Naghdi for II-PK stress gives the time rate of the II-PK, and also the Truesdell rate itself is exactly the time derivation of II-PK stress (Johnson and Bammann, 1984; Nagtegaal and De Jong, 1982). Also, the Lie derivative (Simo, 1988; Yano, 1957) of the GL strain delivers the time derivation of GL strain tensor, because of the nature of the push-forward (from material to spatial configuration) and pull-backward (from spatial to material state) of GL strain tensor. Otherwise, if other stress and strains are employed, the ordinary differential equation (ODE) for the constitutive

model should be revised [see Eq. (4.12)], such that instead of time derivation for strain tensor, Lie derivative should be applied. Also, if the time derivation is applied to the stress tensors in the ODE, it should be replaced by one of the corotational rates. These imply more difficulties to the solution of the ordinary sets of equations.

This three-dimensional non-linear viscoelastic material model is integrated within a displacement-based finite element context. The deviatoric and volumetric responses are decoupled in two ways because of the nature of Lagrangian strain measure in finite deformation framework. The strain tensor is decomposed into instantaneous and hereditary portions. The hereditary strains are updated at the end of each analysis time increment using a recursive formulation, the same approach as proposed by Haj-Ali and Muliana (2004). The method for calculating the trial stress is also enhanced to reduce the number of computational iterations in the material level. Furthermore, in order to guarantee and enhance the convergence of stress state, the consistent tangent compliance matrix is derived regarding to the II-PK stress definition and the method of splitting the Lagrangian strain. The presented equations are derived to be effective in modeling the viscoelastic behavior of isotropic materials in finite strain range.

4.2 Single Viscoelastic Convolutional Integral

In this section, a Schapery-type single integral model is derived based on irreversible thermodynamics process. Schapery showed the energy equation is capable to model the non-linear coupled thermo-viscoelastic materials (Schapery, 1997). In the classical thermodynamic concept, the state of a material can be fully characterized by some independent state variable, which depends on the physical thermodynamic nature

of the system. Because, the Helmholtz free energy under isothermal condition can be explained in terms of stress and strain tensors, and some proper internal state variables (ISVs); thus, Schapery hired the Gibbs energy concept (which is the negative of the complementary energy of the Helmholtz free energy) and introduced it as a function of stress, temperature, and internal state variables. The Gibbs model for describing the thermo-viscoelastic bodies which was presented and used by some researchers (Khan, 2011; Schapery, 1969a; Schapery, 1997), has the following form

$$G = G_0 - A_m \eta_m + \frac{1}{2} B_{mn} \eta_m \eta_n \tag{4.1}$$

where G_0, A_m, and B_{mn} are functions of stress and temperature. In Chapter 3, it was shown that II-PK stress and GL strain are both naturally work-conjugate. Since polymers belong to the class of material with memory (O'Dowd and Knauss, 1995); thus, stress or strain at any time should be determined by the history of deformation gradient. Besides, from thermodynamics, II-PK stress is derived from deformation gradient quantity as

$$S_{ij} = F_{ik}^{-1} \frac{\partial \Psi}{\partial F_{kj}} \tag{4.2}$$

Using the chain rule as: $\frac{\partial \Psi}{\partial F} = \frac{\partial \Psi}{\partial E} \frac{\partial E}{\partial F}$, and also substituting the GL strain relation, $E = \frac{1}{2}\left(F^{\mathrm{T}} F - I\right)$, one can obtain the II-PK stress from the Helmholtz free energy as

$$S_{ij} = \frac{\partial \Psi}{\partial E_{ij}} \tag{4.3}$$

Also, the Helmholtz free energy and the Gibbs energy functions are related by a Legendre transformation. Therefore, the derivation of Gibbs energy with respect to the II-PK stress gives the total GL strain at a certain time, as

$$E_i = -\frac{\partial G}{\partial S_i} \qquad \text{(in vector form)} \tag{4.4}$$

Replacing G by its relation from Eq. (4.1), one can get

$$E_i = -\frac{\partial G_0}{\partial S_i} + \frac{\partial A_m}{\partial S_i}\eta_m + \frac{1}{2}\frac{\partial B_{mn}}{\partial S_i}\eta_m \eta_n \tag{4.5}$$

By neglecting the higher order terms of internal state variables ($\eta_m \eta_n$), the reduced form for the incremental strain can be defined as next

$$\mathrm{d}E_i = \frac{\partial A_m}{\partial S_i}\eta_m \tag{4.6}$$

Based on the second law of thermodynamics, one may write

$$\rho T \dot{\zeta} + \rho \sum \frac{\partial G}{\partial \eta_i}\dot{\eta}_i = S_{ij}\dot{E}_{ij}^{\mathrm{p}} - \nabla_i q_i + \rho \Gamma = 0 \tag{4.7}$$

where ζ is the entropy production in the system. Hence, the entropy production rate is

$$T\dot{\zeta} = -\sum_i \frac{\partial G}{\partial \eta_i}\dot{\eta}_i \geq 0 \tag{4.8}$$

Then, it can be rewritten as: $T\dot{\zeta} = -\dfrac{\partial G}{\partial \eta_m}\dot{\eta}_m$ (summation over m), and substituting Eq. (4.1) into the current relation, and differentiating the related terms, the thermodynamic forces can be found from

$$\frac{\partial G}{\partial \eta_m} = A_m - B_{mn}\eta_n = f_m \tag{4.9}$$

This model is equivalent to the generalized nonlinear Voigt model (Khan, 2011). The sub-indices m and n are the numbers of dashpots. To describe the changes in the internal state variables, η, a set of equations can be introduced as

$$\dot{\eta}_m = \frac{C_{mn}}{a_T} f_n \tag{4.10}$$

This set of evolution equations relates the ISVs to the thermodynamic forces, and in which C_{mn} is presumed constant and symmetric positive-definite matrix, and a_T is a temperature dependent parameter and is called the temperature shift factor. At the reference temperature level it is equal to 1. As a matter of fact, all non-linearity comes from the entropy production through the parameter a_T ($a_T > 0$). Now, by rearranging Eq. (4.10), the forces can be written

$$a_T \dot{\eta}_m = C_{mn} f_n \qquad \Rightarrow \qquad f_m = a_T C_{mn}^{-1} \dot{\eta}_n \tag{4.11}$$

Substituting Eq. (4.11) into Eq. (4.9), then the required differential equations set for finding the ISVs can be expressed as

$$A_m - B_{mn}\,\eta_n = a_T\, C_{mn}^{-1}\,\dot{\eta}_n \qquad \Rightarrow \qquad a_T\, C_{mn}^{-1}\,\dot{\eta}_n + B_{mn}\,\eta_n = A_m \tag{4.12}$$

Now, in order to solve the recent set of equations, under general input conditions (i.e. the coefficients are time dependent), a proper form for the tensor B is required to be assumed. In fact, the relation of B with stress and temperature should be defined. Therefore, similar to the definition of a_T, tensor B can be explained

$$B_{mn} = B_{mn}(S_i, T_R) = b\, K_{mn} \qquad , \qquad b = b(S_i, T_R) \qquad , \qquad b(0, T_R) = 1 \tag{4.13}$$

in which K_{mn} is a constant symmetric tensor, and is defined at reference temperature. Parameter b is a function of stress and temperature, and its magnitude at reference

stress state and temperature is equal to 1. Moreover, the reduced time, ψ, is defined as

$$\mathrm{d}\psi = \frac{\mathrm{d}t}{a_T/b} \qquad \Rightarrow \qquad \psi = \int_0^t \frac{\mathrm{d}t'}{a_T/b} \tag{4.14}$$

The magnitude of $\frac{1}{b}$ is considered as the stress shift factor, a_S. This parameter is also analogous to the strain shift factor, a_ε, when the Helmholtz free energy is utilized to find stress as: $S_i = \frac{\partial \Psi}{\partial E_i}$. Thus, the reduced time will be rewritten as

$$\psi = \int_0^t \frac{\mathrm{d}t'}{a_S a_T} \tag{4.15}$$

Multiplying both sides of Eq. (4.12) by $\frac{1}{b}$ (or a_S) and replacing the time derivative with the reduced time derivative, lead to

$$C_{mn}^{-1} \frac{\mathrm{d}\eta_n}{\mathrm{d}\psi} + K_{mn}\eta_n = \frac{A_m}{b} \tag{4.16}$$

Now, multiplying both sides of the recent equation by C_{lm}, gives

$$C_{lm}C_{mn}^{-1} \frac{\mathrm{d}\eta_n}{\mathrm{d}\psi} + C_{lm}K_{mn}\eta_n = C_{lm}\frac{A_m}{b} \qquad \Rightarrow \qquad \frac{\mathrm{d}\eta_n}{\mathrm{d}\psi} + \left(C_{lm}K_{mn}\right)\eta_n = C_{lm}\frac{A_m}{b} \tag{4.17}$$

With the purpose of solving this system of ODEs, through hidden coordinates one can diagonalize the second order coefficient tensors, C_{lm} and K_{mn}. Because of diagonalizing procedure for Eq. (4.17), the quantity of the ISVs will not be the same as before, even though the same symbol, η, is being used. Thereby, the uncoupled set of equations in terms of internal state variables can be written as

$$\frac{\mathrm{d}\eta_i}{\mathrm{d}\psi} + \left(C_i\, K_i\right)\eta_i = a_S C_i A_i \qquad , \qquad \text{(no summation over } i\text{)} \tag{4.18}$$

This new set of equations has constant coefficients, and they are linear. Schapery (1969a) examined the thermodynamics limitations that affect Eq. (4.18). Briefly, the shift factor is greater than zero, and since C_{mn} and K_{mn} are positive definite matrices, therefore the diagonalized representations are also positive ($C_i > 0$, $K_i > 0$). Moreover, the free energy is independent of all hidden coordinates, and in view of Eq. (4.4), the observed coordinates are unaffected by such hidden coordinates. The term $C_i K_i$ is also defined as $1/\tau_i$ and is called the relaxation time. The goal is expressing the ISVs (η_i) in terms of the applied forces. Henceforth, in order to solve Eq. (4.18), both sides will be multiplied by $\exp\left(\psi/\tau_i\right)$ as the integration factor, and using $C_i = 1/(K_i\tau_i)$, delivers

$$\frac{\mathrm{d}}{\mathrm{d}\psi}\left[\exp\left(\frac{\psi}{\tau_i}\right)\eta_i\right] = \left[a_S\,\frac{A_i}{K_i}\right] \times \left[\frac{1}{\tau_i}\exp\left(\frac{\psi}{\tau_i}\right)\right] \tag{4.19}$$

The solution of the ISVs will be as

$$\eta_i = \exp\left(-\frac{\psi}{\tau_i}\right)\int_0^t \underbrace{\left[a_S\,\frac{A_i}{K_i}\right]}_{V}\underbrace{\left[\left(\frac{1}{\tau_i}\exp\left(\frac{\psi'}{\tau_i}\right)\right)\right]\mathrm{d}\psi'}_{\mathrm{d}U} \tag{4.20}$$

Applying the integration by parts to Eq. (4.20), simply provides

$$\eta_i = \exp\left(-\frac{\psi}{\tau_i}\right)\left[a_S\,\frac{A_i}{K_i}\exp\left(\frac{\psi}{\tau_i}\right)\Bigg|_0^t - \int_0^t \frac{1}{K_i}\exp\left(\frac{\psi'}{\tau_i}\right)\frac{\mathrm{d}\left(a_S A_i\right)}{\mathrm{d}\psi'}\mathrm{d}\psi'\right] \tag{4.21}$$

Since at $t = 0$ the system is in rest, so A_i is zero, and the above expression can be simplified for finding η_i , as

$$\eta_i = \frac{1}{K_i}\int_0^t \left(1-\exp\left(\frac{-(\psi-\psi')}{\tau_i}\right)\right)\frac{\mathrm{d}(a_S A_i)}{\mathrm{d}\psi'}\mathrm{d}\psi' \tag{4.22}$$

The non-linear responses of several materials are recorded and shown that the time-dependent properties can be explained in terms of isothermal linear viscoelastic (Schapery, 1969a). This behavior is obtainable by assuming a form for vector A_i like

$$A_i = \Theta(T) + K_{ij}\,\widehat{S}_j \quad , \quad \text{where: } \widehat{S}_j = \widehat{S}\left(S_j, T\right) \text{ and } \Theta(T_R) = 0 \tag{4.23}$$

in order to characterize the thermo-mechanical performance of the creep function. Here K_{ij} is a constant tensor, S_j is the II-PK stress, and T is temperature and $\Theta(T)$ is a thermal function. Even though in practice the temperature and forces should be applied simultaneously, in this study the effect of temperature is not considered. Thus, based on the new mathematical form for A_i, the next useful expressions may be derived

$$\mathrm{d}\left(a_S A_i\right) = K_{ij}\,\mathrm{d}\left(a_S \widehat{S}_j\right) \quad , \quad \frac{\partial A_m}{\partial S_i} = K_{mj}\frac{\partial \widehat{S}_j}{\partial S_i} \tag{4.24}$$

Substituting Eq. (4.24) into Eq. (4.22), the expressions for the ISVs may be modified to

$$\eta_i = \int_0^t \frac{K_{ij}}{K_m}\left(1-\exp\left(\frac{-(\psi-\psi')}{\tau_m}\right)\right)\frac{\mathrm{d}\left(a_S \widehat{S}_j\right)}{\mathrm{d}\psi'}\mathrm{d}\psi' \quad , \quad \text{(summation over } j \text{ and } m\text{)} \tag{4.25}$$

Replacing this relation for η_i into Eq. (4.6), and after simplifying, the incremental strain, $\mathrm{d}E_i$, will be obtained as

$$\mathrm{d}E_i = \left(\frac{\partial \widehat{S}_j}{\partial S_i}\right)\int_0^t \left(\frac{K_{jl}K_{\ln}}{K_m}\right)\left[1-\exp\left(-\frac{\psi-\psi'}{\tau_m}\right)\right]\frac{\mathrm{d}\left(a_S \widehat{S}_n\right)}{\mathrm{d}\psi'}\,\mathrm{d}\psi' \quad \begin{pmatrix}\text{summation over}\\ m,\ n,\ l, \text{ and } j\end{pmatrix} \tag{4.26}$$

To derive the Schapery-type single integral, the Prony series is introduced as

$$\Delta D_{nj}\left(\psi\right)=\sum_{m=1}^{\mathrm{NP}}\left(\frac{K_{jl}K_{\ln}}{K_{m}}\right)\left[1-\exp\left(\frac{-\psi}{\tau_{m}}\right)\right] \tag{4.27}$$

in which NP is the number of Prony series terms. Utilizing Eqs. (4.26) and (4.27), finally the total strain can be shown to have the form

$$E_{i}=\left(-\frac{\partial G_{o}}{\partial S_{i}}\right)+\left(\frac{\partial \widehat{S}_{n}}{\partial S_{i}}\right)\int_{0}^{t}\Delta D_{nj}\left(\psi-\psi'\right)\frac{\mathrm{d}\left(a_{S}\widehat{S}_{j}\right)}{\mathrm{d}\psi'}\mathrm{d}\psi' \tag{4.28}$$

Here, the following non-linear parameters, as functions of stress state are defined for the viscoelastic formulation

$$g_{0}(S)=-\frac{\partial G_{0}}{\partial S}\frac{1}{D_{0}S}\quad,\quad g_{1}(S)=\frac{\partial \widehat{S}}{\partial S}\quad,\quad g_{2}(S)=a_{S}\frac{\widehat{S}}{S} \tag{4.29}$$

In Eq. (4.29), the functions $g_0(S)$, $g_1(S)$ and $g_2(S)$ characterize the non-linearity of the instantaneous creep response, the effects of the transient compliance, and the effects of loading rate on viscoelastic strain (creep response), respectively. By considering Eq. (4.29), the final viscoelastic formula for investigating the creep response, is expressed according to the II-PK stress and GL strain in the Schapery single integral form as

$$E=D_{0}\,g_{0}\left(S^{\psi}\right)S^{\psi}+g_{1}\left(S^{\psi}\right)\int_{0}^{\psi}\Delta D\left(\psi-\psi'\right)\frac{\mathrm{d}\left(g_{2}\left(S^{\psi}\right)S^{\psi}\right)}{\mathrm{d}\psi'}\mathrm{d}\psi' \tag{4.30}$$

This equation reduces to the linear superposition principle when: $g_0=g_1=g_2=a_S=1$, and was proposed and applied to polymers by several researchers (Leaderman, 1943; Muliana and Khan, 2008; Schapery, 1974). This linear integral form is equal to the first term in the multiple integral form proposed by Green and Rivlin (1957), or the first term of the multiple superposition principal (MSP) by Pipkins and Rogers (1968). Moreover,

Schapery (2000) found out that the MSP model has some restrictions to be applied to multiple step loading and unloading for viscous solids. But on the other hand, the single integral model is able to characterize a wide range of materials (Schapery, 1969b). It should be noted that Eq. (4.28) shows the functions g_1 and g_2 are not independent. For example, if g_1 changes linearly like $g_1(S) = \alpha S + \beta$; then, the general solution for function $\widehat{S}$ is $\widehat{S} = \frac{\alpha}{2} S^2 + \beta S$. Replacing this result to Eq. (4.29) gives the function g_2 as

$$g_2 = a_S \frac{\widehat{S}}{S} = a_S \left(\frac{\alpha}{2} S + \beta \right) \tag{4.31}$$

Eq. (4.29) illustrates that not only g_1 and g_2 are dependent, but the stress shift factor, a_S, and g_2 are also dependent. Thus, if the stress shift factor is considered $a_S = 1$ (in the reference temperature), one can come up with $g_2(S) = (\frac{\alpha}{2})S + \beta$. Considering the inter-dependency of g_1 and g_2, along with $a_S = 1$, makes the viscoelastic model calibration much easier. Schapery (1966) also stated that one may take any finite strain quantities that completely define the nature of deformation, and this choice is arbitrary. For example, he chose Boit as strain and symmetric Kirchhoff (II-PK) as stress. But again regarding to the energy conjugacy concept in Chapter 3, the Boit strain and the II-PK stress are not work conjugate.

4.3 Double Viscoelastic Convolutional Integral (Higher Terms)

In Section 4.2, it was assumed that the higher order terms do not affect the magnitude of the strain, because in small deformation condition, the multiplication of

$\eta_m \eta_n$ is negligible. But, if the strain level is higher than the moderate large deformation range (more 10%); then, the effect of the related terms will be significant and should be incorporated. It means that Eq. (4.5) must be considered instead of Eq. (4.6) to take into account the non-linearity that relates to the contribution of higher order terms of the Gibbs energy (in regarding to the applied stresses). Recall that the tensor B was defined as: $B_{mn} = b\,K_{mn}$, where b is a scalar function of stress. Therefore, the second term of Eq. (4.5) can be expanded as

$$\frac{\partial B_{mn}}{\partial S_i}\eta_m \eta_n = \frac{\partial (bK_{mn})}{\partial S_i}\eta_m \eta_n = K_{mn}\frac{\partial b}{\partial S_i}\eta_m \eta_n \tag{4.32}$$

Now, substituting Eq. (4.22) into Eq. (4.32) leads to

$$\begin{aligned}\frac{\partial B_{mn}}{\partial S_i}\eta_m \eta_n = K_{mn}\frac{\partial b}{\partial S_i}&\left(\int_0^t \frac{K_{mj}}{K_p}\left(1-\exp\left(\frac{-(\psi-\psi')}{\tau_p}\right)\right)\frac{\mathrm{d}\left(\widehat{S}_j/b\right)}{\mathrm{d}\psi'}\mathrm{d}\psi'\right)\\ &\left(\int_0^t \frac{K_{nl}}{K_q}\left(1-\exp\left(\frac{-(\psi-\psi')}{\tau_q}\right)\right)\frac{\mathrm{d}\left(\widehat{S}_l/b\right)}{\mathrm{d}\psi'}\mathrm{d}\psi'\right)\end{aligned} \tag{4.33}$$

Here are summations over the indices. For simplifying the recent equation, one of the integrands coefficients needs to be diagonalized, since there is just one tensor K_{mn} for multiplying to the two integrands coefficients; so, the first integral is diagonalized as

$$\mathrm{diag}\left[\sum_{p=1}^{\mathrm{NP}}\frac{K_{mj}}{K_p}\left(1-\exp\left(\frac{-(\psi-\psi')}{\tau_p}\right)\right)\right] = \sum_{p=1}^{\mathrm{NP}}\delta_{mj}\left(1-\exp\left(\frac{-(\psi-\psi')}{\tau_p}\right)\right) \tag{4.34}$$

Now, multiplying the K_{mn} into the second parentheses, then utilizing the diagonalized relation in Eq. (4.34) through hidden coordinates (Schapery, 1969a), along with the definition of the Prony series in Eq. (4.27), one can rewrite Eq. (4.33) as

$$\frac{\partial B_{mn}}{\partial S_i}\eta_m\,\eta_n = \frac{\partial b}{\partial S_i}\left(\int_0^t \Delta D_{ml}\left(\psi-\psi'\right)\frac{\mathrm{d}\left(\widehat{S}_l/b\right)}{\mathrm{d}\psi'}\mathrm{d}\psi'\right) \left(\int_0^t \sum_{p=1}^{\mathrm{NP}}\left(1-\exp\left(\frac{-\left(\psi-\psi'\right)}{\tau_p}\right)\right)\frac{\mathrm{d}\left(\widehat{S}_m/b\right)}{\mathrm{d}\psi'}\mathrm{d}\psi'\right) \tag{4.35}$$

Henceforth, Eq. (4.5) that is the general form of Eq. (4.6) will be written as

$$\mathrm{d}E_i = \left(\frac{\partial \widehat{S}_m}{\partial S_i}\right)\int_0^t \Delta D_{mj}\left(\psi-\psi'\right)\frac{\mathrm{d}\left(\widehat{S}_j/b\right)}{\mathrm{d}\psi'}\mathrm{d}\psi' + \frac{1}{2}\frac{\partial b}{\partial S_i} \left(\int_0^t \sum_{p=1}^{\mathrm{NP}}\left(1-\exp\left(\frac{-\left(\psi-\psi'\right)}{\tau_p}\right)\right)\frac{\mathrm{d}\left(\widehat{S}_m/b\right)}{\mathrm{d}\psi'}\mathrm{d}\psi'\right)\left(\int_0^t \Delta D_{ml}\left(\psi-\psi'\right)\frac{\mathrm{d}\left(\widehat{S}_l/b\right)}{\mathrm{d}\psi'}\mathrm{d}\psi'\right) \tag{4.36}$$

Eventually, recalling the relations for non-linear parameters in Eq. (4.29), then the mathematical formulations for viscoelastic convolution integral with lower and higher internal state variable terms can be expressed as

$$E = D_0\,g_0\left(S^{\psi}\right)S^{\psi} + g_1\left(S^{\psi}\right)\int_0^{\psi}\Delta D\left(\psi-\psi'\right)\frac{\mathrm{d}\left(g_2\left(S^{\psi}\right)S^{\psi}\right)}{\mathrm{d}\psi'}\mathrm{d}\psi' + \frac{\left(\partial a_S/\partial S^{\psi}\right)}{2\left(a_S\right)^2} \left(\int_0^{\psi}\sum_{p=1}^{\mathrm{NP}}\left(1-\exp\left(\frac{-\left(\psi-\psi'\right)}{\tau_p}\right)\right)\frac{\mathrm{d}\left(g_2\left(S^{\psi}\right)S^{\psi}\right)}{\mathrm{d}\psi'}\mathrm{d}\psi'\right)\left(\int_0^{\psi}\Delta D\left(\psi-\psi'\right)\frac{\mathrm{d}\left(g_2\left(S^{\psi}\right)S^{\psi}\right)}{\mathrm{d}\psi'}\mathrm{d}\psi'\right) \tag{4.37}$$

This equation has the first two terms of Eq. (4.30) which are added by the multiplication of the higher terms of transient compliance. In this case, one can factorize the common term in Eq. (4.37) which is the convolution integral, and present it in the next form

$$E = D_0\,g_0\left(S^{\psi}\right)S^{\psi} + P\left(S^{\psi}\right)\int_0^{\psi}\Delta D\left(\psi-\psi'\right)\frac{\mathrm{d}\left(g_2\left(S^{\psi}\right)S^{\psi}\right)}{\mathrm{d}\psi'}\mathrm{d}\psi' \tag{4.38}$$

where

$$P\left(S^{\psi}\right)=g_1\left(S^{\psi}\right)+\frac{\left(\partial a_S/\partial S^{\psi}\right)}{2\left(a_S\right)^2}\int_0^{\psi}\sum_{p=1}^{\mathrm{NP}}\left(1-\exp\left(\frac{-\left(\psi-\psi'\right)}{\tau_p}\right)\right)\frac{\mathrm{d}\left(g_2\left(S^{\psi}\right)S^{\psi}\right)}{\mathrm{d}\psi'}\mathrm{d}\psi' \quad (4.39)$$

As can be observed, Eq. (4.38) has the same form similar to Eq. (4.30). In fact, the interesting outcome of Eq. (4.38) and (4.39) is that through considering the higher terms of internal state variables in the derivations, the final form of the viscoelastic strain is the same as the single convolution integral presented in Section 4.2. The only difference is that in Eq. (4.38) function $g_1\left(S^{\psi}\right)$ has been replaced by a new function $P\left(S^{\psi}\right)$. In this case, similar to Eqs. (4.30) and (4.31), the non-linear function P is dependent on functions g_1, g_2, and a_S. This outcome basically shows a Schapery-type viscoelastic model in large deformation concept has the same form like the conventional single integral formulation, and only proper stress and strain measures should be hired to transform it into the finite strain range. Therefore, in order to generalize the viscoelastic model to multiaxial framework, from now on Eq. (4.30) will be used, since there is no difference between Eq. (4.30) and (4.38) for finding the function P or g_1. The only difference is the interconnectivity of the non-linear functions.

4.4 Generalizing Single Viscoelastic Convolution Integral to Three-Dimensions

Based on the one-dimensional Schapery model for non-linear viscoelasticity, a three-dimensional constitutive equation is developed for isotropic non-linear viscoelastic materials. Assuming the separation of the hydrostatic and deviatoric responses, the constitutive model is expressed in incremental system. This goal can be achieved by updating the hereditary integrals at the end of each time increment through a recursive

method for both volumetric and distortional portions. The proposed model can be implemented in any finite element package.

4.4.1 Decoupling Volumetric and Deviatoric Strains and Hierarchical Integral

In the previous subsection, it was found that the single convolution integral does not limit to infinite deformation. The derivations proved that considering the lower (approximation) and/or higher terms in Gibbs energy develop the same viscoelastic integral form, which can be assigned to the diagonalization process through the hidden coordinates. Even though Schapery (1969a; 1964), Pipkins and Rogers (1968), and O'Dowd and Knauss (1995), replaced the small strain and Cauchy stress with other strain and stress measures (that are defined for representing finite deformation) to extend the infinite strain to large deformation model, there exist some problems while generalizing and utilizing the single integral form. Generalization from 1D to 3D needs the volumetric and deviatoric part of strain to be defined, and also the consistent tangent should be derived and revised.

The numerical formulation in the previous sections for uniaxial viscoelastic behavior is now employed to be extended as multiaxial (3D) constitutive relations for isotropic materials. Even though Eqs. (4.30) and (4.38) take into consideration the anisotropy, while generalizing these models to multiaxial framework, keeping anisotropy property is difficult and introduces more parameters and concerns. For this purpose, the deviatoric and volumetric stress/strain relations should be decoupled. The procedure can be accomplished by assuming that the total strains are known in each analysis time span, and also the increment of strain rates is constant. This assumption is consistent with

several non-linear constitutive laws that have been implemented within a displacement-based finite element context (Muliana and Khan, 2008). In uniaxial formulation, the single integral form in Eq. (4.30) or (4.38), can be discretized as

$$E(t) = g_o^t D_o S(t) + g_1^t \sum_{n=1}^{\mathrm{NP}} D_n \left(g_2^t S(t) - q_n(t) \right) \tag{4.40}$$

where

$$q_n(t) = \int_0^t \exp(-\lambda_n \Delta\psi^\tau) \frac{\mathrm{d}(g_2^\tau S_{ij}^\tau)}{\mathrm{d}\tau} \mathrm{d}\tau \qquad , \qquad \Delta\psi^\tau = \psi^t - \psi^\tau \tag{4.41}$$

The convolutional integral can be divided to recursive parts, from previous and current time increment. There are two ways to split-up the hereditary integral, with or without assuming that the term $g_2 S$ changes linearly over the current time step, Δt. The variable Δt designates the time increment. The recursive technique along with assuming the linear change of $g_2 S$, can be presented through the next equation, which shows the n^{th} term of the hereditary integral

$$q_n^t = q_n^{t-\Delta t} \exp(-\lambda_n \Delta\psi^t) + \left(g_2^t S^t - g_2^{t-\Delta t} S^{t-\Delta t} \right) \left(\frac{1 - \exp(-\lambda_n \Delta\psi^t)}{\lambda_n \Delta\psi^t} \right) \tag{4.42}$$

For more detail the reader is referred to (Haj-Ali and Muliana, 2004; Lai and Bakker, 1996). On the other hand, if the assumption of linear change of $g_2 S$ is not considered, the hereditary decomposition can be derived as

$$\begin{aligned} q_n^t = & q_n^{t-\Delta t} \exp(-\lambda_n \Delta\psi^t) + \left(g_2^t S^t - g_2^{t-\Delta t} S^{t-\Delta t} \exp(-\lambda_n \Delta\psi^t) \right) \\ & - \left(\frac{\lambda_n}{a_S}\right) \exp(-\lambda_n \Delta\psi^t) \int_{t-\Delta t}^{t} (g_2^\tau S^\tau) \exp(-\lambda_n \Delta\psi^\tau) \mathrm{d}\tau \end{aligned} \tag{4.43}$$

Now, in order to discretize and solve the integral in the recent equation, by utilizing the trapezoidal rule, and simplifying the derived relations, one can get

$$q_n^t = q_n^{t-\Delta t}\exp(-\lambda_n \Delta\psi^t) + g_2^t S^t\left(1-\frac{\lambda_n\Delta\psi^t}{2}\right) - g_2^{t-\Delta t}S^{t-\Delta t}\left(1+\frac{\lambda_n\Delta\psi^t}{2}\right)\exp(-\lambda_n\Delta\psi^t) \quad (4.44)$$

The result of the recent derivation is almost equivalent to Eq. (4.42) since the trapezoidal approximation is also valid when the time increment is small, and in that case the term $g_2 S$ can also change linearly in each analysis time step, Δt, and the result will be the same. Therefore, the recursive form obtained in Eq. (4.42) will be hired for the following derivations. So, in uniaxial formulation the total strain in the single integral form (either Eq. (4.30) or (4.38)), can be discretized as

$$\begin{aligned} E(t) = &\left[g_o^t D_o + g_1^t g_2^t \sum_{n=1}^{\mathrm{NP}} D_n \left(1-\frac{1-\exp(-\lambda_n\Delta\psi^t)}{\lambda_n\Delta\psi^t}\right)\right] S^t \\ &- g_1^t \sum_{n=1}^{\mathrm{NP}} D_n \left[\exp(-\lambda_n\Delta\psi^t) q_n^{t-\Delta t} - g_2^{t-\Delta t}\left(\frac{1-\exp(-\lambda_n\Delta\psi^t)}{\lambda_n\Delta\psi^t}\right) S^{t-\Delta t}\right] \end{aligned} \quad (4.45)$$

In order to generalize Eq. (4.45) to three-dimensions, by inverting Eq. (3.141) (see Chapter 3) and similar to the separation technique in mechanics of material that is also mentioned by Darabi et al. (2011), the decomposition of GL strain with respect to the volumetric and deviatoric parts of II-PK stress, can be obtained as

$$E_{ij} = \frac{1}{3K}S_{ij}^{\mathrm{V}} + \frac{1}{2G}S_{ij}^{\mathrm{D}} = \frac{B}{3}S_{ij}^{\mathrm{V}} + \frac{J}{2}S_{ij}^{\mathrm{D}} \quad , \quad \text{(all are in undamaged configuration)} \quad (4.46)$$

where K and G are the bulk and shear moduli, respectively. Utilizing the latest equation along with considering the new modified Schapery single integral model in Eq. (4.30), and after some simple mathematical manipulations, the constitutive model can be separated to the deviatoric and volumetric components of the non-linear viscoelastic strain (at any typical time), and can be demonstrated as

$$E_{ij}^{\text{dev}} = \frac{1}{2} J_0 \, g_0 S_{ij}^{\text{dev}} + \frac{1}{2} g_1 \int_0^{\psi} \Delta J \left(\psi - \psi'\right) \frac{\mathrm{d}\left(g_2 S_{ij}^{\text{dev}}\right)}{\mathrm{d}\psi'} \mathrm{d}\psi' \tag{4.47}$$

$$E_{ij}^{\text{vol}} = \frac{1}{3} B_0 \, g_0 S_{ij}^{\text{vol}} + \frac{1}{3} g_1 \int_0^{\psi} \Delta B \left(\psi - \psi'\right) \frac{\mathrm{d}\left(g_2 S_{ij}^{\text{vol}}\right)}{\mathrm{d}\psi'} \mathrm{d}\psi' \tag{4.48}$$

$$\begin{aligned} J_0 &= 2(1+\upsilon) D_0 \qquad & \Delta J^{\psi^t} &= 2(1+\upsilon) \Delta D^{\psi^t} \\ B_0 &= 3(1-2\upsilon) D_0 \qquad & \Delta B^{\psi^t} &= 3(1-2\upsilon) \Delta D^{\psi^t} \end{aligned} \tag{4.49}$$

Here, J and B are the transient shear and bulk compliances, and the material constants J_0 and B_0 are the instantaneous effective elastic shear and bulk compliances, respectively. Therefore, the recursive relation in Eq. (4.42), for hereditary integral, will be decoupled to volumetric and deviatoric integral and extended to multiaxial form as

$$q_{ij,n}^{t,\text{dev}} = \exp(-\lambda_n \Delta\psi^t) \, q_{ij,n}^{t-\Delta t,\text{dev}} + \left(g_2^t \, S_{ij}^{t,\text{dev}} - g_2^{t-\Delta t} \, S_{ij}^{t-\Delta t,\text{dev}}\right) \left(\frac{1-\exp(-\lambda_n \Delta\psi^t)}{\lambda_n \Delta\psi^t}\right) \tag{4.50}$$

$$q_{ij,n}^{t,\text{vol}} = \exp(-\lambda_n \Delta\psi^t) \, q_{ij,n}^{t-\Delta t,\text{vol}} + \left(g_2^t \, S_{ij}^{t,\text{vol}} - g_2^{t-\Delta t} \, S_{ij}^{t-\Delta t,\text{vol}}\right) \left(\frac{1-\exp(-\lambda_n \Delta\psi^t)}{\lambda_n \Delta\psi^t}\right) \tag{4.51}$$

With regards to Eqs. (4.45) to (4.51), and decomposing and simplifying the strain components by algebraic manipulations, the volumetric and deviatoric strain tensors can be derived as

$$\begin{aligned} E_{ij}^{t,\text{dev}} = \frac{1}{2} \Bigg[& g_o^t J_o + g_1^t g_2^t \sum_{n=1}^{\text{NP}} J_n \left(1 - \frac{1-\exp(-\lambda_n \Delta\psi^t)}{\lambda_n \Delta\psi^t}\right) \Bigg] S_{ij}^{t,\text{dev}} - \frac{1}{2} g_1^t \sum_{n=1}^{\text{NP}} J_n \Bigg[\\ & \exp(-\lambda_n \Delta\psi^t) q_{ij,n}^{t-\Delta t,\text{dev}} - g_2^{t-\Delta t} \left(\frac{1-\exp(-\lambda_n \Delta\psi^t)}{\lambda_n \Delta\psi^t}\right) S_{ij}^{t-\Delta t,\text{dev}} \Bigg] \equiv \bar{J}^t S_{ij}^{t,\text{dev}} - d_{ij}^t \end{aligned} \tag{4.52}$$

$$\begin{aligned} E_{ij}^{t,\text{vol}} = \frac{1}{3} \Bigg[& g_o^t B_o + g_1^t g_2^t \sum_{n=1}^{\text{NP}} B_n \left(1 - \frac{1-\exp(-\lambda_n \Delta\psi^t)}{\lambda_n \Delta\psi^t}\right) \Bigg] S_{ij}^{t,\text{vol}} - \frac{1}{3} g_1^t \sum_{n=1}^{\text{NP}} B_n \Bigg[\\ & \exp(-\lambda_n \Delta\psi^t) q_{ij,n}^{t-\Delta t,\text{vol}} - g_2^{t-\Delta t} \left(\frac{1-\exp(-\lambda_n \Delta\psi^t)}{\lambda_n \Delta\psi^t}\right) S_{ij}^{t-\Delta t,\text{vol}} \Bigg] \equiv \bar{B}^t S_{ij}^{t,\text{vol}} - V_{ij}^t \end{aligned} \tag{4.53}$$

It should be mentioned that the differences between Eqs. (4.47) to (4.51) and those presented by other researchers (Haj-Ali and Muliana, 2004; Huang et al., 2011a; Lai and Bakker, 1996) is that they are stated in the undamaged (effective) configuration allowing one to couple the viscoelastic model to any damage evolution law. The other difference comes from the nature and definition of Lagrangian strain and II-PK stress (for finite strain) which deliver a volumetric tensor instead of a scalar value (in small deformation form). Hence, the volumetric and deviatoric decoupling provides two strain tensors and also the decomposed hereditary integrals for volumetric portion (Eq. (4.51)) is also a tensor rather than a scalar.

4.4.2 Trial Stress and Corresponding Enhancement

In the Schapery viscoelastic constitutive model, in each analysis time increment, an approximation of the unknown stress increment needs to be determined. This estimation is based on the strain increment, hereditary integrals, and the Prony series. Therefore, a trial stress can be found for the deviatoric and volumetric parts of the strain tensor, and then the other viscoelastic calculations can be conducted based on the computed trial stresses. Here, in order to find the quantity of the trial stresses to have a proper estimation of the stress state, and also to expedite the convergence in the viscoelastic model, the related equations for the trial stresses have been presented, and then a new approach to improve the values of these trial stresses are explained. Recalling the incremental GL strain [see Eq. (3.79)], it is expressed as a function of current and previous strains, and the previous deformation gradient

$$\Delta E_{t+\Delta t} = F_t^{-\mathrm{T}} \left(E_{t+\Delta t} - E_t \right) F_t^{-1} \tag{4.54}$$

Based on Eqs. (4.52) and (4.53), and succeeding the same methodology as Haj-Ali and Muliana (2004) used, the deviatoric and volumetric strain increments for the new modified viscoelastic model can be written as

$$\begin{aligned}\Delta E_{ij}^{t,\mathrm{dev}} &= F_{ij}^{t-\Delta t,\mathrm{dev}^{-\mathrm{T}}}\left[\left(\bar{J}^{t}S_{ij}^{t,\mathrm{dev}}-d_{ij}^{t}\right)-\left(\bar{J}^{t-\Delta t}S_{ij}^{t-\Delta t,\mathrm{dev}}-d_{ij}^{t-\Delta t}\right)\right]F_{ij}^{t-\Delta t,\mathrm{dev}^{-1}}\\ \Delta E_{ij}^{t,\mathrm{vol}} &= F_{ij}^{t-\Delta t,\mathrm{dev}^{-\mathrm{T}}}\left[\left(\bar{B}^{t}S_{ij}^{t,\mathrm{vol}}-V_{ij}^{t}\right)-\left(\bar{B}^{t-\Delta t}S_{ij}^{t-\Delta t,\mathrm{vol}}-V_{ij}^{t-\Delta t}\right)\right]F_{ij}^{t-\Delta t,\mathrm{dev}^{-1}}\end{aligned} \tag{4.55}$$

Substituting the related formula in the above equation, one can get

$$\begin{aligned}&F_{ik}^{t-\Delta t,\mathrm{dev}^{\mathrm{T}}}\,\Delta E_{ij}^{t,\mathrm{dev}}\,F_{jl}^{t-\Delta t,\mathrm{dev}} = \\ &\quad J^{t}S_{kl}^{t,\mathrm{dev}}-J^{t-\Delta t}S_{kl}^{t-\Delta t,\mathrm{dev}}-\frac{1}{2}\sum_{n=1}^{\mathrm{NP}}J_n\left(g_1^{t}\exp(-\lambda_n\Delta\psi^{t})-g_1^{t-\Delta t}\right)q_{kl,n}^{t-\Delta t,\mathrm{dev}}\\ &\quad -\frac{1}{2}g_2^{t-\Delta t}\sum_{n=1}^{\mathrm{NP}}J_n\left[g_1^{t-\Delta t}\left(\frac{1-\exp(-\lambda_n\Delta\psi^{t-\Delta t})}{\lambda_n\Delta\psi^{t-\Delta t}}\right)-g_1^{t}\left(\frac{1-\exp(-\lambda_n\Delta\psi^{t})}{\lambda_n\Delta\psi^{t}}\right)\right]S_{kl}^{t-\Delta t,\mathrm{dev}}\end{aligned} \tag{4.56}$$

$$\begin{aligned}&F_{ik}^{t-\Delta t,\mathrm{vol}^{\mathrm{T}}}\,\Delta E_{ij}^{t,\mathrm{vol}}\,F_{jl}^{t-\Delta t,\mathrm{vol}} = \\ &\quad B^{t}S_{kl}^{t,\mathrm{vol}}-B^{t-\Delta t}S_{kl}^{t-\Delta t,\mathrm{vol}}-\frac{1}{3}\sum_{n=1}^{\mathrm{NP}}B_n\left(g_1^{t}\exp(-\lambda_n\Delta\psi^{t})-g_1^{t-\Delta t}\right)q_{kl,n}^{t-\Delta t,\mathrm{vol}}\\ &\quad -\frac{1}{3}g_2^{t-\Delta t}\sum_{n=1}^{\mathrm{NP}}B_n\left[g_1^{t-\Delta t}\left(\frac{1-\exp(-\lambda_n\Delta\psi^{t-\Delta t})}{\lambda_n\Delta\psi^{t-\Delta t}}\right)-g_1^{t}\left(\frac{1-\exp(-\lambda_n\Delta\psi^{t})}{\lambda_n\Delta\psi^{t}}\right)\right]S_{kl}^{t-\Delta t,\mathrm{vol}}\end{aligned} \tag{4.57}$$

Moreover, for finding a trial stress, since there is no reasonable relation between the amount of the previous and the current time increment, an assumption should be applied. If $\Delta\psi^{t}=\Delta\psi^{t-\Delta t}$ is considerd, then the recent equations will be reduced to the following forms that are appropriate for analysis with fixed time increment

$$\begin{aligned}F_{ik}^{t-\Delta t,\mathrm{dev}^{\mathrm{T}}}\,\Delta E_{ij}^{t,\mathrm{dev}}\,F_{jl}^{t-\Delta t,\mathrm{dev}} &= J^{t}S_{kl}^{t,\mathrm{dev}}-J^{t-\Delta t}S_{kl}^{t-\Delta t,\mathrm{dev}}\\ &\quad -\frac{1}{2}\sum_{n=1}^{\mathrm{NP}}J_n\left(g_1^{t}\exp(-\lambda_n\Delta\psi^{t})-g_1^{t-\Delta t}\right)q_{kl,n}^{t-\Delta t,\mathrm{dev}}\\ &\quad -\frac{1}{2}g_2^{t-\Delta t}\left(g_1^{t-\Delta t}-g_1^{t}\right)\sum_{n=1}^{NP}J_n\left(\frac{1-\exp(-\lambda_n\Delta\psi^{t})}{\lambda_n\Delta\psi^{t}}\right)S_{kl}^{t-\Delta t,\mathrm{dev}}\end{aligned} \tag{4.58}$$

$$
\begin{aligned}
F_{ik}^{t-\Delta t,\mathrm{vol}\,\mathrm{T}}\,\Delta E_{ij}^{t,\mathrm{vol}}\,F_{jl}^{t-\Delta t,\mathrm{vol}} &= B^{t}S_{kl}^{t,\mathrm{vol}} - B^{t-\Delta t}S_{kl}^{t-\Delta t,\mathrm{vol}} \\
&\quad -\frac{1}{3}\sum_{n=1}^{\mathrm{NP}} B_n\left(g_1^{t}\exp(-\lambda_n\Delta\psi^{t}) - g_1^{t-\Delta t}\right)q_{kl,n}^{t-\Delta t,\mathrm{vol}} \\
&\quad -\frac{1}{3}g_2^{t-\Delta t}\left(g_1^{t-\Delta t} - g_1^{t}\right)\sum_{n=1}^{\mathrm{NP}} J_n\left(\frac{1-\exp(-\lambda_n\Delta\psi^{t})}{\lambda_n\Delta\psi^{t}}\right)S_{kl}^{t-\Delta t,\mathrm{vol}}
\end{aligned}
\tag{4.59}
$$

The difference of the incremental volumetric strain in Eq. (4.58) and the one proposed by Haj-Ali and Muliana (2004) is that since GL strain is utilized; thus, the volumetric is a second order tensor (not a scalar). An immediate result of the latest equations is that for computing the trial stress, one also needs to assume some approximations, as

$$
J^{t} \approx J^{t-\Delta t} = J^{t,\mathrm{trial}} \quad , \quad B^{t} \approx B^{t-\Delta t} = B^{t,\mathrm{trial}} \quad , \quad g_1^{t} = g_1^{t-\Delta t} \tag{4.60}
$$

According to these approximation assumptions, one can find the trial incremental volumetric and deviatoric stresses as

$$
\begin{aligned}
J^{t}\,S_{ij}^{\mathrm{dev}}(t) - J^{t-\Delta t}\,S_{ij}^{\mathrm{dev}}(t-\Delta t) &= J^{t,\mathrm{trial}}\,\Delta S_{ij}^{\mathrm{dev,trial}}(t) \\
B^{t}\,S_{ij}^{\mathrm{vol}}(t) - B^{t-\Delta t}\,S_{ij}^{\mathrm{vol}}(t-\Delta t) &= B^{t,\mathrm{trial}}\,\Delta S_{ij}^{\mathrm{vol,trial}}(t)
\end{aligned}
\tag{4.61}
$$

Thus, regarding this equation, Eqs. (4.58) and (4.59) will be reduced to the following relations for computing an estimation of the new stress state (trial stress) in the current time increment as

$$
\Delta S_{ij}^{t,\mathrm{dev,trial}} = \frac{1}{J^{t,\mathrm{trial}}}\left[F_{ik}^{t-\Delta t,\mathrm{dev}\,\mathrm{T}}\,\Delta E_{kl}^{t,\mathrm{dev}}\,F_{lj}^{t-\Delta t,\mathrm{dev}} + \frac{1}{2}g_1^{t,\mathrm{trial}}\sum_{n=1}^{\mathrm{NP}} J_n\left(\exp\left(-\lambda_n\Delta\psi^{t}\right)-1\right)q_{ij,n}^{t-\Delta t,\mathrm{dev}}\right] \tag{4.62}
$$

$$
\Delta S_{ij}^{t,\mathrm{vol,trial}} = \frac{1}{B^{t,\mathrm{trial}}}\left[F_{ik}^{t-\Delta t,\mathrm{vol}\,\mathrm{T}}\,\Delta E_{kl}^{t,\mathrm{vol}}\,F_{lj}^{t-\Delta t,\mathrm{vol}} + \frac{1}{3}g_1^{t,\mathrm{trial}}\sum_{n=1}^{\mathrm{NP}} B_n\left(\exp\left(-\lambda_n\Delta\psi^{t}\right)-1\right)q_{ij,n}^{t-\Delta t,\mathrm{vol}}\right] \tag{4.63}
$$

In these equations for the trial stresses, the effects of the non-linear parameters in the current time have been removed. Thus, for enhancing these trial stresses, because the

estimation for stress state is now available, the effects of the non-linear terms in the current states should be carried out. Therefore, the subsequent scheme can be followed

At first, one needs to compute the stress increments utilizing Eqs. (4.62) and (4.63). Afterwards, the values of the non-linear parameter g_1^t should be computed based on the new updated stress. Therefore, with respect to the following equalities

$$\begin{aligned} J^t S_{ij}^{t,\mathrm{dev}} - J^{t-\Delta t} S_{ij}^{t-\Delta t,\mathrm{dev}} &= \left(J^t - J^{t-\Delta t}\right) S_{ij}^{t-\Delta t,\mathrm{dev}} + J^{t,\mathrm{trial}}\ \Delta S_{ij}^{t,\mathrm{dev,trial}} \\ B^t S_{ij}^{t,\mathrm{vol}} - B^{t-\Delta t} S_{ij}^{t-\Delta t,\mathrm{vol}} &= \left(B^t - B^{t-\Delta t}\right) S_{ij}^{t-\Delta t,\mathrm{vol}} + B^{t,\mathrm{trial}}\ \Delta S_{ij}^{t,\mathrm{vol,trial}} \end{aligned} \tag{4.64}$$

and through substituting the above equalities into Eqs. (4.58) and (4.59), the updated modified trial stresses may be shown as

$$\begin{aligned} \Delta S_{ij}^{t,\mathrm{dev,trial}} = \frac{1}{J^t}\Bigg\{ & F_{ik}^{t-\Delta t,\mathrm{dev\,T}}\ \Delta E_{kl}^{t,\mathrm{dev}}\ F_{lj}^{t-\Delta t,\mathrm{dev}} + \frac{1}{2}\left[\sum_{n=1}^{\mathrm{NP}} J_n \left(g_1^t \exp\left(-\lambda_n \Delta\psi^t\right) - g_1^{t-\Delta t}\right) q_{ij,n}^{t-\Delta t,\mathrm{dev}}\right] \\ & + \frac{1}{2}\left[g_2^{t-\Delta t}\left(g_1^{t-\Delta t} - g_1^t\right)\sum_{n=1}^{\mathrm{NP}} J_n \left(\frac{1-\exp\left(-\lambda_n \Delta\psi^t\right)}{\lambda_n \Delta\psi^t}\right) + \left(J^{t-\Delta t} - J^t\right)\right] S_{ij}^{t-\Delta t,\mathrm{dev}} \Bigg\} \end{aligned} \tag{4.65}$$

$$\begin{aligned} \Delta S_{ij}^{t,\mathrm{vol,trial}} = \frac{1}{B^t}\Bigg\{ & F_{ik}^{t-\Delta t,\mathrm{vol\,T}}\ \Delta E_{kl}^{t,\mathrm{vol}}\ F_{lj}^{t-\Delta t,\mathrm{vol}} + \frac{1}{3}\left[\sum_{n=1}^{\mathrm{NP}} B_n \left(g_1^t \exp\left(-\lambda_n \Delta\psi^t\right) - g_1^{t-\Delta t}\right) q_{ij,n}^{t-\Delta t,\mathrm{vol}}\right] \\ & + \frac{1}{3}\left[g_2^{t-\Delta t}\left(g_1^{t-\Delta t} - g_1^t\right)\sum_{n=1}^{\mathrm{NP}} B_n \left(\frac{1-\exp\left(-\lambda_n \Delta\psi^t\right)}{\lambda_n \Delta\psi^t}\right) + \left(B^{t-\Delta t} - B^t\right)\right] S_{ij}^{t-\Delta t,\mathrm{vol}} \Bigg\} \end{aligned} \tag{4.66}$$

The recursive method introduced by Haj-Ali and Muliana (2004) and is modified here, reduces the computational cost of numerical integration. Also, the modified trial stresses can reduce the number of iterations in the material level.

4.4.3 Consistent Tangent Compliance

According to the essence of incremental solution, with the purpose of accelerating the numerical convergence and also arriving at a correct stress state in each given strain increment, the consistent tangent stiffness should be derived and employed. Otherwise, the strain increments must be very small to satisfy the accuracy of stress updates and also to minimize the errors of linearization. Here, an iterative method is hired by defining the strain residuals. The equation for residual strain may be defined through both the total GL strain, or based on the increments of the GL strain. In the case of the current modified Schapery single integral viscoelastic model (containing II-PK stress and GL strain), the consistent tangent quantity which is a fourth-order tensor and is shown in the next equation, can be derived in two approaches regarding to the formulating of the residual strain tensor

$$C_{ijkl}^{t} = \frac{\partial R_{ij}^{t}}{\partial \Delta S_{kl}^{t}} \tag{4.67}$$

In the first case, based on additively decomposition of the volumetric and deviatoric portions of the incremental strain, the quantity of the residual tensor is expressed

$$R_{ij}^{t} = \Delta E_{ij}^{t,\mathrm{dev}} + \Delta E_{ij}^{t,\mathrm{vol}} - \Delta E_{ij}^{t} \tag{4.68}$$

In this relation, R_{ij}^{t} is the residual tensor and ΔE_{ij}^{t} is the current increment of the GL strain. Now, by substituting Eqs. (4.58) and (4.59), the residual tensor can be written as

$$
\begin{aligned}
R_{ij}^{t} = &-\Delta E_{ij}^{t} + \left(F_{ir}^{t-\Delta t}\right)^{-\mathrm{T}} \Bigg[J^{t} S_{rs}^{t,\mathrm{dev}} - J^{t-\Delta t} S_{rs}^{t-\Delta t,\mathrm{dev}} - \frac{1}{2}\sum_{n=1}^{\mathrm{NP}} J_n \left(g_1^{t} \exp(-\lambda_n \Delta\psi^{t}) - g_1^{t-\Delta t} \right) q_{rs,n}^{t-\Delta t,\mathrm{dev}} \\
&- \frac{1}{2} g_2^{t-\Delta t} \sum_{n=1}^{\mathrm{NP}} J_n \left(g_1^{t-\Delta t} \frac{1-\exp(-\lambda_n \Delta\psi^{t-\Delta t})}{\lambda_n \Delta\psi^{t-\Delta t}} - g_1^{t} \frac{1-\exp(-\lambda_n \Delta\psi^{t})}{\lambda_n \Delta\psi^{t}} \right) S_{rs}^{t-\Delta t,\mathrm{dev}} \\
&+ B^{t} S_{rs}^{t,\mathrm{vol}} - B^{t-\Delta t} S_{rs}^{t-\Delta t,\mathrm{vol}} - \frac{1}{3}\sum_{n=1}^{\mathrm{NP}} B_n \left(g_1^{t} \exp(-\lambda_n \Delta\psi^{t}) - g_1^{t-\Delta t} \right) q_{rs,n}^{t-\Delta t,\mathrm{vol}} \\
&- \frac{1}{3} g_2^{t-\Delta t} \sum_{n=1}^{\mathrm{NP}} J_n \left(g_1^{t-\Delta t} \frac{1-\exp(-\lambda_n \Delta\psi^{t-\Delta t})}{\lambda_n \Delta\psi^{t-\Delta t}} - g_1^{t} \frac{1-\exp(-\lambda_n \Delta\psi^{t})}{\lambda_n \Delta\psi^{t}} \right) S_{rs}^{t-\Delta t,\mathrm{vol}} \Bigg] \left(F_{sj}^{t-\Delta t}\right)^{-1}
\end{aligned}
\tag{4.69}
$$

One can derive the consistent tangent through differentiating the proper terms of Eq. (4.69), and should recall that the derivation of the terms in the previous time increment with respect to the current stress state will vanish. The derivation and simplification of the Lagrangian residual strain tensor with respect to the II-PK stress tensor is explained in detail in Appendix C. However, the simplified result of the viscoelastic tangent compliance tensor is presented here, as

$$
\begin{aligned}
\frac{\partial R_{ij}^{t}}{\partial \Delta S_{kl}^{t}} = \left(F_{ir}^{t-\Delta t}\right)^{-\mathrm{T}} \Bigg[& J^{t} \delta_{rk} \delta_{sl} + \frac{1}{3}\left(B^{t} - J^{t}\right) C_{kl} C_{rs}^{-1} + \frac{\partial B^{t}}{\partial \Delta S_{kl}^{t}} S_{rs}^{t,\mathrm{vol}} + \frac{\partial J^{t}}{\partial \Delta S_{kl}^{t}} S_{rs}^{t,\mathrm{dev}} \\
& - \sum_{n=1}^{\mathrm{NP}} \mathbb{A}_{kl,n}^{1} \exp(-\lambda_n \Delta\psi^{t}) \left(\frac{1}{2} J_n \, q_{rs,n}^{t-\Delta t,\mathrm{dev}} + \frac{1}{3} B_n \, q_{rs,n}^{t-\Delta t,\mathrm{vol}} \right) \\
& + g_2^{t-\Delta t} \sum_{n=1}^{\mathrm{NP}} \left(\frac{1}{2} J_n S_{rs}^{t-\Delta t,\mathrm{dev}} + \frac{1}{3} B_n S_{rs}^{t-\Delta t,\mathrm{vol}} \right) \\
& \left(\mathbb{A}_{kl}^{2} \left(\frac{1-\exp(-\lambda_n \Delta\psi^{t})}{\lambda_n \Delta\psi^{t}} \right) - \mathbb{A}_{kl}^{3} \exp(-\lambda_n \Delta\psi^{t}) \right) \Bigg] \left(F_{sj}^{t-\Delta t}\right)^{-1}
\end{aligned}
\tag{4.70}
$$

With the purpose of modifying the recent outcome in such a way to be a practical derivation for the aim of implementation, this equation should be written based on the increments of effective stress. Because in incremental solution, the derivation of the non-linear material parameters (here: g_1^{t}, a_S^{t}, and also J^{t} and B^{t}) are achievable regarding

to the effective stress. Therefore, the derivation of the effective stress, $\Delta\bar{S}$, with respect to the total stress tensor should be illustrated. This derivation is obtainable as explained in the next relation.

$$\frac{\partial\Delta\bar{S}}{\partial\Delta S_{kl}}=\frac{\partial\Delta\bar{S}}{\partial S_{kl}}=\frac{3}{2}\frac{1}{\Delta\bar{S}}\left(S_{kl}-\frac{1}{3}(C_{kl}C^{-1}_{mn})S_{mn}\right) \tag{4.71}$$

The derivation of the incremental stress regarding the total stress is also explained in Appendix C. Thus, taking into account the latest relation, Eq. (4.70) will be modified as

$$\begin{aligned}\frac{\partial R^{t}_{ij}}{\partial\Delta S^{t}_{kl}}=\left(F^{t-\Delta t}_{ir}\right)^{-\mathrm{T}}\Bigg[& J^{t}\delta_{rk}\delta_{sl}+\frac{1}{3}\left(B^{t}-J^{t}\right)C_{kl}C^{-1}_{rs}+\frac{\partial\Delta\bar{S}}{\partial\Delta S^{t}_{kl}}\Bigg\{\frac{\partial B^{t}}{\partial\Delta\bar{S}}S^{t,\mathrm{vol}}_{rs}+\frac{\partial J^{t}}{\partial\Delta\bar{S}}S^{t,\mathrm{dev}}_{rs}\\ & -\sum_{n=1}^{\mathrm{NP}}\mathbb{B}^{1}_{n}\exp(-\lambda_{n}\Delta\psi^{t})\left(\frac{1}{2}J_{n}\,q^{t-\Delta t,\mathrm{dev}}_{rs,n}+\frac{1}{3}B_{n}\,q^{t-\Delta t,\mathrm{vol}}_{rs,n}\right)\\ & +g^{t-\Delta t}_{2}\sum_{n=1}^{\mathrm{NP}}\left(\frac{1}{2}J_{n}S^{t-\Delta t,\mathrm{dev}}_{rs}+\frac{1}{3}B_{n}S^{t-\Delta t,\mathrm{vol}}_{rs}\right)\\ & \left(\mathbb{B}^{2}\left(\frac{1-\exp(-\lambda_{n}\Delta\psi^{t})}{\lambda_{n}\Delta\psi^{t}}\right)-\mathbb{B}^{3}\exp(-\lambda_{n}\Delta\psi^{t})\right)\Bigg\}\Bigg]\left(F^{t-\Delta t}_{sj}\right)^{-1}\end{aligned} \tag{4.72}$$

where

$$\mathbb{B}^{1}_{n}=\frac{\partial g^{t}_{1}}{\partial\Delta\bar{S}}+\lambda_{n}\Delta\psi^{t}\frac{g^{t}_{1}}{a^{t}_{S}}\frac{\partial a^{t}_{S}}{\partial\Delta\bar{S}}\quad,\quad\mathbb{B}^{2}=\frac{\partial g^{t}_{1}}{\partial\Delta\bar{S}}+\frac{g^{t}_{1}}{a^{t}_{S}}\frac{\partial a^{t}_{S}}{\partial\Delta\bar{S}}\quad,\quad\mathbb{B}^{3}=\frac{g^{t}_{1}}{a^{t}_{S}}\frac{\partial a^{t}_{S}}{\partial\Delta\bar{S}}$$

Now, if in a large deformation problem the time increment becomes larger, or the magnitude of volumetric portion of strain is comparable with its distortional counterpart; then, the additive decomposition of the volumetric and deviatoric strains will not be acceptable. In order to minimize the residual strain, in each time increment the deformation gradient tensor given by Finite Element Analysis (FEA) and the one computed through the constitutive models (here is viscoelasticity) should be close

enough to deliver the same quantity of GL strain. However, instead of comparing the total GL strain, the residual of the incremental GL strain can also be computed and compared. The mentioned inter-span deformation gradient and the related residual in a typical iteration are shown schematically in Fig. 4.1. Therefore, in each increment subsequently after finding the total deformation gradient, the residual of the incremental GL strain can be calculated as

$$\delta E_{(n)} = \frac{1}{2}\left(\Delta F_{(n)}^{\mathrm{T}} \Delta F_{(n)} - I\right) \quad , \quad \text{where: } \Delta F_{(n)} = F^{\mathrm{FEM}} F_{(n)}^{-1} \tag{4.73}$$

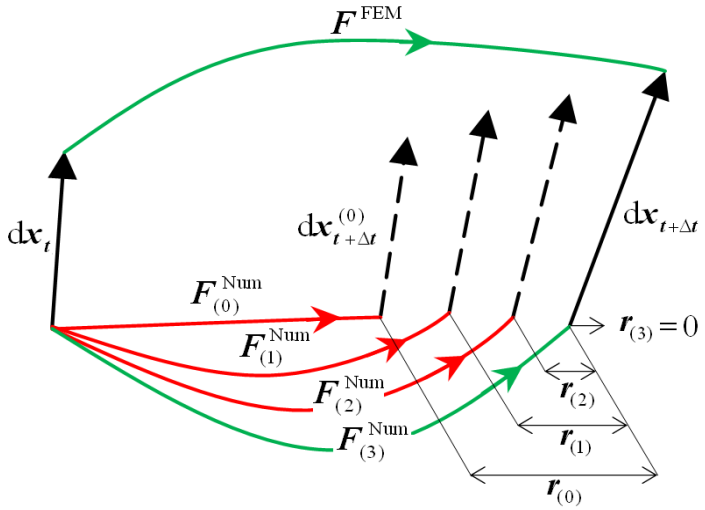

Fig. 4.1. Graphical depiction of iteratively updating deformation gradient tensor and its corresponding residual strain, according to each updated deformation gradient tensor.

In the final iteration, the difference of the deformation gradient, $\Delta F_{(n)}$ will be equal to the identity tensor since $F^{\mathrm{FEM}} = F_{(n)}$. For the rest of expressing the derivations, in the following equations, the iteration number, *n*, is removed from the subscripts. Hence, let's

redefine the residual strain tensor (the same as Eq. (4.73)); thus, the residual strain instead of Eq. (4.68) will be expressed as

$$R_{ij}^{t} = \delta E_{ij}^{t} = \frac{1}{2}\left(\Delta F_{ij}^{\mathrm{T}} \Delta F_{ij} - I\right) \tag{4.74}$$

Therefore, the forth order compliance tensor should be written as the next form

$$\frac{\partial R_{ij}^{t}}{\partial \Delta S_{kl}^{t}} = \frac{1}{2}\left(\left(\frac{\partial \Delta F_{im}}{\partial \Delta S_{kl}^{t}}\right)^{\mathrm{T}} \Delta F_{mj} + \Delta F_{im}^{\mathrm{T}}\left(\frac{\partial \Delta F_{mj}}{\partial \Delta S_{kl}^{t}}\right)\right) \tag{4.75}$$

Through substituting $\Delta F = F^{\mathrm{FEM}} F^{-1}$, and recalling the decoupled F^{ve} to volumetric and deviatoric, and rotation as $F^{\mathrm{ve}} = R U_{\mathrm{dev}}^{\mathrm{ve}} U_{\mathrm{vol}}^{\mathrm{ve}}$ (see Chapter 3); then, the differentiation of incremental deformation gradient with respect to the incremental II-PK stress can be described in this form

$$\frac{\partial \Delta F_{mj}}{\partial \Delta S_{kl}^{t}} = -F_{mp}^{\mathrm{FEM}}\left[K_{pskl}\left(I + 2E^{t,\mathrm{vol}}\right)_{sx}^{-1} + G_{pskl}\left(I + 2E^{t,\mathrm{dev}}\right)_{sx}^{-1}\right] F_{xj}^{\mathrm{ve}\,-1} \tag{4.76}$$

where

$$K_{pskl} = \frac{\partial}{\partial \Delta S_{kl}^{t}}\Bigg[B^{t} S_{ps}^{t,\mathrm{vol}} - B^{t-\Delta t} S_{ps}^{t-\Delta t,\mathrm{vol}} - \frac{1}{3}\sum_{n=1}^{\mathrm{NP}} B_n\left(g_1^{t}\exp(-\lambda_n \Delta\psi^{t}) - g_1^{t-\Delta t}\right) q_{ps,n}^{t-\Delta t,\mathrm{vol}}$$
$$- \frac{1}{3} g_2^{t-\Delta t}\sum_{n=1}^{\mathrm{NP}} J_n\left(g_1^{t-\Delta t}\frac{1-\exp(-\lambda_n \Delta\psi^{t-\Delta t})}{\lambda_n \Delta\psi^{t-\Delta t}} - g_1^{t}\frac{1-\exp(-\lambda_n \Delta\psi^{t})}{\lambda_n \Delta\psi^{t}}\right) S_{ps}^{t-\Delta t,\mathrm{vol}}\Bigg]$$

$$G_{pskl} = \frac{\partial}{\partial \Delta S_{kl}^{t}}\Bigg[J^{t} S_{ps}^{t,\mathrm{dev}} - J^{t-\Delta t} S_{ps}^{t-\Delta t,\mathrm{dev}} - \frac{1}{2}\sum_{n=1}^{\mathrm{NP}} J_n\left(g_1^{t}\exp(-\lambda_n \Delta\psi^{t}) - g_1^{t-\Delta t}\right) q_{ps,n}^{t-\Delta t,\mathrm{dev}}$$
$$- \frac{1}{2} g_2^{t-\Delta t}\sum_{n=1}^{\mathrm{NP}} J_n\left(g_1^{t-\Delta t}\frac{1-\exp(-\lambda_n \Delta\psi^{t-\Delta t})}{\lambda_n \Delta\psi^{t-\Delta t}} - g_1^{t}\frac{1-\exp(-\lambda_n \Delta\psi^{t})}{\lambda_n \Delta\psi^{t}}\right) S_{ps}^{t-\Delta t,\mathrm{dev}}\Bigg]$$

It is important to recall: $U^{\text{vol}} = \sqrt{I + 2E^{\text{vol}}}$ and $U^{\text{dev}} = \sqrt{I + 2E^{\text{dev}}}$ from Chapter 3. Now, by considering the result of Eq. (4.76), and similar to Eq. (4.72), the consistent tangent compliance while the volumetric and deviatoric strains cannot be separated additively, may be written as the next relation, in which $\mathbb{B}^1_n$, $\mathbb{B}^2$, and $\mathbb{B}^3$ are the same as expressed in Eq. (4.72). Similar to the pervious approach of derivations of the compliance tensor, the procedure to get the following equation is explained in Appendix C.

$$\frac{\partial R^t_{ij}}{\partial \Delta S^t_{kl}} = -\text{symm}\left(F^{-\text{T}}_{iy} C^{\text{FEM T}}_{yp} \left[K_{pskl} \left(I + 2E^{t,\text{vol}} \right)^{-1}_{sx} + G_{pskl} \left(I + 2E^{t,\text{dev}} \right)^{-1}_{sx} \right] F^{\text{ve}\,-1}_{xj} \right) \quad (4.77)$$

where

$$K_{pskl} = \frac{1}{3}\left(C_{kl}C^{-1}_{ps}\right)B^t + \frac{\partial \Delta \bar{S}}{\partial S^t_{kl}} \left[\frac{\partial B^t}{\partial \Delta \bar{S}} S^{t,\text{vol}}_{ps} - \frac{1}{3}\sum_{n=1}^{\text{NP}} \left[B_n \exp(-\lambda_n \Delta \psi^t) q^{t-\Delta t,\text{vol}}_{ps,n} \mathbb{B}^1_{kl,n} \right] \right.$$
$$\left. + \frac{1}{3} g_2^{t-\Delta t} \sum_{n=1}^{\text{NP}} \left[B_n \left(\mathbb{B}^2_{kl} \left(\frac{1 - \exp(-\lambda_n \Delta \psi^t)}{\lambda_n \Delta \psi^t} \right) - \mathbb{B}^3_{kl} \exp(-\lambda_n \Delta \psi^t) \right) \right] S^{t-\Delta t,\text{vol}}_{ps} \right]$$

$$G_{pskl} = J^t \left(\delta_{pk}\delta_{sl} - \frac{1}{3} C_{kl} C^{-1}_{ps} \right) + \frac{\partial \Delta \bar{S}}{\partial S^t_{kl}} \left[\frac{\partial J^t}{\partial \Delta \bar{S}} S^{t,\text{dev}}_{ps} - \frac{1}{2}\sum_{n=1}^{\text{NP}} \left[J_n \exp(-\lambda_n \Delta \psi^t) q^{t-\Delta t,\text{dev}}_{ps,n} \mathbb{B}^1_{kl,n} \right] \right.$$
$$\left. \left. + \frac{1}{2} g_2^{t-\Delta t} \sum_{n=1}^{\text{NP}} \left[J_n \left(\mathbb{B}^2_{kl} \left(\frac{1 - \exp(-\lambda_n \Delta \psi^t)}{\lambda_n \Delta \psi^t} \right) - \mathbb{B}^3_{kl} \exp(-\lambda_n \Delta \psi^t) \right) \right] S^{t-\Delta t,\text{dev}}_{ps} \right] \right]$$

4.5 Summary

A Schapery-type non-linear viscoelastic material model based on II-PK stress and GL strain has been derived through Gibbs energy, to enhance the Schapery single integral viscoelastic model to a large deformation framework. The state variables in this approach are strain-based. Here, it has been shown that the derived model through using the higher order terms of internal state variables in the Gibbs energy delivers the same

mathematical form when the lower terms are used. The effects of the additional higher order non-linear terms can be taken into account to the computational model through function $g_1(S)$, which is designated to capture the effects of the transient compliance.

Because the volumetric and deviatoric effects are incorporated in the material properties of the model, and also the distortion and dilatation components of the stress measure are separated, as well as the strain components; thereby, the model is capable to distinguish the differences between the compression and tension responses of polymers.

The developed computational method for the numerical integration is built on Lai and Bakker (1996) approach for the 3D representation of non-linear viscoelastic model, and also Haj-Ali and Muliana (2004) recursive integration along with an iterative scheme in order to satisfy the constitutive strain residual. Because the nature of the employed stress and strain measures was different than the ones used by the previous researchers, thus the consistent tangent compliance is identified and revised to ensure and expedite the convergence of the computational model.

Also, the derived constitutive law is suitable only for small and large deformation gradient viscoelastic problems under quasi-static loading.

CHAPTER V

APPLYING UNIFIED LARGE DEFORMATION VISCOELASTIC-VISCOPLASTIC-VISCODAMAGE CONSTITUTIVE MODEL TO POLYMERIC MATERIALS

5.1 Introduction

Polymers and polymer composites are complex materials that are increasingly being used to fabricate structural components in many industrial applications (Ericson and Berglund, 1993; Lee and Jang, 1999; Megnis et al., 2001). Polymeric materials offer a wide range of advantages, such as high strength-to-weight ratio, impact resistance (through mixing with particles and/or different fibers), high flexibility, recyclability, corrosion resistance, low cost, and fast processing times, that make them very attractive materials for many industries (e.g. automotive, defense, sport, civil, aerospace, health, etc.). Here, a combination of non-linear thermo-viscoelastic (Schapery's non-linear viscoelastic model for predicting the recoverable strain), thermo-viscoplastic (Perzyna's viscoplastic theory for addressing the hardening) laws, similar to the recent work by Huang et al. (2011a) is used as a unified model. Then, the unified models are generalized to finite deformation framework. The required algorithms for extending the small strain elastoplastic models to large deformation range are discussed in detail in Chapter 3. Moreover, the generalized Schapery viscoelastic model used to predict the large deformation behavior, is derived and explained in Chapter 4. By utilizing the proposed algorithms in Chapters 3 and 4, the unified non-linear thermo-viscoelastic, -viscoplastic,

and -viscodamage models are modified to be able to capture the large deformation response of polymers and polymer composites. Afterwards, the generalized unified models have been implemented into the well-known commercial finite element code ABAQUS (2008) via the user material subroutine, UMAT.

The outline of this chapter is as follows. In Section 5.2, the coupled models for non-linear viscoelastic, viscoplastic, and viscodamage is presented. In Section 5.3, the numerical algorithms and computational implementation of the constitutive equations in the finite element code ABAQUS (2008) are presented. Section 5.4 is devoted to the calibration of model parameters. Section 5.5 contains the comparison of the predictions of implemented models and the response of PMMA (Polymethyl-metacrylate) polymer by using a set of creep-secondary, creep-tertiary tests, and also stress-strain behavior at three different strain rates, in two temperature levels. And finally, conclusions are summarized in Section 5.6.

5.2 Constitutive Models

5.2.1 Effective Configuration (Power Equivalence Hypothesis)

Kachanov (1958) was the pioneer of the concept of continuum damage mechanics (CDM). He introduced a scalar quantity that is called continuity, ζ, and physically has been defined by Rabotnov (1969) as

$$\zeta = \frac{\bar{A}}{A} \tag{5.1}$$

Here $\bar{A}$ is the effective area (undamaged or intact area), and A is the whole area, which is capable to carry the applied load. In 1961, Odqvist and Hult (1961) introduced another

variable, ϕ , which defines the reduction of area due to micro-damages

$$\phi = 1 - \zeta = \frac{A - \bar{A}}{A} = \frac{A^{D}}{A} \tag{5.2}$$

where A^{D} is the area of micro-damages, and ϕ is the damage density variable, which evolves from $\phi = 0$ for intact (undamaged) material to $\phi = 1$ for total rupture. In fact, complete rupture happens when $\phi = \phi^{c}$, where ϕ^{c} is the critical damage density that is a material property (Abu Al-Rub and Voyiadjis, 2003). The relation between stresses in the undamaged material and damaged material is defined next (Chaboche, 2003)

$$\bar{\sigma}_{ij} = \frac{\sigma_{ij}}{1 - \phi} \tag{5.3}$$

where σ_{ij} and $\bar{\sigma}_{ij}$ are the components of the effective Cauchy stress tensor in the nominal and effective (undamaged) configurations, respectively. Since, in generalization framework the second Piola-Kirchhoff (II-PK) stress measure is used; thereby, similar to recent equation, Eq. (5.3) can be rewritten as

$$\bar{S}_{ij} = \frac{S_{ij}}{1 - \phi} \tag{5.4}$$

where S_{ij} and $\bar{S}_{ij}$ are the components of the II-PK stress tensor in the nominal and damaged configurations. In order to model the degradation in strength and stiffness regarding to the damage evolution, Cicekli et al. (2007) and Abu Al-Rub and Voyiadjis (2009) have concluded that Eq. (5.3) is more accurately defined as

$$\bar{\sigma}_{ij} = \frac{\sigma_{ij}}{(1 - \phi)^{2}} \tag{5.5}$$

And in the same manner, Eq. (5.5) will be converted to

$$\bar{S}_{ij} = \frac{S_{ij}}{(1-\phi)^2} \tag{5.6}$$

In this work, Eq. (5.6) is adopted, because $\bar{\sigma}_{ij}$ is the true effective stress which drives the non-linear behaviors (here: viscoelastic, viscoplastic, and viscodamage), and the constitutive equations in the subsequent sections are presented in terms of the effective (undamaged) stress components, $\bar{\sigma}_{ij}$. The evolution law for the damage density, ϕ, will be discussed in Subsection 5.2.5.

A transformation hypothesis is also required to relate the nominal strains, E_{ij}, to the strains in the undamaged (effective) configuration, $\bar{E}_{ij}$. To achieve it, one can either adapt the strain equivalence hypothesis (i.e., the strains in nominal and effective configurations are equal) or the strain energy equivalence hypothesis (i.e., any form of strain energy in the nominal configuration is equal to the corresponding strain energy in the effective configuration) (Abu Al-Rub and Voyiadjis, 2003). Although, the strain energy equivalence hypothesis is intuitively more physically sound, it greatly complicates the constitutive models and their numerical implementation (Abu Al-Rub and Voyiadjis, 2003). Therefore, for the sake of simplicity and ease in the finite element implementation of these complex constitutive equations, the strain equivalence hypothesis is adopted. Hence, it is assumed that the nominal strain components, E_{ij}, are equal to their counterparts in the effective configuration, $\bar{E}_{ij}$.

5.2.2 Multiplicative/Additive Decomposition of Lagrangian Strain

The total distortion of a solid domain subjected to an applied stress can be decomposed into recoverable and irrecoverable constituents, where the amount of each is mainly affected by time, temperature, and loading rates. As explained in Chapter 3, in small strain concept, additive decomposition of total strain to viscoelastic (recoverable) and viscoplastic (irrecoverable) components is acceptable. But in this work, because the response of polymeric materials under finite distortion is being investigated, the viscoelastic and viscoplastic portions of strain and strain rates should be separated with respect to the requirements of large deformation concepts. Henceforth, the deformation gradient can be multiplicatively decomposed into viscoelastic, F^{ve}, and viscoplastic, F^{vp}, components as was shown in Fig. 3.1 (Kröner, 1960; Lee and Liu, 1967), such that

$$F_{ij} = F^{ve}_{ik} F^{vp}_{kj} \quad , \quad \text{where: } \det(F) > 0 \ , \ \det(F^{ve}) > 0 \ , \ \det(F^{vp}) > 0 \qquad (5.7)$$

Through using Eq. (5.7) and the definition of the Green-Lagrange (GL) strain, the decomposition of GL strain and strain rate is derived in Chapter 3.

The key point for using large deformation concept in incremental procedure is that the deformation gradient tensor is supposed to be known in each time increment of the analysis (finite element softwares provide this tensor), and moreover it is constant during the applied load in that time increment. Also, in all iterations inside a time increment, the total rigid body rotation is assumed to be constant and equal to its value at the end of that increment. Converting the pure multiplicative decomposition of the deformation gradient to the additive-multiplicative decomposition approach of the GL strain and strain rate and their issues are fully explained in Chapter 3, and based on that

the procedures for extending the small strain constitutive models to its equivalent finite strain framework, are itemized as follows:

1) The incremental Lagrangian strain tensor for the current time increment should be computed using Eq. (3.76) or (3.79).
2) The total rigid body rotation, R, is calculated by Eqs. (3.68) to (3.70).
3) Based on the modified viscoelastic model, the trial stress should be found (Eqs. (4.65) and (4.66)), and the yielding condition should be checked. If the trial stress state does not violate the yield condition, then no plasticity occurred and $F^{vp} = I$.
4) If trial stress satisfies the yield condition, the plastic corrector should be activated.
5) The strain rate, $\dot{E}^{vp}$, in the flow rule for viscoplastic in infinite strain models should be replaced by the rate of deformation tensor, D^{vp} (Eq. (3.80)).
6) Utilizing the Eqs. (3.85) to (3.94), gives the plastic stretch tensor, U^{vp}, according to the estimated trial stress. Then, the viscoplastic deformation gradient tensor and the viscoplastic strain rate can be computed correspondingly by: $F^{vp} = RU^{vp}$ and $\dot{E}^{vp} = F^{vp^T} D^{vp} F^{vp}$.
7) For the elastic part, at first the total Lagrangian viscoelastic strain tensor should be calculated (see Chapter 3). Then by hiring Eqs. (3.100) and (3.102) the viscoelastic stretch tensor, U^{ve} and its rate, $\dot{U}^{ve}$, will be found.
8) The tangent stiffness modulus is then computed through Eq. (3.156), and subsequently the II-PK stress will be updated by Eq. (3.151).

9) Afterwards the computed incremental Lagrangian strain tensor in step 1, should be compared with Eq. (3.54) or Eq. (3.55) to check the convergence. If the convergence is not satisfied, then the procedure from step 4 should be repeated.

5.2.3 Non-Linear Thermo-Viscoelastic Model

In this study, the modified Schapery non-linear viscoelastic model that was derived in Chapter 4 is employed to numerically predict the viscoelastic response of the polymer (PMMA). In the one-dimensional case, the single integral viscoelastic model can be expressed in terms of the effective stress concept, as

$$E^{\mathrm{NVE},t} = \bar{D}_0\, g_0\left(\bar{S}^t, T^t\right)\bar{S}^t + g_1\left(\bar{S}^t, T^t\right)\int_0^t \Delta D\left(\psi^t - \psi^\tau\right)\frac{\mathrm{d}\left(g_2\left(\bar{S}^\tau, T^t\right)S^\tau\right)}{\mathrm{d}\psi^\tau}\mathrm{d}\psi^\tau \qquad (5.8)$$

where $\bar{D}_0$ is the instantaneous elastic compliance for undamaged material, $\Delta\bar{D}$ is the transient compliance for the undamaged material, and g_0, g_1, and g_2 are non-linear parameters that are functions of the effective stress and temperature at any specific time, τ. Parameter g_0 is the non-linear instantaneous compliance that measures the reduction or increase in the instantaneous elastic compliance. The transient non-linear parameter g_1 measures the non-linearity effect in the transient compliance, and the parameter g_2 accounts for the loading rate effect on the creep response, as well. In the case of linear viscoelastic materials $g_0 = g_1 = g_2 = 1$, such that the Eq. (5.8) reduces to the Boltzmann superposition integral. Also, in Eq. (5.8), ψ^t is the reduced time that is given by

$$\psi^t = \int_0^t \frac{\mathrm{d}t}{a_T\, a_s} \qquad (5.9)$$

where a_T and a_s are the temperature and stress (or strain) time-shift factors, respectively. For numerical convenience, the Prony series are commonly used to represent the transient compliance $\Delta\bar{D}$ as follows

$$\Delta\bar{D}^{\psi^t} = \sum_{n=1}^{N} \bar{D}_n \left[1 - \exp\left(-\lambda_n \psi^t\right)\right] \tag{5.10}$$

where N is the number of Prony series terms, $\bar{D}_n$ is the n^{th} coefficient term of the Prony series associated with the n^{th} retardation time, $1/\lambda_n$. As proposed by Lai and Bakker (1996), the one-dimensional non-linear viscoelastic model in Eq. (5.8) can be generalized to the three-dimensional form by decomposing the viscoelastic response into deviatoric and volumetric portions. According to Chapter 4, by assuming that the Poisson's ratio $\bar{\nu}$ is time- and temperature-independent, and using the Prony series for the transient compliance, Eq. (5.8) is split-up to deviatoric and volumetric strains, and also expressed in terms of the hereditary integral, as

$$\begin{aligned} E_{ij}^{t,\text{dev}} = {} & \frac{1}{2}\left[g_o^t \bar{J}_o + g_1^t g_2^t \sum_{n=1}^{\text{NP}} \bar{J}_n \left(1 - \frac{1-\exp(-\lambda_n \Delta\psi^t)}{\lambda_n \Delta\psi^t}\right)\right] \bar{S}_{ij}^{t,\text{dev}} \\ & - \frac{1}{2} g_1^t \sum_{n=1}^{\text{NP}} \bar{J}_n \left[\exp(-\lambda_n \Delta\psi^t) q_{ij,n}^{t-\Delta t,\text{dev}} - g_2^{t-\Delta t} \left(\frac{1-\exp(-\lambda_n \Delta\psi^t)}{\lambda_n \Delta\psi^t} \right) \bar{S}_{ij}^{t-\Delta t,\text{dev}} \right] \end{aligned} \tag{5.11}$$

$$\begin{aligned} E_{ij}^{t,\text{vol}} = {} & \frac{1}{3}\left[g_o^t \bar{B}_o + g_1^t g_2^t \sum_{n=1}^{\text{NP}} \bar{B}_n \left(1 - \frac{1-\exp(-\lambda_n \Delta\psi^t)}{\lambda_n \Delta\psi^t}\right)\right] S_{ij}^{t,\text{vol}} \\ & - \frac{1}{3} g_1^t \sum_{n=1}^{\text{NP}} \bar{B}_n \left[\exp(-\lambda_n \Delta\psi^t) q_{ij,n}^{t-\Delta t,\text{vol}} - g_2^{t-\Delta t} \left(\frac{1-\exp(-\lambda_n \Delta\psi^t)}{\lambda_n \Delta\psi^t} \right) S_{ij}^{t-\Delta t,\text{vol}} \right] \end{aligned} \tag{5.12}$$

where the superscript Δt designates the increment of discretized time, and the variables $q_{ij,n}^{\text{dev}}$ and $q_{ij,n}^{\text{vol}}$ are the n^{th} term of deviatoric and volumetric hereditary integrals. These

expressions were derived in Chapter 4, as well. The above equations are very useful for the numerical implementation of the non-linear viscoelastic model as will be shown in Section 5.3. It is noteworthy to mention that the difference between Eqs. (5.11) to (5.12) and those presented in Haj-Ali and Muliana (2004) and Huang et al. (2011b) is that they are expressed in the effective (undamaged) configuration, which allows one to easily couple viscoelasticity to damage evolution, and are also extended to finite deformations. Besides, the other difference comes from the nature and the GL strains and the II-PK stresses that provide tensor quantities for volumetric measures instead of a scalar value, unlike what appears in small deformation formula.

5.2.4 Thermo-Viscoplastic Model

In order to calculate the viscoplastic deformations in polymers, a Perzyna-type (Perzyna, 1966) viscoplastic constitutive model can be utilized, but modified here in terms of the effective stress tensor instead of the nominal stress tensor. This is argued as once the material is damaged, further loading can only affect the undamaged (effective) regions inside a body, such that the undamaged parts can flow plastically. Since large deformation theory and measures should be used, the viscoplastic rate of deformation, D_{ij}^{vp}, can be expressed using the following flow rule

$$D_{ij}^{\text{vp}} = \dot{\gamma}^{\text{vp}} \frac{\partial g}{\partial \bar{S}_{ij}} \tag{5.13}$$

where $\dot{\gamma}^{\text{vp}}$ is the viscoplastic multiplier, and g is the viscoplastic potential function. Physically, $\dot{\gamma}^{\text{vp}}$ is a positive scalar, which determines the magnitude of D_{ij}^{vp}, whereas

$\partial g / \partial \overline{S}_{ij}$ determines the direction of D_{ij}^{vp}. In this approach, as discussed in Chapter 3, unlike the other researchers that consider irrotational flow (Anand and Ames, 2006; Anand and Gurtin, 2003; Gurtin and Anand, 2005; Wagner, 1978); here, the viscoplastic deformation gradient contains the rigid body rotation (rotational flow). Therefore the vorticity tensor will not vanish. After calculating D_{ij}^{vp} in each time increment, using Eqs. (3.85) to (3.92); then, the viscoplastic deformation gradient and finally the strain rate tensors can be computed in a straightforward manner.

Perzyna (1971) expressed the viscoplastic multiplier in terms of an overstress function and a viscosity parameter that relates the rate of viscoplastic deformation to the current stresses, such that $\dot{\gamma}^{\text{vp}}$ can be expressed as

$$\dot{\gamma}^{\text{vp}} = \Gamma^{\text{vp}}(T)\left\langle \Phi(f) \right\rangle^{N} \tag{5.14}$$

where $\langle\ \rangle$ is the Macauley bracket, $N > 0$ is the viscoplastic rate sensitivity parameter, and $\Gamma^{\text{vp}}(T)$ is the viscoplastic viscosity parameter such that $1/\Gamma^{\text{vp}}$ represents the viscoplasticity relaxation time according to the notion given by Perzyna. This viscosity parameter is temperature-dependent such that

$$\Gamma^{\text{vp}} = \Gamma_{\text{ref}}^{\text{vp}}\,\theta^{\text{vp}}(T) \qquad , \qquad \theta^{\text{vp}}(T) = \exp\left[\theta(T - T_{\text{ref}})/T_{\text{ref}}\right] \tag{5.15}$$

in which $\Gamma_{\text{ref}}^{\text{vp}}$ is the viscosity parameter at a reference temperature T_{ref} and θ is a material parameter. In Eq. (5.14), Φ is the overstress function which is expressed in terms of the yield function f, and the following expression is assumed for function Φ

$$\left\langle \Phi(f) \right\rangle = \begin{Bmatrix} 0 & \Phi(f) \le 0 \\ \dfrac{f}{S_y^0} & \Phi(f) > 0 \end{Bmatrix} \tag{5.16}$$

where S_y^0 is a yield stress quantity used to normalize the overstress function and can also be assumed unity. In this study, a modified Drucker-Prager yield function (f) is used that can distinguish between the distinct behavior of polymers in compression and tension, and also is able to take into account the confining pressures. But, this modified Drucker-Prager yield function is expressed as a function of the effective (undamaged) stresses, $\bar{S}_{ij}$, as

$$f = \bar{\Sigma} - \frac{\alpha}{3}\bar{I}_1 - \kappa(E_{\text{eff}}^{\text{vp}}) \le 0 \tag{5.17}$$

where α is a material parameter designated to the material's internal friction or entanglement. $\bar{I}_1 = \bar{S}_{kk}$ is the first invariant of the effective stress tensor, $\kappa(E_{\text{eff}}^{\text{vp}})$ is an isotropic hardening function associated with the cohesive characteristics of the material and depends on the equivalent or effective viscoplastic strain, $E_{\text{eff}}^{\text{vp}}$. The stress $\bar{\Sigma}$ is the deviatoric effective shear stress and is assumed to have the following form

$$\bar{\Sigma} = \frac{\sqrt{\bar{J}_2}}{2}\left[\left(1+\frac{1}{d}\right)+\left(1-\frac{1}{d}\right)\frac{\bar{J}_3}{\sqrt{\bar{J}_2^3}}\right] \tag{5.18}$$

in which $\bar{J}_2 = \frac{3}{2}\bar{S}_{ij}^{\text{dev}}\bar{S}_{ij}^{\text{dev}}$ and $\bar{J}_3 = \frac{9}{2}\bar{S}_{ij}^{\text{dev}}\bar{S}_{jk}^{\text{dev}}\bar{S}_{ki}^{\text{dev}}$ are the second and third deviatoric stress invariants of the effective stresses $\bar{S}_{ij}$, respectively. The material parameter d is the ratio of the yield stress in uniaxial tension to that in compression. Therefore, d gives

the distinction of polymer's behavior in contraction and extension loading conditions, where $d=1$ implies that $\bar{\Sigma}=\sqrt{\bar{J}_2}$. The value of d should have a range of $0.778 \le d \le 1$ in order to ensure that the yield surface is convex. Applying a uniaxial compression stress, then $\bar{\Sigma}=\sqrt{\bar{J}_2}=\bar{S}_{11}$; whereas under uniaxial tension $\bar{\Sigma}=\sqrt{\bar{J}_2}/d=\bar{S}_{11}/d$. This indicates that at the same stress level, the material in tension yields earlier than in compression. Following the work of Lemaitre and Chaboche (1994), one can express the isotropic hardening function, $\kappa(E_{\text{eff}}^{\text{vp}})$, as an exponential function of the equivalent viscoplastic strain $E_{\text{eff}}^{\text{vp}}$, such that

$$\kappa(E_{\text{eff}}^{\text{vp}})=\kappa_0+\kappa_1\left[1-\exp\left(-\kappa_2 E_{\text{eff}}^{\text{vp}}\right)\right]\theta^{\text{vp}}(T) \tag{5.19}$$

where κ_0, κ_1, and κ_2 are material parameters; κ_0 defines the initial yield stress, $\kappa_0+\kappa_1$ determines the saturated yield stress level, and κ_2 is the strain hardening rate and shows how fast a material hardens. Because polymers viscoplastic deformation is generally complex; thus, a non-associated viscoplastic effect should be assumed. Hence, the viscoplastic potential function, g, in Eq. (5.13) is not equal to the yield function f. Thus, the direction of the viscoplastic strain increment is not normal to the yield surface, but is normal to the viscoplastic potential surface. This can be simply achieved by assuming a generalized Drucker-Prager-type viscoplastic potential function as

$$g=\bar{\Sigma}-\frac{\beta}{3}\bar{I}_1 \tag{5.20}$$

where the parameter β describes the dilation-contraction response of the material. Then, the effective viscoplastic strain rate $\dot{E}_{\text{eff}}^{\text{vp}}$ in Eq. (5.19) can be expressed as

$$\dot{E}_{\text{eff}}^{\text{vp}} = A^{-1}\sqrt{\dot{E}_{ij}^{\text{vp}}\dot{E}_{ij}^{\text{vp}}} = A^{-1}\sqrt{\left(F_{ki}^{\text{vp}}D_{kl}^{\text{vp}}F_{lj}^{\text{vp}}\right)\left(F_{ki}^{\text{vp}}D_{kl}^{\text{vp}}F_{lj}^{\text{vp}}\right)} \quad , \quad A = \sqrt{1+2\left(\frac{0.5+\beta/3}{1-\beta/3}\right)^2} \tag{5.21}$$

and from Eq. (5.20), one can easily write

$$\frac{\partial g}{\partial \bar{S}_{ij}} = \frac{\partial \bar{\Sigma}}{\partial \bar{S}_{ij}} - \frac{1}{3}\beta\,\delta_{ij} \tag{5.22}$$

Considering $\partial \bar{J}_2 / \partial \bar{S}_{ij} = 3\bar{S}_{ij}^{\text{dev}}$ and $\partial \bar{J}_3 / \partial \bar{S}_{ij} = \frac{27}{2}\bar{S}_{ik}^{\text{dev}}\bar{S}_{kj}^{\text{dev}} - 3\bar{J}_2\,\delta_{ij}$; $\partial \bar{\Sigma} / \partial \bar{S}_{ij}$ is given by

$$\frac{\partial \bar{\Sigma}}{\partial \bar{S}_{ij}} = \frac{1}{2}\left[\left(1+\frac{1}{d}\right)\left(\frac{\partial \bar{J}_2}{\partial \bar{S}_{ij}}\right)\frac{1}{2\sqrt{\bar{J}_2}} + \left(1-\frac{1}{d}\right)\left(\frac{\partial \bar{J}_3}{\partial \bar{S}_{ij}}\bar{J}_2 - \frac{\partial \bar{J}_2}{\partial \bar{S}_{ij}}\bar{J}_3\right)\frac{1}{\bar{J}_2^2}\right] \tag{5.23}$$

According to Wang et al. (1997), one can define a consistency condition for rate-dependent plasticity (viscoplasticity) similar to the classical rate-independent plasticity theory such that a dynamic (rate-dependent) yield surface, χ, is expressed from Eqs. (5.14), (5.16), and (5.17) as

$$\chi = \left(\bar{\Sigma} - \frac{\alpha}{3}\bar{I}_1 - \kappa(E_{\text{eff}}^{\text{vp}})\right) - S_y^0\left(\frac{\dot{\gamma}^{\text{vp}}}{\Gamma^{\text{vp}}}\right)^{1/N} \le 0 \tag{5.24}$$

The Kuhn-Tucker loading-unloading conditions for the dynamic yield surface χ are

$$\chi \le 0 \qquad \dot{\gamma}^{\text{vp}} \ge 0 \qquad , \qquad \dot{\chi} = 0 \qquad \dot{\gamma}^{\text{vp}}\chi = 0 \tag{5.25}$$

One of the main points in the non-linear incremental computation scheme is that the system of equation of the constitutive models should arrive at a converged stress state at the end of each analysis time increment. For such guarantee, the idea of consistent tangent stiffness is the key role; therefore, in order to find the proper tangent stiffness tensor for the presented models, the following derivations for the viscoplastic part should

be hired. One may recall that the compliance tensor for the viscoelastic part is derived and explained in Chapters 3 and 4, and Appendix B, C, and D. Now, to find the expression for viscoplastic tangent stiffness, one must discern that the compliance tensor is a combination of the compliance of both viscoelastic and viscoplastic models. Thus, regarding the definition of residual strain in Chapter 4, $R_{ij}^{t} = \frac{1}{2}\left(\Delta F_{ik}^{\mathrm{T}} \Delta F_{kj} - I\right)$, and using $\Delta F = F^{\mathrm{FEM}} F^{-1}$ and $F = F^{\mathrm{ve}} F^{\mathrm{vp}} = R U^{\mathrm{ve}} U^{\mathrm{vp}}$; the compliance tensor can be found through deriving the residual strain with respect to the incremental II-PK stress, as

$$\frac{\partial R_{ij}^{t}}{\partial \Delta S_{kl}^{t}} = \frac{1}{2}\left(\left(\frac{\partial \Delta F_{im}}{\partial \Delta S_{kl}^{t}}\right)^{\mathrm{T}} \Delta F_{mj} + \Delta F_{im}^{\mathrm{T}}\left(\frac{\partial \Delta F_{mj}}{\partial \Delta S_{kl}^{t}}\right)\right) \tag{5.26}$$

where

$$\frac{\partial \Delta F_{ij}}{\partial \Delta S_{kl}^{t}} = F_{ip}^{\mathrm{FEM}}\left[\frac{\partial U_{pr}^{\mathrm{vp}\,-1}}{\partial \Delta S_{kl}^{t}} U_{rq}^{\mathrm{ve}\,-1} + U_{pr}^{\mathrm{vp}\,-1}\frac{\partial U_{rq}^{\mathrm{ve}\,-1}}{\partial \Delta S_{kl}^{t}}\right] R_{qj}^{\mathrm{T}}$$

Now, through using the definition of the viscoelastic and viscoplasic stretch, one may find the compliance tensor for the combination of both constitutive models as

$$\begin{aligned}\frac{\partial R_{ij}^{t}}{\partial \Delta S_{kl}^{t}} = -\mathrm{symm}\Bigg(F_{iy}^{-\mathrm{T}} C_{yp}^{\mathrm{FEM}} U_{py}^{t,\mathrm{vp}\,-1}\Bigg[\Delta t\ \frac{\partial \mathbb{X}_{yr}^{t}}{\partial \Delta S_{kl}^{t}} \\ + K_{pskl}\left(I + 2E^{t,\mathrm{vol}}\right)_{sx}^{-1} + G_{pskl}\left(I + 2E^{t,\mathrm{dev}}\right)_{sx}^{-1}\Bigg] F_{xj}^{\mathrm{ve}\,-1}\Bigg)\end{aligned} \tag{5.27}$$

where

$$\frac{\partial \mathbb{X}_{yr}^{t}}{\partial \Delta S_{kl}^{t}} = \Delta t\ \Gamma^{\mathrm{vp}}\left(\frac{f}{S_{\mathrm{yield}}^{0}}\right)^{N} R_{ya}^{t\ \mathrm{T}}\left[\frac{N}{f}\frac{\partial g}{\partial \Delta \bar{S}_{ab}}\frac{\partial f}{\partial \Delta \bar{S}_{kl}} + \frac{\partial^{2} g}{\partial \Delta \bar{S}_{ab}\partial \Delta \bar{S}_{kl}}\right] R_{br}^{t}$$

Furthermore, the derivations of these equations are explained in detail in Appendix D.

5.2.5 Thermo-Viscodamage Model

Time-, rate-, and temperature-independent evolution equations for evaluating the damage variable, ϕ, are not proper to predict the damage nucleation and growth in polymeric materials. In general, the damage evolution, $\dot{\phi}$, can be explained as a function of the total stress (in effective state), $\bar{S}_{ij}$, hydrostatic stress, $\bar{S}_{ij}^{\text{vol}}$, strain, E_{ij}, strain rate, $\dot{E}_{ij}$, temperature, T, and damage history, ϕ, schematically as

$$\dot{\phi} = F\left(\bar{S}_{ij}(t),\ \bar{S}_{ij}^{\text{vol}}(t),\ E_{ij}(t),\ \dot{E}_{ij}(t),\ T(t),\ \phi(t)\right) \tag{5.28}$$

The first time-dependent (creep) damage law, which was proposed by Kachanov (1958) and later modified by Rabotnov (1969), has the following form

$$\dot{\phi} = C_1 \sigma^{C_2} (1-\phi)^{-C_3} \tag{5.29}$$

Here $C_{i\ (i=1,2,3)}$ are material constants. However, for other types of loading conditions, the damage evolution should also depend on strain. Belloniet et al. (1979) proposed the following creep damage law, which was later slightly modified by Cozzarelli (1981) and Lee (1986), in which C_1 to C_4 are material constants, and t is time

$$\phi = C_1\, \varepsilon^{C_2}\, \sigma^{C_3} t^{C4} \tag{5.30}$$

Schapery (1990) used his theory of viscoelastic fracture mechanics (Schapery, 1975) along with the elastic-viscoelastic correspondence principle and continuum damage mechanics to model the growth of damage in a viscoelastic domain. He also proposed the following power-law evolution equation for a damage parameter, S, as

$$\dot{S} = \left(-\frac{\partial W^{R}}{\partial S}\right)^{\alpha} \tag{5.31}$$

α is a material constant, and W^R is the pseudo elastic strain energy density defined as

$$W^R = \frac{1}{2} E^R \left(\varepsilon^R\right)^2 \qquad , \qquad \varepsilon^R = \frac{1}{E^R} \int_0^t E\left(\psi^t - \psi^\xi\right) \frac{\mathrm{d}\varepsilon}{\mathrm{d}\xi} \mathrm{d}\xi \tag{5.32}$$

with ε^R is the pseudo strain, $E(t)$ is the relaxation modulus in uniaxial loading, E^R is a reference modulus (e.g. $E^R = 1$), and ψ^t is the reduced time as defined in Eq. (5.9). But, unlike the current damage variable, ϕ, there is no clear physical meaning for the damage variable S in Schapery's model. Moreover, there is no defined relation between the damaged relaxation modulus E and S. Voyiadjis et al. (2003, 2004) and Abu Al-Rub and Voyiadjis (2006a) have proposed a viscodamage evolution law for metallic materials

$$\dot{\phi} = \left\langle \frac{\bar{Y}}{K(\phi)} - 1 \right\rangle^m \tag{5.33}$$

where $\bar{Y} = \bar{\tau}_{ij} \bar{\varepsilon}_{ij} / 2$ is the damage driving force and interpreted as the energy release rate, m is a material constant, and $K(\phi)$ is a damage isotropic hardening function that incorporates the damage history effect to the model. Motivated and guided by the above damage evolution laws, Darabi et al. (2011) have proposed the viscodamage evolution law for multiaxial state of stress, as

$$\dot{\phi} = \Gamma^{\mathrm{vd}} \left\langle \frac{\bar{Y}}{Y_0} \left(1 - \phi\right)^2 \right\rangle^q \exp\left(k E_{\mathrm{eff}}\right) G(T) \tag{5.34}$$

where $\Gamma^{\mathrm{vd}} = \Gamma_0^{\mathrm{vd}} G(T)$ with Γ_0^{vd} is the damage viscousity parameter evaluated at a reference temperature T_{ref} and $G(T) = \exp\left(\delta (T - T_{\mathrm{ref}}) / T_{\mathrm{ref}}\right)$; δ, k, and q are material

constants; $E_{\text{eff}} = \sqrt{\frac{2}{3} E_{ij} E_{ij}}$ is the effective or equivalent total strain; and Y_0 is the damage thereshold that specifies at which effective stress level damage initiates; and $\bar{Y} = \left\langle \bar{\Sigma} - \beta \bar{I}_1 / 3 \right\rangle$ is the damage driving force where $\bar{\Sigma}$ is given in Eq. (5.18). This form for $\bar{Y}$ allows one to incorporate the difference in damage behavior under contraction and extension loading conditions (or compression and tension under uniaxial loading), and also under confining pressures. Besides, note that E_{eff} includes both viscoelastic and viscoplastic quantity of strains, which allows simplicit time, rate, and temperature to be coupled. This viscodamage evolution law has been successfully used by Abu Al-Rub and Tehrani (2011) and Tehrani and Abu Al-Rub (2011) for modeling polymers and polymer composites. Eq. (5.34) is used in this work for modeling damage evolution. To make the damage model compatible with viscoelastic and viscoplastic formulation in the framework of large strain measures (as discussed in previous chapters), the role of engineering strain should be replaced by Lagrangian strain measure.

For completeness, a general thermodynamic framework for deriving the presented coupled viscoelastic-viscoplastic-viscodamage constitutive model is outlined in Appendix E. In the following sections, numerical algorithms for implementing the presented thermo-mechanical viscoelastic, viscoplastic, and viscodamage evolution equations are explained in detail and the associated material constants will be identified based on available experimental data.

5.3 Finite Element Implementation

In this section, numerical algorithms for applying the presented unified thermo-mechanical evolution equations in the finite deformation framework are discussed. Using the effective stress concept in the undamaged configuration greatly simplifies the numerical implementation of the proposed constitutive models. One can first update the effective II-PK stress, $\overline{S}_{ij}$, based on the non-linear viscoelasticity and viscoplasticity equations, which are expressed in the effective (undamaged) state. Then the damage density based on Eq. (5.34), and finally the updated nominal stresses can be computed (Abu Al-Rub et al., 2010). Given the deformation gradients at the previous, $F_{ij}^{t-\Delta t}$, and current time, F_{ij}^{t}, the incremental GL strain can be computed by Eq. (3.79) or $\Delta E_t = F_{t-\Delta t}^{-\mathrm{T}}\left(E_t - E_{t-\Delta t}\right)F_{t-\Delta t}^{-1}$. Using Eq. (3.46), the total GL strain will be

$$E_t = \frac{1}{2}\left(C_t - I\right) \qquad , \qquad C_t = F_t^{\mathrm{T}} F_t \tag{5.35}$$

Afterwards, the next important task is determining the value of the incremental volumetric and deviatoric quantities of the GL strain tensor, that are presented as

$$\Delta E_{ij}^{t,\mathrm{vol}} = \frac{1}{2}\left(\left(J_{t-\Delta t}^{-1} J_t\right)^{2/3} - 1\right) I_{ij} \qquad , \qquad \Delta E_{ij}^{t,\mathrm{dev}} = J_t^{-2/3}\left[\Delta E_{ij}^{t} - \Delta E_{ij}^{t,\mathrm{vol}}\right] \tag{5.36}$$

Here, $J_t = \det(F_{ij}^{t})$. In the next step, the deviatoric and volumetric increments of the trial stresses to initiate the coupled viscoelastic and viscoplastic models, are found as follows

$$\Delta S_{ij}^{t,\mathrm{dev,trial}} = \frac{1}{\overline{J}^{t,\mathrm{trial}}}\left[F_{ik}^{t-\Delta t,\mathrm{dev}\,\mathrm{T}}\,\Delta E_{kl}^{t,\mathrm{dev}}\,F_{lj}^{t-\Delta t,\mathrm{dev}} + \frac{1}{2} g_1^{t,\mathrm{trial}} \sum_{n=1}^{\mathrm{NP}} J_n \left(\exp\left(-\lambda_n \Delta\psi^t\right) - 1\right) q_{ij,n}^{t-\Delta t,\mathrm{dev}}\right] \tag{5.37}$$

$$\Delta S_{ij}^{t,\text{vol,trial}} = \frac{1}{\bar{B}^{t,\text{trial}}}\left[F_{ik}^{t-\Delta t,\text{vol T}}\, \Delta E_{kl}^{t,\text{vol}}\, F_{lj}^{t-\Delta t,\text{vol}} + \frac{1}{3} g_1^{t,\text{trial}} \sum_{n=1}^{\text{NP}} B_n \left(\exp\left(-\lambda_n \Delta\psi^t\right) - 1 \right) q_{ij,n}^{t-\Delta t,\text{vol}} \right] \tag{5.38}$$

where

$$\bar{J}^t = \frac{1}{2}\left[g_0^t \bar{J}_0 + g_1^t g_2^t \sum_{n=1}^{N} \bar{J}_n \left(1 - \frac{1-\exp(-\lambda_n \Delta\psi^t)}{\lambda_n \Delta\psi^t} \right) \right]$$

$$\bar{B}^t = \frac{1}{3}\left[g_0^t \bar{B}_0 + g_1^t g_2^t \sum_{n=1}^{N} \bar{B}_n \left(1 - \frac{1-\exp(-\lambda_n \Delta\psi^t)}{\lambda_n \Delta\psi^t} \right) \right]$$

But the non-linear viscoelastic parameters (i.e. g_0, g_1, g_2) are assumed to be functions of the last converged effective stresses. Therefore, if enhanced quantities are required for $\Delta\bar{S}_{ij}^{t,\text{dev,trial}}$ and $\Delta\bar{S}_{ij}^{t,\text{vol,trial}}$ to reduce the number of iterations in material level, or to increase the time increment, one can hire Eq. (4.65) and (4.66). Also to find the total undamaged II-PK stress, one can compute it as

$$\begin{aligned} S_{t+\Delta t} &= J^t\, F^{t\,-1}\left(\bar{\sigma}^{t-\Delta t}\right) F^{t\,-\text{T}} + J^{t-\Delta t}\, F^{t-\Delta t\,-1}\left(\Delta\bar{S}^t\right) F^{t-\Delta t\,-\text{T}} \\ \Delta\bar{S}^t &= \Delta\bar{S}_{ij}^{t,\text{vol,trial}} + \Delta\bar{S}_{ij}^{t,\text{dev,trial}} \end{aligned} \tag{5.39}$$

The undamaged volumetric and deviatoric portions of II-PK stress can be calculated as

$$\bar{S}^{\text{vol}} = \frac{1}{3}(\bar{S} : C)C^{-1} \qquad , \qquad \bar{S}^{\text{dev}} = \bar{S} - \bar{S}^{\text{vol}} \tag{5.40}$$

Then, the undamaged hydrostatic and deviatoric components of viscoelastic strain increments can be expressed from Eqs. (4.56) and (4.57) as

$$\begin{aligned} \Delta E_{ij}^{t,\text{dev}} = F_{ik}^{t-\Delta t\,-\text{T}} \Bigg[& \bar{J}^t \bar{S}_{kl}^{t,\text{dev}} - \bar{J}^{t-\Delta t} \bar{S}_{kl}^{t-\Delta t,\text{dev}} - \frac{1}{2}\sum_{n=1}^{\text{NP}} J_n \left(g_1^t \exp(-\lambda_n \Delta\psi^t) - g_1^{t-\Delta t} \right) q_{kl,n}^{t-\Delta t,\text{dev}} \\ & - \frac{1}{2} g_2^{t-\Delta t} \sum_{n=1}^{NP} J_n \left[g_1^{t-\Delta t} \left(\frac{1-\exp(-\lambda_n \Delta\psi^{t-\Delta t})}{\lambda_n \Delta\psi^{t-\Delta t}} \right) - g_1^t \left(\frac{1-\exp(-\lambda_n \Delta\psi^t)}{\lambda_n \Delta\psi^t} \right) \right] \bar{S}_{kl}^{t-\Delta t,\text{dev}} \Bigg] F_{lj}^{t-\Delta t\,-1} \end{aligned} \tag{5.41}$$

$$\Delta E_{ij}^{t,\mathrm{vol}} = F_{ik}^{t-\Delta t\ -\mathrm{T}}\left[\bar{B}^{t}\bar{S}_{ij}^{t,\mathrm{vol}} - \bar{B}^{t-\Delta t}\bar{S}_{ij}^{t-\Delta t,\mathrm{vol}} - \frac{1}{3}\sum_{n=1}^{\mathrm{NP}} B_n\left(g_1^{t}\exp(-\lambda_n\Delta\psi^{t}) - g_1^{t-\Delta t}\right)q_{kl,n}^{t-\Delta t,\mathrm{vol}}\right.$$
$$\left. -\frac{1}{3}g_2^{t-\Delta t}\sum_{n=1}^{NP} B_n\left[g_1^{t-\Delta t}\left(\frac{1-\exp(-\lambda_n\Delta\psi^{t-\Delta t})}{\lambda_n\Delta\psi^{t-\Delta t}}\right) - g_1^{t}\left(\frac{1-\exp(-\lambda_n\Delta\psi^{t})}{\lambda_n\Delta\psi^{t}}\right)\right]\bar{S}_{kl}^{t-\Delta t,\mathrm{vol}}\right]F_{lj}^{t-\Delta t\ -1} \tag{5.42}$$

In the recent equations and Eqs. (5.37) and (5.38), the variables $q_{ij,n}^{t-\Delta t,\mathrm{dev}}$ and $q_{ij,n}^{t-\Delta t,\mathrm{vol}}$ are the deviatoric and volumetric hereditary integrals for n^{th} term of Prony series at the previous time step, respectively. After stress state convergence, the hereditary integrals should be updated and stored [see Eqs. (4.50) and (4.51)] at the end of every converged time increment, which will be used for the next time increment, and their expressions are

$$q_{ij,n}^{t,\mathrm{dev}} = \exp(-\lambda_n\Delta\psi^{t})q_{ij,n}^{t-\Delta t,\mathrm{dev}} + \left(g_2^{t}S_{ij}^{t,\mathrm{dev}} - g_2^{t-\Delta t}S_{ij}^{t-\Delta t,\mathrm{dev}}\right)\left(\frac{1-\exp(-\lambda_n\Delta\psi^{t})}{\lambda_n\Delta\psi^{t}}\right) \tag{5.43}$$

$$q_{ij,n}^{t,\mathrm{vol}} = \exp(-\lambda_n\Delta\psi^{t})q_{ij,n}^{t-\Delta t,\mathrm{vol}} + \left(g_2^{t}S_{ij}^{t,\mathrm{vol}} - g_2^{t-\Delta t}S_{ij}^{t-\Delta t,\mathrm{vol}}\right)\left(\frac{1-\exp(-\lambda_n\Delta\psi^{t})}{\lambda_n\Delta\psi^{t}}\right) \tag{5.44}$$

Since the total rigid body rotation is lumped to the plastic part, then: $F_{ij}^{\mathrm{ve}} = U_{ij}^{\mathrm{ve}}$

$$E_t^{\mathrm{vol}} = E_{t-\Delta t}^{\mathrm{vol}} + F_{t-\Delta t}^{\mathrm{T}}\left(\Delta E_t^{\mathrm{vol}}\right)F_{t-\Delta t} \quad , \quad E_t^{\mathrm{dev}} = E_{t-\Delta t}^{\mathrm{dev}} + F_{t-\Delta t}^{\mathrm{T}}\left(\Delta E_t^{\mathrm{dev}}\right)F_{t-\Delta t} \tag{5.45}$$

The deviatoric viscoelastic stretch tensor can be computed simply as (like Eq. (3.101))

$$U_t^{\mathrm{dev}} = \sqrt{I + 2E_t^{\mathrm{dev}}} \tag{5.46}$$

Once the total GL strain is computed through $E_t^{\mathrm{ve}} = U_t^{\mathrm{dev}}\left(E_t^{\mathrm{vol}}\right)U_t^{\mathrm{dev}} + E_t^{\mathrm{dev}}$, then using Eq. (3.101), the viscoelastic deformation gradient is calculated as $F = U^{\mathrm{ve}} = \sqrt{I + 2E^{\mathrm{ve}}}$. Or, similar to Eq. (5.46), one can write: $U_t^{\mathrm{vol}} = \sqrt{I + 2E_t^{\mathrm{vol}}}$. Then, viscoelastic deformation gradient as: $F^{\mathrm{ve}} = U^{\mathrm{ve,dev}}U^{\mathrm{ve,vol}}$.

Rigid body rotation has not been decomposed to elastic and plastic portions, and both have been lumped to one rotation tensor that is considered as the plastic rotation tensor. The rotation can be determined exactly through the deformation gradient tensor, not through incremental integration, and is presented in the next equation

$$B = FF^{\mathrm{T}} = V^{2} \qquad , \qquad V = \sqrt{FF^{\mathrm{T}}} \qquad , \qquad R = V^{-1}F = B^{-1/2}F \tag{5.47}$$

$B^{-1/2}$ is evaluated as next, where λ_i and v are the eigenvalues and eigenvectors tensor.

$$B^{-1/2} = \left(v\ \lambda v^{\mathrm{T}}\right)^{-1/2} = v\ (\lambda)^{-1/2}\, v^{\mathrm{T}} = v \begin{bmatrix} \lambda_1^{-1/2} & 0 & 0 \\ 0 & \lambda_2^{-1/2} & 0 \\ 0 & 0 & \lambda_3^{-1/2} \end{bmatrix} v^{\mathrm{T}} \tag{5.48}$$

At this point, all of the calculations related to viscoelasticity are completed; and now, with the purpose of computing the viscoplastic portion of deformation, through utilizing Eq. (5.13) to (5.24), one can systematically track the following procedures, that explains the computation of viscoplastic rate of deformation.

$$\Delta t\, D_{ij}^{\mathrm{vp}} = \Delta\gamma^{\mathrm{vp}} \frac{\partial g}{\partial \bar{S}_{ij}} \qquad , \qquad \Delta\gamma^{\mathrm{vp}} = \Gamma^{\mathrm{vp}} \left\langle \frac{\bar{\Sigma} - \frac{\alpha}{3}\bar{I}_1 - \kappa(E_{\mathrm{eff}}^{\mathrm{vp}})}{S_y^0} \right\rangle^{N} \tag{5.49}$$

where

$$\bar{\Sigma} = \frac{1}{2}\left[\left(1+\frac{1}{d}\right)\sqrt{\bar{J}_2} + \left(1-\frac{1}{d}\right)\frac{\bar{J}_3}{\bar{J}_2}\right]$$

$$\frac{\partial g}{\partial \bar{S}_{ij}} = \frac{1}{2}\left[\left(1+\frac{1}{d}\right)\left(\frac{\partial \bar{J}_2}{\partial \bar{S}_{ij}}\right)\frac{1}{2\sqrt{\bar{J}_2}} + \left(1-\frac{1}{d}\right)\left(\frac{\partial \bar{J}_3}{\partial \bar{S}_{ij}}\bar{J}_2 - \frac{\partial \bar{J}_2}{\partial \bar{S}_{ij}}\bar{J}_3\right)\frac{1}{\bar{J}_2^2}\right] - \frac{1}{3}\beta\,\delta_{ij}$$

Therefore, by taking into account the calculated rotation in Eq. (5.47), the value of time increment, and the viscoplastic rate of deformation from Eqs. (5.49), then the viscoplastic stretch tensor, U_t^{vp}, will be computed through a successive multiplicative mapping update as next

$$U_t^{\text{vp}} = U_{t-\Delta t}^{\text{vp}} \exp\left(R_t^{\text{T}} D^{\text{vp}} R_t \, \Delta t\right) \tag{5.50}$$

Afterwards, one can find the viscoplastic deformation gradient as

$$F_{ij}^{\text{vp},t} = R_{ik}^{t} \, U_{kj}^{\text{vp},t} \tag{5.51}$$

By substituting Eqs. (5.13) and (5.21) into Eq. (3.119), the equivalent viscoplastic strain can be written as

$$E_{\text{eff}}^{\text{vp},\,t} = E_{\text{eff}}^{\text{vp},\,t-\Delta t} + \Delta E_{\text{eff}}^{\text{vp},\,t} \tag{5.52}$$

where

$$\Delta E_{\text{eff}}^{\text{vp},t} = \Delta\gamma^{\text{vp},t} A^{-1} \sqrt{\left(F_{ki}^{\text{vp},t} \frac{\partial g}{\partial \bar{S}_{ij}^{t}} F_{lj}^{\text{vp},t}\right)\left(F_{ki}^{\text{vp},t} \frac{\partial g}{\partial \bar{S}_{ij}^{t}} F_{lj}^{\text{vp},t}\right)} \quad , \quad A = \sqrt{1+2\left(\frac{0.5+\beta/3}{1-\beta/3}\right)^2}$$

A trial dynamic yield surface function, χ^{trial}, can be defined from Eq. (5.24) as

$$\chi = \bar{\Sigma}^{\text{trial}} - \alpha \, \bar{I}_1^{\text{trial}} - \kappa(E_{\text{eff}}^{\text{vp},\,t-\Delta t}) - S_y^0 \left(\frac{\Delta\gamma^{\text{vp},\,t-\Delta t}}{\Delta t \;\; \Gamma^{\text{vp}}}\right)^{1/N} \tag{5.53}$$

In order to calculate $E_{\text{eff}}^{\text{vp},t}$, the magnitude of viscoplastic stretch can be found iteratively using the Newton-Raphson scheme. When $\Delta\gamma^{\text{vp},t}$ is obtained, $F_{ij}^{\text{vp},t}$ can be calculated from Eq. (5.49) to (5.51). In the Newton-Raphson method, the differential of χ with respect to $\Delta\gamma^{\text{vp}}$ is needed, which can be expressed as

$$\frac{\partial \chi}{\partial \Delta \gamma^{\mathrm{vp}}} = -\frac{\partial \kappa}{\partial \Delta E_{\mathrm{eff}}^{\mathrm{vp}}} \frac{\partial \Delta E_{\mathrm{eff}}^{\mathrm{vp}}}{\partial \Delta \gamma^{\mathrm{vp}}} - \frac{S_y^0}{\Delta \gamma^{\mathrm{vp}} N} \left(\frac{\Delta \gamma^{\mathrm{vp}}}{\Delta t \ \Gamma^{\mathrm{vp}}} \right)^{\frac{1}{N}} \tag{5.54}$$

Therefore, at the $(\mathrm{k+1})^{\mathrm{th}}$ iteration, the viscoplastic multiplier is then calculated by

$$\left(\Delta \gamma^{\mathrm{vp},t} \right)^{\mathrm{k+1}} = \left(\Delta \gamma^{\mathrm{vp},t} \right)^{\mathrm{k}} - \left[\left(\frac{\partial \chi}{\partial \Delta \gamma^{\mathrm{vp},t}} \right)^{\mathrm{k}} \right]^{-1} \chi^{\mathrm{k}} \tag{5.55}$$

Then, substituting the converged $\Delta \gamma^{\mathrm{vp},t}$ into Eq. (5.49) yields a new $F_{ij}^{\mathrm{vp},t}$ which then can be used in calculating the viscoplastic strains $E_{ij}^{\mathrm{vp},t}$ using Eq. (5.35). The above recursive-iterative algorithm with the Newton-Raphson method can be employed to obtain the current effective stresses and the updated values of the viscoelastic and viscoplastic strains by minimizing the residual strain increments, $\prod_{ij}^{t}$, which by following the nature of Lagrangian strain (Eq. (3.54) and (3.55)), can be defined as

$$\prod_{ij}^{t} = F^{\mathrm{vp\ T}} \left[\Delta E_{ij}^{\mathrm{ve},t} + \left(F^{\mathrm{vp}\ -1} F^{\mathrm{ve}} \right)^{\mathrm{T}} \Delta E_{ij}^{\mathrm{vp},t} \left(F^{\mathrm{vp}\ -1} F^{\mathrm{ve}} \right) \right] F^{\mathrm{vp}} \ - \ \Delta E_{ij}^{t} \tag{5.56}$$

The stress increment at the $(\mathrm{k+1})^{\mathrm{th}}$ iteration can be calculated by

$$\left(\Delta \bar{S}_{ij}^{t} \right)^{\mathrm{k+1}} = \left(\Delta \bar{S}_{ij}^{t} \right)^{\mathrm{k}} - \left[\left(\frac{\partial \prod_{ij}^{t}}{\partial \Delta \bar{S}_{kl}^{t}} \right)^{\mathrm{k}} \right]^{-1} \left(\prod_{ij}^{t} \right)^{\mathrm{k}} \tag{5.57}$$

The differential of $\prod_{ij}^{t}$ gives the consistent tangent compliance, which is necessary only for speeding up the convergence of the solution and can be derived as

$$\frac{\partial \prod_{ij}^{t}}{\partial \Delta \bar{S}_{kl}} = F^{\mathrm{vp\ T}} \left[\frac{\partial \Delta E_{ij}^{\mathrm{ve},t}}{\partial \Delta \bar{S}_{kl}} + \left(F^{\mathrm{vp}\ -1} F^{\mathrm{ve}} \right)^{\mathrm{T}} \frac{\partial \Delta E_{ij}^{\mathrm{vp},t}}{\partial \Delta \bar{S}_{kl}} \left(F^{\mathrm{vp}\ -1} F^{\mathrm{ve}} \right) \right] F^{\mathrm{vp}} \tag{5.58}$$

where $\partial \Delta E_{ij}^{ve} / \partial \Delta \bar{S}_{kl}$ and $\partial \Delta E_{ij}^{vp} / \partial \Delta \bar{S}_{kl}$ are the non-linear viscoelastic and viscoplastic tangent compliances, respectively. However, the complete derivations of the compliance tensors are expressed in Appendices C and D.

Damage can also be implemented by using the effective stress concept. As mentioned earlier, once the updated effective stress increment is calculated from Eq. (5.57), the total updated effective stress is calculated from Eq. (5.39), and the final viscoelastic and viscoplastic strains are calculated from Eqs. (5.35). Then one can use Eq. (5.34) to compute the rate of the damage density, as

$$\phi^t = \phi^{t-\Delta t} + \dot{\phi}^t \Delta t \tag{5.59}$$

Then, the final nominal stresses, S_{ij}, can be calculated using Eq. (5.6). Since most of the commercial finite element software work with the Cauchy stress measure; therefore, the nominal II-PK stress should be converted to Cauchy stress as

$$\sigma_{ij}^t = \frac{1}{J^t} F_{ik}^t \, S_{kl}^t \, F_{lj}^{t\,\mathrm{T}} \tag{5.60}$$

The effective stress concept is numerically attractive, since it allows the calculations of the effective stresses to be decoupled from damage. The above formulated numerical procedures have been implemented in the user material subroutine (UMAT) of the well-known finite element code ABAQUS, as part of this research.

5.4 Application of the Constitutive Models to Polymer

In this section, af first the main steps for identifing and determining the material parameters associated with the presented constitutive model will be summarized.

Subsequently, the model is used for predicting the viscoelastic, viscoplastic, and damage response of PMMA polymer under different loading conditions and temperatures.

The procedure for determining the combined viscoelastic and viscoplastic model parameters in a systematic way by using the single/repeated creep-recovery test has been thoroughly discussed by Huang et al. (2011a). It is important to mention that it is practically impossible to determine the instantaneous compliance, $\bar{D}_0$, from the creep or creep-recovery tests, because the instantaneous strain is very difficult to measure, and usually the average of $\bar{D}_0$ is used. Hence, $\bar{D}_0$ is determined from the initial response using the monotonic constant strain rate test at the reference temperature. Viscoelastic parameters are separated into two categories. The first category of parameters is the Prony series coefficients, $\bar{D}_n$ and λ_n (Eq. (5.10)) associated with the linear viscoelastic response for undamaged material. The second category contains the non-linear viscoelastic parameters, g_0, g_1, and g_2, and the stress time-shift factor, a_σ. The first step to identify these parameters is separating the viscoelastic and viscoplastic strains in a single creep-recovery test at low stress and strain levels for which one can assume that the induced damage in the material is negligible. It is obvious the result of a small strain model and its extended to large strain are the same, while a body is subjected to small deformation. Schematic diagrams are shown in Fig. 5.1 for a single creep-recovery test.

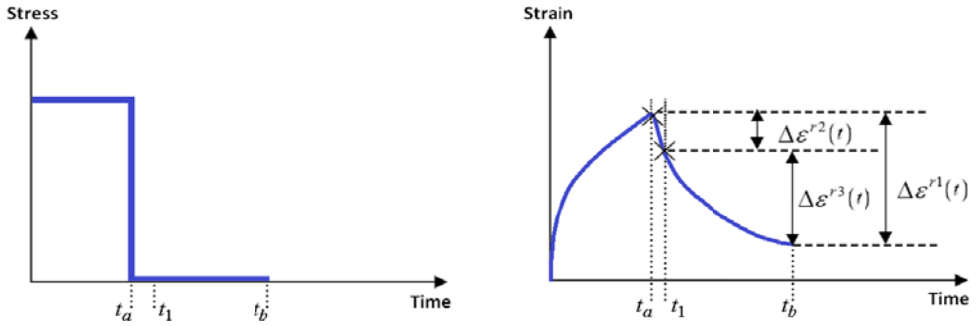

Fig. 5.1. Schematic depiction of single creep-recovery test.

One can then express the creep and recovery strains for this test (in one-dimension) from Eqs. (5.8) and (5.9) at reference temperature where the temperature-shift factor is 1, as

$$\varepsilon^{c}(t)=\varepsilon^{rec}(t)+\varepsilon^{irrec}(t)\ =\left[g_0\bar{D}_0+g_1 g_2\ \Delta\bar{D}\left(\frac{t}{a_s}\right)\right]\bar{S}+\varepsilon^{irrec}(t)\quad,\quad \text{for: } 0<t<t_a \qquad (5.61)$$

$$\varepsilon^{r}(t)=\varepsilon^{rec}(t)+\varepsilon^{irrec}(t_a)=g_2\bar{S}\left[\Delta\bar{D}(\psi)-\Delta\bar{D}(t-t_a)\right]+\varepsilon^{irrec}(t_a)\quad,\quad \text{for: } t_a<t<t_b \qquad (5.62)$$

where ε^{c} is the total creep strain, ε^{r} is the total strain during recovery (or unloading), ε^{rec} is the recoverable strain (i.e. viscoelastic strain), ε^{irrec} is the irrecoverable strain (i.e. viscoplastic strain), $\psi=t/a_s+t-t_a$, and t_a is the loading time shown in Fig. 5.1. Notice that the instantaneous strain $g_o\bar{D}_o\bar{\sigma}$ is neglected from Eq. (5.61) due to the difficulty in measuring it. The first step of the analysis procedure is to obtain the Prony series coefficients $\bar{D}_n$ and λ_n in Eq. (5.10) from a linear viscoelastic response at a low stress level. Since the viscoplastic strain during the relaxation process is constant, which is equal to its value at the end of the loading step (or equivalently at the end of the unloading step), $\bar{D}_n$ and λ_n are determined first by analyzing the recovery strain. The analysis employs the strain $\Delta\varepsilon^{r1}$ shown in Fig. 5.1, which is the recovered strain

between t_a and t_b in order to obtain $\bar{D}_n$ and λ_n at the lowest stress level without damage (i.e., one can assume $g_0 = g_1 = g_2 = a_s = 1$). The expression for $\Delta\varepsilon^{r1}(t)$ can be derived from Eqs. (5.61), (5.62), and (5.10), such that

$$\begin{aligned}\Delta\varepsilon^{r1}(t) &= \varepsilon^{c}(t_a) - \varepsilon^{r}(t) \\ &= \bar{S}\left\{\bar{D}_0 + \sum_{n=1}^{N}\bar{D}_n[1-\exp(-\lambda_n t_a)] - \sum_{n=1}^{N}\bar{D}_n \exp[-\lambda_n(t-t_a)][1-\exp(-\lambda_n t)]\right\}\end{aligned} \tag{5.63}$$

which can be simplified to

$$\begin{aligned}\Delta\varepsilon^{r1}(t) &= \varepsilon^{c}(t_a) - \varepsilon^{r}(t) \\ &= \bar{S}\left\{\bar{D}_0 + \sum_{n=1}^{N}\bar{D}_n\left[1-\exp(-\lambda_n t_a) - \exp[-\lambda_n(t-t_a)] + \exp[-\lambda_n(2t-t_a)]\right]\right\}\end{aligned} \tag{5.64}$$

Then, $\bar{D}_n$ and λ_n are determined by minimizing the error between the measurements of $\Delta\varepsilon^{r1}(t)$ and Eq. (5.63). The non-linear viscoelastic expressions in Eqs. (5.61) and (5.62) with the identified $\bar{D}_n$ and λ_n can then be used to analyze the experimental data at higher stress levels to determine the non-linear parameters. At higher stress levels, the next expression for the recovered strain $\Delta\varepsilon^{r3}(t)$ from $t = t_a$ to $t = t_b$ (Fig. 5.1) can be derived from Eq. (5.62) and then used to determine the non-linear parameter g_2, as

$$\begin{aligned}\Delta\varepsilon^{r3}(t) &= \varepsilon^{r}(t_1) - \varepsilon^{r}(t) \\ &= g_2\bar{S}\sum_{n=1}^{N}D_n \exp(-\lambda_n t_a)[1-\exp(-\lambda_n \frac{t_a}{a_s})][\exp(-\lambda_n t_1) - \exp(-\lambda_n t)]\end{aligned} \tag{5.65}$$

Once the non-linear parameter g_2 is obtained, the expression for $\Delta\varepsilon^{r2}(t)$, which can be derived from Eqs. (5.61) and (5.62), is fitted to the experimental data from $t = t_a$ to $t = t_1$ (Fig. 5.1) in order to get the non-linear parameters g_1 and a_s, such that

$$\Delta\varepsilon^{r2}(t) = \varepsilon^{c}(t_a) - \varepsilon^{r}(t)$$
$$= \bar{S}\left\{ g_0 \bar{D}_0 + g_2 \left(\sum_{n=1}^{N} \bar{D}_n [1 - \exp(-\lambda_n \frac{t_a}{a_s})] \left[g_1 - \exp\left(-\lambda_n (t - t_a)\right) \right] \right) \right\} \tag{5.66}$$

Following the above procedure, for PMMA polymer, the Prony series and non-linear viscoelastic parameters can be extracted from the experimental data presented by Lai and Bakker (1995) and Hasan and Boyce (1995) at different stresses and temperatures. The trend of the identified viscoelastic parameters are illustrated in Fig. 5.2. Moreover, Table 5.1 presents the calibrated viscoelastic model parameters. Here, the non-linear parameters are functions of the effective stress, $\hat{\bar{S}}$.

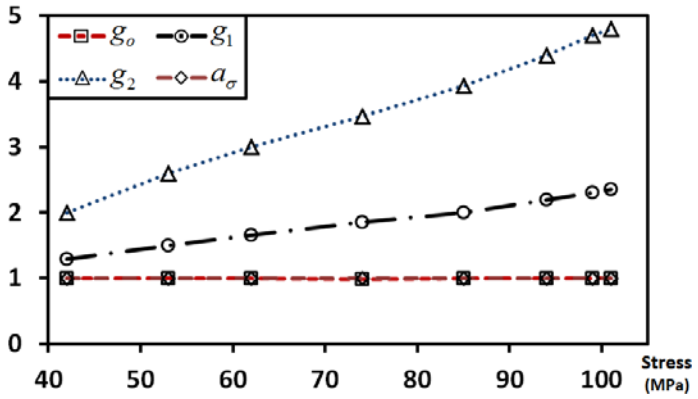

Fig. 5.2. Variation of non-linear viscoelastic parameters versus stress levels at 296 K.

Table 5.1: Viscoelastic material parameters for PMMA polymer.

Linear viscoelastic model parameters									
N	1	2	3	4	5	6	7	8	9
λ_n (s^{-1})	1.0	0.1	0.01	10^{-3}	10^{-4}	10^{-5}	10^{-6}	10^{-7}	10^{-8}
$\bar{D}_n$ (MPa^{-1})$\times 10^{-6}$	10.34	14.66	16.84	19.58	27.28	41.06	61.23	80.50	160.23
$\bar{D}_0$ (MPa^{-1})	200×10^{-6}								
Non-linear viscoelastic parameters									
$g_0 = \exp\left(7.037\,(T - T_0)/T_0\right)$ $\quad$ $a_s = \exp\left(-23.24\,(T - T_0)/T_0\right)$									
$g_1 = \begin{cases} 1.0 & \hat{\bar{S}} \le 20 \\ 0.0175(\hat{\bar{S}} + 32.11) & \hat{\bar{S}} > 20 \end{cases} \times \exp\left(0.459\,(T - T_0)/T_0\right)$									
$g_2 = \begin{cases} 1.0 & \hat{\bar{S}} \le 20 \\ 0.0467(\hat{\bar{S}} + 1.093) & \hat{\bar{S}} > 20 \end{cases} \times \exp\left(0.459\,(T - T_0)/T_0\right)$									
Temperature time-shift factor									
$a_T\ (T_o = 296\ \mathrm{K}) = 1.0$, $a_T\ (T = 323\ \mathrm{K}) = 0.5$									

Once the linear and non-linear viscoelasticity model parameters are obtained from the separated viscoelastic strain, one can subtract the viscoelastic strain from the total strain measurements to obtain the viscoplastic strain. Viscoplastic model parameters can then be determined from the extracted viscoplastic response. From the dynamic yield surface in Eq. (5.24), one can obtain and use the next expression in case of uniaxial compression test, such that

$$\frac{\Delta\gamma^{\mathrm{vp},t}}{\Delta t} = \Gamma^{\mathrm{vp}}\left[\left((1-\frac{\alpha}{3})\bar{S} - \left(\kappa_0 + \kappa_1\left[1-\exp\left(-\kappa_2\varepsilon_{\mathrm{eff}}^{\mathrm{vp}}\right)\right]\right)\right)\Big/\tau_y^0\right]^N \tag{5.67}$$

where $\bar{S}$ is the applied uniaxial compressive stress in the absence of damage. The increment of plastic multiplier, $\Delta\gamma^{\mathrm{vp},t}$, can be obtained from the separated $\Delta\varepsilon^{\mathrm{vp},t}$, through using the experimental data in case of uniaxial compression by considering the expression derived from Eq. (5.13), as

$$\Delta\gamma^{\text{vp},t} = \frac{\Delta E^{\text{vp},t}}{\partial g / \partial \bar{S}} = \frac{\Delta E^{\text{vp},t}}{(1-\beta/3)} \tag{5.68}$$

The quantity of viscoplastic parameters: Γ^{vp}, N, κ_0, κ_1, and κ_2, can be obtained numerically by minimizing the error between the measurements and Eq. (5.67). Using the experimental data presented by Lai and Bakker (1995) and Hasan and Boyce (1995), the viscoplastic material constants are obtained. The loading times in these tests were rather short; hence, one can assume that the material is not damaged during these experiments, or at least the introduced damage is not signifcant at lower stress levels. The identified viscoplastic material parameters are listed in Table 5.2.

Table 5.2: Viscoplastic material parameters for PMMA polymer.

α	β	$\Gamma^{\text{vp}}_{\text{ref}}$ (s^{-1})	N	d	κ_0 (MPa)	κ_1 (MPa)	κ_2	θ	T_{ref} (K)	S_y^o (MPa)
0.3	0.15	2×10^{-4}	1.3	0.85	80	75	30	3.78	296	1.0

The viscodamage model has four distinct material parameters: (i) Γ_0^{vd} is the reference damage viscousity parameter, (ii) Y_0 is the reference damage force obtained at a reference stress from a single creep test, (iii) q shows the dependency of the damage model on stress, and (iv) k is a constant showing how much the evolution of damage density depends on the total effective strain. To find the viscodamage parameters, one can select Y_0 as the smallest stress level at which damage initiates. Then, one can assume that the value of $\bar{Y}(1-\phi)^2/Y_0$ is almos constant in the stress level that damage

initiates; thus, the value of these terms: $\Gamma_0^{\text{vd}}\left[\bar{Y}(1-\phi)^2/Y_0\right]^q$ is constant, and variable q can be set as: $q=0$ at the first try. Then proper values for the whole of the recent expression and parameter k can be found by using just one creep-tertiary curve at one certain stress level (which can be the curve with the lowest stress level). Afterwards, by repeating the same procedure using another stress level data for the tertiary-creep test, with the obtained parameter k, the new value for the whole term of $\Gamma_0^{\text{vd}}\left[\bar{Y}(1-\phi)^2/Y_0\right]^q$ can be found. In the next step, by dividing the value of the expression for both stress levels, a constant value for Γ_0^{vd} and then q can be computed. In Table 5.3, the viscodamage material parameters are listed.

Table 5.3: Viscodamage material parameters for the PMMA polymer.

$\Gamma_{\text{ref}}^{\text{vd}}$ (s^{-1})	Y_0 (MPa)	q	k
2×10^{-6}	85	15	1.8

Now, similar to Eq. (5.34), one can easily write the damage viscousity parameter as

$$\Gamma^{\text{vd}}=\Gamma_{\text{ref}}^{\text{vd}}G(T)=2.0\times10^{-6}\times\exp\left[69.175\left(\frac{T-296}{296}\right)\right] \tag{5.69}$$

In Section 5.5, the comparison of creep and recovery results and creep-damage predictions based on experimental data, are illustrated.

5.5 Model Predictions

In order to demonstrate the capabilities and predictions of all three unified constitutive models that are generalized to large deformation framework, the numerical

analyses have been conducted and shown in the small and large strain range. The components of models in the creep tests (secondary and tertiary) have been decomposed to VE, VE+VP, and VE+VP+VD which stand for viscoelastic, viscoelastic–viscoplastic, and viscoelastic–viscoplastic–viscodamage, respectively, in the following figures. The comparison of experimental values and just viscoelastic model predictions for both creep and recovery at lower stress levels (15-40 MPa) at room temperature (Lai and Bakker (1995)), using the numerical model described in Eqs. (5.36) to (5.46), are plotted in Fig. 5.3 (a) and (b).

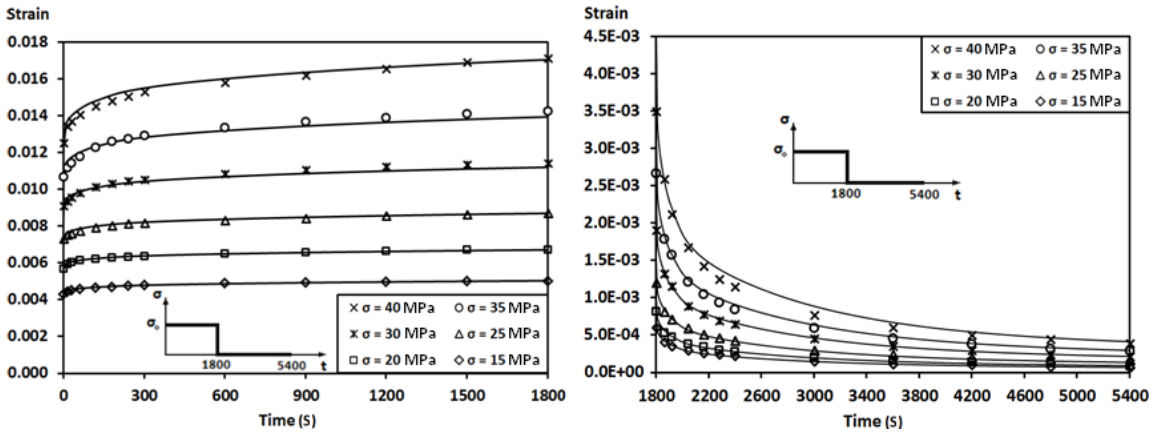

(a) Creep test (30 minutes) (b) Recovery test (60 minutes)

Fig. 5.3. Predictions for PMMA behavior under tensile loading in lower stress level ranges (15-40 MPa).

It should be noted that, the non-linear viscoelastic functions in Table 5.1 were calibrated by using this range of data (25 to 35 MPa), and then those functions are hired to predict the creep behavior in other stress ranges. Also, it should be clarified that in order to find the viscoelastic material parameters of PMMA, the data presented by Lai and Bakker

(1995) is used. This data set is in small deformation range, and is proper for calibrating the Prony series terms and their corresponding relaxation time variables. After finding the viscoelastic parameters, to calibrate the viscoplastic and viscodamage models, since they are in large strain range (more than 5%), the data presented by Hasan and Boyce (1995) is used (Figs. 5.4 - 5.5, and Figs. 5.7 - 5.8).

The results of creep-secondary for higher stresses (Hasan and Boyce (1995)), which are in the range of 42 to 74 MPa at 296 K have been illustrated in Figs. 5.4 (a) to (d). The predictions for 42 and 53 MPa do not show any plasticity, and as can be seen, the viscoelastic and viscoplastic and also viscodamage simulations exactly coincide. In fact, as can be studied in open reports about yield stress of the PMMA (glassy amorphous polymer), the irrecoverable deformation begins around 50-55 MPa at room temperature. This is the reason why the viscoelastic model under predicts the behavior when stress is 62 MPa, (see Fig. 5.4 (c)), which is mostly due to the initiation of plastic phenomenon. By focusing on the stress level at 85 MPa, the combination of viscoelastic and viscoplastic underpredicts the real behavior of material, which can be attributed to the damage initiation. As shown in Fig. 5.4 (e), by adding the damage law the behavior has been precisely captured. In Figs. 5.4 (f) to (h), the differences between the models are easily recognizable.

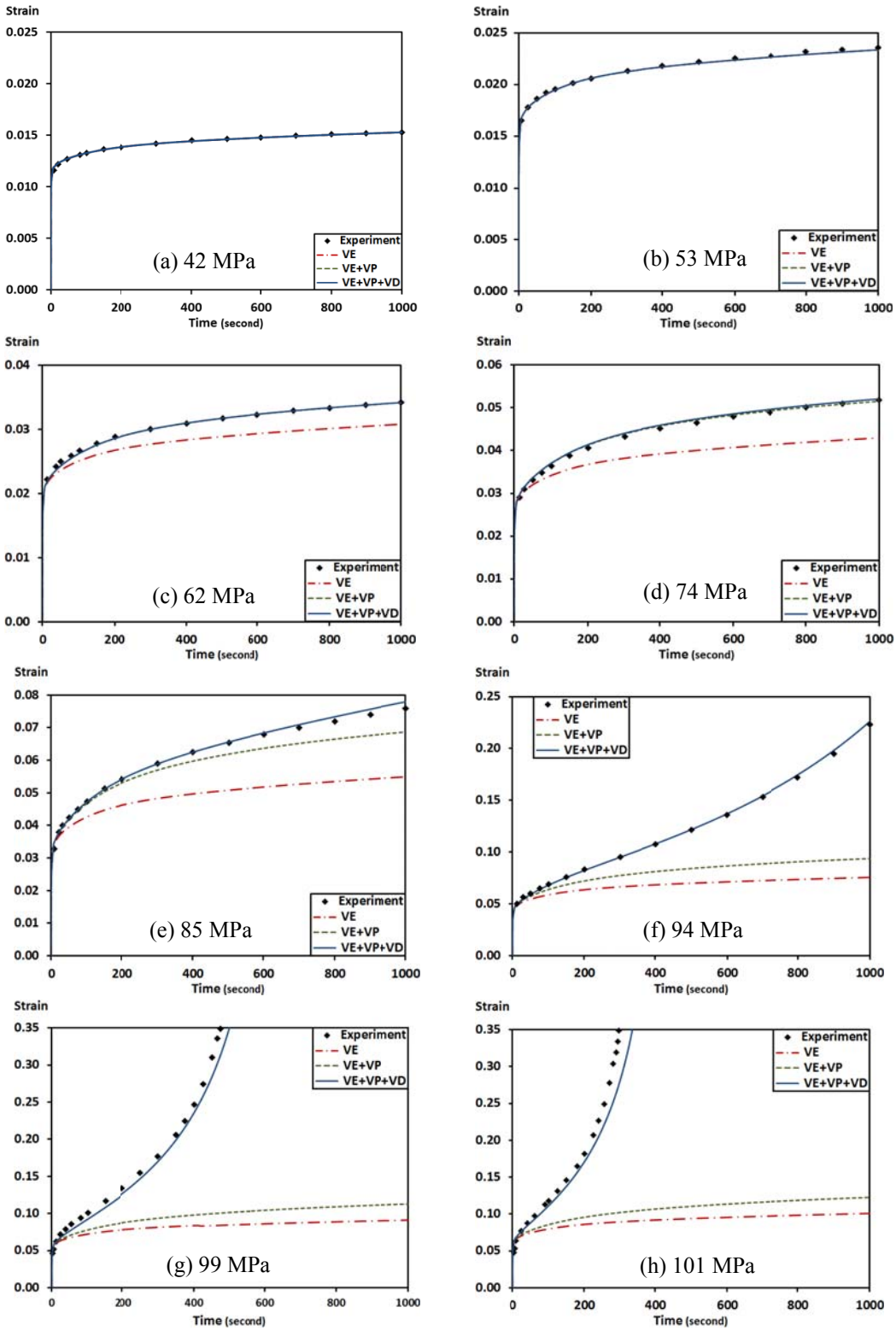

Fig. 5.4. Experimental data and numerical predictions for eight stress levels at 296 K.

The viscodamage model prediction on 94 MPa is precise, but the simulations at 99 and 101 MPa in Fig. 5.4 (g) and (h) slightly underpredict the experimental tests. Fig. 5.5 shows the total comparisons for all the experimental data and the predictions validations of the numerical models in one diagram.

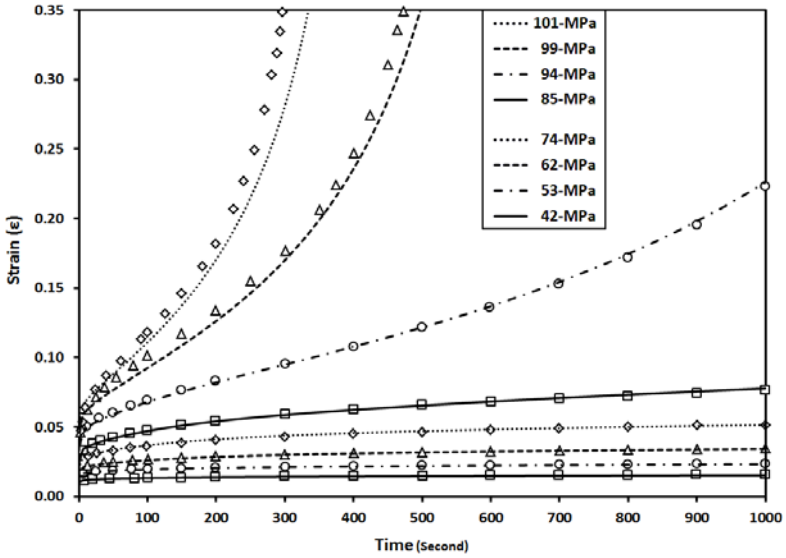

Fig. 5.5. Experimental data versus predictions for all stress levels (296 K = 23 ^{o}C).

In addition, in Fig. 5.6 (a) and (b) the changes of Damage Density Φ, Eq. (5.34), versus time and strain are depicted only for higher stress levels (85, 94, 99, and 101 MPa), since as can be recognized from Fig. 5.4 (a) to (d) there are no effects of damage initiation or evolution in these stress control tests at lower stress levels.

The behavior of PMMA polymer at a higher temperature (323 K) is shown here. Fig. (5.7) (a) and (b) present that the behavior at lower stresses (22 and 32 MPa) is governed by just viscoelasticity. Fig. 5.7 (c) and (d) depicts the behavior of PMMA at 42 and 52 MPa, and show that plastic phenomenon initiated around 40 MPa.

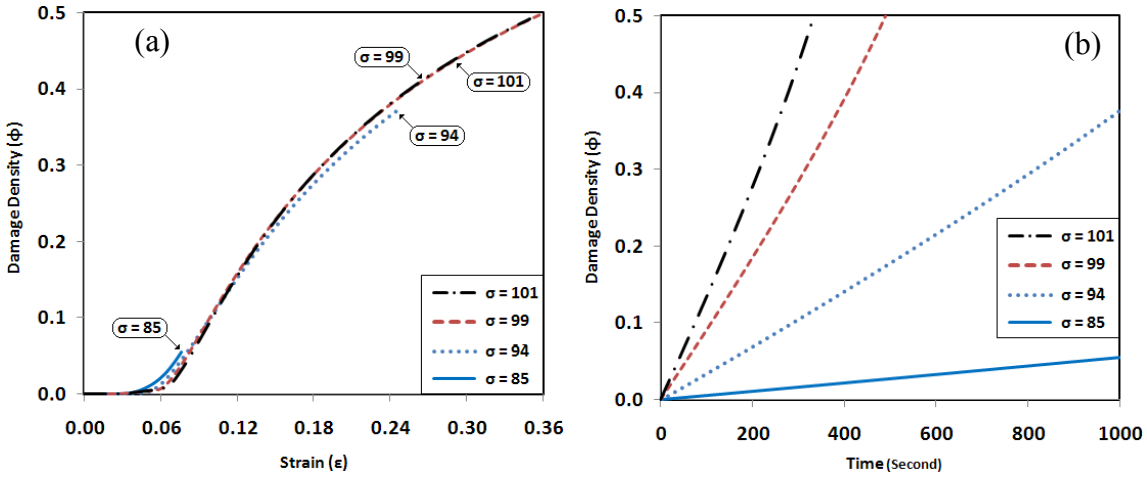

Fig. 5.6. Damage density versus: (a) strain, and (b) time, for creep tests in the range of 85 to 101 MPa, at room temperature (296 K).

Also, as can be observed there is no damage in these stress levels. One can compare the initiation of irrecoverable behavior at both temperatures. In Fig. 5.7 (e) to (h), like the simulations at room temperature the models differences in prediction are easily identifiable.

The temperature variables for transforming the viscoelastic material parameters from room temperature (296 K) to 323 K, in Table 5.1, is achieved by calibrating the model response with the experimental data sets in 22 and 32 MPa, at 323 K. Moreover, the temperature factor in the exponential expression in the viscoplastic model (the Arrhenious temperature form) is obtained based on calibrating the viscoplastic model with just experimental data in 42 MPa at 323 K. Also, in order to find the temperature variable for viscodamage viscous parameters, this parameter is calibrated with the data in 66 MPa stress level at 323 K. These calibrated parameters are used to validate the models in other stress levels.

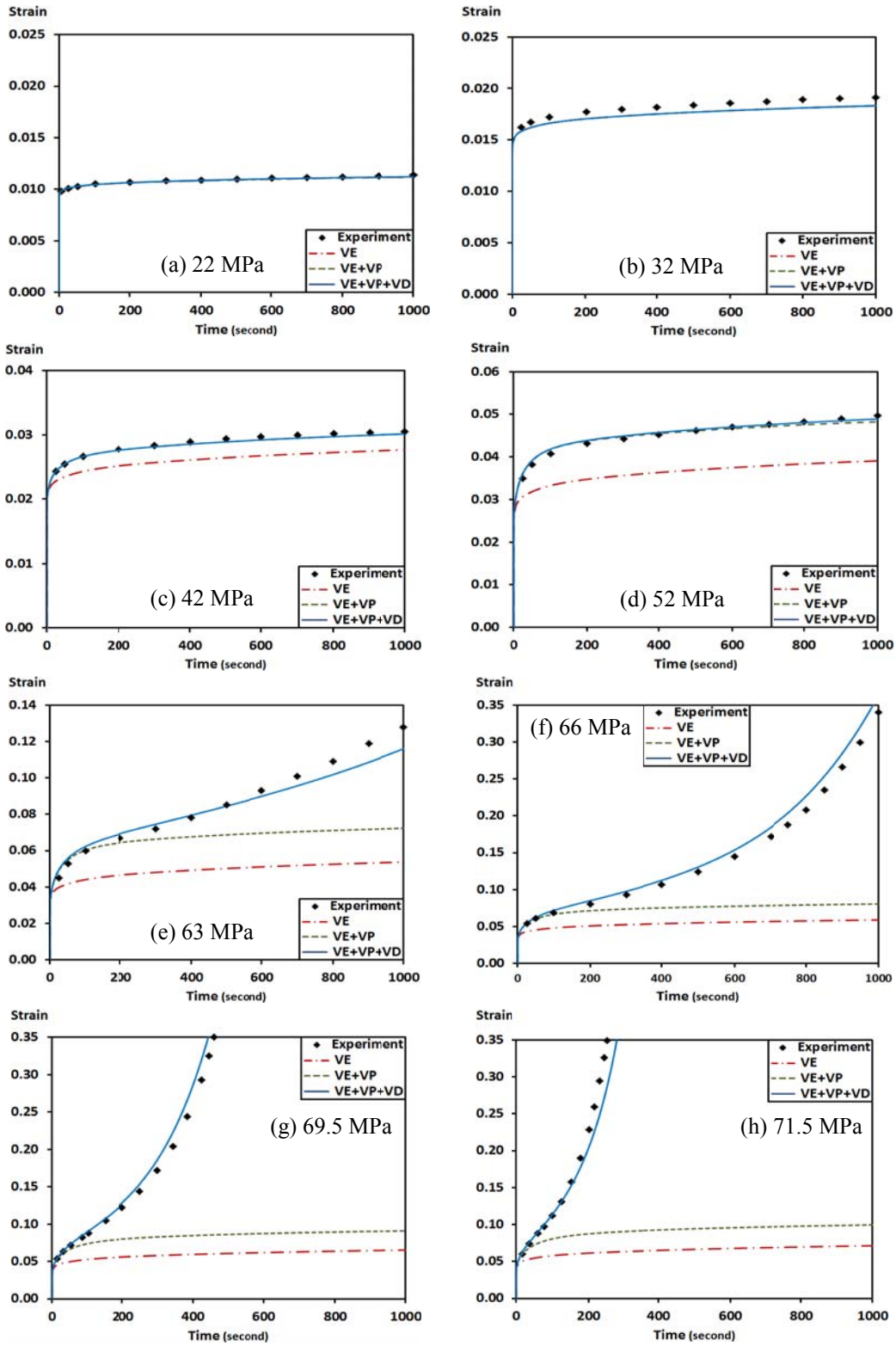

Fig. 5.7. Experimental data and numerical predictions for eight stress levels at 323 K.

As seen, although the model predictions differ slightly from experimental data sets, they are in acceptable ranges. Fig. 5.8 presents the predictions versus the experimental data of all stress levels in one view.

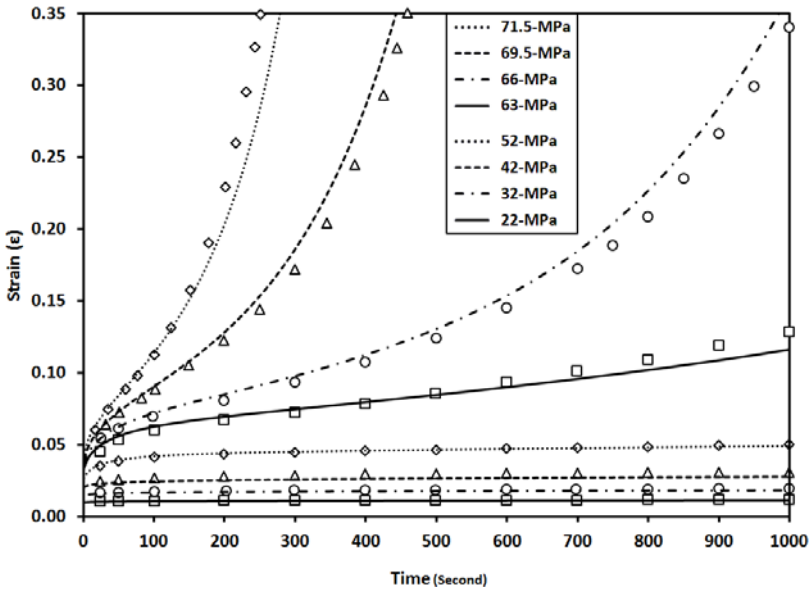

Fig. 5.8. Experimental data versus predictions for all stress levels (323 K = 50 ^{o}C).

The results of predictions for higher stress levels at 323 K show that the temperature parameters in the unified models were well-calibrated in such a way that the results of numerical simulation are also in good agreement with the experimental data in this temperature level. Moreover, the variations of Damage Density (Φ) versus ture strain and time for higher stress levels (63, 66, 69.5, and 71.5 MPa) at 323 K are illustrated in Fig. 5.9 (a) and (b). In practice, by setting the temperature parameter in the related formula (Arrhenious exponential forms) for all material model parameters, one can predict the behavior of PMMA in other temperatures and stresses.

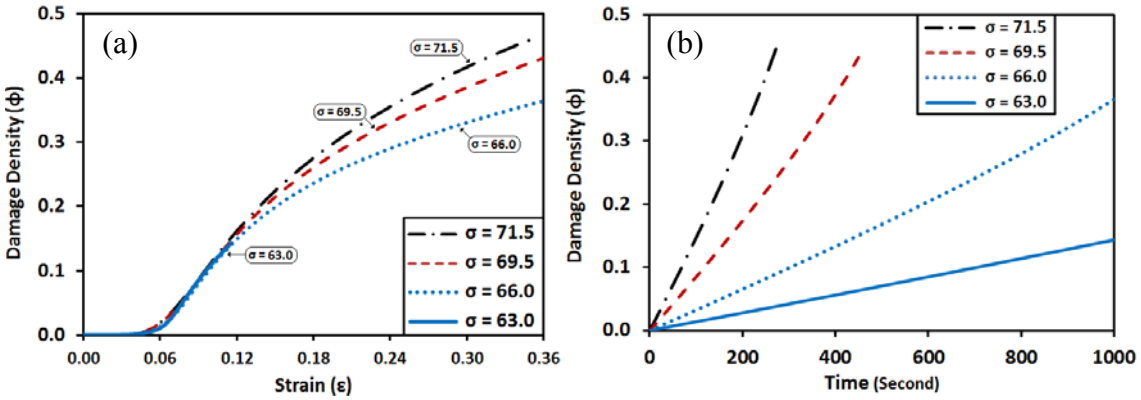

Fig. 5.9. Damage Density versus: (a) strain and (b) time for creep tests in the range of 63 to 71.5 MPa at 323 K.

To study the capabilities of the calibrated models for stresses higher than the available data (more than 101 MPa at 296 K, and more than 71.5 MPa at 323 K), in Fig. 5.10 (a) and (b), forecasting the creep tertiary response of PMMA, are displayed. It is a virtual experiment performed to find the stress level (in stress control test) at which rupture will occur.

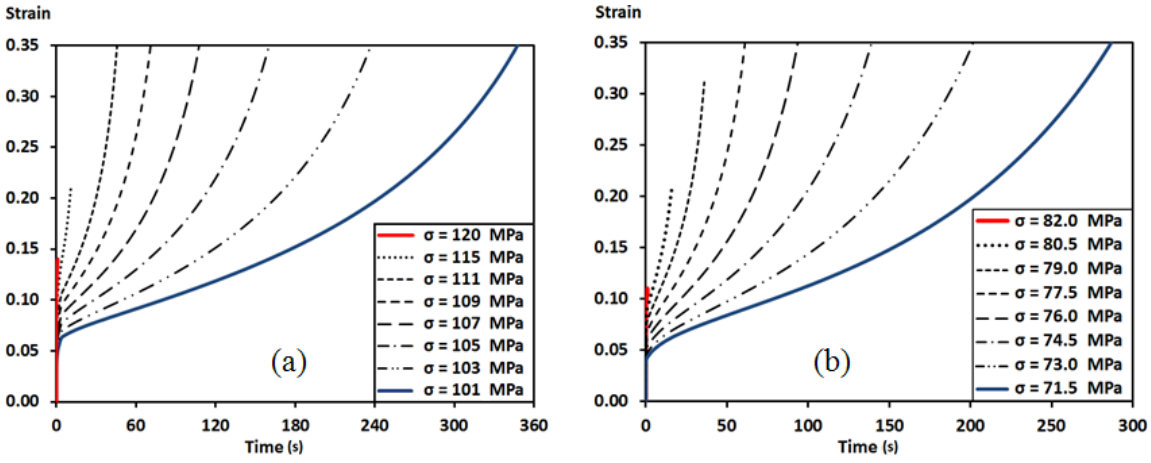

Fig. 5.10. Forecasting the behavior of PMMA under high stress levels for finding the stress where rupture will occur: (a) 296 K, and (b) 323 K.

The simulations show that the failure stress occurs around 120 MPa at room temperature and 75 MPa at the other temperature level,which is compatible with the experiments mentioned by Kondo et al. (1992) and in ASTM D 695.

Additionally, after setting and calibrating the required material parameters for all of the numerical models by using the creep and recovery tests (mentioned at the beginning of this section), several simulations are conducted to check and compare the calibrated models with stress-strain responses of PMMA at different strain rates and temperatures. Thus, in Fig. 5.11 (a) and (b), the comparison between numerical simulations and the experiments for stress-strain tests (displacement control), for three different strain rates at both temperature levels, have been presented. The required material parameters for these simulations come from the calibrated parameters (presented in Fig. 5.4 and 5.7) for creep-secondary and -tertiary (stress control) tests.

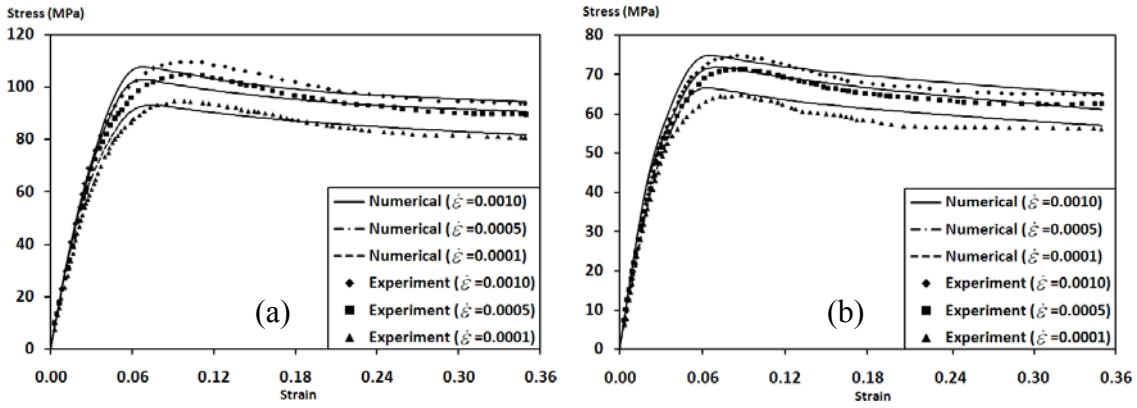

Fig. 5.11. Comparison between experimental data and calibrated numerical models for displacement control tests, at three different strain rates: (a) 296 K, and (b) 323 K.

Fig. 5.12 (a) and (b) display how damage density changes versus true strain at different strain rates at both temperatures in the simulations illustrated in Fig. 5.11 (a) and (b). It is obvious that the increase of damage density accelerates at higher temperature. Moreover, forecasting the behavior of PMMA at the other strain rates, from low to high rates, at both temperatures are displayed in Fig. 5.13 (a) and (b). It has been simulated to show how PMMA acts while subjected to a range of strain rates loading.

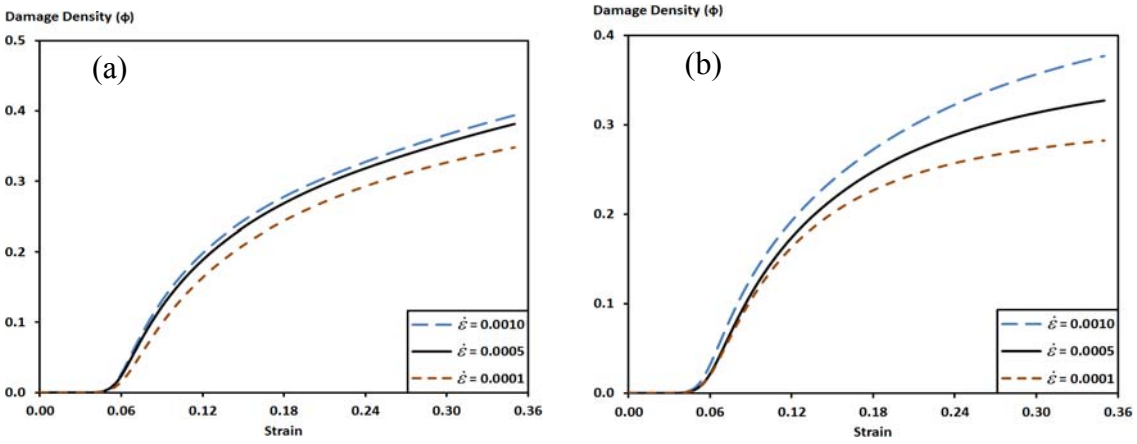

Fig. 5.12. Damage density versus strain, at three strain rates: (a) 296 K, and (b) 323 K.

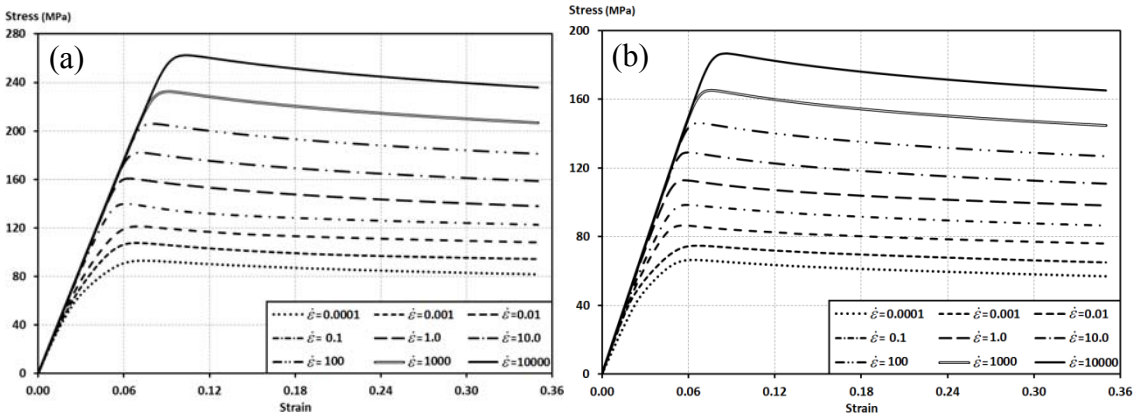

Fig. 5.13. Forecasting the stress-strain behavior of PMMA, in low and high strain rates (nine different strain rates): (a) at 296 K, and (b) at 323 K.

5.6 Summary

This chapter contains the generalization of unified constitutive models from small strain range to large deformation, and then applying a temperature, rate, and time-dependent continuum damage model (viscodamage) with the coupling of temperature-dependent viscoelastic, viscoplastic, and viscodamage models for accurately predicting the non-linear behavior of PMMA polymer. Computational algorithms are presented for numerically integrating and implementing the proposed constitutive models using finite element methods via UMAT in ABAQUS (2008).

Based on creep-secondary and -tertiary tests conducted over a stress range (42 to 101 MPa) at room temperature (296 K) and another stress range (22 to 71.5 MPa) at 323 K (50 C), it is observed that the PMMA polymer exhibits non-linear viscoelastic-viscoplastic behavior. Also, it has been found that the behavior of this material around 52 MPa at 296 K and 38 MPa at 323 K becomes a combination of non-linear viscoelastic and viscoplastic up to about 80 MPa (296 K) and 60 MPa (323 K). As demonstrated, after 80 MPa (296 K) and 60 MPa (323 K) the damage behavior becomes important, in such a manner that in 85 MPa (296 K) and 63 MPa (323 K) the tertiary part of creep behavior is obvious.

The predictions of the developed models are in good agreement with the experimental sets in both creep-secondary and -tertiary responses of PMMA polymer in high stress levels at both temperatures. The creep-tertiary response directly relates to the effect of damage phenomenon, which is the corrspondece of FLV (free local volumes) in polymers. In addition, the potential of the proposed calibrated models for forecasting the

failure stress of PMMA, which occurs around 120 MPa at room temperature and 80 MPa at 50 C, is demonstrated. Also, the results of the predictions of stress versus strain (displacement control test) employing the combined viscoelastic, viscoplastic, and viscodamage models demonstrate acceptable predictions for all stress-strain diagrams in different strain rates and at both temperatures. Using the material parameters found from creep responses, shows the validation of the calibrated model. Although the peak points of the numerical predictions have a shift in comparison to experimental data, they are in acceptable ranges.

The current time-integration scheme is also shown to be computationally efficient and accurate. The proposed algorithm is the extension of small strain models to large deformation context, and is designed to be compatible with finite elements (FE) framework. The FE simulations show the ability of the proposed combination methods for effectively predicting the time dependent responses of PMMA polymers, and also can be applied to other polymer and polymer composite materials.

CHAPTER VI

GENERATING REPRESENTATIVE VOLUME ELEMENTS (RVE) FOR COMPLEX MICROSTRUCTURES

6.1 Introduction

Considerable efforts have been dedicated to employ materials with lightweight structures, which are highly desirable to be used to increase energy efficiencies in different commercial and industrial divisions (Corum et al., 2001; Dahl et al., 2005; Jacob et al., 2006). The thermo-mechanical properties of randomly dispersed particles or fiber reinforced composites (PRC or FRC) are of paramount importance for their special applications in lightweight structures (Pan et al., 2008). Mass production of random particle or fiber based composites with different volume fractions, establishes PRCs or FRCs as the alternating candidate materials for developing and manufacturing lightweight components in the sports, automotive, army, aerospace, and other industries.

In this chapter, numerical methods for generating RVEs (Representative Volume Elements) for random PRCs or FRCs are reviewed, and another technique will be introduced. The required techniques and algorithms are discussed and proposed for generating RVEs containing randomly distributed reinforcing inclusions. The software developed as part of this research (RVE_Maker) for generating different types of RVEs in both 2D and 3D is presented here. This program creates RVEs in order to be analyzed for obtaining specific physical (thermo-mechanical) properties of the composite material using finite element analysis (FEA).

6.2 Comprehensive Idea for Creating Microstructures

To generate various RVEs with different types of particles, geometrical knowledge of the shapes, orientations, location and distribution pattern of the reinforcing inclusions is mandatory. Geometrical entities that morphologically match to the reinforcing inclusions can be inserted in a 2D rectangular region, or a 3D cuboid (box) by following a predefined distribution outline (locations with a certain orientation).

Based on the above idea, several researchers employed different techniques and approaches to automatically generate RVEs. Okereke et al. (2002) developed a MATLAB code based on the Monte Carlo Method or Hard Core algorithm, in which a definite 2D rectangular RVE is occupied randomly until a predefined volume fraction is obtained. They also applied a constraint of periodicity of material on the generated RVE. Okereke's code creates straight fibers by extruding a 2D circular model in the third dimension. A typical 3D RVE generated using the above approach is similar to Fig. 6.1. In addition, Digimat MF software provides a mean field homogenization of multi-phase materials, such that the model can be treated as a material with one set of parameters.

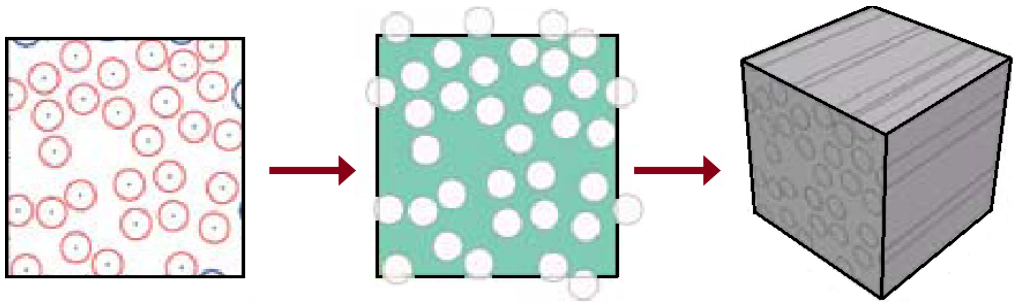

Fig. 6.1. 2D circular particles are extruded to create 3D model (Okereke et al. (2002)).

Digimat FE is a software program that creates a 3D RVE structure (van Melick and Govaert, 2009). However, this software generates straight unidirectional fibers, and cannot consider the waviness of fibers. To expand the use of fibers in composites and accurately characterizing these types of inclusions in composite materials, as mentioned in Section 6.1, is needed. The main challenge in completely virtually exploring the capabilities of the FRCs can be ascribed to the obvious barriers of effectively modeling their geometry at the micro-level. This complexity becomes even more apparent while modeling the waviness of fibers and also modeling fibers with high aspect ratios (HAR).

In this section, the concerns and issues for generating 2D and 3D composite models are categorized and listed from the simplest type of inclusions in 2D to the most complex one (Hybrid) in 3D. Nano-ceramic particles have the simplest but most fundamental geometry, which has a 2D circular shape. Now, in order to create them, as demonstrated in Fig. 6.2, the particles with the largest radius should be generated at first, through randomly locating their center and their radius.

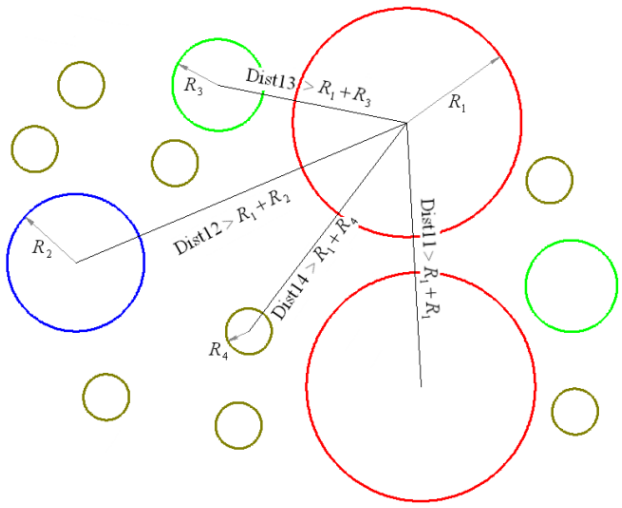

Fig. 6.2. Graphically illustrating how to check the intersection of 2D-circular particles.

Afterwards, the other particles can be created with respect to their radii successively from the large one to the smaller one. For checking the intersections, while locating a new center for a new particle, the distance between the central points of the newest particle should be greater than the summation of its radius and the radius of each of the previously generated particles.

The next category of well-known nanocomposites is nanoclay/polymer composites. Nanoclay particles in both intercalated and exfoliated conditions have ellipsoidal shape (but different aspect ratios and properties) (Sheng et al., 2004). As TEM images have revealed (Khan, 2011, c; Yung et al., 2006), the main geometrical characteristic of nanoclay particles is their high aspect ratios, in such a way that they can be considered as a planar sheet in fully exfoliated condition. Therefore, in order to virtually generating these inclusions in two-dimensions, one should note that the cross sections of these particles are ellipse-shape with high aspect ratio. The procedure for generating the ellipse-shape geometry is firstly locating the center of the particle in a random way. Then, the end point of the major axis should be identified, through the length of the major axis, and then the angle of rotation. Finally, the length of the minor axis and/or the point at the end of this axis is required to define the geometry (Fig. 6.3 (a)). Now, for generating the next elliptical particles, the same procedure should be followed, and moreover the intersections of the newest particle and the previous ones need to be checked. There are two ways to check the intersection of these geometrical entities. The first and most costly one is mathematically checking the intersection of ellipses, through solving a system of non-linear equations of conical equations in matrix form. This method is not practical, since the geometries should be finally meshed, and

using this method accepts very close particles as not intersected ones. This condition causes problems in meshing and analyzing the RVE; therefore, the second method needs to be introduced. In this approach, since these particles have high aspect ratios, they can be approximated by their closed bounding rectangle regions. This method has two advantages: (1) Checking the intersections of two rectangles are computationally less costly than solving a system of non-linear equation, because the intersections of line segments should be checked, and (2) Preventing the highly closeness of the clay particles is intrinsically required for FEA, similar to Fig. 6.3 (c).

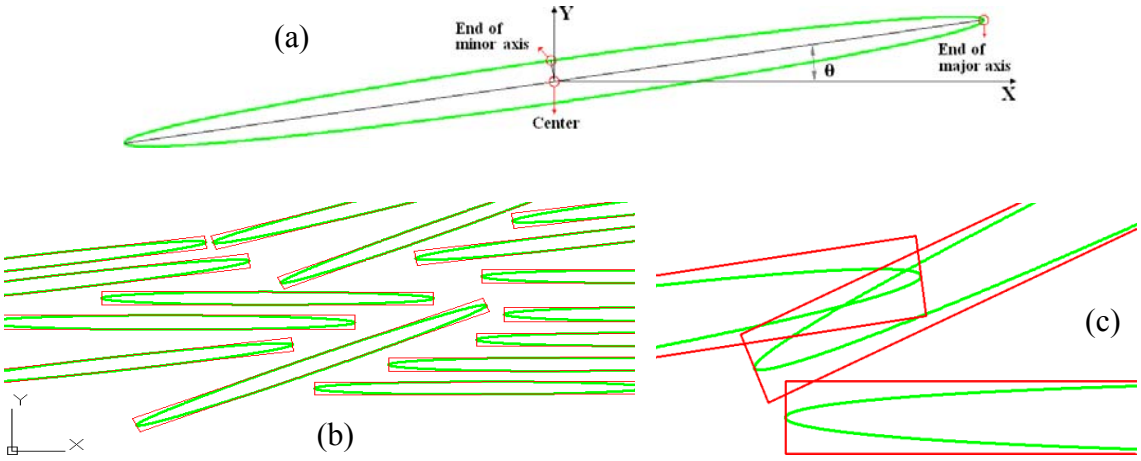

Fig. 6.3. 2D caly particles geometrical parameters and intersections: (a) Parameters for drawing ellipse. (b) Clay particles and the related bounding regions. (c) Illustrating how to check the intersection of elliptical particles through using the bounding rectangles.

Circular and elliptical particles are regular geometries, but the cross-sections of many types of composite materials show irregular fuzzy shape domains. In this case, there is no mathematical formula to check the overlaps or intersections of such irregular regions. Therefore, one way is defining a second order array containing zeros for all

cells of the array. The size of the array should be equal to the dimensions (length and width) of the RVE, which is divided by the required grids size. One can reduce the size of the grids to increase the accuracy of creating the irregular regions. Then after creating each particle or region, the related cells (or grids) in the main array that are inside the particle's boundary, should be updated by a number that identifies the related phase. For example in Fig. 6.4 (b), the cells in the white domain are zero (the matrix), the green ones are 1 (phase 1), reds are 2 (phase 2), and number 3 has been assigned to the yellow regions which are phase 3.

To generate a fuzzy irregular shape, the center of the particle or region should be located randomly, and checked not to be inside the other particles or phases. Then, as demonstrated in Fig. 6.5, the use of a series of radii that vary using a Fourier series formula in between a predefined range, leads to the creation of boundary of the irregular phase. The geometry can be enhanced by increasing the number of discretizing grids. Hiring more Fourier terms delivers more sophisticated geometries.

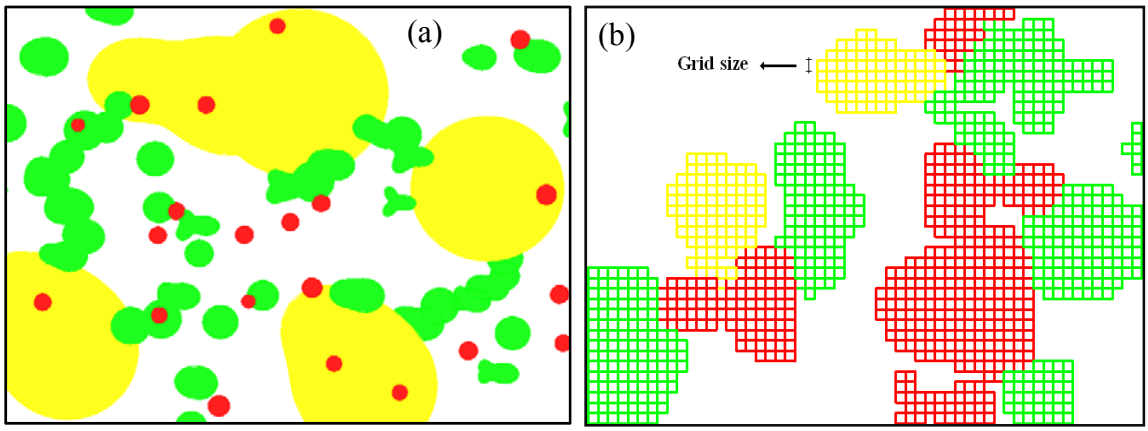

Fig. 6.4. Materials with irregular phases: (a) Different phases and their overlaps and intersections. (b) Contact faces or overlaps of different phases through using an array.

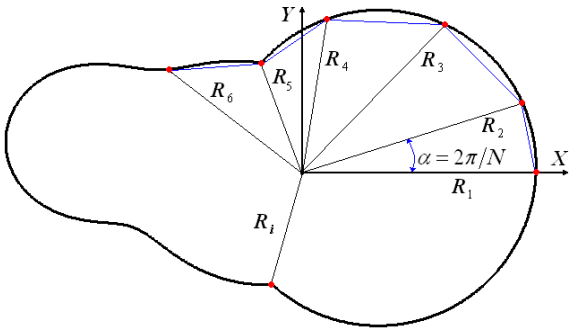

Fig. 6.5. Presenting how to generate an irregular phase using a center and variable radii.

Today, due to powerful computers along with the capabilities of high visualization devices, researchers can create more realistic and sophisticated models to better investigate the behavior of materials. Therefore, creating and analyzing three dimensional RVEs is more desirable.

In reality, ceramics are almost spherical shape particles, where a cross section of such a composite contains 2D circular shape inclusions, as shown in Fig. 6.6. The procedure for generating spherical particles is similar to the method explained for 2D circular particles. The only difference is that the central point of the particles should be randomly defined in a 3D space (inside a box), and the 3D distance between the centers of the spheres should be checked for intersections. The most important significant idea in this case is meshing a spherical particle inside a 3D RVE. A sphere has no edge on the surface, therefore one cannot seed mesh nodes on the surface of it; thus, so many elements will be generated while meshing these entities using the commercial software. This forces the mesh generator engine to create more meshes around the particles and inside the RVE. It is obvious that simulating a model containing a huge number of 3D elements is not a proper decision. Therefore, as can be seen in Fig. 6.6, the spheres

should be sliced to two parts, and the edge of the slices will let the particles be seeded for reducing the number of generated meshes.

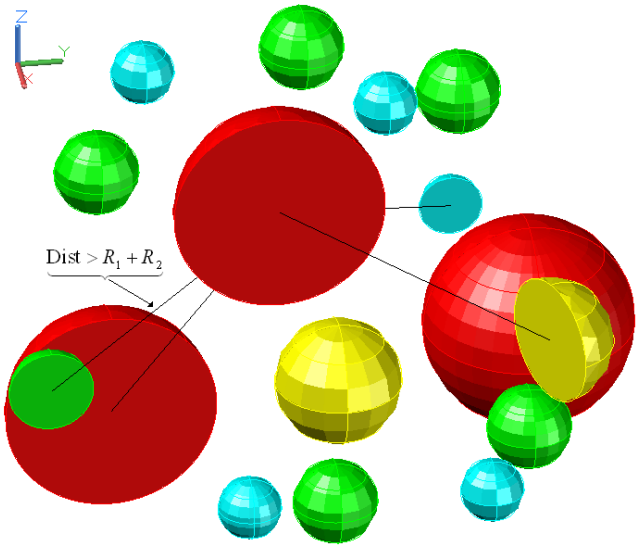

Fig. 6.6. Checking the intersections of 3D-Spherical particles.

For creating 3D nanoclay particles, which is the realistic shape of these particles (as mentioned before), there are more issues while generating them in comparison to the 2D cases. In fact, to geometrically identify these particles, one needs to specify the length of the major axis, the aspect ratios of both mean and minor axes (with respect to the major axis), and the three angles of rotation in three-dimensional space. Fig. 6.7 (a) depicts these required parameters. Simulating RVEs containing 3D ellipsoids with such high aspect ratios has no difference in comparison to the ones containing thin plate shape objects. Also, creating such 3D ellipsoids makes some problems; for example, these ellipsoids have sharp edges which need so many elements to discretize it smoothly. Moreover, creating them in both AutoCAD and ABAQUS is very difficult. Now, since

3D ellipsoids have no advantage in comparison to the 3D thin disk-shape particles; therefore, 3D nanoclay particles can be approximated by very thin platelet objects as shown in Fig. 6.7 (a) and (b). After generating these 3D objects, there are two ways for checking their overlaps or intersections. As discussed for the 2D ellipses, the first way is mathematically checking the intersection of 3D ellipsoids, which needs a non-linear system of equations to be solved in matrix form. This method is very time consuming. But, the second way is checking the positions of these particles through using the bounding box around each of them.

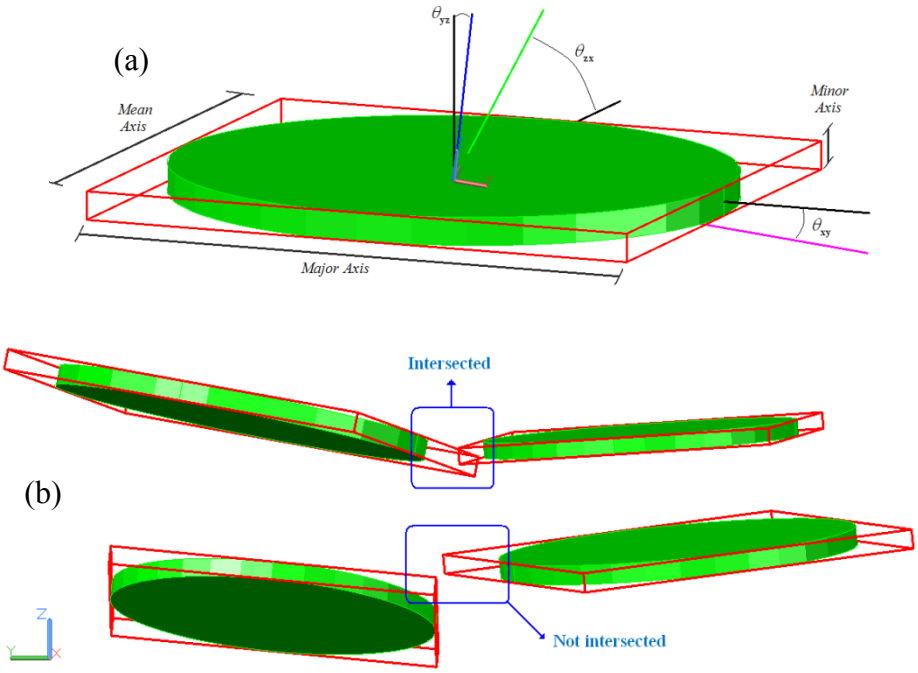

Fig. 6.7. 3D caly particles geometrical parameters and intersections: (a) Drawing ellipse parameters. (b) Checking the intersection of ellipsoidal particles using bounding boxes.

The cuboids as shown in Fig. 6.7 can be utilized for probing the overlaps of these objects. This technique has two advantages; at first it is faster than solving the equations,

and secondly it prevents the highly closeness of these particles (that makes problems while meshing and analyzing). It is worth mentioning that when checking the intersections of ellipses or ellipsoids, and even other objects, there is no need to consider and compare all the particles with each other. In fact, just the particles in the vicinity of a newly created particle can be checked out.

One of the most interesting and important inclusions for enhancing the thermo-mechanical responses of composites (especially polymer based composites) are carbon nano tubes (CNTs) or carbon nano fibers (CNFs). Almost all the models generated by different researchers have been made of well dispersed straight fibers (Chen and Liu, 2004; Mishnaevsky, 2007; Muliana and Kim, 2007; Okereke et al., 2002; Ostoja-Starzewski, 2002; Song and Youn, 2006). However, the TEM images in that scale reveal that during manufacturing processes, these fibers become wavy because of the very high aspect ratios that cause no resistance to bending. In the open literature, there are many debates regarding the effects of CNTs on nanocomposites, in such a way many claimed substantial improvements have been achieved using CNTs (Ajayan et al., 2000; Moisala et al., 2006; Qian et al., 2002), but others mentioned just modest enhancement can be obtained (Chen et al., 2006; Gojny et al., 2006; Zhu et al., 2004). Besides, most of the researchers have modeled the CNTs as straight objects in three dimensions, or as wavy thread-shape objects through using beam or truss elements in 3D RVEs, that all are approximations for simply producing these inclusions. Therefore, it was decided to create realistic 3D geometry of the CNTs as straight, rod, and curved shape objects. In the following, the procedure for randomly generating these inclusions is explained.

The main problem in creating the three-dimensional fibers is how to apply waviness to bend these objects in a 3D space, and then how to check the intersection between the generated fibers. To solve these issues, at first creating wavy fibers is clarified. The length of fibers change in a range; so, one can select a random length in that range. Then, the chosen length should be divided to several segments. The next parameter for identifying the waviness is the bending angle between two segments. Now, this algorithm should be followed to create a 3D fiber.

1) One random point should be selected inside an RVE, as the start point of the first segment of the fiber.
2) A random point should be chosen on the surface of the sphere that its center is the first selected point, and its radius is the length of the segments (see Fig. 6.8).

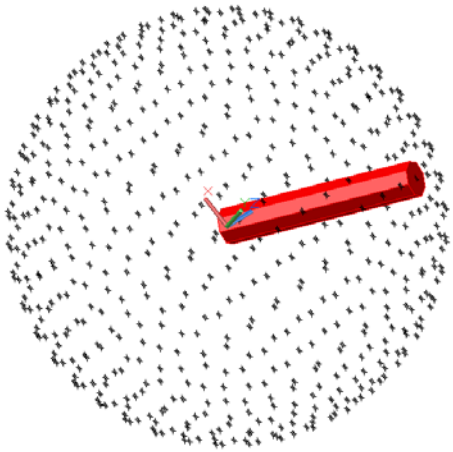

Fig. 6.8. possible points on surface of a sphere for creating the first segment of a fiber.

3) Then, the first segment of the fiber can be generated by constructing a 3D cylinder that has two points and its radius is the fiber's radius.

4) In order to find the other segments successively, as shown in Fig. 6.9, a cone of possible points must be considered in front of the previous constructed segments, such that the view angle of the cone is twice of the bending angle. In fact, the possible points are laying on the surface of a sphere cut by a cone that its angle of view is twice of the bending angle.

5) One point should be selected randomly from that 3D rotated cone, like Fig. 6.9.

6) Using the selected point on the 3D cone, and similar to step (3), the cylindrical segment can be built.

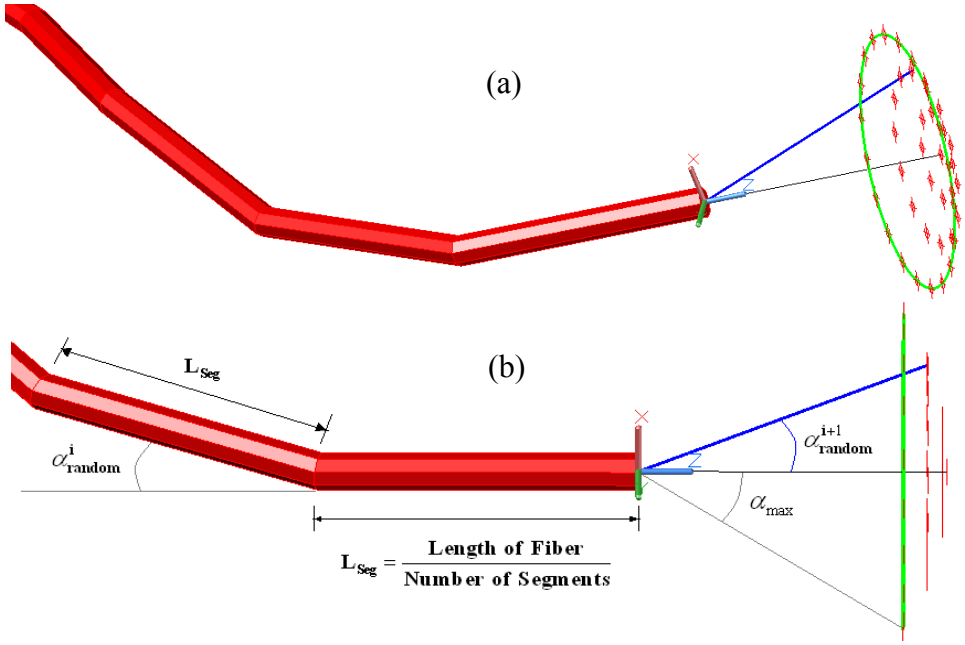

Fig. 6.9. Possible points in front of each segment of a 3D fiber: (a) Rotated view to show the cone, (b) Side view depiction of cone and segments. (The coordinate triad is just schematic; black line is in direction of axis of previous segment).

The technique of assuming a cone is employed instead of selecting a random bending angle, because finding a random angle is proper for a 2D case and not a 3D one. Since in

a 3D space, such point can be located through using three rotation angles. But, the main problem occurs when the new segment faces to the previously generated fibers (or particles in hybrid cases), as seen in Fig. 6.10.

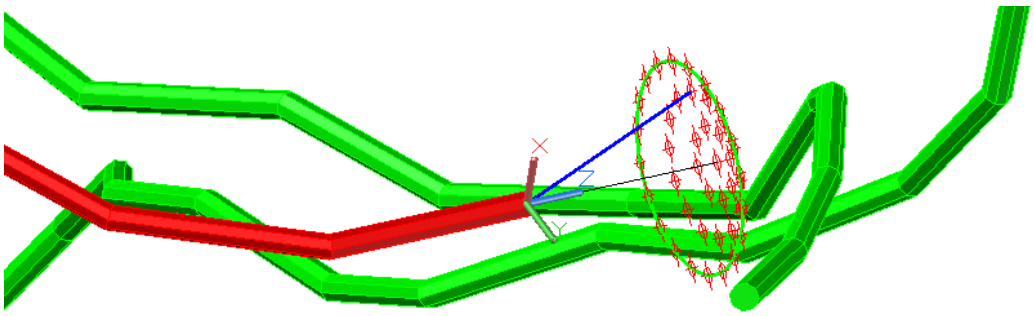

Fig. 6.10. Depiction of possible points that can be selected in a traceable manner not to intersect the previously generated fibers.

For example, if only three random angles are selected and the related cylinder segment intersects with other inclusions, the number of repetition to escape from the entrapped situation will be too high with no satisfactory achievement. Fig. 6.10 shows how the possible points on the cone in front of each segment of a 3D-Fiber provide a predefined traceable condition to bypass the fibers (or particles). After creating the first fiber, while creating the segments of other fibers, the intersections of a new segment with the previously generated segments should be investigated. As demonstrated in Fig. 6.11, the minimum distance between the line segments of the axis of two cylinders must be calculated, and compared with a critical length.

To make a smooth geometry of the fibers, two approaches can be followed. Firstly one may divide the total length of each fiber to many small segments, and the other one is converting the 3D axis line of the current generated fiber to a 3D spline.

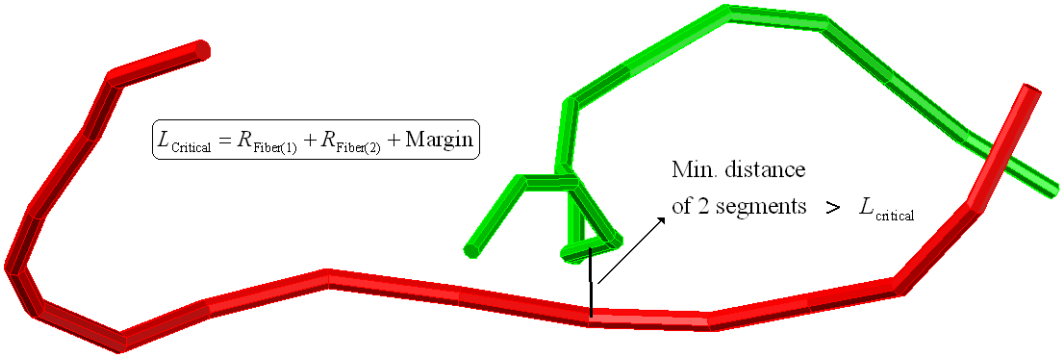

Fig. 6.11. Checking the closeness of 3D segments of two fibers.

In Figs. 6.8 to 6.11, none of the abovementioned ways to make smooth fibers is used to illustrate the segments, their connection, bending angles, and the front probable points on a conical region. It is obvious if the maximum bending angle is considered to be zero, the fibers are created as straight unidirectional or randomly oriented rod shape objects. The corresponding image for straight or rod fibers are demonstrated in the next section.

The most complex geometry for a 3D RVE is a combination of wavy fibers in the neighborhood of particles. These combinations can be carbon nanotubes and nano ceramics, as well as carbon nanotubes and nanoclay particles. In order to create such hybrid composites, the same procedure as previously explained for each of the inclusions must be followed. However, while generating each of them the intersections should be checked out. For creating a mixture of spherical ceramics and fibers, at first the nano ceramic particles can be generated, and afterwards the fibers. During the construction of each fiber, the position of cylindrical segments and the neighboring spherical particles must be checked. This task can be accomplished by finding the minimum distance of the center of a sphere and the nearest cylindrical segment. As demonstrated in Fig. 6.12, the

calculated distance should be greater than the summation of the radii of the fiber and the sphere, and a defined margin (the margin can be a ratio of the both mentioned radii). For the case of hybrid composite containing fibers and nanoclays, the same procedure as previously explained for each of the inclusions must be pursued. Here again, at first the clay particles are generated, and subsequently the fibers.

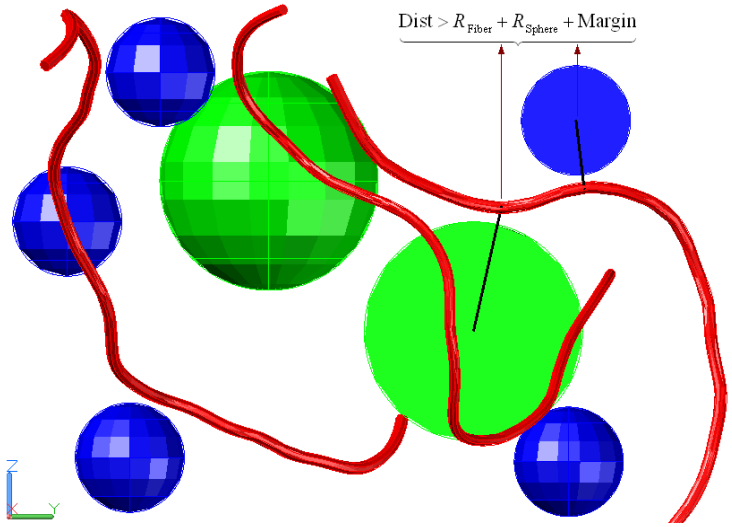

Fig. 6.12. Checking the intersection of 3D spherical particles, and 3D fiber inclusions.

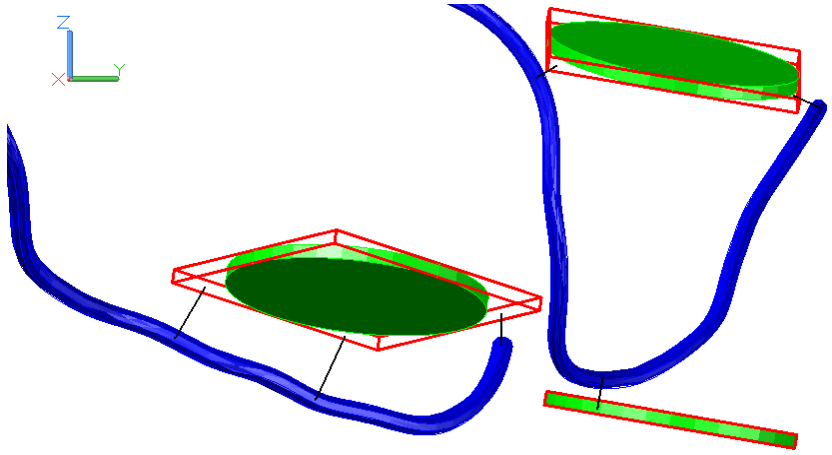

Fig. 6.13. Checking the intersection of 3D ellipsoidal particles, and 3D fiber inclusions.

Now, during the construction of each fiber, the position of cylindrical segments of fibers and the neighboring cuboids (the bounding box) surrounding the clays should be probed, as demonstrated in Fig. 6.13.

6.3 RVE_Maker, Microstructural FE Models Generator

In this section, the computational code that has been developed for modeling micro/nano composites is presented. In order to virtually (numerically) investigate the mechanical behavior of various polymer composites, creating geometrical representative models for different types of particles and inclusions is mandatory. Because manually generating complex models is almost impossible, to overcome this issue, innovative technical software called RVE_Maker is designed and developed through utilizing Borland C++ Builder 6. RVE_Maker is designed to create simple and complex geometries for composite materials, in both 2D and 3D. It is capable to automatically generate RVEs for composites that contain randomly dispersed particles. The first screen shot of the RVE_Maker and a sample page for identifying geometrical parameters are displayed in Fig. 6.14.

To generate random numbers for geometrical parameters, such as locating centers of particles, length, aspect ratios, diameters, etc., a pseudo random number generator is used to produce a real number from a uniform distribution between zero and one ($x \in [0,1]$). Then, this selected number is converted to the proper range for each of the parameters, through a linear transformation, as follows

$$\text{Random Number} = a + (b - a) \times \text{rand}(0\ ,1)/\text{MaximumRand} \qquad (6.70)$$

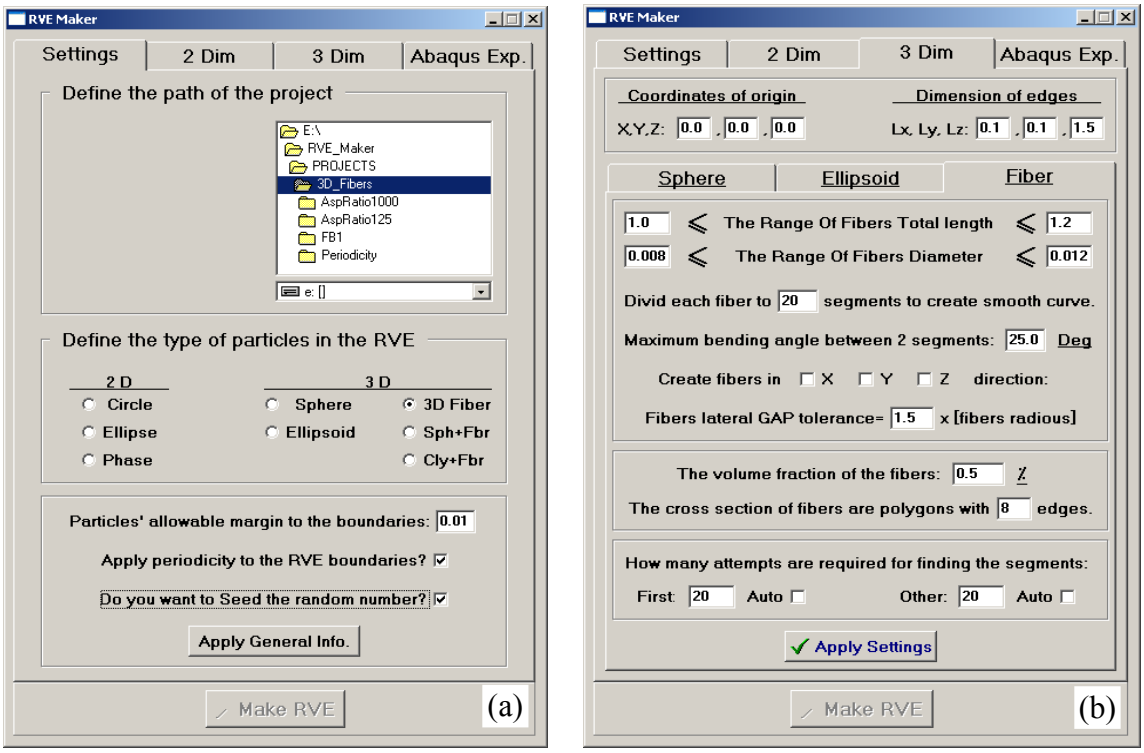

Fig. 6.14. Screen shots of RVE_Maker software: (a) first page, and (b) page for identifying geometrical parameters of 3D fibers.

where a and b are the lower and higher limitations of the parameters range, respectively. The variable "MaximumRand" is used to normalize the calculated random number, which depends on the compiler and operating system (OS), which are for this study Borland C++ and Windows 64 bit, respectively. This program is capable of generating and dispersing different types of particles and inclusions for micro/nano composite materials. From the menus and options in the software, one can set the required geometrical parameters for automatically generating a desired model. It should be noted here that not only the positions of particles are random, but the nature of the inclusions' shape and size are also random. Thus, the geometrical parameters can be picked randomly from a reasonable range, to depict random shapes, size and distribution

patterns. Then, the program randomly checks the available unoccupied positions inside the RVE region (rectangle or cube) for creating particles. Afterwards, with respect to the geometrical parameters, such as radius, thickness, aspect ratios, orientations, etc., the program checks the intersections of the newest inclusion according to the previously generated objects. If there is no overlap or intersection, then the new particle is inserted to its proper location, and its geometrical properties will be recorded in a data bank.

The program creates the inclusions up to the desired volume (3D) or area (2D) fraction. The geometrical data in the recorded data bank should be drawn in proper software. Henceforth, the program automatically writes the required script files (which are also called command files) for AutoCAD. When the first script file is played in AutoCAD, it automatically draws the geometry entities, and when the second script is run, it converts the entities to standard geometrical files (.SAT files, Standard ACIS Text) that can be read by other CAD family software.

In order to create finite element representations from the generated numerical models; here ABAQUS (2008) software is employed. Thus, the generated depicted entities in AutoCAD must be exported to ABAQUS. ABAQUS is able to be managed by C++ codes or Python script codes; therefore, the RVE_Maker program automatically generates the required Python command code, as well. This code imports the created geometry (.SAT file) from AutoCAD to ABAQUS. Subsequently, the Python code applies all the required options and settings to the model to create a complete finite element representation as a CAE (Computer-Aided Engineering) file.

The most important task of the Python code is generating elements for meshing the RVE. This task can be accomplished by carefully seeding each edge of the inclusions

in order to optimize the number of generated elements. The program can use 3-node (Trigonal) or 4-node (Quadrilateral) elements to mesh a 2D RVE. For the three dimensional cases, 3D-Stress elements containing 4 nodes (Tetrahedral) should be used to mesh a complex 3D domain.

For both 2D and 3D cases, a free meshing method in which mapping technique and element size growth are allowed, has been employed. Even though utilizing 8-nodes (Hexahedral) elements are more efficient in comparison to the Tetrahedral elements (create less elements), and also its numerical solution is more stable; it is almost impossible to mesh a complex 3D model with Hexahedral elements, even for simple spherical particles.

The next essential task of the Python code is assigning the material properties to each particle or region inside the RVE. These mentioned tasks are much more critical while creating complex geometries. The Python code also applies constraints to the RVEs edges; for 2D cases at the bottom side in the vertical direction (Y-direction) and at the left side in the horizontal direction (X-direction), whereas periodic boundary conditions (BC) are applied to the right edge of the RVE to force the right side nodes to move simultaneously with each other, Fig. 6.14.

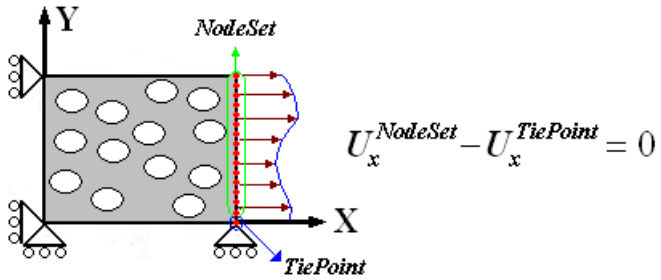

Fig. 6.15. Demonstrating periodic boundary conditions in a 2D RVE.

Actually, the horizontal displacement of nodes on the right edge (all nodes but one = NodeSet) should be the same as the displacement of the node (Tie-Point) at the corner of right and bottom edges (both Fig. 6.14 and Fig. 6.15 (a)).

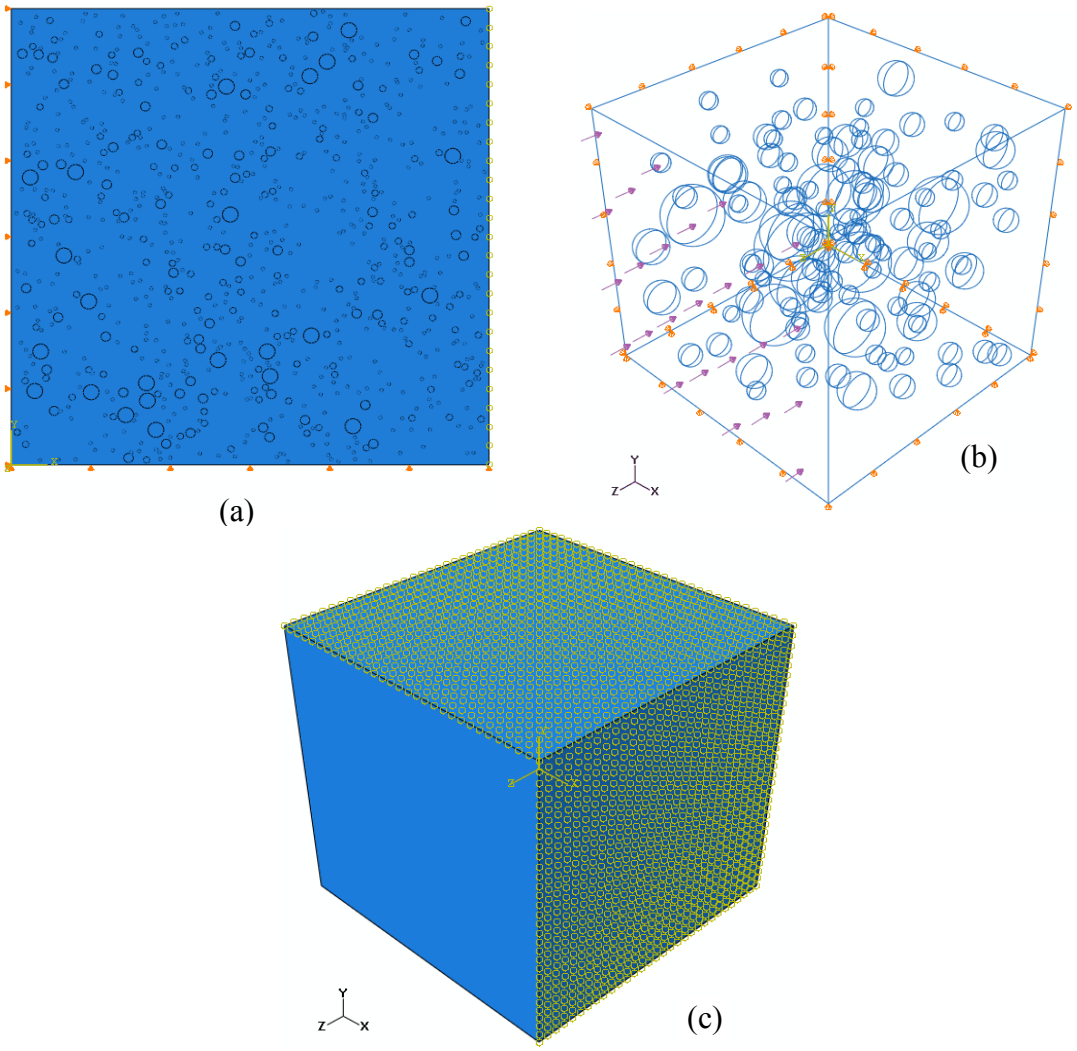

Fig. 6.16. Boundary conditions and constraints: (a) on 2D RVE, (b) BCs and forces on 3D RVE, and (c) Constraints on lateral faces of 3D RVE.

For the case of 3D RVEs, the XY-, YZ-, and ZX-faces at the lower level coordinates are constrained with roller supports, respectively not to move in Z, X, and Y directions.

Similar to 2D cases, the nodes on the other faces are constrained to move with each other. Actually, only the nodes on every boundary face are tied to a point in space (on the same face) such that the boundary face does not curve, and stays flat (Fig. 6.15 (b)).

The RVEs in two dimensions can be simulated through Plane-Strain, and the three dimensions ones may be simulated by using 3D-stress finite element analysis. Both displacement control and force control tests can be conducted.

This program (RVE_Maker) can produce and handle two dimensional particles, such as circular (for ceramics or rubber) and elliptical (for nanoclay) particles, and also irregular phases (e.g. TRIP steel phases). For three dimensional cases, it is able to generate spherical (for ceramics or rubber) and ellipsoidal (for nanoclay) particles, 3D-fibers (for Carbon Nano Tube or Carbon Nano Fiber), and 3D-fibers with neighboring spherical or elliptical particles. In the following, some samples of the geometries that can be created by this software are demonstrated. Firstly, two dimensional RVEs are shown in Figs. 6.16 to 6.18, and then 3D samples have been depicted in Figs. 6.19 to 6.23.

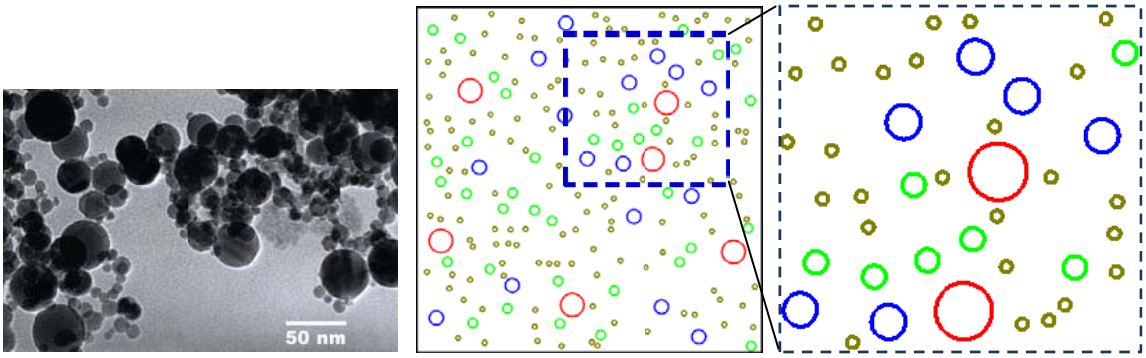

(a) (b) (c)

Fig. 6.17. Circular shape of ceramic particles: (a) TEM image of ceramic particles, (b) Extended zoom of geometrical model created in ACAD, (c) Close up zoom of image (b).

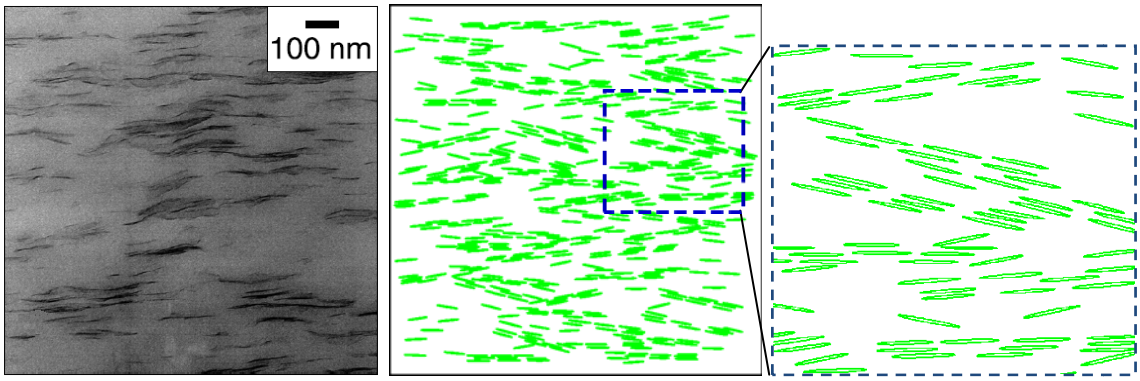

(a) (b) (c)

Fig. 6.18. Elliptical shape of clay particles: (a) TEM image of clay particles. (b) Extended zoom of geometrical model created in ACAD, (c) Close up zoom of image (b).

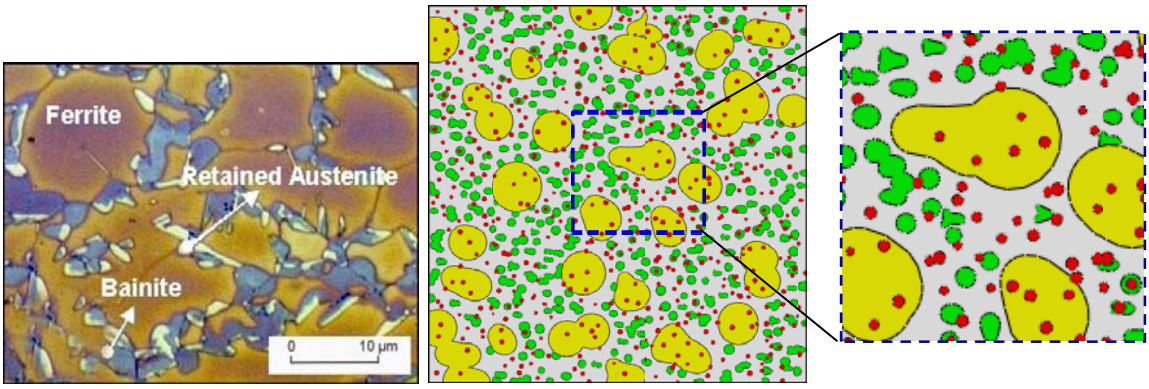

(a) (b) (c)

Fig. 6.19. Irregular geometry of multi-phases material: (a) Real image of irregular multi-phases material (TRIP steel), (b) Extended zoom of geometrical model created in ACAD, (c) Close up zoom of image (b).

Fig. 6.18 is a generated sample for a 2D cross section of different precipated phases inside metallic materials. Such representative model is not studied in this research. This is just accomplished for the sake of another research for investigating the responses of advance high strength steels. In the following, the capability of the RVE_Maker program in creating three-dimensional RVEs is demonstrated.

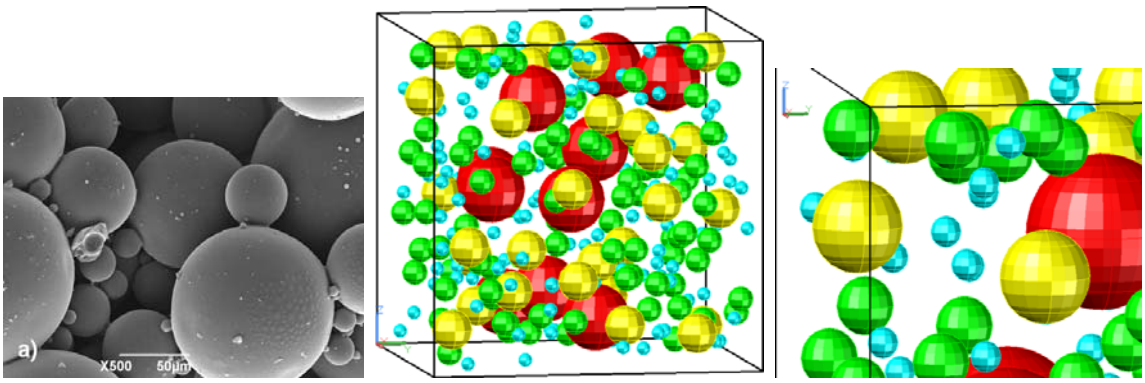

(a) (b) (c)

Fig. 6.20. Spherical shape of ceramic particles: (a) Real 3D TEM image of NCRP, (b) Extended zoom of geometrical model created in ACAD, (c) Close up zoom of image (b).

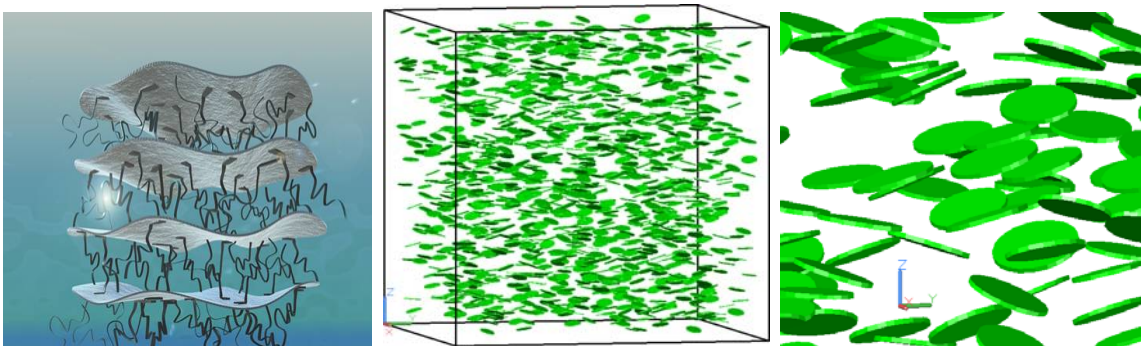

(a) (b) (c)

Fig. 6.21. Ellipsoidal shape of clay particles: (a) Schematic image of exfoliated NCLP (thin platelet disk), (b) Extended zoom of geometrical model created in ACAD, (c) Close up zoom of image (b).

RVE_Maker program is able to generate all types of the straight, random rods, and curved shape fibers. This capability provides possibility for analyzing and comparing different realistic fiber configurations. Comparing Fig. 2.2 that was generated by Meso3DFiber software with Figures 6.21 to 6.23, clearly illustrates the capability of the RVE_Maker software for creating complex nano-composites geometries with fibers.

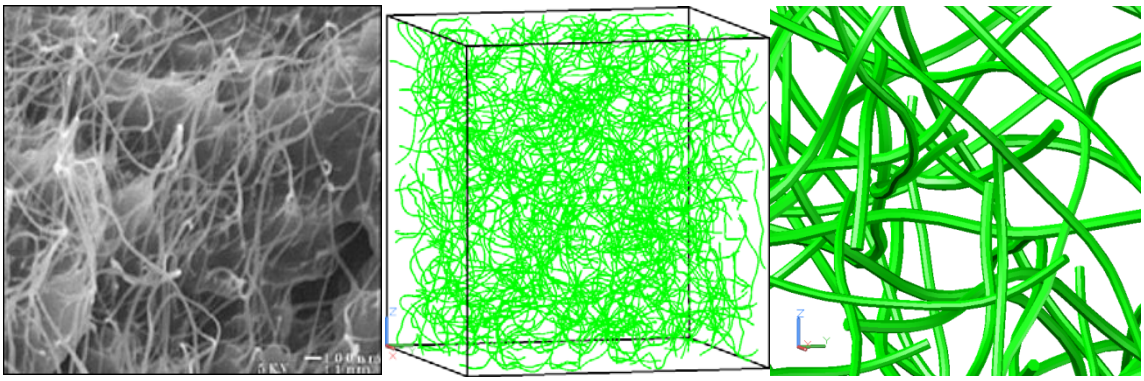

(a) Curved shape CNTs. (b) Model's extended view in ACAD. (c) Close up view of (b).

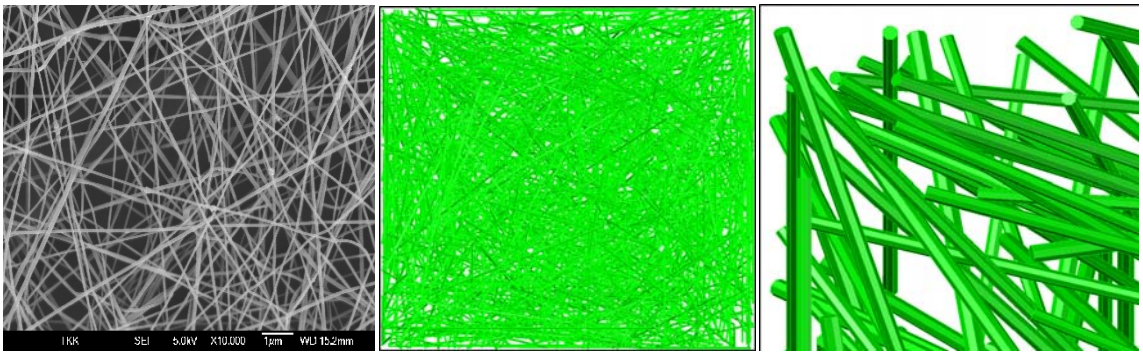

(d) Rod shape CNTs. (e) Model's extended view in ACAD. (f) Close up view of (e).

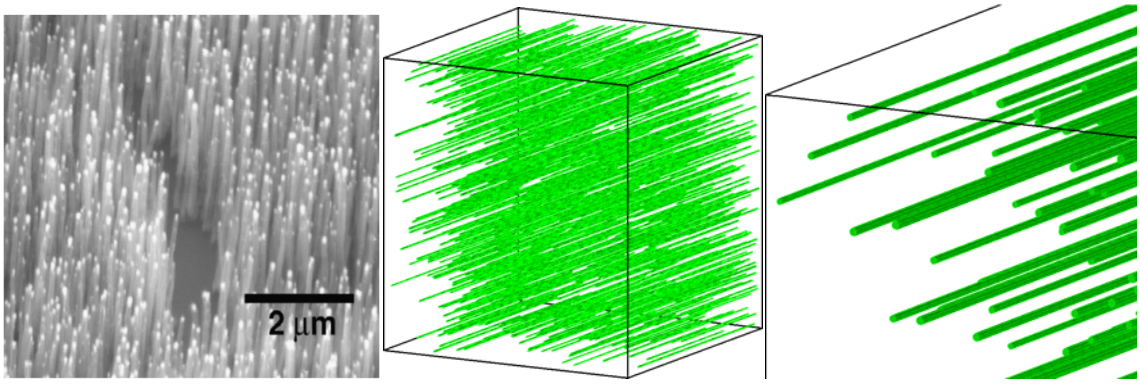

(g) Unidirectional CNTs. (h) Model's extended view in ACAD. (i) Close up view of (h).

Fig. 6.22. Different types of nano fibers or nano tubes generated by RVE_Maker. Images in (a), (d), and (g) are three-dimensional TEMs.

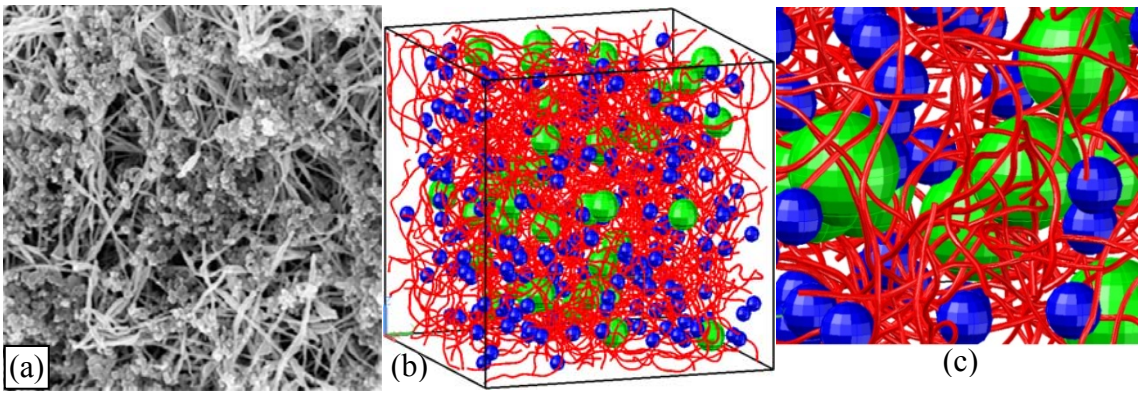

Fig. 6.23. Hybrid composite consist of CNT and spherical particles: (a) 3D SEM image of nano platinum particles (NPP) and CNT, (b) Extended zoom of created model in ACAD. (c) Close up zoom of (b).

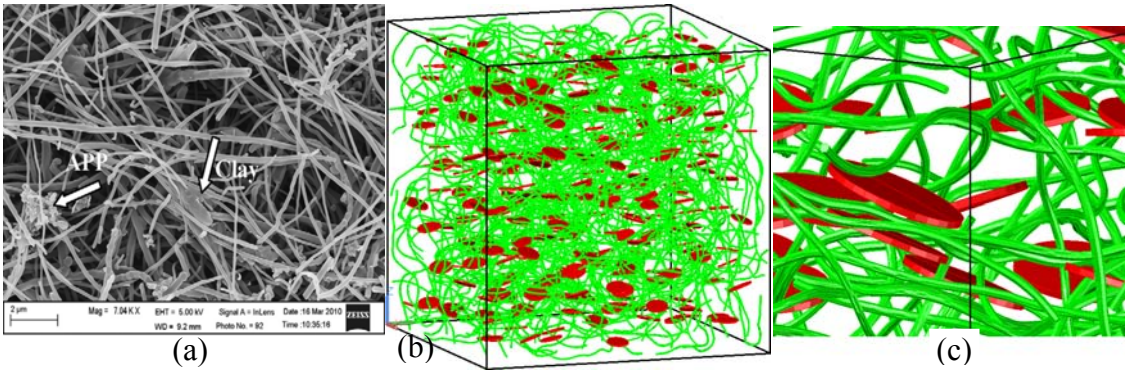

Fig. 6.24. Hybrid composite consist of carbon nano fiber (CNF) and naoclay particles: (a) 3D SEM image of nano clay particles and CNF, (b) Extended zoom of created model in ACAD, (c) Close up zoom of image (b).

In order to simulate a desired created RVE, the mechanical behavior of the inclusions should be determined. In many cases, because the matrices of the composites are much softer than the inclusions; therefore, just elastic mechanical properties are enough to be considered for the inclusions. However, in some cases, if the amount of the transferred load from matrix to inclusions is very high, then the elastic response of the particles will not be enough to represent the realistic behavior of the composites. Thus,

elastic-plastic or elastic-damage behavior may be considered and utilized (for the inclusions) in these meso-scale finite element simulations, in order to reasonably characterize the response of the composites.

6.4 Proper RVE Size

The homogenized responses for simulating RVEs highly depend on the distribution of the inclusions inside an RVE. One RVE must guarantee and deliver a certain accuracy of the estimated property that is attained by spatial averaging of the given criteria.

If the size of an RVE is small, then it may not have all possible orientation and distribution for particles. Thus, if another random distribution is considered, then the desired response will be way different from the response of the previous distribution, which means the response of the RVE in that size is not reliable. Henceforth, the size of the RVE should be large enough as compared to the characteristic size of the inclusions, such that the RVE statistically engulfs all different particles distributions and orientations, so that the response of the RVE deviates in a small acceptable range, and the size effect of the RVE is negligible. Therefore, in order to determine the proper size of an RVE, a number of realizations of the microstructure (RVEs with different sizes, for example: 1.0×1.0, 1.5×1.5, 2.0×2.0, $2.5 \times 2.5\ \mu m^2$) should be generated. Then several random distributions of the inclusions for each size should be produced. At least five different distributions for each size are required to study and compare the responses. Afterwards, all the created microstructure models must be submitted for simulation, under the same loading and periodic boundary conditions. Then the achieved properties

should be recorded. From the recorded results of the various simulated random distributions; the maximum, minimum, mean value and variance of the obtained response should be computed.

The desired response can be listed as: Young's modulus of the composite, the peak stress of the stress-strain curve, the toughness modulus (the area under the stress-strain diagram), or the maximum of the creep response after a definite time. Then, one can explore that after which size, the deviation of minimum and maximum of the response converge to a certain constant range. This means the behavior of the RVEs that are larger than the obtained optimum size, with any random distribution of that type of particle, results in the same acceptable range, and the effect of the RVE size on the ultimate strength of the nano-composite response will be negligible. Again, the number of realizations should be sufficient for each volume size.

CHAPTER VII

MICROMECHANICAL RESPONSES OF POLYMER NANO-COMPOSITES USING VISCOELASTIC CONSTITUTIVE MODEL

7.1 Introduction

In engineering and industrial fields, utilizing the particulate-filled polymer composites has been encouraged by their interesting material properties for different types of applications. Adding rigid (or elastic) particles to polymers or other matrices as the host materials, can provide a number of desirable effects, such as: reduction in the thermal expansion coefficient, increase in stiffness modulus, enhancement in the creep resistance, and also improving the fracture toughness of polymer composites (Ahmed and Jones, 1990).

The enhancement in the physical characteristics of a filled polymer results from a complex interaction between the properties of the different phases or inclusions (the matrix, the particles and the interfacial regions). The results of experimental data support this statement and reveal that the distribution of the reinforcing particles and the randomness pattern of the constituents can greatly influence the mechanical behavior of the composites (Chawla et al., 1998; Watt et al., 1996). Through extensive observations it is revealed agglomeration and network formation of the particles are responsible for the high levels of reinforcement, and also the breakdown of networks and the de-agglomeration are the main source of the non-linear responses of strain (Heinrich et al., 2002; Kraus, 1984). It means that the overall macroscopic behavior of particulate

composites is governed by the size, shape, aspect ratios, and the statistical random distribution of the reinforcing inclusions. Therefore, in order to design the best structural arrangement for a composite material, it is crucial to determine the overall macroscopic behaviors of the composites and understanding the responses of each component, when the composite is subjected to different types of external loadings.

However, theoretically the effects of these constituents have not been satisfactorily modeled. The specific surface area of the constituents extremely increases once the average particle sizes is smaller than 600 nm, which leads to a strong tendency to agglomeration (Osman and Atallah, 2006). Also in nano-composites, more clusters can be formed in comparison to micro-composites, due to their large contact area (surface energy) between the particles. In addition, these clusters are stronger than the ones in micro-composites, and can be packed much better than the roughly spherical micro-particles, which improve the modulus and viscosity. Several researchers have claimed that the primary fundamental mechanism for reinforcement and non-linear behavior appears to be the filler-matrix interactions, but not filler agglomerations (Osman and Atallah, 2006). In addition, micromechanical simulations predict that the viscoelastic and mechanical properties of PCMs do not depend on the size of particles (Barnes et al., 1989; Choi and Krieger, 1986). Nevertheless, there exist contradictions in the literature data and results, and the consequences of circular micro-inclusions on the viscoelasticity are still debatable (Cai and Salovey, 1999; Vollenberg and Heikens, 1989). Unfortunately, there is fairly little data regarding non-linear viscoelastic responses and performance at low volume fraction particulated polymer composites. In open literatures, the main focus was on fiber reinforced composite, and fairly few studies

have been conducted to analyze the viscoelastic responses of polymer composite materials, based on particles shapes and properties.

To have a fundamental understanding on the effects of the presence of particles and their properties on the overall response of composites, various micromechanical models have been formulated (Nemat-Nasser and Hori, 1999). As mentioned in Chapter 2, the homogenization studies focused on just elastic or heat conduction response of PCMs. Though, there is no analytical solution for complicated constitutive models. In most researches, micro-macro approach is assumed to determine the homogenized viscoelastic response of a composite (Khan and Muliana, 2009), and then the deformation in the composite is measured at multiple length scales. There is no analytical and/or homogenization technique for studying complex geometries that is governed by advanced constitutive models. Henceforth, the only possible way is finite element approach. Furthermore, in many cases, it is not computationally practical to incorporate every detailed characteristic of the inclusions and all microstructural geometry features, such as: considering cohesive contacts or cohesive elements for the interface of inclusion-matrix modeling (especially in complicated geometries), and also realistic 3D irregular shape of inclusions for a large scale representative volume element (RVE). Creating and simulating such RVEs and then analyzing their performances in order to design a better microstructural composite, may be very difficult.

Polymethyl methacrylate (PMMA) is widely used in different applications, and is usually mixed with various minerals (e.g. nano-clay or nano-ceramics) to customize its properties to the requirements of certain purposes. Spherical particles have been used in different studies as the simplest type of inclusions, since creating and handling these

geometries are easy (as explained in Chapter 6). Actually, there is no need to take care of the orientation of circular and spherical (in 2D and 3D) particles while loading. But, in the case of non-spherical ones such as platelet, ellipsoids, and tubular shape inclusions the degrees of orientations with respect to the applied stress are important factors.

Several micromechanical creep-recovery and cyclic loading simulations have been conducted and presented for predicting the viscoelastic responses of particulate-filled PMMA polymer composites, in small strain range. Therefore, Schapery's three-dimensional non-linear viscoelastic model based on recursive method for updating hereditary strains is employed (Haj-Ali and Muliana, 2004). Moreover, the stress predictor for the trial stress has been modified in order to decrease the number of iterations for viscoelastic convergence. The first part of this chapter is a review and simulations of just viscoelastic behavior of two and three dimensional particulate reinforcement polymer composite materials (PCMs), in small strain range. In the second part, the overall effects of shape and weight fractions of nano-clays and nano-ceramics on viscoelastic, viscoplastic, and viscodamage response of PCMs are studied and demonstrated, for quite a few 3D micromechanical models.

7.2 Constitutive Model

7.2.1 Non-Linear Viscoelastic Model in Small Strain Framework

Even though in Chapter 4 the derivation of Schapery model is presented, it is in large deformation concept, and in order to capture the viscoelastic response of PCMs in small strain range, the conventional Schapery single integral model should be employed. Therefore in this section, the Schapery's non-linear viscoelastic model (Schapery, 1969

b) is used to model the viscoelastic response of PMMA polymer which is the matrix of the composites. The Schapery's viscoelastic one-dimensional convolution single integral model is expressed in terms of the Cauchy stress, σ, as

$$\varepsilon^{\mathrm{NVE},t} = g_0(\sigma^t)D_0\sigma^t + g_1(\sigma^t)\int_0^t \Delta D\left(\psi^t - \psi^\tau\right)\frac{\mathrm{d}\left(g_2(\sigma^\tau)\sigma^\tau\right)}{\mathrm{d}\tau}\,\mathrm{d}\tau \tag{7.1}$$

where D_0 is the instantaneous compliance, and ΔD is the transient compliance. g_0, g_1, and g_2 are non-linear parameters related to the stress level, σ, at specific time τ. The parameter g_0 measures the increase or reduction in the instantaneous compliance, the parameter g_1 deals with the non-linearity effect in the transient compliance, and the parameter g_2 accounts for the loading rate effect on the creep response. Also ψ^t is the reduced time and expressed similar to Eqs. (4.15) or (5.9). The a_T and a_s are the temperature, and strain-or-stress shift factors, respectively. Here, since the viscoelastic response in the reference temperature is studied, thus: $a_T = 1$. For the purpose of representing the transient part of a viscoelastic response two methods are usually used: power laws and exponential Prony series. Thus, for numerical purpose, the Prony series is utilized to capture the transient compliance, ΔD, the same as Eq. (5.10). As proposed by Lai and Bakker (1996), the one-dimensional nonlinear viscoelastic model in Eq. (7.1) can be generalized to three-dimensional problems by decomposing the viscoelastic response into deviatoric and volumetric parts, such that

$$\underset{\approx}{\varepsilon}^{\mathrm{ve}} = \underset{\approx}{\varepsilon}^{\mathrm{ve}}_{\mathrm{dev}} + \frac{1}{3}\varepsilon^{\mathrm{ve}}_{\mathrm{vol}}\underset{\approx}{1} = \frac{1}{2G}\underset{\approx}{\sigma}_{\mathrm{dev}} + \frac{1}{9K}\sigma_{\mathrm{vol}}\underset{\approx}{1} = \frac{J}{2}\underset{\approx}{\sigma}_{\mathrm{dev}} + \frac{B}{3}\sigma_{\mathrm{vol}}\underset{\approx}{1} \tag{7.2}$$

Here, $\underset{\approx}{1}$ is the identity tensor (Kronecker delta). $\underset{\approx}{\varepsilon}_{\text{dev}}^{\text{NVE}}$ and $\varepsilon_{\text{vol}}^{\text{NVE}}$ are deviatoric (tensor) and volumetric (scalar) strain, respectively. G and K are the shear and bulk moduli, respectively, which are related to the Young's modulus, E, and Poisson's ratio, υ, as

$$G = E\,/\,2(1+\upsilon) \qquad , \qquad K = E\,/\,3\left(1-2\upsilon\right) \tag{7.3}$$

$\underset{\approx}{\sigma}_{\text{dev}} = \underset{\approx}{\sigma} - \frac{1}{3}\sigma_{\text{vol}}\underset{\approx}{1}$ and σ_{vol} are deviatoric (tensor) and volumetric (scalar) stress in the current configuration. Using the Schapery's integral constitutive law, Eq. (7.1), and after some mathematical manipulations (Lai and Bakker, 1996), the deviatoric and volumetric non-linear viscoelastic strain components can be partitioned and expressed at time t, as

$$\underset{\approx}{\varepsilon}_{\text{dev}}^{\text{NVE},t} = \frac{1}{2} g_0^t J_0 \underset{\approx}{\sigma}_{\text{dev}}^t + \frac{1}{2} g_1^t \int_0^t \Delta J^{(\psi^t - \psi^\tau)} \frac{\mathrm{d}(g_2^\tau \underset{\approx}{\sigma}_{\text{dev}}^\tau)}{\mathrm{d}\tau}\,\mathrm{d}\tau \tag{7.4}$$

$$\varepsilon_{\text{vol}}^{\text{NVE},t} = \frac{1}{3} g_0^t B_0\, \sigma_{\text{vol}}^t + \frac{1}{3} g_1^t \int_0^t \Delta B^{(\psi^t - \psi^\tau)} \frac{\mathrm{d}(g_2^\tau \sigma_{\text{vol}}^\tau)}{\mathrm{d}\tau}\,\mathrm{d}\tau \tag{7.5}$$

$$\begin{aligned} J_0 &= 2(1+\upsilon)D_0 & \Delta J^{\psi^t} &= 2(1+\upsilon)\Delta D^{\psi^t} \\ B_0 &= 3(1-2\upsilon)D_0 & \Delta B^{\psi^t} &= 3(1-2\upsilon)\Delta D^{\psi^t} \end{aligned} \tag{7.6}$$

J and B are the shear and bulk compliances, and the material constants J_0 and B_0 are the instantaneous effective elastic shear and bulk compliances, respectively. Similar to Chapters 4 and 5 the Poisson's ratio ν is assumed not to be a function of time. Using the Prony series for the transient compliance, the deviatoric strain tensor, $\underset{\approx}{\varepsilon}_{\text{dev}}^{\text{NVE}}$, and the volumetric strain, $\varepsilon_{\text{vol}}^{\text{NVE}}$, can be expressed in terms of the hereditary integral formulation as (Haj-Ali and Muliana, 2004)

$$\begin{aligned}\underset{\sim}{\varepsilon}_{\text{dev}}^{\text{NVE},t} &= \frac{1}{2}\left[g_0^t J_0 + g_1^t g_2^t \sum_{n=1}^{\text{NP}} J_n \left(1 - \frac{1-\exp(-\lambda_n \Delta\psi^t)}{\lambda_n \Delta\psi^t} \right) \right] \underset{\sim}{\sigma}_{\text{dev}}^t \\ &\quad - \frac{1}{2} g_1^t \sum_{n=1}^{\text{NP}} J_n \left[\exp(-\lambda_n \Delta\psi^t) \underset{\sim}{q}_{n,\text{dev}}^{t-\Delta t} - g_2^{t-\Delta t} \frac{(1-\exp(-\lambda_n \Delta\psi^t))}{\lambda_n \Delta\psi^t} \underset{\sim}{\sigma}_{\text{dev}}^{t-\Delta t} \right]\end{aligned} \tag{7.7}$$

$$\begin{aligned}\varepsilon_{\text{vol}}^{\text{NVE},t} &= \frac{1}{3}\left[g_0^t \bar{B}_0 + g_1^t g_2^t \sum_{n=1}^{\text{NP}} B_n \left(1 - \frac{1-\exp(-\lambda_n \Delta\psi^t)}{\lambda_n \Delta\psi^t} \right) \right] \sigma_{\text{vol}}^t \\ &\quad - \frac{1}{3} g_1^t \sum_{n=1}^{\text{NP}} \bar{B}_n \left[\exp(-\lambda_n \Delta\psi^t) q_{\text{vol},n}^{t-\Delta t} - g_2^{t-\Delta t} \frac{(1-\exp(-\lambda_n \Delta\psi^t))}{\lambda_n \Delta\psi^t} \sigma_{\text{vol}}^{t-\Delta t} \right]\end{aligned} \tag{7.8}$$

Eqs. (7.7) and (7.8) are very useful for the numerically implementing the nonlinear viscoelastic model in finite element codes or software. The values of viscoelastic material parameters are presented in Table 7.1 and 7.2.

Table 7.1: Viscoelastic material parameters for the PMMA (Lai and Bakker, 1996).

N	1	2	3	4	5	6	7	8	9
λ_n (s^{-1})	1.0	0.1	0.01	10^{-3}	10^{-4}	10^{-5}	10^{-6}	10^{-7}	10^{-8}
D_n (MPa^{-1})$\times 10^{-6}$	23.63	5.66	14.84	18.88	28.58	40.06	60.42	79.65	162.18
D_0 (MPa^{-1})$\times 10^{-6}$	271								

Table 7.2: Non-linear viscoelastic parameters for the PMMA (Lai and Bakker, 1996).

Stress (MPa)	15	20	25	30	35	40
a_σ	1.0	1.0	1.0	1.018	1.067	1.493
g_0	1.0	1.0	0.973	0.946	0.897	0.861
g_1	1.0	1.0	1.045	1.197	1.345	1.197
g_2	1.0	1.0	1.197	1.600	1.919	2.677

Based on the experimental data published by Lai and Bakker, the creep and recovery simulations in different stress levels for pure PMMA polymer are conducted, checked, and shown in Fig. 7.1. These data are the ones which are used in Chapter 5 to calibrate the large deformation viscoelastic model. Thus, in Fig. 7.1, the numerical model is conducted using small strain Schapery model. These experimental data are also used to compare the effects of the presence of different types of particles in the overall creep and recovery response of the composites.

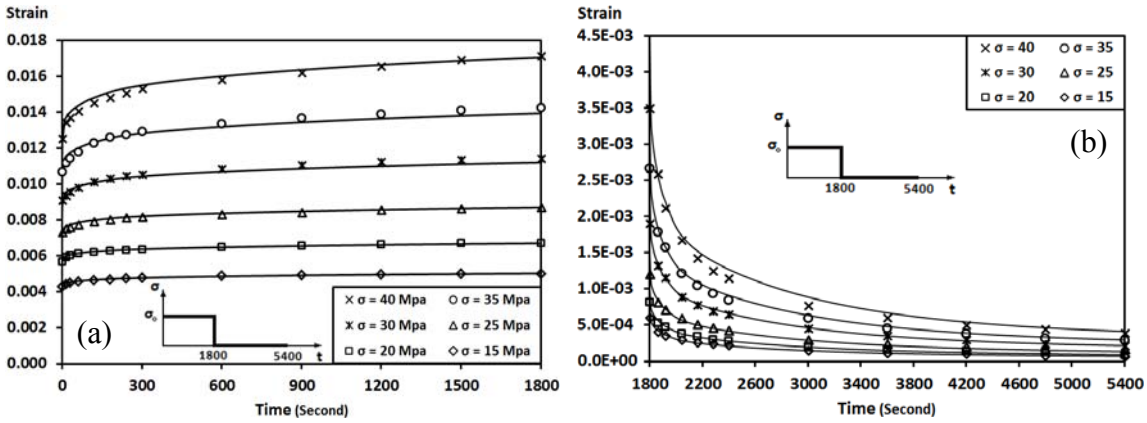

Fig. 7.1. Predicting the behavior of PMMA under a range of tensile loading at T=296 K. (a) Creep Test (30 minutes), (b) Recovery Test (60 minutes).

7.2.2 Trial Stress and Corresponding Enhancement

In the Schapery viscoelastic constitutive model, in each analysis time increment, an approximation of the unknown stress increment need to be determined. This estimation is based on the strain increment, hereditary integrals, and Prony series. Therefore, a trial stress should be found for the deviatoric and volumetric part of strain, and then the other viscoelastic calculations can be conducted based on these computed

trial stresses. Comparable to the Subsections 4.4.2 and 5.3, here in order to enhance the value of the trial stresses to expedite the convergence in the viscoelastic model, the related equations for the trial stresses are presented, and then the new equations for the improved trial stresses are explained. According to Eqs. (4.55) to (4.57) the deviatoric and volumetric strain increment in small deformation framework can be written as

$$\begin{aligned}\Delta\varepsilon_{ij}^{t} &= J^{t}S_{ij}^{t} - J^{t-\Delta t}S_{ij}^{t-\Delta t} - \frac{1}{2}\sum_{n=1}^{\mathrm{NP}} J_n\left(g_1^{t}\exp\left[-\lambda_n\Delta\psi^{t}\right] - g_1^{t-\Delta t}\right)q_{ij,n}^{t-\Delta t} \\ &\quad -\frac{1}{2}g_2^{t-\Delta t}\sum_{n=1}^{\mathrm{NP}}\left[J_n\left(g_1^{t-\Delta t} - g_1^{t}\right)\times\frac{1-\exp\left[-\lambda_n\Delta\psi^{t}\right]}{\lambda_n\Delta\psi^{t}}\right]S_{ij}^{t-\Delta t}\end{aligned} \tag{7.9}$$

$$\begin{aligned}\Delta\varepsilon_{kk}^{t} &= B^{t}\sigma_{kk}^{t} - B^{t-\Delta t}\sigma_{kk}^{t-\Delta t} - \frac{1}{3}\sum_{n=1}^{\mathrm{NP}} B_n\left(g_1^{t}\exp\left[-\lambda_n\Delta\psi^{t}\right] - g_1^{t-\Delta t}\right)q_{kk,n}^{t-\Delta t} \\ &\quad -\frac{1}{3}g_2^{t-\Delta t}\sum_{n=1}^{\mathrm{NP}}\left[B_n\left(g_1^{t-\Delta t} - g_1^{t}\right)\times\frac{1-\exp\left[-\lambda_n\Delta\psi^{t}\right]}{\lambda_n\Delta\psi^{t}}\right]\sigma_{kk}^{t-\Delta t}\end{aligned} \tag{7.10}$$

For computing the trial stress, one needs to assume some approximations, like

$$J^{t} \approx J^{t-\Delta t} = J^{t,\mathrm{trial}} \quad , \quad B^{t} \approx B^{t-\Delta t} = B^{t,\mathrm{trial}} \quad , \quad g_1^{t} = g_1^{t-\Delta t} \tag{7.11}$$

Therefore, Eqs. (7.9) and (7.10) will be reduced to the following relations for making an estimation of the stress state in the current time increment.

$$\begin{aligned}\Delta S_{ij}^{t,\mathrm{trial}} &= \frac{1}{J^{t,\mathrm{trial}}}\left[\Delta e_{ij}^{t} + \frac{1}{2}g_1^{t,\mathrm{trial}}\sum_{n=1}^{\mathrm{NP}} J_n\left(\exp\left[-\lambda_n\Delta\psi^{t}\right]-1\right)q_{ij,n}^{t-\Delta t}\right] \\ \Delta\sigma_{kk}^{t,\mathrm{trial}} &= \frac{1}{B^{t,\mathrm{trial}}}\left[\Delta\varepsilon_{kk}^{t} + \frac{1}{2}g_1^{t,\mathrm{trial}}\sum_{n=1}^{\mathrm{NP}} B_n\left(\exp\left[-\lambda_n\Delta\psi^{t}\right]-1\right)q_{kk,n}^{t-\Delta t}\right]\end{aligned} \tag{7.12}$$

In these equations, the effects of the non-linear parameters in the current time increment have been removed. Thus, for enhancing these trial stresses, at first Eq. (7.12) should be computed and then through considering Eq. (4.64), the updated trial stresses may be modified as

$$\Delta S_{ij}^{t,\text{trial}} = \frac{1}{J^t}\left\{\Delta e_{ij}^t + \frac{1}{2}\left[\sum_{n=1}^{\text{NP}} J_n\left(g_1^t \exp\left(-\lambda_n \Delta\psi^t\right) - g_1^{t-\Delta t}\right) q_{ij,n}^{t-\Delta t}\right]\right.$$
$$\left. + \left[\frac{1}{2} g_2^{t-\Delta t} \sum_{n=1}^{\text{NP}}\left(J_n\left(g_1^{t-\Delta t} - g_1^t\right) \times \frac{1-\exp\left(-\lambda_n \Delta\psi^t\right)}{\lambda_n \Delta\psi^t}\right) + \left(J^{t-\Delta t} - J^t\right)\right] S_{ij}^{t-\Delta t}\right\} \tag{7.13}$$

$$\Delta\sigma_{kk}^{t,\text{trial}} = \frac{1}{B^t}\left\{\Delta\varepsilon_{kk}^t + \frac{1}{3}\left[\sum_{n=1}^{\text{NP}} B_n\left(g_1^t \exp\left(-\lambda_n \Delta\psi^t\right) - g_1^{t-\Delta t}\right) q_{kk,n}^{t-\Delta t}\right]\right.$$
$$\left. + \left[\frac{1}{3} g_2^{t-\Delta t} \sum_{n=1}^{\text{NP}}\left(B_n\left(g_1^{t-\Delta t} - g_1^t\right) \times \frac{1-\exp\left(-\lambda_n \Delta\psi^t\right)}{\lambda_n \Delta\psi^t}\right) + \left(B^{t-\Delta t} - B^t\right)\right] \sigma_{kk}^{t-\Delta t}\right\} \tag{7.14}$$

7.2.3 Energy Dissipation Through Viscoelasticity

The increase in temperature is attributed to the dissipation of energy and is due to the viscoelastic deformation in the viscoelastic constitutive model. Viscoelastic solid materials are categorized as dissipative materials, and during the mechanical deformation, significant amount of heat could be generated which affects the temperature of the viscoelastic domain. For investigating the energy dissipation through mechanical deformation, studying the entropy and specific heat is mandatory. The entropy relation for Schapery's viscoelastic model, based on Gibbs complementary energy, G, was expressed in Eq. (4.1) which is written based on functions and tensors of stress and temperature, and also the internal state variables (ISVs). ISVs represent the equivalent springs and dashpots in the model. Recalling Eqs. (4.9) to (4.11)

$$\frac{\partial G}{\partial \eta_m} = A_m - B_{mn}\eta_n \qquad , \qquad \frac{\partial G}{\partial \eta_m}^{\text{def}} = a_T C_{mn}^{-1} \dot{\eta}_n \tag{7.15}$$

here C_{mn} is a positive definite symmetric coefficient tensor, and a is a positive scalar that is a function of temperature and stress. Solving the above equations together (see

Chapter 4 and (Khan, 2011) for more detail) delivers η_m (ISVs) that can be expressed

$$\eta_m = \frac{1}{K_m}\int_0^{\psi}\left(1-\exp(-\lambda_m(\psi-\psi'))\right)\frac{\mathrm{d}}{\mathrm{d}\psi'}\left(\frac{A_m}{b}\right)\mathrm{d}\psi' \tag{7.16}$$

λ_m is the inverse of positive retardation time. b is the inverse of stress shift factor (Eq. (4.14)). In thermodynamics, Gibbs free energy is defined as

$$G(p,T) = H - TS \tag{7.17}$$

Here H is enthalpy, S is the entropy, T is absolute (Kelvin) temperature, and p is the applied pressure. Also, entropy is defined as the rate of changes of Gibbs free energy with respect to the absolute temperature, i.e.: $\frac{\partial G}{\partial T} = -\frac{\partial G}{\partial T}(TS) = -S$. Replacing Eq. (4.1) into this relation

$$S = -\frac{\partial G}{\partial T} = -\frac{\partial G_0}{\partial T} + \frac{\partial A_m}{\partial T}\eta_m \tag{7.18}$$

The mathematical form for A_m that characterizes the master creep function was introduced in Eq. (4.23), and considering the Cauchy stress it can be expressed as

$$A_m = K_{mj}\hat{\sigma}_j + \alpha_m\hat{\phi} \tag{7.19}$$

in which α_m is the thermal expansion coefficients, and $\hat{\sigma}$ is a function of stress and temperature, but $\hat{\phi}$ is just a function of temperature. By substituting Eqs. (7.16) and (7.19) in the recent formula for entropy, one can come up with

$$S = -\frac{\partial G_0}{\partial T} + \frac{\partial \hat{\varphi}}{\partial T}\int_0^{\psi^t}\mathrm{d}\alpha_k(\psi^t-\psi)\frac{\mathrm{d}}{\mathrm{d}\psi}\left(\frac{\hat{\sigma}_k}{b}\right)\mathrm{d}\psi + \frac{\partial \hat{\varphi}}{\partial T}\int_0^{\psi^t}\mathrm{d}D(\psi^t-\psi)\frac{\mathrm{d}}{\mathrm{d}\psi}\left(\frac{\hat{\varphi}}{b}\right)\mathrm{d}\psi \tag{7.20}$$

where $\mathrm{d}\alpha_k(\psi)$ is the creep compliance thermal expansion, and $\mathrm{d}D(\psi)$ is the transient components of the specific heat (in a certain stress level) which are expressed as

$$\mathrm{d}\alpha_k(\psi) = \sum_m \frac{K_{mk}\alpha_m}{K_m}\left(1-\exp(-\lambda_m\psi)\right) \quad , \quad \mathrm{d}D(\psi) = \sum_m \frac{\alpha_m^2}{K_m}\left(1-\exp(-\lambda_m\psi)\right) \tag{7.21}$$

K_m is the diagonalized terms of the second rank tensor K_{mn}. The specific heat capacity (or thermal capacity) in a certain pressure is defined and expressed as

$$C_p(\sigma) = T\left(\frac{\partial S}{\partial T}\right)\Big|_\sigma = -T\left(\frac{\partial^2 G}{\partial T^2}\right)\Big|_\sigma \tag{7.22}$$

Replacing Eqs. (7.20) and (7.21) in the equation expressing the specific heat capacity, the specific heat capacity can be obtained as

$$C_p = -T\frac{\partial^2 G_0}{\partial T^2} + T\frac{\partial}{\partial T}\left\{\frac{\partial \hat{\varphi}}{\partial T}\int_0^{\psi^t} \mathrm{d}\alpha_k(\psi^t-\psi)\frac{\mathrm{d}}{\mathrm{d}\psi}\left(\frac{\hat{\sigma}_k}{b}\right)d\psi + \frac{\partial \hat{\varphi}}{\partial T}\int_0^{\psi^t} \mathrm{d}C(\psi^t-\psi)\frac{\mathrm{d}}{\mathrm{d}\psi}\left(\frac{\hat{\varphi}}{b}\right)d\psi\right\} \tag{7.23}$$

According to the first and second thermodynamics laws, the internal entropy production rate, *S* can be explained (Rice (1971), Schapery (1964, 1966)). As a result, the rate of generated internal entropy may be written

$$\Pi_{\text{disp}}^{\text{ve}} = T\dot{S} = -\frac{\partial G}{\partial \zeta_m}\dot{\zeta}_m \tag{7.24}$$

By substituting Eq. (7.16) into Eq. (7.24), one can get

$$
\begin{aligned}
T\dot{S} = & \left\{ K_{mj} \left(\hat{\sigma}_j - b \int_0^{\psi^t} \left(1 - \exp(-\lambda_m (\psi - \psi^t))\right) \frac{\mathrm{d}(g_2 \hat{\sigma})}{\mathrm{d}\psi} \mathrm{d}\psi \right) \right. \\
& \left. - b \int_0^{\psi^t} \left(1 - \exp(-\lambda_m (\psi - \psi^t))\right) \frac{\mathrm{d}}{\mathrm{d}\psi} \left(\frac{\alpha_m \hat{\varphi}}{b}\right) \mathrm{d}\psi + \alpha_m \hat{\varphi} \right\} \\
& \left\{ \frac{1}{K_m} \frac{\mathrm{d}}{\mathrm{d}t} \left(\int_0^{\psi^t} \left(1 - \exp(-\lambda_m (\psi - \psi^t))\right) \frac{\mathrm{d}}{\mathrm{d}\psi} \left(\frac{K_{mj} \hat{\sigma} + \alpha_m \hat{\varphi}}{b}\right) \mathrm{d}\psi \right) \right\}
\end{aligned}
\tag{7.25}
$$

Simplifying the recent equation and removing the specific heat retardation and the thermal transient parts, the following relation can be achieved

$$
T\dot{S} = b \left\{ g_2 \sigma_j - \int_0^{\psi} \left(1 - \exp(-\lambda_m (\psi - \psi'))\right) \frac{\mathrm{d}(g_2 \sigma_j)}{\mathrm{d}\psi'} \mathrm{d}\psi' \right\} \left\{ \frac{\mathrm{d}}{\mathrm{d}t} \int_0^{\psi} \Delta D_{jk} (\psi - \psi') \frac{\mathrm{d}(g_2 \sigma_k)}{\mathrm{d}\psi'} \mathrm{d}\psi' \right\}
\tag{7.26}
$$

The reader is referred to Appendix A of (Khan, 2011) for more detail about the derivations of energy dissipation through viscoelastic model. Eventually, one can derive an equation which relates the temperature, rate of temperature change, and dissipated energy through viscoelastic components.

$$
\begin{aligned}
\rho c_p \dot{T} + T \alpha \dot{\sigma}_{vol} = & -q_{i,i} + g_2 \left\{ \sum_{m=1}^{\mathrm{NP}} \int_0^{\psi^t} \exp(-\lambda_m (\psi - \psi^t)) \frac{\mathrm{d}(g_2 \sigma)}{\mathrm{d}\psi} \mathrm{d}\psi \right\} \\
& \left\{ \frac{\mathrm{d}}{\mathrm{d}t} \sum_{m=1}^{\mathrm{NP}} D_m \left[g_2 \sigma - \int_0^{\psi^t} \exp(-\lambda_m (\psi - \psi^t)) \frac{\mathrm{d}(g_2 \sigma)}{\mathrm{d}\psi} \mathrm{d}\psi \right] \right\}
\end{aligned}
\tag{7.27}
$$

If there exists no external heat flux, Eq. (7.27) will be re-written as

$$
\begin{aligned}
\rho c_p \dot{T} = & g_2 \left\{ \sum_{m=1}^{\mathrm{NP}} \int_0^{\psi^t} \exp(-\lambda_m (\psi - \psi^t)) \frac{\mathrm{d}(g_2 \sigma)}{\mathrm{d}\psi} \mathrm{d}\psi \right\} \\
& \left\{ \frac{\mathrm{d}}{\mathrm{d}t} \sum_{m=1}^{\mathrm{NP}} D_m \left[g_2 \sigma - \int_0^{\psi^t} \exp(-\lambda_m (\psi - \psi^t)) \frac{\mathrm{d}(g_2 \sigma)}{\mathrm{d}\psi} \mathrm{d}\psi \right] \right\}
\end{aligned}
\tag{7.28}
$$

Recalling the hereditary integral from Eq. (4.41), then Eq. (7.28) can be modified as

$$\rho c_p \dot{T} = g_2 \left\{ \sum_{m=1}^{\mathrm{NP}} q_m^t \right\} \left\{ \frac{\mathrm{d}}{\mathrm{d}t} \sum_{m=1}^{\mathrm{NP}} D_m \left[g_2 \sigma - q_m^t \right] \right\} \tag{7.29}$$

The derivation in the third term in the RHS can be numerically simplified as

$$\frac{\mathrm{d}}{\mathrm{d}t}\left(g_2 \sigma - q_m^t \right) = \frac{\mathrm{d}\left(g_2 \sigma \right)}{\mathrm{d}t} - \frac{\mathrm{d}q_m^t}{\mathrm{d}t} = \left(\frac{\mathrm{d}g_2}{\mathrm{d}t} \sigma + \frac{\mathrm{d}\sigma}{\mathrm{d}t} g_2 \right) - \frac{\mathrm{d}q_m^t}{\mathrm{d}t} \tag{7.30}$$

Discretizing the continues time (replacing $\mathrm{d}t$ to Δt), and after some manipulation

$$\frac{\mathrm{d}}{\mathrm{d}t}\left(g_2 \sigma - q_m^t \right) \equiv \frac{1}{\Delta t}\left[(g_2^t - g_2^{t-\Delta t})\sigma^t + g_2^t(\sigma^t - \sigma^{t-\Delta t}) - (q_m^t - q_m^{t-\Delta t}) \right] \tag{7.31}$$

Therefore, Eq.(7.29) can be re-written (summation over *i* and *j*) as

$$\rho c_p \Delta T = g_2 \sum_{m=1}^{\mathrm{NP}} q_{ij,m}^t \left\{ \sum_{m=1}^{\mathrm{NP}} D_m \left[(g_2^t - g_2^{t-\Delta t})\sigma_{ij}^t + g_2^t(\sigma_{ij}^t - \sigma_{ij}^{t-\Delta t}) - (q_{ij,m}^t - q_{ij,m}^{t-\Delta t}) \right] \right\} \tag{7.32}$$

Finally the incremental change in temperature may be computed as

$$\Delta T = \frac{g_2}{\rho c_p} \sum_{m=1}^{\mathrm{NP}} q_{ij,m}^t \left\{ \left[(g_2^t - g_2^{t-\Delta t})\sigma_{ij}^t + g_2^t(\sigma_{ij}^t - \sigma_{ij}^{t-\Delta t}) \right] \sum_{m=1}^{\mathrm{NP}} D_m - \sum_{m=1}^{\mathrm{NP}} D_m (q_{ij,m}^t - q_{ij,m}^{t-\Delta t}) \right\} \tag{7.33}$$

In this equation, the summation over hereditary integral can be calculated, and $q_{ij,m}^t$ should be stored to be used in the next increment.

$$\sum_{m=1}^{\mathrm{NP}} q_{ij,m}^t = \sum_{m=1}^{\mathrm{NP}} \left(q_{ij,m}^{\mathrm{dev},t} + \frac{1}{3} q_m^{\mathrm{vol},t} \delta_{ij} \right) \tag{7.34}$$

The required material parameters for computing the change of temperature during loading are presented in Table 7.3.

Table 7.3: Material properties for computing temperature changes.

Matrix	Density (ρ)	Specific Heat (c_p)
PMMA	1200 kg/m^3	1470 $J/(kg\,K)$

7.3 2D and 3D Microstructural Models

In this section, two and three dimensional dispersed perfectly bonded intercalated nano-clay particles (NCLP) and also nano-ceramic particles (NCRP) (with two different radii) in a PMMA polymer matrix are studied. The effects of particles distribution and shape on viscoelastic response of the composites, through micromechanical simulation of the RVEs that are subjected to uniaxial compressive load under isothermal condition are presented. In Fig. 7.2, some samples of the generated 2D RVEs are shown, which depict the applied loads and boundary conditions. These images demonstrate the random distribution of NCLPs and two different sizes of NCRPs inside the polymer composites. In Fig. 7.3, one 3D RVE sample shows the compressive load on the top surface, the boundary conditions on lower surfaces, and periodic boundary conditions on the other three faces that force the nodes on those faces move with each other in a same direction.

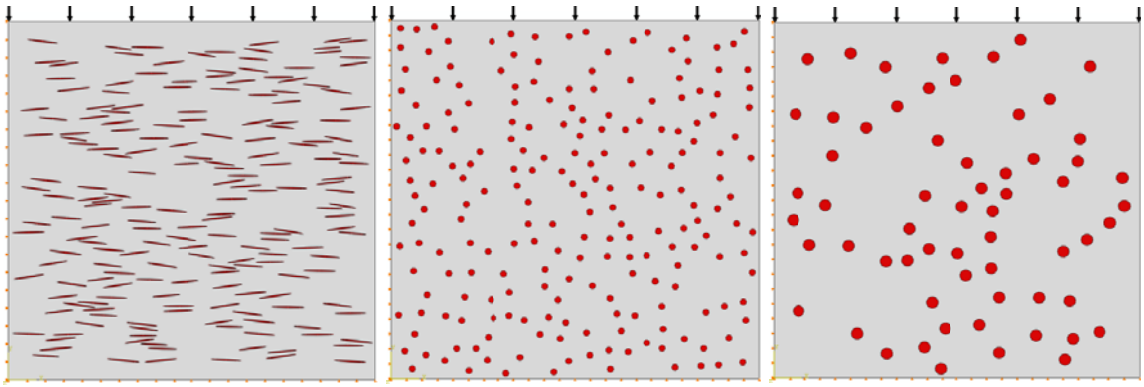

(a) NCLP (aspect ratio≈0.05) (b) NCRP (R=0.0175 µm) (c) NCRP (R=0.032 µm)

Fig. 7.2. Boundary condition and applied load on RVE samples (5% weight fraction).

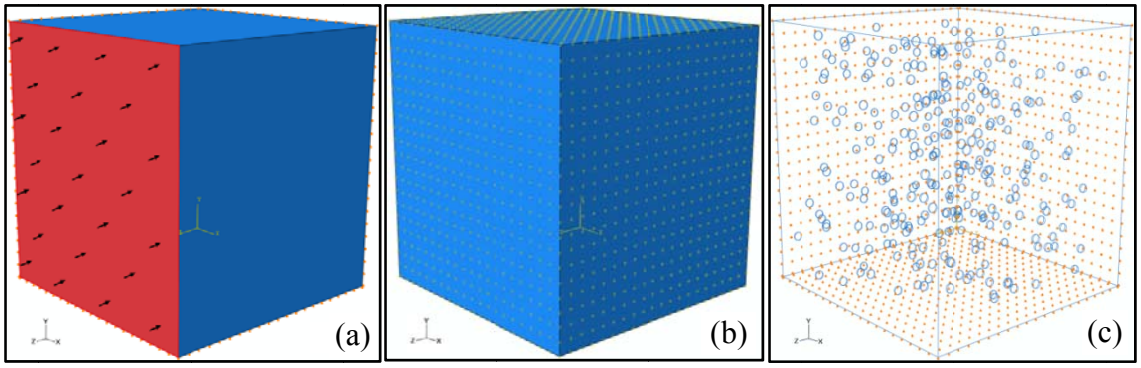

Fig. 7.3. General 3D RVE: (a) Loading condition, (b) Equation on three faces of the RVE, (c) Boundary conditions on other three faces of the RVE.

For creating these geometries, as mentioned in Chapter 6, the developed RVE_Maker software is utilized. The elastic properties and also geometrical variables to create the elliptical shape of the NCLP, which are presented by Sheng et al. (2004), are listed in Table 7.4. These parameters are employed in the current study for micro-scale finite element simulations.

Table 7.4: Mechanical and geometrical properties of nano-clay particles.

Nanoclay particles	E (GPa)	Poisson's Ratio	Length (nm)	Thickness (nm)	Angle of orientation	Aspect Ratio
Intercalated	136	0.28	150 - 180	7.0 – 9.0	$-10^o \leq \alpha \leq 10^o$	$0.048 \leq \text{A.R.} \leq 0.05$

In order to compare the results of the RVEs containing elliptical and circular particles, the mechanical properties of the circular particles are assumed to be the same as the ones in clay particles. This is done because the comparisons of the effect of shapes and patterns are desired and not the realistic effect of constituents mechanical properties on the overall response of the RVEs. The same boundary conditions that were mentioned in Chapter 6, and depicted through Figs. 6.14 and 6.15, are applied to these RVEs. Plane strain and 3D-Stress elements are considered for meshing and analyzing the 2D and 3D models, respectively. The finite element simulations were conducted under stress control tests for compressive loading. Figs. 7.4 and 7.5 illustrate the micromechanical models in 2D that were simulated to study the viscoelastic response. In spite of the limitations, 2D analyses are still a viable approach to gain qualitative insight, rather than to evaluate the quantitative response, of the material response at the microstructural level. However, in this chapter the results of 2D and 3D models are compared.

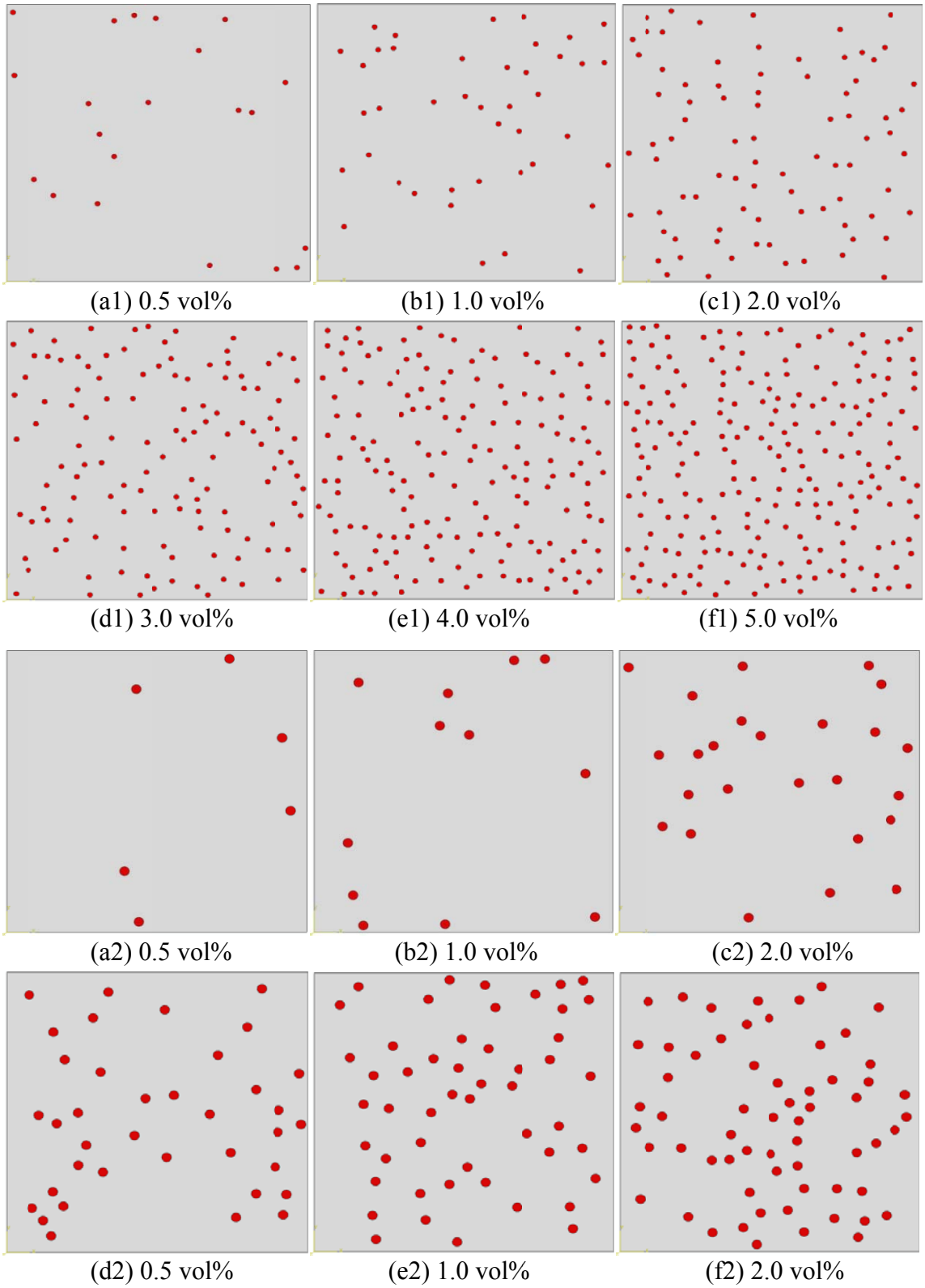

Fig. 7.4. 2D RVEs with NCRP: (a1)-(f1) R1 = 0.032 μm, (a2)-(f2) R2 = 0.0175 μm.

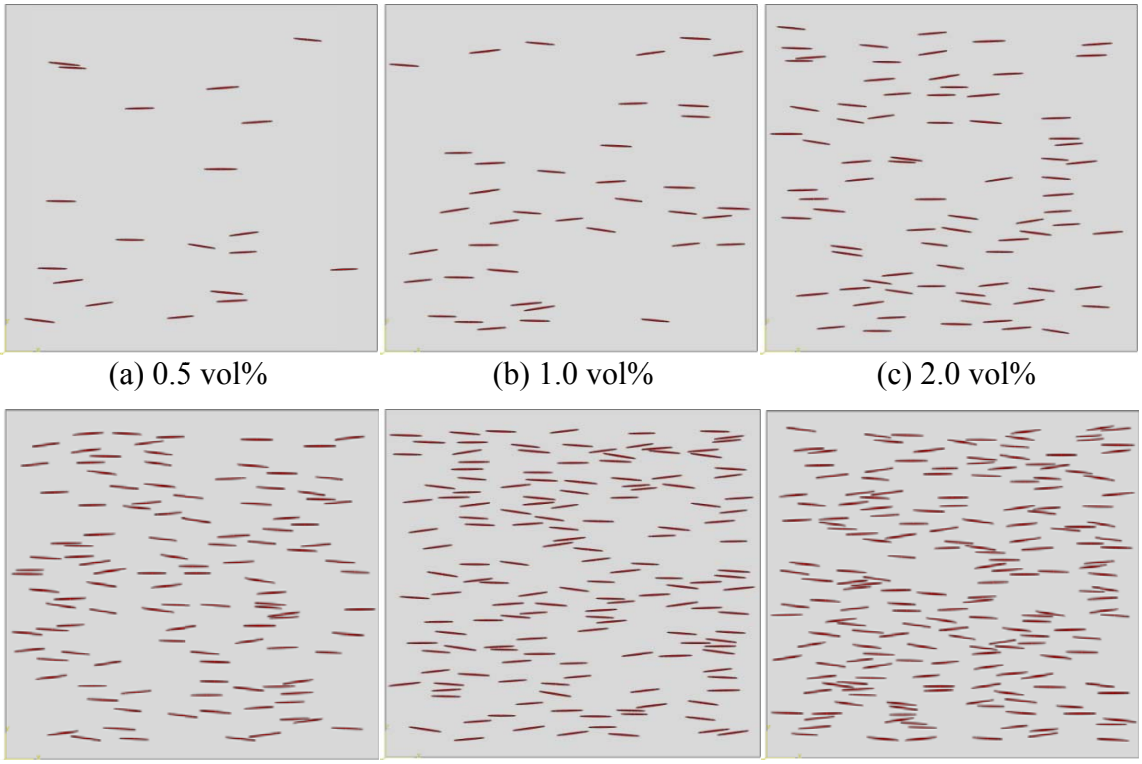

(a) 0.5 vol% (b) 1.0 vol% (c) 2.0 vol%

(d) 3.0 vol% (e) 4.0 vol% (f) 5.0 vol%

Fig. 7.5. 2D RVEs with intercalated NCLP (ellipse shape) (aspect ratio ≈ 0.05).

Moreover, the 3D RVEs containing 3D particles are shown in Figs. 7.6 and 7.7. It can be observed the particles are sliced to two pieces. It is done to create additional edges on the surface of the particles (both spherical and elliptical). The presence of such additional edges can help to reduce the number of generated elements through controlling the mesh seeding numbers on the additional boundaries (edges) for meshing the complex geometries. In this study, the particles are elastic and the matrix is made of isotropic viscoelastic PMMA polymer subjected to small deformation gradients. Perfect bonding is assumed for the particle-matrix interfaces.

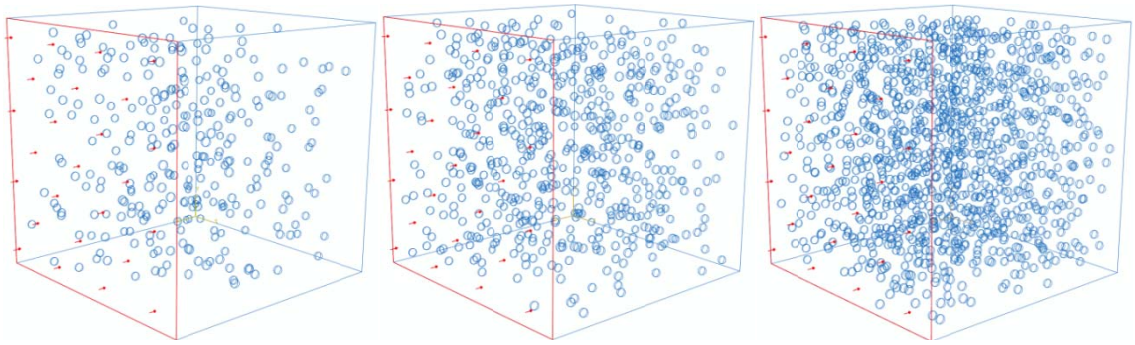

(a) 0.5 vol% (b) 1.0 vol% (c) 2.0 vol%

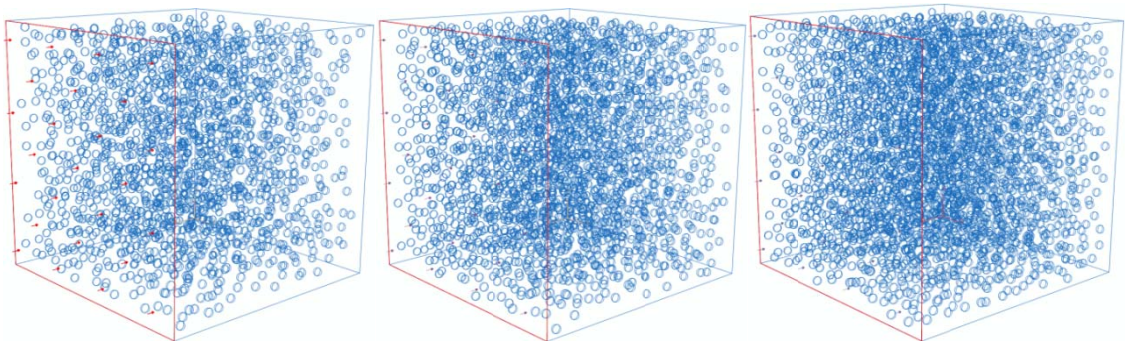

(d) 3.0 vol% (e) 4.0 vol% (f) 5.0 vol%

Fig. 7.6. 3D RVEs with NCRP (spherical shapes), Radius = 0.032 μm.

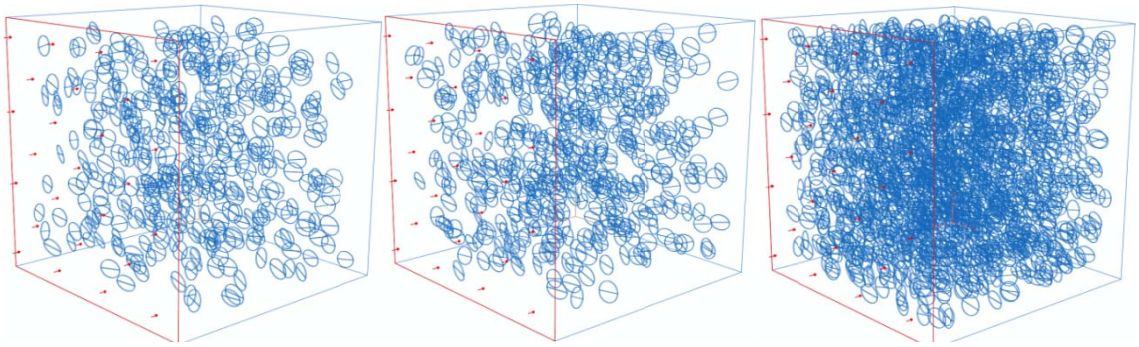

(a) 0.5 vol% (b) 1.0 vol% (c) 2.0 vol%

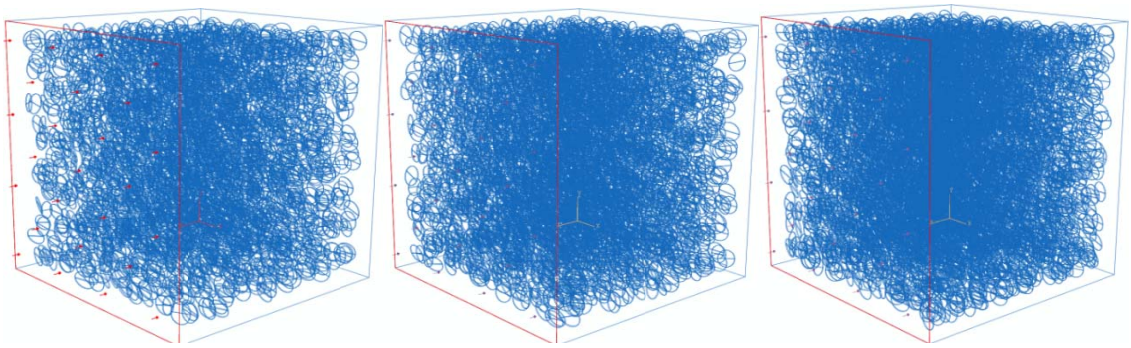

(d) 3.0 vol% (e) 4.0 vol% (f) 5.0 vol%

Fig. 7.7. 3D RVEs with intercalated NCLP. Aspect ratio of the ellipsoidal ≈ 0.05.

7.4 Determining Proper RVE Size

One of the main goals of solid mechanics of heterogeneous materials is to derive some effective properties from the knowledge of the constitutive models and the distribution of the components. For this purpose, as discussed in Chapter 6, the concept of RVE is used such that the overall response of a certain physical property (thermal, mechanical, and etc.) of a geometrical model in smaller scale can explain the response of the whole material in larger scale. It means that, the proper size for an RVE can be determined for a given physical property and for another property the size may vary. For

such determination, it is also necessary to consider the precision of the estimation of the favorite property(s).

The size of one RVE should be large enough as compared to the characteristic size of the inclusions so that the size effect of the RVE is negligible. However, in this study none of the homogenization techniques has been employed. Henceforth, a number of realizations are required to generate different geometrical models. In order to decide about the proper statistical representative size for a desired RVE, one should be able to conduct several FEA simulations for various random geometrical distribution samples. Hence, for this purpose, numerous RVEs with different sizes each containing various random distributions of NCLP and also NCRP have been generated and simulated, for both 2D and 3D cases. The geometrical RVE models are created with different sizes for 2D as: $0.5\times0.5, 1.0\times1.0, 1.5\times1.5, 2.0\times2.0$ and $2.5\times2.5\ \mu m^2$, and for 3D cases as: $0.5\times0.5\times0.5, 1.0\times1.0\times1.0, 1.5\times1.5\times1.5, 2.0\times2.0\times2.0$ and $2.5\times2.5\times2.5\ \mu m^3$. For the realization, several random sets (totally five sets for each size) of distributed particles were generated for each size of the 2D and 3D models. By simulating these geometrical models, it is shown the idea that there exists just one single possible minimal RVE size, must be relinquished. As can be seen in Fig. 7.8, for each type of particle and RVE size, there is a range that the desired characteristics deviate in between the range.

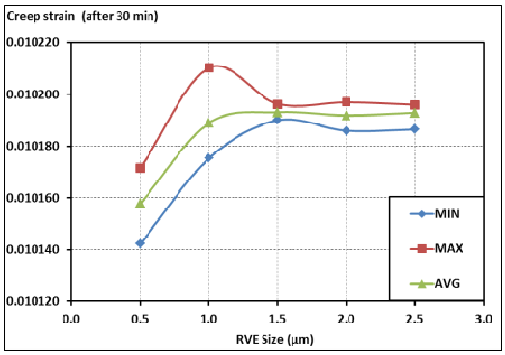

(a) 2D-Elliptical particles.

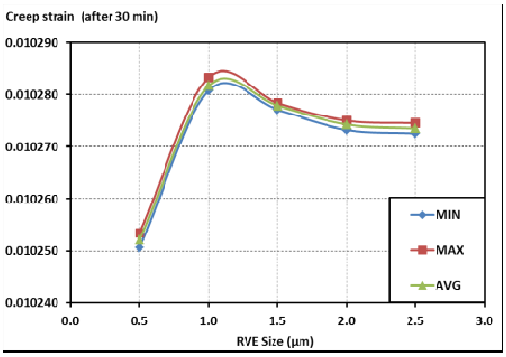

(b) Circular particles (R1).

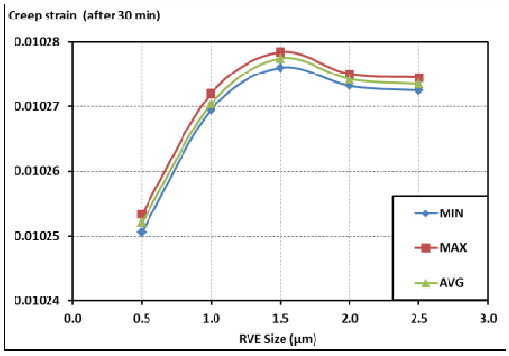

(c) Circular particles (R2).

Fig. 7.8. Comparing amount of maximum, minimum, and average of creep strain simulations for 2D models. Particles weight fraction for all cases is 2%.

Therefore, from the computational point of view a proper size for an RVE can be redefined as: it is the size in which the variation of the range of the desired physical property does not change by increasing the size of the model. The three diagrams in Fig. 7.8 (a) to (c) demonstrate that the response (here: ultimate creep strain up to 30 minutes) of any RVE larger than $2.5\times2.5\ \mu m^2$ with any random distribution of nano-clay and/or nano-ceramic particles results almost the same quantity, and the response will not depend on RVE size. It is worthy to mention that the other mechanical properties (e.g.,

initial Young's modulus) which are not reported here, are also RVE size-independent when the RVE is larger than $2.5\times2.5\ \mu m^2$.

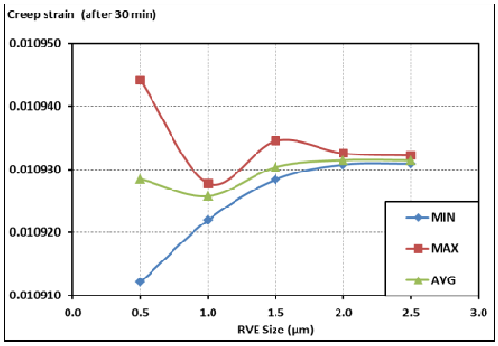

(a) 3D-Ellipsoidal particles.

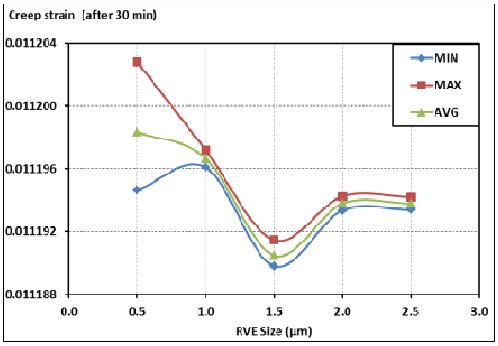

(b) 3D-Spherical particles.

Fig. 7.9. Comparing amount of maximum, minimum, and average of creep strain simulations for 3D models. Particles weight fraction for all cases is 2%.

The same analogy is valid for simulations of 3D RVEs. The results of creep tests for 3D models are presented in the diagrams of Fig. 7.9 (a) and (b). They show that the creep strains do not change through increasing the RVE size more than $2.5\times2.5\times2.5\ \mu m^3$.

7.5 Computational Results

In this section, the results of the micromechanical simulations are presented. At first, in Figs. 7.10 to 7.12, the creep and recovery responses of the generated 2D composites are depicted. Six different weight fractions (vol% = 0.5, 1.0, 2.0, 3.0, 4.0, and 5.0) as mentioned in Section 7.4, are simulated, but for the sake of conciseness, just the results of minimum (0.5%), medium (2.0%), and maximum (5.0%) particles weight fractions are presented.

As can be observed in Figs. 7.10 to 7.12, for both creep and recovery simulations, the presence of the elastic inclusions can reduce the amount of creep and recovery strains during 30 minutes applying loads or 60 minutes removing loads, respectively. Furthermore, it is recognized that for all types of the particles, increasing the weight fraction of inclusions can just a little affect the overall creep and recovery responses. Here, it should be mentioned that in order to extracting the required numerical data, for the purpose of computing and illustrating the average strain, dissipated energy, and temperature at a constant stress level of each of the RVEs, the weighted average integral over the whole volume of the RVE (Nemat-Nasser and Hori, 1999) can be utilized, as

$$\left\langle \varepsilon_{yy} \right\rangle = \frac{1}{V}\int_v V_i \varepsilon_{yy,i}\, \mathrm{d}v \qquad , \qquad \left\langle D \right\rangle = \frac{1}{V}\int_v V_i D_i\, \mathrm{d}v \qquad , \qquad \left\langle T \right\rangle = \frac{1}{V}\int_v V_i T_i\, \mathrm{d}v \qquad (7.35)$$

where $\left\langle \varepsilon_{yy} \right\rangle$, $\left\langle D \right\rangle$, and $\left\langle T \right\rangle$ are sequentially the overall macroscopic response of: the strain in the y direction, the dissipated energy, and the temperature. Also, V_i is the volume (or area in 2D models) of the i^{th} element, and V is the volume (or area in 2D) of the whole RVE. Therefore, the overall macroscopic behavior can be computed through numerical discretized form as

$$\left\langle \varepsilon_{yy} \right\rangle \approx \frac{1}{V}\sum_{i=1}^{\mathrm{NOEL}} V_i \varepsilon_{yy,i} \qquad , \qquad \left\langle D \right\rangle \approx \frac{1}{V}\sum_{i=1}^{\mathrm{NOEL}} V_i D_i \qquad , \qquad \left\langle T \right\rangle \approx \frac{1}{V}\sum_{i=1}^{\mathrm{NOEL}} V_i T_i \qquad (7.36)$$

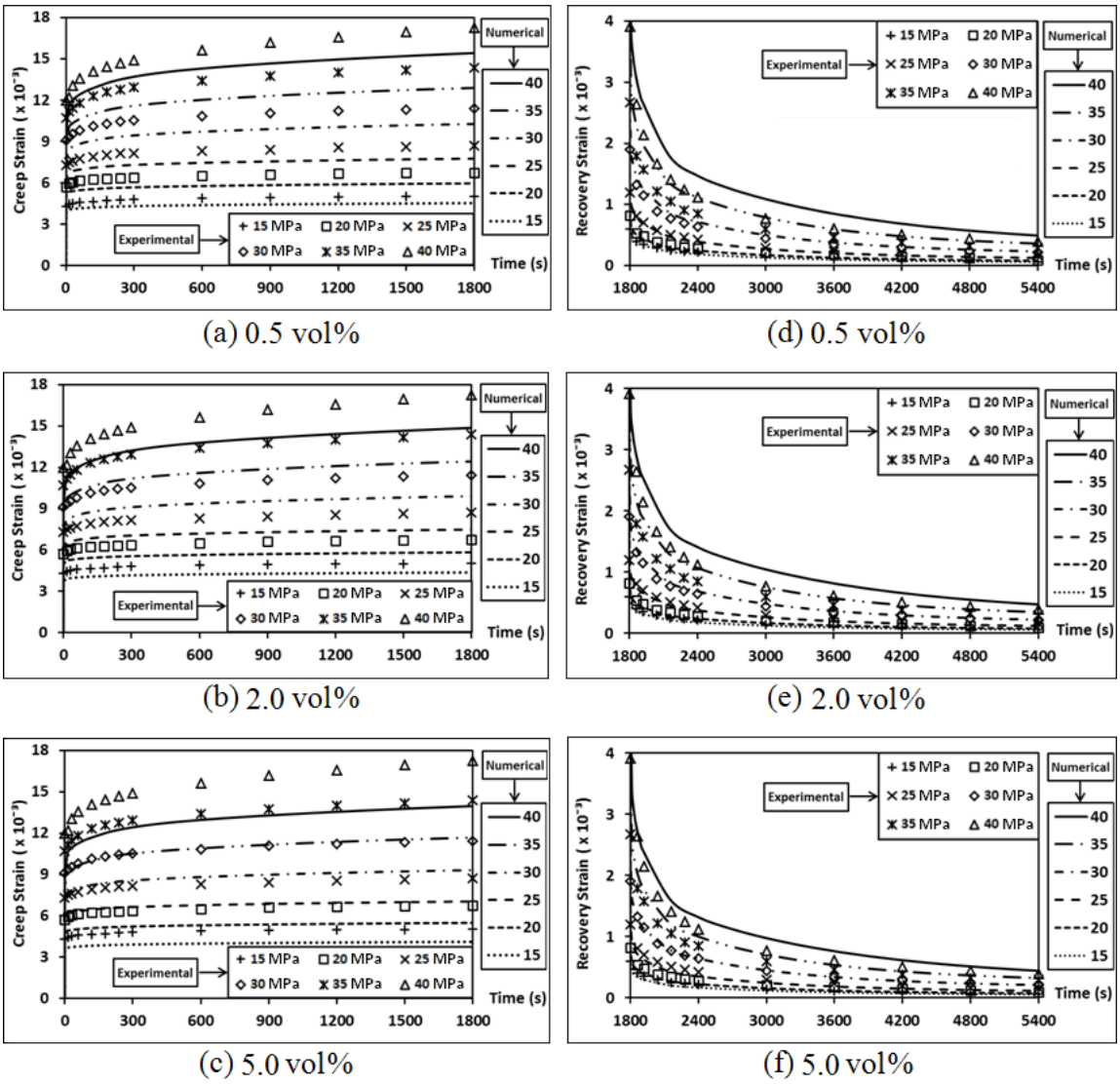

Fig. 7.10. Comparing creep and recovery strain of 2D NCLPs simulations with respect to three different weight fractions and various stress levels. (a) to (c) Creep. (d) to (f) Recovery. Stress unit is MPa.

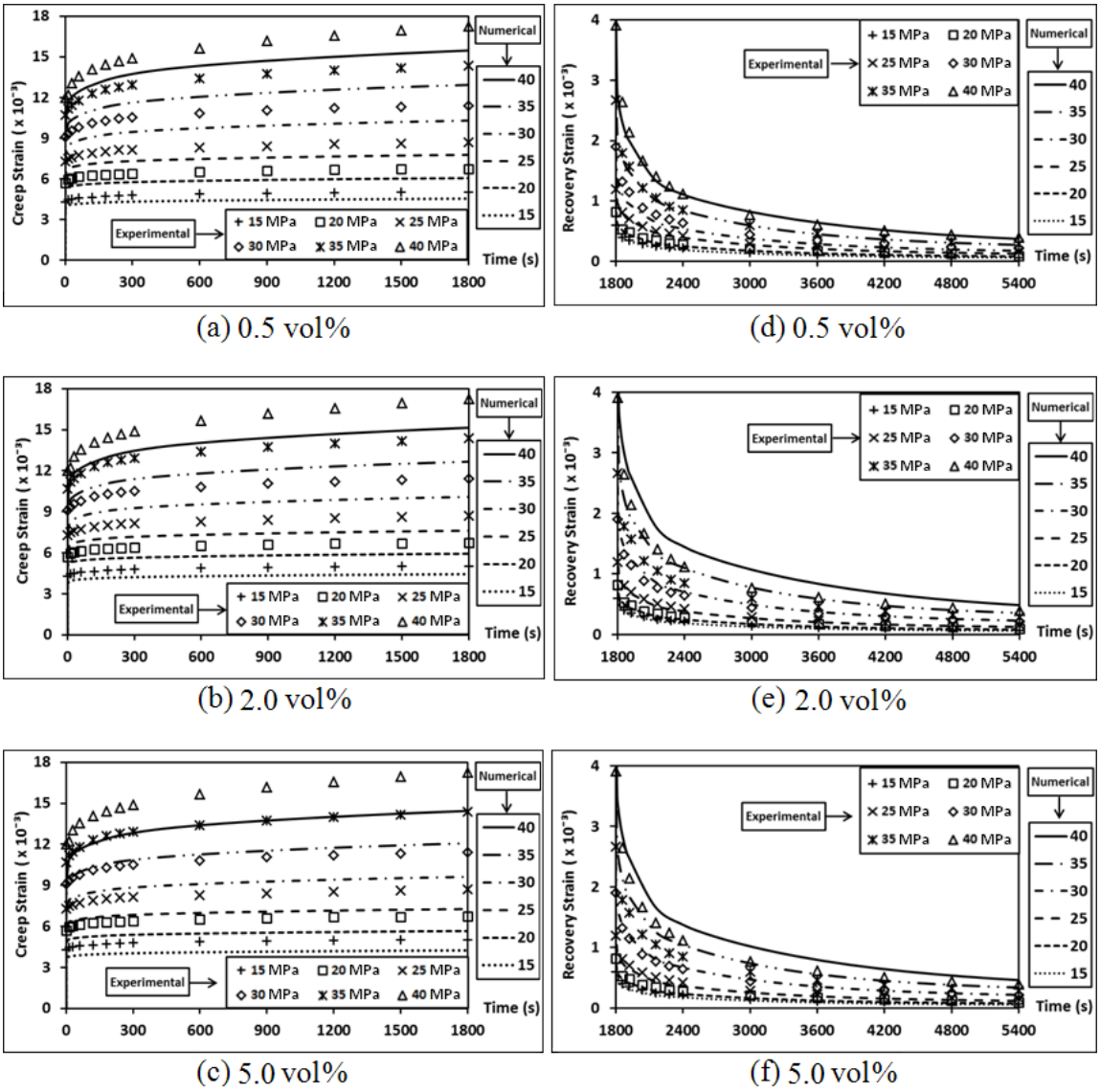

Fig. 7.11. Comparing creep and recovery strain of NCRPs (2D-Circle, R1) simulations according to three different weight fractions and various stress levels. (a) to (c) Creep. (d) to (f) Recovery. Stress unit is MPa.

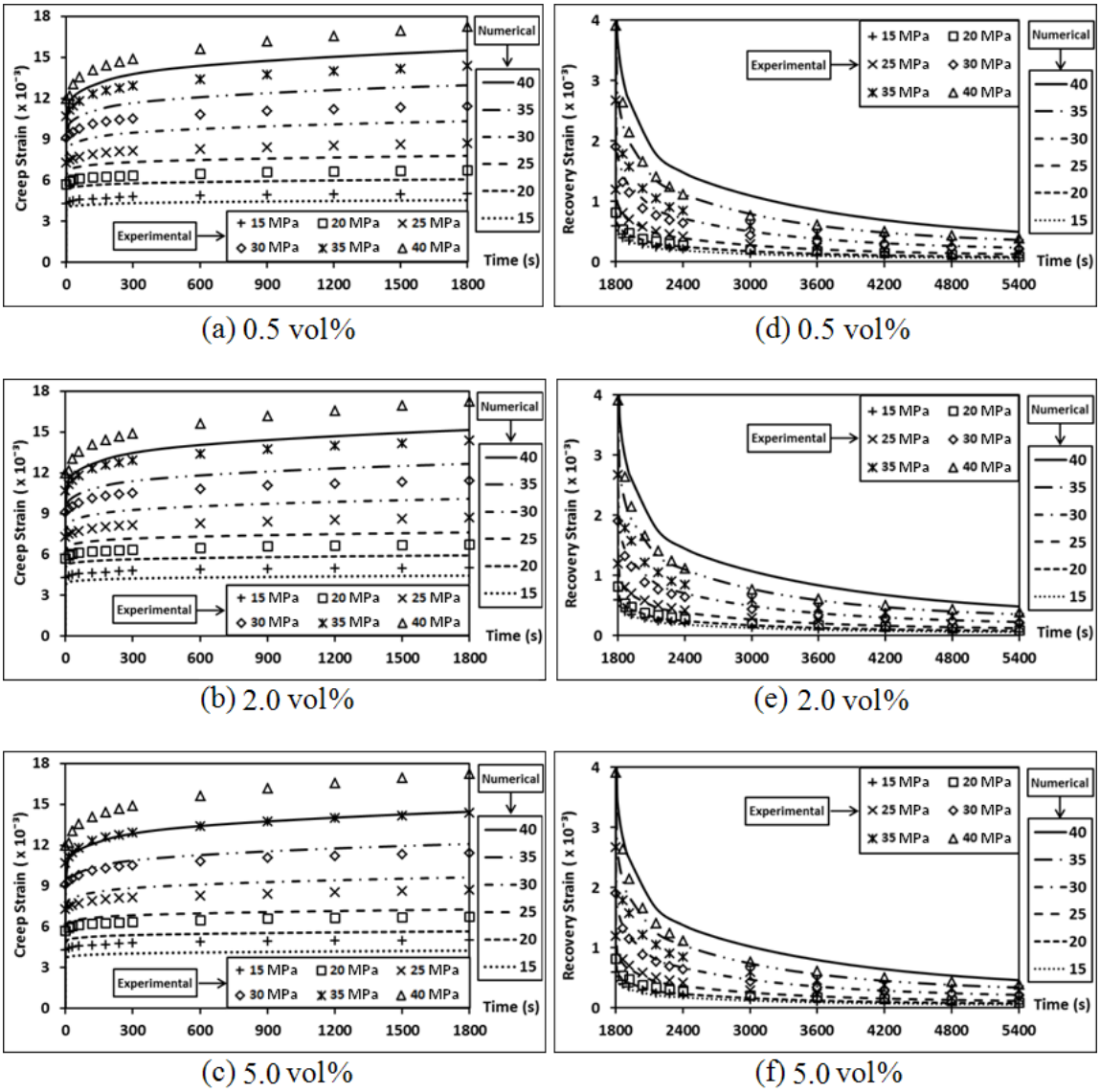

Fig. 7.12. Comparing creep and recovery strain of NCRPs (2D-Circle, R2) simulations according to three different weight fractions and various stress levels. (a) to (c) Creep. (d) to (f) Recovery. Stress unit is MPa.

The maximum effects of particles for enhancing the viscoelastic response (i.e. the reduction in creep strain) of composites may be observed while the RVE is subjected to higher stress levels in all types of the inclusions. It is an immediate result of comparing

the creep in the minimum ($\sigma = 15\,\text{MPa}$) and maximum ($\sigma = 40\,\text{MPa}$) stress levels in the above depicted diagrams. Also, the amount of strain reductions in the creep and recovery tests for elliptical shape particles is greater than the ones in the circular particles (in both the lowest and highest stress levels). The numerical evaluation and comparison for understanding that how much particles can boost the resistance of the composites against creep (stress control) loading, is stated in Table 7.5.

Table 7.5: Comparing the enhancement of different particles on creep and recovery.

Weight Fraction 5.0 %	Load	Creep (30 minutes)			Recovery (60 minutes)		
	Particle Type	Elliptical	Circle (R1)	Circle (R2)	Elliptical	Circle (R1)	Circle (R2)
	$\sigma = 15\,\text{MPa}$	18.0%	15.4%	15.35%	3.24%	1.88%	1.87%
	$\sigma = 40\,\text{MPa}$	19.1%	16.29%	16.23%	5.1%	3.2%	3.19%

By simple analogy from Table 7.5, it can be understood that in the same particles volume fraction the effects of shape is more important on creep rather than size. Furthermore, from the simulations for circular particles, it may be concluded that there is almost no difference between the responses of the RVEs containing larger or smaller particles circular inclusions.

Secondly, for the case of 3D models, in Figs. 7.13 to 7.14, the creep and recovery responses of the 3D composites (shown in Figs. 7.6 and 7.7) are depicted. Similar to the 2D cases, six different weight fractions are simulated, but for the sake of brevity, just the results of minimum (0.5%), medium (2.0%), and maximum (5.0%) particles weight fractions are presented.

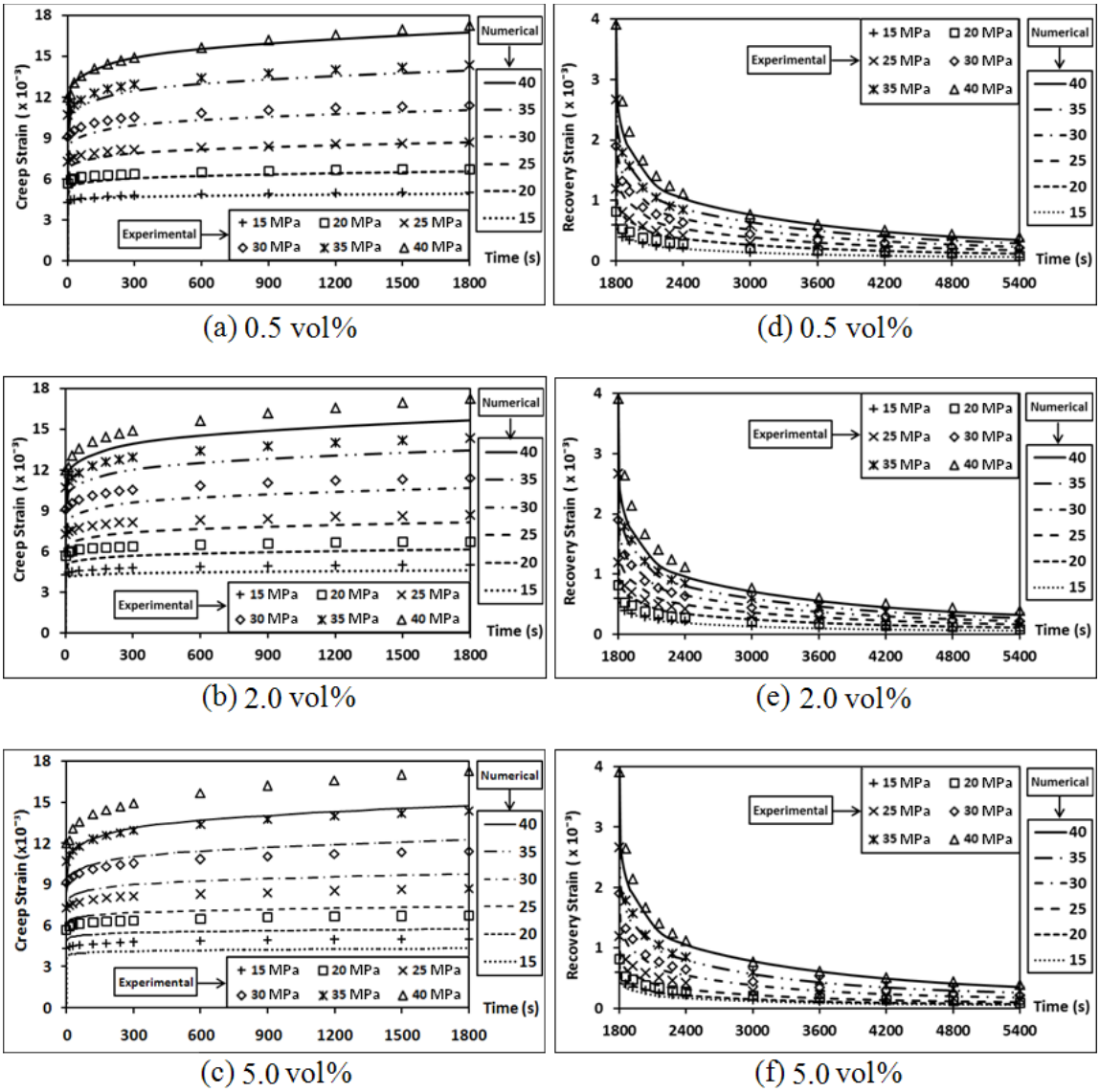

Fig. 7.13. Comparing creep and recovery strain of 3D NCLPs (3D-Ellipsoid) simulations according to three different weight fractions and various stress levels. (a) to (c) Creep. (d) to (f) Recovery. Stress unit is MPa.

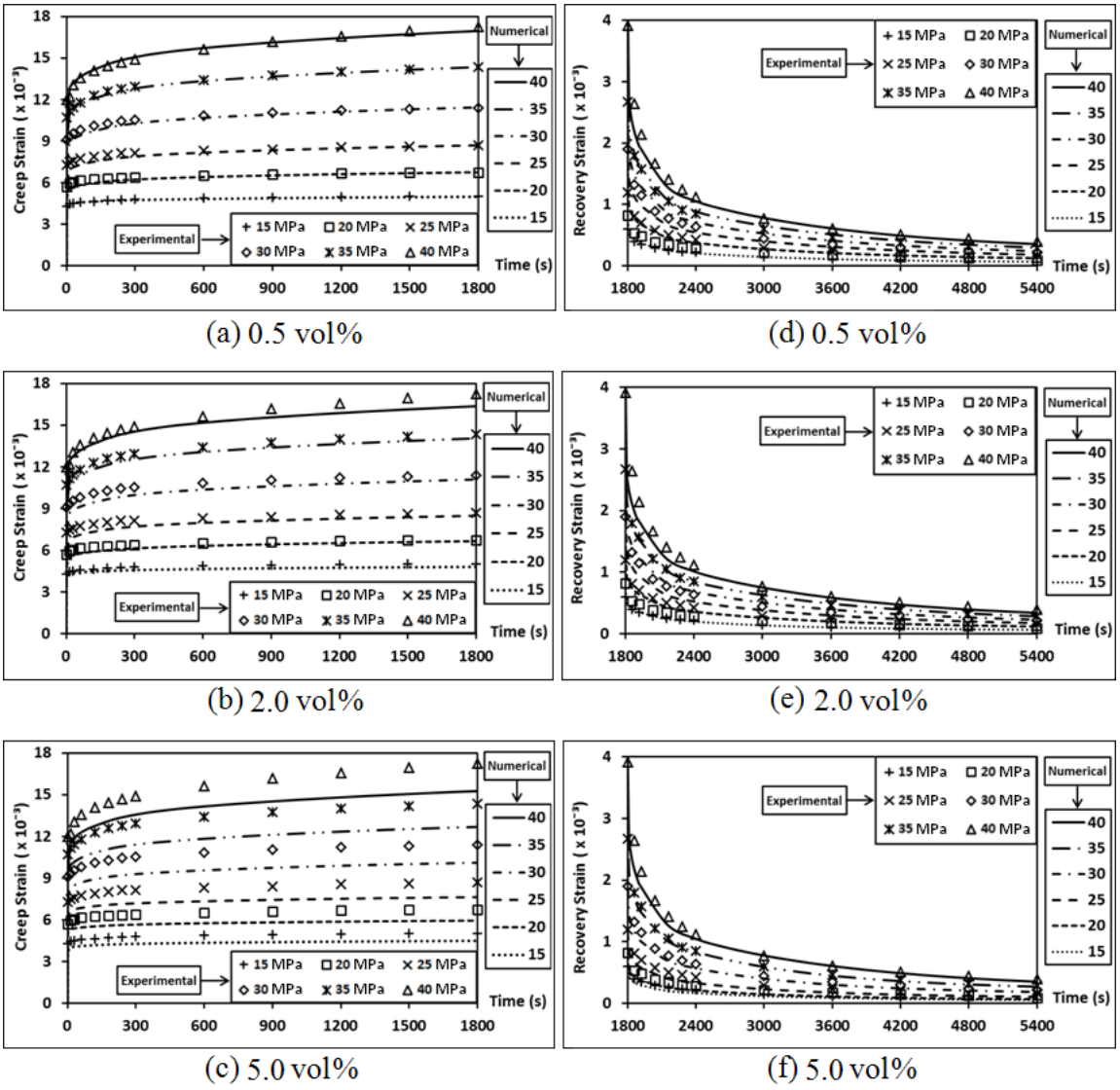

Fig. 7.14. Comparing creep and recovery strain of 3D NCRPs (3D-Spherical) simulations according to three different weight fractions and various stress levels. (a) to (c) Creep. (d) to (f) Recovery. Stress unit is MPa.

Table 7.6: Different particles enhancement on creep and recovery response.

Weight Fraction 5.0 %	Load	Creep (30 minutes)		Recovery (60 minutes)	
	Particle Type	Ellipsoidal	Spherical (R2)	Ellipsoidal	Spherical (R2)
	$\sigma = 15\,\text{MPa}$	17.6%	13.6%	3.17%	1.66%
	$\sigma = 40\,\text{MPa}$	18.34%	14.28%	4.89%	2.81%

Similar to Table 7.5 (for 2D), Table 7.6 (for 3D) shows that in the same particles volume fraction the effect of shape is more important on creep rather than size. Moreover, comparing Tables 7.5 and 7.6 demonstrates that the responses of composite with 2D-Ellipse are close to 3D-Ellipsoid one. For example, the creep strain in the 2D-Ellipse case is 1.031 times (or 3%) greater than the 3D one, for both minimum (15 MPa) and maximum (40 MPa) stress level. But the difference is higher for round shape particles, i.e. the creep strains in the 2D-Circular particles are approximately 1.136 times (or 13.6%) greater than the one for spherical shape particles, for both 15 and 40 MPa. This result affirms the effect of particles shape on composite response is more important in comparison to particles size.

In Fig. 7.15, the trends of creep and recovery strains in the RVEs including 2D and 3D NCLPs are demonstrated. It is apparent that the effect of particles to resist against creeping is highest for the RVE that contains 5% of nano-clay particles. Also, for both cases, it is obvious that adding 5% of nano-clays may improve the creep resistance about 9.5% comparing to the RVE containing 0.5% of the particles. In this figure, the diagrams related to 3D models show a slight waviness in responses that can be assigned to particles distributions. As explained in Figs. 7.8 and 7.9, when RVE size is determined it means that the response of the RVEs with that certain size deviates in a range. Therefore, it is probable to capture such deviation in RVEs responses. Also, judging against Fig. 7.15 (a) and (b) with (c) and (d) shows the 2D models are less sensitive to the particle distribution in comparison to the 3D ones.

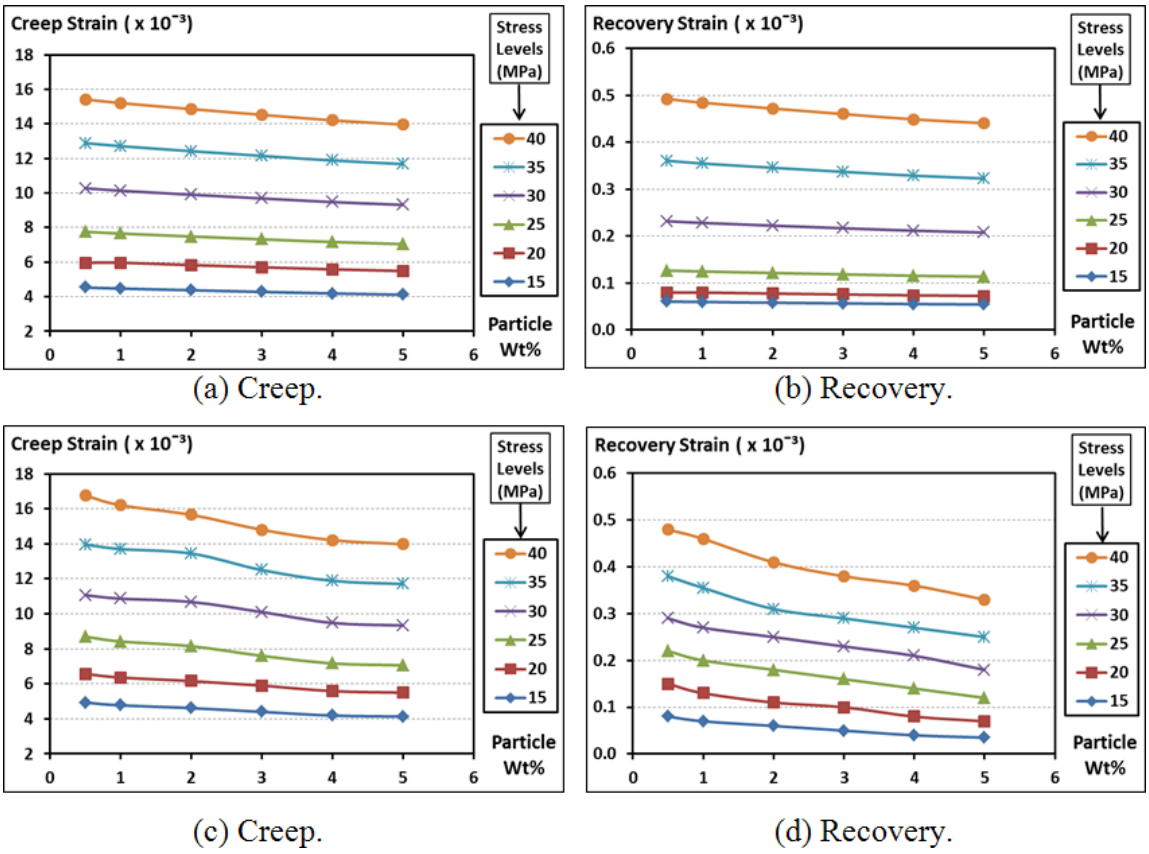

Fig. 7.15. Comparing final strain values in creep (30 min) and recovery (60 min) simulations of: (a)-(b) 2D-Ellipses, and (c)-(d) 3D-Ellipsoids, with respect to different weight fractions subjected to various compressive stress levels.

Fig. 7.16 (a) to (c) depicts the non-linear viscoelastic strain distribution in RVEs containing elliptical particles. Also, Fig. 7.17 (a) to (c) and (d) to (f) illustrate the distribution of the same variable in RVEs including circular particles with two radii: R = 0.0175 μm and R = 0.032 μm, respectively. In all images in Figs. 7.16 and 7.17, the elastic particles are shown in blue navy. The presence of these inclusions produces some localized strain field regions. In all the 2D RVEs with vol = 0.5% particles, the localized regions are dispersed sporadically. But, by adding more inclusions the localized regions

connect to each other and govern more areas inside the RVEs. It is apparent that the effect of elliptical particles is more pronounced. An immediate result of the viscoelastic strain distributions is that the presence of particles is the source of heterogeneous strain distribution, and more inclusions in all cases generate more heterogeneity.

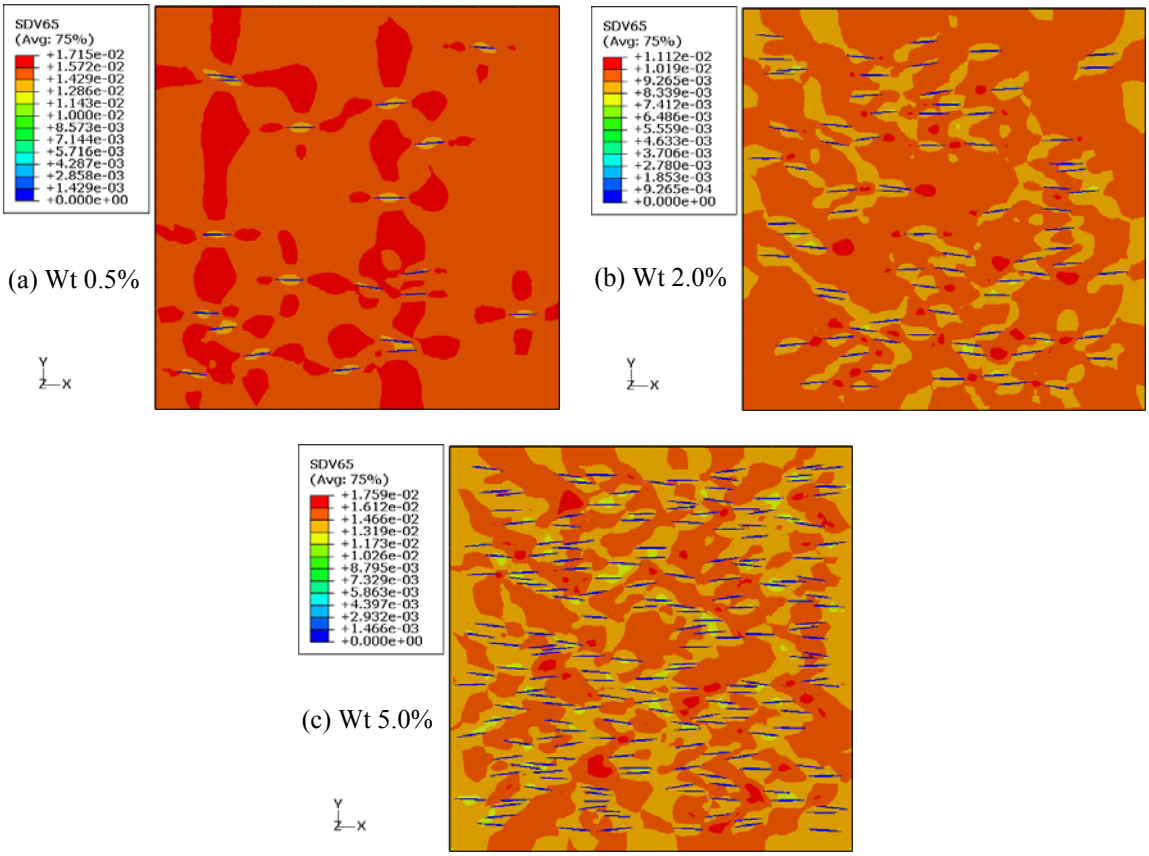

Fig. 7.16. Distribution of non-linear viscoelastic strain ($\varepsilon_{yy}^{\mathrm{NVE}}$), for elliptical NCLP.

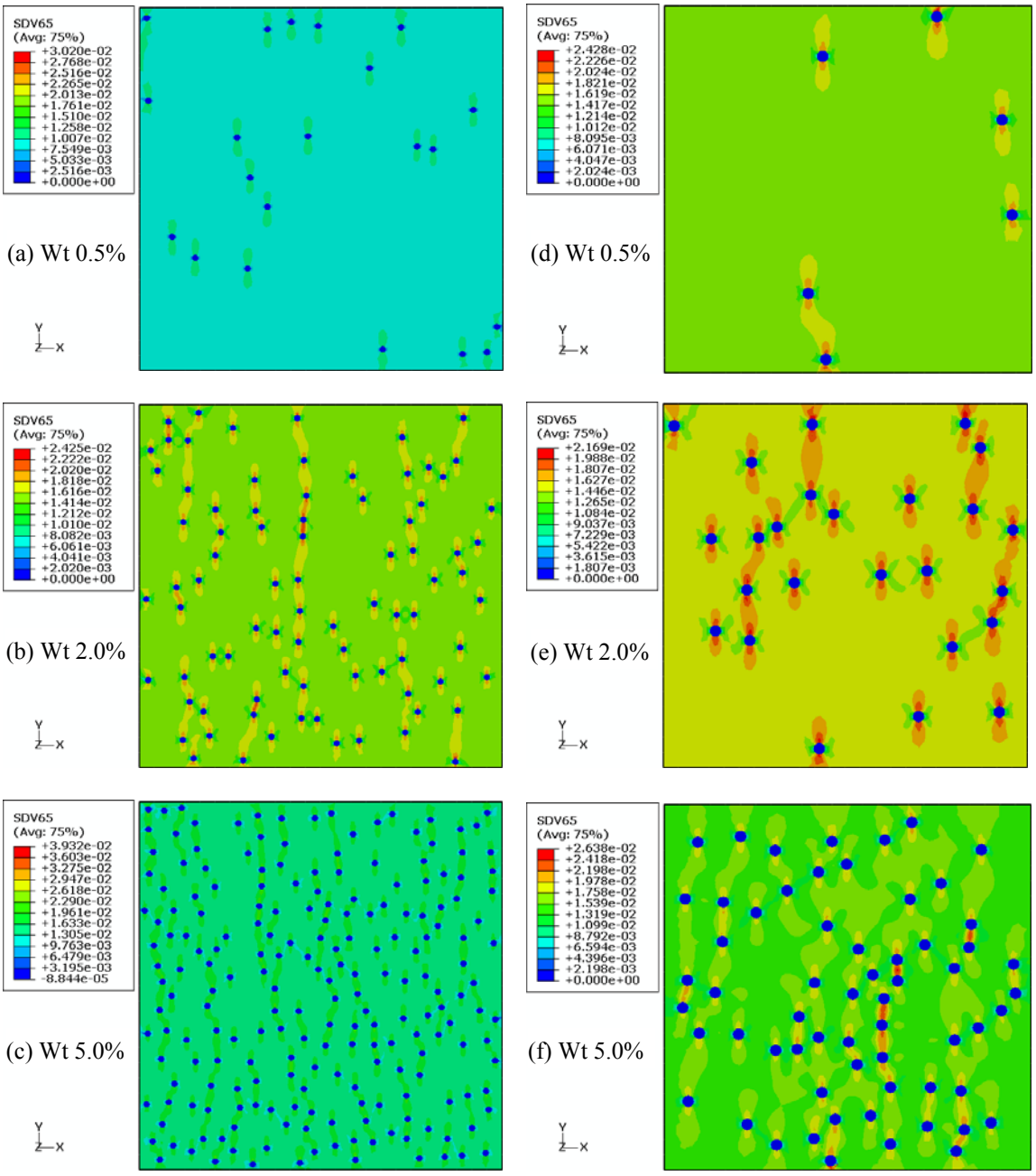

Fig. 7.17. Distribution of non-linear viscoelastic strain ($\varepsilon_{yy}^{\mathrm{NVE}}$), for circular NCRP. (a) to (c) NCRP (R = 0.0175 μm). (d) to (f) NCRP (R = 0.032 μm).

In Fig. 7.18, the view cut (cross section) of the 3D RVEs are shown and the elastic particles are in blue navy. Comparing Fig. 7.18 (a) to (c) with Fig. 7.16 (a) to (c) reveals that in the 3D simulations the ellipsoidal particles show better distribution for non-linear viscoelastic strain and less localized regions. For the circular particles, through comparing Fig. 7.18 (d) to (f) with Fig. 7.17 (d) to (f), it can be concluded that the presence of the 2D circular particles cause localized strain regions inside the composites; however, in the 3D spherical particles the localized regions are not formed as intense as the one shown in 2D models. In Fig. 7.18, similar to Fig. 7.16 and 7.17, the presence of particles is the main source of the heterogeneous strain distribution, and more inclusions in all cases produce more perturbation and localization.

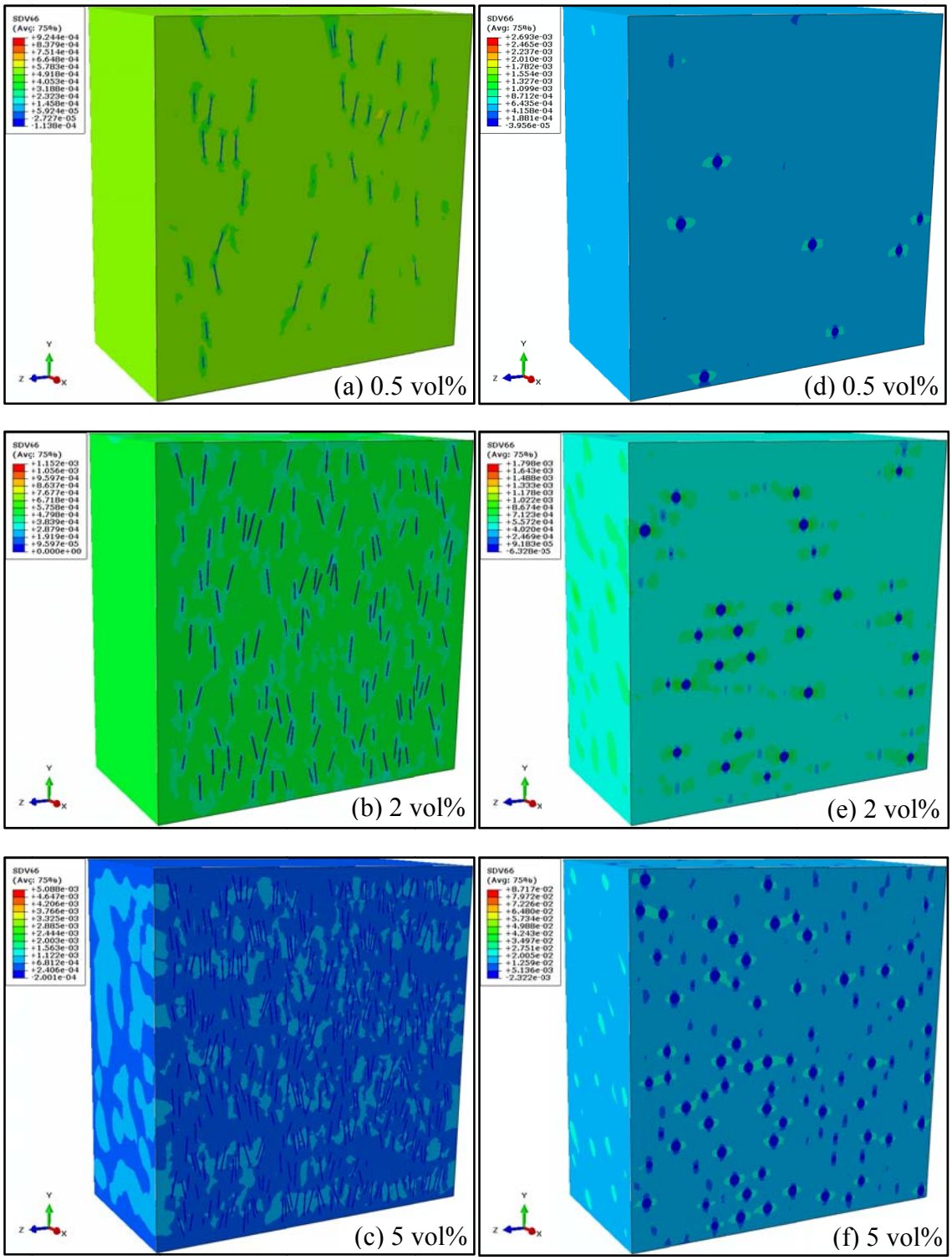

Fig. 7.18. Distribution of non-linear viscoelastic strain ($\varepsilon_{yy}^{\mathrm{NVE}}$). (a) to (c) Ellipsoidal particles. (d) to (f) Spherical particles (R = 0.032 μm).

In the following, in both Figs. 7.19 and 7.20 from (a1) to (c1), the average growth of temperature in the composites while subjected to creep tests at different stress levels is illustrated. It is evident that adding more particles increases the amount of dissipated energy, since they cause heterogeneity in stress and strain fields and subsequently in their distribution pattern. To study the dissipated energy, the reader is referred to Appendix E.

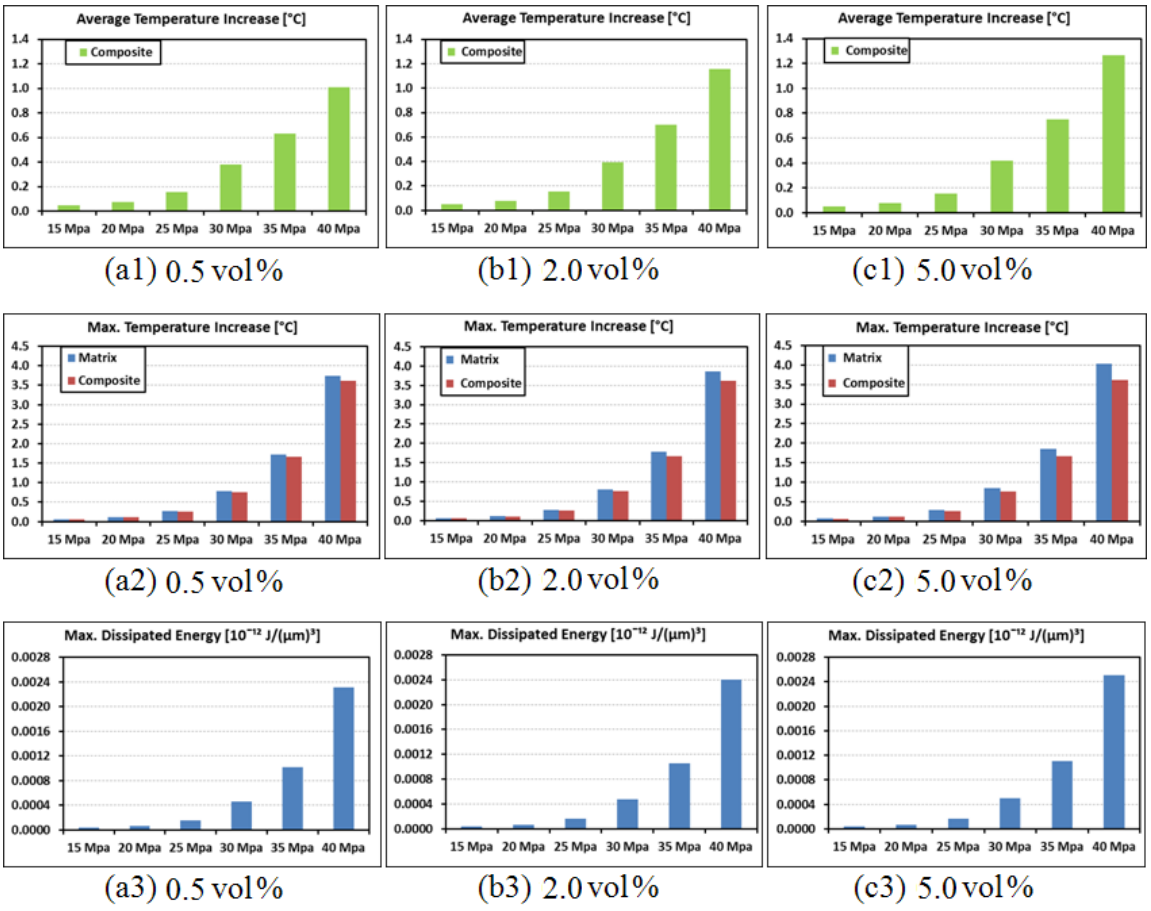

Fig. 7.19. Comparing different aspects of 2D RVEs containing NCLPs, during creep tests: (a1) to (c1) average temperature increase. (a2) to (c2) Maximum temperature increase in PMMA matrix and whole composites. (a3) to (c3) Maximum amount of energy dissipation.

Thus, adding more particles generates more heat and the overall temperature of the samples increase. Also, Figs. 7.19 and 7.20 from (a2) to (c2) point wisely illuminate the amount and growth of the maximum temperature increase inside the RVEs. The images from (a3) to (c3) show the maximum calculated energy dissipation inside the RVEs.

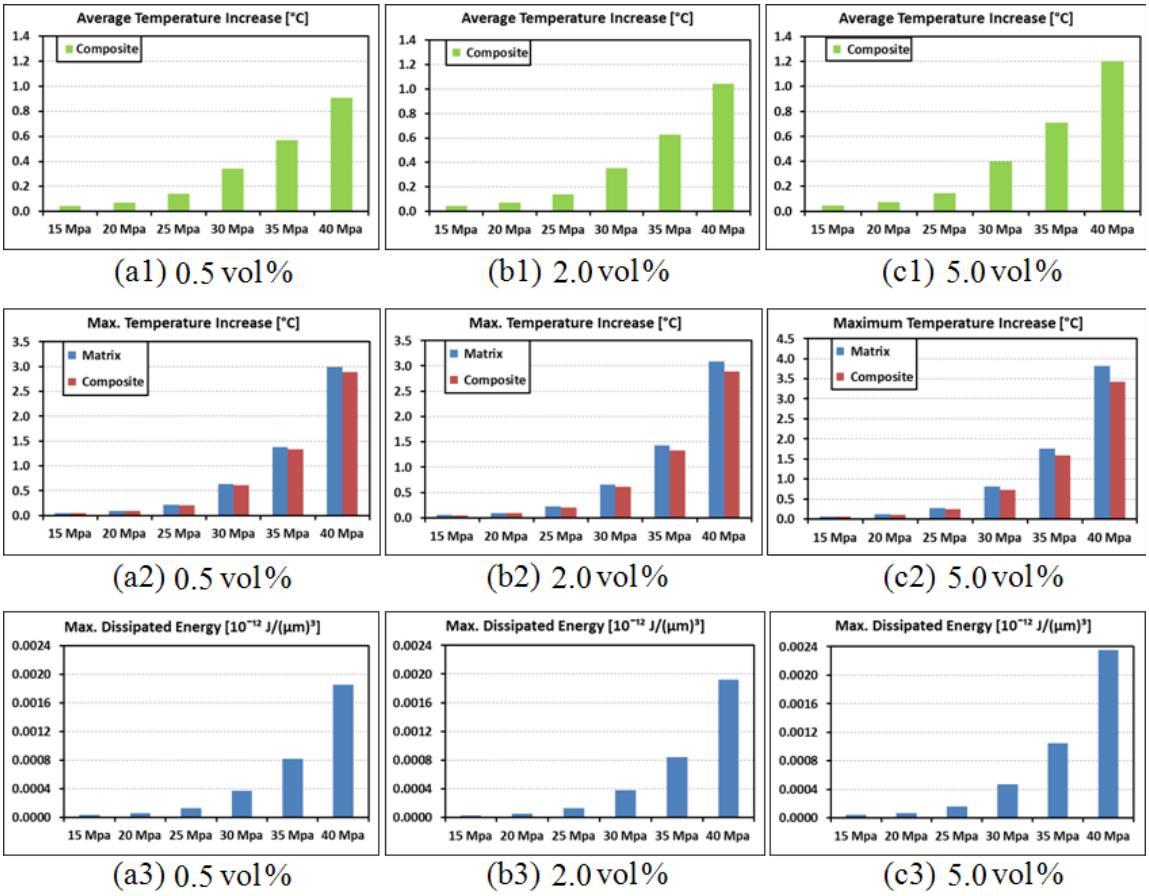

Fig. 7.20. Comparing different aspects of 2D RVEs containing NCRP (R1), during creep tests: (a1) to (c1) average temperature increase. (a2) to (c2) Maximum temperature increase in PMMA matrix and whole composites. (a3) to (c3) Maximum energy dissipation.

For the case of circular particles, since the differences between the results of the two circular particles are negligible; so, for the sake of briefness, the related diagrams for

circular particles with larger radius are not presented. Now, in Figs. 7.21 and 7.22, the trends of dissipated energy, the average increase of temperature inside the whole RVEs and also point wisely in polymer matrix are presented for 3D models.

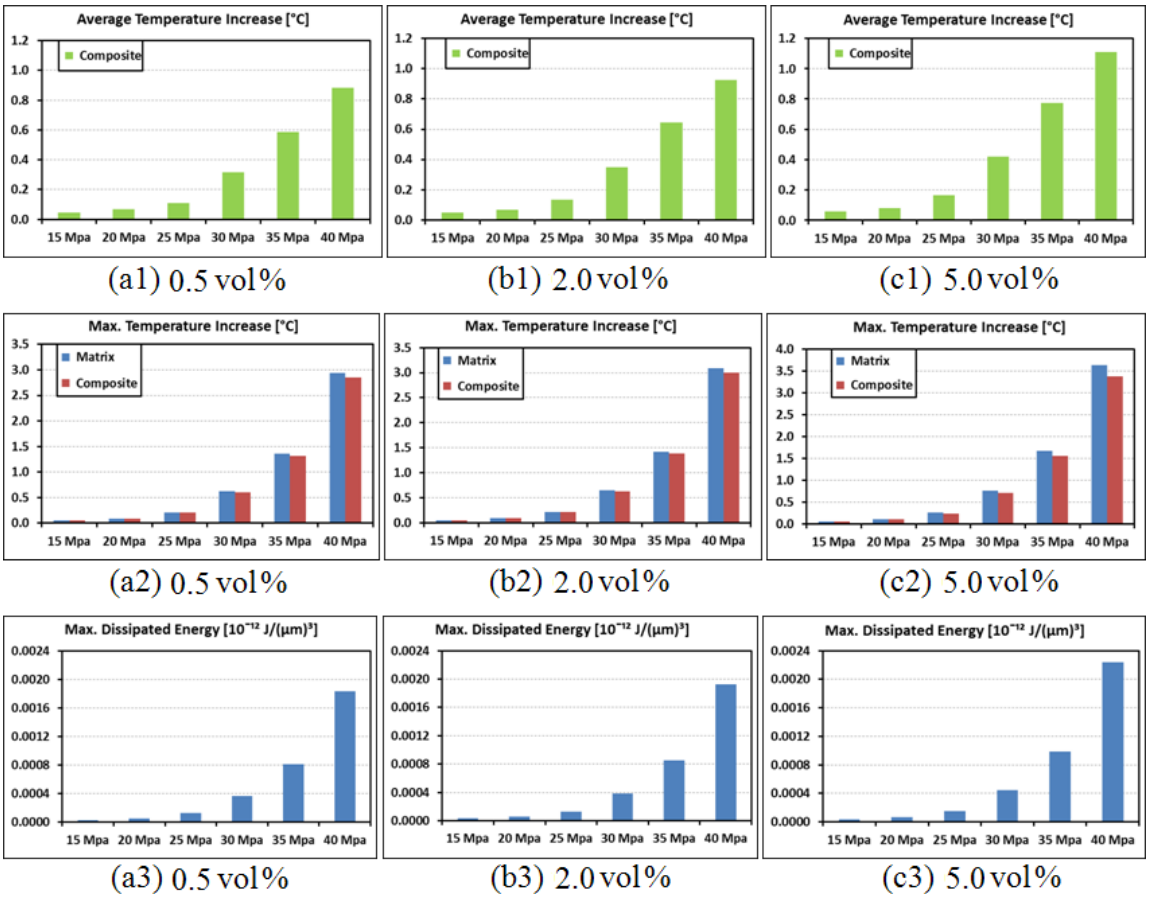

Fig. 7.21. Comparing different aspects of 3D RVEs containing NCLPs, during creep tests: (a1) to (c1) average temperature increase. (a2) to (c2) Maximum temperature increase in PMMA matrix and whole composites. (a3) to (c3) Maximum amount of energy dissipation.

Through comparing these Figs. 7.21 and 7.22 with Figs. 7.19 and 7.20 (for both ellipse and ellipsoids, and circular and spherical), it is observable that the amount of the generated heat and dissipated energy are less than that in the 2D cases. As was discussed

previously, the strain localization (and also stress localization, which is not demonstrated here) is the paramount reason of heterogeneity in the composites which leads to the increase of dissipated energy and heat.

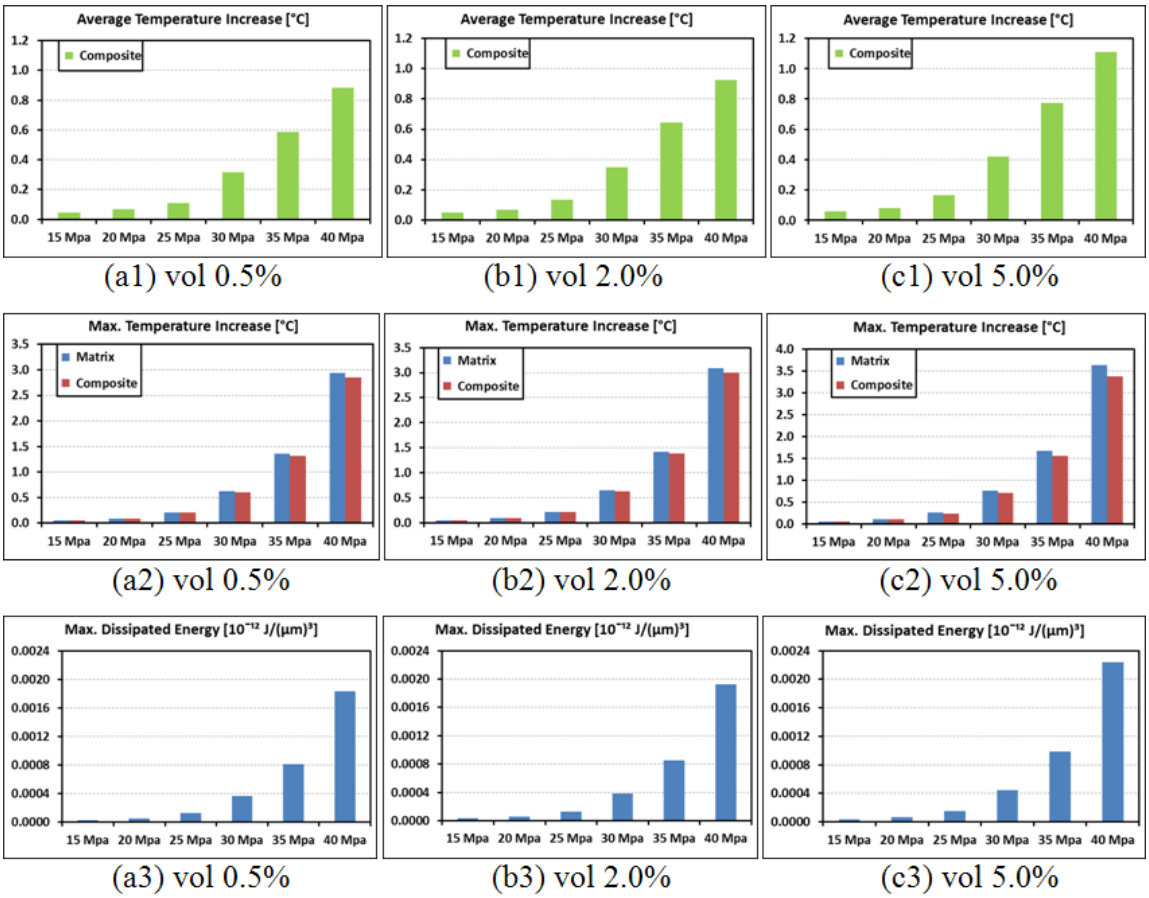

Fig. 7.22. Comparing different aspects of 3D RVEs containing NCRPs, during creep tests: (a1) to (c1) average temperature increase. (a2) to (c2) Maximum temperature increase in PMMA matrix and whole composites. (a3) to (c3) Maximum amount of energy dissipation.

In this part of the computational results section, the effects of particles on the response of RVEs subjected to cyclic loads are briefly studied and presented. At first, in Fig. 7.23, for the sake of brevity just one sample of the applied cyclic loads on the

generated RVEs is shown. Fig. 7.23 (a) depicts the applied load with the frequency of $10.0/\mathrm{s}$. The main formula for expressing stress in terms of time and frequency is

$$\sigma(t) = \sigma_0 + \sum_{n=1}^{N} A_n \cos(\omega t) + B_n \sin(\omega t) \tag{7.37}$$

Using $N = 1$, $\sigma_0 = \frac{\sigma}{2}$, and $A_1 = -\frac{\sigma}{2}$, Eq. (7.37) is simplified to $\sigma(t) = \frac{\sigma_0}{2}\left(1 - \cos(\omega t)\right)$.

Fig. 7.23 (b) also demonstrates the combination of the applied stress and strain in one chart. Through performing several simulations, it is checked that after 25 load cycles the values of strain reach a saturated level; therefore, in order to find complex modulus the RVEs should be simulated up to 25 loading cycles.

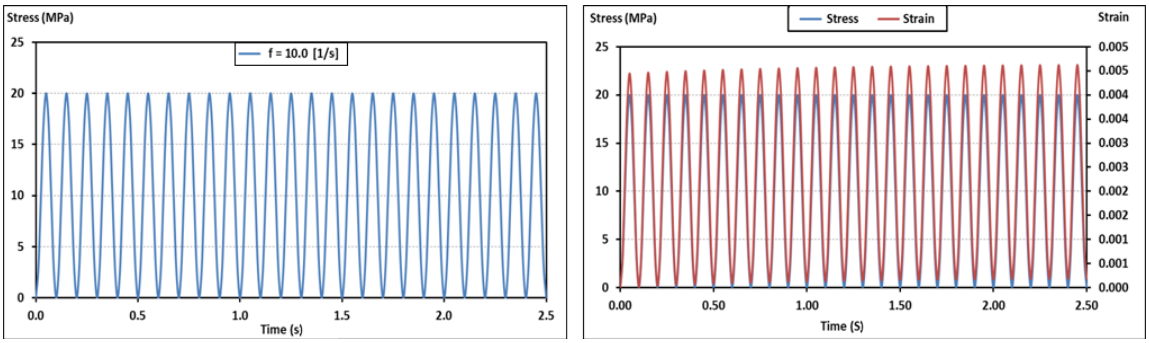

(a) (b)

Fig. 7.23. (a) Applied cyclic stress. (b) Both applied stress and its strain response.

Then, after simulating each RVE under different frequencies, the complex modulus can be simply found through the next procedure. After 25 cycles, as seen in Fig. 7.24, the value of strain in the pinnacle (or base) of the strain response curve should be picked and then the complex modulus is: $E^*_{\text{avg}} = \sigma/\varepsilon$. In the simulated cases, the values of strain in different frequencies were obtained, when the maximum stress (20 MPa) occurred.

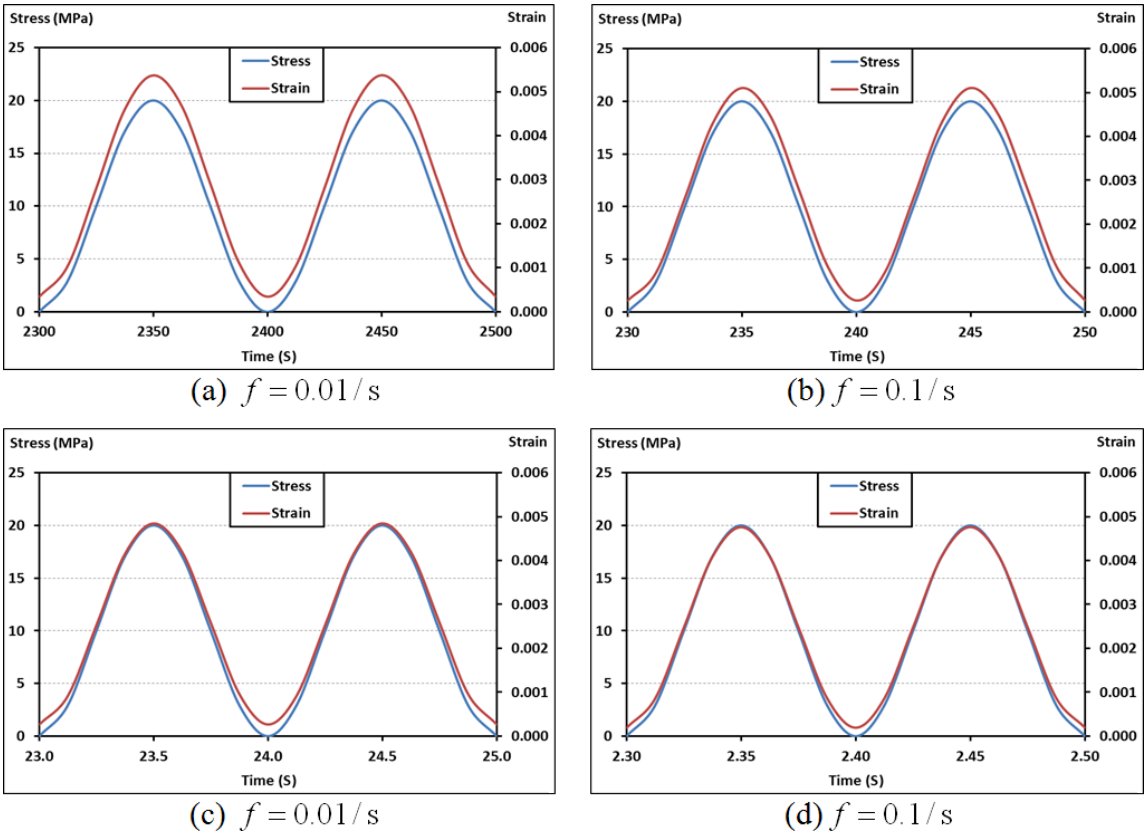

Fig. 7.24. Comparing applied stresses and strain responses in the saturation region of strain, according to different frequencies. RVEs contains 5 vol% of NCLP.

Fig. 7.25 shows the trend of complex modulus changes for each composite versus the cyclic loading frequencies. For the purpose of understanding the amount of development complex modulus of these composites, 3 (particles type) × 6 (frequency) × 6 (weight fraction) = 108 simulations have been accomplished just for the 2D models. The 2D models are the ones demonstrated in Figs. 7.4 and 7.5. As can be seen in the diagrams of Fig. 7.25 (a) and (b), the size of the circular particles does not affect the complex modulus, and just volume fraction governs the response. However, in diagram (c) that relates to the RVEs containing elliptical particles, the complex modulus has been improved a little, which can be attributed to the shape of elliptical inclusions.

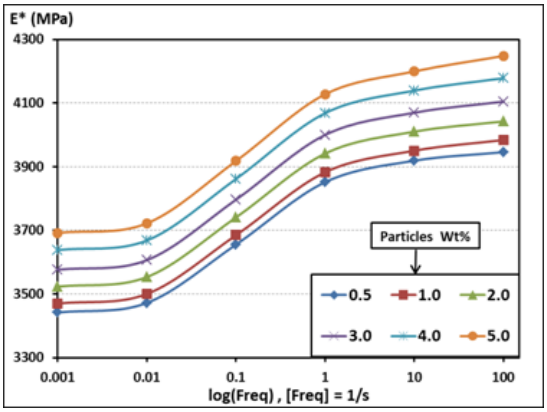

(a) Circular particles (R2).

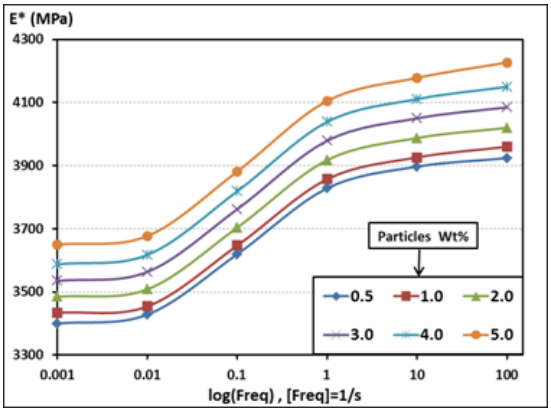

(b) Circular particles (R1).

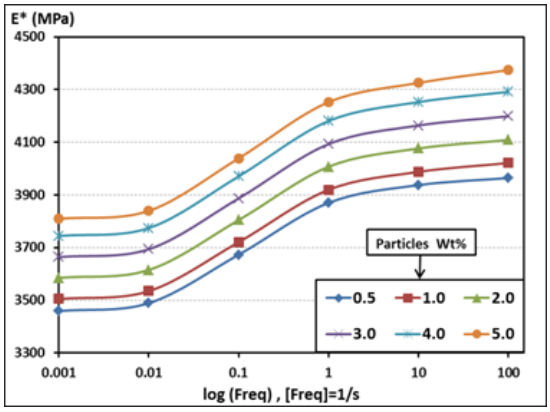

(c) Elliptical particles.

Fig. 7.25. Comparing composites complex modulus versus cyclic loads frequencies, for 2D RVEs.

The same outcome can be concluded from Fig. 7.26 (a) and (b) for the 3D models. The complex modulus of diagram (b) has been slightly enhanced in comparing to diagram (a) which is related to the shape of the ellipsoidal inclusions. For simulating the 3D models in Fig. 7.26 (a) and (b), 2 (particles type) × 6 (frequency) × 6 (weight fraction) = 72 simulations have been accomplished. Here, the 3D models are the ones shown in Figs. 7.6 and 7.7.

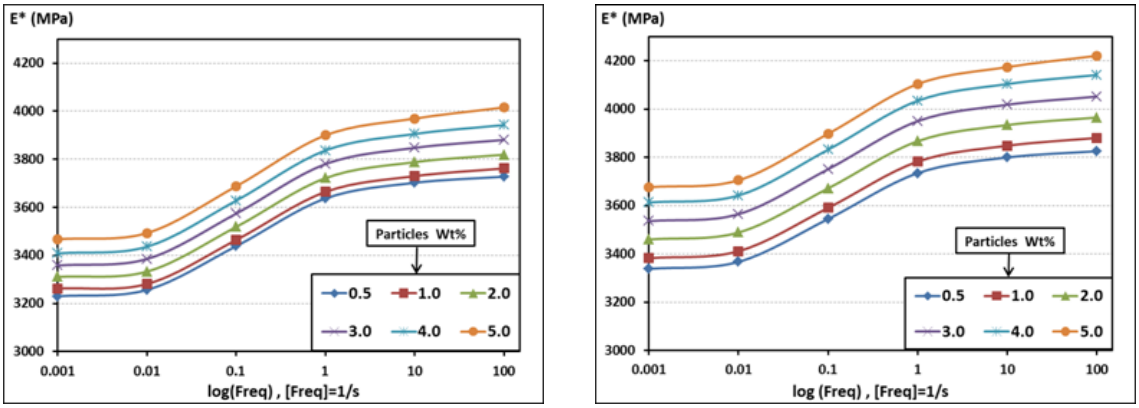

(a) Spherical particles (R1). (b) Ellipsoidal particles.

Fig. 7.26. Comparing composites complex modulus versus cyclic loads frequencies, for 3D RVEs.

From Fig. 7.23 and 7.24 it can be concluded that even though the amount of complex modulus in 2D cases are higher than the ones in 3D models, the magnitude of enhancement of 3D ellipsoidal particles, with respect to 3D spherical ones, is higher than the magnitude of enhancement of 2D ellipses with respect to 2D circular particles. For example in Fig. 7.23 the complex modulus enhancement of ellipse particles regarding to circular ones, for 5 vol%, is about 145 MPa. However, according to Fig. 7.24, the modulus enhancement for the 3D RVEs is about 210 MPa.

7.6 Summary

The nature of the shape and distribution of the filler particles were shown that affect the macroscopic response of particulate filled composites. However, it is observed that the size of the circular particles did not affect the response of both creep and recovery, and also cyclic loadings. In all types of loadings, the obtained results demonstrate that the higher modulus of the nano-composites in cyclic loads and decrease

in creep strains is a direct consequence of the volume fraction of constituents. But, in the same volume fraction, the shape of particles (elliptical and circular) affects the behavior.

Moreover, the maximum effect of those types of particles for enhancing the viscoelastic response of the composites is observed while the RVE is subjected to higher stress levels. Adding more particles is also found to almost linearly affect the viscoelastic responses of all the simulated composites.

It is shown that the radius of circular particles has no outcome on either creep-recovery (loading-unloading) or complex modulus (cyclic loading). Also, it is shown that the complex modulus in 2D simulations is higher than their counterpart in 3D models. Furthermore, the magnitude of enhancement of 3D ellipsoidal particles, with respect to 3D spherical ones is shown higher than the magnitude of enhancement of 2D ellipses with respect to 2D circular particles.

There is no significant increase in the composite complex modulus with respect to adding more particles to the RVEs. It may relate to the fact that the cyclic loads have been measured at lower strain and stress levels at room temperature. Further, since PMMA is a glassy amorphous polymer, and it is mostly elastic in the room temperature; hence, the complex modulus does not change a lot in these conditions. The pure viscous component of the viscoelastic properties means that the enhancement in modulus is analogous to the increase of viscosity.

Calculations show the average temperature increase in the simulated RVEs is about 1.0 to 1.2 C for 2D and 0.8 to 1.0 C for the 3D models, even though in some points (elements) the temperature has increased up to 4 C. It is also obvious that the elliptical

particles dissipate more energy that increases the internal generated heat in comparison to circular ones. An immediate result of the viscoelastic strain distribution in 2D models illustrates that adding more inclusions merges the localized viscoelastic regions and affects more areas inside the RVEs. On the other hand, the connection between localized regions does not occur in the 3D models with lower volume fractions, and is observable just in the highest volume fraction (5 vol%). It is achieved that the effects of the elliptical (2D) and ellipsoidal (3D) particles are more noticeable.

CHAPTER VIII

VIRTUALLY INVESTIGATING ELASTIC RESPONSE OF CNT-BASED POLYMER COMPOSITES IN SMALL DEFORMATION RANGE

8.1 Introduction

Carbon nanotubes (CNTs) have been the main research focus in composite materials when they were discovered by Iijima (1991). Now, they are being investigated for many purposes and applications in conventional and new areas, such as: lightweight structural composites, electronics, field emissions, and nano-mechanical devices, actuators, medical applications and nano-robotics (Qian et al. (2002), Thostenson et al. (2001), Baughman et al. (2002)). Due to CNTs extremely high stiffness, strength, resilience, as well as superior electrical and thermal properties, they may become ideal reinforcing materials for the new class of composites.

Numerous experimental studies and simulations have been performed to investigate the properties of CNT reinforced composites. Empirical models have been employed to compute the elastic properties of single and multilayered nanotubes and it has been proven that the shear and Young's modulus are comparable to that of diamond (Lu, 1997). CNT/Polystyrene composites were characterized by (Qian et al., 2000) and it was shown that adding 1 vol% CNTs in PS results to 25% increase in the tensile strength and an increase in the elastic stiffness of the composite in a range of 36% and 42%. Using short-fiber composite theory have demonstrated that adding 10 vol% of the CNF

(carbon nano fibers) increases the elastic modulus which is equivalent to the increase in modulus by adding just 1 vol% of CNTs (Thostenson et al., 2001).

CNTs are extremely small in size, and their strengths are 20 times that of high strength steel alloys, half as dense as aluminum and also having high current carrying capacities approximately 1000 times that of copper. Investigating the effects of large aspect ratios of these cylinders (i.e., length to diameter ratio as large as 10^2 to 10^5) is a field of interest (Gade, 2005). CNTs diameters are in the nanometer scale and their length can be even in nano up to micrometer order (Smalley and Colbert, 1996). CNTs are generally classified as single-walled carbon nanotubes (SWNT) and multi-walled carbon nanotubes (MWNT). SWNT is a hollow structure formed by covalently bonded carbon atoms and it looks like a thin graphene sheet rolled into a cylindrical shape (Gade, 2005). Both ends of CNTs can be sealed using end caps, and are called as hemispherical caps. These SWNTs typically have diameters ranging from 0.7 to 20.0 nm with thickness of 0.14 to 0.34 nm (Ruoff and Lorents, 1995) and the experimental and theoretical results show that their Young's modulus can reach up to 1 TPa (Salvetat et al., 1999a; 1999b; Zhou and Shi, 2002).

The CNTs load carrying capacities in composites have been demonstrated in many preliminary simulations (Chen and Liu, 2004; Liu et al., 2005; Liu and Chen, 2003) and experiments (Qian et al., 2000; Schadler et al., 1998; Wagner et al., 1998). Although significant efforts (Bower et al., 1999; Qian et al., 2000; Schadler et al., 1998; Xiao and Zhang, 2004) have been accomplished, characterizing the mechanics in CNT-based nano-composites directly in that scale is still a perplexing complex task. On the other hand, simulations of discrete (Mokashi et al., 2007) and continuum based models

have provided useful perspectives and insights for better understanding the mechanics of the nano-composites. Since the discovery of CNTs, attentions have been focused on their remarkable stiffness, high strength-to-weight ratios, toughness, and other mechanical properties. But, there are many issues that should be considered and studied before the potential of CNT-based composites can be employed in real engineering requests. Actually, the most amazing property of CNTs is their incomparable increase in stiffness when combined with other materials, and it has been proved experimentally by several researchers (Thostenson et al., 2001). Several techniques have been proposed to understand the mechanical properties of the composites. From which, the computational approaches play a significant role in the characterization of the nano-composites. Yet, gaining these outstanding characters even at macro-scale makes considerable challenges. To better comprehend the ways for obtaining these requirements, extensive experimental and virtual test studies are required.

At nano-scale, the analytical models are almost limited to simple geometries. Also conducting such experimental tests to evaluate their behavior are very expensive. However, modeling and simulating the nano-composites may be achieved in a cost effective manner through using even one powerful desktop computer. One of the interesting methods is Molecular Dynamics (MD) simulations that have been shown to be a brilliant scheme in characterizing nano-composites behavior. MD approach at the molecular level requires a lot of memory, CPU-hours and catches on a computer to solve even one semi large-scale problem. Therefore, MD is limited to just small nano-scale samples because of its extreme computational costs. This significant obstacle leads the development and usage of other alternate approaches for characterizing and evaluating

the CNT-reinforced composites at micro-scale. MD simulations can be used for small-scale models, whereas continuum mechanics (CM) is a typical approach used for large-scale models. The CM method can overcome the abovementioned issues, since it is computationally effective and easier for characterizing large-scale models. The two most commonly used numerical techniques in CM are the FEM and BEM (finite and boundary element method). In this chapter, the continuum mechanics approach using FEM, which is one of the alternative methods, is adopted to assess the effective modulus of the CNT-based composites. It is successfully validated using the rule of mixtures (analytical) and MD methods.

The effects of waviness of CNTs on overall response of these composites are studied here for the first time. It is also shown that long CNTs reinforced composites produce higher effective modulus compared to the ones with short CNTs. The outcomes are found to be in good agreement with the obtained result of using MD and analytical approaches. Different elements for modeling the CNTs are compared to illustrate which geometries and elements can be used for better modeling the CNTs inside a composite. Moreover, many large-scale CNT-based models are developed and simulated in this work through using 3D solid elements. In these models, different possible mixtures of CNT-based composite scenarios are numerically investigated.

In many researches (Fu et al., 2008; Tjong, 2006; Xie et al., 2005), it has been claimed that outstanding properties can be achieved by adding a little amount of CNTs to a polymer matrix, indicating these fibers have the potential to be as perfect reinforcing materials for polymers. However, the results of the simulations for RVEs containing even a single CNT (for both hollow and solid CNTs) illustrate that a little bending and

curvature in the geometry of a CNT can cause significant reduction in the elastic modulus of the composite. Also, it is shown that the amount of the matrix thickness around a fiber has a profound effect on Young's modulus of the composites. Furthermore, the amount of CNTs Poisson's ratios is studied to determine the effect of this material parameter on the overall responses of such RVEs.

8.2 Computational Methods for Assessing CNT-Reinforced Composites

In order to evaluate the outstanding effective properties of nano-composites at the nano-scale, MD simulations (Alder and Wainwright, 1957), continuum mechanics - FEM, constitutive modeling techniques (Odegard et al., 2003) are some of the most popular techniques used in this research field. In the following, each of the methods will be explained briefly, and afterwards, at first some 3D simple models the same as what were developed by Griebel and Hamaekers (2004) for using molecular dynamics approach have also been developed. The FEM models developed here are to demonstrate and prove that the continuum mechanics framework can be a substantial substitute for calculating the overall responses of nano-composites.

8.2.1 Molecular Dynamics (MD)

The elastic moduli of nanotube/polymer composites were examined by Griebel and Hamaekers (2004) through molecular dynamics approach. The stress-strain curves were derived from the simulations on a composite with single-walled CNTs embedded in polyethylene matrix, for the application of external stresses. Besides, the results from the MD simulations for the Young's modulus of a CNT/polyethylene composite were

compared with the rule of mixtures predictions for long, continuous CNTs. Also the extended rule for short, fully embedded CNT in polyethylene matrix was studied.

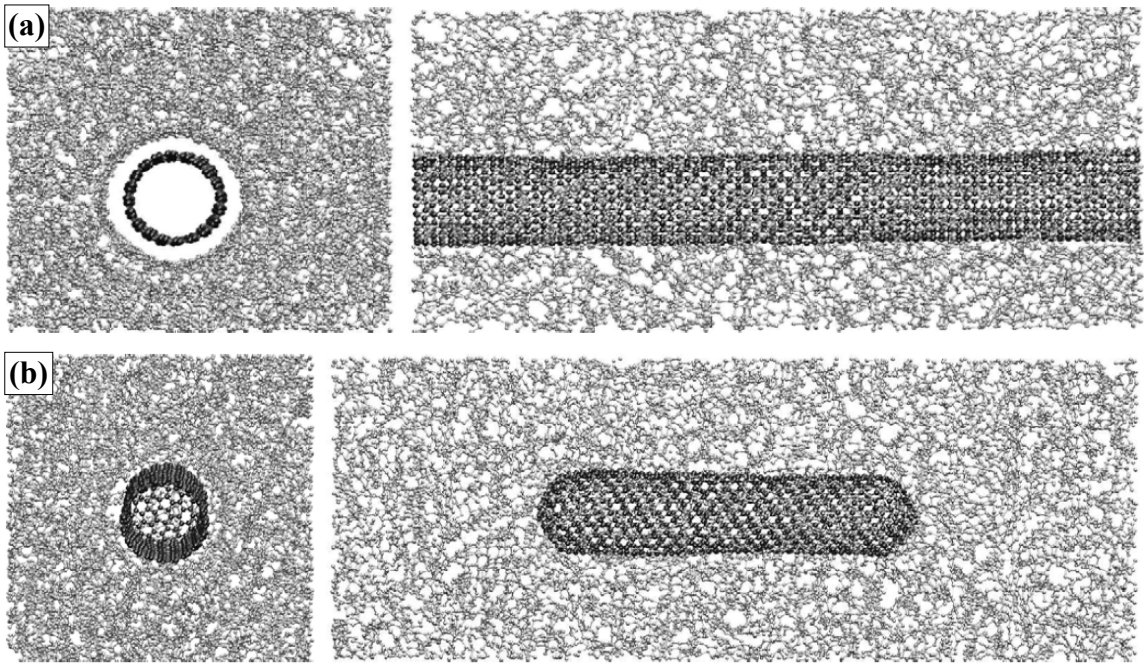

Fig. 8.1. Front and side view of finite tube within the unit cell containing one CNT in polymer matrix system: (a) Long CNT, (b) Short CNT (Griebel and Hamaekers, 2004).

8.2.2 CNT Constitutive Model

Frankland et al. (2003), Odegard et al. (2002), and Odegard et al. (2003) have developed a new technique for evolving constitutive models for composite materials reinforced with SWNT, based on an equivalent-continuum modeling procedure. This scheme considers the atomistic interactions at the nano-scale, and also the interfacial properties of the CNTs and the surrounding matrix by using MD simulations.

8.2.3 Continuum Mechanics (CM)

A continuum mechanics method using FEM was introduced in evaluating the effective material properties of CNT-based composites by Fisher et al. (2003) and Liu and Chen (2003, 2007). These numerical examples that are based on 3D RVEs containing both long and short CNTs were developed utilizing the FEM and BEM approaches. These models have shown significant load carrying capacities of the CNTs in a polymer matrix. Also, these results proved to be in excellent agreement with the rule of mixtures (ROM) results and are reported to be consistent with some of the experimental results in literature.

The results reported in this chapter answer and illustrate the efficiency of continuum mechanics using the FEM for nano-scale RVE models as well as for large scale 3D models containing numerous CNTs in a polymer matrix, for all sorts of CNT morphologies for the first time, such as: straight, random rods, and curved shape CNTs. The computational outcomes of modeling CNT based composites will be reviewed in the following sections. Also, the strength of materials (ROM) technique for estimating the response of fiber-reinforced composites and the extension of this method for the nano-composites reinforced with long and short CNTs are discussed in the next section. In continuum mechanics (CM) concept, a material is considered as a continuous media, which is a collection of material points interconnected by inter-atomic forces. In simple words, continuum mechanics method deals with Newton's laws of motion and the governing principles are conservation of mass, momentum, and energy (Xu and Liao, 2001). Most of continuum problems are focused on the macroscopic characters of

materials rather than the microscopic properties. Even though the CM theory has been proposed to study the macroscopic response of materials, it is shown to be reasonably accurate for studying the micro- and nano-mechanics in which the typical length scales approach are needed, but it is still larger than those of individual atoms. Even though the nature of CM and MD are totally different, here it is assumed the material is homogeneous and continuous in its character.

The first main task is to employ 3D elastic solid elements that replace beam and shell elements for modeling composites containing CNTs. This is fundamental to ensure the accuracy and compatibility between the CNTs and the polymer matrix in the composite. For this issue, SWCNTs have been usually modeled as 3D thin shells, but the shell thickness and Young's modulus reported in literatures exhibit a large scattering range. The order of error to approximate SWCNTs as thin shells was studied by Peng et al. (2008) through an atomistic-based finite-deformation shell theory. In their methodology, the shell thickness and Young's modulus were avoided, but it linked the tension and bending rigidities directly to the inter-atomic potential. Also, they showed for the second order of error, the tension and bending rigidities of SWCNTs can be modeled by an elastic orthotropic thin shell, but the thickness and elastic modulus cannot, and just for the first order of error, a constant shell thickness can be defined, and SWCNTs can be modeled as an elastic isotropic thin shell. The consistent Young's modulus also fluctuates by an order of magnitude, which is so called the Yakobson's paradox (Shenderova et al., 2002).

In the next sections, different elements are studied to observe which one can work properly for modeling 3D CNTs, and it is shown that all cases as: 3D shell, 3D thin solid, or equivalent full 3D solid element work in the same way and one can employ each of these options to model the CNTs. Henceforth, 3D solid elements (to assure the second order accuracy) for both CNTs and matrix have been used in this work and a simple sample of that is demonstrated in Fig. 8.2.

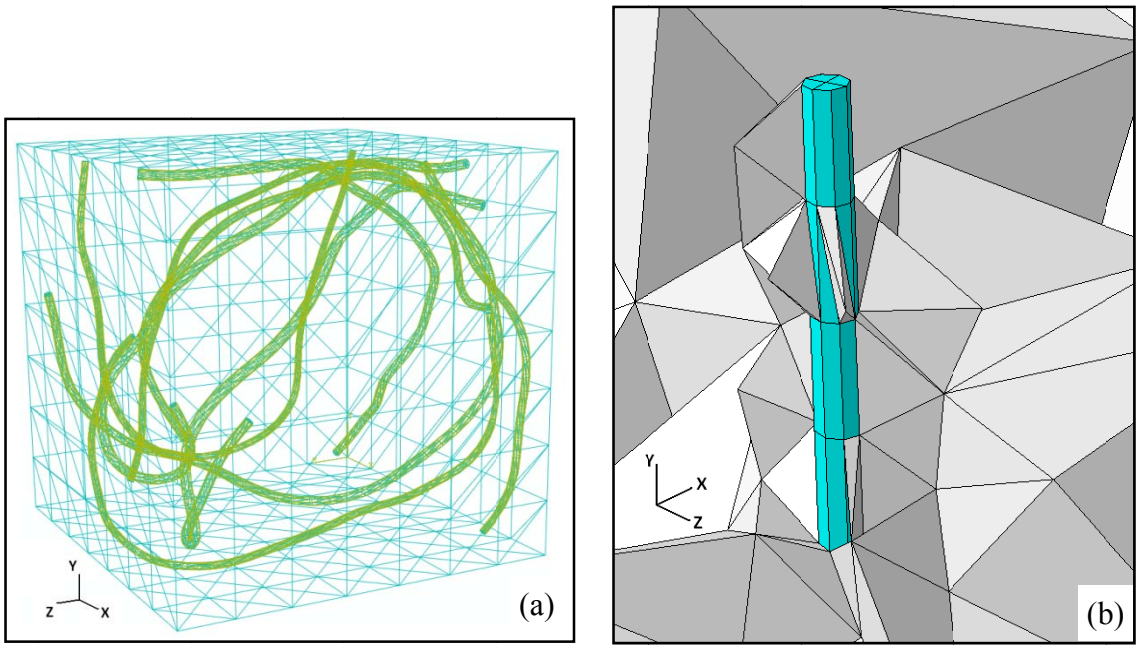

Fig. 8.2. Meshed RVE sample with 3D elements: (a) Full view of rendered wireframe elements. (b) Close up view of 3D solid elements for CNT and surrounding matrix.

In the work by Liu and Chen (2003), a short CNT is surrounded by a cylinder shape matrix, but such assumption cannot be considered in realistic large-scales models. Nevertheless, as shown in Fig. 8.2, one of the advantages of this work in comparison to other works is the realistic geometries of the generated and analyzed models.

8.2.4 Rule of Mixtures Theory for Composites

8.2.4.1 Long Fibers

Predicting the effective material properties of a CNT-composite based on the concepts of the strength of materials is employed by simple analytical expressions which is the ROM. The ROM and its generalized form for some cases of particle- or fiber-reinforced composites have been successfully applied in the past for composites. Yet, this theory is not accurate for evaluating complex geometries and also interfacial stress (the load transferring through the interface), but it has been found to be simple, efficient and accurate for predicting the effective material constants (Young's modulus, Poisson's ratio) in just the axial and transverse direction of the RVEs. It should be recalled that applying load to the same direction of fibers axis is equivalent to a system of materials that are parallelly attached, and studying the transverse direction is equivalent to a series of materials, which can be predicted through utilizing the conceptual theories of the strength of materials. The first analysis delivers the upper bound of the response and the latter one gives the lower bound. In the model used here, there are certain assumptions that should be made before developing the rule of mixtures expression:

- CNTs are uniform, parallel and continuous.
- Perfect bonding between CNT and matrix is considered.
- Load produces same longitudinal strain in CNT, matrix, and the whole composite.

According to these assumptions, the equivalent Young's Modulus of the composite can be derived and explained as

$$E_{\text{Comp}} = E_{\text{CNT}} V_{\text{CNT}} + E_{\text{Matrix}} \left(1 - V_{\text{CNT}}\right) \tag{8.1}$$

8.2.4.2 Short Fibers

Salvetat et al. (1999a) demonstrated through MD simulations, and Ruoff and Lorents (1995) showed by continuum mechanics simulations that the effective modulus of the composite using short CNTs is far less compared to the increase in modulus using continuous long CNTs. The short CNT-reinforced composites that are analyzed in this chapter show they are not being as strong as the composites containing long continuous CNTs; therefore, these constituents are not recommended to be used for critical structural applications. The effective modulus, E_C, for a short fiber reinforced composite, that is illustrated in Fig. 8.3, using the extended rule of mixtures (EROM) by Chen and Liu (2004) is expressed as

$$E_C = \frac{L}{\frac{L_e}{E_M} + \frac{L_{CNT}}{E_{CNT}}\frac{A}{A_M}} \quad , \quad A = 4a^2 \quad , \quad A_M = A - \pi r_i^2 \tag{8.2}$$

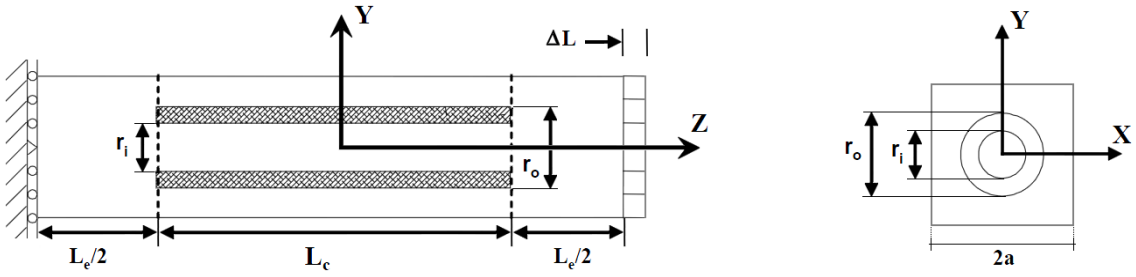

Fig. 8.3. Short fiber reinforcing inside a composite (Chen and Liu, 2004).

The EROM, Eq. (8.2), is applied to assess and validate the FEM simulations for the effective Young's modulus of short CNT reinforced nano-composite models, when the applied load and fibers are in the same direction. Also, the computations and estimations

based on these analytical equations can illustrate that how much is the difference between the effective modulus of composites containing straight CNTs (as upper bound) and the one contains curved shape fibers, while the volume fraction of the fibers are the same.

8.3 Developing FEM Models for CNT-Reinforced RVEs

This section discusses the development of different scenarios of nano-composites with various volume fractions and geometries (aspect ratios and distribution pattern) for evaluating the overall response of such composites. The average effective Young's modulus of the CNT reinforced composite is of certain interest and it has been calculated and assessed using numerical methods. Here, in order to characterize the virtually generated RVEs for the nano-composites, finite element method using ABAQUS commercial software tool is employed. The obtained results from analyzing the developed models in this chapter have been successfully validated using molecular dynamics (just for some cases) and other analytical approach ROM.

The preliminary results obtained in this study can be compared with the available experimental and MD results from similar models reported in the literature (Griebel and Hamaekers, 2004; Liu and Chen, 2003). In most of the studies performed in literatures, CNTs are considered as homogeneous and isotropic materials and are represented by continuum beam, shell, and 3D solid elements (Chen and Liu, 2004; Govindjee and Sackman, 1999; Liu and Chen, 2003; Qian et al., 2003; Sohlberg et al., 1999). Here, before simulating large scale RVEs, the main parameters and concerns about modeling CNTs are studied.

8.3.1 Investigating RVEs with One CNT

Depending on the problem characterization and structure (i.e., material properties, boundary conditions and geometry) two or three dimensional studies can be performed. In fact, 2D analysis has been mainly used to reduce the computational resources. Although 2D simulations are less time consuming, it is also less accurate. However, a 3D analysis is computationally time consuming approach, and this type of modeling is relatively more precise than the 2D analysis. 3D models are used in situations where 2D degeneration model does not sound physical or is not possible. Since a sample of 2D fibers is planar and they intersect with each other, which does not occur in reality; therefore, 3D CNTs are modeled. In the following simulations, the matrix is polyethylene and the CNTs are considered as isotropic materials. The geometrical and material parameters for creating and analyzing these RVEs are stated in Table 8.1 (Gade, 2005).

Table 8.1: Elastic properties and morphological parameters for the CNTs and matrix.

CNT Length (nm)	Inner Radius (nm)	Thickness (nm)	Aspect Ratio	Vol (%)	*E* (MPa)	Poisson's Ratio
11.25	0.5	0.34	6.696	6.5	430850	0.23

Matrix Length (nm)	Width × Height (nm^2)	Matrix Volume (nm^3)	*E* (MPa)	Poisson's Ratio
11.25	4.8 × 4.8	259.2	614.2	0.485

In almost all the RVEs generated by other researchers (Griebel and Hamaekers, 2004; Liu et al., 2005; Liu and Chen, 2007; Odegard et al., 2003) in the field of CNT/polymer

nano-composites the long CNTs have been inserted in a matrix from one end to the other end in the longitudinal direction. But here for the first time, curved CNTs are studied to observe how their curvatures affect the overall performance of a composite. In this section, the main strategy is to comprehend the effect of hollow and solid CNTs, matrix thickness, Poisson's ratio, and CNT curvature on the elastic response and behavior of CNT-reinforced composites before exploring large-scale complex models. Fig. 8.4 depicts different virtual case studies for better understanding the above mentioned items. The results of simulating such models are discussed in the following.

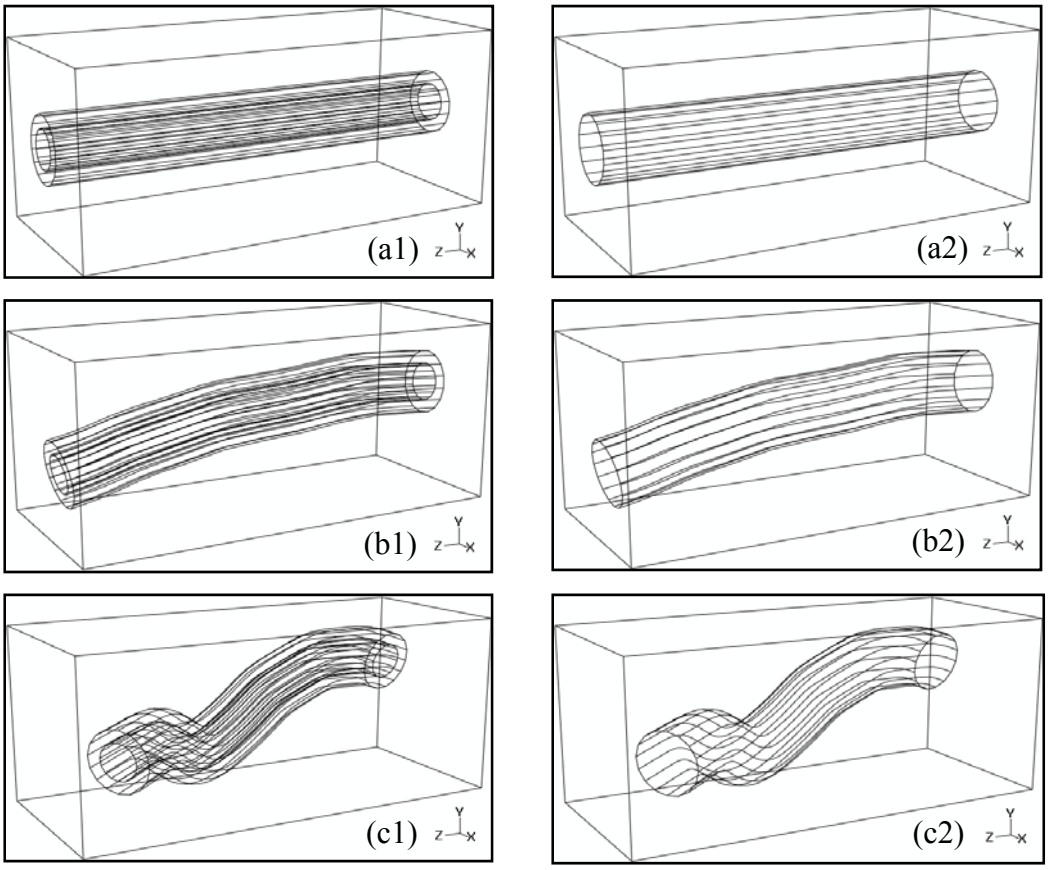

Fig. 8.4. RVEs containing one hallow or equivalent solid CNT, with different segmental bending angles; Straight: (a1)-(a2) α=0°, Curved: (b1)-(b2) α=5°, (c1)-(c2) α=25°.

One of the main arguments in the literature is the value of Poisson's ratio for CNTs. Its range has been mentioned from 0.05 (close to zero) to 0.23. Therefore, several simulations were conducted to demonstrate the effect of this material parameter on the RVE's response. In the diagrams shown in Fig. 8.5, comparisons between different approaches (MD, ROM, and FEM) for analyzing these RVE responses are presented. It can be observed that even though the natures of the mentioned methods are different, the total response of the RVE with one straight hollow CNT, Fig. 8.4 (a1), is in the same range. For the case of ROM, the differences can be attributed to the assumptions of the ROM method, since it especially does not consider the Poisson's ratio, and it almost over-estimates the elastic behavior. For the MD case, Fig. 8.1 (a), the differences can be attributed to the nature of the MD method (which is based on inter-molecular forces) and the FEM which considers the material as homogeneous solid domains, and the boundary conditions which affect the response. The outcomes show the response from FEM is in between the ROM and MD methods, and Table 8.2 shows the elastic modulus computed through FEM is almost 7% higher than the one obtained by MD, and 7% less than the ROM. Such molecular model was simulated by Zhou and Shi (2002), and its value is used here to check and assess the FEM method. The simulations related to Fig. 8.4 are presented in Fig. 8.5 and Fig. 8.6. In Fig. 8.5 (a1) to (c1) the Poisson's ratio is $\upsilon = 0.05$, and in (a2) to (c2) it is $\upsilon = 0.23$. These simulations show that for all cases (straight, slightly curved, and highly curved), the stress distribution for both Poisson's ratio values are the same in either polymer matrix or the CNT. This means that Poisson's ratio does have negligible influence on the whole response of these RVEs. As shown in Fig. 8.5 (c1) and (c2), because of the highly curved shape of the fiber, the cross-section to view a

proper cut of the fiber does not pass through the axis of the fiber; therefore, in both Figs. 8.5 and 8.6 (c1) and (c2), the cross section of the fiber is not as perfect as the ones in (a1)-(a2) and (b1)-(b2).

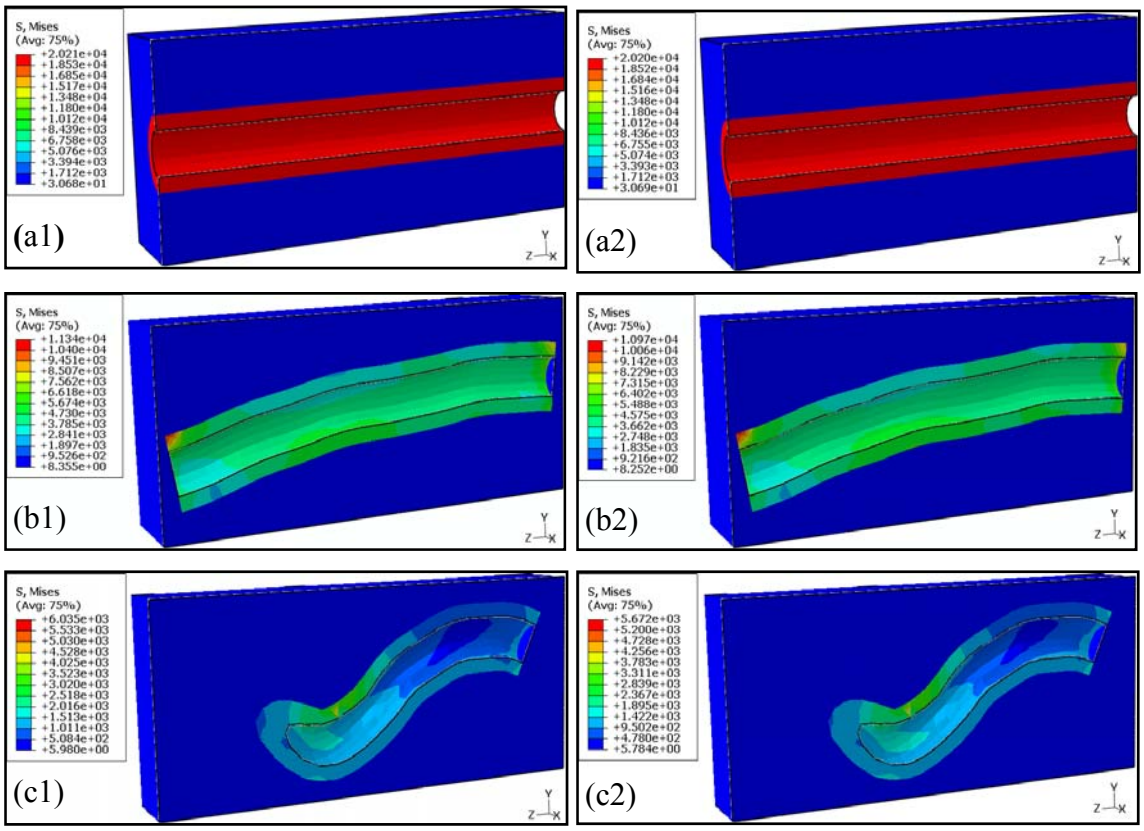

Fig. 8.5. Von Mises stress (MPa) in RVEs with one hollow CNT, and different segmental bending angles (α); Straight: (a1)-(a2) α=0°, Curved: (b1)-(b2) α=5°, (c1)-(c2) α=25°.

Then, the hollow CNTs are replaced by solid fibers, to see whether the equivalent solid CNTs can represent the same behavior as thin hollow CNT or not. The stress contours, in Fig. 8.6 are in one to one relation with the images in Fig. 8.5; and although the stress distribution in the solid and hollow CNTs are different (and they should be), the average

of the von Mises stress in the polymer matrices is almost the same. The averages of the stresses in the matrices have been computed by Python scripting code in ABAQUS, for both hollow and solid CNTs and the results are presented in Table 8.2.

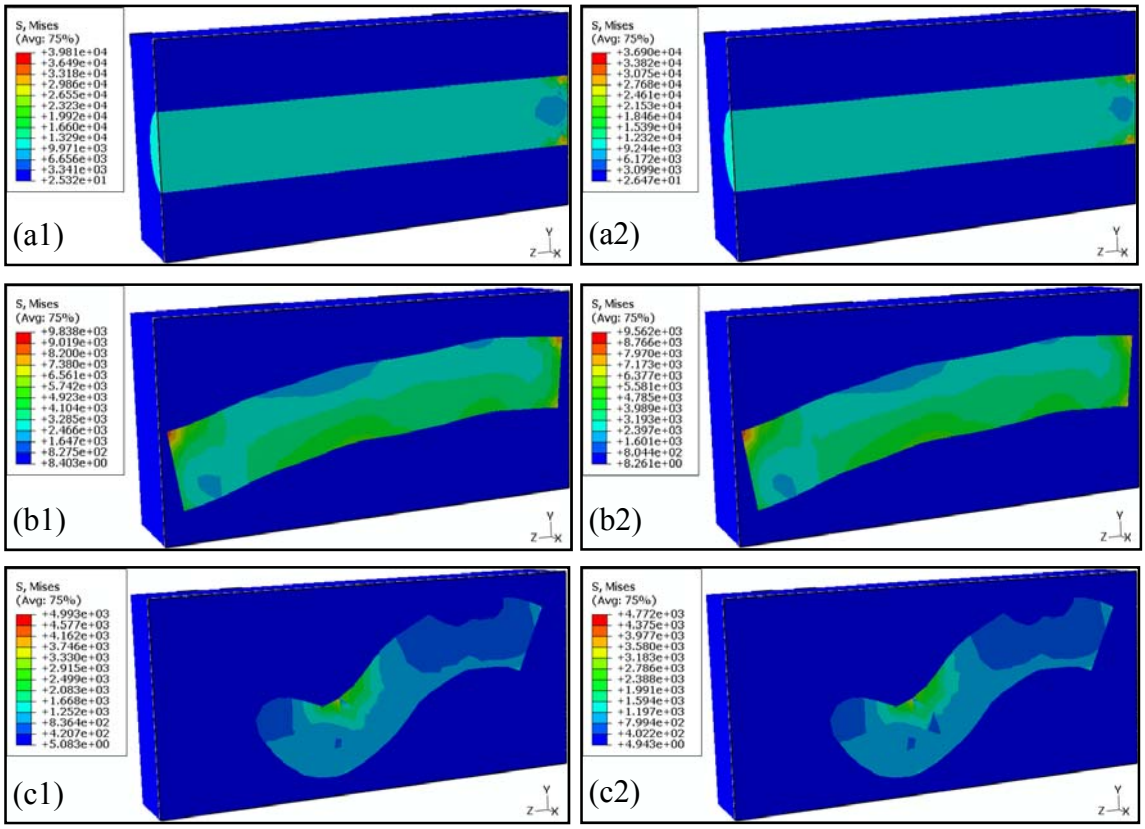

Fig. 8.6. Von Mises stress (MPa) in RVEs with one solid CNT, and different segmental bending angles (α); Straight: (a1)-(a2) α=0°, Curved: (b1)-(b2) α=5°, (c1)-(c2) α=25°.

Table 8.2: Comparing the average of von Mises and σ_{zz} in the RVEs matrices.

	Average von Mises stress (MPa)			Average σ_{zz} stress (MPa)		
CNT Type	$\theta = 0^{o}$	$\theta = 5^{o}$	$\theta = 25^{o}$	$\theta = 0^{o}$	$\theta = 5^{o}$	$\theta = 25^{o}$
Hallow	31.11	68.55	44.96	32.53	105.67	46.41
Solid	31.34	66.50	43.10	33.76	101.89	44.01

Moreover, comparison of elastic response of the RVE with hallowed CNT, Fig. 8.4 (a1), with other methods is presented here in Table 8.3. Such comparisons are presented just to show that how much FEM can be effective to model the CNT-based nano-composites. Besides, in the depicted diagrams in Fig. 8.7, it is conceivable that a little curvature in the CNTs consequences to a remarkable reduction in the elastic response of the RVEs.

Table 8.3: Young's modulus achieved by different methods.

	MD	FEM	ROM
E (MPa)	23395.0	25017.3	26824.5
Increase (%)	0	6.9	14.7

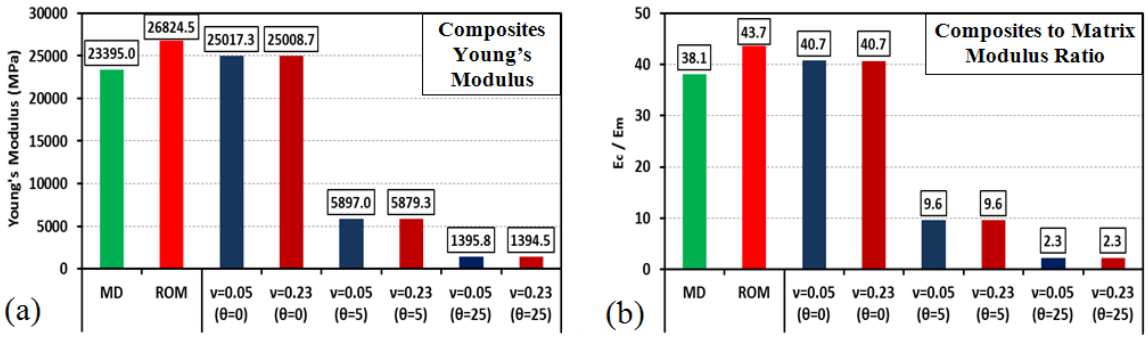

Fig. 8.7. Comparing results achieved through MD, ROM, and FEM methods for RVE with one hollow straight CNT, and effect of curvatures on performance.

Trends of stress-strain curves for both hallow and equivalent solid CNTs with different Poisson's ratios and different curvatures are also shown in Fig. 8.8.

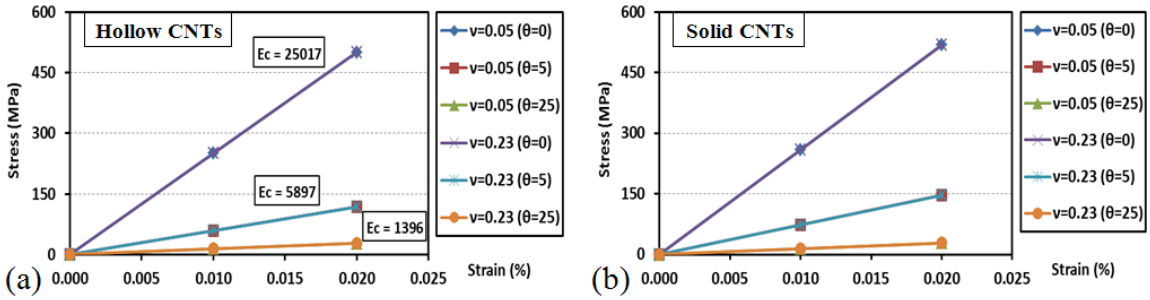

Fig. 8.8. Effects of curvature and Poisson's ratio on overall elastic modulus (MPa).

These diagrams indicate the CNTs can be modeled as either thin 3D hollow tubes or 3D full solid elements. The stress distributions in Fig. 8.5 and Fig. 8.6, the average stresses in Table 8.2, and also stress-strain curves for solid and tubular shape CNTs in Fig. 8.8; altogether lead to this conclusion that the CNTs can be considered as both hollow and equivalent solid, and also the Poison's ratio of the CNT does not affect the response of the composite in the small strain range for just finding the elastic modulus.

One of the items that should be investigated is the effect of the matrix thickness as a cover around an inclusion. Therefore, the previously generated models in Fig. 8.4 (a1) to (c1) were reconstructed such that there is more matrix coverage in front of the longitudinal axis of the CNTs, but the volume fractions of the CNTs are the same as before. Table 8.4 gives the matrix parameters, and the CNT parameters are the same as presented in Table 8.1.

Table 8.4: Morphological and elastic parameters for the RVEs with thicker matrix.

Matrix Length (nm)	Width × Height (nm^2)	Matrix Volume (nm^3)	*E* (MPa)	Poisson's Ratio
13.5	4.4 × 4.4	259.2	614.2	0.485

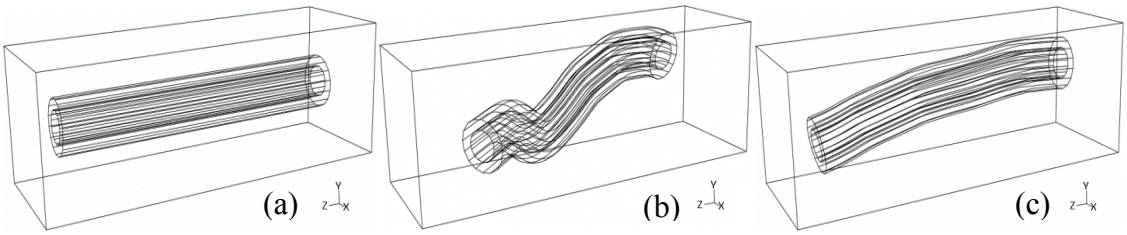

Fig. 8.9. RVEs containing one hollow CNT, with thicker matrix cover in front of the CNT. Different bending angles; Straight: (a) α=0°, Curved: (b) α=5°, and (c) α=25°.

The outcomes of the simulations for the recent models are presented in Figs. 8.10 and 8.11. Fig. 8.10 shows stress distribution in the matrix and the hollow CNTs, and it can be observed that the amounts of the average stress in matrices are in the same range and order.

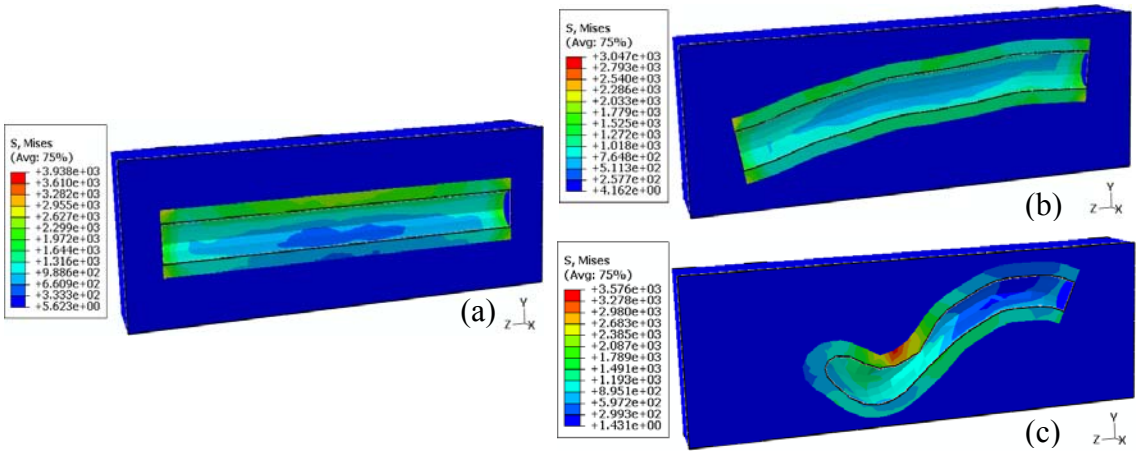

Fig. 8.10. Von Mises stress (MPa) in RVEs with more polymer cover along fibers axis containing one hollow CNT, with different bending angles (α). Straight: (a) α=0°. Curved: (b) α=5°, and (c) α=25°.

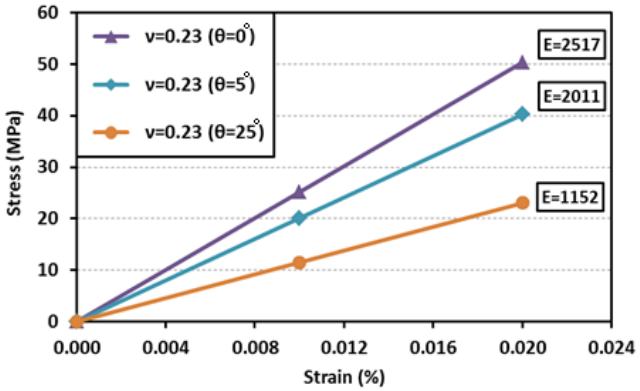

Fig. 8.11. Trends of elastic modulus (MPa) of RVEs with more matrix cover.

Also, Fig. 8.11 demonstrates the trend of the stress-strain curves with respect to the CNT's bending and curvature. This diagram illustrates that the elastic modulus of the composite with straight CNT (Fig. 8.9 (a)) is 25% (or 1.25 times) greater than the RVE with a little curvature (Fig. 8.9 (b)) and is 118% (or 2.18 times) greater than the modulus of the RVE with highly curved CNT (Fig. 8.9 (c)). Comparing this diagram, Fig. 8.11, and the diagrams in Fig. 8.8 prove a significant reduction in the Young's modulus when the matrix cover in front of the CNTs are thicker. This numerical comparisons and evaluations between the elastic responses of these RVEs with different scenarios are presented in the diagrams in Fig. 8.12.

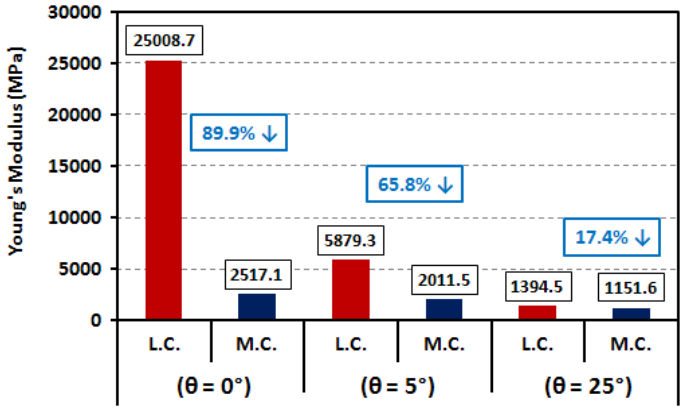

Fig. 8.12. Comparing effect of less and more matrix covers around CNTs on overall response of RVEs. (L.C. = Less Cover, and M.C. = More Cover).

The abovementioned simulations displayed in Fig. 8.5, Fig. 8.6, and Fig. 8.10 along with the diagrams shown in Fig. 8.8, Fig. 8.11, and 8.12 reveal that the amount of matrix thickness around or in front of the CNT constituents in a composite has profound effect on the overall behavior of the RVE sample. The volume fractions of the models in Fig. 8.5 and 8.10 are equal, but because the models in Fig. 8.10 have thicker matrix covers in front of the tip of the CNTs; therefore, the Young's moduli have diminished a lot. If the matrix is not thick, most of the applied load transfers to the CNTs and stress field in these constituents are activated earlier, and the overall response of such RVE is closer to the behavior of the inclusions. That is the main reason why the elastic modulus of the RVEs in Fig. 8.4 (a1) and (a2) are much higher than the ones presented in Fig. 8.9 (a).

In the study conducted by Gade (2005) and Liu and Chen (2007), very short CNTs were also considered, which are re-simulated in this work just to understand the FEM capabilities range for analyzing that scale. For this purpose, one RVE model containing a short hollow CNT with end caps is constructed here (see Fig. 8.1 (b)). The

required geometrical parameters are given in Table 8.5, and for better understanding some parameters, the reader is referred to Fig. 8.3. The generated model is shown in Fig. 8.13. It should be mentioned that the applied loads in all RVE cases in this chapter are aligned in 'Z' direction.

Table 8.5: Elastic properties and geometrical parameters for short CNT and the matrix.

CNT Length (nm)	Inner Radius (nm)	Outer Radius (nm)	Remaining Length (nm)	Aspect Ratio	Vol (%)	*E* (MPa)	Poisson's Ratio
5.0	0.5	0.84	6.25	2.976	2.8	430850	0.23

Matrix Length (nm)	Width × Height (nm²)	Matrix Volume (nm³)	*E* (MPa)	Poisson's Ratio
11.25	4.8 × 4.8	259.2	614.2	0.485

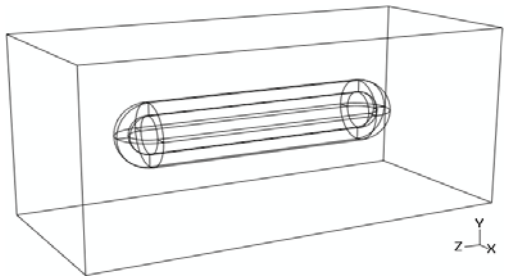

Fig. 8.13. RVE containing one short hallow CNT, with straight structure.

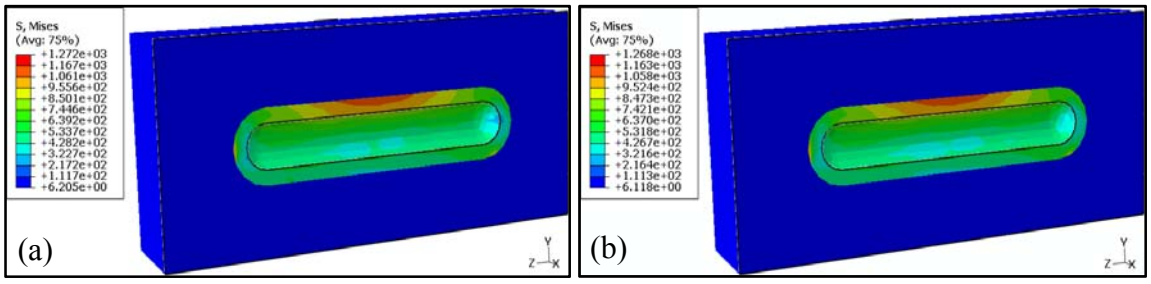

Fig. 8.14. Mises stress (MPa) in RVE with short hallow CNT: (a) $\upsilon = 0.05$, (b) $\upsilon = 0.23$.

Elastic response of the recent models shows the effect of Poisson's ratio is also negligible in the short CNT cases. These elastic modulus are compared with the MD model and extended rule of mixture (EROM), Eq. (8.2), and illustrated in Fig. 8.15. The assessments show the modulus achieved by FEM and EROM methods are almost 25% less than the one simulated by MD method. Hence, based on the result of the short and long CNTs, the Young's Modulus from MD method is higher than the FEM technique.

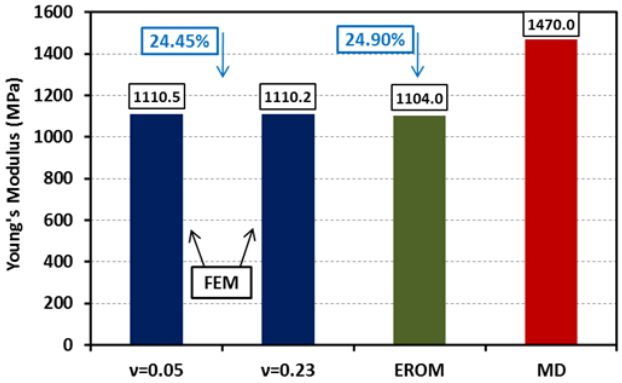

Fig. 8.15. Comparing short CNT responses through FEM, MD, and EROM.

8.3.2 Analyzing Additional Factors Affecting RVEs with One CNT

In this section, CNTs with higher aspect ratios are analyzed, and the differences between modeling the CNTs through different 3D elements are studied. Then the effect of the element types on the elastic response is shown. At first, long straight CNTs are placed in a long box shape matrix, with proper matrix cover in front of the fiber axis. The cover is considered because the load should be applied to the surface of the matrix and not directly to the CNTs, as explained in the previous section. The matrix is PMMA

and the CNTs are Multi-walled nanotubes (MWNT). The geometrical parameters required for generating the RVEs and mechanical properties for analysis are given in Table 8.6. In this table, the aspect ratio and volume fraction is measured based on the equivalent full solid state.

Table 8.6: Elastic properties and morphological parameters for short CNT and matrix.

CNT Length (nm)	Inner Radius (nm)	Outer Radius (nm)	Matrix Cover (nm)	Aspect Ratio	Vol (%)	*E* (MPa)	Poisson's Ratio
580	5	5.15	10	≈ 58	8.43	1000	0.05

Matrix Length (nm)	Width × Height (nm^2)	Matrix Volume (nm^3)	*E* (MPa)	Poisson's Ratio
600	30 × 30	54×10^4	2500	0.35

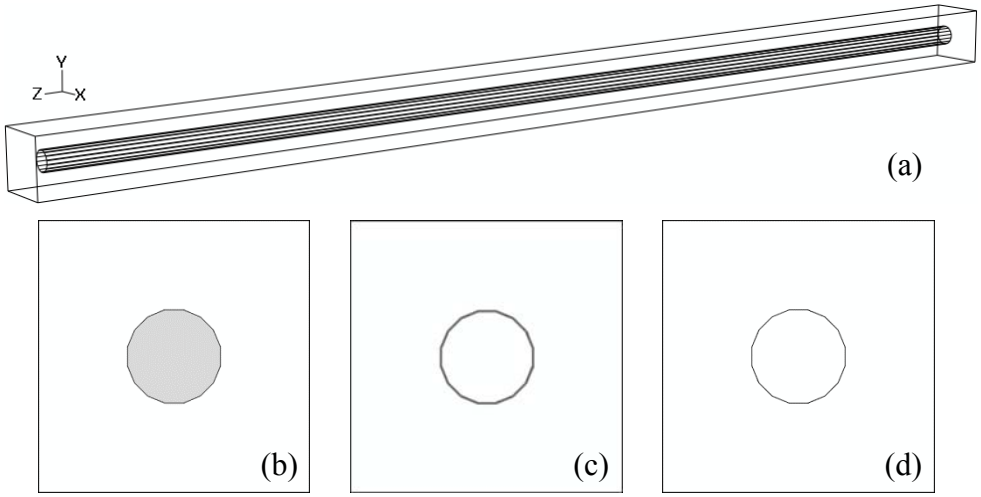

Fig. 8.16. Illustration of RVE with one straight CNT. (a) Full 3D perspective view. Front view of RVE with different geometry: (b) Full solid, (c) Thin solid, (d) Hollow shell.

Then, the models required for evaluating different 3D elements are generated and demonstrated in Fig. 8.16. After simulating the mentioned RVEs, the contours of stress

distribution in both matrix and CNTs are shown in Fig. 8.17. As can be observed, the average of von Mises stress in the matrices for the three RVEs is almost the same. Also, stress-strain curves of these RVEs are presented in Fig. 8.18, and the Young's modulus are stated in Table 8.7, where *t* is the virtual thickness of the simulated 3D shell. Based on the achieved results, it is obvious that for the straight CNTs, different elements behave in the same way, and they are equivalent.

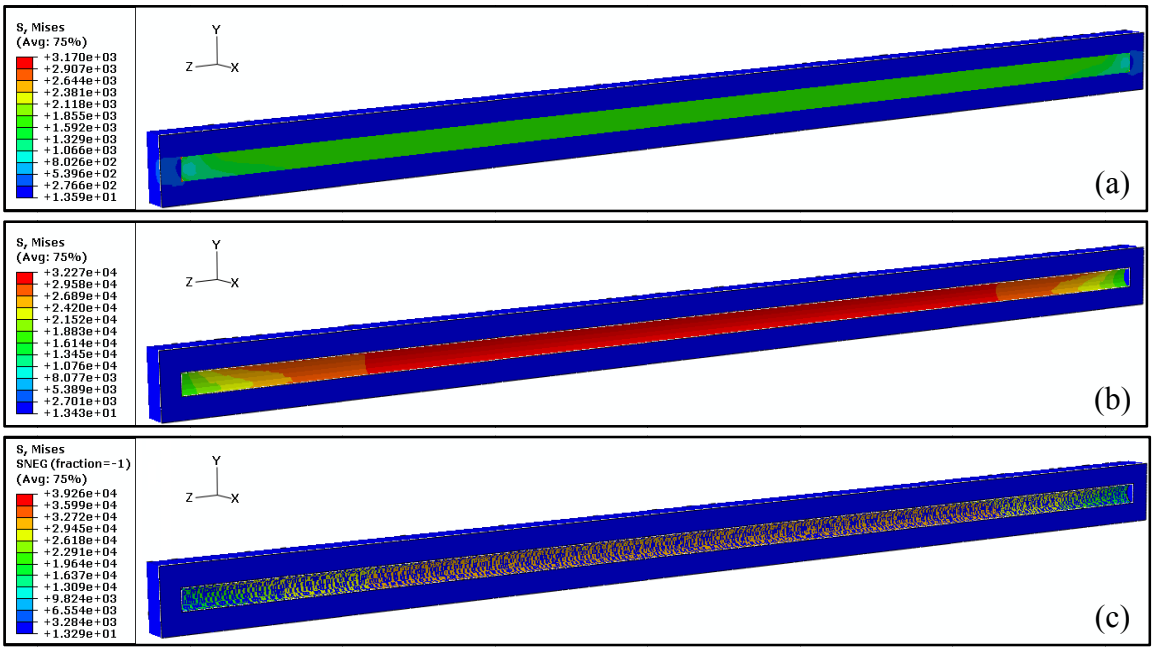

Fig. 8.17. Comparison of von Mises stress (MPa) distribution in RVEs containing long straight CNT: (a) Full solid, (b) Thin solid, (c) 3D hollow shell.

Table 8.7: Comparing the ratio of Young's Moduli for different straight CNT structure.

CNT structure	Equivalent Solid	Thin Solid	Shell ($t = 0.01$)	Shell ($t = 0.15$)
$E_{\text{compo}}/E_{\text{matrix}}$	7.06	6.92	1.59	6.97

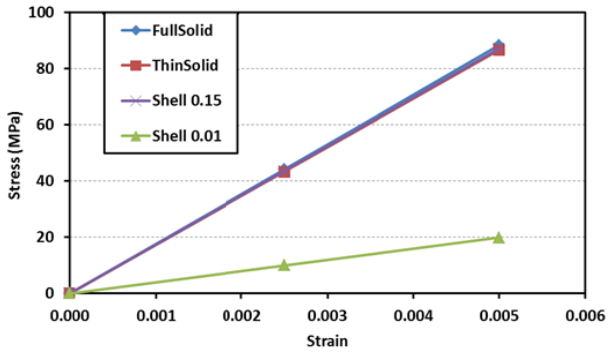

Fig. 8.18. Comparison of stress-strain responses of long straight CNT as: 3D hollow shell with two thicknesses, 3D thin-hollow solid, and 3D solid elements.

Even though the thickness 0.01 nm is not realistic, here it is used as the thickness of the 3D shell element and analyzed just to give a perspective to have a better sense as to how the thickness of shell can affect the overall response of the model. However, only studying straight CNTs are not enough to decide about selecting a certain element type. In reality, CNTs are curved or highly curved in a composite; thus, the effect of applied load on curved solid and shell elements should be explored, as well.

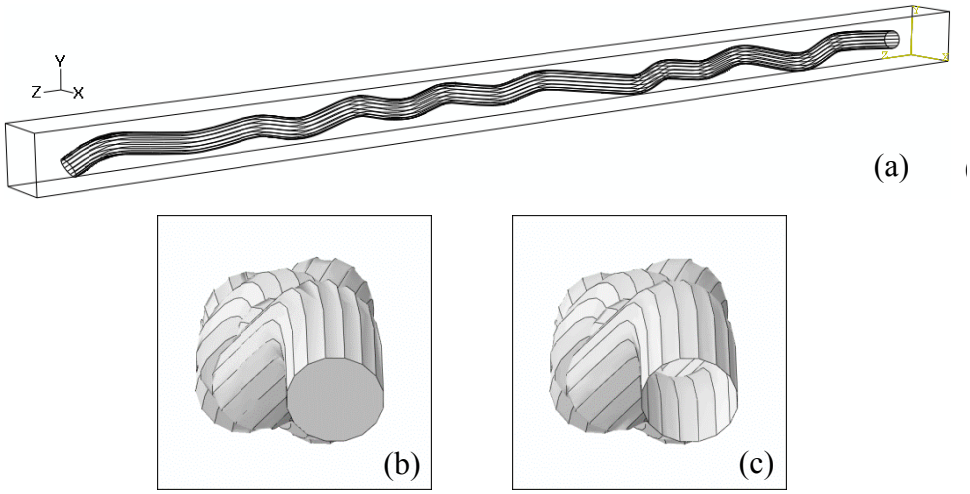

Fig. 8.19. Illustrating RVE with one curved CNT. (a) Full 3D perspective view. Front view of RVEs with different geometries: (b) Full solid, (c) 3D hollow shell.

Henceforth, two RVEs containing one curved CNT were generated; one is made of 3D full solid and the other one is made of 3D tubular shell, as portrayed in Fig. 8.19. The results are presented in Fig. 8.20 and 8.21. The stress distribution contours are illustrated in Fig. 8.20 and the average stress in the matrices are in the same range. Moreover, Fig. 8.21 shows the elastic curves of the models response. As can be seen, in elastic range the diagrams are equivalent, and the ratios of the composite's modulus with respect to the matrix modulus are almost the same. As can be observed, the response of the equivalent full solid and thin hollow solid are close to each other.

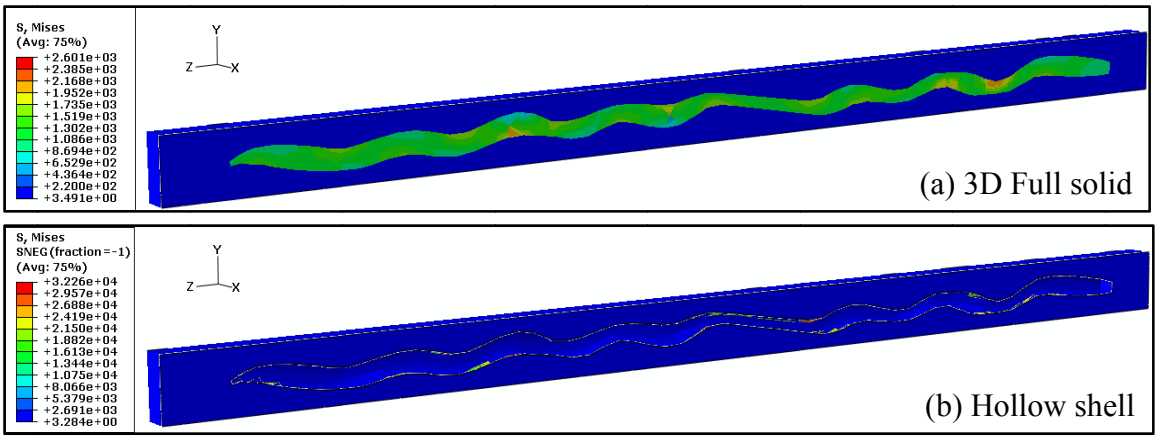

Fig. 8.20. Von Mises stress (MPa) distribution in RVEs with long highly curved CNT.

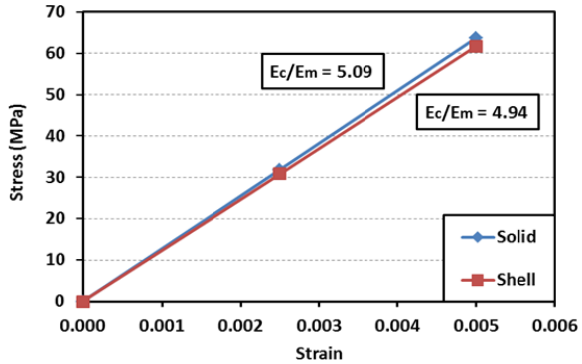

Fig. 8.21. RVE elastic response with long curved CNT (3D hollow shell vs full solid).

This means when CNTs are exactly aligned or not aligned in the direction of the applied force on the RVE, each of the above mentioned elements can be employed to model the CNTs. In this part of the study, the main focus is placed on probing the effect of curvature on RVEs including one long CNT. For this purpose, four models are generated. Fig. 8.22 (a1) to (d1) show the cross sections of the RVEs with different curvatures, and Fig. 8.22 (a2) to (d2) which are in one to one relation with Fig. 8.22 (a1) to (d1), depict 3D perspective view of the same RVEs.

Table 8.7: Morphological and elastic parameters for short CNT and the matrix.

CNT Length (nm)	Radius (nm)	Bending Angle	Aspect Ratio	Vol (%)	E (MPa)	Poisson's Ratio
1200	5.0	$-25^o < \alpha < 25^o$	120	0.758	1000	0.05

Matrix Length (μm)	Width × Height (μm²)	Matrix Volume (μm³)	E (MPa)	Poisson's Ratio
1.3	0.1 × 0.1	13×10^{-3}	2500	0.35

One is noted, since importing highly curved 3D fibers with circular cross section to the FEM software ABAQUS has many technical issues; therefore, as seen in Fig. 8.22, the cross sections of the fibers are polygon. Such cross section provides more stable geometry while extrusion through a highly curved 3D spline. However, since the area of a circle is greater than the area of a polygon with the same exterior radius (e.g, if octagon is used, 10% reduction in cross section area takes place); therefore, in order to gain the same area for the cross section and consequently the proper volume for a 3D fiber, the circumferential radius of the polygon should be proportionally increased and matched.

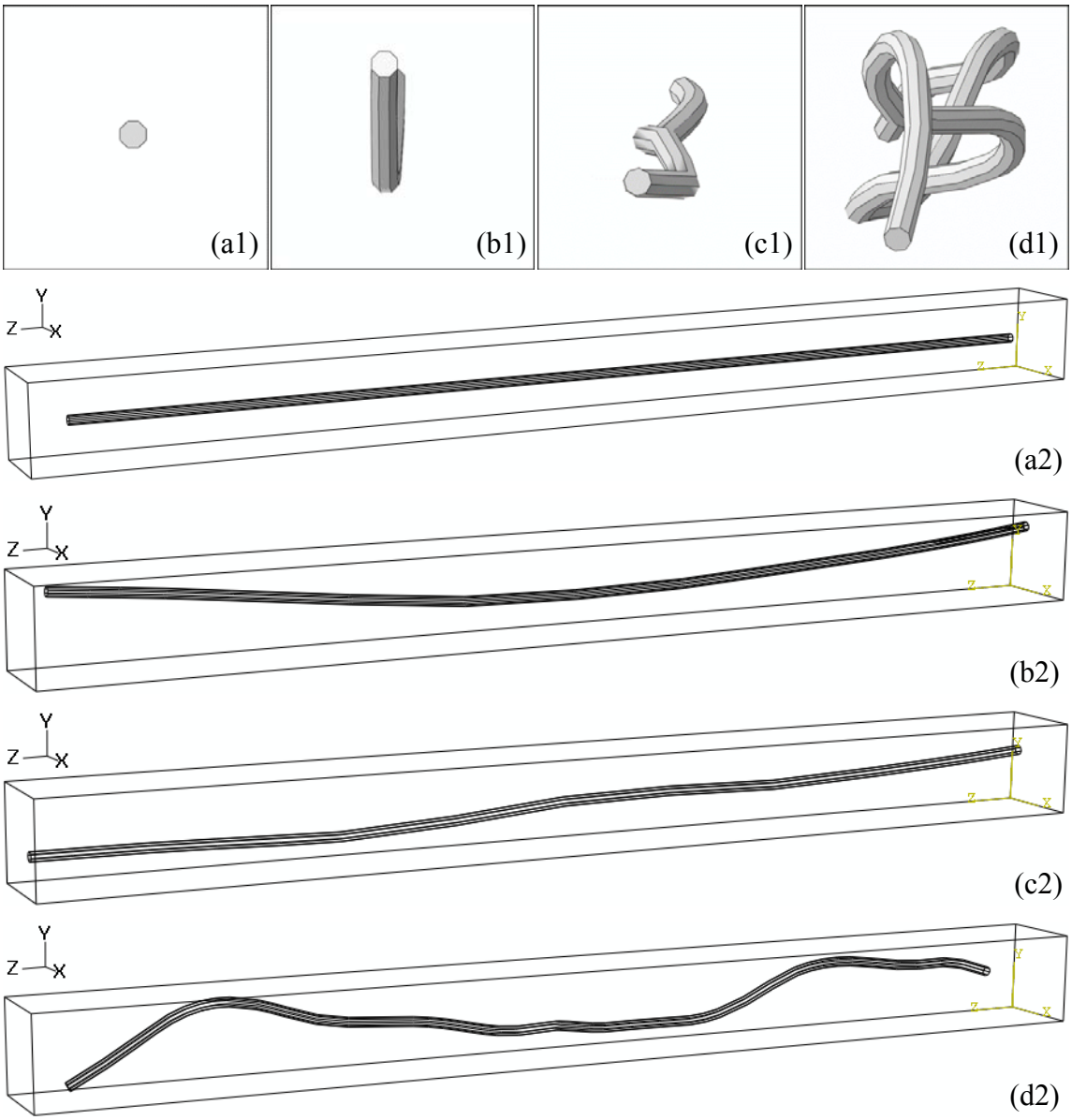

Fig. 8.22. RVEs containing one CNT with high aspect ratio (≈120) and different bending angles: (a1)-(a2) α=0°. (b1)-(b2) α=2°. (c1)-(c2) α=5°. (d1)-(d2) α=25°.

The stress distribution contours of these generated RVEs are shown in Fig. 8.23. It is observed that the middle part of the fibers carry more load comparing to the end segments. As proved previously, the straight segments of each fiber in the direction of applied load have the capacity to carry more loads. Besides, Fig. 8.23 (a) to (c) reveals

that when a fiber bends, the maximum stress transferring through the segments parallel to the direction of applied load are higher than the fiber which is completely straight. The amount of stress in the fiber in Fig. 8.23 (d) is slightly smaller because it does not even have a tiny segment parallel to the load. In the following, the simulations of the same RVEs (similar to Fig. 8.23) are presented such that the nodes on each face of them are not tied to move together.

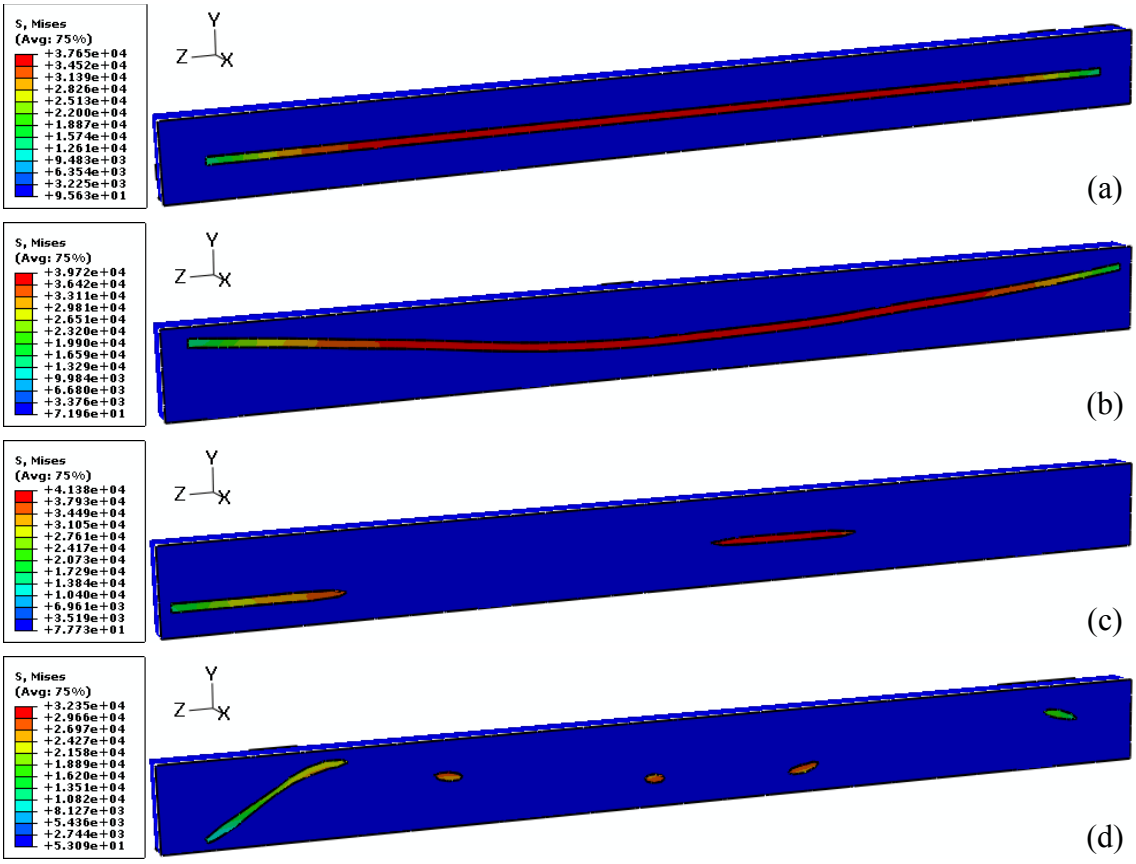

Fig. 8.23. Comparing von Mises stress (MPa) contours for RVEs with different curvatures and the nodes on each face of RVEs are tied to move simultaneously. Bending angle: (a) α=0°, (b) α=2°, (c) α=5°, (d) α=25°.

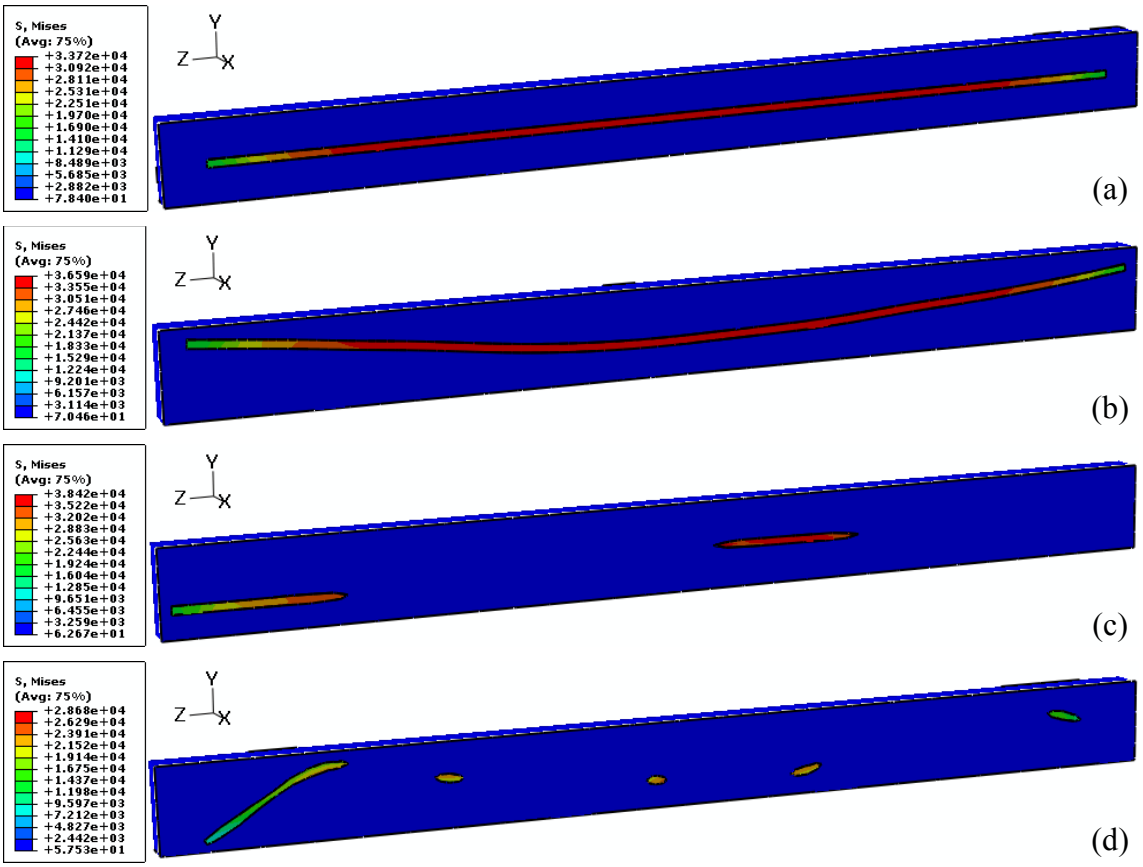

Fig. 8.24. Comparing von Mises stress (MPa) contours for RVEs with different curvatures, with no equation on faces to tie nodes to move simultaneously. Bending angle: (a) α=0°, (b) α=2°, (c) α=5°, (d) α=25°.

The average of the von Mises stress in both matrix and CNT in each of the RVEs shown in Fig. 8.23 and 8.24, are demonstrated in Fig. 8.25. It can be observed from Fig. 8.25 (a) that, for both tied and not tied faces, the minimum stress in the polymer matrix is occurred in the RVE containing the fully straight CNT. As bending angle increases, the average stress in the matrix intensifies almost linearly. From Fig. 8.25 (b) it can be concluded that the average stress in the CNT placed fully straight is less than the ones when the bending angle is $\alpha = 2^o$ or $\alpha = 5^o$. Also, the average stress in both matrix and the CNTs in the tied models are higher than that in the models with not tied faces, and

the ratio is almost 10%. As the simulations of Figs. 8.23 and 8.24 shows, tying the nodes on the RVEs surfaces, in order to model the periodic boundary conditions affect the overall response of the RVEs.

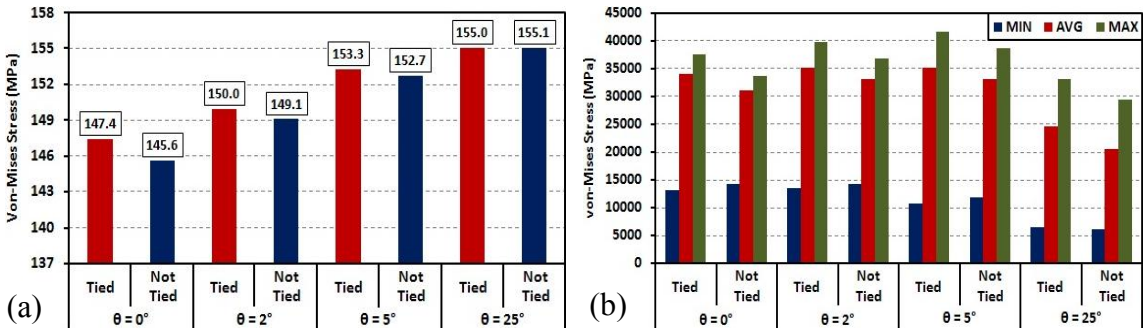

Fig. 8.25. Comparing trend of von Mises stress for RVEs with different CNT curvatures, with tied and not tied nodes on each face.

For this purpose, Fig. 8.26 illustrates the perturbation produced because of not tying the nodes on RVE faces. This perturbation is the consequence of different curvatures along the fibers axis, which create heterogeneous stiffness in each slice of the RVE along the direction of the fibers axis.

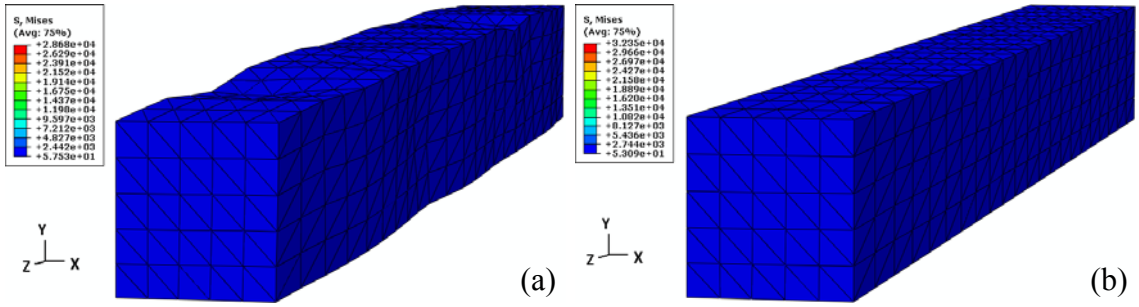

Fig. 8.26. Comparing von Mises stress (MPa) distribution on RVEs with a curved CNT, bending angle is 25°: (a) Without tied equation on faces, (b) With tied equation on faces.

Comparison of Young's moduli of the mentioned RVEs in Figs. 8.23 and 8.24 are depicted in Fig. 8.27. This figure reveals that considering the tied surfaces can cause the elastic modulus of a composite increase, which are calculated and shown in the labels above each RVE test. As seen, the elastic modulus of the RVEs with free faces have been diminished approximately 6%.

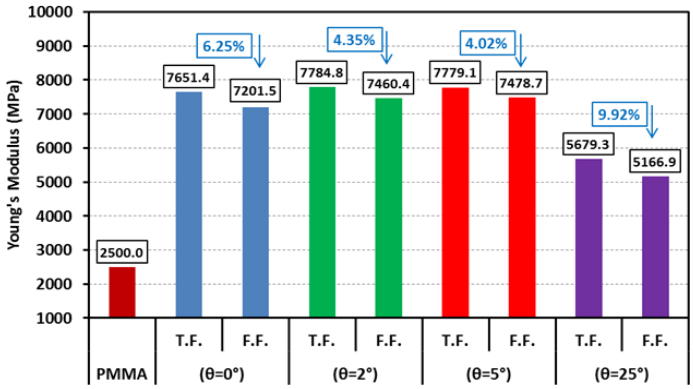

Fig. 8.27. Comparing elastic response of RVEs with tied face (TF) and free face (FF).

8.3.3 Primary Discussion for RVEs Containing One CNT

The effective Young's modulus of several CNT-based composites has been evaluated, and as an initial step in this process, the continuum mechanics concept is shown to be valid through using 3D RVE models of the composite. Numerical examples for both long and short CNT-reinforced composites have been conducted and validated using the available MD results and the strength of materials technique. The results are in complete agreement enlightening that the CM method can deliver a proper approximation in estimating the overall response of these types of composites. Although perfect bonding is assumed , actually in small strain range the applied load does not cause debonding,

which reduces the mechanical performance of the composites. Longer CNTs in these RVEs exhibit considerably better load transfer when compared to the short CNT cases.

In the following, large-scale models of the composites reinforced with multiple nanotubes for various volume fractions are studied. The results for the effective Young's modulus of the CNT/polymer composites are exhibited in terms of nanotube aspect ratio (AR), volume fraction, and morphology. It is worthy to mention, both FEM and constitutive modeling results (Odegard et al., 2002) show similar behavior with less improvement in the modulus after the length of 200 nm.

8.4 Large Scale CNT-Reinforced Polymer Composite

As explained in Chapter 6 and this chapter, 3D solid elements are employed for the CNTs instead of 3D shells, because modeling CNTs with shell elements have been a controversial subject in literatures; thus, the equivalent 3D solid elements are employed. Here, sweeping mesh technique using C3D8 (brick elements) for CNTs are considered. Also, free mapped meshing along with interior element growth using C3D4 (tetrahedral elements) are utilized for the matrix regions in ABAQUS software. Different models are created using the RVE_Maker software (see Chapter 6) containing: 0.5, 1.0, 2.0, and 3.0 vol% for the CNTs. Moreover, the morphologies of the CNTs can be listed as:

- Straight rod shapes of randomly dispersed CNTs:
  - Parallel to the direction of the applied load (is called *Z*-dir).
  - Perpendicular to the direction of the applied load (is called *X*-dir).
  - Fully random rods.
- Curved shape CNTs.

The most challenging models in the above list are the ones containing the curved shape CNTs. The structural and mechanical factors to generate these large-scale RVEs are given in Table 8.8, and the related sample geometries are illustrated in Fig. 8.28.

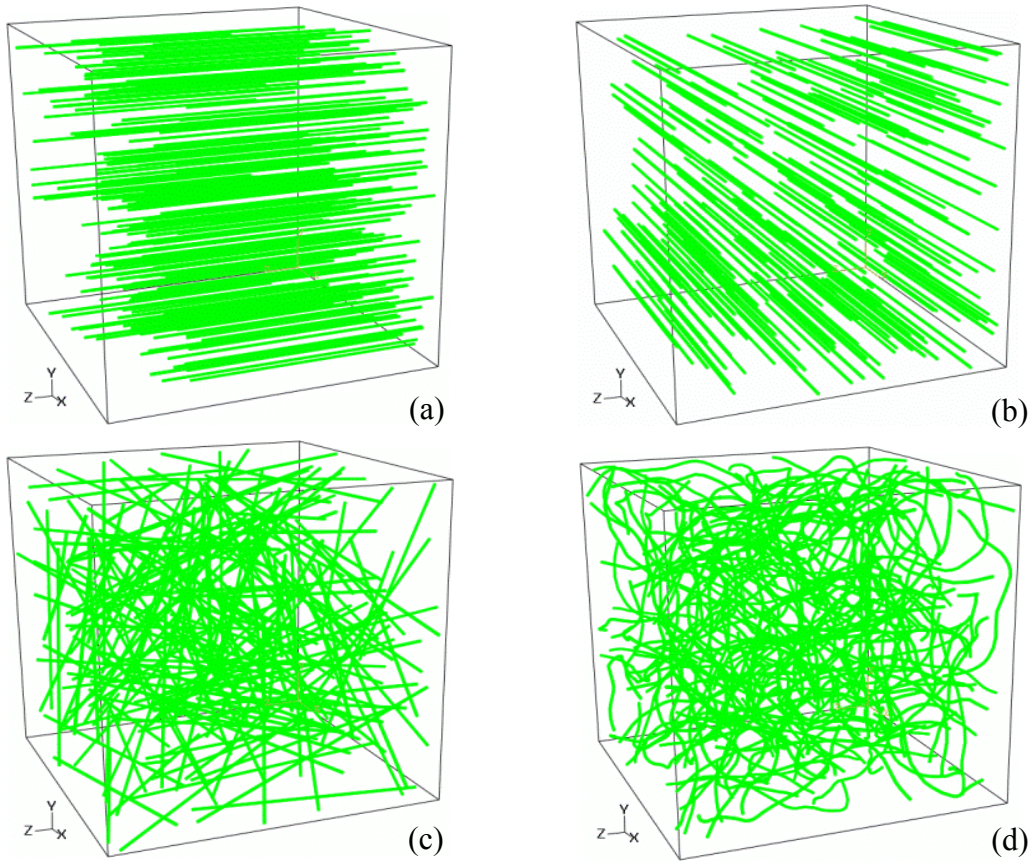

Fig 8.28. Different CNT morphologies for large-scale modeling. Samples volume fraction is 0.5%. (a) *Z*-direction. (b) *X*-direction. (c) Random Rods. (d) Curved.

Table 8.8: Geometrical and mechanical parameters for large-scale CNT-based RVEs.

Diameter (nm)	Length (μm)	Bending Angle	Aspect Ratio	*E* (TPa)	Poisson's Ratio
$8 < \phi < 12$	$1.0 < L < 1.2$	$-25 < \alpha < 25^{o}$	$AR \approx 120$	1.0	0.05

Matrix (Length × Width × Height) (μm³)	*E* (MPa)	Poisson's Ratio
2.5 × 2.5 × 2.5	2500	0.35

To ensure about the simulations results, at first proper mesh density and RVE size should be checked. Therefore, one RVE with different mesh densities were created to determine how to seed CNTs and the RVE edges to have a converged Young's modulus. In Figs. 8.29 and 8.30 the RVE samples with different mesh densities are shown. The RVEs contain 1 vol% CNT.

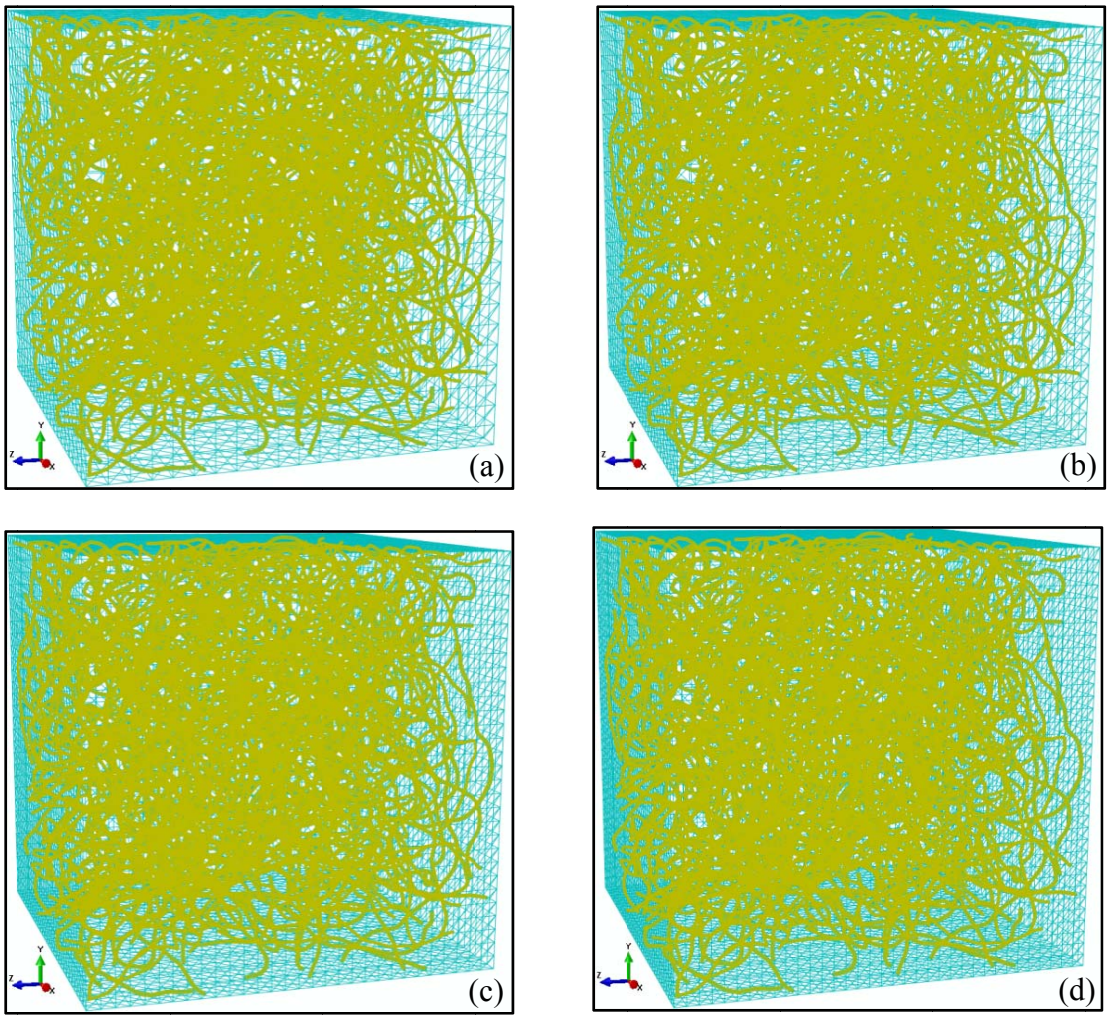

Fig. 8.29. Mesh density of RVEs with curved CNTs. (a) Case 1, (b) Case 2, (c) Case 3, (d) Case 4.

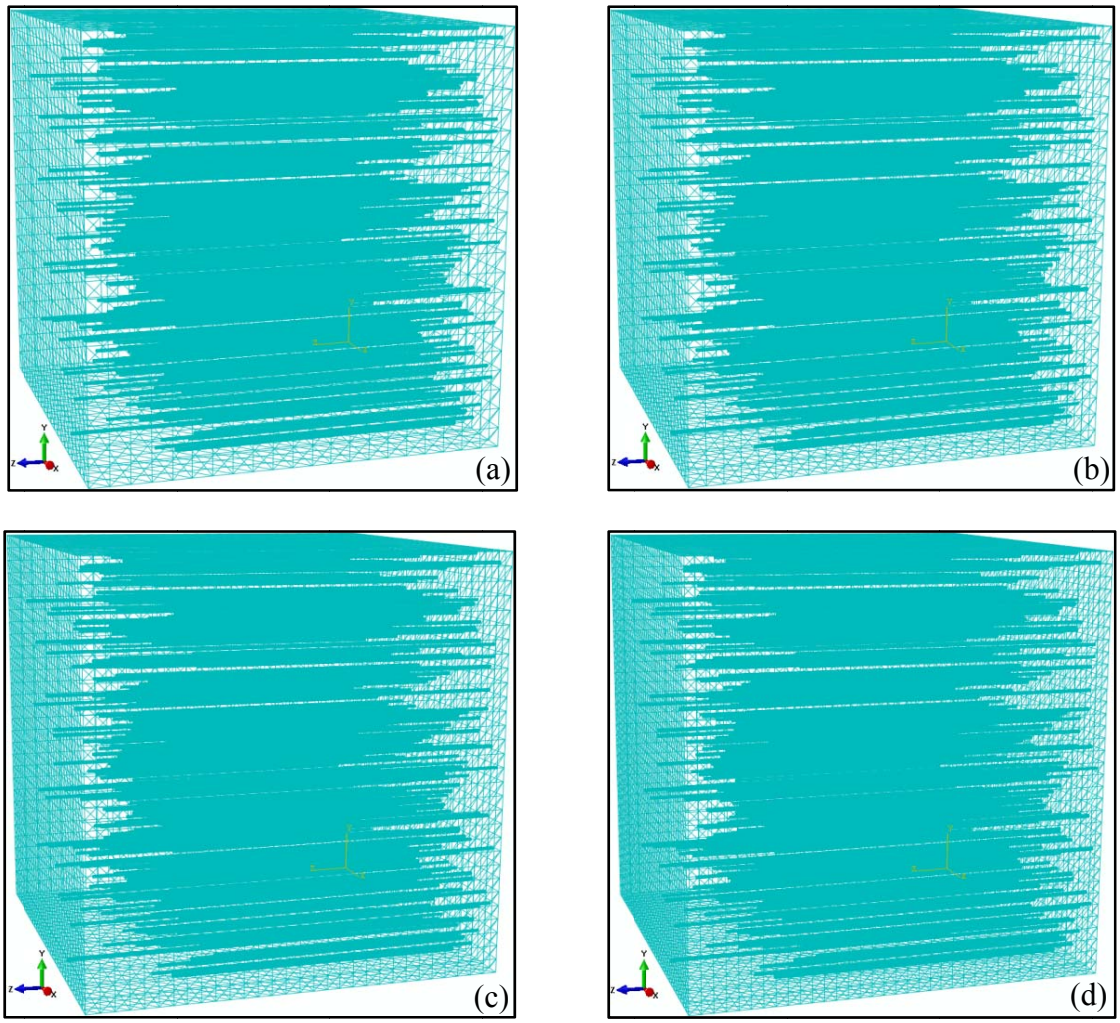

Fig. 8.30. Mesh density of RVEs with straight CNT. (a) Case 1, (b) Case 2, (c) Case 3, (d) Case 4.

The results of simulating these RVEs with different mesh densities are given and compared in Tables 8.9 and 8.10 for curved and straight fibers, respectively. In Fig. 8.31 the exact values and fashion of modulus convergence according to the mesh densities are illustrated. Based on the obtained elastic modulus for the curved fibers, it is obvious that after increasing the mesh seeding number in Case 3, the elastic response has changed

less than 0.054%, which shows the mesh density in both Case 3 and 4 are proper for virtually modeling the RVEs containing this type of CNTs. Similarly, for straight fibers, through increasing the mesh seeding number in Case 3, the elastic modulus has converged less than 0.031%. Therefore, there is no difference between the mesh densities in Case 3 or 4.

Table 8.9: Elastic response of RVEs with different mesh densities (Curved CNTs).

	Case 1		Case 2		Case 3		Case 4	
RVE Entities	CNTs	Matrix	CNTs	Matrix	CNTs	Matrix	CNTs	Matrix
Mesh Seed #	≈ 45	20	≈ 49	25	≈ 53	30	≈ 57	35
NO. Elements	67872	1634092	74032	1843154	80192	2060845	86352	2289248
E (MPa)	3172.96		3157.10		3143.76		3142.05	

Table 8.10: Elastic response of RVEs with different mesh densities (Straight CNTs).

	Case 1		Case 2		Case 3		Case 4	
RVE Entities	CNTs	Matrix	CNTs	Matrix	CNTs	Matrix	CNTs	Matrix
Mesh Seed #	≈ 45	21	≈ 49	25	≈ 53	30	≈ 57	35
NO. Elements	69964	1326625	76176	1392564	82388	1681424	88600	1896234
E (MPa)	7599.0		7520.1		7476.33		7474.01	

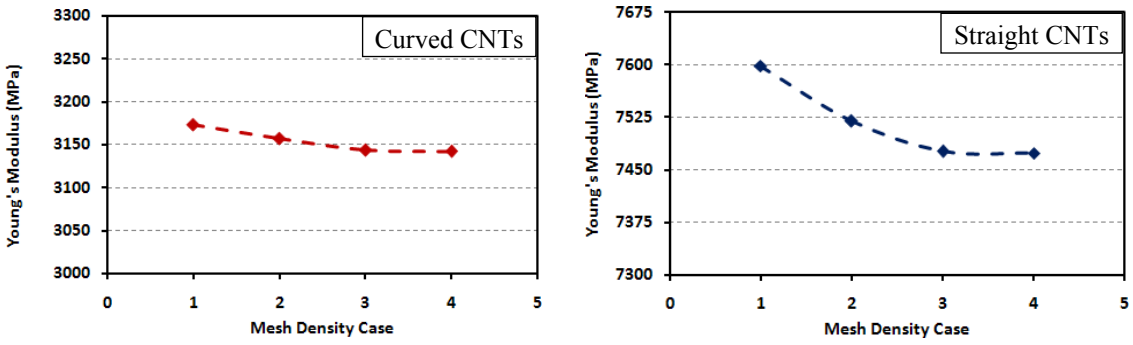

Fig. 8.31. Elastic response of RVEs with different mesh densities (CNT 1 vol%).

In order to determine the proper RVE size, several virtual tests should be conducted. Therefore, 30 models (6 sizes and 5 random sample of each size) with curved CNTs were generated for each RVE size, and then all the RVEs were simulated and the minimum, average, and maximum elastic responses (which is the desired critical response) of them are plotted in Fig. 8.32. This diagram shows the proper RVE size for this study is $2.5\,\mu m^3$, since after that size the criteria for evaluating the proper size changed a little. The trend of RVE size convergence is demonstrated in Fig. 8.31. It should be noted that, handling the RVEs with larger sizes with the available software and computers is a barely possible task.

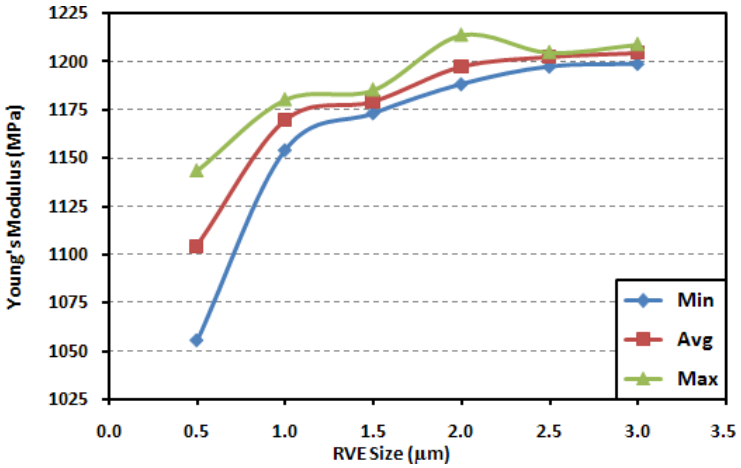

Fig. 8.32. Elastic response trend of curved CNTs to find proper RVE size.

After determining the RVE size, many RVEs with different morphologies are created. Periodic and non-periodic geometrical boundaries are considered for the RVEs. For each of these two main categories, CNTs with four different arrangements as explained and shown in Fig. 8.28 are generated. Finally, for each CNTs arrangement,

four different volume fractions (0.5, 1.0, 2.0, and 3.0 vol%) are created. Thus, 32 models are virtually modeled and simulated. Because numerous models are generated; just some of the stress contours of the models are demonstrated in the following images. In Fig. 8.33, the elements of the matrices are removed, and then the von Mises stress distributions in the CNTs of the simulated non-periodic RVEs with 1 vol% CNTs and high aspect ratios (AR ≈ 120) are shown.

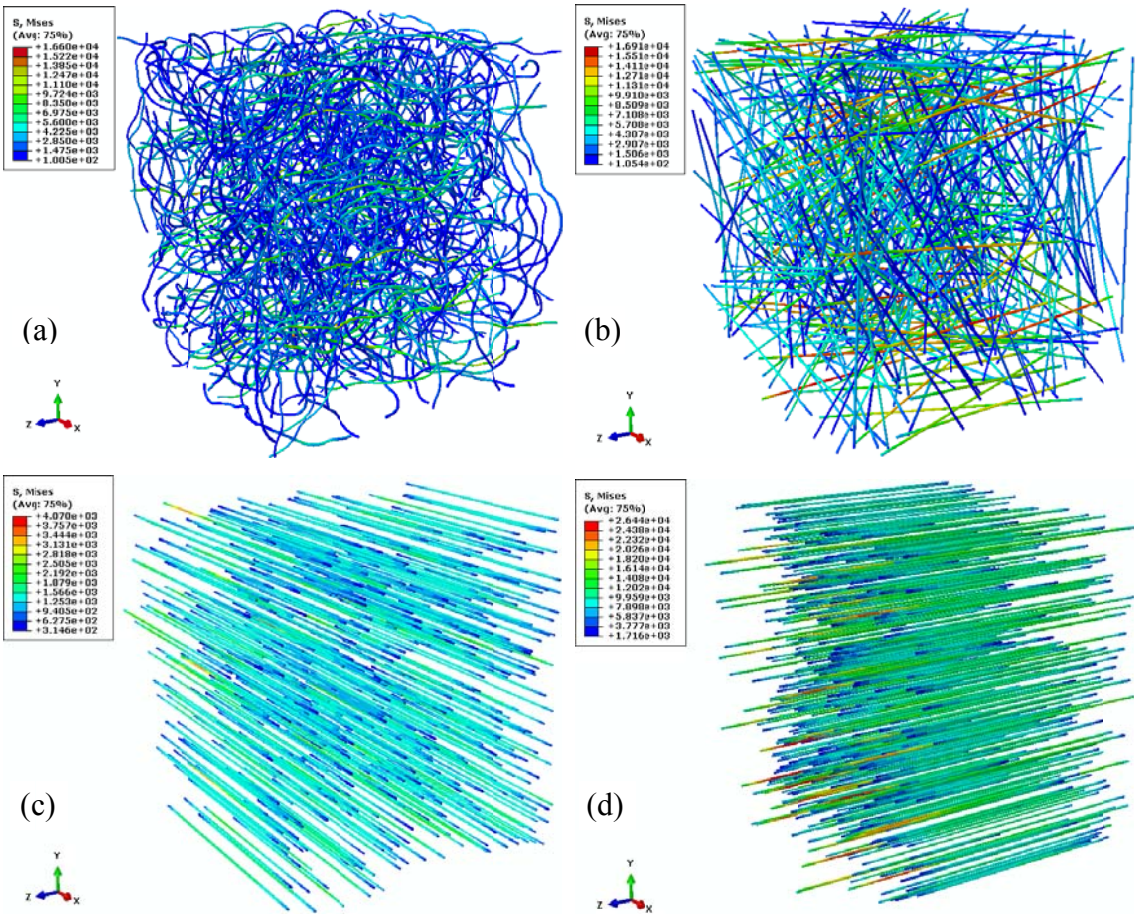

Fig. 8.33. Von Mises stress (MPa) distribution in CNTs of simulated non-periodic RVEs (110 < Aspect Ratios < 120). (a) Curved. Straight: (b) Random Rod, (c) *X*-direction, and (d) *Z*-direction. CNTs volume fraction is 1%.

Table 8.11 provides the average of stress produced in CNTs for each model. In order to perceive the CNTs arrangements effects on the RVEs response, the von Mises stress of these non-periodic RVEs for all the four CNT configurations are compared in Fig. 8.34.

Table 8.11: Average von Mises stress (MPa) in CNTs for different non-periodic RVEs.

	CNT Type			
CNT vol%	Curved	Random Rods	*Z*-Dir	*X*-Dir
0.5	3309	4959	11688	2070
1.0	2422	4554	9918	1345
2.0	2579	4501	8095	831
3.0	2738	4801	6936	636

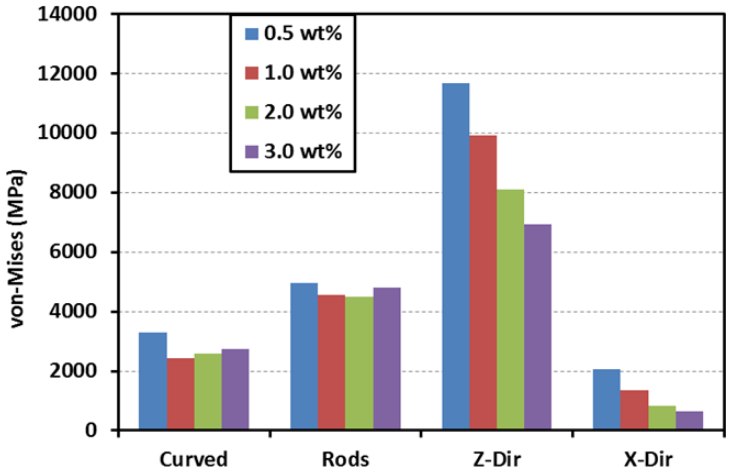

Fig. 8.34. Trends of average von Mises stress produced in CNTs of non-periodic RVEs.

Fig. 8.34 illustrates the fashions of average stress in CNTs for each of the non-periodic models. The average stress has a sorted pattern in the well-arranged fibers (*X*- and *Z*-dir). But, in other cases (curved and rods), irregular pattern is observed; however, the fibers in the RVEs with 0.5 vol% are stressed more than the other weight fractions. Since the

distribution pattern of CNTs are fully random, although weight fractions are increased in the latter cases, their average stress may vary irregularly. It is obvious that the amount of stress in the CNTs placed in the direction of the applied loads (*Z*-dir) is the highest one and the minimum relates to the *X*-dir arrangements.

For the RVEs with non-periodic geometry, Fig. 8.35 shows the trends of Young's modulus for the composites with different types of CNTs. Based on the presented data in diagrams in Fig. 8.35 and 8.36, it can be concluded that adding more CNT to the composites, linearly enhance the elastic modulus of the composite. Also, it is apparent that adding more CNTs perpendicular to the direction of the applied load just increase the elastic modulus from 2665 MPa (vol 0.5%) up to 3000 MPa (vol 3.0%). It means increasing the volume fraction in the perpendicular direction does not boost the Young's modulus of the composite.

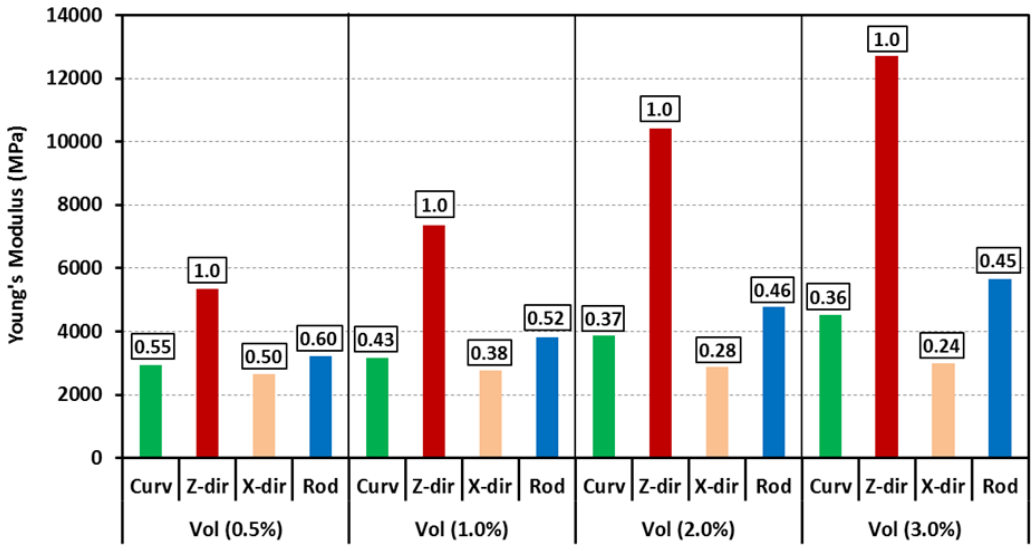

Fig. 8.35. Young's modulus trends for composites containing different types of CNTs (AR ≈ 120), with non-periodic geometries.

Similarly, one can detect in Fig. 8.36 (a) a slight curvature in the response of the composites that have straight CNTs in the *Z*-dir (the direction of the applied load) up to 3 vol%, which may lead to a saturation level or decelerate of enhancement while adding more carbon nanotubes. However, more simulations are conducted to find the correct path and pattern of elastic modulus improvement. Therefore, as plotted in Fig. 8.36 (b), after 3 vol% of CNTs the RVEs elastic modulus improvement accelerates through adding more CNTs to the composites.

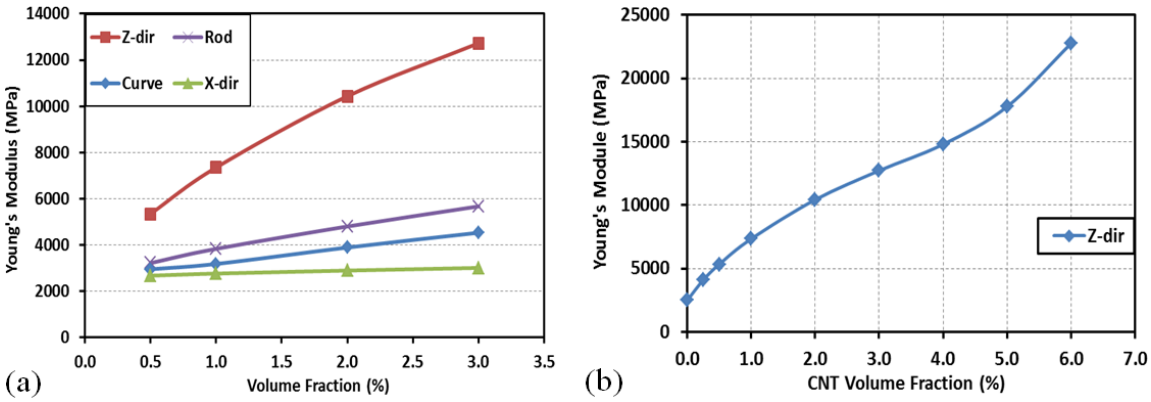

Fig. 8.36. Trends of elastic modulus variations of CNT/PMMA nano-composites with non-periodic geometry, for different CNT morphologies and volume factions (AR ≈ 120): (a) All CNT configurations, (b) Just straight CNT configuration.

In Fig. 8.37, a sample of a close range zoom inside a RVE is shown to better depict stress distribution in some fibers. It is observed those fibers segments that are aligned parallel to the applied load direction carry the highest portions of stress, and other CNTs that are randomly dispersed and curved to other directions, just transfer a very little portion of the applied load.

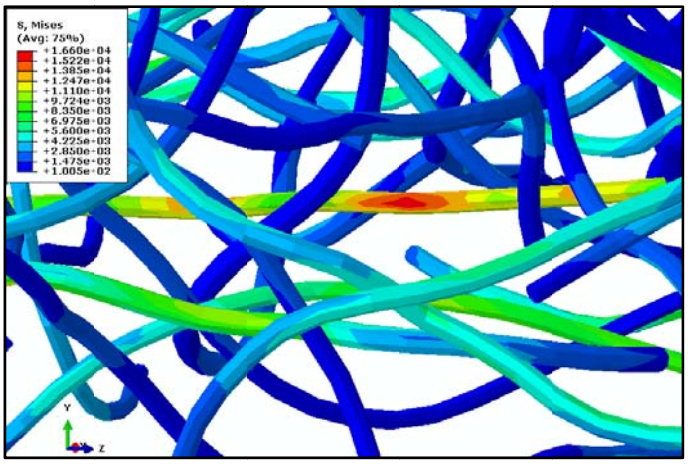

Fig. 8.37. Close range view of von Mises stress (MPa) state in some CNTs inside an RVE (1 vol% CNTs) to demonstrate their load carrying capacity.

Since experimentally creating random rod shape CNTs are difficult to almost impossible, and besides the most interesting morphologies are the curved and straight fibers; therefore, in order to study periodic geometry condition on overall elastic behavior of the CNT-based composites, just curved and straight CNTs are considered. Thus, several models with different volume fractions are created and presented in Fig. 8.38. This figure demonstrates the stress distribution in the fibers for the simulated RVEs with periodic geometry.

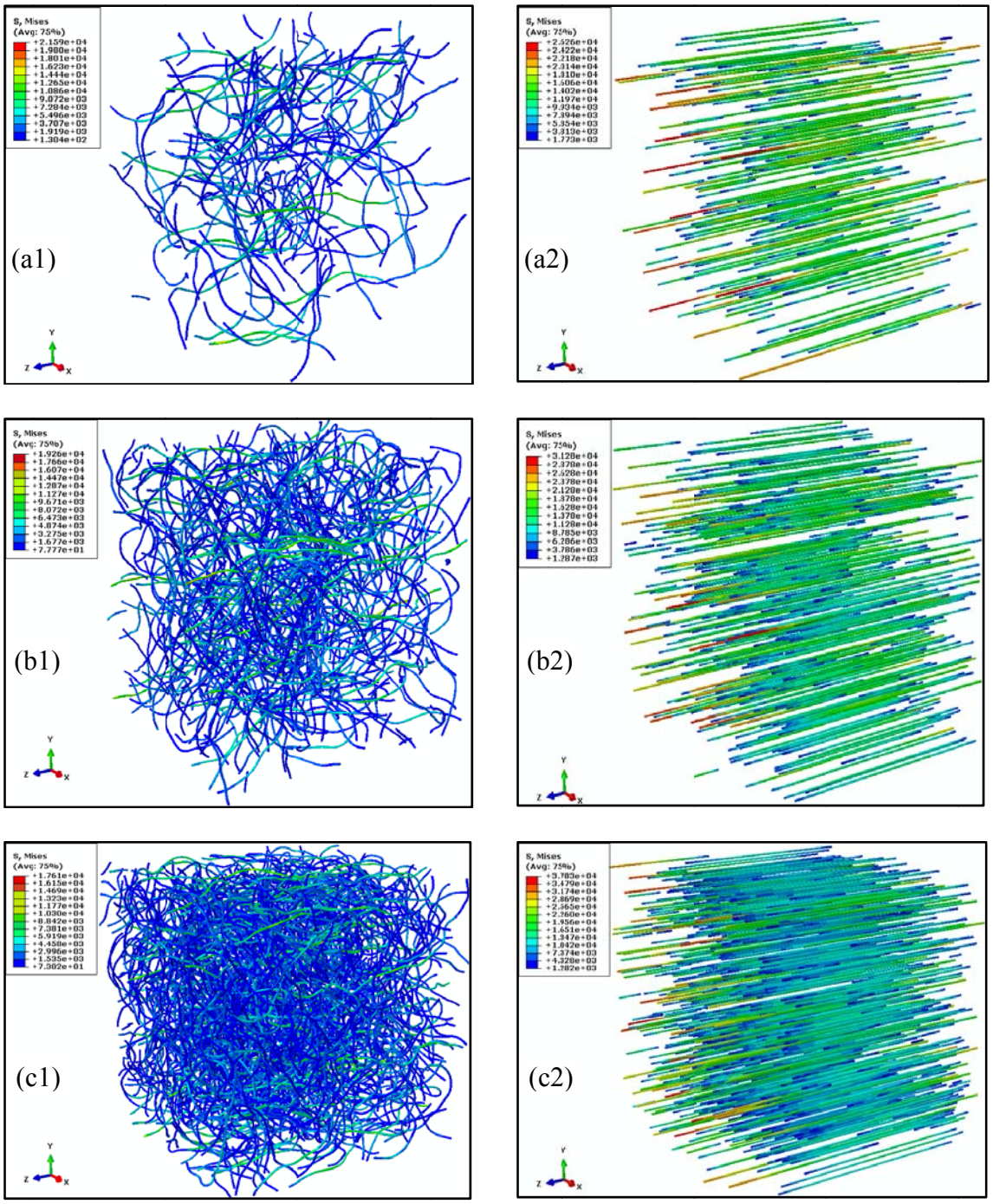

Fig. 8.38. Von Mises stress (MPa) distribution in CNTs of simulated periodic RVEs, (110 < AR < 120). (a1) to (d1) are curved CNTs, and (a2) to (d2) are straight CNTs. CNTs volume fractions are: (a1)-(a2) 0.5%, (b1)-(b2) 1%, (c1)-(c2) 2%, (d1)-(d2) 3%.

Fig. 8.38. Continued.

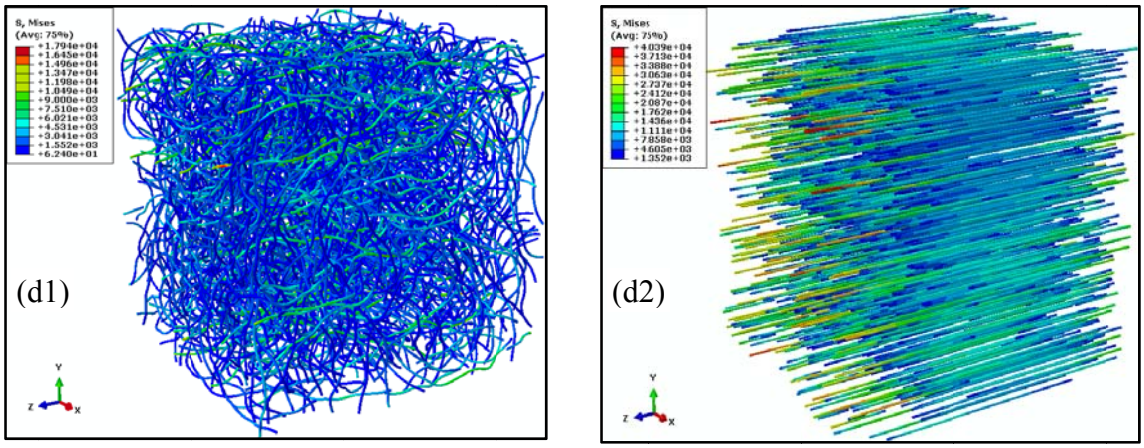

The average produced stresses in fibers of the presented RVEs in Fig. 8.38 are given in Table 8.12. Fig. 8.39 is drawn regarding this table and illustrates the pattern of average stress in CNTs for each of the periodic models. Average stress has a linearly sorted outline in the well-arranged CNTs (*Z*-dir). But in the curved ones, irregular changes are observed; however, fibers in the RVE containing 0.5 vol% CNTs is stressed more than the ones in other volume fractions. Similar to Fig. 8.34, the irregular pattern can be assigned to the randomness and heterogeneity of the curved fibers placed in the RVE.

Table 8.12. Average von Mises stress (MPa) in CNTs for different periodic RVEs.

	CNT Type	
CNT vol%	Curved	*Z*-Dir
0.5	2805	13098
1.0	2503	12707
2.0	2109	12083
3.0	2430	11763

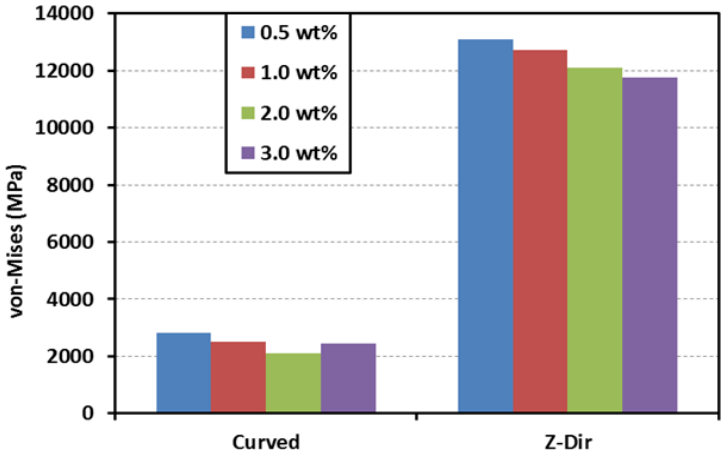

Fig. 8.39. Trends of average von Mises stress produced in CNTs of non-periodic RVEs.

Also, in diagrams depicted in Fig. 8.40, the fashions of elastic modulus improvements for periodic RVEs are shown. This diagram demonstrates that the growth of the elastic modulus is linear for both straight and curved CNTs (up to 3 vol%). It is observable that the enhancement regarding to both curved and straight (*Z*-dir) CNTs are linear, and the *Z*-dir improvement is more intense. Based on these results, it can be achieved that the straight fibers are stressed two to three times more than the curved fibers.

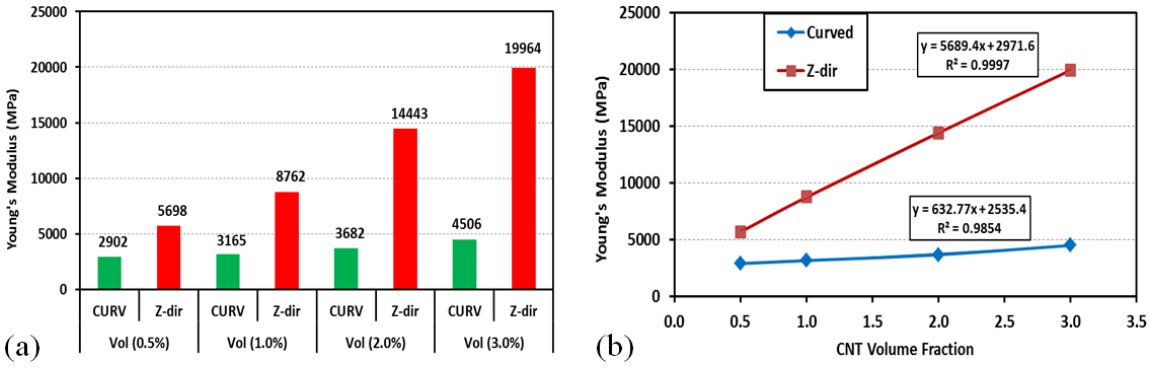

Fig. 8.40. Comparing composites containing two CNT types (AR ≈ 120), with periodic geometries. (a) Elastic moduli comparisons. (b) Trends of Young's modulus growth.

Moreover, the comparisons between the response of the periodic and non-periodic geometries are clarified in Table 8.13 and Fig. 8.41. In this figure, two morphologies for curved and straight CNTs with different volume fractions are shown (AR ≈ 120). Also, the ratios of modulus enhancement for just straight CNTs are inserted in the table. From Fig. 8.41 and Table 8.13, it can be achieved the RVEs with periodic geometry give higher elastic modulus for the same volume fractions. As the volume fraction increases the ratios of Young's moduli of the periodic with respect to the non-periodic are escalated just for the RVEs containing aligned CNTs in the direction of the applied load. However, in the RVEs with curved CNTs, for both periodic and non-periodic cases the overall elastic modulus are almost the same, and no degradation and/or enhancement is observed. From the mentioned table and diagram, it can also be obtained that the differences of the modulus in periodic and non-periodic cases increase, and as calculated, the ratio of periodic to non-periodic increases linearly. Such improvement in comparison to the non-periodic condition can be attributed to the fact that the CNTs cutting the faces of the RVEs carry more loads; since the load is directly applied to those fibers. Thus, as studied for small RVEs with just one CNT in Section 8.2.5.1 (see: Figs. 8.4 and 8.5, and also Figs. 8.9 and 8.10); the large-scale samples with periodic conditions reveal more carrying load capacities, as well.

Table 8.13: Youngs modulus (MPa) of periodic and non-periodic RVEs and their ratios.

	Vol (0.5%)		Vol (1.0%)		Vol (2.0%)		Vol (3.0%)	
CNT Type	Curve	*Z*-dir	Curve	*Z*-dir	Curve	*Z*-dir	Curve	*s*-dir
Periodic	2902	5699	3165	8762	3886	14443	4529	19964
Non-Periodic	2941	5339	3173	7345	3883	10430	4524	12725
Prd / Non-Prd	0.987	1.067	0.998	1.193	1.001	1.385	1.001	1.569

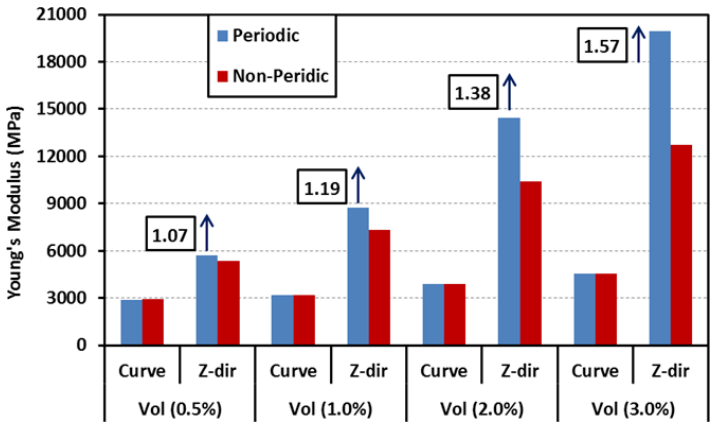

Fig. 8.41. Comparing elastic modulus of RVEs with periodic and non-periodic CNTs.

Since, the aspect ratio is one of the main parameters that affect the behavior of the composites; therefore, several models with less aspect ratios ($10 < AR < 12$), which is about one tenth of the previously modeled CNTs in Figs. 8.33 and 8.38, were generated to study the effect of this parameter on the large scale models. Similarly as an example, stress contours of just one series of the non-periodic RVEs with 1 vol% CNT and $AR \approx 11$ are demonstrated in Fig. 8.42.

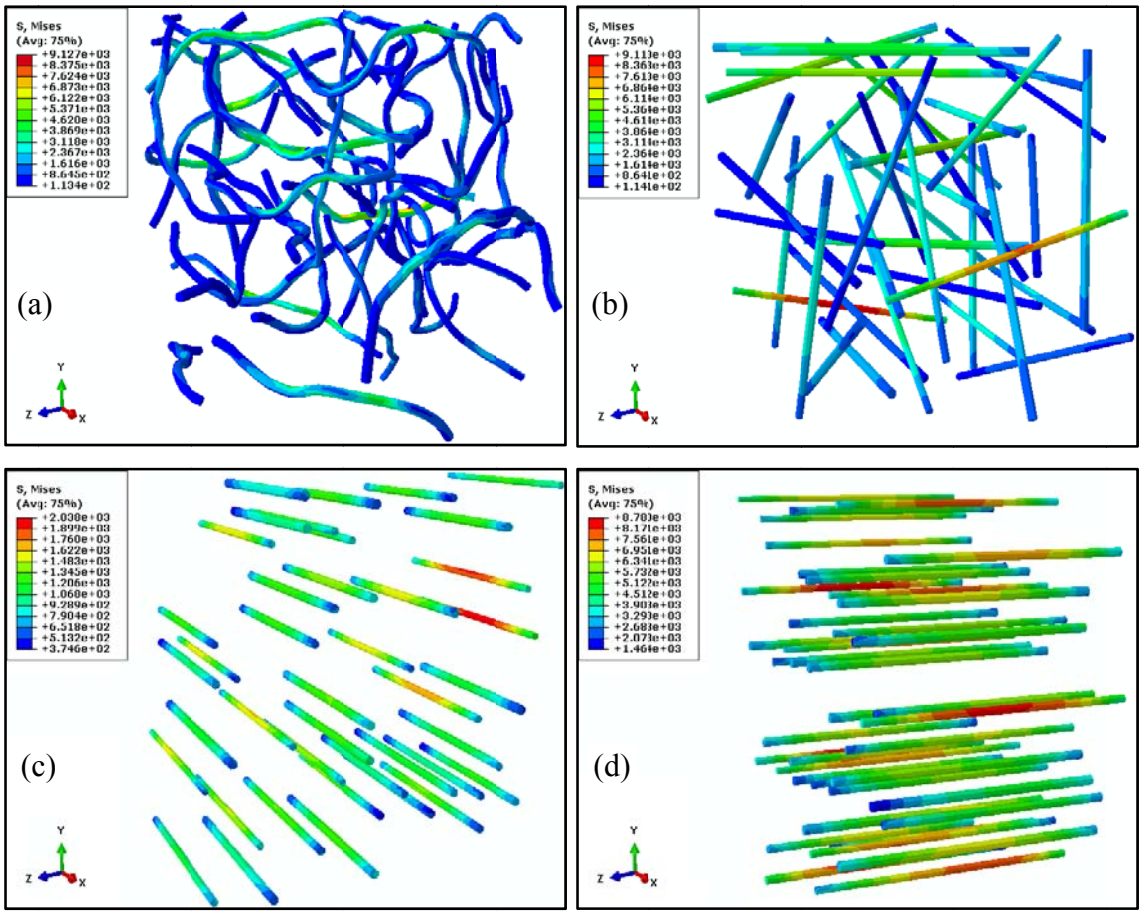

Fig. 8.42. Von Mises stress (MPa) distribution in CNTs of simulated non-periodic RVEs (10 < AR < 12). (a) Curved. (b) Random Rod, (c) *X*-direction, and (d) *Z*-direction.

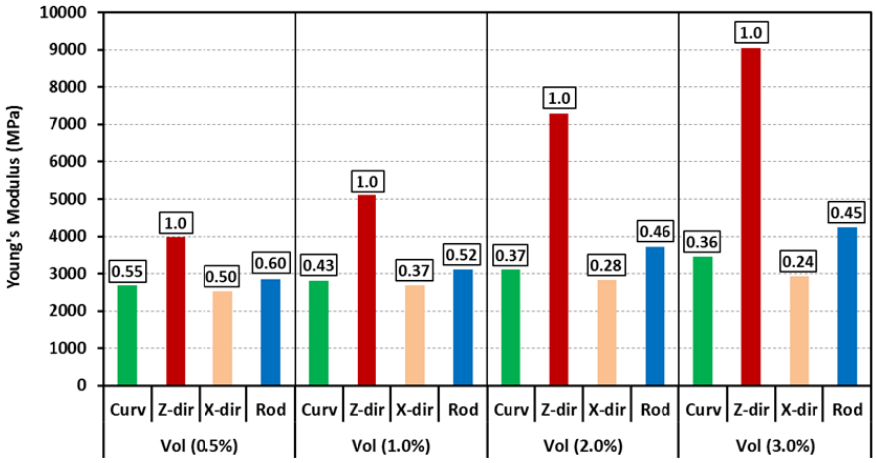

Fig. 8.43. Young's modulus trend of non-periodic CNT composites (10 < AR < 12).

The amounts and trends of modulus enhancement, regarding Fig. 8.42, for a variety of CNT morphologies and volume fractions are provided and shown in Figs. 8.43 and 8.44. The ratios of modulus enhancement for each CNT arrangement regarding to the highest one in their categories (which are the *Z*-dir arrangements) are also noted in the chart. All of the different CNT arrangements show a linear modulus improvement for each case up to 3 vol%, and these trends are depicted in Fig. 8.44.

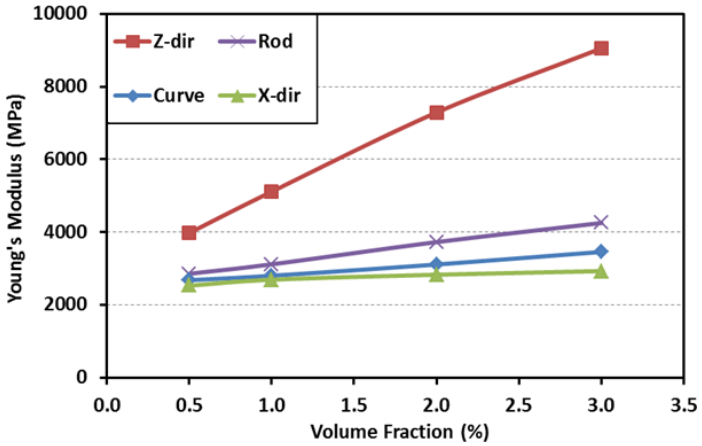

Fig. 8.44. Elastic modulus trends of CNT-reinforved nano-composites with non-periodic geometry, for different CNT morphologies and volume factions (AR ≈ 11).

Furthermore, elastic responses of the RVEs with two different AR are compared and shown in Figs. 8.45. The percentages of modulus reduction for each model with respect to its counterpart in the RVEs with higher aspect ratio are given. It illustrates that the maximum reduction relates to the *Z*-dir cases which is about 40% drop. The minimum decrease relates to the *X*-dir arrangements, which is about 2%. Regarding to Fig. 8.45, it is observed that through changing the values of aspect ratios of the CNTs, the modulus reduction can be sorted in a descending manner as: straight (*Z*-dir), straight (rod),

curved, and straight (*X*-dir). In addition, as the volume fraction increases, the amount of the elastic modulus reduction in all types (but *X*-dir) converges to about 38%.

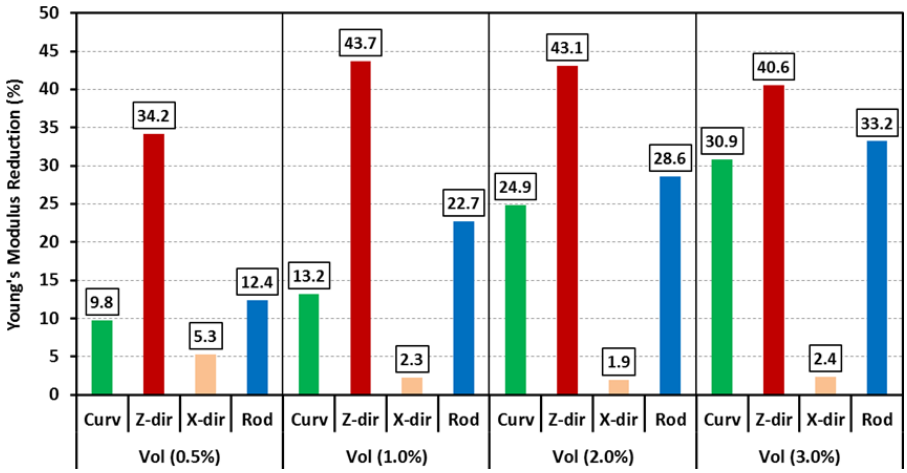

Fig. 8.45. Young's modulus reduction (percentage) of CNT-reinforced composites with AR ≈ 11 regarding the composites containing CNTs with AR ≈ 120.

The comparisons between Figs. 8.35, 8.43 and 8.45 proves that long CNTs contribute more to enhance a CNT-reinforced composite; hence, this geometrical parameter (aspect ratio) has a key role for improving the overall elastic behavior of the composites. Also, Fig. 8.46 shows the average value of von Mises stress in the polymer matrix of the RVE samples of Figs. 8.33 and 8.42. Different CNT morphologies regarding to two AR are considered, and the results confirm that in small strain range, increasing AR parameter reduces the average stress produced in the whole matrix. The reduction here for just 1 vol% is approximately 4%. This phenomenon can be ascribed to the pattern of CNT distribution, which relates to the AR parameter of these constituents.

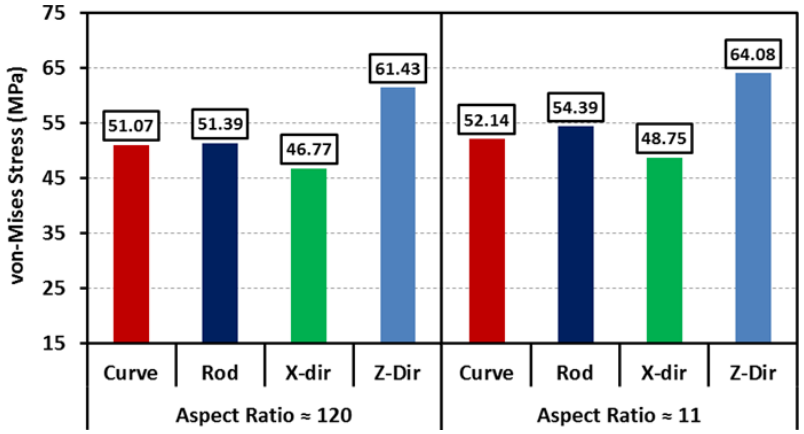

Fig. 8.46. Comparing average value of von Mises stress (MPa) in RVEs with different CNT arrangements, and two different ARs. In all cases, CNT volume fraction is 1%.

In fact, the CNTs with higher AR are finer and can be dispersed homogeneously and perfectly inside an RVE and cover the whole matrix, such that the fibers are available everywhere inside the RVE domain, and they can locally carry the internal loads. Thus, CNTs with higher aspect ratios deliver lower level of stress inside the RVEs matrices.

8.5 Summary

The properties of fiber reinforced composites strongly depend on the direction of measurement. It is shown that the strength and Young's modulus of fiber-reinforced composites attain the maximum value when they are measured in the longitudinal direction of the fibers. At any other angle of measurement and even a slight bending or curvature in the fibers lower the performances, and the minimum elastic modulus is obtained while the load is perpendicular to the longitudinal direction of the fibers. The outcomes of this method indicate that long nanotubes aligned parallel to the loading direction should be used for effective load transferring between the fibers and matrix.

Furthermore, the effect of Poisson's ratio of the CNTs is studied and it is shown that it almost does not affect the overall responses of the RVEs.

The research performed in this chapter successfully validates the FEM results with MD, and rule of mixtures as well, for just single carbon nanotube that is surrounded by polyethylene matrix, for two aspect ratios. It is also shown that instead of modeling the CNTs as hollow tubes; they can be modeled as long solid cylinders with their Young's modulus reduced equivalently. This validation and agreement of the continuum mechanics with MD and ROM results can play a significant role for the finite element approach that can be used for characterizing larger models.

It can be stated that the CM approach using FEM can deliver promising outcomes for nano-scale models as well as for large-scale models, when the results are focused on the overall responses instead of the interfacial properties of the composite. Emphasis is placed on modeling large-scale complex composite models using 3D solid elements instead of 3D truss, beam, or shell elements. The results shown here indicate that FEM can be utilized as an excellent estimation approach for evaluating elastic moduli of large-scale complex models; hence, FEM can be used for characterizing nano-composites, which can significantly reduce computational time and resources (memory and cpu hours) in comparison to the MD method.

CHAPTER IX

LARGE STRAIN MICROMECHANICAL RESPONSES OF POLYMER NANO-COMPOSITES USING UNIFIED VISCOELASTIC-VISCOPLASTIC-VISCODAMAGE MODLES

9.1 Introduction

There have been very few attempts to conduct more realistic large scale simulations of nanocomposites with random distribution of nano particles (e.g., carbon nanotubes/nanofibers, nano-clays, nano-ceramics, and hybrid inclusions) with different morphologies; even based on small strain concept let alone large deformation frameworks, which is the main focus of this chapter.

Experimental studies revealed that the enhancement in the multifunctional properties of nanocomposites strongly depends on the morphologies (size, aspect ratio, volume fraction, and distribution) and properties of the nano-inclusions (see Chapters 1, 2, 7, and 8). Although there are many experimental studies on nanoclay/nanotubes/ nanofibers polymer-based composites, very little research has been done in the three-dimensional micromechanical computational modeling of such composites.

Numerous experimental studies have shown that the material response of PCMs are very complex and is time-, rate-, and temperature-dependent and exhibits both recoverable and irrecoverable deformations (see Chapter 5). Besides, because polymer and polymer composites experience large deformation during both mechanical and thermal loading, investigating the response of such composites in large strain regime is

mandatory. However, as explained in Chapters 3, 4, and 5, the viscoelastic, viscoplastic and viscodamage constitutive models were generalized to be able to properly capture and measure the stress and strain fields in the large deformation range.

Therefore, the main objective of this chapter is to employ the unified coupled time and rate dependent models in large strain framework (as explained in Chapter 5) in order to study the mesomechanical behavior of these composites. Hence, damage evolution in nano-composites containing PMMA (Polymethyl methacrylate) polymer embedded with silicate nanoclay particles (NCLP), nano-ceramic particles (NCRP), carbon nanotubes (CNT), and hybrid nano particles (HNP) (e.g. NCLP and CNT, or NCRP and CNT) are simulated through using the mentioned models. Also, the simulations are conducted in order to obtain and compare the overall macroscopic mechanical responses in terms of key microstructural features. The RVE models are subjected to uniaxial tension and compression at different strain rates.

9.2 Constitutive Laws Mesh Sensitivity

The accuracy of the FEA method depends on the sizeof the elements. To study the mesh sensitivity of the calibrated numerical models, the following simulations is conducted. One 2D RVE is chosen containing 2 vol% of intercalated nanoclay particles, and the RVE size is: $2.5\times2.5\ \mu m^2$. Five different mesh densities are generated, and their configurations and number of elements in each case are demonstrated in Fig. 9.1.

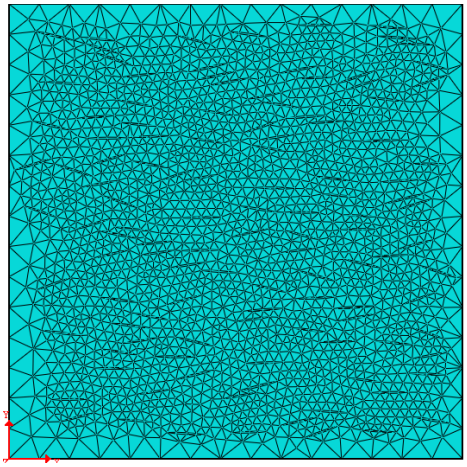

(a) Coarse mesh (Elem # 4096)

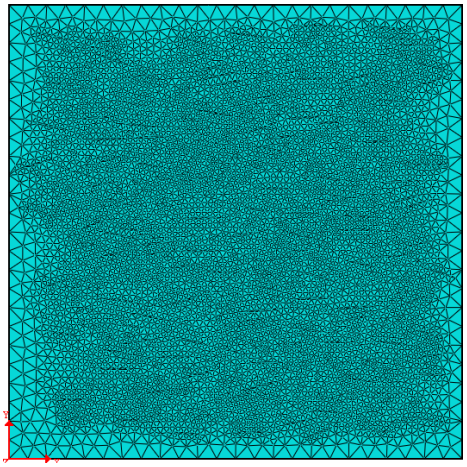

(b) Fine mesh (Elem # 13726)

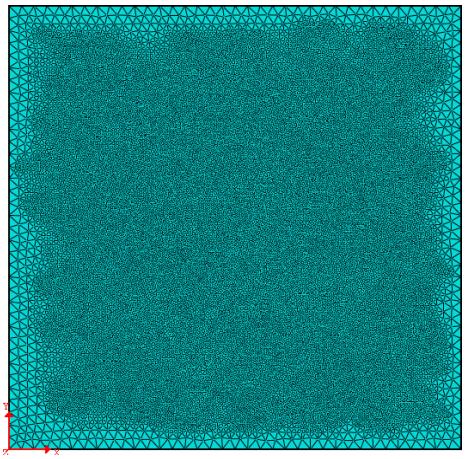

(c) Finer mesh (Elem # 27262)

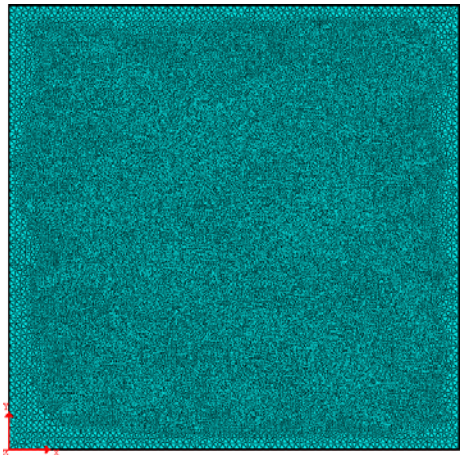

(d) Finer mesh (Elem # 59774)

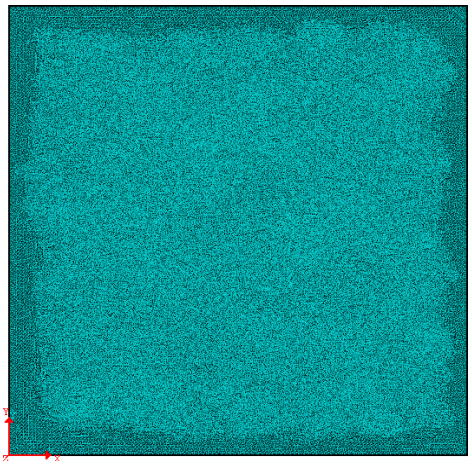

(e) Finest mesh (Elem # 160192)

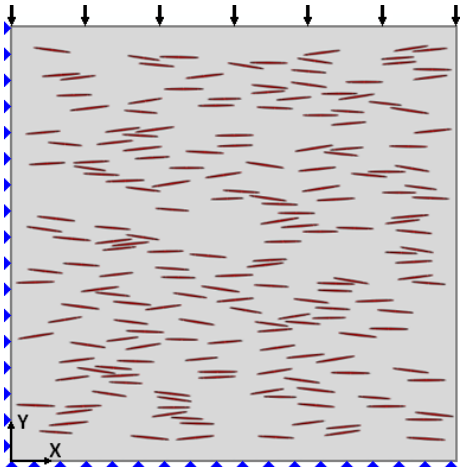

(f) Load & Boundary Condition

Fig. 9.1. Different mesh density for one 2D RVE with 2% nanoclay.

Displacement (or strain) and force (or stress) control tests have been performed. Fig. 9.2 depicts the stress-strain responses for the RVEs with different mesh densities through using the unified models. In images (a) and (b), the differences of the unified models when the considered stress and strain measures are work-conjugate (as mentioned in Section 3.2.1) and non work-conjugate (as mentioned in Section 3.2.2) are shown. One can observe that the non-conjugate models are highly mesh sensitive. However, the work-conjugate models also show mesh dependency which is in an acceptable range.

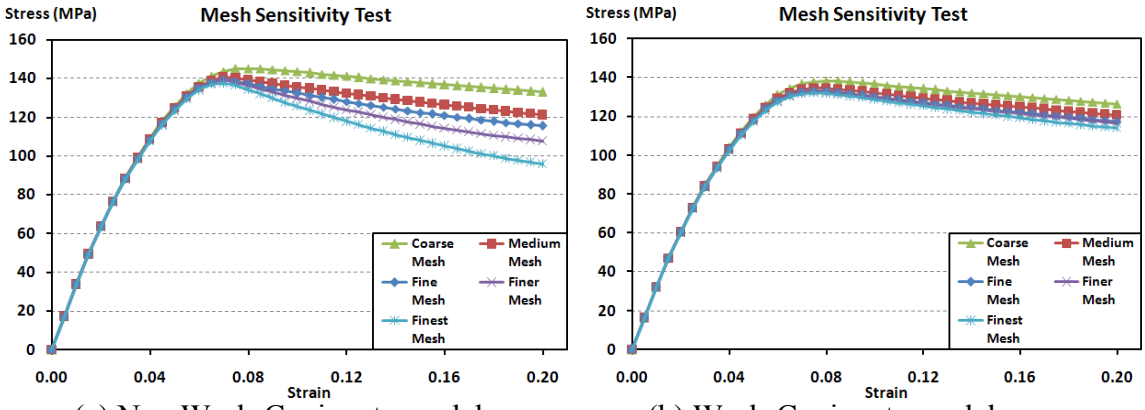

(a) Non Work-Conjugate models. (b) Work-Conjugate models.

Fig. 9.2. Stress-strain diagrams (displacement control simulation) for all mesh densities for both work-conjugate and non work-conjugate.

In the following, Fig. 9.3 shows the damage distribution in the RVEs for the coarse, medium, and fine mesh scenarios. In this figure from (a1) to (c1), the depicted damage distributions relate to the unified constitutive models when they are written based on a non work-conjugate stresses and strains. Also, Fig. 9.3 (a2) to (c2) show the damage distributions according to the constitutive models written based on II-PK stress and GL strains which are the work-conjugate case, and were calibrated in Chapter 5.

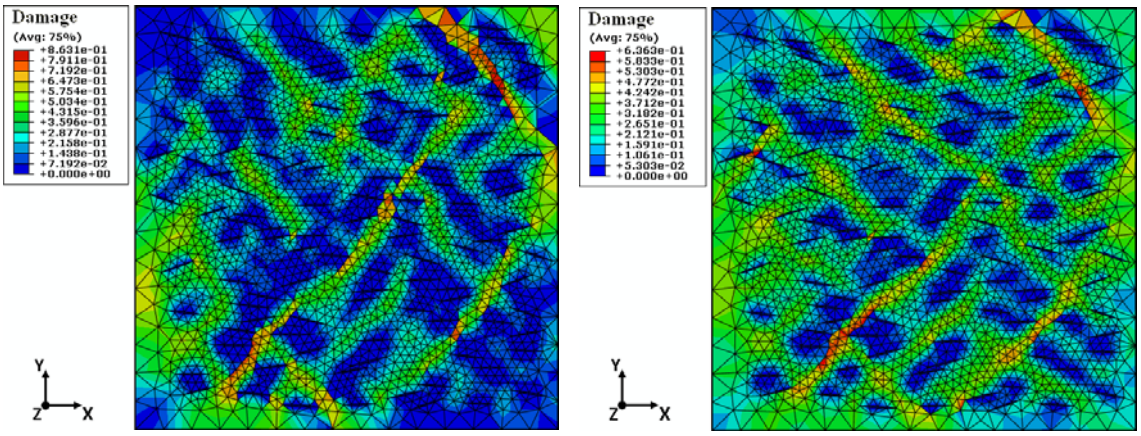

(a1) Elem # 4096 (Coarse) (a2) Elem # 4096 (Coarse)

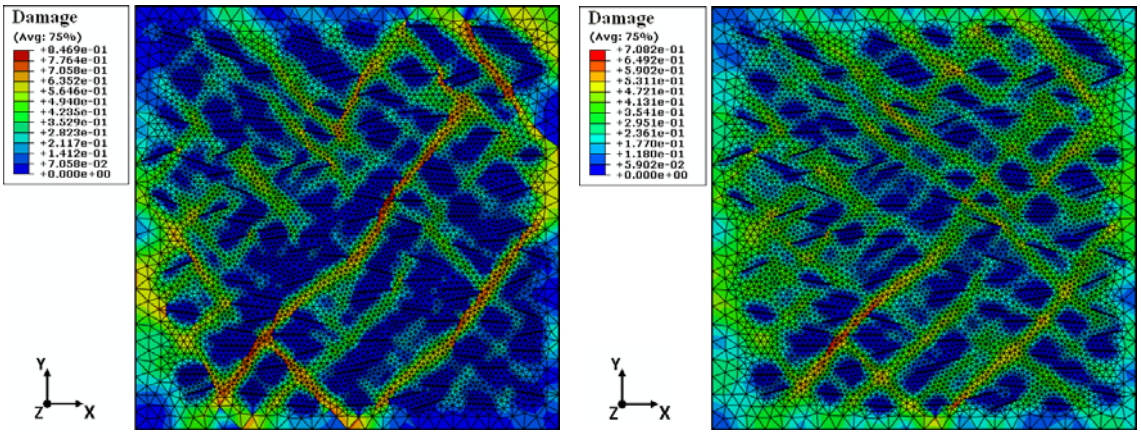

(b1) Elem # 13726 (Medium) (b2) Elem # 13726 (Medium)

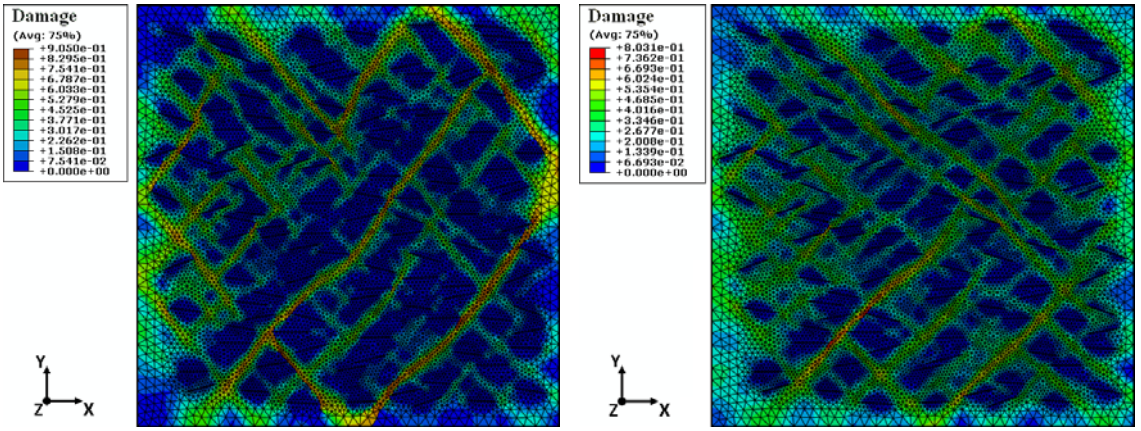

(c1) Elem # 27262 (Fine) (c2) Elem # 27262 (Fine)

Fig. 9.3. Damage distribution of strain-control simulation for Coarse, Medium, and Fine mesh densities: (a1) to (c1) Stress and strain are not work-conjugate. (a2) to (c2) II-PK stress and GL strain (work-conjugate).

In Fig. 9.3, for both cases, the RVEs have been illustrated in company with their discretized mesh element edges, just to show that the widths of the damaged regions are in the range of element sizes. Fig. 9.4 is continuing Fig. 9.3 for demonstrating damage distribution in the highly discretized RVEs. The same order is considered in this figure, i.e. images (a1) and (b1) relate to the non conjugate models and (a2) and (b2) are the results of the work-conjugate stresses and strains.

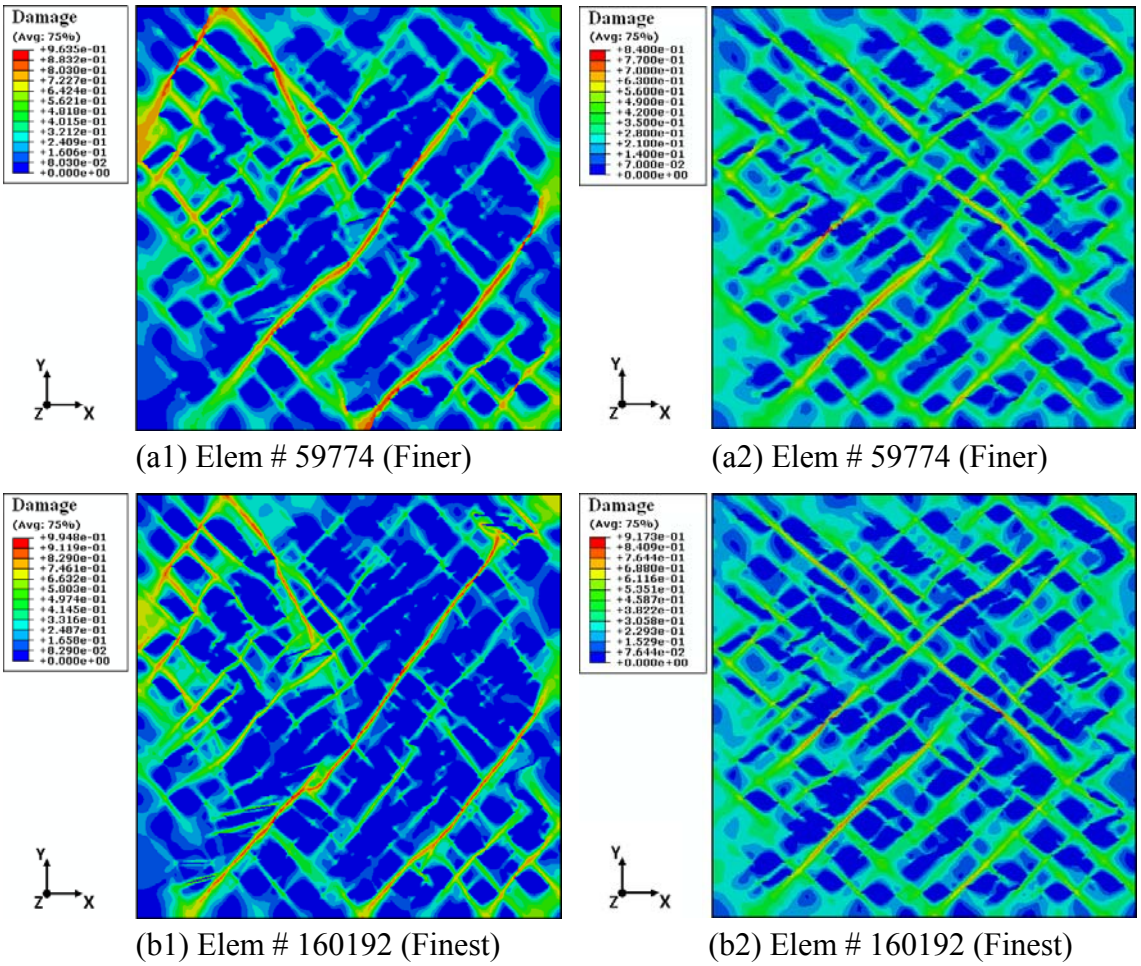

(a1) Elem # 59774 (Finer) (a2) Elem # 59774 (Finer)

(b1) Elem # 160192 (Finest) (b2) Elem # 160192 (Finest)

Fig. 9.4. Damage distribution of strain-control simulation for Finer and Finest mesh densities: (a1) to (c1) Stress and strain are not work-conjugate. (a2) to (c2) II-PK stress and GL strain (work-conjugate).

In Fig. 9.4, in the contrary of Fig. 9.3, since in Finer and Finest mesh densities the size of meshes are very small (see Fig. 9.1 (d) and (e)); thus, mesh edges are removed to show the damaged areas much clearly. One can observe from Fig. 9.3 and 9.4 that in the non conjugate models, as the sizes of meshes become smaller, the damaged band regions are narrower and also the value of damage variable increases. Besides, the creep and recovery simulation results in Fig. 9.5 show that the used viscoelastic and viscoplastic constitutive laws are not sensitive to discretization; i.e. these time- and rate-dependent models intrinsically have length scale which makes them as mesh independent models.

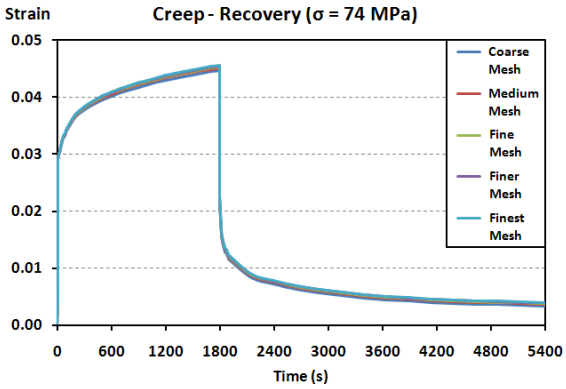

(a) Viscoelastic model.

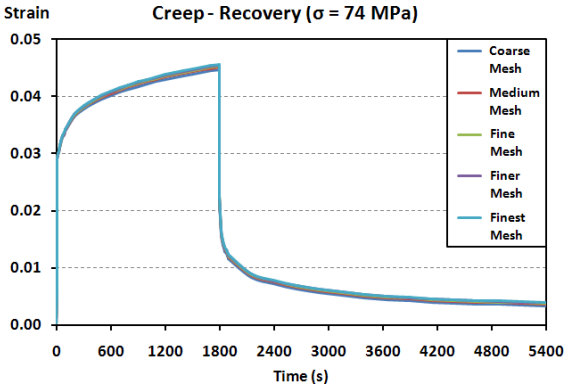

(b) Viscoelastic and viscoplastic model.

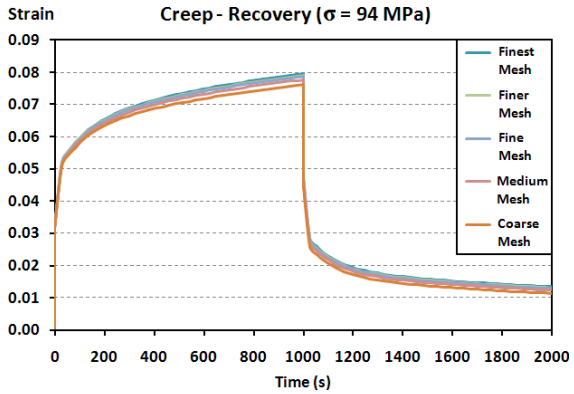

(c) Viscoelastic, viscoplastic, and viscodamage model.

Fig. 9.5. Stress control simulations, creep-recovery, for all mesh densities.

Comparing the images in Fig. 9.5 reveals that the responses of the composite models are mesh dependent when the viscodamage law is utilized (at 94 MPa). In this figure, as the meshes becomes finer, the strain (especially in tertiary creep) increases. However, the responses are in an acceptable range.

9.3 3D Microstructural Models

In this subsection, three-dimensional microstructure-based representative volume elements (RVEs) have been arbitrarily generated with different distributions and patterns. The main sample geometries of the simulated models are shown in the following figures.

At first, nanoclay and nano ceramic particles are demonstrated in Fig. 9.6. For creating these geometries the developed RVE_Maker software as explained in Chapter 6 is used. The volume fractions of both NCLP (nano-clay particles) and NCRP (nano-ceramics particles) are 1, 2, and 3%. Just three volume fractions are probed; because, here the main focus is studying the effects of the 3D particles in nucleation and growth of damage in these polymer composites, and also the trend of the overall responses of the composites. Furthermore, simulating, running, and extracting data for composites with higher volume fractions excruciates the computer resources and time. Therefore, for these types of inclusions, 6 RVE models are generated (3 of each), and totally 6 (RVEs) × 2 (strain rate) × 2 (tension and compression) = 24 simulations are conducted. The mechanical properties and geometrical variables of NCLPs are the same as presented in Table 7.4. In order to compare the effects of particles shape on RVEs responses, the mechanical properties of NCRPs are assumed to be the same as NCLPs.

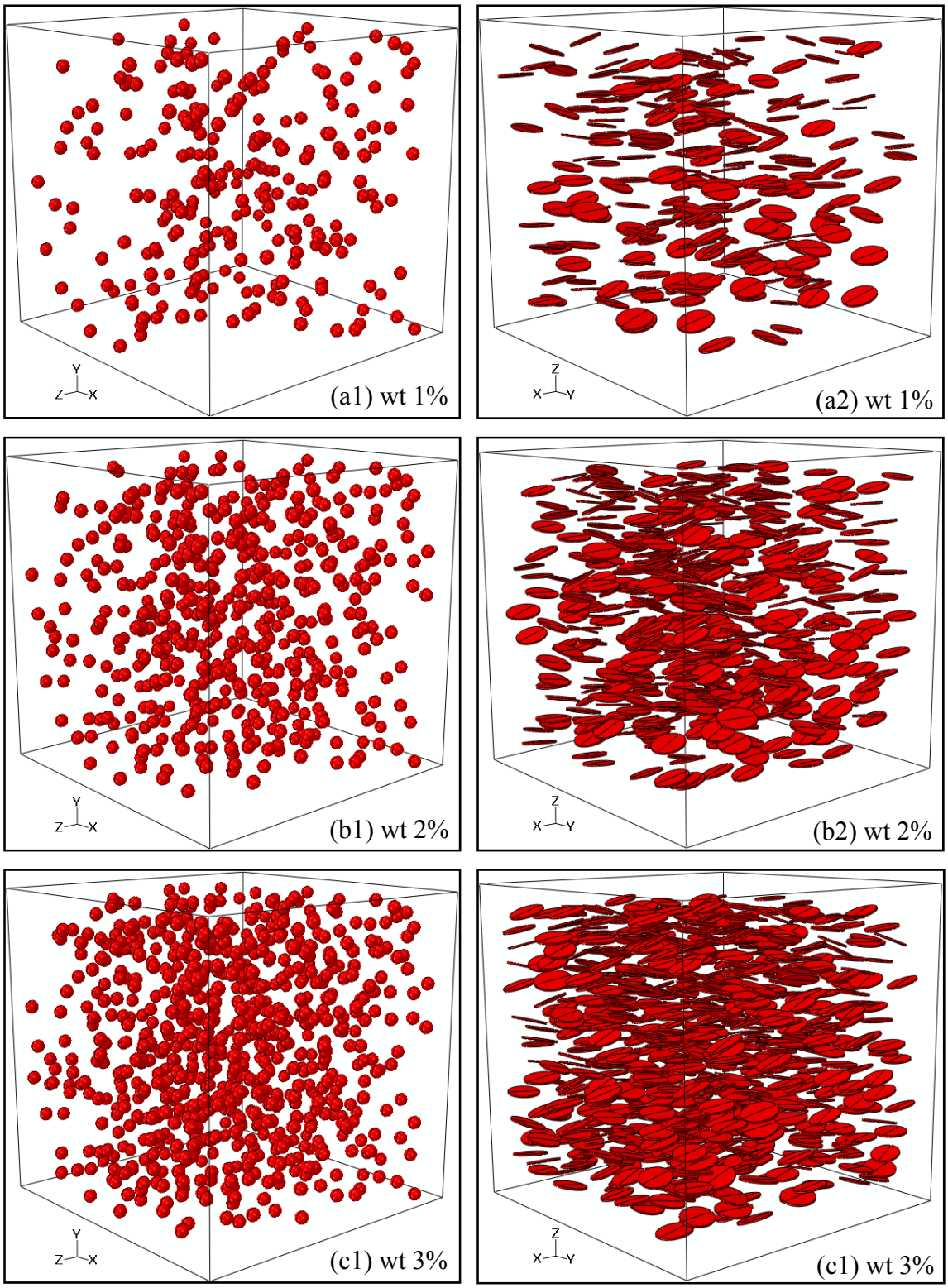

Fig. 9.6. Microstructures with NCRPs (a1 to c1) and NCLPs (a2 to c2).

For the purpose of studying the effects of CNTs on polymer composites, CNTs with two different AR are investigated. The AR of one series is about 120, and the other one is about 11 ($10 < AR < 12$). Four different volume fractions are generated for CNTs with AR ≈ 120 as: 0.1, 0.5, 1.0 and 2.0%. Also, four different volume fractions are generated for CNTs with AR ≈ 11 as: 0.5, 1.0, 2.0, and 3.0%. Henceforth, for fibers with AR ≈ 120; 8 RVE models are generated (2 (curved and straight) × 4 vol%). So, totally 8 (RVEs) × 2 (strain rate) × 2 (tension and compression) = 32 simulations are performed. The geometrical variables and mechanical parameters for these CNT-based RVEs are presented in Table 8.9. In Fig. 9.7, for the sake of conciseness, just two RVE samples of the RVE models are presented, showing the morphology of the curved and straight CNTs with higher aspect ratios. One is noted to Chapter 8 that generating CNTs as random rods for higher volume percent is impossible, and fibers perpendicular to the applied load direction are not interested.

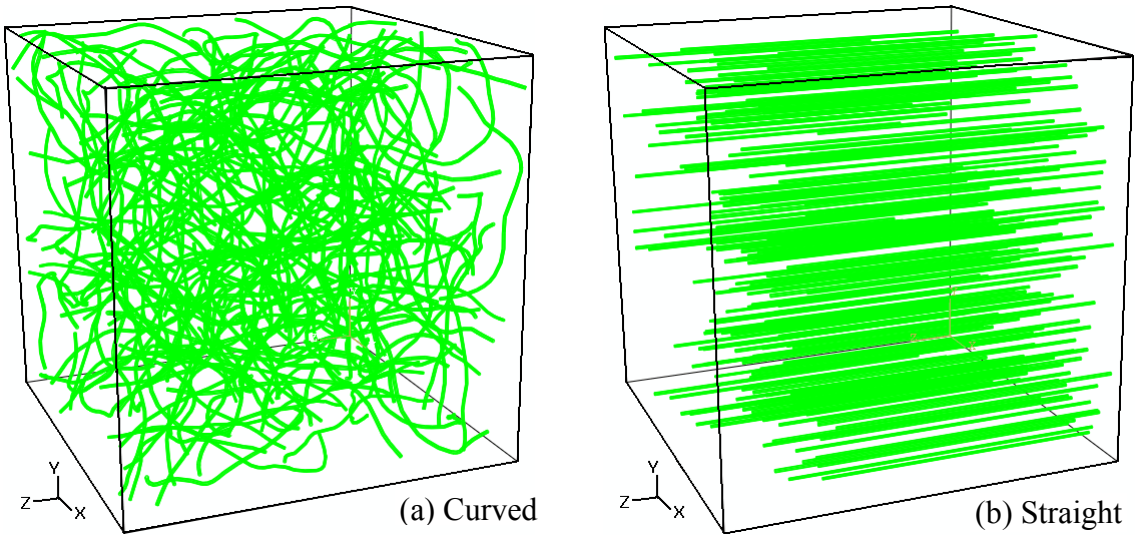

Fig. 9.7. Microstructures containing 1% volume fraction CNTs with aspect ratio ≈ 120.

Fig. 9.8 illustrates 4 RVE morphologies with AR ≈ 11. The geometrical and mechanical parameters for these CNTs are the same as CNTs with AR ≈ 120, but only the diameter of these fibers is almost 10 times larger. Henceforth, for this case totally 16 RVEs (4 morphology × 4 vol%) × 2 (strain rate) × 2 (tension and compression) = 64 simulations are performed. Thus, all in all, 96 simulations are conducted for both CNT ARs.

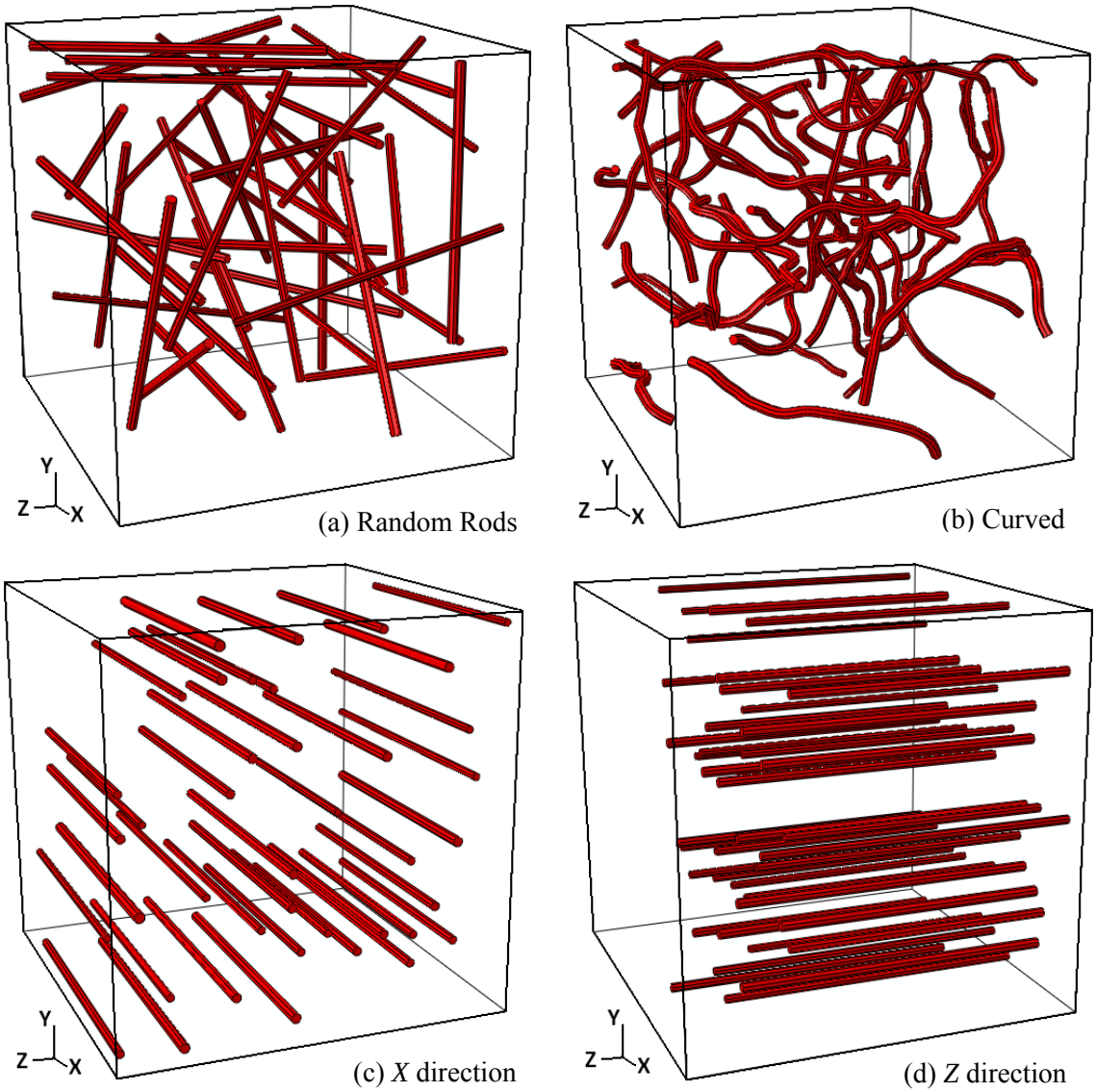

Fig. 9.8. Microstructures containing 1% volume fraction CNTs with aspect ratio ≈ 10.

In this work, two hybrid polymer composites are studied. One is the hybridation of CNTs and NCLPs, and the other one is the mixture of CNTs and NCRPs. For these cases, the idea is virtually computing the effects of CNTs volume percentages versus NCLPs or NCRPs volume percentages. Therefore, three volume fractions are considered for particles (1, 2, and 3%), and three volume fractions are created for CNTs. This means, 2 (particle types) × 3 (particles vol%) × 3 (CNTs vol%) = 18 RVE models are generated. As a result, 18 (RVEs) × 2 (strain rate) × 2 (tension and compression) = 64 simulations. Here, in Fig. 9.9, two samples of hybrid composites are demonstrated.

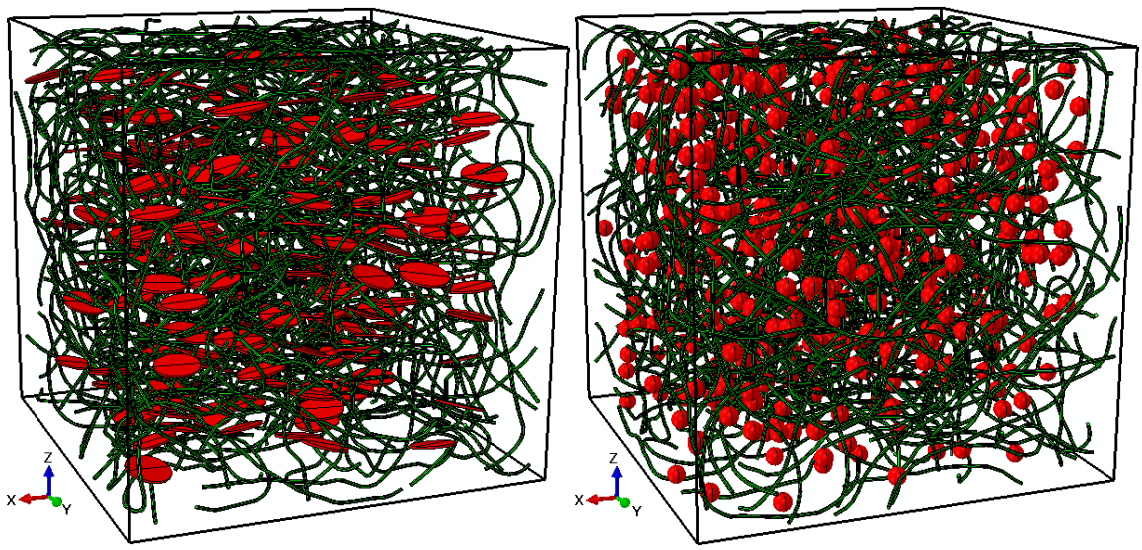

(a) Curved CNTs and NCLPs. (b) Curved CNTs and NCRPs.

Fig. 9.9. Hybrid microstructures containing 1% CNT (AR ≈ 120) and 1% nano particles.

In Fig. 9.10 (a), one 3D RVE sample shows the location of the applied load on the RVEs top surface. Fig. 9.10 (b) of this figure also demonstrates the boundary conditions on lower surfaces which constraint the RVEs translations in the global Cartesian directions.

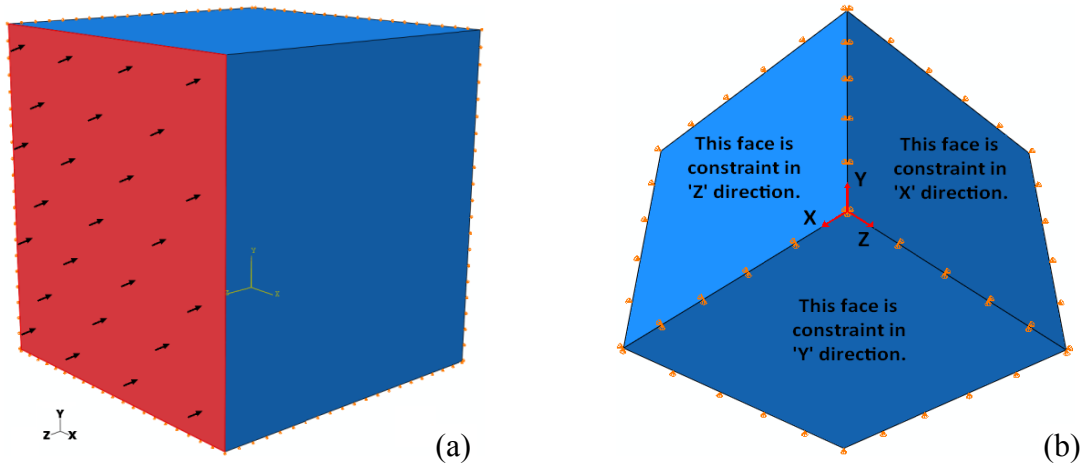

Fig. 9.10. Boundary conditions of 3D RVE: (a) Applied load, (b) Boundary conditions.

In Fig. 9.11, the periodic boundary conditions (PBC) on the other three faces are shown. It means nodes on these faces will move with each other in one of X, Y, or Z directions. In another word, the translation of the defined node set on one face will be equal to the amount of the translation of the related tie point on the same face, as formulated below

$$U_X^{\text{TiePoint}} - U_X^{\text{TiedNodeSet}} = 0 \tag{9.1}$$

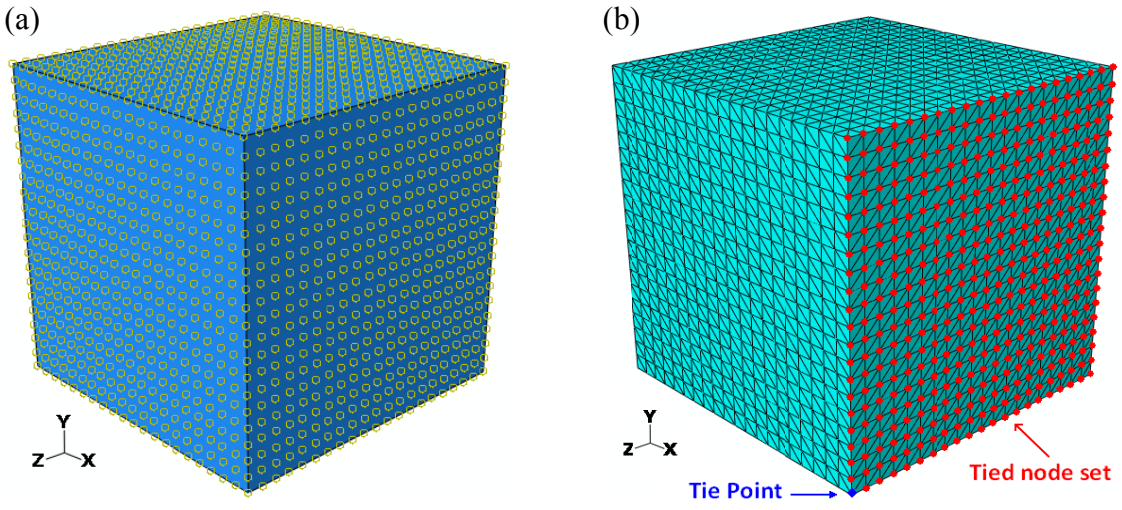

Fig. 9.11. Periodic boundary condition on RVE sample: (a) Illustrating all faces with periodic boundary condition, (b) Tied Node Set and related Tie Point shown on one face.

9.4 Computational Results of Large Deformation Models

In this section the damage distribution contours of the simulated RVEs are shown from Figs. 9.12 to 9.45. Besides, the stress-strain curves of the models under compression and tension loads are shown to present how the volume fraction and shape of inclusions can improve the maximum stress and toughness of the nano-composites.

9.4.1 Intercalated Nanoclay Polymer Composites

The damage initiation and growth in nanoclay particles are demonstrated in Figs. 9.12 to 9.14 for both compression and tension loadings.

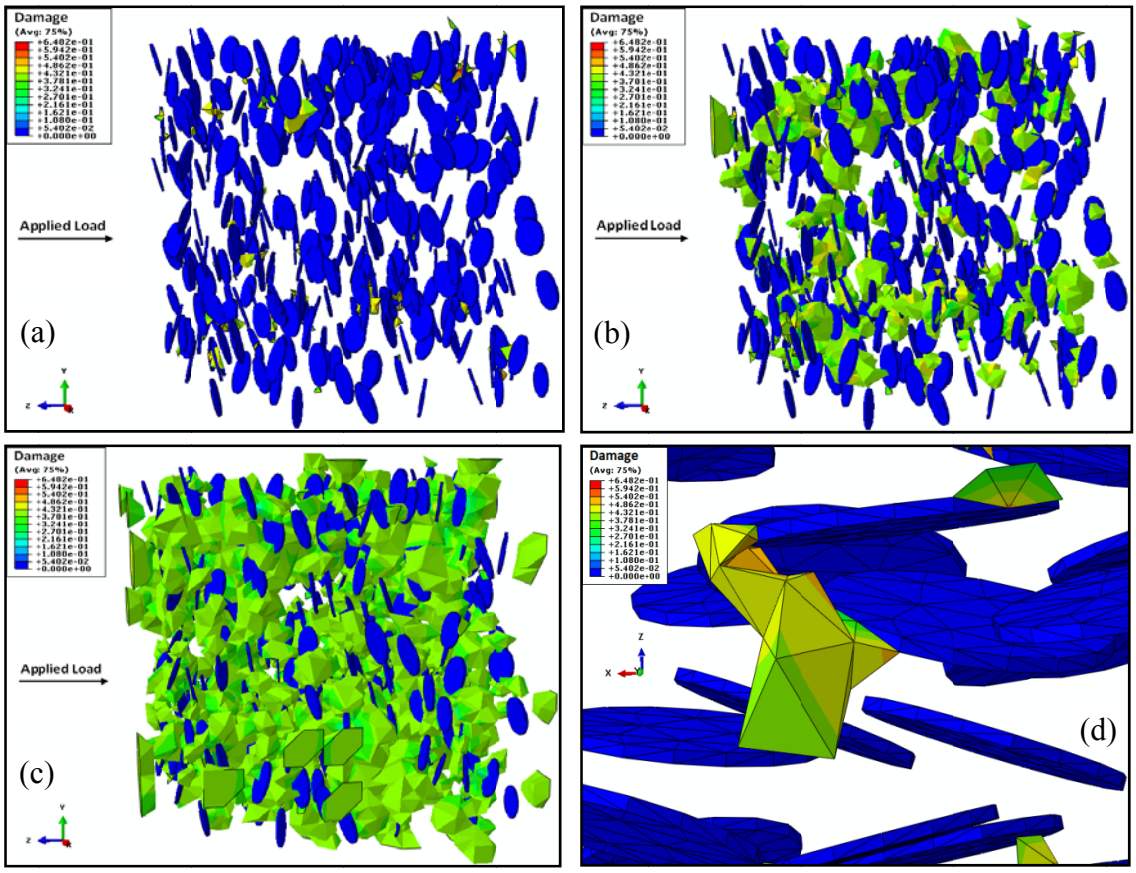

Fig. 9.12. Damage evolution in RVE with 1 vol% NCLPs, in compression: (a) to (c) Growth of damage, (d) Close view of damage propagation between particles and matrix.

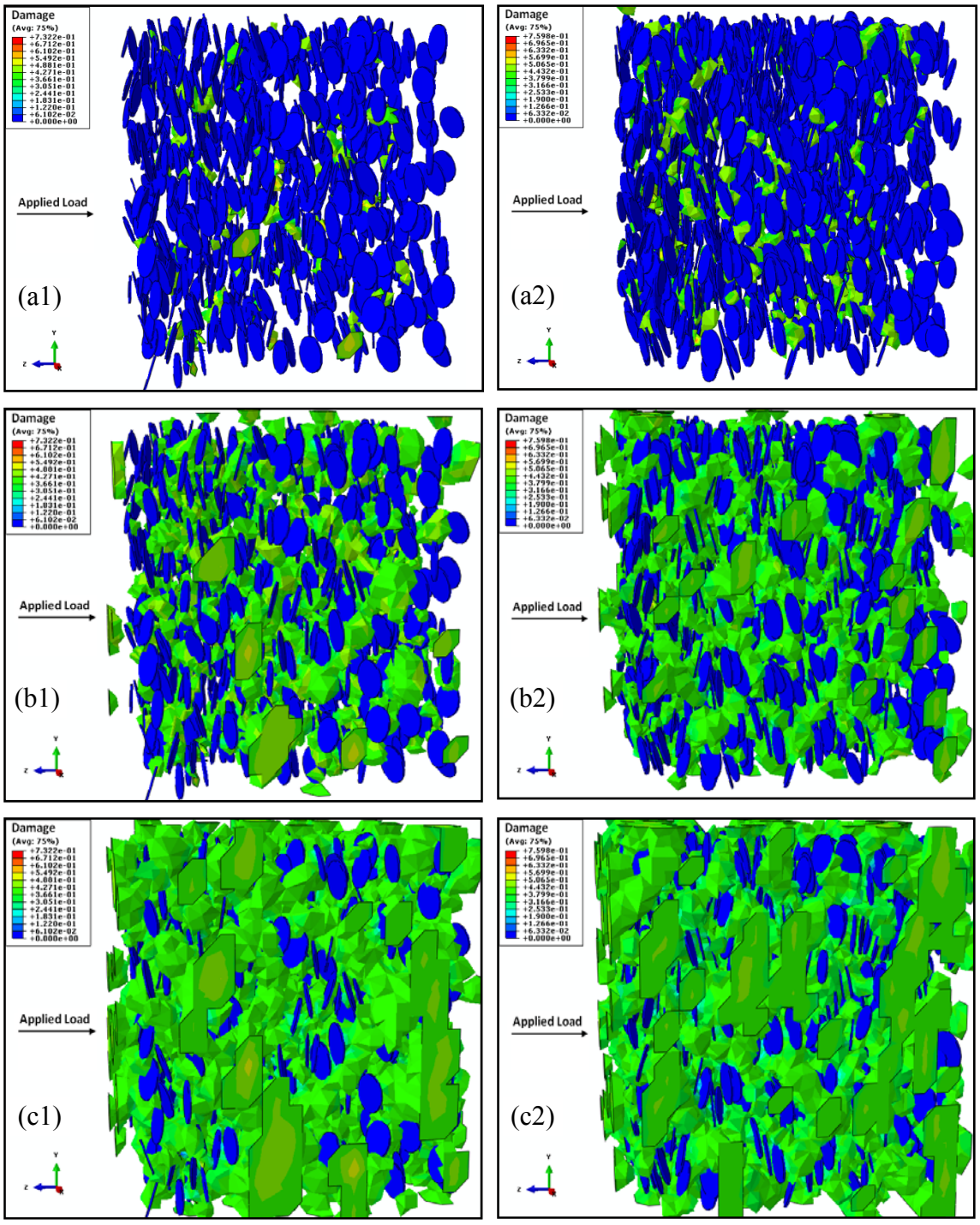

Fig. 9.13. Damage evolution in RVEs with NCLPs, in compression: (a1) to (c1) 2 vol%, and (a2) to (c2) 3 vol%.

Several finite element RVE models under displacement control test (both tension and compression) up to 30% strain were conducted, for simulating intercalated 3D NCLPs embedded in PMMA matrix. In the following, for the sake of conciseness, just the models under $\dot{\varepsilon} = 0.001/s$ displacement control test are depicted, unless mentioned. Comparing the magnitude and pattern of damage distribution in the polymer matrices, one can observe that although the maximum damage variable is higher as the particles volume fractions increase, the average value of damaged regions are less. In the following, the stress strain responses of the RVEs subjected to compressive load applied almost perpendicular to the major plane of the NCLPs are depicted in Fig. 9.14.

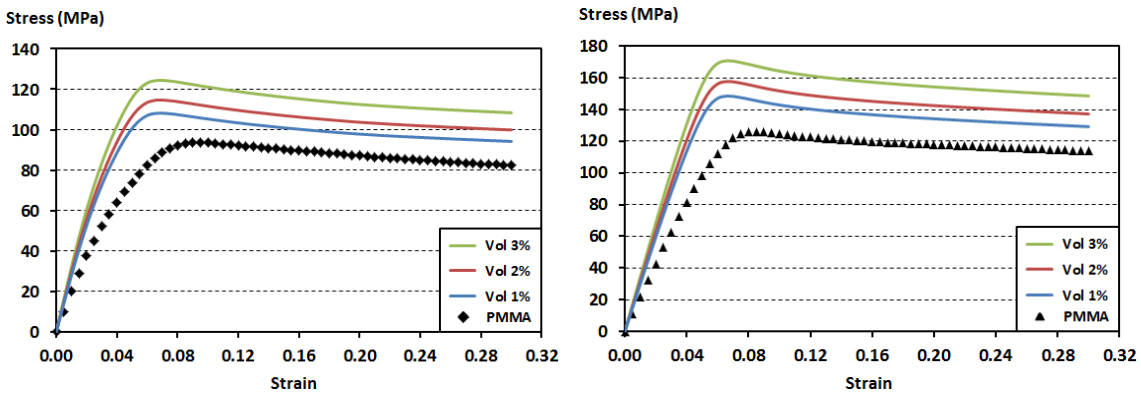

(a) $\dot{\varepsilon} = 0.001/\mathrm{s}$. (b) $\dot{\varepsilon} = 0.1/\mathrm{s}$.

Fig. 9.14. Stress-Strain response of RVEs containing NCLPs, in compression.

For the sake of briefness, in Fig. 9.15, the damage evolution of the RVE containing 3% NCLP which is subjected to tension load is shown. The same as damage distribution through compressive loading, the presence of particles is the main stimulation of damage initiation and propagation.

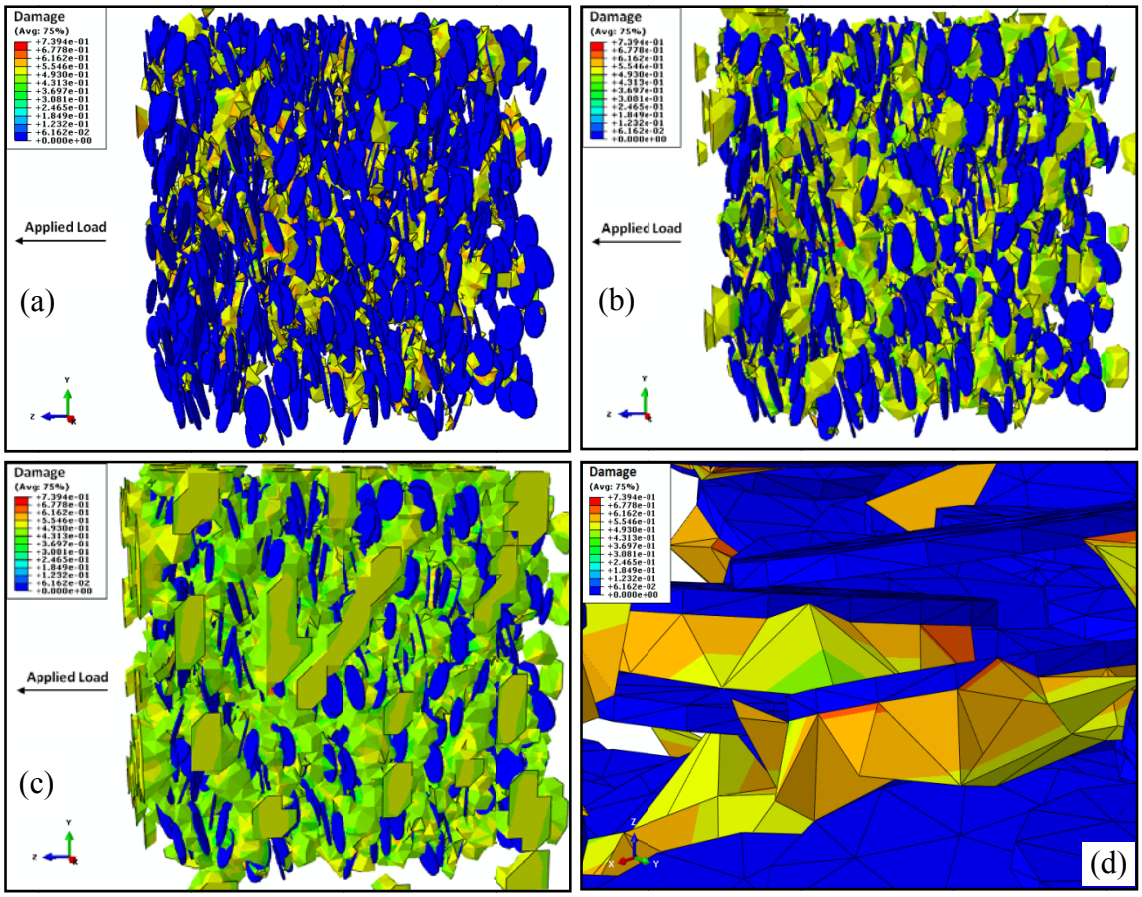

Fig. 9.15. Damage evolution in RVE with 3 vol% NCLPs, in tension: (a) to (c) Growth of damage, (d) Close view of damage propagation between particles and matrix.

The damage distribution contours (Fig. 9.12 (d)) for compression reveal that the damages nucleate at the tip (at the edge in front of the clay's major axis) of the clay particles, and then propagate through the inter-space gap between the major plane sheets of the particles. However, it can be seen in tension simulations (Fig. 9.15 (d)) that damage nucleation is initiated in between the clay plates, although in several sporadic locations damage is inspired at the tip of the particles, and the recent type of propagation is due to the 3D orientation of the NCLPs. Also, through using a Python script code in ABAQUS, the average value of the damage variable (φ; $0 < \varphi < 1$) can be computed and it is $\varphi \approx$

0.3, in compression and φ ≈ 0.42 in tension for the RVEs containing 3% NCLPs. It simply shows the amount of damage is more intense in tension comparing to compression load case, and it means 40% increase in the damaged regions has occurred. Moreover, the diagrams in Fig. 9.16 illustrate the stress-strain response of the NCLP/PMMA composites at two strain rates in tension, for three different volume fractions. It can be concluded that the trend of these curves and the magnitude of maximum stress changes linearly regarding the particles volume fractions. Also, no increase in elastic modulus is observable in these curves, regarding particles volume fractions. It can be seen that, the composites behave almost the same as each other up to 3% strain. As presented in Fig. 9.14 and 9.16, by comparing the responses of the composites with the behavior of pure polymer matrix (PMMA), the main enhancement in toughness and maximum strength happened when 1% NCLP is added to the matrix, and after that a linear enhancement trend is observed. Comparing Figs. 9.14 and 9.16, one can obtain the mechanical improvements of these composites are more pronounced during compressive load.

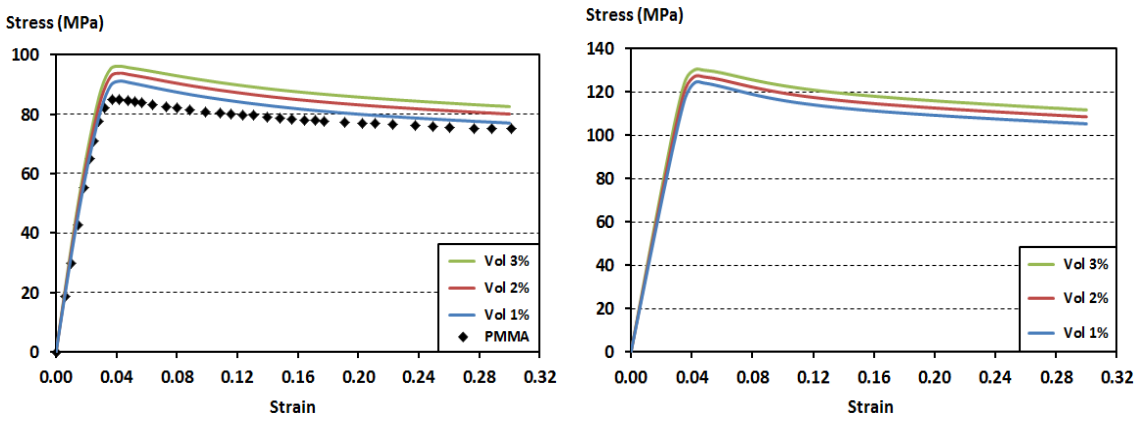

(a) $\dot{\varepsilon} = 0.001/\mathrm{s}$ (b) $\dot{\varepsilon} = 0.1/\mathrm{s}$

Fig. 9.16. Stress-Strain response of RVEs containing NCLPs, in tension.

9.4.2 Nano-Ceramics Polymer Composites

In this part, the damage initiation and evolution in the RVEs containing NCRPs are shown and discussed. The images of the damage contours inside the RVEs are separated and presented in two figures, Fig. 9.17 and Fig 9.18.

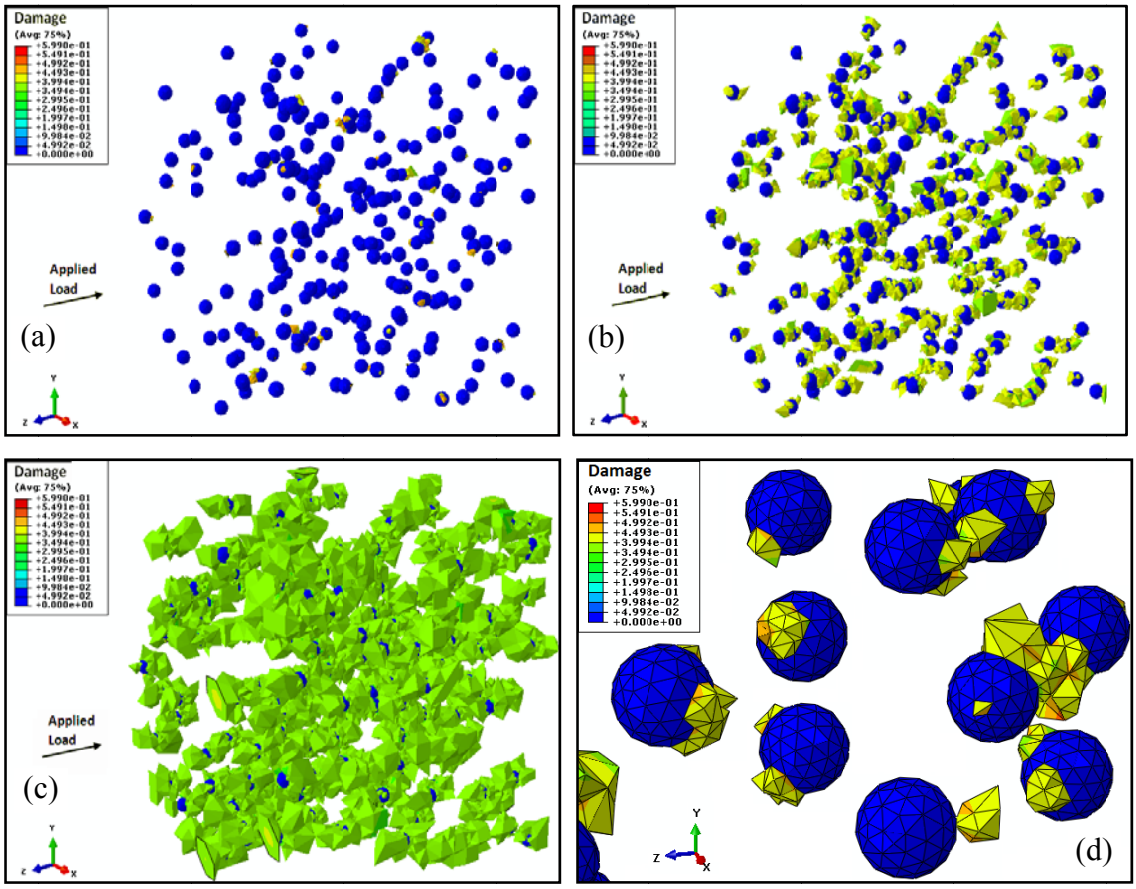

Fig. 9.17. Damage evolution in RVE with 1 vol% NCRPs, in compression: (a) to (c) Growth of damage, (d) Close view of damage propagation between particles and matrix.

In Fig. 9.17 from images (a) to (c), and Fig. 9.18 (a1) to (c1) and (a2) to (c2), one may observe that the damaged regions at first emerge at the top of the spherical particles, exactly in the direction of the applied compressive load.

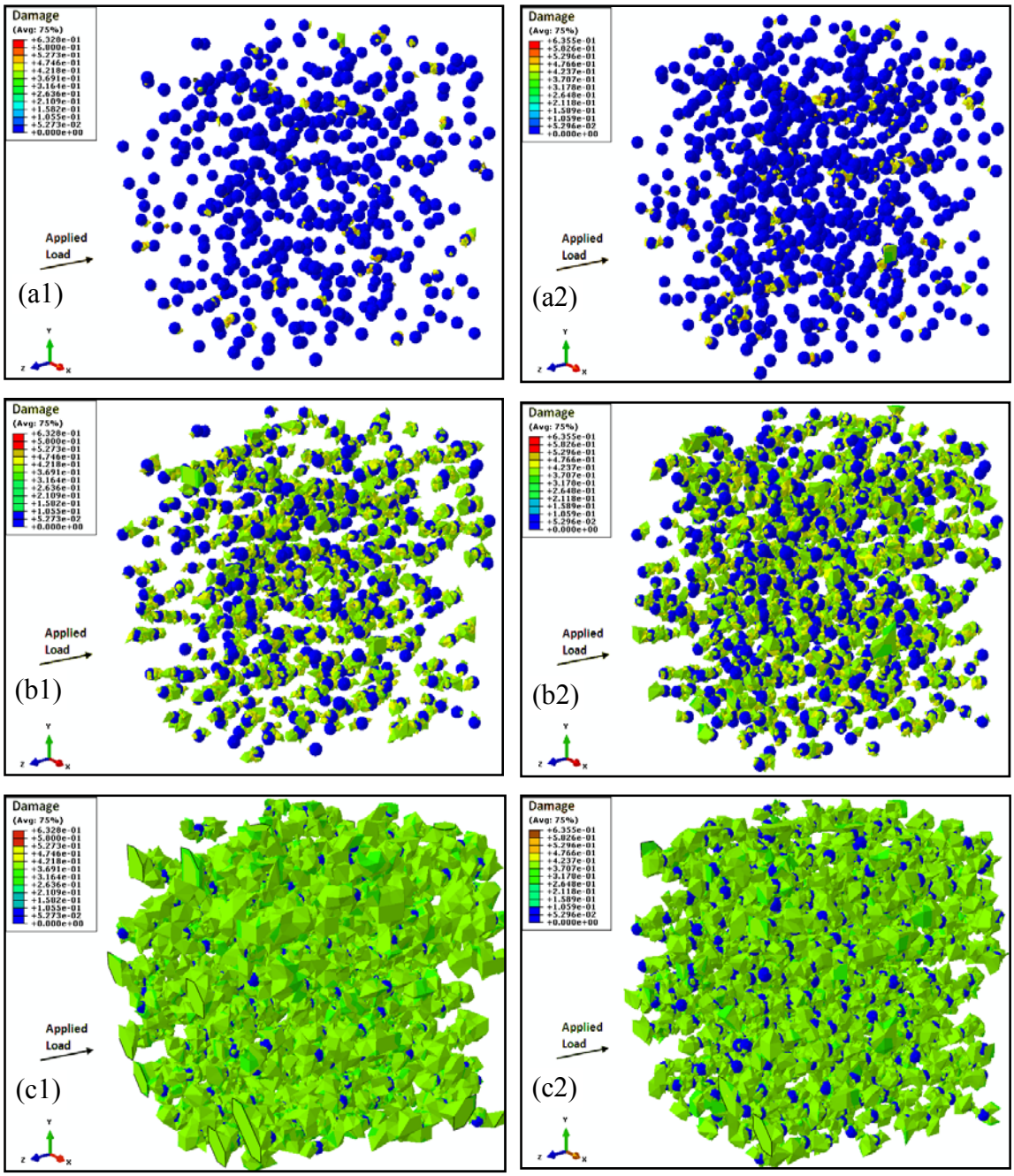

Fig. 9.18. Illustration of damage growth in RVEs with 2 and 3% NCRPs, in compressive load: (a1) to (c1) 2 vol%, and (a2) to (c2) 3 vol%.

Then the degraded parts of matrix at the top of the spheres turn around the same particles, and afterwards spread in the direction of the applied load in between the

neighboring inclusions. Thus, the damaged regions linearly propagate and merge together in the direction of load, which provide dispersed weak columns inside the RVE and lead to less stiffness. This phenomenon is better illustrated in Fig. 9.17 (d). The same damage initiation and growth pattern in tensile load can also be seen in the RVE with 3% NCRP in Fig. 9.19 (a) to (c). Fig. 9.19 (d), which is a close zoom of the particles and damaged elements, shows a better perspective of this damage evolution outline. Furthermore, the stress-strain diagrams of the simulated RVEs containing spherical ceramics subjected to two strain rates in both tension and compression are demonstrated.

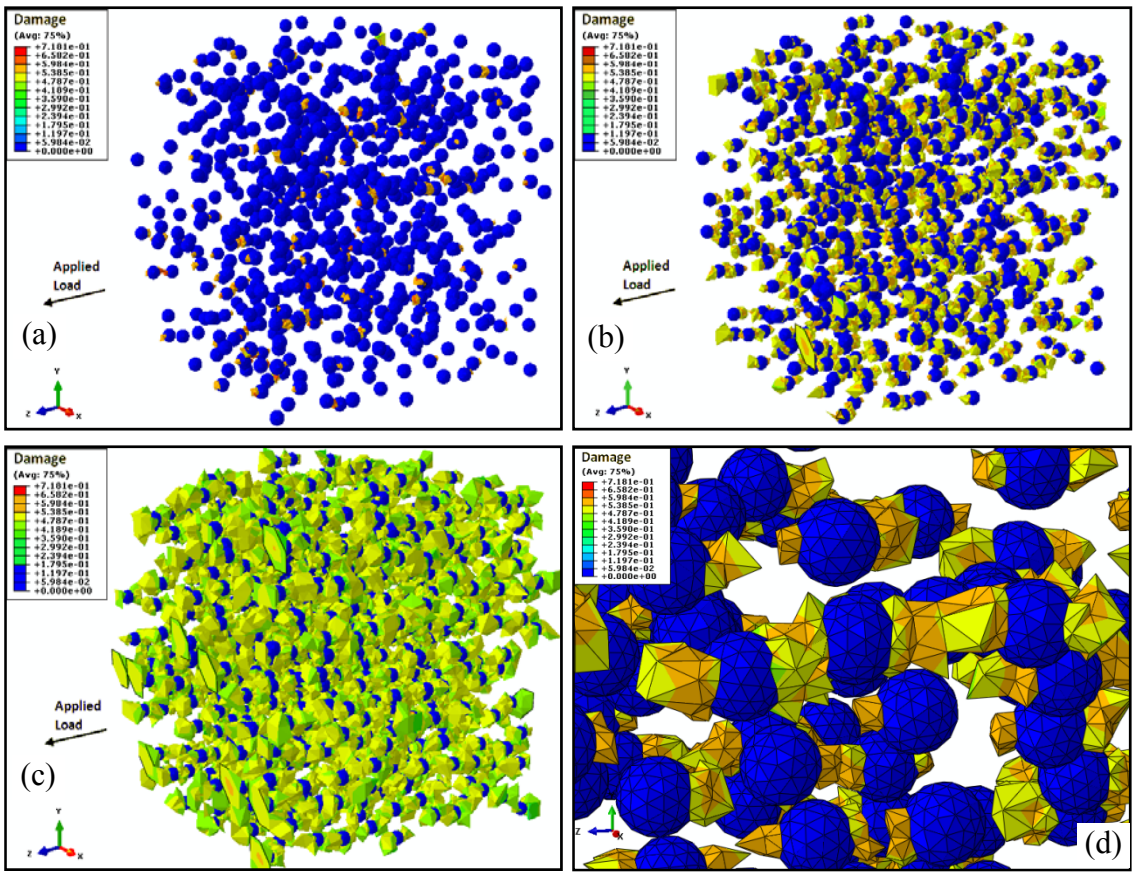

Fig. 9.19. Damage evolution in RVE with 3 vol% NCRPs, in tension: (a) to (c) Growth of damage, (d) Close view of damage propagation between particles and matrix.

As depicted in all images of Fig. 9.20, slight linear improvements in composites Young's modulus along with linear enhancement of the maximum peak stress and toughness are observable. Although maximum stress is increased, no considerable enhancement in toughness is seen in tensile simulations. It can be attributed to the presence of particles that stimulate more damage in the RVEs which leads to stiffness reduction of the host material. The spherical nano-ceramics show the same trend of stress-strain behavior similar to the nano-clay particles. Also, the mechanical effects of these particles are more evident in compressive loads rather than in tensile loads.

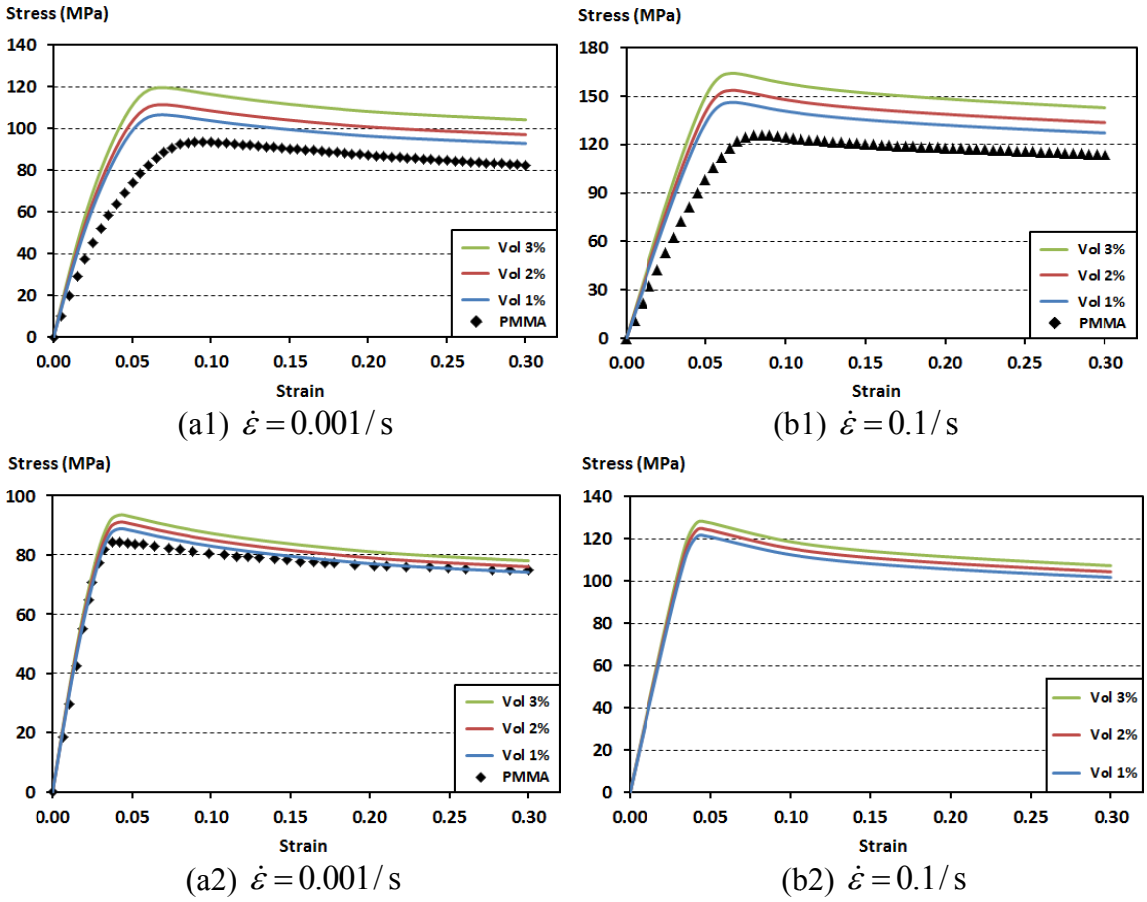

Fig. 9.20. Stress-Strain responses of RVEs containing NCRPs, at two different strain rates: (a1) and (b1) Compression load, (a2) and (b2) Tension load.

9.4.3 Carbon Nanotubes Polymer Composites

In this section, the damage growth in the RVEs containing CNTs are presented and discussed. At first, the CNTs with higher aspect ratios, as explained in section 9.3 are shown. Afterwards, the CNTs with smaller aspect ratios will be demonstrated and then compared with the ones with higher ARs. In Fig. 9.21, the formation of damage inside a composite containing a little amount of CNTs (0.1 vol%) subjected to compressive load is depicted. Damage is initiated from CNTs tips, and at first gradually propagates perpendicular to the CNTs axis, and then parallel to the CNT axis.

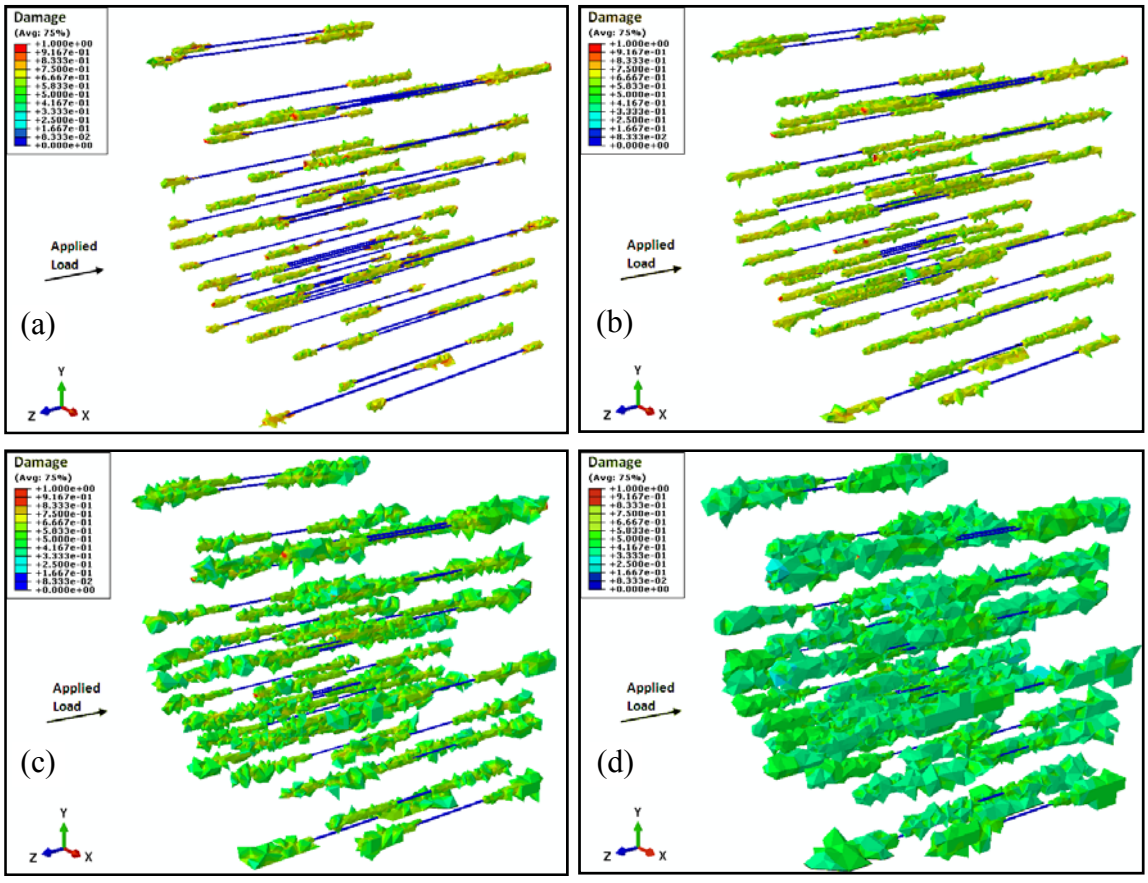

Fig. 9.21. Damage evolution in RVE with 0.1 vol% oriented CNTs in the direction of applied load, in compression: (a) to (c) shows the growth of damage.

It means the damaged regions at the CNT tips stimulate and drive more damage to the matrix, rather than the amplitude of the stress transformed between the CNTs and matrix.

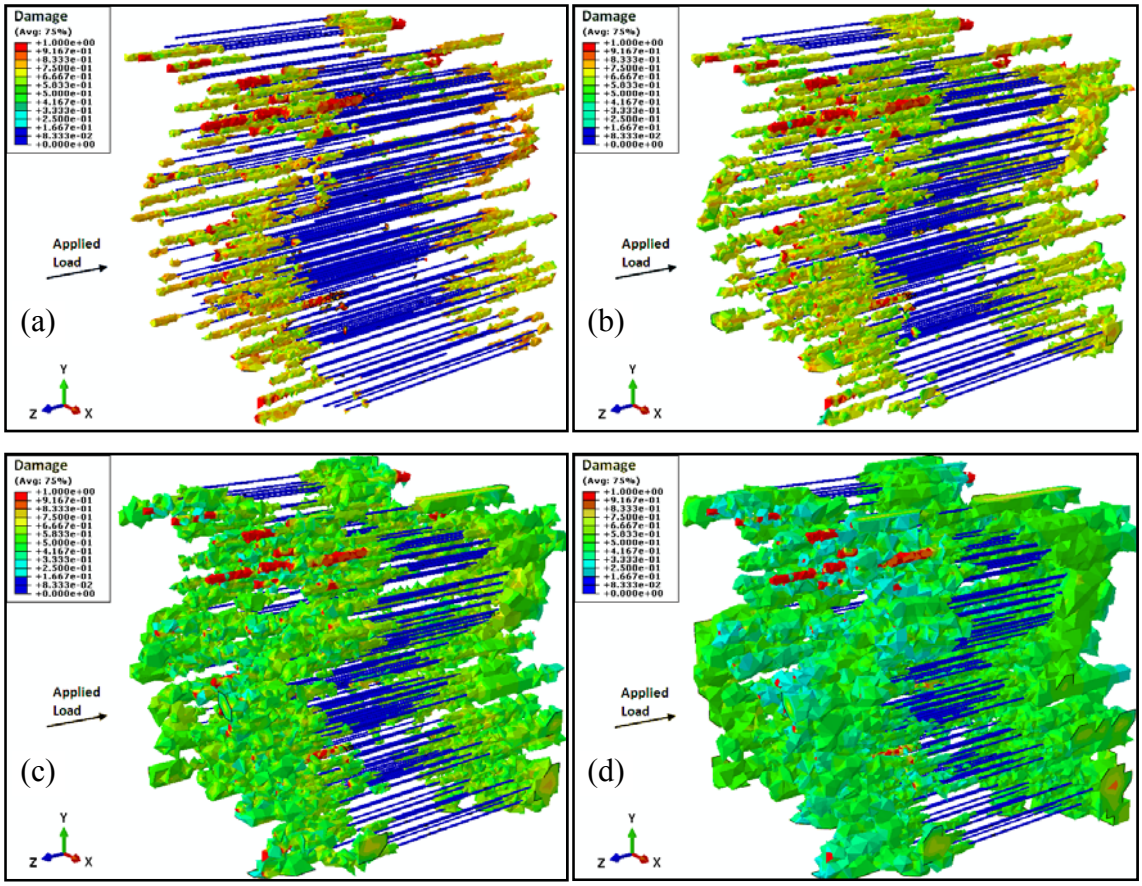

Fig. 9.22. Damage evolution in RVE with 0.5 vol% oriented CNTs in the direction of applied load, in compression: (a) to (c) shows the growth of damage.

This phenomenon can be attributed to the fact that, the straight CNTs are similar to rebars in reinforced concrete. But here, the polymer matrix is softer than concrete paste and the CNTs are stiffer than the steel rebars; therefore, the CNT rods are stiffer than the PMMA matrix in two orders of magnitude (about several hundred). Thus, applying compressive load to the top surface of the RVEs in the direction of CNTs is equivalent

to piercing the polymer matrix by the tiny CNT rods. Moreover, since the CNTs have two sharp stiff ends; hence, while compressing the RVEs, the both ends cause piercing the matrix and the initial damage occurs in those locations.

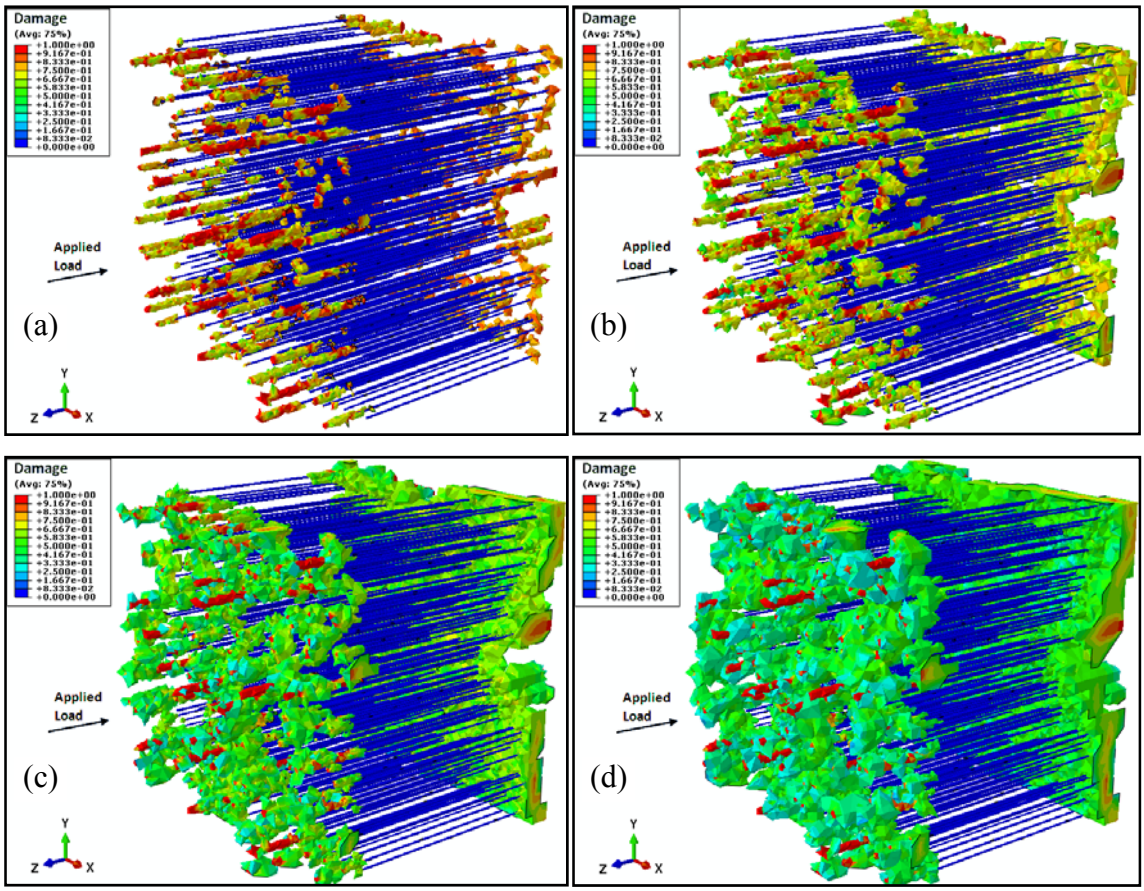

Fig. 9.23. Damage evolution in RVE with 1.0 vol% oriented CNTs in the direction of applied load, in compression: (a) to (c) shows the growth of damage.

As the volume fraction of CNTs increases (Figs. 9.22 and 9.23), more piercing damage happens, and less damage development regarding the transferred load between CNTs and matrix is observable. In tension (Fig. 9.24), similar to compression, the tips of the fibers induce damage. But in this case, large amounts of stress fields are canalized and

transferred to the CNTs at first via their tips and not their main body. Thus, the amount of the transferred stress at the tips leads to the initiation of damage in matrix.

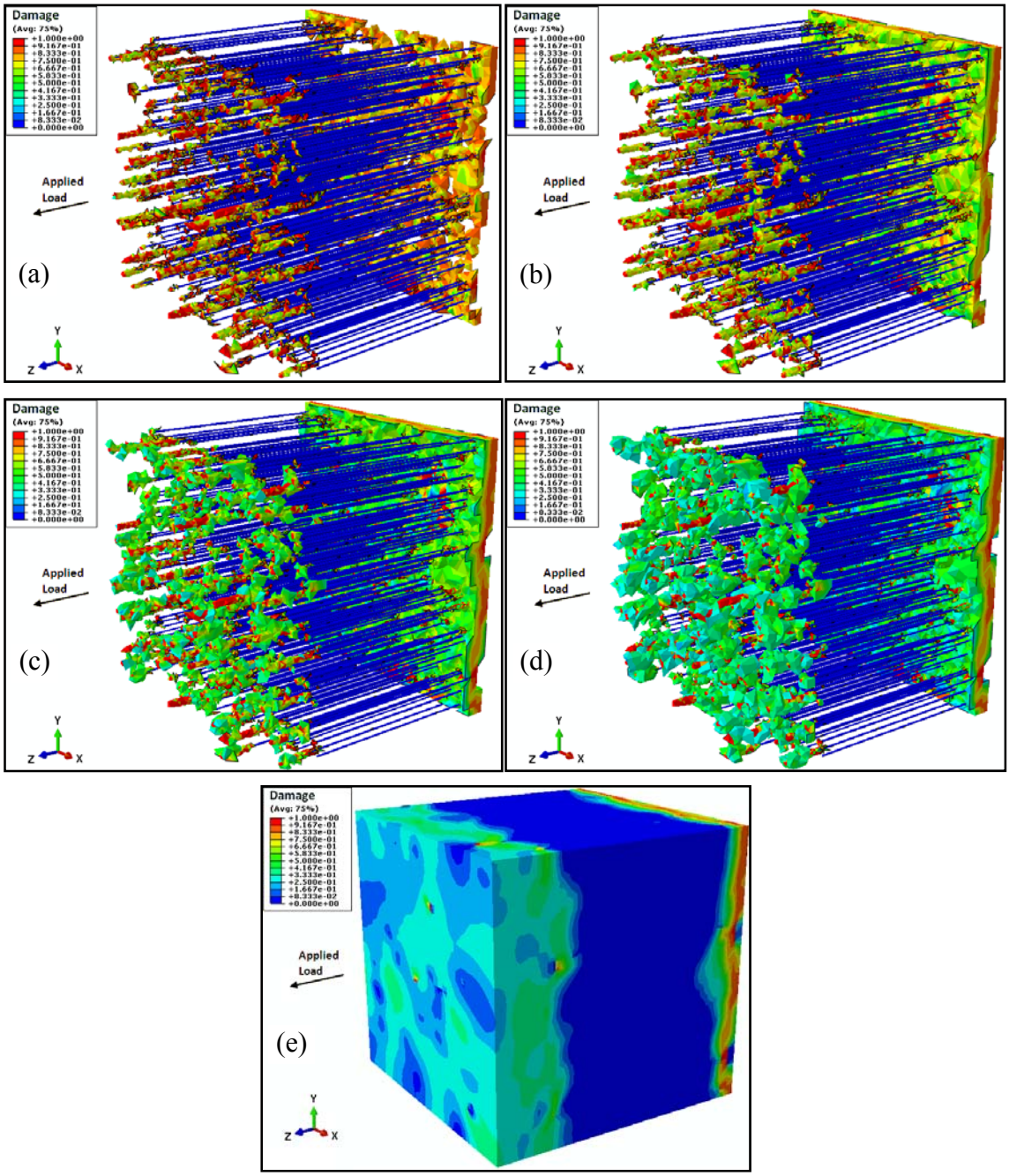

Fig. 9.24. Damage evolution in RVE with 1 vol% oriented CNTs aligned to tensile load: (a) to (d) Damage initiation and growth, (e) Overall view of damage pattern on RVE.

Here, the continuum damage concept is used; however, debonding of fibers and matrix should be probed in another study. As can be seen in previous models under compressive and tensile load, damage is high at the CNT tips and is very low around the main body of the reinforcing fibers, such that the middle parts almost do not induce damage into the surrounding matrix. For instance, Fig. 9.24 (e) shows the large middle part of the RVE is undamaged, and all damaged elements are concentrated at both ends of the tiny fibers. It leads to conclude that failure happens at the applied load surface and the constraint supporting faces. The stress fields in fibers confirm and explain this idea, as well.

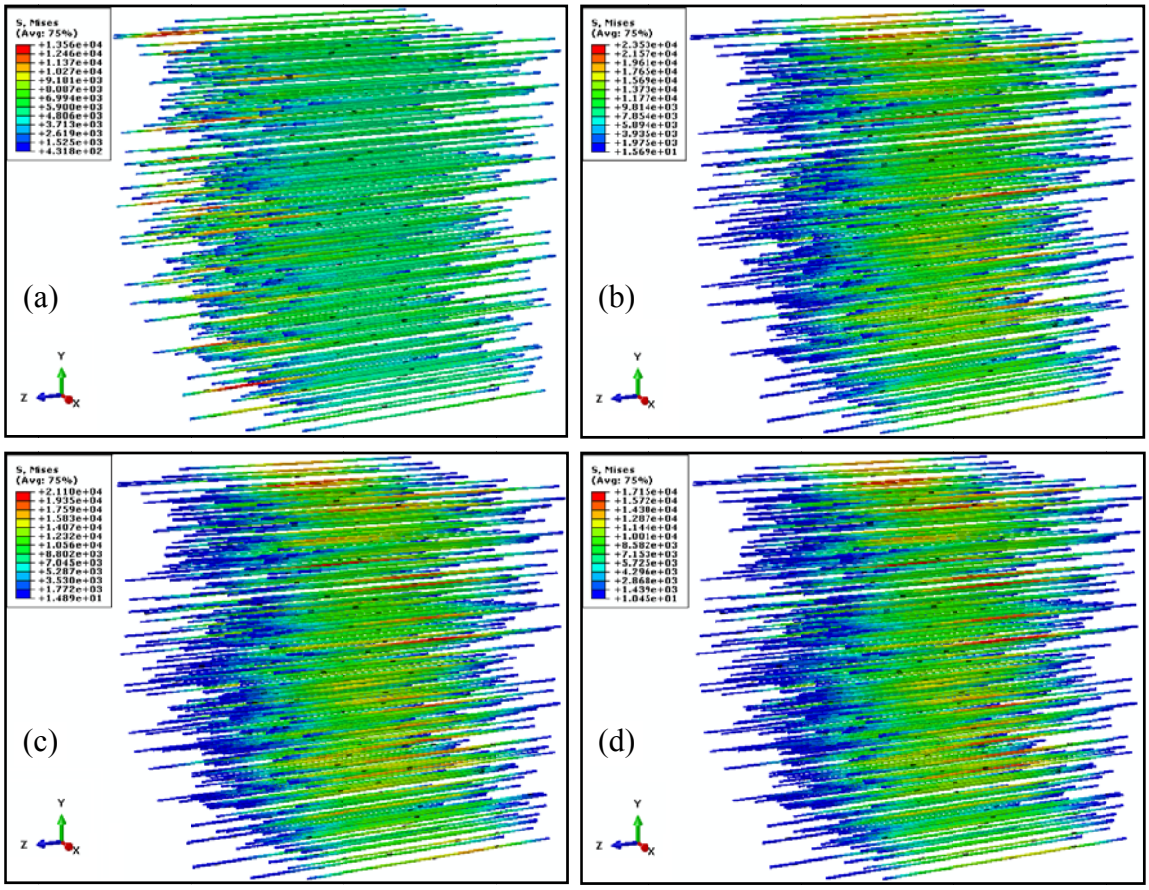

Fig. 9.25. Von Mises stress (MPa) during increasing load, in RVE with 1 vol% oriented CNTs, in compression, and $\dot{\varepsilon} = 0.001/\mathrm{s}$: (a) to (d) increase and distribution of stress.

Thus, in order to better explain this event, the distributions of von Mises stress for both loading cases are shown in Figs. 9.25 and 9.26. In these figures, one can observe the magnitudes of stress, at first (images (a)), at CNT tips are higher than the other segments. But, as the load increases (images (b) to (d)), and since the transferred load at the tips stimulate damage into the matrix, and damaged parts cannot carry more load; then, loads are conveyed via the main CNT bodies providing more contact surface in comparing to the tips. The damage distribution and the stress contours show the internal stress in RVEs is well transferred to CNTs and carried by them such that no damage is generated.

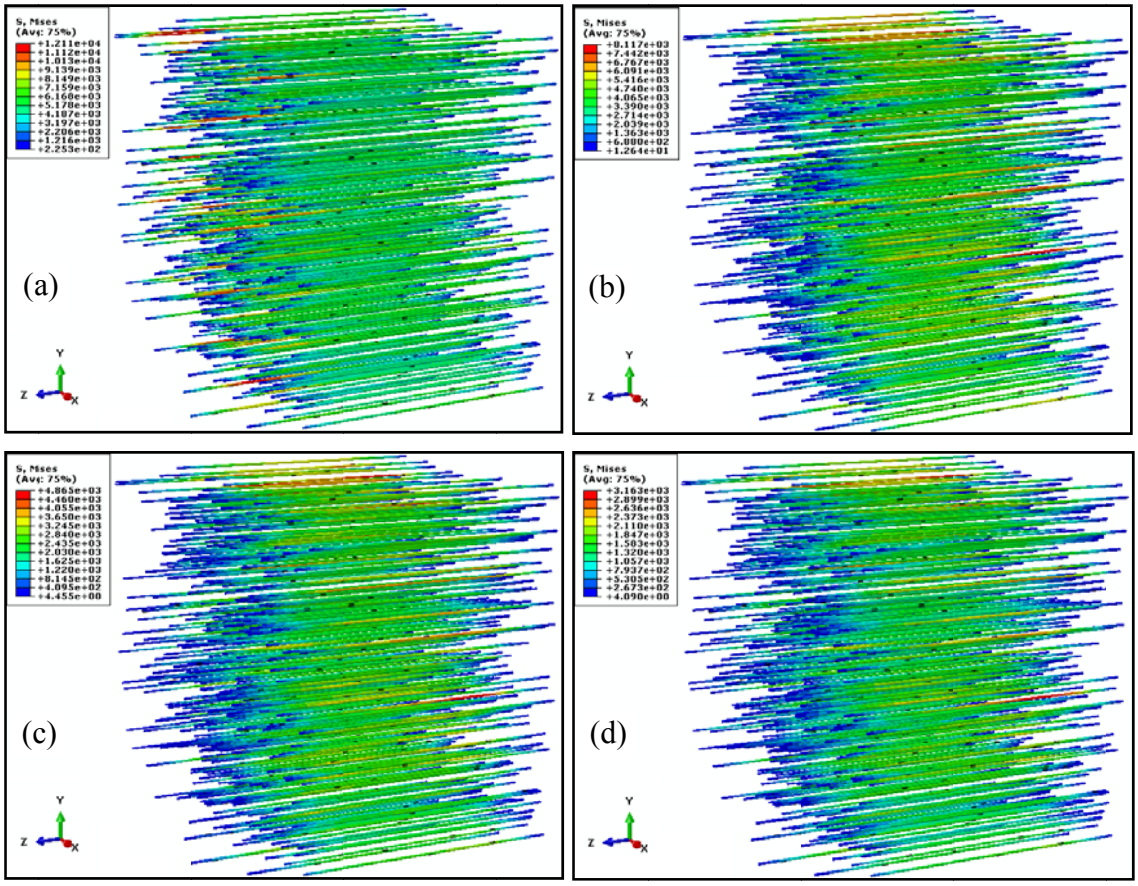

Fig. 9.26. Von Mises stress (MPa) during increasing load, in RVE with 1 vol% oriented CNTs, in tension, and $\dot{\varepsilon} = 0.001/\mathrm{s}$: (a) to (d) increase and distribution of stress.

Also, the stress-strain curves of the simulated samples, for the CNTs with higher aspect ratios, oriented in the direction of applied tension or compression, at two strain rates, are portrayed in Fig. 9.27. It is seen that the stress-strain response of the polymer composites is enhanced by increasing the volume percent of CNTs. Young's modulus, maximum strength, and strain hardening rates increase a little, and almost in linear outline, while increasing the CNTs. The damage intensification reduces the performance of the composites in tensile tests (images (a2) and (b2)), and it is more obvious while adding more CNT to the system.

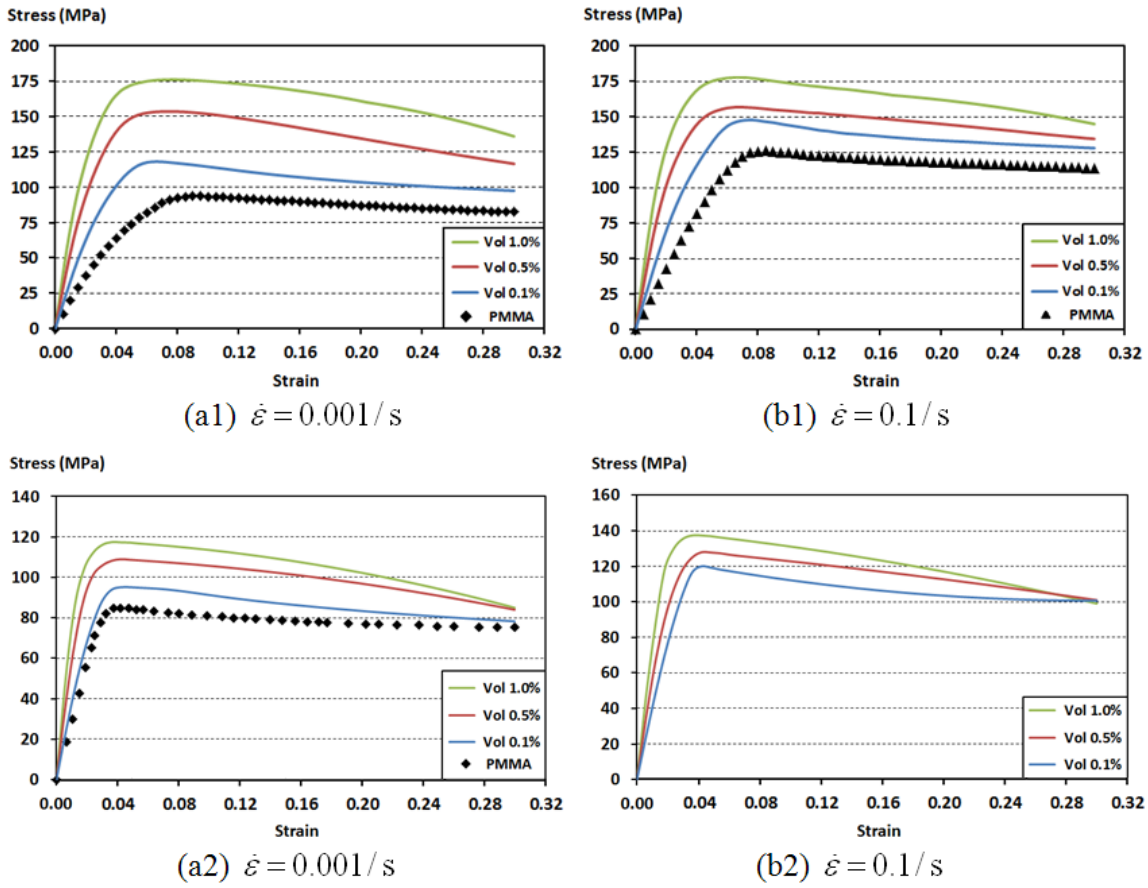

Fig. 9.27. Stress-strain response of RVEs containing oriented CNTs, at two different strain rates: (a1) and (b1) Compressive load, (a2) and (b2) Tensile load.

In the following, the overall responses and damage initiation and evolutions in the RVEs containing curved CNTs are presented, in Figs. 9.28 to 9.33.

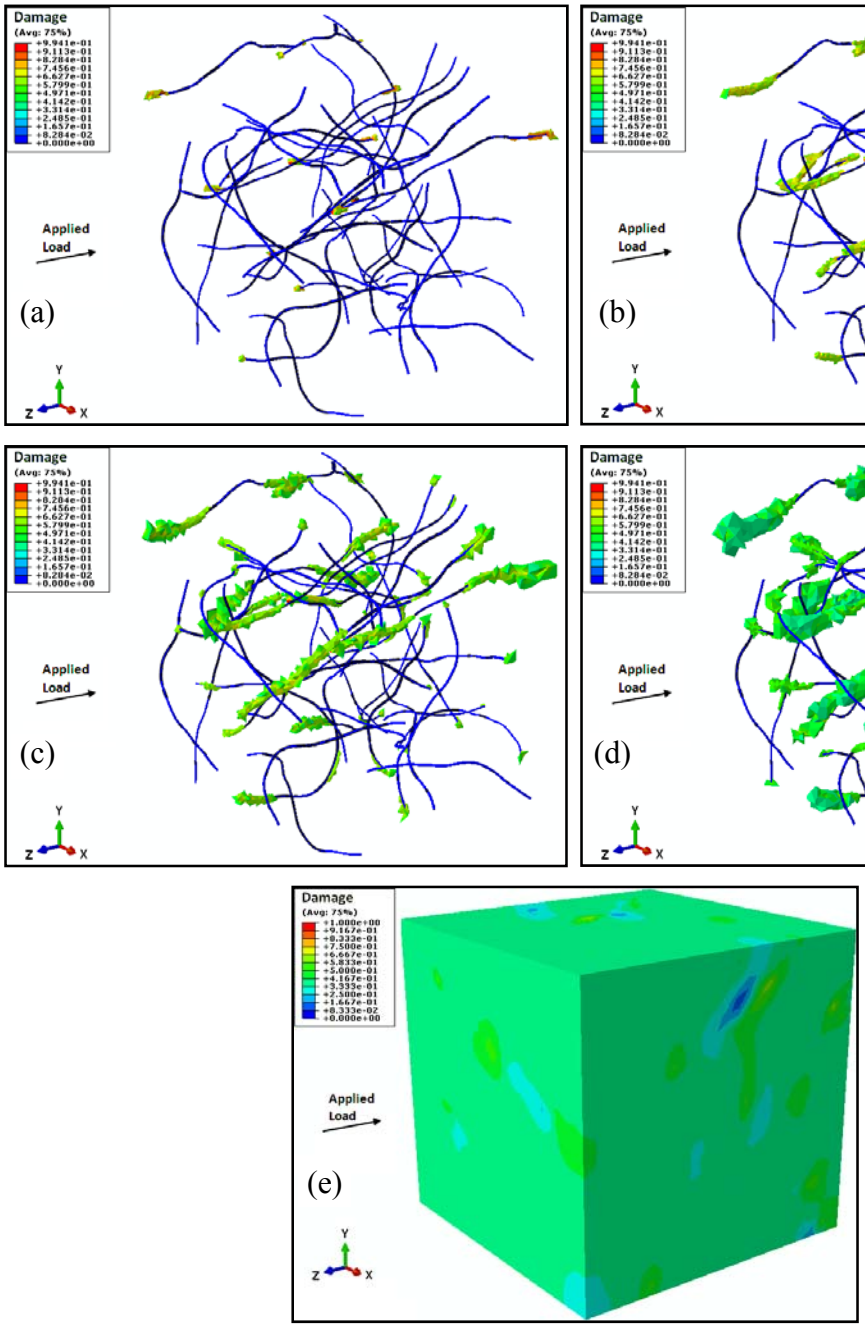

Fig. 9.28. Damage evolution in RVE with 0.1 vol% curved CNTs, under compression: (a) to (d) Damage initiation and growth, (e) Overall view of damage pattern on RVE.

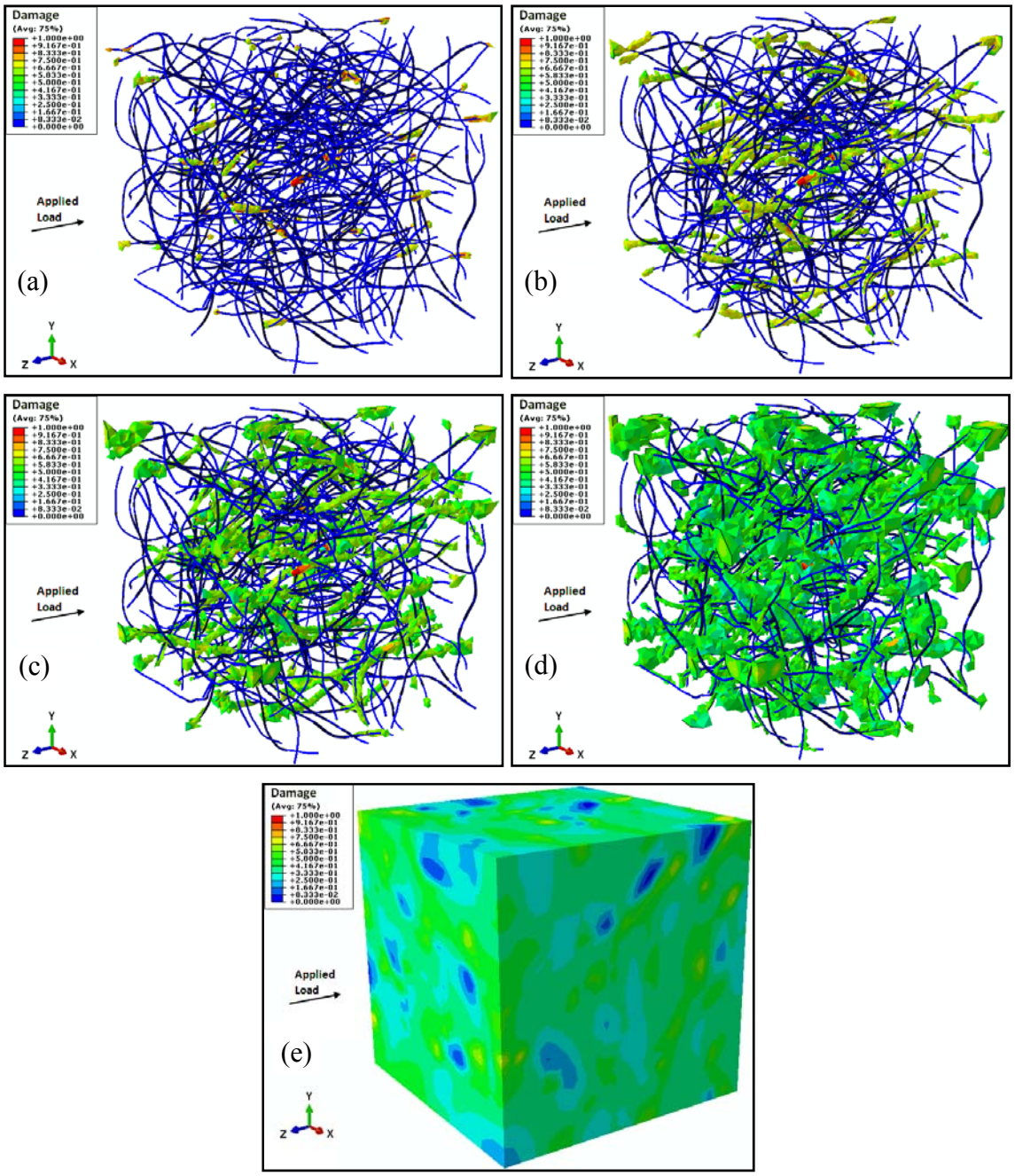

Fig. 9.29. Damage evolution in RVE with 0.5 vol% curved CNTs, under compression: (a) to (d) Damage initiation and growth, (e) Overall view of damage pattern on RVE.

Similar to the straight CNT cases under compressive load, damage is very high at the tip of CNTs and is very low around their main bodies, such that the central parts of the

fibers almost do not generate damage into the surrounding polymer matrix. But, just those CNT tips that are parallel to the direction of the applied load cause initial damage.

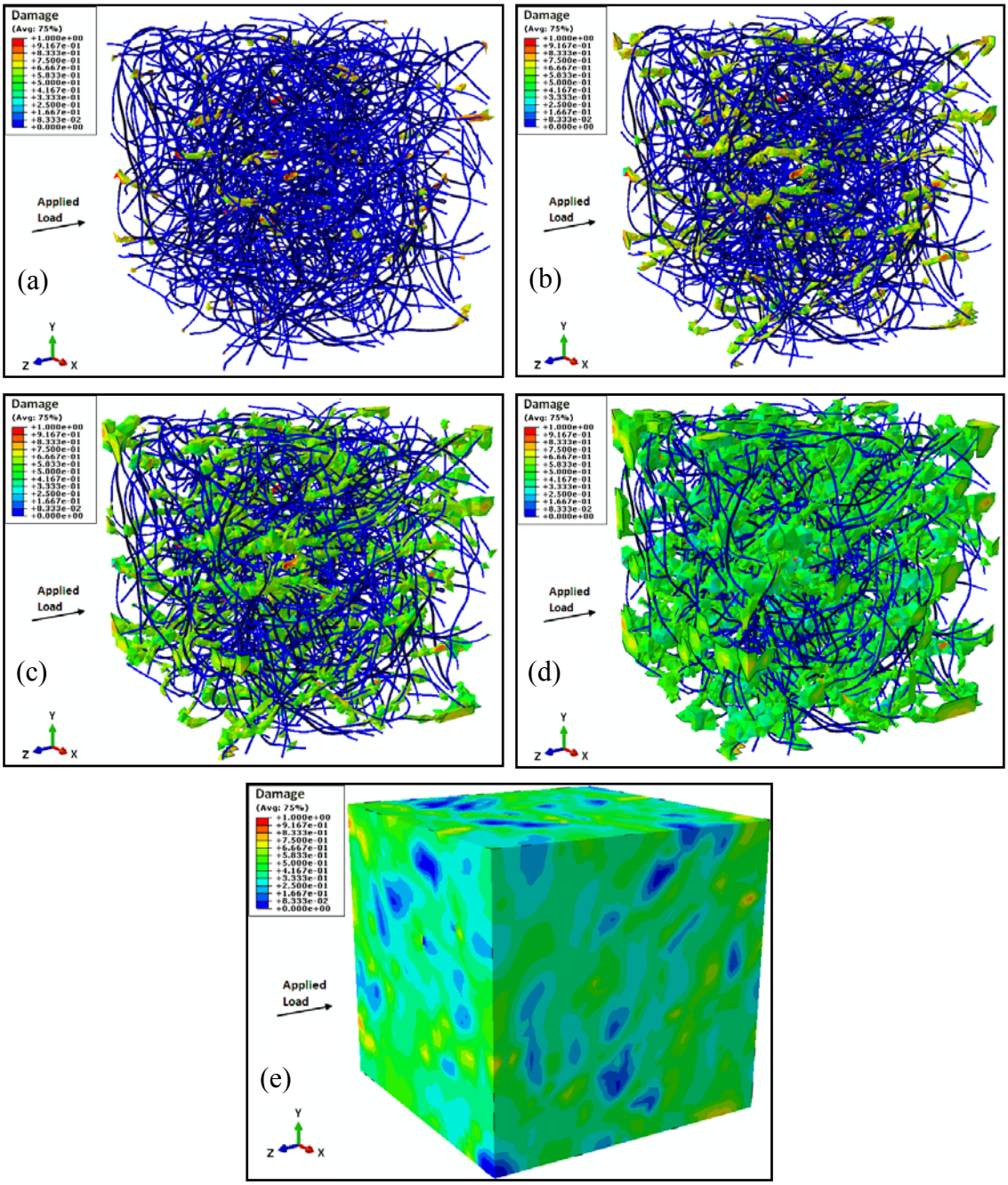

Fig. 9.30. Damage evolution in RVE with 1.0 vol% curved CNTs, under compression: (a) to (d) Damage initiation and growth, (e) Overall view of damage pattern on RVE.

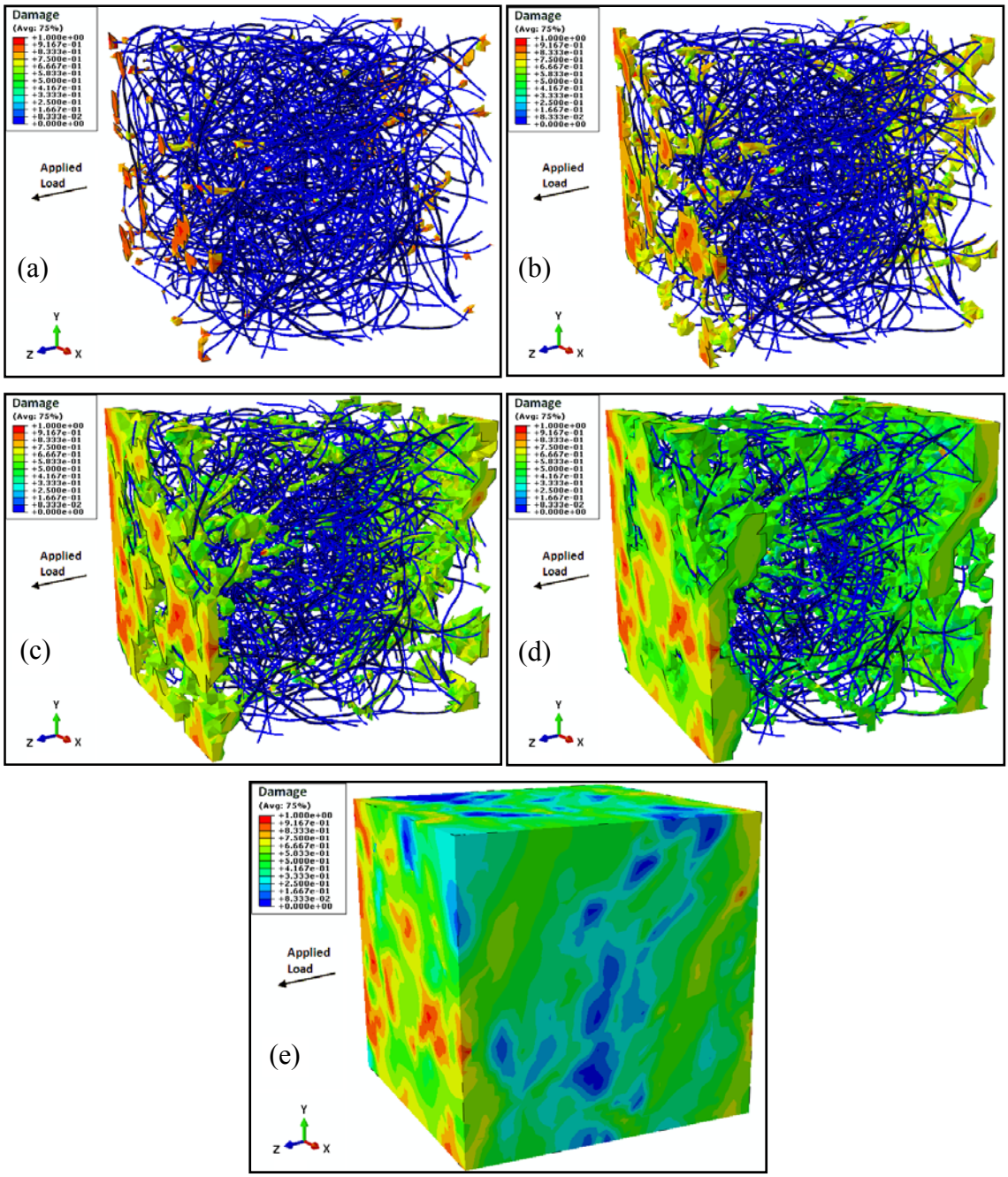

Fig. 9.31. Damage evolution in RVE with 1.0 vol% curved CNTs, under compression: (a) to (d) Damage initiation and growth, (e) Overall view of damage pattern on RVE.

The same scenario is repeated in tensile loading (Fig. 9.31); i.e. the damage in the host material (PMMA) commences at the CNT tips whose fiber segments are parallel to the

applied tension load. This performance is similar to the behavior of the CNTs oriented to the applied load. Curved fibers are bent inside the matrix of the RVEs under both tension and compression, and besides since the curved fibers with high aspect ratios do not resist against bending moments (they perform as wires or threads); thus, the fibers main curved bodies do not act to carry a big portion of the applied load. Analogous to the oriented CNTs (shown in Fig. 9.25 and 9.26), in the following the distribution of von Mises stresses in the curved CNTs are depicted.

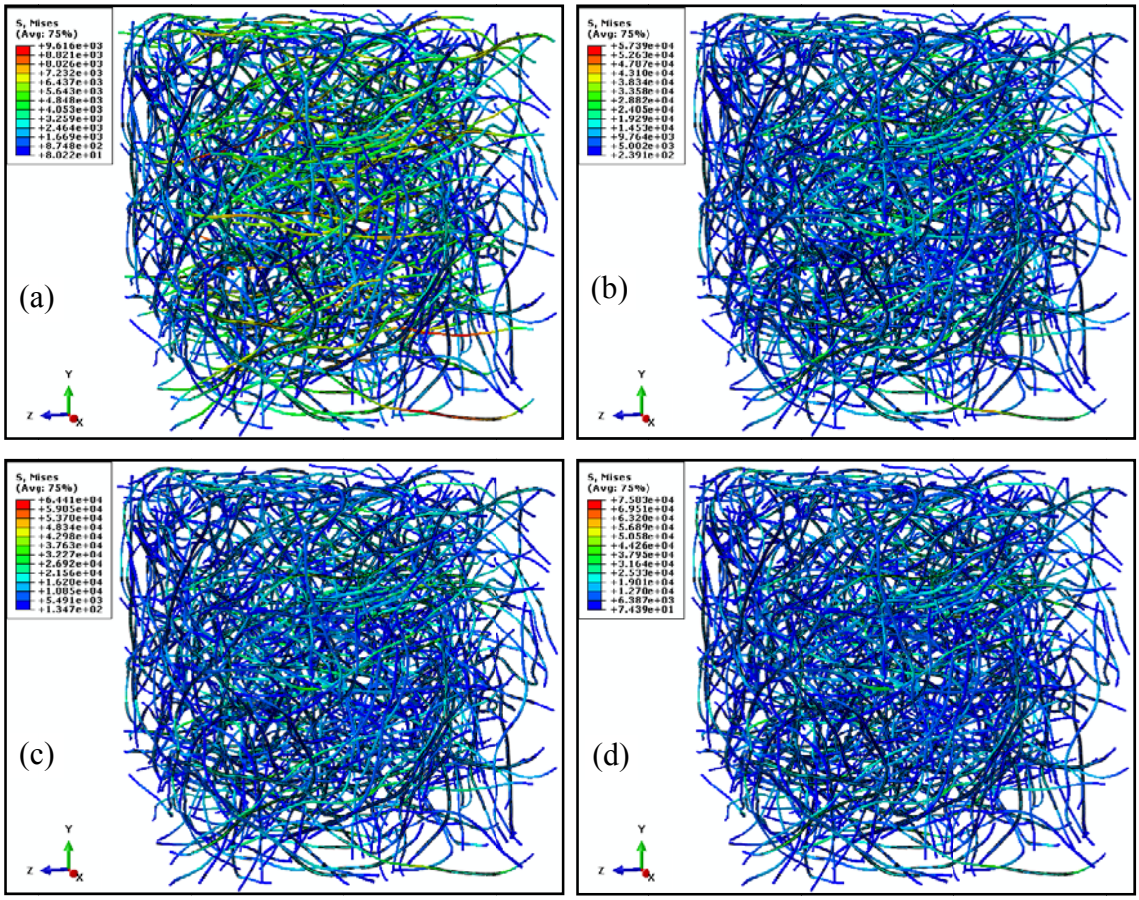

Fig. 9.32. Von Mises stress (MPa) during increasing load, in RVE with 1 vol% curved CNTs, in compression, and $\dot{\varepsilon} = 0.001/\mathrm{s}$: (a) to (d) increase and distribution of stress.

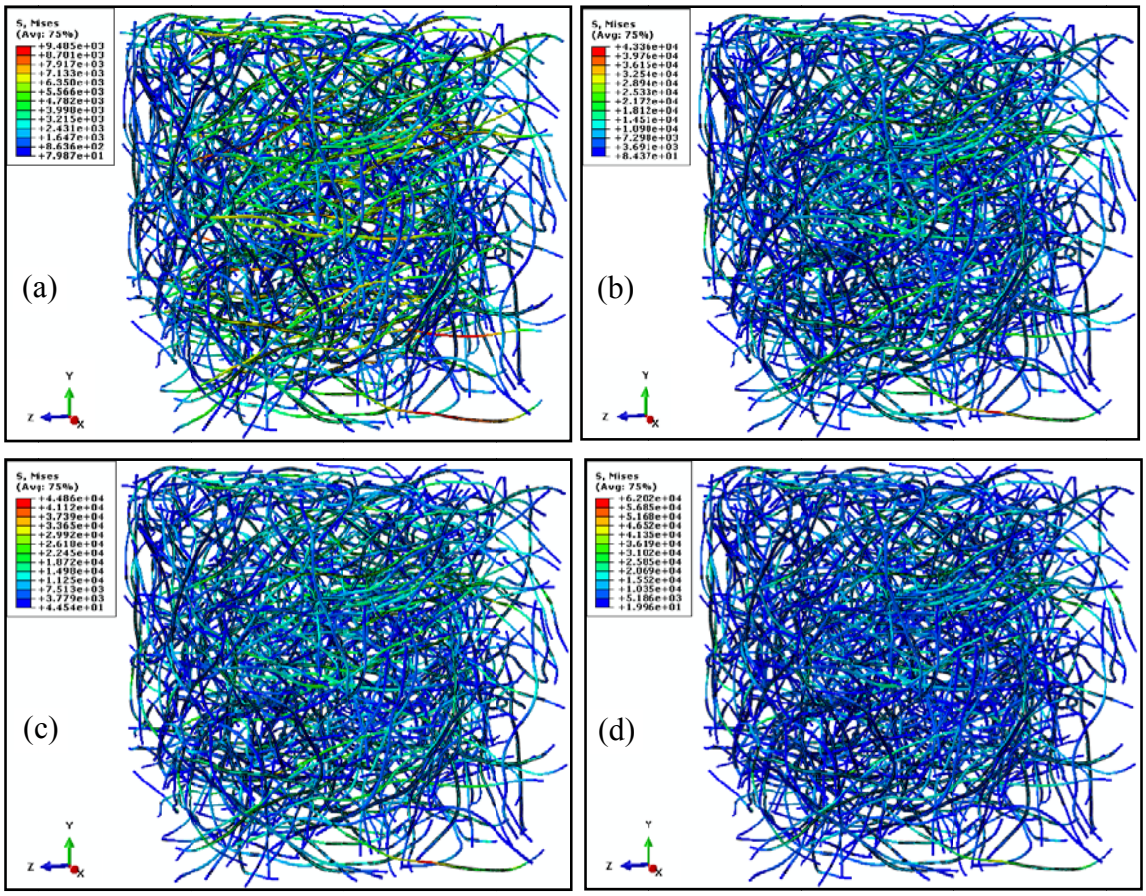

Fig. 9.33. Von Mises stress (MPa) during increasing load, in RVE with 1 vol% curved CNTs, in tension, and $\dot{\varepsilon} = 0.001/\mathrm{s}$: (a) to (d) increase and distribution of stress.

Figs. 9.32 and 9.33 show that at first (in images (a)) the tips of those CNT segments aligned in the applied load direction carry more stress that induce damage to the matrix. Then, the internal stresses fields are transferred to the CNT segments aligned to the load direction, which cause the tips of the CNTs relieve the carried load. However, the von Mises stress contours demonstrate the CNT segments which are not placed in the direction of the applied load do not experience to carry load, and consequently no damage is stimulated by their curved segments. Also, the stress-strain curves of the simulated RVEs, for the curved CNTs with higher aspect ratios subjected to tension or

compression loads (at two strain rates), are portrayed in Fig. 9.34. The diagrams reveal that in compression tests, a linear trend of enhancement of Young's modulus, maximum stress and toughness can be obtained due to increasing the curved CNTs. The same trend is observed in tension tests, as well. However, since the magnitude of damage is more intensive in tensile tests, adding more CNTs causes reduction in toughness.

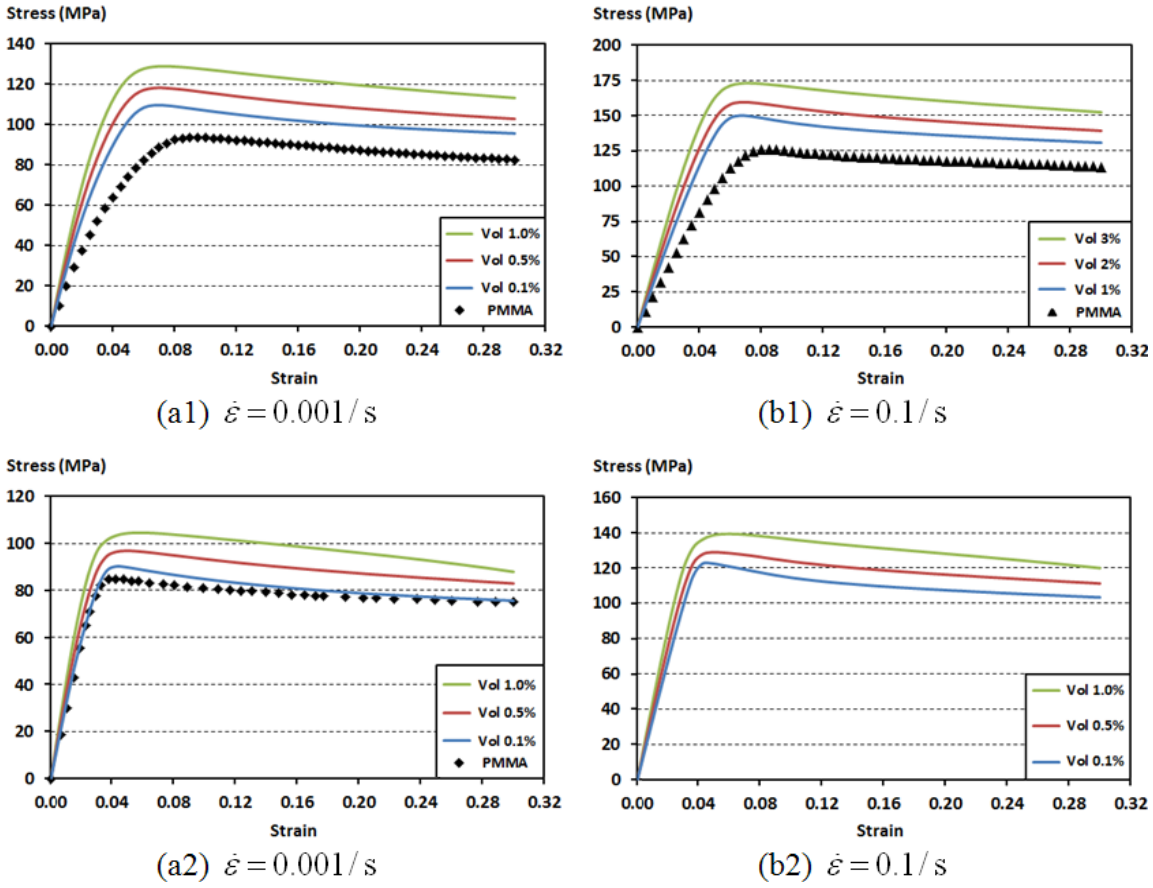

Fig. 9.34. Stress-Strain response of RVEs containing curved CNTs, at 2 different strain rates: (a1) and (b1) Compression load, (a2) and (b2) Tension load.

One of the main parameters governing the CNT-based composite behavior is the fibers aspect ratios; thus here, the effects of this geometrical variable on the overall response of

the RVEs are presented and discussed. At first, all CNT configurations are shown in Figs. 9.35 and 9.36, and for briefness just oriented and curved CNTs are depicted.

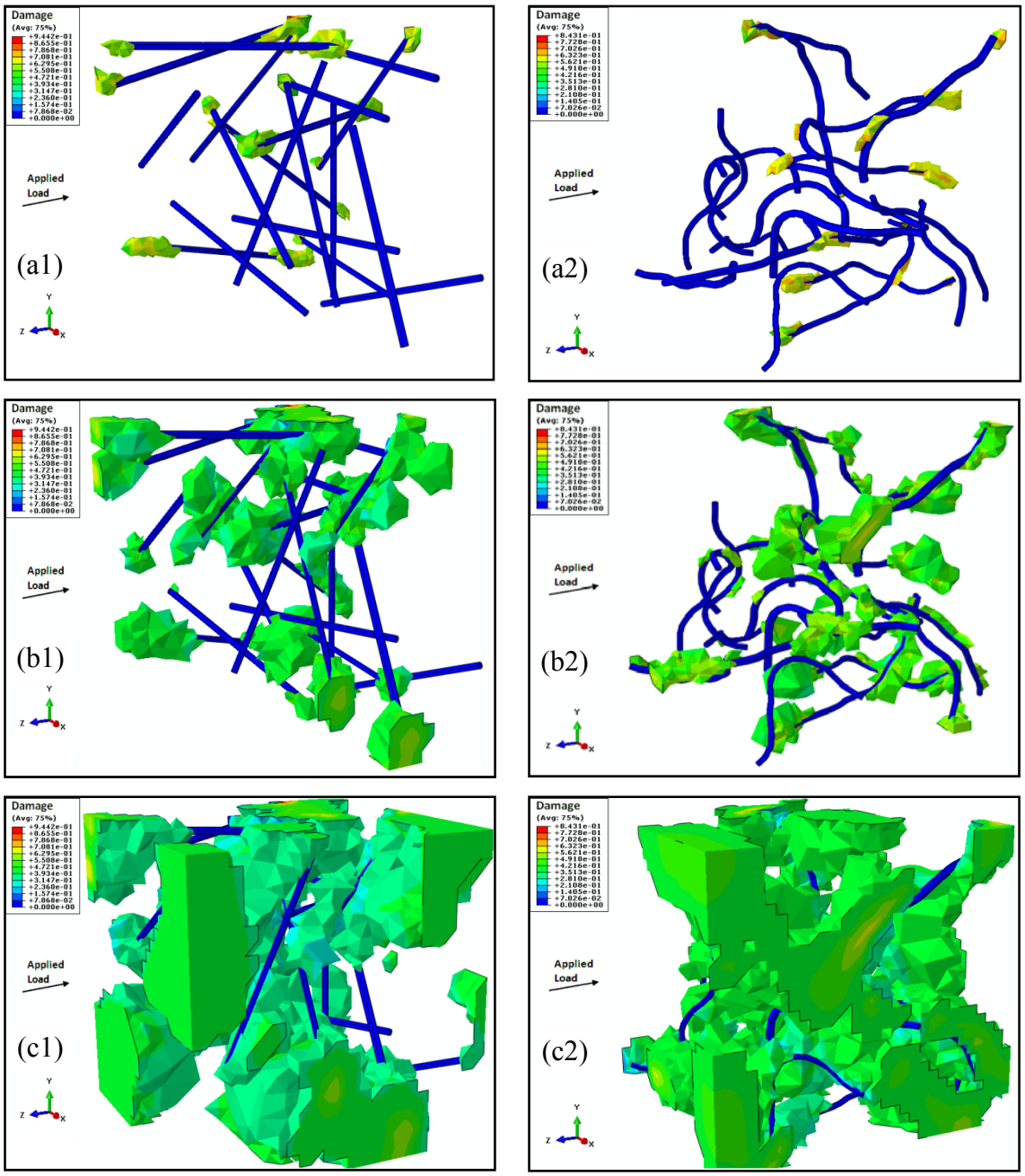

Fig. 9.35. Damage nucleation and growth inside RVEs with 0.5% CNT (AR ≈ 11), under compressive load: (a1) to (c1) Random rod CNTs, and (a2) to (c2) Curved CNTs.

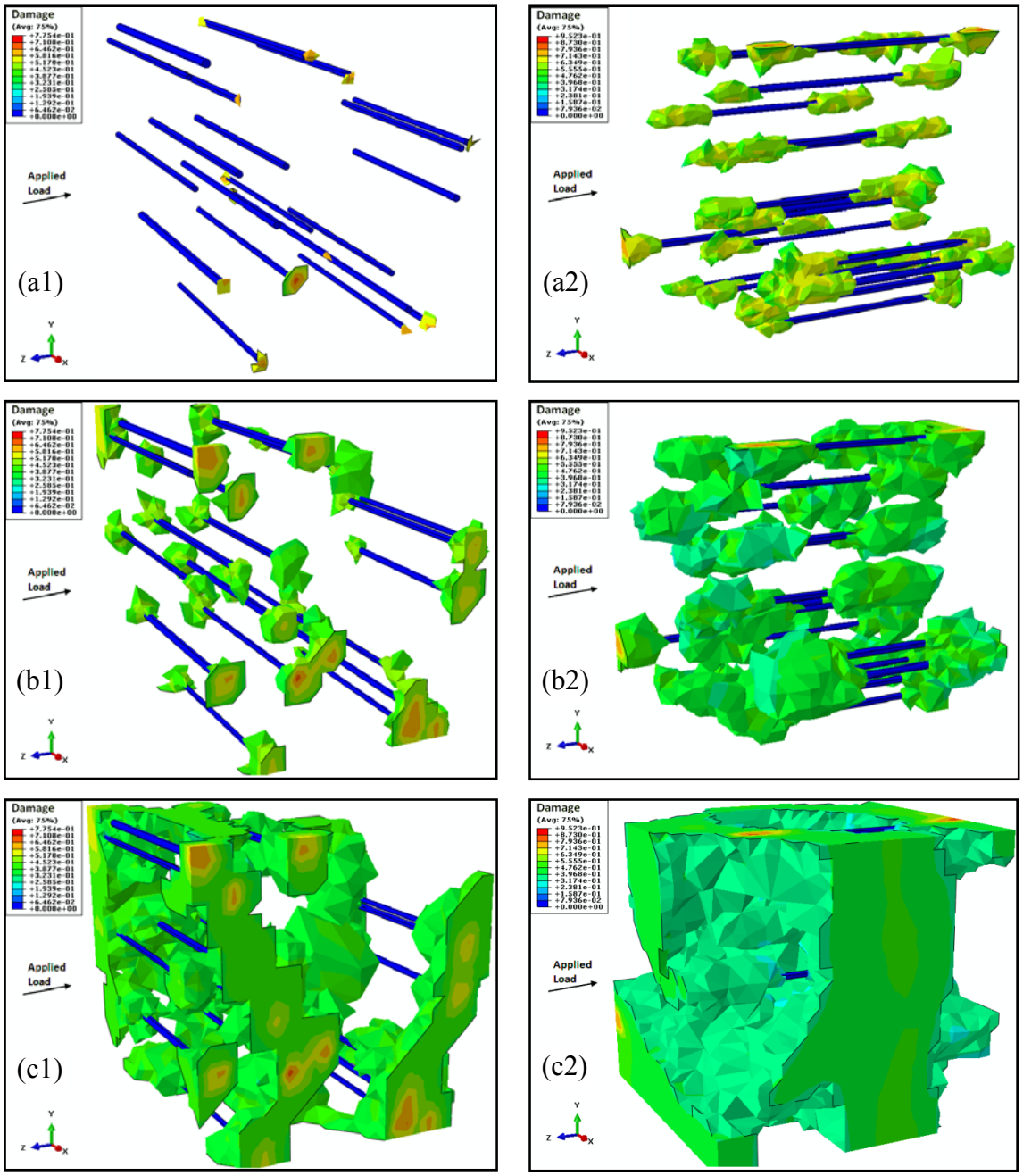

Fig. 9.36. Damage nucleation and growth in RVEs with 0.5 vol% CNT (AR ≈ 11) under compressive load; CNTs oriented in: (a1) to (c1) *X*-direction and (a2) to (c2) *Z*-direction.

According to Figs. 9.35 and 9.36, for all cases, damage is stimulated and initiated at the tips of CNTs. However, the magnitude of damage is highest when the fibers are oriented

in load direction, and is lowest when aligned perpendicular to the load. The maximum and average magnitude of damage in curved and *X*-direction cases are almost the same.

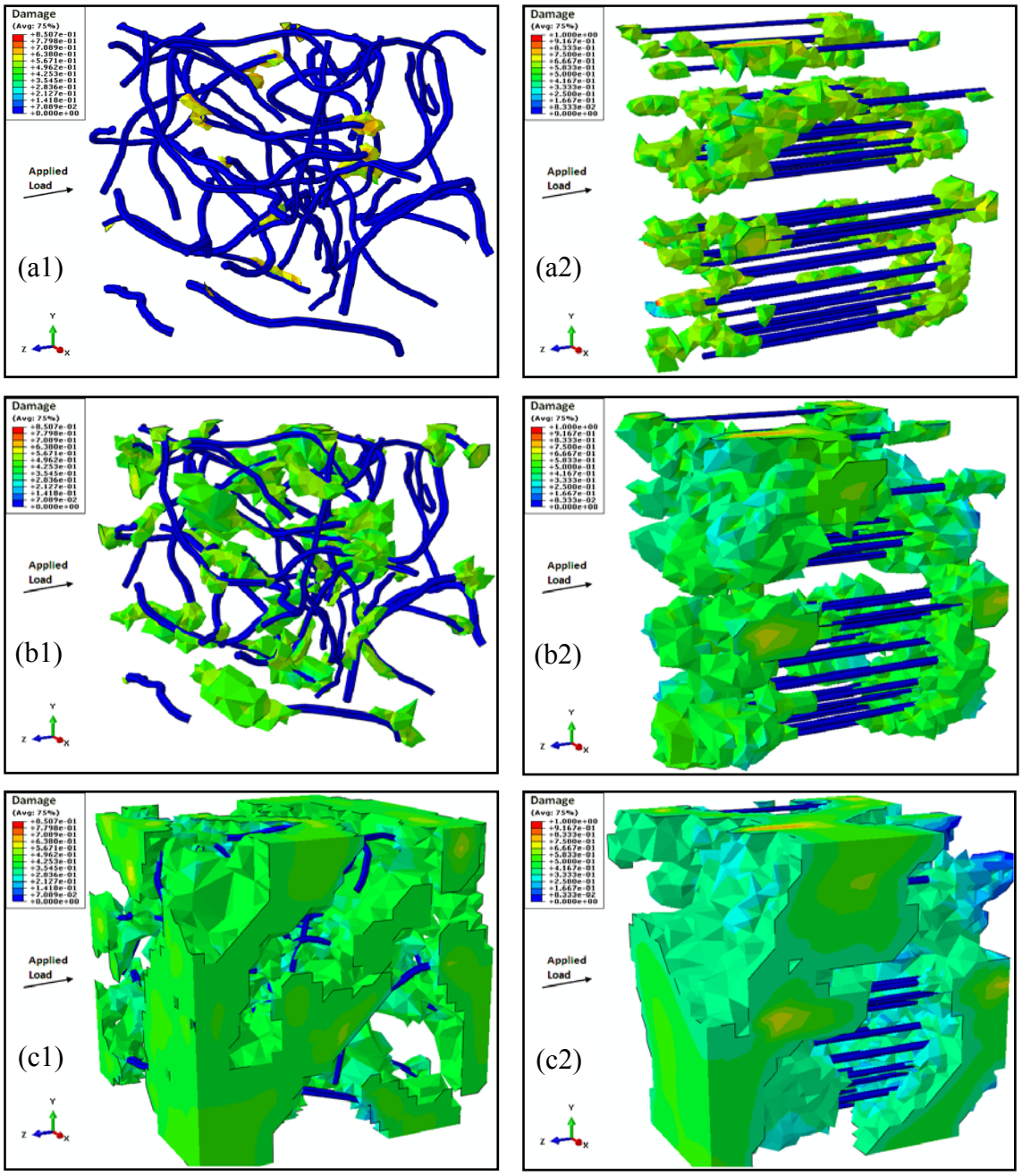

Fig. 9.37. Damage nucleation and growth in RVEs with 1.0 vol% CNT (AR ≈ 11) under compressive load; CNTs oriented in: (a1) to (c1) Curved, and (a2) to (c2) *Z*-direction.

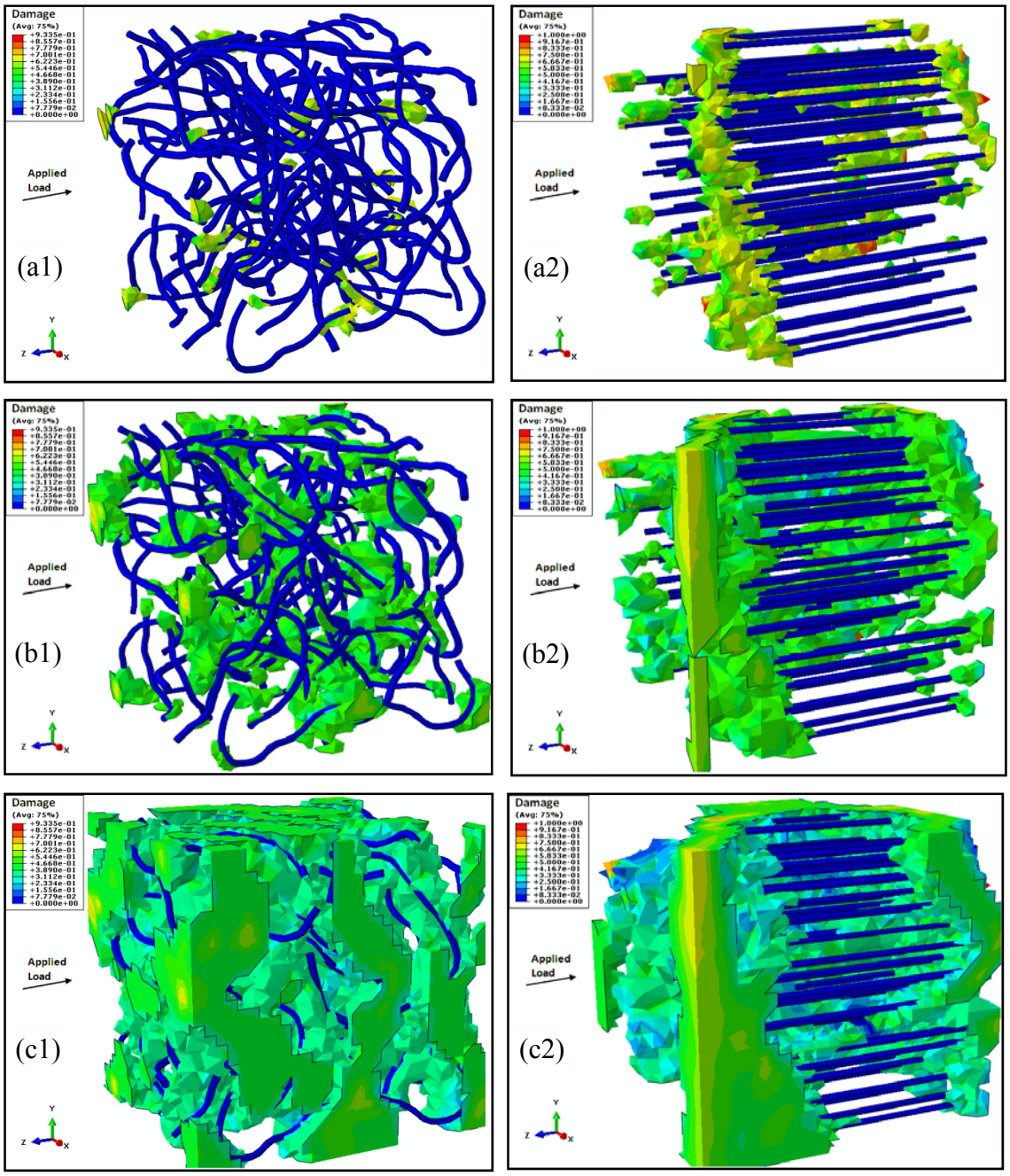

Fig. 9.38. Damage nucleation and growth in RVEs with 2.0 vol% CNT (AR ≈ 11) under compressive load; CNTs oriented in: (a1) to (c1) Curved, and (a2) to (c2) *Z*-direction.

Here, similar to the CNTs with AR≈120, damage is highest in oriented CNTs comparing to the curved ones. But, the amplitude of damage is less in AR≈11, because the cross

section areas of the fibers with AR≈11 are much greater than the one with AR≈120; thus, the CNTs cannot penetrate as easy as CNTs with higher aspect ratios.

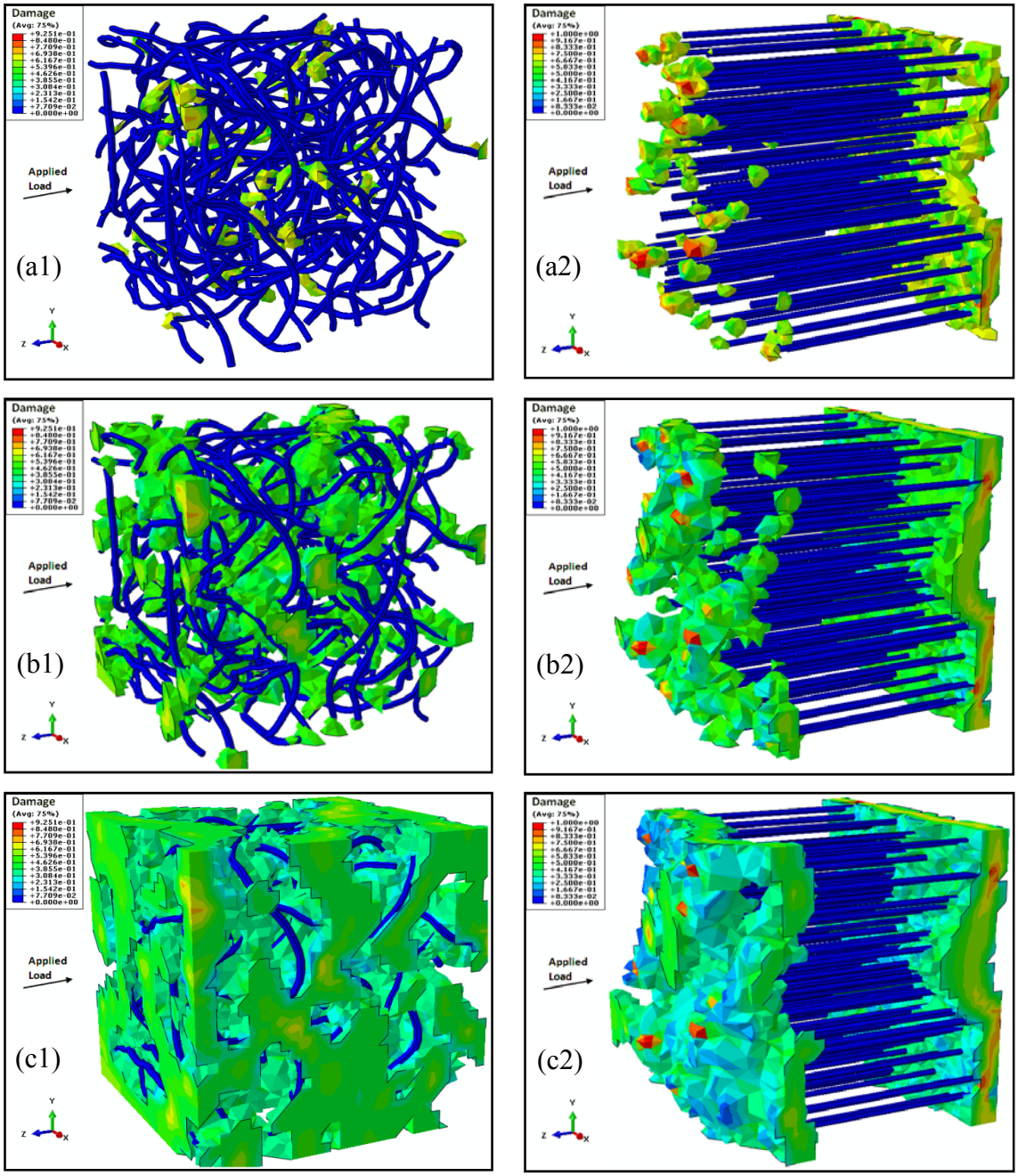

Fig. 9.39. Damage nucleation and growth in RVEs with 3.0 vol% CNT (AR ≈ 11) under compressive load; CNTs oriented in: (a1) to (c1) Curved, and (a2) to (c2) *Z*-direction.

For CNTs with both ARs under compression, it is obvious that damage is localized at both ends of the oriented CNTs, but heterogeneously distributed in RVEs with curved CNTs. Also, the average magnitude of damage in curved ones is less than oriented ones. Again, similar to CNTs with higher AR, the main mechanism of failure for the straight fibers is due to the CNT tips and the surrounding matrix in that location. In the following, in Figs. 9.40 and 9.41, the stress strain diagrams of the simulated RVEs with AR≈11 are shown and compared to each other and to pure polymer matrix responses.

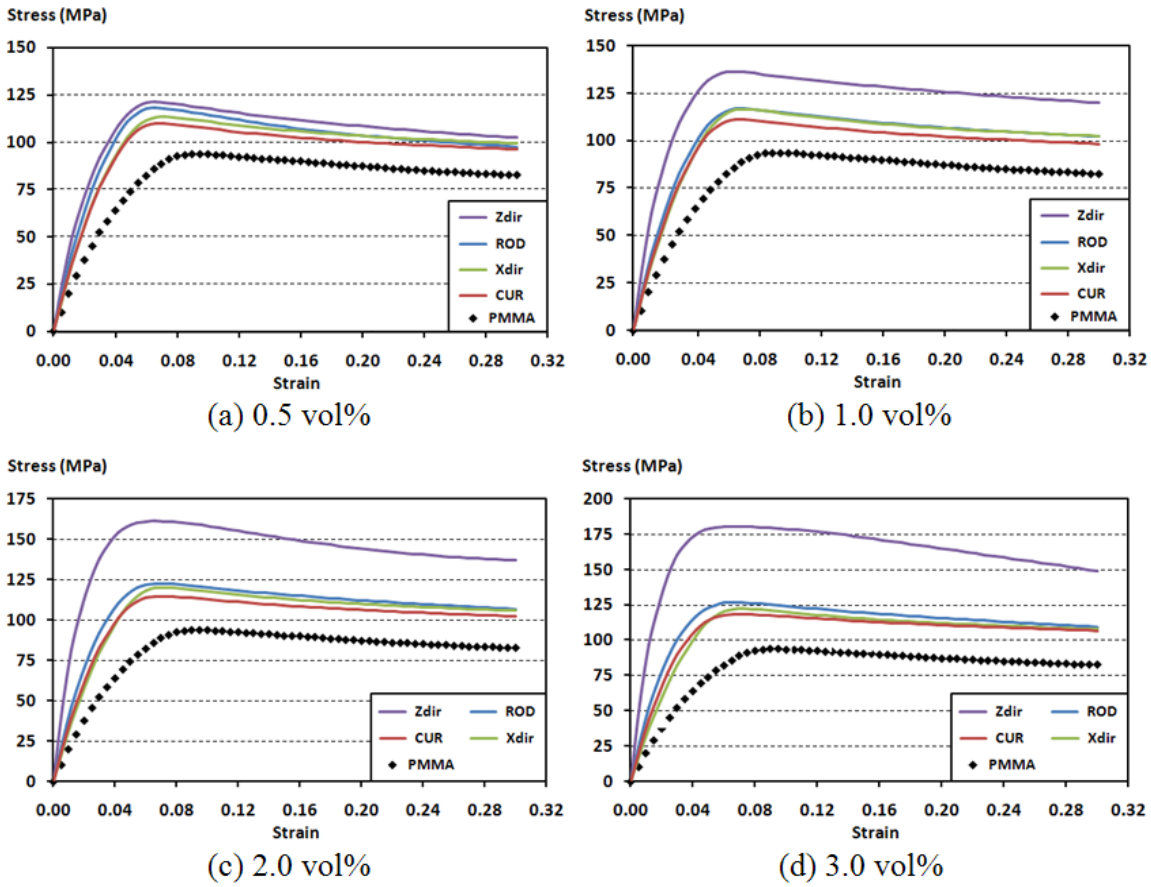

Fig. 9.40. Stress-strain responses of RVEs (AR≈11), containing all CNT configurations, under compressive load, $\dot{\varepsilon} = 0.001/\mathrm{s}$.

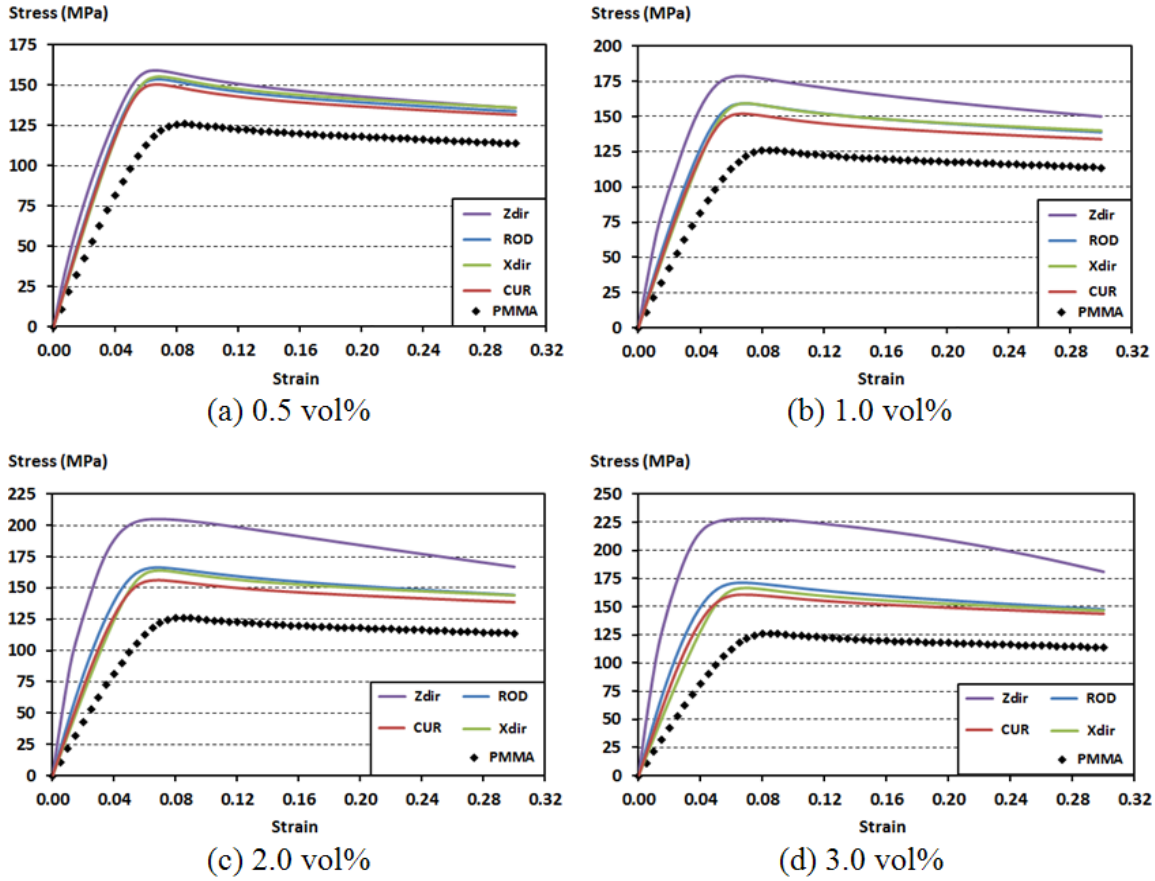

Fig. 9.41. Stress-strain responses of RVEs (AR≈11), containing all CNT configurations, in compression, $\dot{\varepsilon} = 0.1/\mathrm{s}$.

Due to the recent presented diagrams, it is concluded that the maximum peak stress, Young's modulus, and toughness can be achieved through using oriented CNTs, and the minimum values for these mechanical properties are obtained according to the curved CNTs; even though the amplitude of damage in curved CNTs is less than the one in oriented CNTs. In the lowest volume fraction (0.5%), the differences between the mentioned mechanical properties are little, and while adding more CNTs to the composites just the oriented CNTs show better enhancement, and the mechanical improvements regarding other CNT configurations is very small. Moreover, comparing

the trend of stress strain curves relating to the oriented fibers, one can recognize that the overall damage is increased in RVEs while increasing the fibers volume percentages. This causes the stress-strain curves slope down (images (c) and (d) of Figs. 9.40 and 9.41) which means the composite systems after 10% strain absorb less energy.

In the following, damage initiation and growth in these RVEs (AR≈11), but under tension is shown; and for the sake of briefness, just maximum CNT volume fraction, 3%, for both curved and oriented CNTs are displayed, in Figs. 9.42 and 9.43. Here, similar to compression, the curved CNTs show better damage distribution in RVE domain.

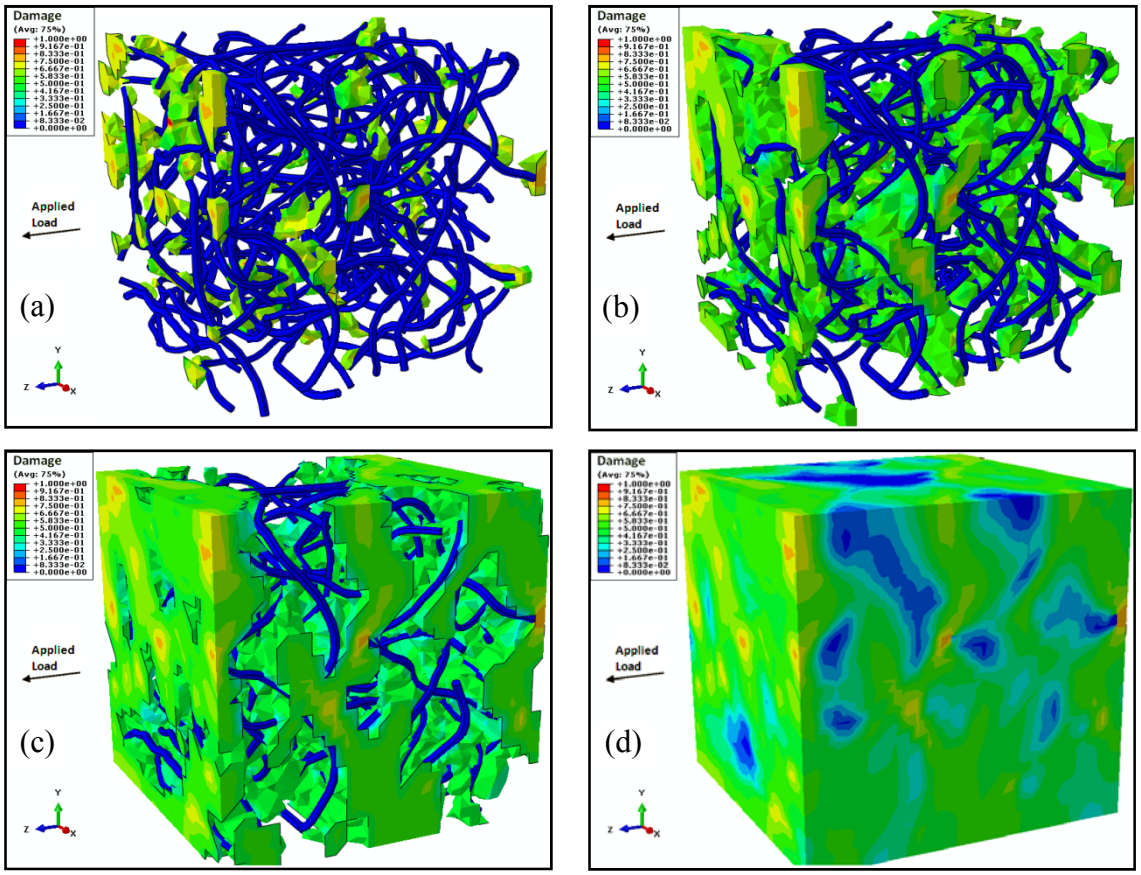

Fig. 9.42. Damage distribution in RVE with 3% curved CNT, AR≈11, under tension: (a) to (d) Damage initiation and growth.

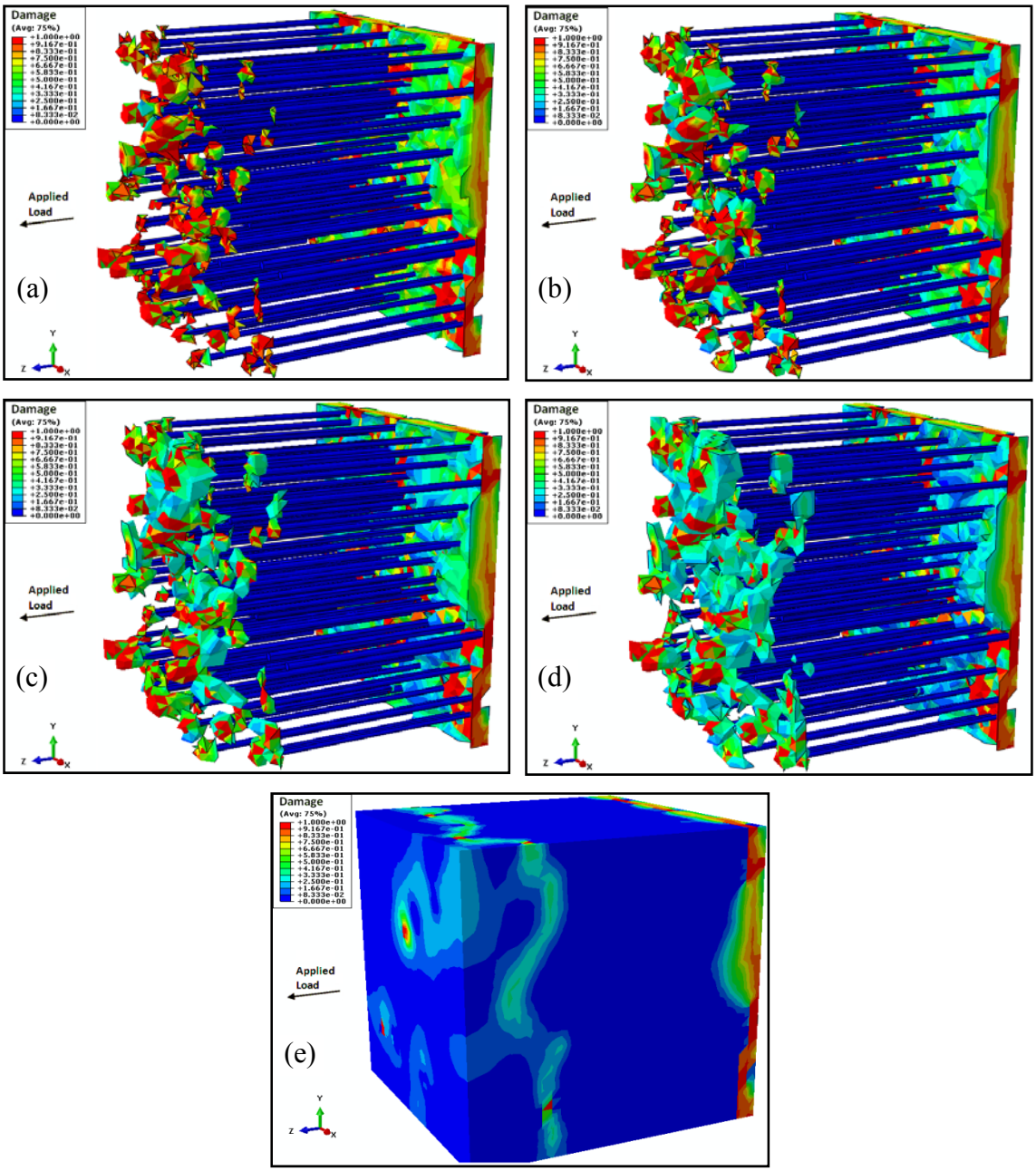

Fig. 9.43. Damage distribution in RVE with 3% curved CNT, AR≈11, under tension: (a) to (d) Damage initiation and growth, and (e) Damage distribution over the whole RVE.

But, in the RVE with oriented CNTs, Fig. 9.43, damage is almost not created in most of the RVE domain, and just localized near both CNT ends. In Fig. 9.43 (e), it is obvious

that the failure mechanism is the rupture at both CNT tips. It means, in this case the whole RVE is not strained, and just both pieces of polymer matrix in front of both CNT end tips are being strained. In this part, in Figs. 9.44 and 9.45, the stress-strain diagrams of the simulated RVEs with AR≈11, subjected to tensile loads, are shown and compared to each other and to the pure polymer matrix. These RVEs also show the same trend similar to the RVEs containing CNTs with AR≈120. Here, since the magnitude of damage is smaller than CNTs with AR≈120; thus, adding more fibers to the RVEs can improve the mechanical responses of the composites a little more.

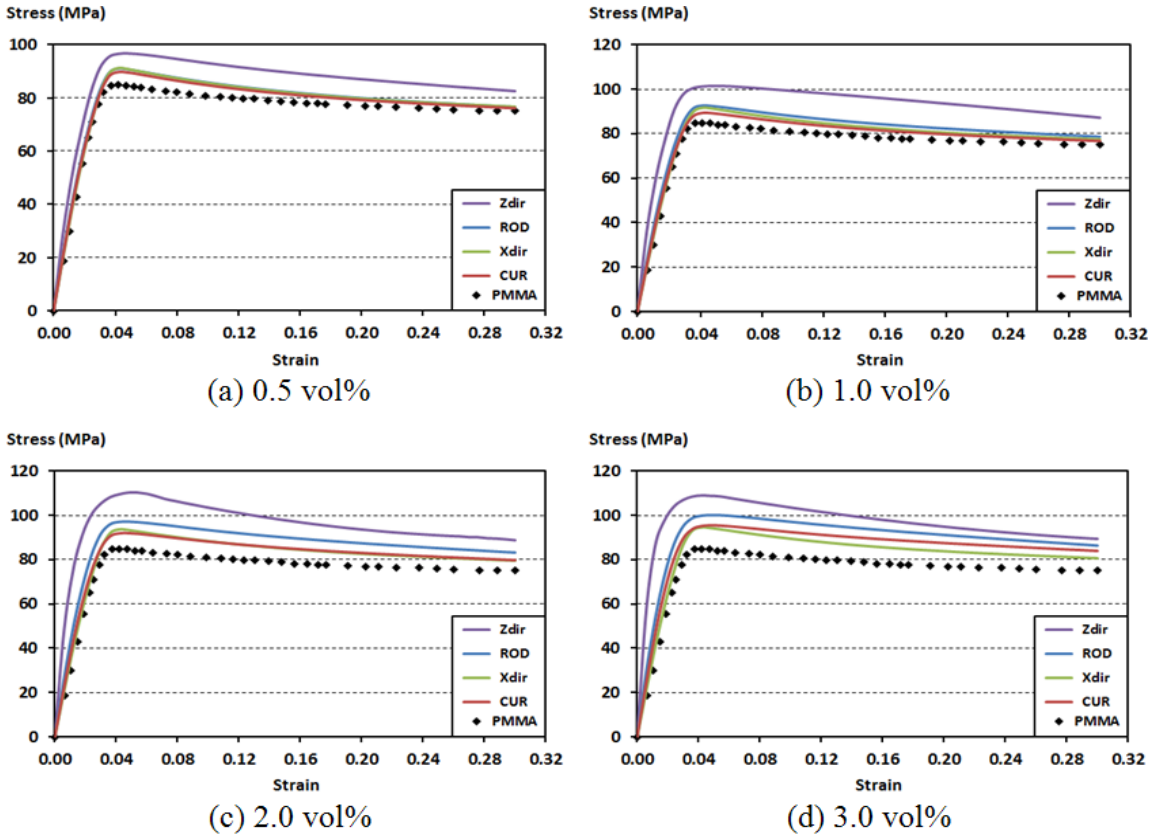

Fig. 9.44. Stress-strain responses of RVEs (AR≈11), containing all CNT configurations, under tensile load, $\dot{\varepsilon} = 0.001/\mathrm{s}$.

However, adding inclusion causes more damage inside the composites and degrades the maximum stress and the overall toughness. This reduction is more critical in higher strain levels (Fig. 9.43). Similar to the CNTs with higher AR, mechanical enhancement can be achieved if the fibers are fully placed in the direction of the applied load.

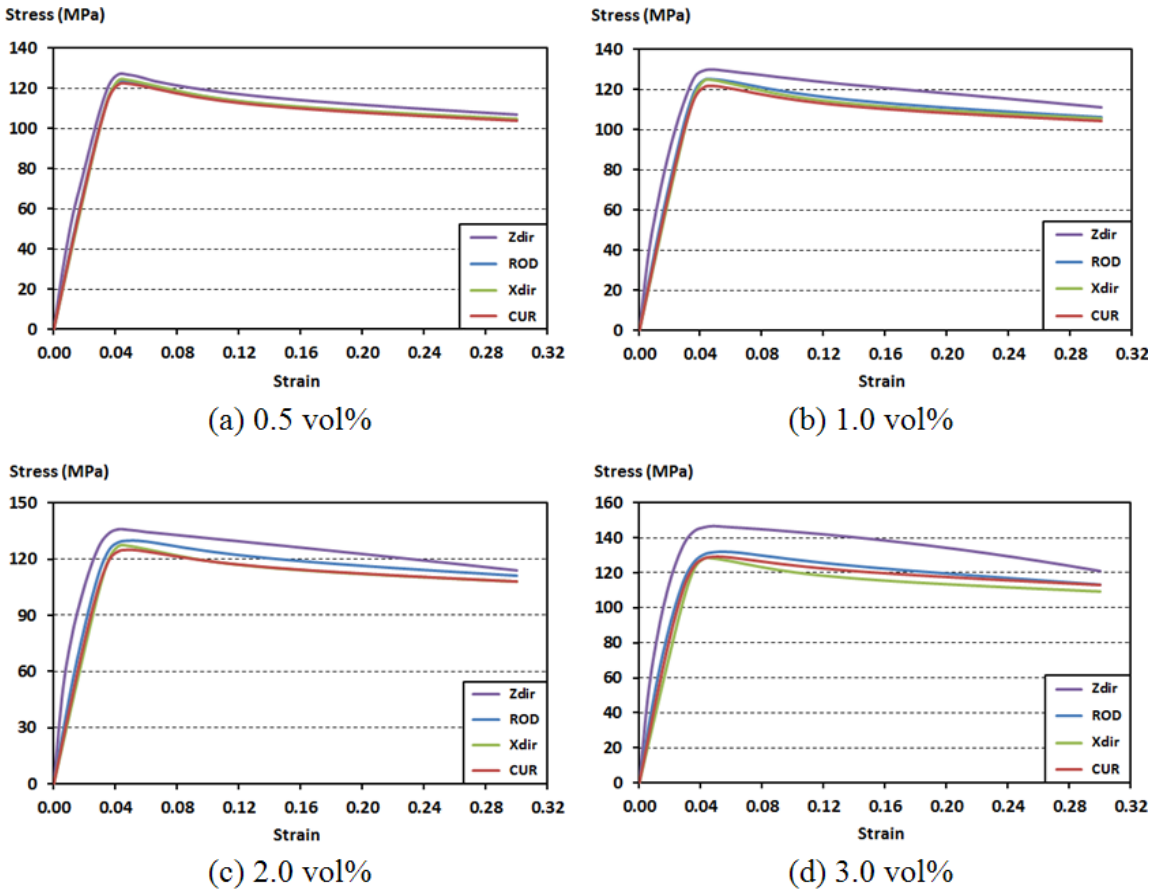

Fig. 9.45. Stress-strain responses of RVEs (AR≈11), containing all CNT configurations, under tensile load, $\dot{\varepsilon} = 0.1/\mathrm{s}$.

9.4.4 Hybrid Polymer Nano Composites

In this section, damage initiation and distribution in hybrid composites are demonstrated. Here, similar to previous sections, the emergence of damage is studied to

find out which type of inclusions at first stimulates and drives damage inside the host material (polymer matrix).

9.4.4.1 Hybrid CNTs and NCLPs Composites

In this subsection, the damage distribution pattern and the mechanical responses of mixed CNTs and NCLPs are studied and shown. Three different CNT volume fractions (0.5, 1, and 2%) with AR ≈ 120, and three NCLP volume fractions (1, 2, and 3 %) are mixed, and nine different micro structures are generated. Figs. 9.46 and 9.47 illustrate the initiation of degradation (damage) in PMMA, under compressive load, and similar to Section 9.4.3, the tips of those CNTs that are placed in the direction of applied loads, stimulate damage.

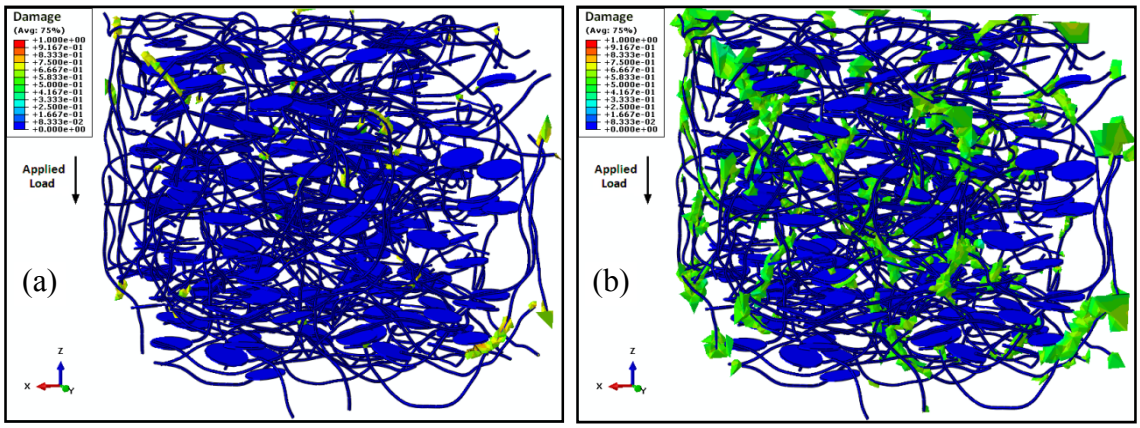

Fig. 9.46. Damage evolution in RVE with 0.5 vol% curved CNT (AR ≈ 120) and 1% NCLP, in compression: (a) to (c) Damage nucleation and growth, and (d) Close view of damage propagation between CNTs and NCLPs inside matrix.

Fig. 9.46. Continued.

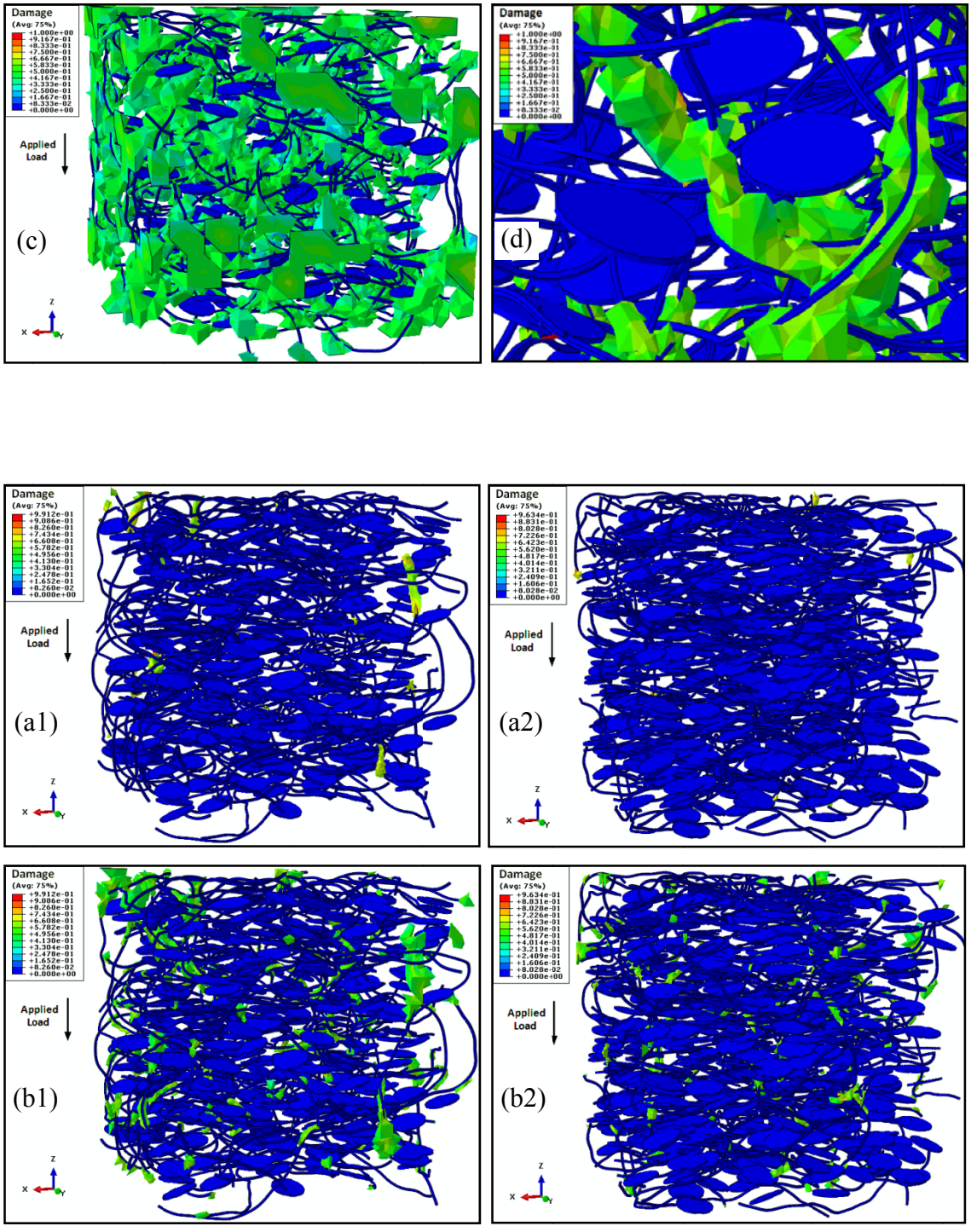

Fig. 9.47. Damage nucleation and growth inside RVEs with 0.5% curved CNT (AR ≈ 120) and: (a1) to (c1) 2% NCLP, and (a2) to (c2) 3% NCLP, under compressive load. Fig. 9.47 Continiued.

Fig. 9.47. Continued.

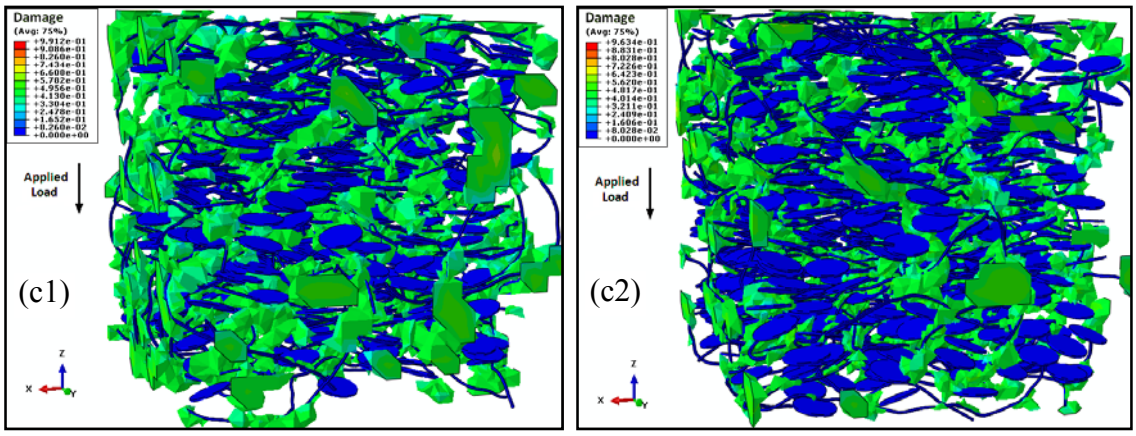

Furthermore, the degradations in the matrix evolve along the main body of the mentioned CNTs. Subsequently, as seen in Figs 9.46 and 9.47, the damaged regions expand perpendicular to the CNTs segments through the interspace gap between the clay particles. Other CNTs (the ones are not placed in the direction of applied load) do not show any effect on matrix degradation. In both figures, it can be seen that the presence of clay particles do not generate damage inside the RVEs, and this can be observed better in Fig. 9.46 (d). Moreover, comparing Figs. 9.46 and 9.47, one may understand that by increasing the clay contents, the volume of damaged regions and their average magnitudes decrease. It means the presence of clay particles is able to postpone the propagation of damage inside the CNT-based composites.

In Figs. 9.48 and 9.49, the same amount of clay contents as shown in Figs. 9.46 and 9.47 are mixed to the RVE systems, but the volume fraction of nanotubes are four times larger than the previous models (from 0.5% to 2%). As seen, and similar to Figs. 9.46 and 9.47, the initiation of damage is due to the CNT segments that are parallel to

the applied forces. Then, the damaged regions expand and propagate at first along the CNTs major axis, and afterwards evolve perpendicular to the CNTs major axis. This phenomenon can be observed better in Fig. 9.48 (d). Similar to all the previous RVE models containing curved CNTs, the fibers which are not placed along the direction of the applied load do not stimulate the matrix to be damaged.

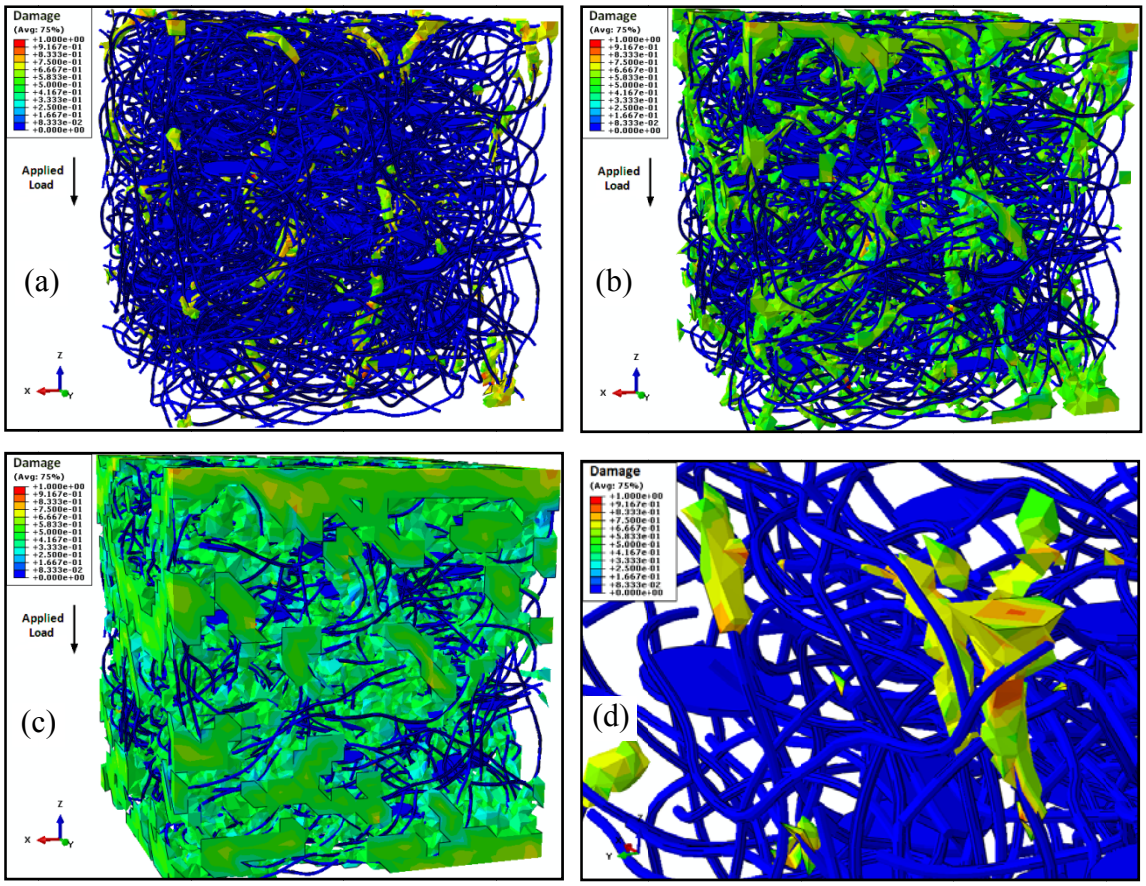

Fig. 9.48. Damage evolution in RVE with 2 vol% curved CNT (AR ≈ 120) and 1% NCLP, in compression: (a) to (c) Damage nucleation and growth, and (d) Close view of damage propagation between CNTs and NCLPs inside matrix.

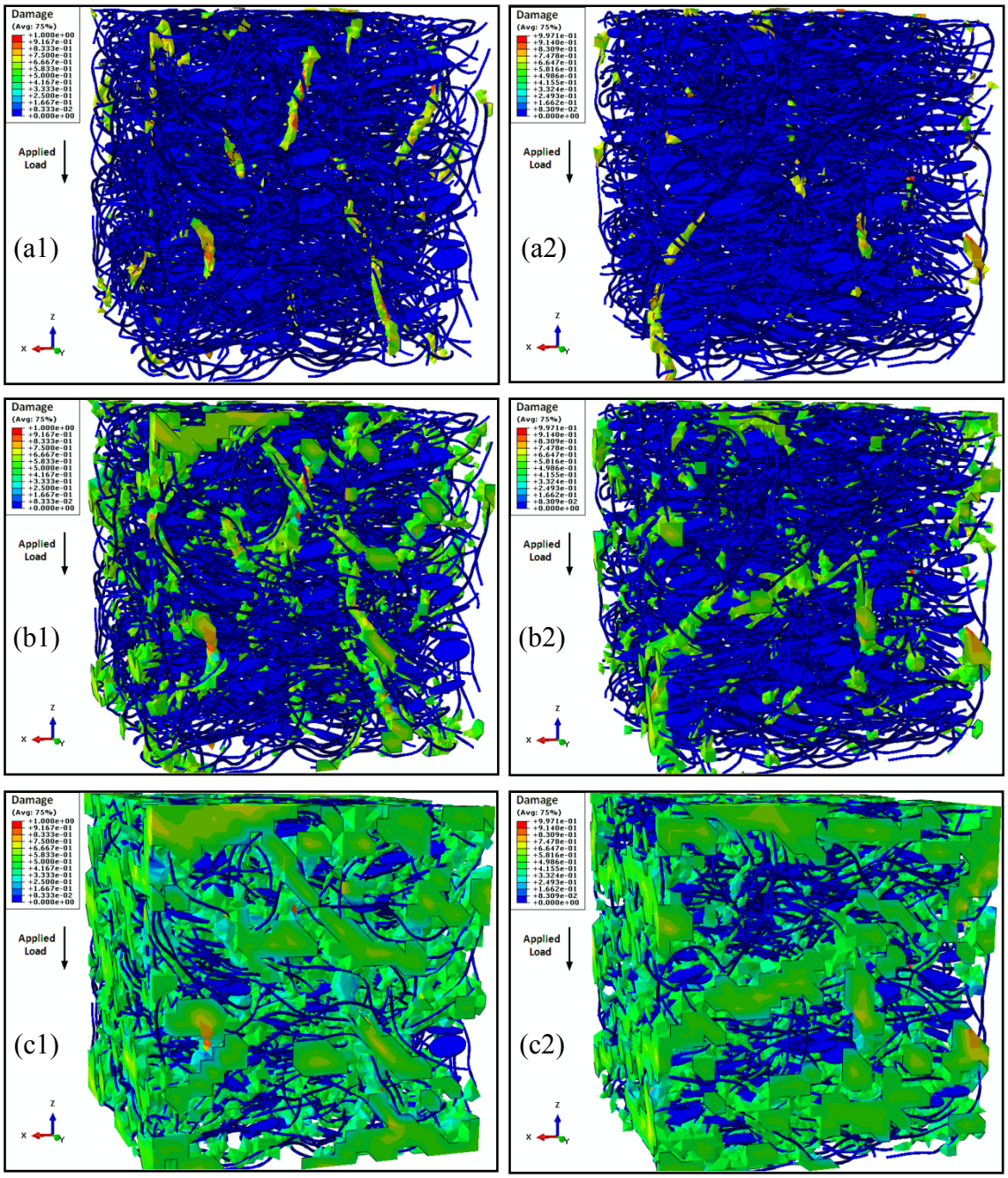

Fig. 9.49. Damage nucleation and growth inside RVEs with 2% curved CNT (AR ≈ 120) and: (a1) to (c1) 2% NCLP, and (a2) to (c2) 3% NCLP, under compressive load.

By comparing Figs. 9.48 and 9.49, not only the existence of NCLPs does not generate damage, but also reduces the degraded regions and their magnitudes. Therefore briefly,

regarding the presented damage distribution in the RVEs under compressive loads (Figs. 9.46 to 9.49), the reinforcing curved fibers cause damage and the platelet configuration of NCLPs diminishes the damage evolution. Here, 18 simulations were performed to gain and illustrate the overall RVEs stress-strain responses with different particles mixture scenarios, and they are presented in Fig. 9.50.

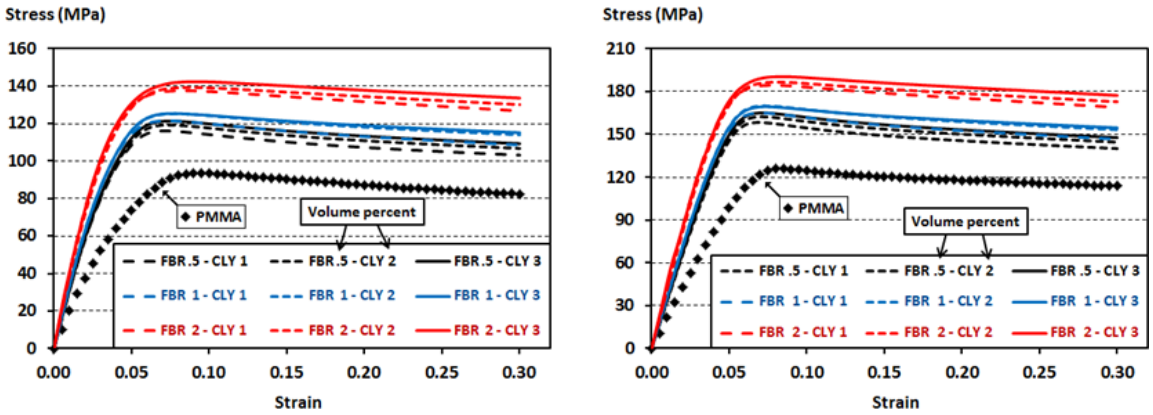

(a) $\dot{\varepsilon} = 0.001/\mathrm{s}$ (b) $\dot{\varepsilon} = 0.1/\mathrm{s}$

Fig. 9.50. Stress-strain response of RVEs containing reinforcing curved CNTs and NCLPs, subjected to compressive load, at 2 strain rates.

In these diagrams (Fig. 9.50), Young's modulus, maximum stress, and toughness are increased while increasing both types of inclusions. In both strain rates, there are curve overlaps between different NCLP mixtures of the RVEs containing 0.5% and 1% CNT; but, the responses of the models with 2% CNT are considerably higher, and they have no overlap with 1% CNT mixtures. Thus, it can be obtained that the main enhancement is due to the presence of CNTs, and then adding the NCLPs can improve the mechanical responses a little more. Although the changes of CNTs volume faction are less than the changes of NCLPs volume faction, the CNT effects are more pronounced in composites.

Similar to compression, in tensile simulations, the CNTs initiate the degradation inside the polymer matrix, rather than the NCLPs. Also, dissimilar to the models containing just NCLPs (Subsection 9.4.1) under tension, damage starts at the tips of the NCLPs instead of the space between their major planes. This occurs not for NCLPs orientation and shape, but because damage is mainly governed (controlled and propagated) by fibers inside the RVEs, which can be seen in Figs. 9.51 and 9.52. Also, while adding more NCLPs in each series of hybrid mixture, similar to compressive tests, the amplitude of damage decrease.

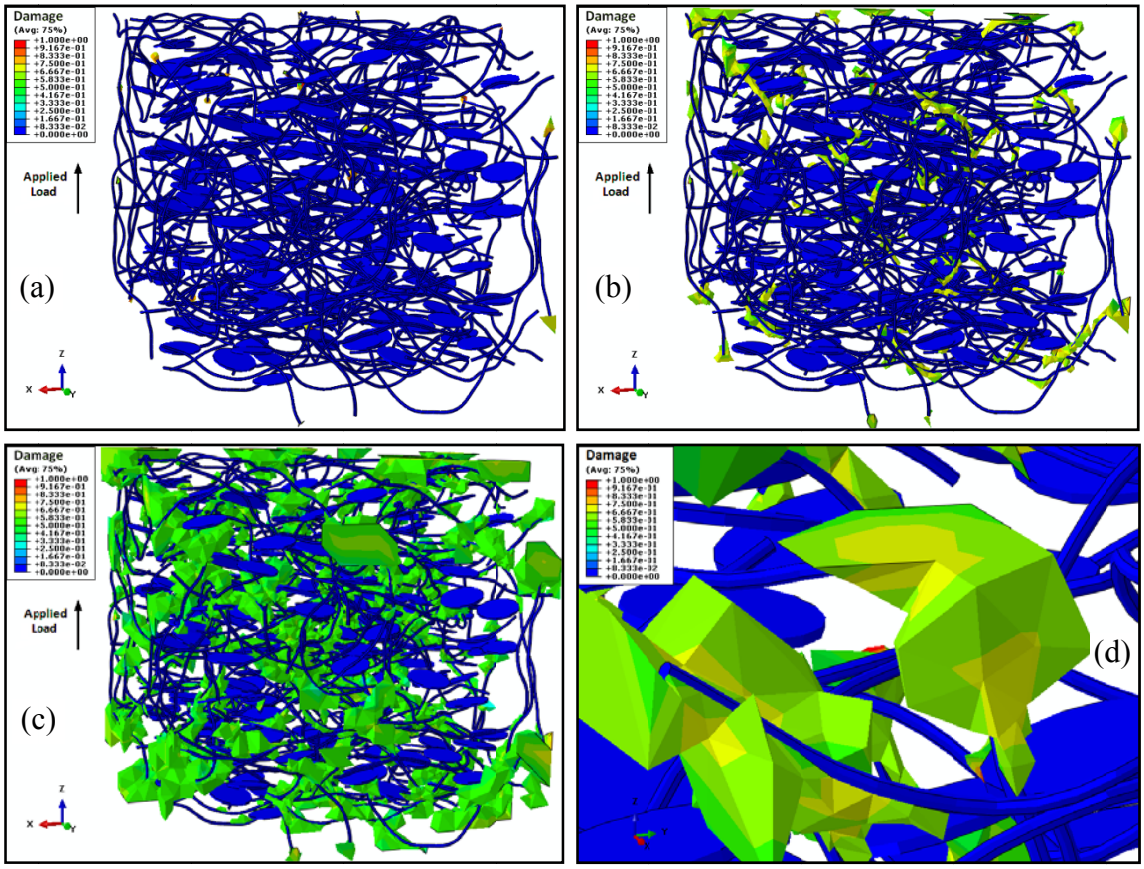

Fig. 9.51. Damage evolution in RVE with 0.5 vol% curved CNT (AR ≈ 120) and 1% NCLP, under tension: (a) to (c) Damage nucleation and growth, and (d) Close view of damage propagation between CNTs and NCLPs inside matrix.

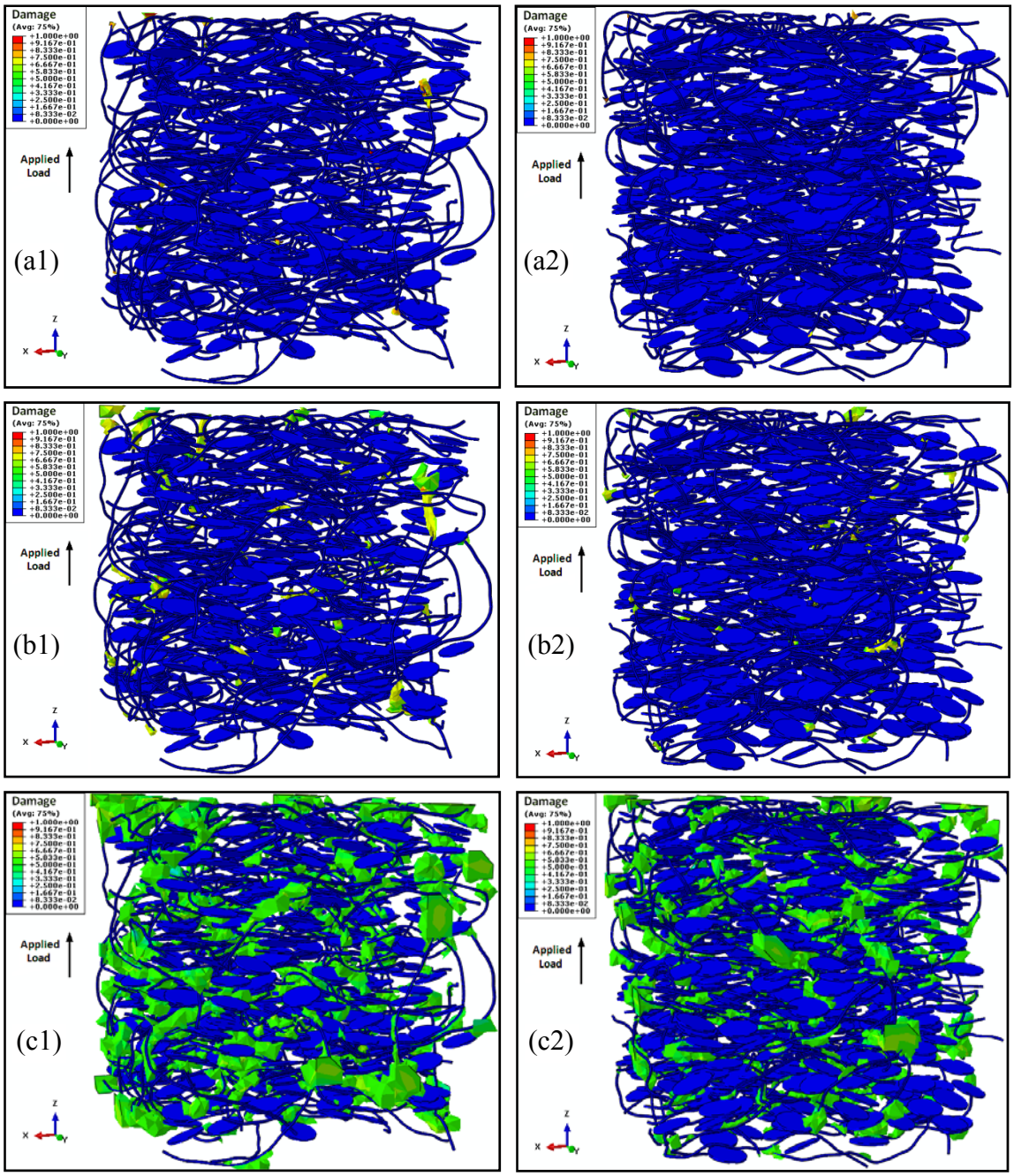

Fig. 9.52. Damage nucleation and growth inside RVEs with 0.5% curved CNT (AR ≈ 120) and: (a1) to (c1) 2% NCLP, and (a2) to (c2) 3% NCLP, under tensile load.

In the following the damaged regions inside the RVE containing 2% CNT and three different NCLPs volume fractions are depicted. As seen in Fig. 9.53, damage initiates at

the tip of all CNTs that are close to the surface boundary conditions. On the contrary of the previous simulations, damages are formed at the CNT tips, no matter they are parallel to the applied load or not. It shows that, huge amounts of stresses are localized in both top (applied load) and bottom (boundary condition) surfaces of the RVEs, which are transferred to the CNTs via their tips. However, damage initiation and growth inside the RVEs under tension are similar to the models under compression (it initiates at CNT tips, growes along major axis, and then extend perpendicular to the fibers major axis).

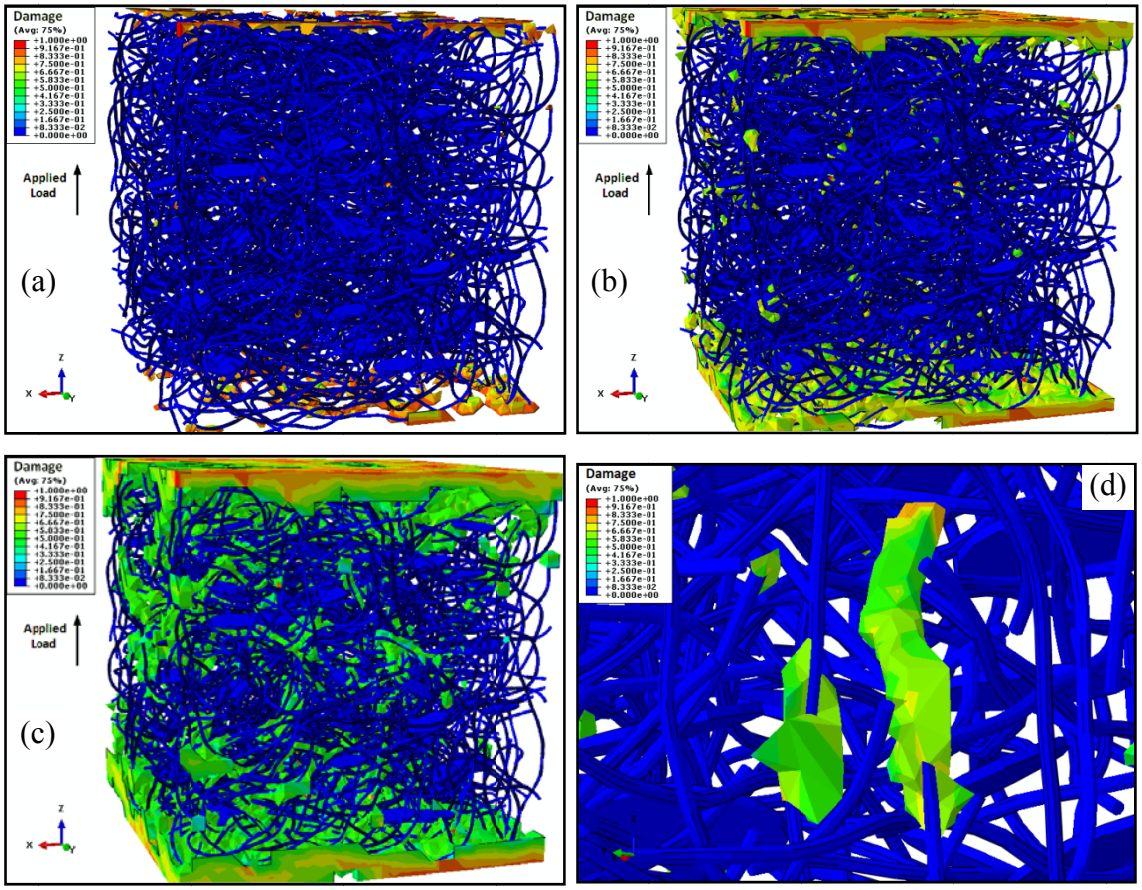

Fig. 9.53. Damage evolution in RVE with 2 vol% curved CNT (AR ≈ 120) and 1% NCLP, under tension: (a) to (c) Damage nucleation and growth, and (d) Close view of damage propagation between CNTs and NCLPs inside matrix.

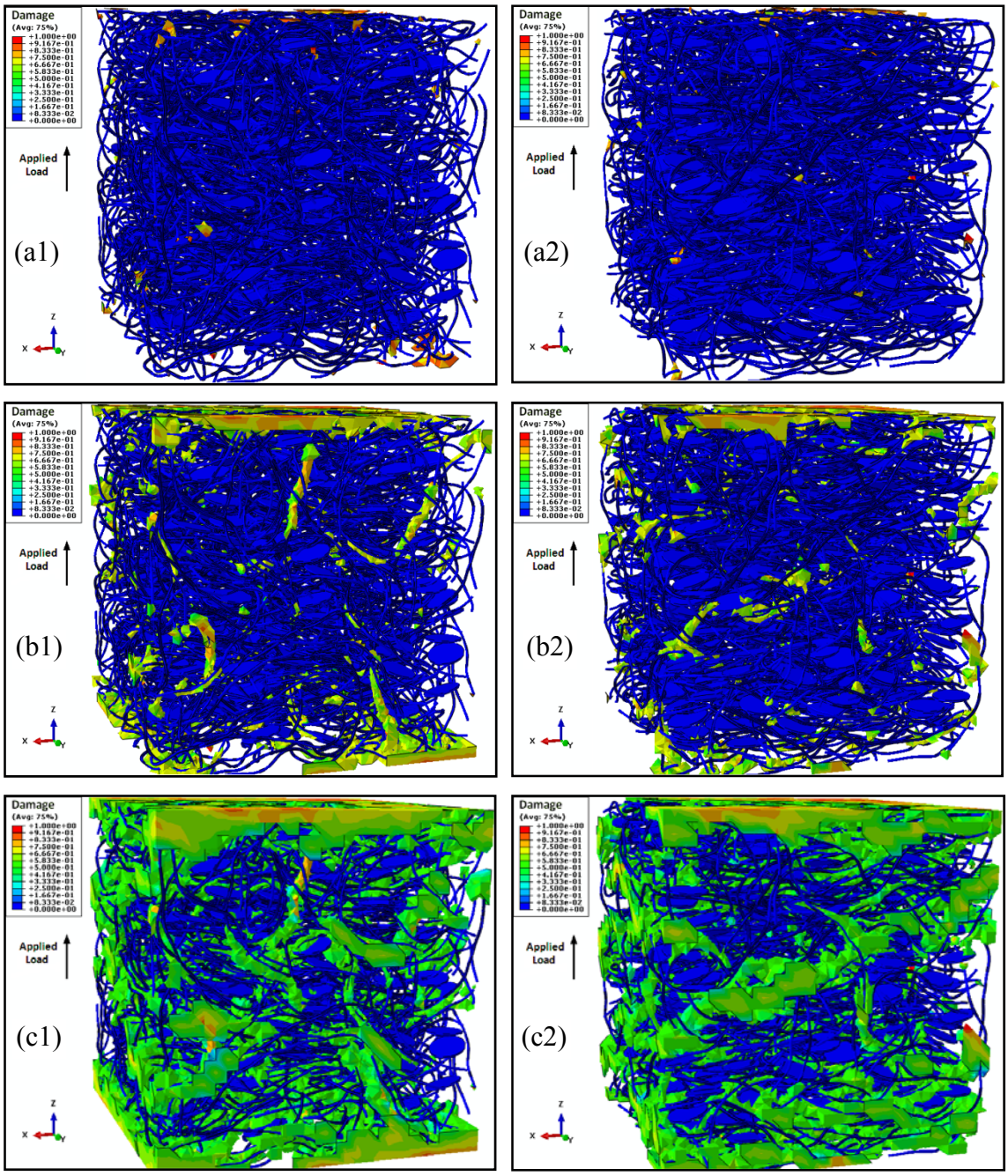

Fig. 9.54. Damage nucleation and growth inside RVEs with 2% curved CNT (AR ≈ 120) and: (a1) to (c1) 2% NCLP, and (a2) to (c2) 3% NCLP, under tensile load.

In addition, like previous RVE models, increasing the volume fraction of clay particles causes reduction in damage growth in the polymer matrix. This behavior which is called

damage growth shielding can be found by comparing Figs. 9.53 and 9.54. Moreover, the stress-strain responses of the tensile simulations are depicted in Fig. 9.55. Both diagrams show the effect of curved CNTs are more pronounced than the NCLPs, such that the CNTs mainly improve the mechanical behavior of the RVEs, and adding clays to the models just enhance it a little. Comparing Fig. 9.50 and 9.55, one may recognize that the effects of NCLPs are more considerable in compressive loads, and almost negligible in tensile loading condition.

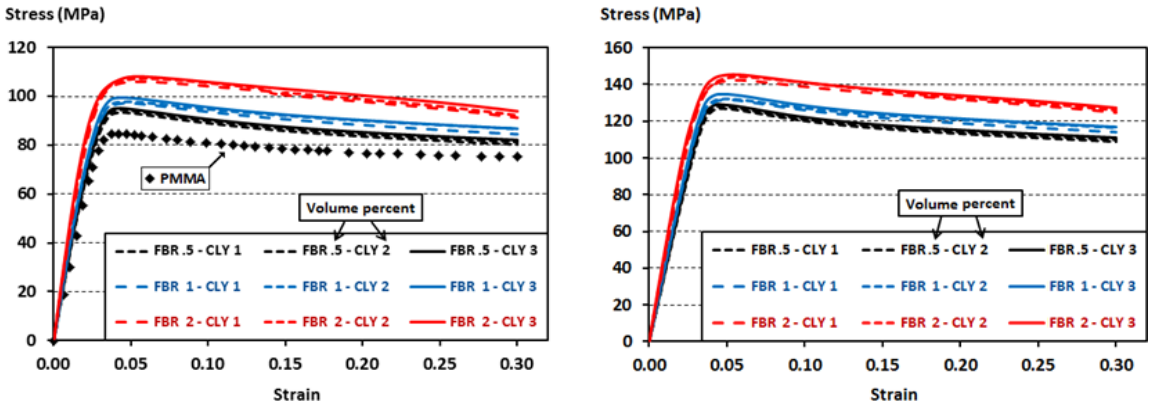

(a) $\dot{\varepsilon} = 0.001/\mathrm{s}$ (b) $\dot{\varepsilon} = 0.1/\mathrm{s}$

Fig. 9.55. Stress-strain response of RVEs containing reinforcing curved CNTs and NCLPs, subjected to tensile load, at two strain rates.

In the following, the magnitude of toughness modulus for the simulated hybrid composites are shown in Fig. 9.56. The trends of the toughness modulus are linear for all hybrid cases (inclusions volume fractions), in both compression and tension loading, at two different strain rates. It can be found out that there is no significant improvement in toughness modulus, and the trend and rate of toughness modulus enhancement are the same in compression and tension.

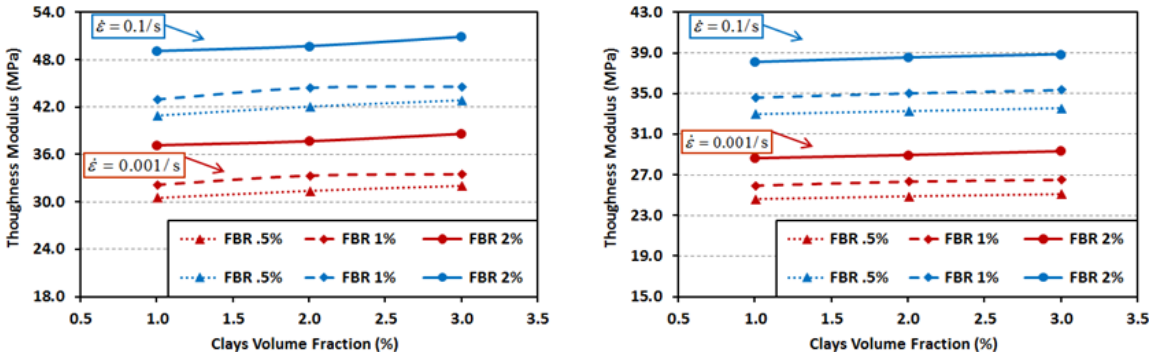

(a) Compression (b) Tension

Fig. 9.56. Toughness modulue of RVEs containing reinforcing curved CNTs and NCLPs, at two strain rates.

9.4.4.2 Hybrid CNTs and NCRPs Composites

In this subsection, the effects of spherical particles on the overall response of PMMA-based nano composites containing CNTs are illustrated and discussed. The same as previous subsection, three different CNT volume fractions (0.5, 1, and 2 %) with aspect ratio ≈ 120, and three NCLP volume fractions (1, 2, and 3 %) are mixed, and 9 different micro structures are generated. Figs. 9.57 and 9.58 depict the initiation of degradation in the matrix, which are subjected to compressive load. They show the presence of the spherical particles does not affect the initiation of damage inside the RVEs containing CNTs. This can be observed better in Fig. 9.57 (d). As seen, the NCRPs do not provoke the polymer matrix to be damaged in the presence of CNTs. Here, according to Figs. 9.57 and 9.58, the degradations are incited around the CNT tips, and evolve in the direction of fibers major axis, and then propagate perpendicular to the axis through the space between the spherical particles. This damage distribution pattern is similar to the one in subsection 9.4.4.1, which means the tips of those CNTs that are placed in the direction of applied loads stimulate damage in matrix.

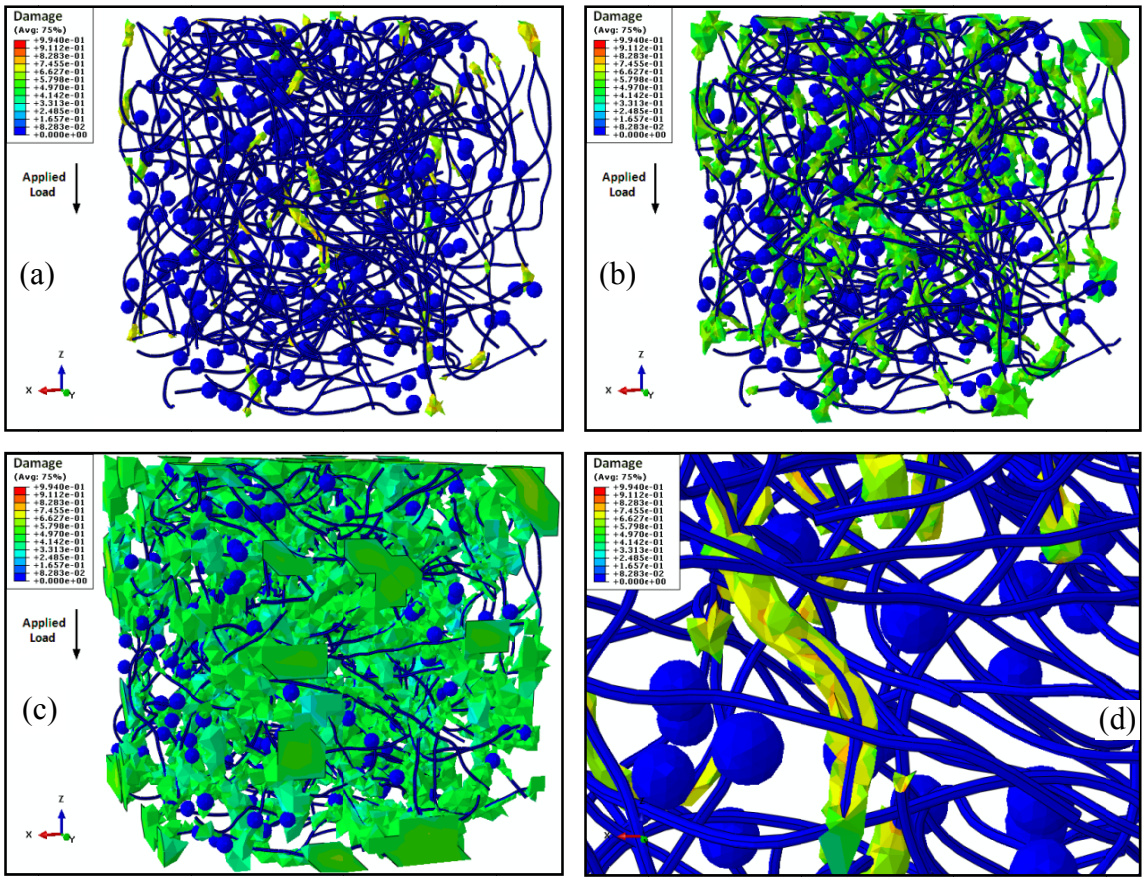

Fig. 9.57. Damage evolution in RVE with 0.5 vol% curved CNT (AR ≈ 120) and 1% NCRP, in compression: (a) to (c) Damage nucleation and growth, and (d) Close view of damage propagation between CNTs and NCRPs inside matrix.

Afterwards, the degradations in the matrix evolve gradually around the main body of the CNTs and NCRPs. Other CNTs (the ones are not placed in the direction of applied load) do not show any effect on matrix degradation. Moreover, comparing Figs. 9.57 and 9.58, one may observe that by increasing the amount of ceramic contents, the volume of damaged regions and their average magnitudes do not decrease. This is in the contrary to the achievement in the previous hybrid model (CNT and NCLP), in which increasing the volume percent of ceramic particles reduced the damaged regions and their average

magnitudes. It means the presence of the spherical particles cannot postpone the propagation of damage inside such CNT-based composites.

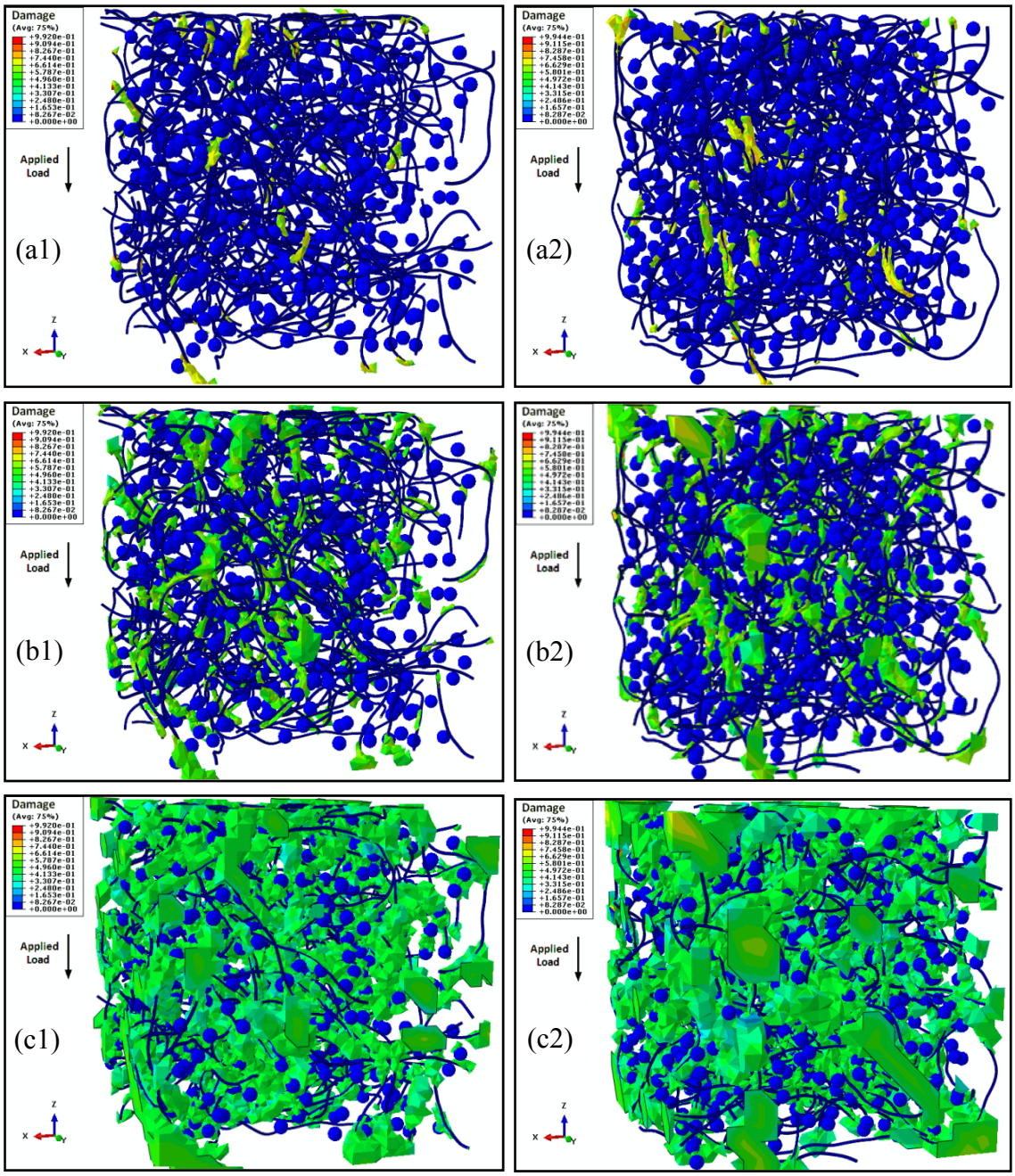

Fig. 9.58. Damage nucleation and growth inside RVEs with 0.5% curved CNT (AR ≈ 120) and: (a1) to (c1) 2% NCRP, and (a2) to (c2) 3% NCRP, under compressive load.

To see the effect of CNTs with higher volume fraction on damage distribution, in Fig. 9.59 and 9.60, the damage contours inside the RVEs containing 2 vol% CNTs are displayed. In this case, the same damage propagation pattern is seen in both figures, and this pattern is better depicted in Fig. 9.59 (d). Similar to Figs. 9.57 and 9.58, by comparing Fig. 9.59 and 9.60, it can be found out that increasing the volume fraction of spherical particles does not enhance the composites functionality against damage propagation. It means, in this type of hybrid composite just CNTs govern the matrix degredation.

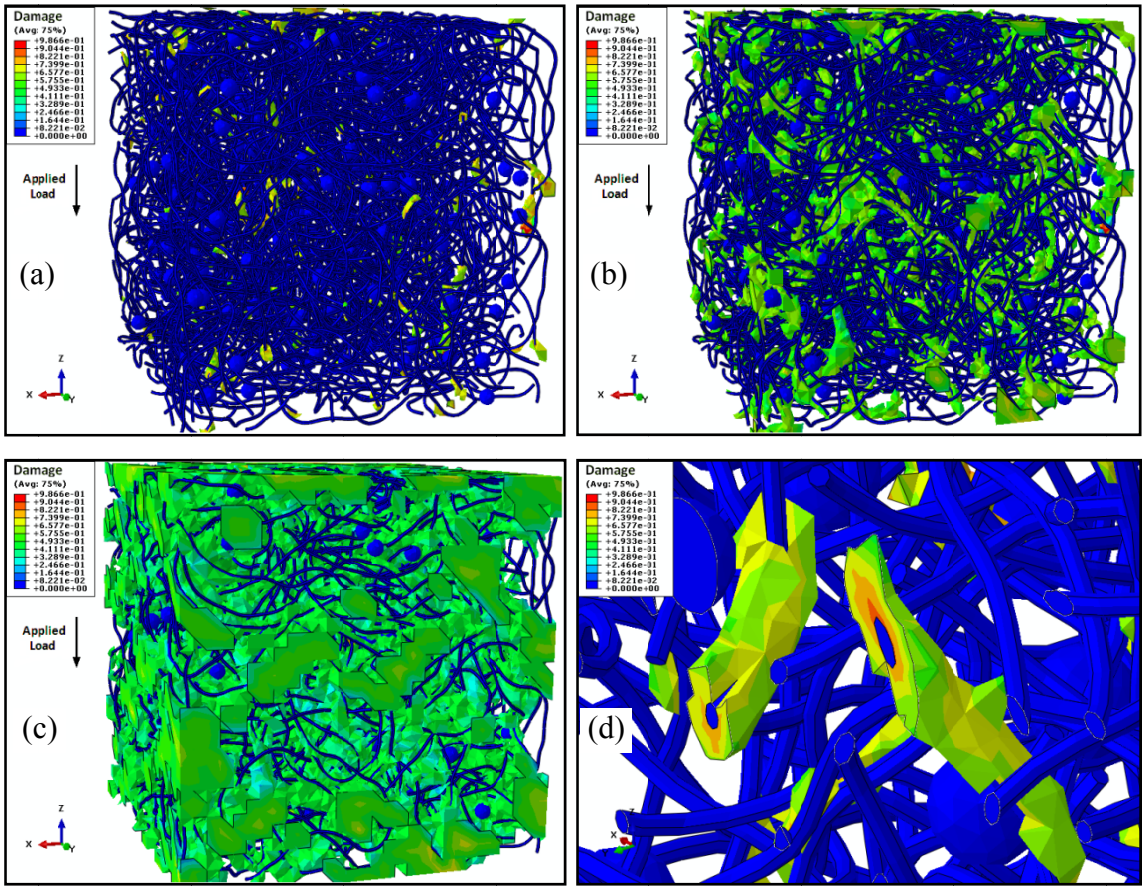

Fig. 9.59. Damage evolution in RVE with 2 vol% curved CNT (AR ≈ 120) and 1% NCRP, in compression: (a) to (c) Damage nucleation and growth, and (d) Close view of damage propagation between CNTs and NCRPs inside matrix.

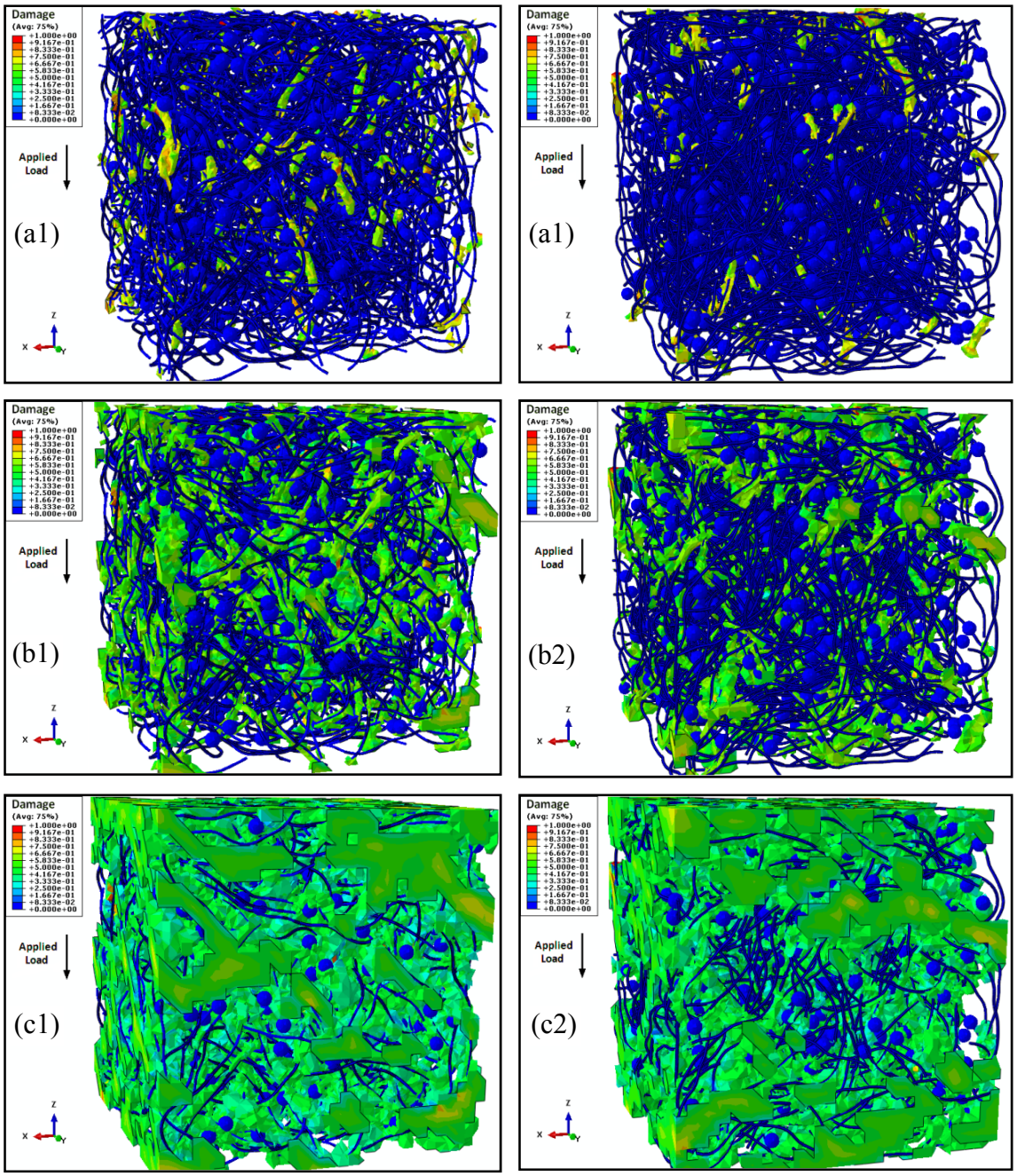

Fig. 9.60. Damage nucleation and growth inside RVEs with 2% curved CNT (AR ≈ 120) and: (a1) to (c1) 2% NCRP, and (a2) to (c2) 3% NCRP, under compressive load.

The overall stress-strain responses of the hybrid RVEs containing CNTs and NCRPs, at two strain rates, are shown in Fig. 9.61. The diagrams show that the effect of CNTs are

more significant than the NCRPs, such that the CNTs mostly enhance the mechanical behavior of the composites, and adding spherical particles to the system just improve it a little. Both diagrams illustrate that the best improvement regarding to the NCRPs happens when they are mixed with the composites containing more fibers. Therefore, when the CNTs volume fractions is higher, the NCLP's can better improve the RVE's responses, under compressive load.

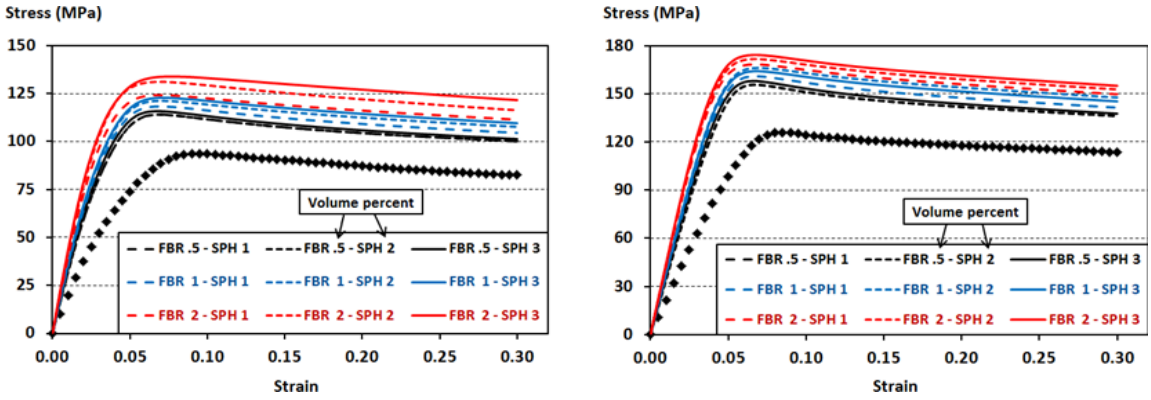

(a) $\dot{\varepsilon} = 0.001/\mathrm{s}$ (b) $\dot{\varepsilon} = 0.1/\mathrm{s}$

Fig. 9.61. Stress-strain response of RVEs containing reinforcing curved CNTs and NCRPs, subjected to compressive load, at two strain rates.

In the following, to study the effect of particles on damage distribution pattern under tension in this type of hybrid composites, the same models are subjected to tensile loads. In Fig. 9.62 (d), the damage distribution around one single CNT, under tensile load, is displayed. As illustrated in Figs. 9.62 and 9.63, increasing the amount of NCRPs does not affect the damage distribution pattern in the composites under tensile load. This phenomenon shows that spherical particles (NCRPs) dissimilar to platelet particles (NCLPs) are not able to provide resistance shield against damage propagation inside the

composite model. Therefore, in tension as well as compression, the behavior of composite is almost controlled by the embedded fibers.

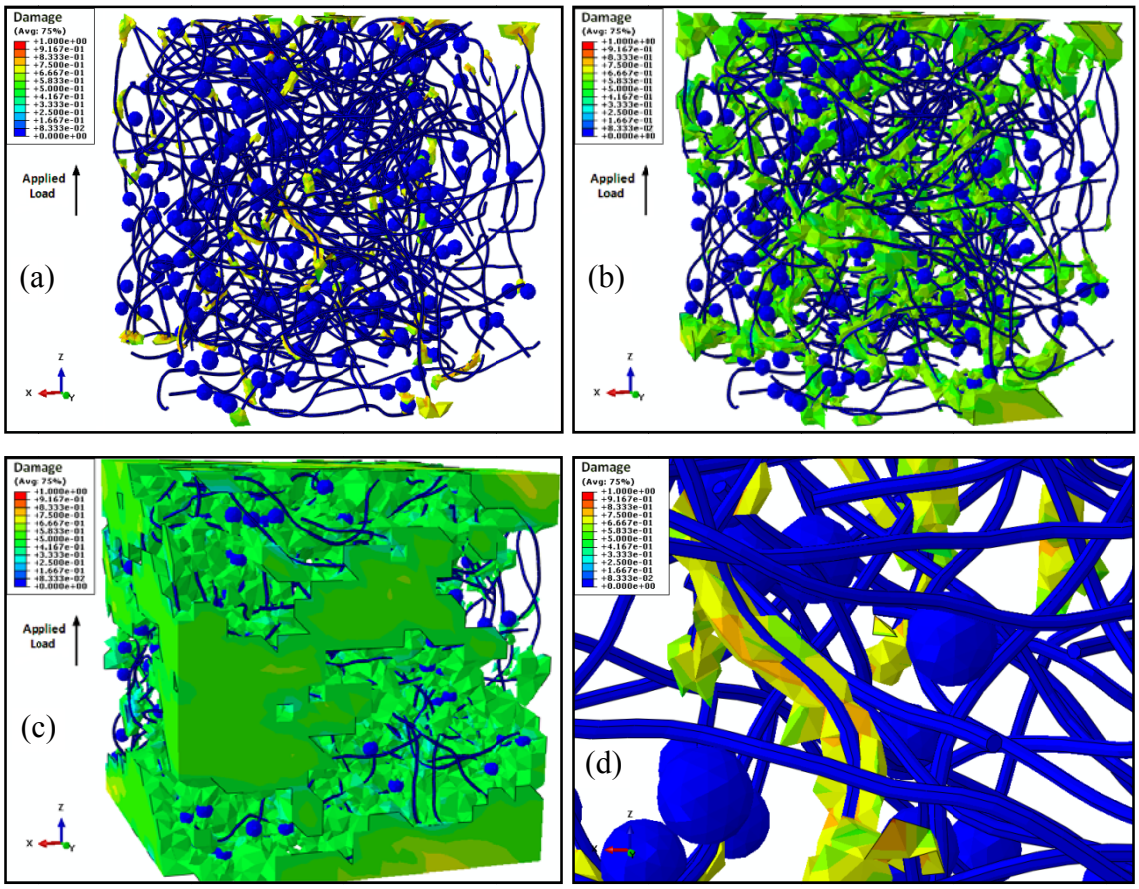

Fig. 9.62. Damage evolution in RVE with 0.5 vol% curved CNT (AR ≈ 120) and 1% NCRP, under tension: (a) to (c) Damage nucleation and growth, and (d) Close view of damage propagation between CNTs and NCRPs inside matrix.

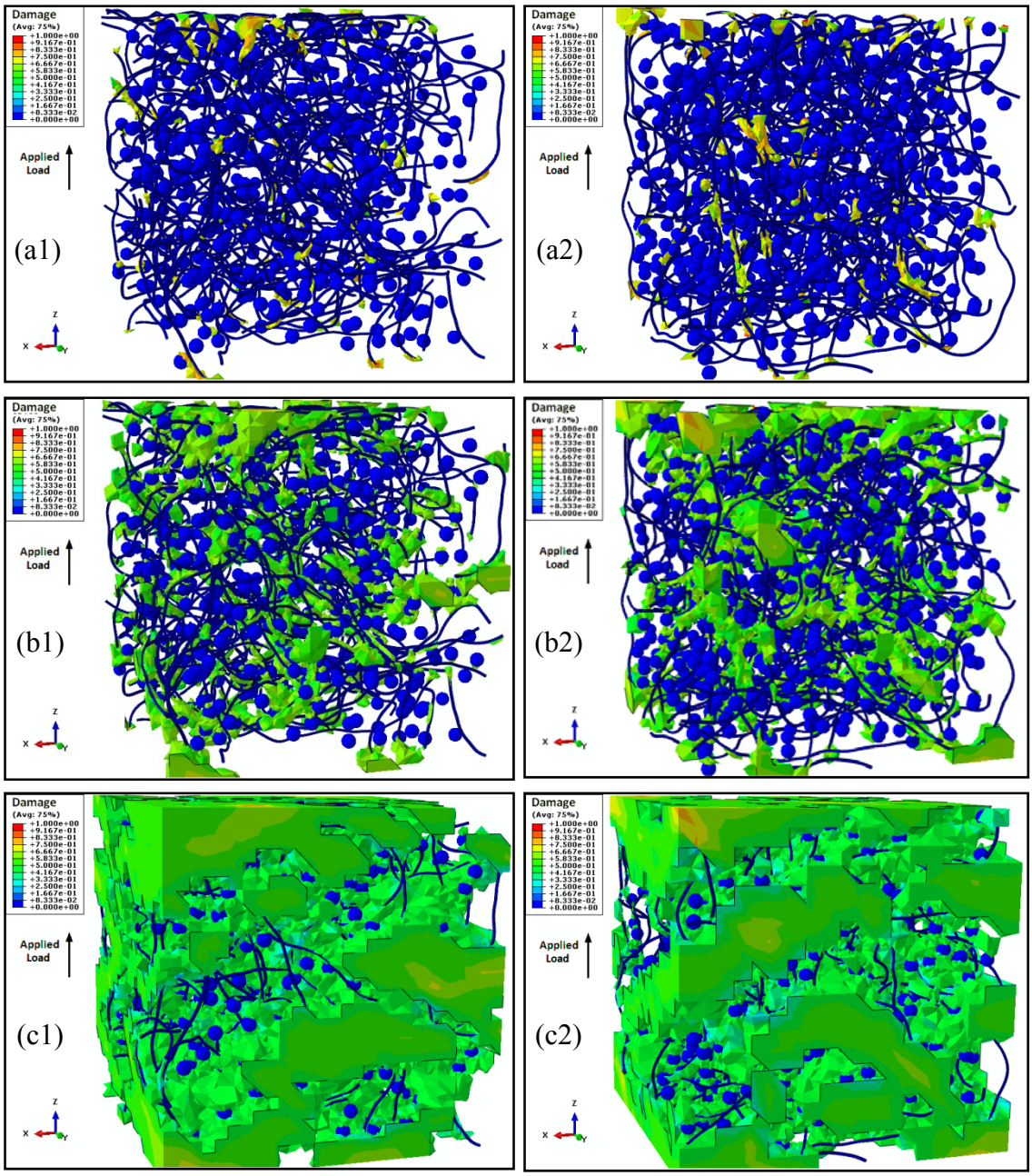

Fig. 9.63. Damage nucleation and growth inside RVEs with 0.5% curved CNT (AR ≈ 120) and: (a1) to (c1) 2% NCRP, and (a2) to (c2) 3% NCRP, under compressive load.

In Fig. 9.64, the same damage pattern, as presented in Figs. 9.62 and 9.63, is observable when the volume fraction of CNTs is increased. Thus, increasing the amount of CNTs, up to 2%, can not highly change the trend of the hybrid composites behavior.

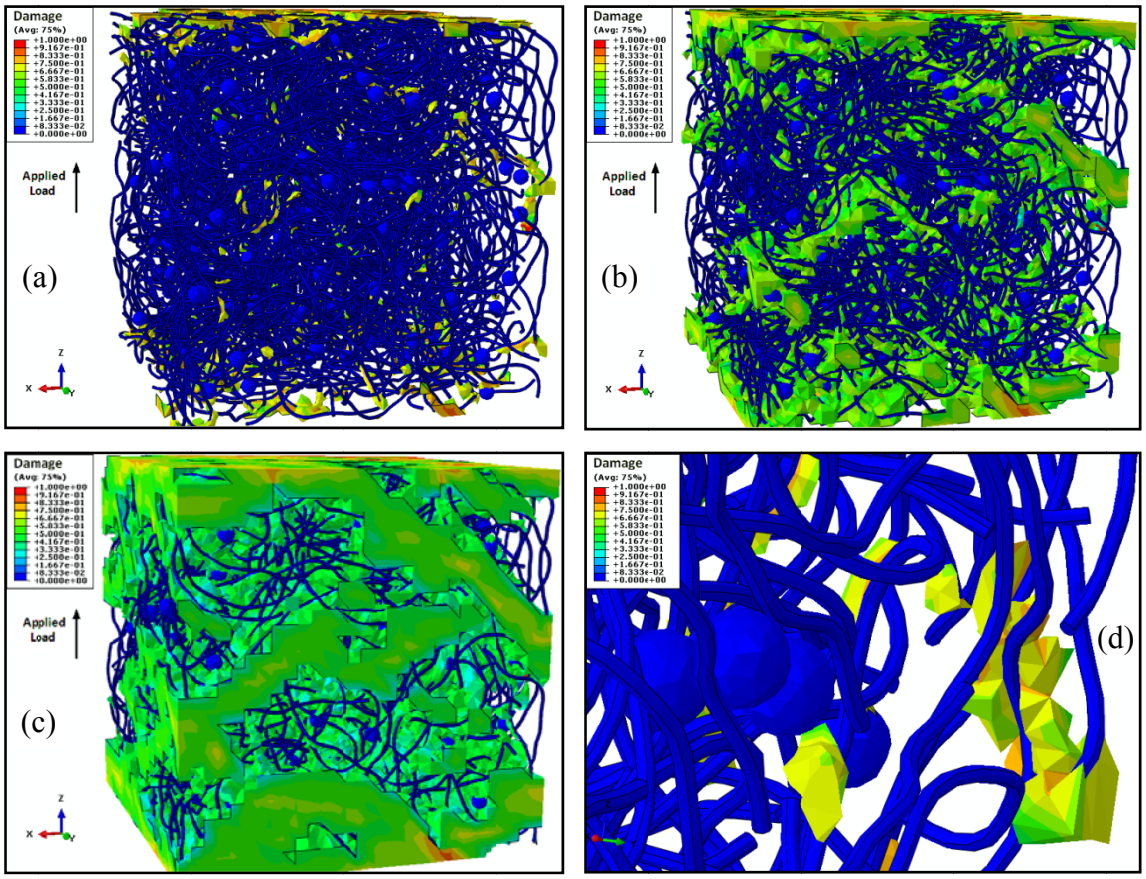

Fig. 9.64. Damage evolution in RVE with 2 vol% curved CNT (AR ≈ 120) and 1% NCRP, under tension: (a) to (c) Damage nucleation and growth, and (d) Close view of damage propagation between CNTs and NCRPs inside matrix.

Here, the overall stress-strain curves of these RVEs under tension, at two strain rates, are displayed in Fig. 9.65, and similar to the compressive loading cases, adding up the NCRPs to the RVE systems just a little improve the response. Moreover, these diagrams

once more confirm that when the CNTs volume fractions is higher, the effect of NCLPs are more significant for improving the RVE's responses. Also, the Young's modulus of the composites are almost linearly enhanced, according to the CNTs and NCRPs. At first, all the mechanicl aspects of the composites are improved by the amount of CNTs, and then slightly enhanced by adding the ceramic particles.

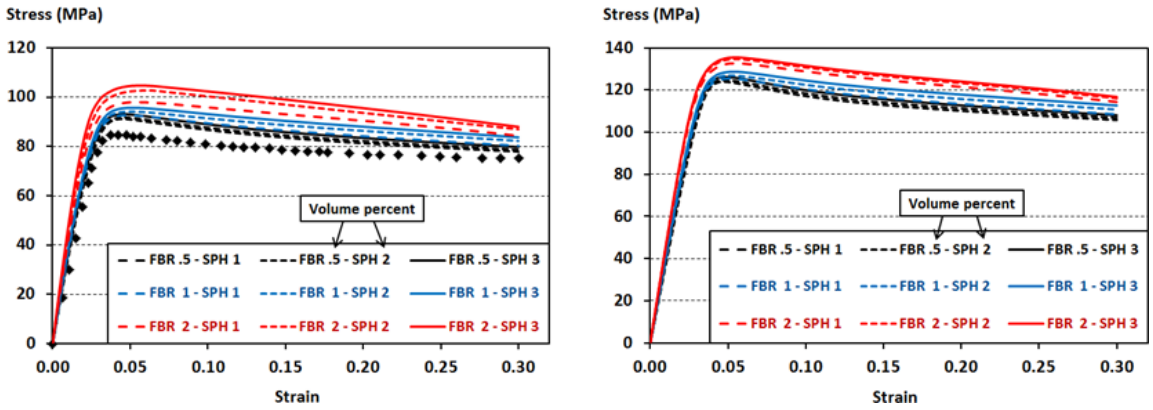

(a) $\dot{\varepsilon} = 0.001/\mathrm{s}$ (b) $\dot{\varepsilon} = 0.1/\mathrm{s}$

Fig. 9.65. Stress-strain response of RVEs containing reinforcing curved CNTs and NCRPs, subjected to tensile load, at two strain rates.

Comparing Fig. 9.61 and 9.65, one may recognize that the effects of NCRPs are more considerable in compression rather than in tension. The magnitude of toughness modulus for these hybrid composites are shown in Fig. 9.66, and their trends are almost linear for all cases, in compression and tension loading, at both strain rates. It can be found out that there is no significant improvement in toughness modulus and the trend and the rate of toughness modulus enhancement are the same in compression and tension.

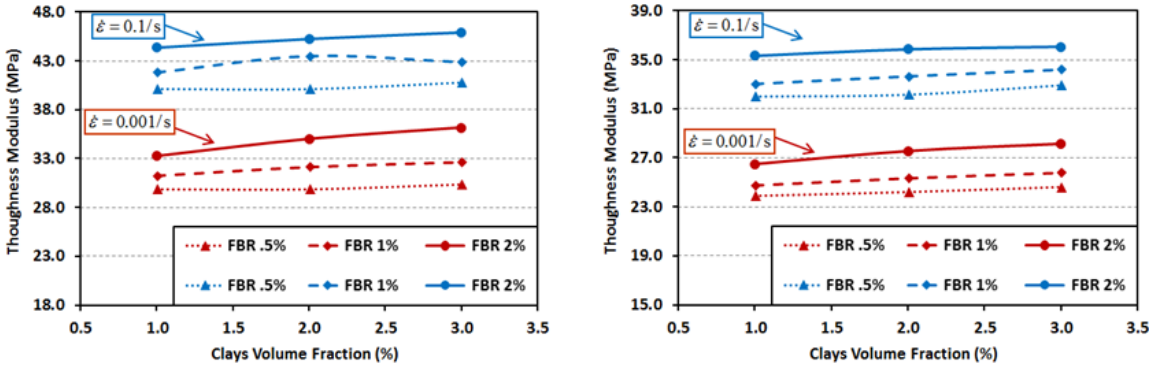

(a) Compression (b) Tension

Fig. 9.66. Toughness modulus of RVEs containing reinforcing curved CNTs and NCLPs, at two strain rates.

9.5 Summary

In this chapter, numerous 3D simulations, under strain control, subjected to both compression and tension load, for different kinds of nano inclusions are performed. In total, 184 simulations are conducted. For each type of inclusion, the magnitude of mechanical enhancement (Young's modulus, maximum strength, amd toughness), and damage distribution inside the composites are computed through FE simulations. Also, damage in RVEs are presented, because their behavior key parameter is damage, and each inclusion type changes the damage distribution pattern.

It is shown that the NCLPs can better improve the behavior of the composites in comparison to the spherical particles. However, NCLPs initiate and drive more damage in the models. Similarly, the NCRPs show almost the same damage distribution pattern; but, according to their shape, they cannot resist against damage evolusion path, and damage can bypath their round surfaces. Thus, NCLPs are able to perform as damage shielding or crack tip pinning to halt damage distribution, which toughens the composite.

CNTs with two ARs are investigated and shown to be able to improve the mechanical response, and the one with higher AR showed better enhacement. The main problem of CNTs is the small area of their tips, which stimulate the polymer matrix to be damaged. CNTs with higher AR generate more damage. In compression, damage initiates at CNT tips, because of their small cross section area, and CNTs penetrate into the matrix. Similarly in tension, damage initiates at the tips of CNTs, not for CNTs penetration but for the significant load transferred from matrix to the CNTs main bodies via their tips. Furthermore, damage initiation and propagation in all CNT forms have the same pattern.

In the studied hybrid composites (CNT-NCLPs, and CNT-NCRPs), damage growth patterns are the same as models containing just CNTs. It is observed that the presence of particles do not stimulate damage inside the RVEs. In case of NCLPs, by increasing the particle contents, the damaged regions and their average magnitudes decrease; but, NCRPs do not have such effect. Hence, NCLPs are able to shield the composites against matrix degradation while mixed with CNTs. For both hybrid cases, it is found that the main enhancement is due to the presence of CNTs, and adding particles improves the mechanical responses a little more. Also, it is realized that the best improvement regarding the particles happens when they are mixed with the composites containing more fibers. Thus, when the CNTs volume fractions is higher, the effect of the particles are more pronounced. Also, the trends of toughness modulus are linear for both hybrids.

CHAPTER X

CONCLUSIONS AND RECOMMENDATIONS

Polymer based structural components are widely used for numerous applications. Experiments reveal polymers are dissipative in nature and show rate and time dependent behavior under different loads, whether in the small or large strain regime. Also, several research studies show that mixing polymers with minute particles enhances composites thermo-mechanical properties. The idea is that dissipation phenomenon can be controlled by tiny particles; hence, composites behavior can be tailored by adding different particles into homogeneous polymer matrix. Thus, the goal is to provide recipes for virtually assessing the optimum combination of particles to customize composites for specific applications. For this purpose, the effects of randomly distributed particles in RVEs are virtually investigated on Young's modulus and heat generation (in small strain), as well as damage distribution and stress-strain response (SSR) of composites in the large strain range. Therefore, significant number of simulations are conducted to examine the above mentioned behavior.

10.1 Conclusions

Several achievements of the present dissertation are listed as follows:

1) An integrated framework for generalizing viscoelastic and viscoplastic constitutive laws from small to an arbitrarily large strain range has been formulated. The generalization is purely kinematic based; thus, it is applicable to different material types in the additive/multiplicative split-up framework of elastic and plastic strains.

2) A Schapery-type non-linear viscoelastic model based on II-PK stress and GL strain is derived utilizing Gibbs energy, to measure viscoelastic response in the large strain range. It is shown that the derived model using higher order ISV terms in Gibbs energy, and delivers similar mathematical form when lower terms are used. The effects of higher order terms are mapped to the model by the scalar function to capture the transient compliance.
3) The generalized viscoelastic and a Perzyna-type viscoplastic to large strain, and a viscodamage model are implemented in ABAQUS user material subroutine. The models were calibrated for PMMA by stress control tests, and they are validated by strain control experimental data sets.
4) A research software tool RVE_Maker, is designed and developed for creating micro/ nano RVEs. The RVE_Maker is able to create 2D and 3D composites. In 3D geometries, it is also able to generate hybrid particle-fiber composites.
5) Numerous FE analyses using only viscoelastic model in small strain were performed on 2D and 3D RVEs. The following observation were made:
    - The circular and spherical particles sizes do not affect the RVE responses for all creep, recovery, and cyclic loads. The effects of elliptical particles are more noticeable as compared to round shape particles.
    - Higher Young's modulus of the nano-composites in cyclic loads and diminishing in creep strains is a direct result of particles volume fractions. In the same volume fraction, particle shape governs the behavior.
    - The complex modulus in 2D simulations is higher than their counterpart in 3D models, and elliptical particles better enhance the behavior than the round ones.

- Energy dissipation and heat generation are found to be accelerated by adding particles to the system, or by increasing the applied load. The average temperature increase in the RVEs is about $1.1^{o}C$ in 2D and $0.9^{o}C$ in 3D models. Elliptical particles showed more generated heat comparing to circular ones.
- The 2D models artificially show localized viscoelastic strain regions; but in 3D models, such strain localization occurs when the particle volume fraction is high.

6) The overall elastic modulus of several small scale CNT-reinforced composites are evaluated and the FEM results were validated with MD and ROM, just for one single CNT. This agreement play a significant role, because it means FEA can be used for characterizing the overall response of large 3D composites with acceptable accuracy. Moreover the following results are achieved:
   - Longer CNTs exhibit considerably better load transfer compared to shorter ones, and CNTs Poisson's ratio does not affect the overall responses of the composites.
   - It is shown when a CNT is attached to the applied load face of an RVE, because the load directly acts on the CNT, the RVE elastic modulus is just governed by the embedded CNT. But, in reality load is applied to the matrix; and a very thin matrix layer in front of CNT tips significantly drops the modulus (10 times). Also, slight curvature in CNTs may drop the modulus about 2.2 times. In actual cases, because the load is applied on the matrix, and fibers are slightly or highly bent, and the bondings to matrix are imprefect; thus, obtaining extraordinary modulus enhancement is impossible.

- The composites behavior strongly depend on CNTs alignment, and the maximum mechanical responses are attained when assessed in the longitudinal direction of fibers. RVEs performances lower at any other fiber direction or a slight bending.
- Several large scale RVEs with two ARs are probed. The results indicate nanotubes with higher ARs aligned to the loading direction deliver the best load transferring between fibers and matrix. Adding CNTs with any morphologies (up to 3 vol%) linearly improve the non-periodic and periodic RVE modulus, and periodic ones show better enhancement. The effects of CNTs with smaller ARs are almost the same as higher ARs, but with lower improvement. Because CNTs with higher AR are finer and better dispersed in an RVE domain to locally carry smaller portion of internal forces. Straight aligned CNTs with smaller ARs show extra modulus reduction (≈40%) but in perpendicular direction minimum reduction is seen (≈3%).

7) Numerous large scale micromechanical models are generated and their responses regarding particles morphologies on overall responses are studied.
   - Micromechanical simulations show NCLPs can better enhance the composites SSR comparing to NCRPs. NCLPs shows damage shielding or crack tip pinning behavior to halt damage growth, which toughens the composite.
   - In compression, damage initiates at the NCLPs major tips and propagates in the direction of their major axis. But in tension, damages occur in between the major plates, then evolve either around particles or propagate to the undamaged regions.
   - NCRPs almost show the same damage distribution pattern; but, according to their shape, they cannot resist against damage growth path, and damage paths (cracks) bypass their round surfaces.

- CNTs with two ARs displayed enhancement in composites SSR, and higher AR showed better enhacement. But, CNTs with higher AR stimulate more damage, because their cross-sections are smaller and they penetrate into the matix. In tension, damage initiates at CNT tips, because of the significant load transferred via the tips. For both ARs, straight CNTs showed maximum improvement; but, they generate more damage in the RVEs, which expedites the SSR degradation.
- In all CNT configurations, adding more CNTs that are not placed in the direction of load does not enhance the composite SSR, especially for the curved CNT state. But in all CNT forms, damage pattern are the same; it initiates at fibers tips, and evolves along major axis direction, and then propagates perpendicular to the axis.
- Damage growth patterns in both hybrid cases are the same as RVEs containing just CNTs. The presence of particles almost do not stimulate damage inside the RVEs. In CNT-NCLP, by increasing the NCLP contents, the damaged regions and their average magnitudes decrease; but, NCRPs do not show such property. Thus, NCLPs can better shield the composites against damage growth while mixed with CNTs. For both hybrid cases, the main enhancement is due to the presence of CNTs and adding particles a little improves the performance. When the CNT volume fraction is higher, the effect of the particles is more pronounced, as well.

10.2 Computational Expenses

Creating, simulating, and extracting data from the mentioned micromechanical RVEs are cumbersome and very time consuming. One should notice that because heterogeneous composites having actual microstructural details are generated (discretization

contains millions of elements) are studied in large deformation range, also in each computational increment all model coordinates are updated, and many tensorial products must be computed; thus, very powerful computer resources are required to handle such FE problems, especially when numerous RVEs must be simulated and investigated. To overcome this problem, the numerical models should be professionally implemented in the ABAQUS-UMAT subroutine to minimize the arithmetic computations, checking conditions, and calling and passing of variables. In addition, internal subroutines in the UMAT subroutine must be implemented in a way to be compatible to be used by multiple CPUs (i.e., the subroutines should work simultaneously with several CPUs). Also, the amount of designated memory and the band for transferring data (catches) must be appropriate to the amount of data buffered and transferred in each increment by one CPU. If such items are considered and applied to the codes, and the computer resources are all set; then, huge RVEs can be simulated very fast. For example, simulating one 3D RVE containing 3 million elements, with the explained models without optimizing the FORTRAN code in UMAT and without applying parallelization capabilities to it (using one CPU) takes almost six weeks to be finished. But, applying the abovementioned code optimizations and other considerations allowed the simulation to be accomplished in just 1.8 days with 8 CPUs. One should note that utilizing 8 CPUs can approximately hasten such simulation just four times than using 1 CPU; thus, optimizing the code is more important.

10.3 Recommendations for Future Researches

The current research and study can be extended to cover more physical aspects of the actual behavior of micro/nano polymer composites, as follows:

1) The amount of dissipated energy and generated heat due to viscoplasticity and damage are more significant than the viscoelastic portion in particulated composites. Although, required equations are derived and mentioned in Appendix E, their values are not computed and presented in this work. Energy dissipation and temperature are highly recommended to be computed due to the three combined constitutive models, and the effects of the generated heat should be incorporated into the numerical models. This allows the degradation of material response due to the internal generated heat is measured while mechanical loads are applied, especially for high stress levels or strain rates.
2) The interfaces between the studied inclusions and polymer matrix can be considered and modeled through Cohesive Contact Elements (CCE) or Cohesive Zone Models (CZM). This allows virtual simulation of the traction separation damage; or, the debonding of inclusions from the surrounding matrix can be analyzed. One important future idea is to calculate and apply the generated heat corresponding to the separation of particles from matrix. This is of interest because of the local generated heat at the interfaces degrades the stiffness of the surrounding matrix, and then gradually distributes through the whole RVE.
3) In this work, particles and fibers are considered as just elastic materials. But, their actual behaviors are elastic-damage, or elastoplastic. For example, the mechanical

properties of NCLPs or CNTs are different in each direction. Because, inclusions carry high portions of internal forces, their actual response can locally affect the microstructure and then affect the overall response of the RVEs.

4) These time- and rate-dependent constitutive models can be modified to incorporate the effects of moisture diffusion (environmental condition), and aging (long term service) on polymer composites.
5) Thermal conductivity of carbon nanofibers/nanotubes are remarkably high. So, heat conduction can be studied while a composite is subjected to a heat flux load, or when heat is generated due to a mechanical load. The thermal coefficients can also be time dependent since the polymer matrix is time dependent.

After incorporating the mentioned recommendations, the responses of the whole models are qualified to be compared with experimental data. However, each of these items takes significant time and effort to be fully studied and practically implemented.

REFERENCES

ABAQUS: User's Manual, 2008. Version 6.8., Habbitt, Karlsson and Sorensen, Inc, Providence, RI.

Abu Al-Rub, R.K., 2008. Interfacial gradient plasticity governs scale-dependent yield strength and strain hardening rates in micro/nano structured metals. International Journal of Plasticity 24, 1277-1306.

Abu Al-Rub, R.K., Darabi, M.K., 2012. A thermodynamic framework for constitutive modeling of time- and rate-dependent materials, Part I: Theory. International Journal of Plasticity 34, 61-92.

Abu Al-Rub, R.K., Darabi, M.K., Little, D.N., Masad, E.A., 2010. A micro-damage healing model that improves prediction of fatigue life in asphalt mixes. International Journal of Engineering Science 48, 966-990.

Abu Al-Rub, R.K., Tehrani, A.H., 2011. Thermo-mechanical viscoelastic, viscoplastic, and viscodamage model for polymers and polymer composites, 52nd AIAA/ASME/ASCE/ AHS/ASC, Structures, Structural Dynamics and Materials Conference, Denver, CO.

Abu Al-Rub, R.K., Voyiadjis, G.Z., 2003. On the coupling of anisotropic damage and plasticity models for ductile materials. International Journal of Solids and Structures 40, 2611-2643.

Abu Al-Rub, R.K., Voyiadjis, G.Z., 2004a. Analytical and experimental determination of the material intrinsic length scale of strain gradient plasticity theory from micro-and nano-indentation experiments. International Journal of Plasticity 20, 1139-1182.

Abu Al-Rub, R.K., Voyiadjis, G.Z., 2004b. Determination of the material intrinsic length scale of gradient plasticity theory. International Journal for Multiscale Computational Engineering 2, 377-400.

Abu Al-Rub, R.K., Voyiadjis, G.Z., 2006a. A finite strain plastic-damage model for high velocity impact using combined viscosity and gradient localization limiters: Part I - Theoretical formulation. Int J Damage Mech 15, 293-334.

Abu Al-Rub, R.K., Voyiadjis, G.Z., 2006b. A physically based gradient plasticity theory. International Journal of Plasticity 22, 654-684.

Abu Al-Rub, R.K., Voyiadjis, G.Z., 2009. Gradient-enhanced coupled plasticity anisotropic damage model for concrete fracture: Computational Aspects and Applications. Int J Damage Mech 18, 115-154.

Ahmed, S., Jones, F.R., 1990. A review of particulate reinforcement theories for polymer composites. Journal of Materials Science 25, 4933-4942.

Aifantis, K.E., Willis, J.R., 2005. The role of interfaces in enhancing the yield strength of composites and polycrystals. Journal of the Mechanics and Physics of Solids 53, 1047-1070.

Ajayan, P.M., Schadler, L.S., Giannaris, C., Rubio, A., 2000. Single-walled carbon nanotube–polymer composites: Strength and weakness. Advanced Materials 12, 750-753.

Alder, B.J., Wainwright, T.E., 1957. Phase transition for a hard sphere system. The Journal of Chemical Physics 27, 1208-1209.

Altenbach, J., Altenbach, H., 1995. Einführung in die kontinuumsmechanik. Teubner Studienbücher, Stuttgart, Germany.

Anand, L., Ames, N.M., 2006. On modeling the micro-indentation response of an amorphous polymer. International Journal of Plasticity 22, 1123-1170.

Anand, L., Gurtin, M.E., 2003. A theory of amorphous solids undergoing large deformations, with application to polymeric glasses. International Journal of Solids and structures 40, 1465-1487.

Arruda, E.M., Boyce, M.C., 1993. Evolution of plastic anisotropy in amorphous polymers during finite straining. International Journal of Plasticity 9, 697-720.

Baek, S., Gleason, R.L., Rajagopal, K.R., Humphrey, J.D., 2007. Theory of small on large: Potential utility in computations of fluid–solid interactions in arteries. Computer Methods in Applied Mechanics and Engineering 196, 3070-3078.

Bandstra, J.P., Koss, D.A., Geltmacher, A., Matic, P., Everett, R.K., 2004. Modeling void coalescence during ductile fracture of a steel. Materials Science and Engineering: A 366, 269-281.

Bardenhagen, S.G., Kober, E.M., 2004. The generalized interpolation material point method. Computer Modeling in Engineering and Sciences 5, 477-496.

Barnes, H.A., Hutton, J.F., Walters, K., 1989. An introduction to rheology. Elsevier Science Limited, London, UK.

Başar, Y., Weichert, D., 2000. Nonlinear continuum mechanics of solids: Fundamental mathematical and physical concepts. Springer Verlag, Berlin, Germany.

Bathe, K.J., Ramm, E., Wilson, E.L., 1975. Finite element formulations for large deformation dynamic analysis. International Journal for Numerical Methods in Engineering 9, 353-386.

Baughman, R.H., Zakhidov, A.A., de Heer, W.A., 2002. Carbon nanotubes, the route toward applications. Science 297, 787-792.

Bažant, Z.P., 1971. A correlation study of formulations of incremental deformation and stability of continuous bodies. J. Appl. Mech 38, 9-19.

Bažant, Z.P., 1996. Finite strain generalization of smallstrain constitutive relations for any finite strain tensor and additive volumetric-deviatoric split. International Journal of Solids and Structures 33, 2887-2897.

Bažant, Z.P., Adley, M.D., Carol, I., Jirásek, M., Akers, S.A., Rohani, B., Cargile, J.D., Caner, F.C., 2000. Large-strain generalization of microplane model for concrete and application. Journal of Engineering Mechanics 126, 971-980.

Bažant, Z.P., Cedolin, L., 2010. Stability of structures: Elastic, inelastic, fracture and damage theories. World Scientific Pub Co Inc, Danvers, MA.

Bažant, Z.P., Oh, B.H., 1983. Crack band theory for fracture of concrete. Materials and Structures 16, 155-177.

Belloni, G., Bernasconi, G., Piatti, G., 1979. Creep damage models. Creep of engineering materials and structures. Applied Science Publishers, Ltd. London, UK.

Beran, M., 1965. Statistical continuum theories. Transactions of the Society of Rheology 9, 339-355.

Besson, J., Cailletaud, G., Chaboche, J.L., Forest, S., 2001. Mécanique non linéaire des matériaux. Hermès Science Publ., Paris, France.

Bocchieri, R.T., 2001. Time-dependent deformation of a nonlinear viscoelastic rubber-toughened fiber composite with growing damage. University of Texas at Austin, Texas.

Böhm, H.J., Eckschlager, A., Han, W., 2002. Multi-inclusion unit cell models for metal matrix composites with randomly oriented discontinuous reinforcements. Computational Materials Science 25, 42-53.

Bonet, J., Wood, R.D., 1997. Nonlinear continuum mechanics for finite element analysis. Cambridge University Press, London, UK.

Bower, A.F., 2009. Applied mechanics of solids. CRC Press, Boca Raton, FL.

Bower, C., Rosen, R., Jin, L., Han, J., Zhou, O., 1999. Deformation of carbon nanotubes in nanotube–polymer composites. Applied Physics Letters 74, 3317-3319.

Boyce, M.C., Parks, D.M., Argon, A.S., 1988. Large inelastic deformation of glassy polymers. Part I: Rate dependent constitutive model. Mechanics of Materials 7, 15-33.

Bruhns, O.T., 2009. Eulerian elastoplasticity: Basic issues and recent results. Theoretical and Applied Mechanics 36, 167-205.

Bruhns, O.T., Xiao, H., Meyers, A., 2001. Large simple shear and torsion problems in kinematic hardening elasto-plasticity with logarithmic rate. International Journal of Solids and Structures 38, 8701-8722.

Bucknall, C.B., 1977. Toughened plastics. Elsevier Science & Technology, London, UK.

Bucknall, C.B., Partridge, I.K., 1983. Phase separation in epoxy resins containing polyethersulphone. Polymer 24, 639-644.

Buryachenko, V.A., Roy, A., 2005. Effective elastic moduli of nanocomposites with prescribed random orientation of nanofibers. Composites Part B: Engineering 36, 405-416.

Cai, J.J., Salovey, R., 1999. Model filled rubber. II. Particle composition dependence of suspension rheology. Journal of Polymer Science Part B: Polymer Physics 37, 815-824.

Caiazzo, A.A., Costanzo, F., 2000. On the constitutive relations of materials with evolving microstructure due to microcracking. International Journal of Solids and Structures 37, 3375-3398.

Carol, I., Rizzi, E., Willam, K., 1994. A unified theory of elastic degradation and damage based on a loading surface. International Journal of Solids and Structures 31, 2835-2865.

Caruthers, J.M., Adolf, D.B., Chambers, R.S., Shrikhande, P., 2004. A thermodynamically consistent, nonlinear viscoelastic approach for modeling glassy polymers. Polymer 45, 4577-4597.

Cassenti, B.N., Annigeri, B.S., 1989. Thermodynamic constraints on stress rate formulations in constitutive models. Computational Mechanics 4, 429-432.

Chaboche, J.L., 2003. Damage mechanics. Comprehensive Structural Integrity 2, 213-284.

Chailleux, E., Davies, P., 2003. Modelling the non-linear viscoelastic and viscoplastic behaviour of aramid fibre yarns. Mechanics of Time-Dependent Materials 7, 291-303.

Chailleux, E., Davies, P., 2005. A non-linear viscoelastic viscoplastic model for the behaviour of polyester fibres. Mechanics of Time-Dependent Materials 9, 147-160.

Chawla, N., Jones, J.W., Andres, C., Allison, J.E., 1998. Effect of SiC volume fraction and particle size on the fatigue resistance of a 2080 Al/SiC p composite. Metallurgical and Materials Transactions A 29, 2843-2854.

Chen, W., Tao, X., Liu, Y., 2006. Carbon nanotube-reinforced polyurethane composite fibers. Composites Science and Technology 66, 3029-3034.

Chen, X.L., Liu, Y.J., 2004. Square representative volume elements for evaluating the effective material properties of carbon nanotube-based composites. Computational Materials Science 29, 1-11.

Choi, G.N., Krieger, I.M., 1986. Rheological studies on sterically stabilized model dispersions of uniform colloidal spheres: II. Steady-shear viscosity. Journal of Colloid and Interface Science 113, 101-113.

Christensen, R.M., 1966. On obtaining solutions in nonlinear viscoelasticity. Division Of Applied Mechanics, AD0651183. DTIC Document, University of California, Berkeley, CA.

Christensen, R.M., 2003. Theory of viscoelasticity: An introduction. Dover Pubns, New York, NY.

Cicekli, U., Voyiadjis, G.Z., Abu Al-Rub, R.K., 2007. A plasticity and anisotropic damage model for plain concrete. International Journal of Plasticity 23, 1874-1900.

Colak, O.U., 2005. Modeling deformation behavior of polymers with viscoplasticity theory based on overstress. International Journal of Plasticity 21, 145-160.

Coleman, B.D., Noll, W., 1961. Foundations of linear viscoelasticity. Reviews of Modern Physics 33, 239.

Corum, J.M., Battiste, R.L., Ruggles, M.B., Ren, W., 2001. Durability-based design criteria for a chopped-glass-fiber automotive structural composite. Composites Science and Technology 61, 1083-1095.

Cozzarelli, G., 1981. Non-linear creep damage under one-dimensional variable tensile stress. International Journal of Non-Linear Mechanics 16, 27-38.

Crissman, J.M., Zapas, L.J., 1985. On the mechanical preconditioning of ultrahigh-molecular-weight polyethylene at small uniaxial deformations. Journal of Polymer Science: Polymer Physics Edition 23, 2599-2610.

Cuitino, A., Ortiz, M., 1992. A material-independent method for extending stress update algorithms from small-strain plasticity to finite plasticity with multiplicative kinematics. Engineering Computations 9, 437-437.

Dahl, J.S., Smith, G., Houston, D., Berger, L., 2005. The influence of fiber tow size on the performance of chopped carbon fiber reinforced composites, Materials and Processing Technologies for Revolutionary Applications, 37th ISTC, Washington, D.C.

Darabi, M.K., Abu Al-Rub, R.K., Masad, E.A., Huang, C.W., Little, D.N., 2011. A thermo-viscoelastic-viscoplastic-viscodamage constitutive model for asphaltic materials. International Journal of Solids and Structures 48, 191-207.

Darabi, M.K., Abu Al-Rub, R.K., Masad, E.A., Little, D.N., 2012. A thermodynamic framework for constitutive modeling of time-and rate-dependent materials. Part II: Numerical aspects and application to asphalt concrete. International Journal of Plasticity 35, 67-69

Dienes, J.K., 1979. On the analysis of rotation and stress rate in deforming bodies. Acta Mechanica 32, 217-232.

Dierickx, P., Verdu, C., Rouais, J.C., Reynaud, A., Fougères, R., 1997. Study of physico-chemical mechanisms responsible for damage of heat treated and as-cast ferritic spheroidal graphite cast irons. Advanced Materials Research 4, 153-160.

Dill, E.H., 2007. Continuum mechanics: Elasticity, plasticity, viscoelasticity. CRC Press, Boca Raton, FL.

Donald, A.M., Kramer, E.J., 1982. Plastic deformation mechanisms in poly (acrylonitrile-butadiene styrene)[ABS]. Journal of Materials Science 17, 1765-1772.

Doyle, T.C., Ericksen, J.L., 1956. Non-linear elasticity. Advances in Applied Mechanics. 4, 53-115.

Duschlbauer, D., Böhm, H.J., Pettermann, H.E., 2006. Computational simulation of composites reinforced by planar random fibers: Homogenization and localization by unit cell and mean field approaches. Journal of Composite Materials 40, 2217-2234.

Dvorkin, E.N., 2010. Advanced topics in computational solid mechanics. Industrial Applications Section 3: Stress measures., Mechanical Engineering. Stanford University, Stanford, CA.

Ehlers, W., Markert, B., 2003. A macroscopic finite strain model for cellular polymers. International Journal of Plasticity 19, 961-976.

Ericson, M.L., Berglund, L.A., 1993. The effect of microstructure on the elastic modulus and strength of performed and commercial GMTs. Polymer Composites 14, 35-41.

Eshelby, J.D., 1957. The determination of the elastic field of an ellipsoidal inclusion, and related problems. Proceedings of the Royal Society of London. Series A. Mathematical and Physical Sciences 241, 376-396.

Fardshisheh, F., Onat, E.T., 1974. Representation of elastoplastic behavior by means of state variables. A.Sawczuk(Ed.), Problems of Plasticity, Leiden: Noordhoff International Publishing, 1974, 89-115.

Findley, W.N., Onaran, K., 1974. Incompressible and linearly compressible viscoelastic creep and relaxation. J Appl Mech-T ASME 41, 243-248.

Fisher, F.T., Bradshaw, R.D., Brinson, L.C., 2003. Fiber waviness in nanotube-reinforced polymer composites I: Modulus predictions using effective nanotube properties. Composites Science and Technology 63, 1689-1703.

Flory, P.J., 1961. Thermodynamic relations for high elastic materials. Trans. Faraday Soc. 57, 829-838.

Frank, G.J., Brockman, R.A., 2001. A viscoelastic-viscoplastic constitutive model for glassy polymers. International Journal of Solids and Structures 38, 5149-5164.

Frankland, S.J.V., Harik, V.M., Odegard, G.M., Brenner, D.W., Gates, T.S., 2003. The stress–strain behavior of polymer–nanotube composites from molecular dynamics simulation. Composites Science and Technology 63, 1655-1661.

Fremond, M., Nedjar, B., 1996. Damage, gradient of damage and principle of virtual power. International Journal of Solids and Structures 33, 1083-1103.

Fu, S.Y., Feng, X.Q., Lauke, B., Mai, Y.W., 2008. Effects of particle size, particle/matrix interface adhesion and particle loading on mechanical properties of particulate–polymer composites. Composites Science and Technology Part B 39 (2008) 933–961.

Fu, Y.B., Ogden, R.W., 2001. Nonlinear elasticity: Theory and applications. Cambridge Univ Pr, Cambridge, UK.

Gade, S., 2005. Characterization of the mechanical properties of carbon nanotube-based composite using the finite element method, Department of Mechanical, Industrial and Nuclear Engineering. University of Cincinnati, Cincinnati, OH.

Gearing, B.P., Anand, L., 2004. Notch-sensitive fracture of polycarbonate. International Journal of Solids and Structures 41, 827-845.

Gojny, F.H., Wichmann, M.H.G., Fiedler, B., Kinloch, I.A., Bauhofer, W., Windle, A.H., Schulte, K., 2006. Evaluation and identification of electrical and thermal conduction mechanisms in carbon nanotube/epoxy composites. Polymer 47, 2036-2045.

Govindjee, S., Sackman, J.L., 1999. On the use of continuum mechanics to estimate the properties of nanotubes. Solid State Communications 110, 227-230.

Green, A.E., Naghdi, P.M., 1965. A general theory of an elastic-plastic continuum. Archive for Rational Mechanics and Analysis 18, 251-281.

Green, A.E., Naghdi, P.M., 1971. Some remarks on elastic-plastic deformation at finite strain. International Journal of Engineering Science 9, 1219-1229.

Green, A.E., Rivlin, R.S., 1957. The mechanics of non-linear materials with memory. Archive for Rational Mechanics and Analysis 1, 1-21.

Griebel, M., Hamaekers, J., 2004. Molecular dynamics simulations of the elastic moduli of polymer–carbon nanotube composites. Computer Methods in Applied Mechanics and Engineering 193, 1773-1788.

Gudmundson, P., 2004. A unified treatment of strain gradient plasticity. Journal of the Mechanics and Physics of Solids 52, 1379-1406.

Gurtin, M.E., 1981. An introduction to continuum mechanics. Academic Pr, New York, NY.

Gurtin, M.E., 2003. On a framework for small-deformation viscoplasticity: Free energy, microforces, strain gradients. International Journal of Plasticity 19, 47-90.

Gurtin, M.E., Anand, L., 2005. A theory of strain-gradient plasticity for isotropic, plastically irrotational materials. Part I: Small deformations. Journal of the Mechanics and Physics of Solids 53, 1624-1649.

Gusev, A., Heggli, M., Lusti, H.R., Hine, P.J., 2002. Orientation averaging for stiffness and thermal expansion of short fiber composites. Advanced Engineering Materials 4, 931-933.

Gusev, A.A., 1997. Representative volume element size for elastic composites: A numerical study. Journal of the Mechanics and Physics of Solids 45, 1449-1459.

Haj-Ali, R.M., Muliana, A.H., 2004. Numerical finite element formulation of the Schapery non-linear viscoelastic material model. International Journal for Numerical Methods in Engineering 59, 25-45.

Hall, R.B., 2005. A thermodynamic framework for viscoplasticity based on overstress (VBO). Journal of Engineering Materials and Technology 127, 369.

Hao, S., Liu, W.K., Moran, B., Vernerey, F., Olson, G.B., 2004. Multi-scale constitutive model and computational framework for the design of ultra-high strength, high toughness steels. Computer Methods in Applied Mechanics and Engineering 193, 1865-1908.

Hasan, O.A., Boyce, M.C., 1993. Energy storage during inelastic deformation of glassy polymers. Polymer 34, 5085-5092.

Hasan, O.A., Boyce, M.C., 1995. A constitutive model for the nonlinear viscoelastic viscoplastic behavior of glassy polymers. Polymer Engineering and Science 35, 331-344.

Hashin, Z., Shtrikman, S., 1963. A variational approach to the theory of the elastic behaviour of multiphase materials. Journal of the Mechanics and Physics of Solids 11, 127-140.

Haupt, P., Lion, A., Backhaus, E., 2000. On the dynamic behaviour of polymers under finite strains: constitutive modelling and identification of parameters. International Journal of Solids and Structures 37, 3633-3646.

Heinrich, G., Klüppel, M., Vilgis, T.A., 2002. Reinforcement of elastomers. Current opinion in solid state and materials science 6, 195-203.

Hibbitt, H.D., Karlsson, B.I., Sorensen, E.P., 2008. ABAQUS TM, 6.8 ed. Hibbit, Karlsson and Sorensen Inc, Providence, RI.

Hill, R., 1963. Elastic properties of reinforced solids: some theoretical principles. Journal of the Mechanics and Physics of Solids 11, 357-372.

Hill, R., 1968. On constitutive inequalities for simple materials-I. Journal of the Mechanics and Physics of Solids 16, 229-242.

Hill, R., Rice, J.R., 1973. Elastic potentials and the structure of inelastic constitutive laws. SIAM Journal on Applied Mathematics, 448-461.

Hoa , S.V., Liu , W., Pugh, M., 2004. Augmentation of fracture toughness of modified epoxy using nanoclay, Fifth Canada Japan Workshop on Composites., Yonezawa, Japan.

Hoger, A., Carlson, D.E., 1984. On the derivative of the square root of a tensor and Guo's rate theorems. Journal of elasticity 14, 329-336.

Holzapfel, G.A., 2000. Nonlinear solid mechanics: A continuum approach for engineering.

Holzapfel, G.A., Gasser, T.C., Ogden, R.W., 2000. A new constitutive framework for arterial wall mechanics and a comparative study of material models. Journal of elasticity 61, 1-48.

Huang, C.W., Abu Al-Rub, R.K., Masad, E.A., Little, D.N., Airey, G.D., 2011a. Numerical implementation and validation of a nonlinear-viscoelastic and viscoplastic model for asphalt concrete mixes. International Journal of Pavement Engineering 12, 433-447.

Huang, C.W., Al-Rub, R.K.A., Masad, E.A., Little, D.N., 2011b. Three-dimensional simulations of asphalt pavement permanent deformation using a nonlinear viscoelastic and viscoplastic model. Journal of Materials in Civil Engineering 23, 56.

Iijima, S., 1991. Helical microtubules of graphitic carbon. Nature 354, 56-58.

Ivanov, I., Tabiei, A., 2001. Three-dimensional computational micro-mechanical model for woven fabric composites. Composite Structures 54, 489-496.

Jacob, G.C., Starbuck, J.M., Fellers, J.F., Simunovic, S., Boeman, R.G., 2006. Crashworthiness of various random chopped carbon fiber reinforced epoxy composite materials and their strain rate dependence. Journal of Applied Polymer Science 101, 1477-1486.

Jeulin, D., Ostoja-Starzewski, M., 2002. Mechanics of random and multiscale microstructures. SpringerWien, New York, NY.

Ji, W., Waas, A.M., Bažant, Z.P., 2010. Errors caused by non-work-conjugate stress and strain measures and necessary corrections in finite element programs. Journal of Applied Mechanics 77, 044504.

Johnson, G.C., Bammann, D.J., 1984. A discussion of stress rates in finite deformation problems. International Journal of Solids and Structures 20, 725-737.

Kachanov, L.M., 1958. Time of the rupture process under creep conditions. Isv. Akad. Nauk. SSR. Otd Tekh. Nauk 8, 26-31.

Kanit, T., Forest, S., Galliet, I., Mounoury, V., Jeulin, D., 2003. Determination of the size of the representative volume element for random composites: statistical and numerical approach. International Journal of Solids and Structures 40, 3647-3679.

Kari, S., Berger, H., Gabbert, U., 2007. Numerical evaluation of effective material properties of randomly distributed short cylindrical fibre composites. Computational Materials Science 39, 198-204.

Khan, A.S., Lopez-Pamies, O., Kazmi, R., 2006. Thermo-mechanical large deformation response and constitutive modeling of viscoelastic polymers over a wide range of strain rates and temperatures. International Journal of Plasticity 22, 581-601.

Khan, K. A., 2011. A multiscale model for coupled heat conduction and deformations of viscoelastic composites. Texas A&M University, Mechanical Engineering Department, College Station, TX.

Khan, K.A., Muliana, A.H., 2009. A multi-scale model for coupled heat conduction and deformations of viscoelastic functionally graded materials. Composites Part B: Engineering 40, 511-521.

Khan, S.U., Iqbal, K., Munir, A., Kim, J.K., 2011. Quasi-static and impact fracture behaviors of CFRPs with nanoclay-filled epoxy matrix. Composites Part A: Applied Science and Manufacturing 42, 253-264.

Kim, J.S., Muliana, A.H., 2009. A time-integration method for the viscoelastic-viscoplastic analyses of polymers and finite element implementation. International Journal for Numerical Methods in Engineering 79, 550-575.

Kinloch, A.J., Shaw, S.J., Hunston, D.L., 1983. Deformation and fracture behaviour of a rubber-toughened epoxy: 2. Failure criteria. Polymer 24, 1355-1363.

Kinloch, A.J., Williams, J.G., 1980. Crack blunting mechanisms in polymers. Journal of Materials Science 15, 987-996.

Kiser, M.T., Zok, F.W., Wilkinson, D.S., 1996. Plastic flow and fracture of a particulate metal matrix composite. Acta Materialia 44, 3465-3476.

Kondo, H., Tanaka, T., Masuda, T., Nakajima, A., 1992. Aging effects in 16 years on mechanical properties of commercial polymers. Pure and Applied Chemistry 64, 1945-1958.

Kraus, G., 1984. Mechanical losses in carbon-black-filled rubbers. Journal of Applied Polymer Science: Applied Polymer Symposium, 39, 75-92.

Krempl, E., Ho, K., 1998. An overstress model for solid polymer deformation behavior applied to nylon 66. Time Dependent and Nonlinear Effects in Polymers and Composites, 118-137.

Kröner, E., 1960. Allgemeine kontinuumstheorie der versetzungen und eigenspannungen. Archive for Rational Mechanics and Analysis 4, 273-334.

Kröner, E., 1980. Linear properties of random media: the systematic theory. Comportements Rhéologiques et Structure des Matériaux, CR 15ème Coll. GFR. Paris, France.

Kunz-Douglass, S., Beaumont, P.W.R., Ashby, M.F., 1980. A model for the toughness of epoxy-rubber particulate composites. Journal of Materials Science 15, 1109-1123.

Lai, J., Bakker, A., 1995. An integral constitutive equation for nonlinear plasto-viscoelastic behavior of high-density polyethylene. Polymer Engineering and Science 35, 1339-1347.

Lai, J., Bakker, A., 1996. 3-D Schapery representation for non-linear viscoelasticity and finite element implementation. Computational Mechanics 18, 182-191.

Leaderman, H., 1943. Elastic and creep properties of filamentous materials and other high polymers. The Textile Foundation, Washington, D.C.

Lee, E.H., 1969. Elastic-plastic deformation at finite strains. Journal of Applied Mechanics 36, 1.

Lee, E.H., Liu, D.T., 1967. Finite-strain elastic-plastic theory with application to plane-wave analysis. Journal of Applied Physics 38, 19-27.

Lee, F.A., 1986. One-dimensional strain-dependent creep damage in inhomogeneous materials. International Journal of Non-Linear Mechanics 21, 303-314.

Lee, J.H., Shishidou, T., Zhao, Y.J., Freeman, A.J., Olson, G.B., 2005. Strong interface adhesion in Fe/TiC. Philosophical Magazine 85, 3683-3697.

Lee, N.J., Jang, J., 1999. The effect of fibre content on the mechanical properties of glass fibre mat/polypropylene composites. Composites Part A: Applied Science and Manufacturing 30, 815-822.

Lemaitre, J., Chaboche, J.L., 1994. Mechanics of solid materials. Cambridge University Press, Cambridge, UK.

Liefeith, D., Kolling, S., 2007. An anisotropic material model for finite rubber viscoelasticity, LS-DYNA FORUM; D-II-02 Dyna More, Stuttgart , Germany.

Liu, T., Tjiu, W.C., Tong, Y., He, C., Goh, S.S., Chung, T.S., 2004. Morphology and fracture behavior of intercalated epoxy/clay nanocomposites. Journal of Applied Polymer Science 94, 1236-1244.

Liu, Y., Nishimura, N., Otani, Y., 2005. Large-scale modeling of carbon-nanotube composites by a fast multipole boundary element method. Computational Materials Science 34, 173-187.

Liu, Y.J., Chen, X.L., 2003. Evaluations of the effective material properties of carbon nanotube-based composites using a nanoscale representative volume element. Mechanics of Materials 35, 69-81.

Liu, Y.J., Chen, X.L., 2007. Continuum models of carbon nanotube-based composites using the boundary element method. Electronic Journal of Boundary Elements 1, 316-335.

Lloyd, D.J., 1994. Particle reinforced aluminium and magnesium matrix composites. International Materials Reviews 39, 1-23.

Lockett, F.J., 1972. Nonlinear viscoelastic solids. Academic Press London, London, UK.

Lu, J.P., 1997. Elastic properties of single and multilayered nanotubes. Journal of Physics and Chemistry of Solids 58, 1649-1652.

Lubarda, V.A., Benson, D.J., 2001. On the partitioning of the rate of deformation gradient in phenomenological plasticity. International Journal of Solids and Structures 38, 6805-6814.

Lubliner, J., 1986. Normality rules in large-deformation plasticity. Mechanics of Materials 5, 29-34.

Lubliner, J., 1990. Plasticity theory. University California at Berkeley, Berkeley, CA.

Makradi, A., Ahzi, S., Gregory, R.V., Edie, D.D., 2005. A two-phase self-consistent model for the deformation and phase transformation behavior of polymers above the glass transition temperature: application to PET. International Journal of Plasticity 21, 741-758.

Megnis, M., Varna, J., 2003. Nonlinear viscoelastic, viscoplastic characterization of unidirectional GF/EP composite. Mechanics of Time-Dependent Materials 7, 269-290.

Megnis, M., Varna, J., Allen, D.H., Holmberg, A., 2001. Micromechanical modeling of viscoelastic response of GMT composite. Journal of Composite Materials 35, 849.

Mehrabadi, M.M., Nemat-Nasser, S., 1987. Some basic kinematical relations for finite deformations of continua. Mechanics of Materials 6, 127-138.

Meraghni, F., Desrumaux, F., Benzeggagh, M.L., 2002. Implementation of a constitutive micromechanical model for damage analysis in glass material reinforced composite structures. Composites Science and Technology 62, 2087-2097.

Meyers, A., Xiao, H., Bruhns, O., 2003. Elastic stress ratchetting and corotational stress rates. Technische Mechanik 23, 92-102.

Miller, M.N., 1969. Bounds for effective electrical, thermal, and magnetic properties of heterogeneous materials. Journal of Mathematical Physics 10, 1988.

Milton, G.W., 1982. Bounds on the elastic and transport properties of two-component composites. Journal of the Mechanics and Physics of Solids 30, 177-191.

Mishnaevsky, J.L., 2007. Computational mesomechanics of composites. John Wiley and Sons, London, UK.

Mishnaevsky, J.L., 2012. Micromechanics of hierarchical materials: A brief overview. Rev. Adv. Mater. Sci 30, 60-72.

Mishnaevsky, J.L., Brondsted, P., 2009. Micromechanisms of damage in unidirectional fiber reinforced composites: 3D computational analysis. Composites Science and Technology 69, 1036-1044.

Moisala, A., Li, Q., Kinloch, I.A., Windle, A.H., 2006. Thermal and electrical conductivity of single-and multi-walled carbon nanotube-epoxy composites. Composites Science and Technology 66, 1285-1288.

Mokashi, V.V., Qian, D., Liu, Y., 2007. A study on the tensile response and fracture in carbon nanotube-based composites using molecular mechanics. Composites Science and Technology 67, 530-540.

Moran, B., Ortiz, M., Shih, C.F., 1990. Formulation of implicit finite element methods for multiplicative finite deformation plasticity. International Journal for Numerical Methods in Engineering 29, 483-514.

Mori, T., Tanaka, K., 1973. Average stress in matrix and average elastic energy of materials with misfitting inclusions. Acta Metallurgica 21, 571-574.

Morman, K.N., 1985. Rubber viscoelasticity: A review of current understanding. Ford Motor Company, Dearborn, MI.

Mott, P.H., Argon, A.S., Suter, U.W., 1993. Atomistic modelling of plastic deformation of glassy polymers. Philosophical Magazine A 67, 931-978.

Muliana, A.H., Haj-Ali, R.M., 2008. A multi-scale framework for layered composites with thermo-rheologically complex behaviors. International Journal of Solids and Structures 45, 2937-2963.

Muliana, A.H., Khan, K.A., 2008. A time-integration algorithm for thermo-rheologically complex polymers. Computational Materials Science 41, 576-588.

Muliana, A.H., Kim, J.S., 2007. A concurrent micromechanical model for predicting nonlinear viscoelastic responses of composites reinforced with solid spherical particles. International Journal of Solids and Structures 44, 6891-6913.

Murakami, S., Kamiya, K., 1997. Constitutive and damage evolution equations of elastic-brittle materials based on irreversible thermodynamics. International Journal of Mechanical Sciences 39, 473-486.

Naghdi, P.M., 1990. A critical review of the state of finite plasticity. Z. Angew. Math. Phys. 41, 315–394.

Nagtegaal, J.C., De Jong, J.E., 1982. Some aspects of non-isotropic work-hardening in finite strain plasticity. Plasticity of Metals at Finite Strain: Theory, Experiment and Computation 65, 102.

Nemat-Nasser, S., 1982. On finite deformation elasto-plasticity. International Journal of Solids and Structures 18, 857-872.

Nemat-Nasser, S., Hori, M., 1999. Micromechanics: overall properties of heterogeneous materials. Elsevier Amsterdam, Amesterdam, Netherlands.

Nemat-Nasser, S., Yu, N., Hori, M., 1993. Bounds and estimates of overall moduli of composites with periodic microstructure. Mechanics of Materials 15, 163-181.

Norris, A.N., 2008. Eulerian conjugate stress and strain. Journal of Mechanics of Materials and Structures 3, 1-20.

O'Dowd, N.P., Knauss, W.G., 1995. Time dependent large principal deformation of polymers. Journal of the Mechanics and Physics of Solids 43, 771-792.

Odegard, G.M., Gates, T., Wise, K.E., Park, C., Siochi, E., 2003. Constitutive modeling of nanotube–reinforced polymer composites. Composites Science and Technology 63, 1671-1687.

Odegard, G.M., Gates, T.S., Nicholson, L.M., Wise, K.E., 2002. Equivalent-continuum modeling of nano-structured materials. Composites Science and Technology 62, 1869-1880.

Odqvist, F.K., Hult, J.G., 1961. Some aspects of creep rupture. Arkiv för Fysik 19, 379-382.

Ogden, R.W., 1997. Non-linear elastic deformations. Courier Dover Publication, Mineola, NY.

Okereke, M.I., Buckley, C.P., Hieu, L.C., 2002. Micromechanical modelling of finite deformation of thermoplastic matrix composites. University of Greenwich, London, UK.

Oleynik, E.F., Baer, E., Moet, S., 1990. High performance polymers. Hauser: Munich, 79.

Ortiz, M., Martin, J.B., 1989. Symmetry-preserving return mapping algorithms and incrementally extremal paths: A unification of concepts. International Journal for Numerical Methods in Engineering 28, 1839-1853.

Osman, M.A., Atallah, A., 2006. Effect of the particle size on the viscoelastic properties of filled polyethylene. Polymer 47, 2357-2368.

Ostoja-Starzewski, M., 2002. Microstructural randomness versus representative volume element in thermomechanics. Transactions-American Society of Mechanical Engineers Journal Of Applied Mechanics 69, 25-35.

Painter, P.C., Coleman, M.M., 1997. Fundamentals of polymer science. Recherche 67, 02.

Pan, Y., Iorga, L., Pelegri, A.A., 2008. Numerical generation of a random chopped fiber composite RVE and its elastic properties. Composites Science and Technology 68, 2792-2798.

Pasricha, A., Tuttle, M.E., Emery, A.F., 1995. Time-dependent response of IM7/5260 composites subjected to cyclic thermo-mechanical loading. Composites Science and Technology 55, 49-56.

Peng, J., Wu, J., Hwang, K.C., Song, J., Huang, Y., 2008. Can a single-wall carbon nanotube be modeled as a thin shell? Journal of the Mechanics and Physics of Solids 56, 2213-2224.

Perzyna, P., 1966. Fundamental problems in viscoplasticity. Advances in Applied Mechanics 9, 244-368.

Perzyna, P., 1971. Thermodynamic theory of viscoplastcity. Advances in Applied Mechanics 11, 313-354.

Pipkin, A.C., Rogers, T.G., 1968. A non-linear integral representation for viscoelastic behaviour. Journal of the Mechanics and Physics of Solids 16, 59-72.

Qian, D., Dickey, E.C., Andrews, R., Rantell, T., 2000. Load transfer and deformation mechanisms in carbon nanotube-polystyrene composites. Applied Physics Letters 76, 2868-2870.

Qian, D., Liu, W.K., Ruoff, R.S., 2003. Load transfer mechanism in carbon nanotube ropes. Composites Science and Technology 63, 1561-1569.

Qian, D., Wagner, G.J., Liu, W.K., Yu, M.F., Ruoff, R.S., 2002. Mechanics of carbon nanotubes. Applied Mechanics Reviews 55, 495.

Quek, S.C., Waas, A., Shahwan, K.W., Agaram, V., 2004. Compressive response and failure of braided textile composites: Part 2-computations. International Journal of Non-Linear Mechanics 39, 649-663.

Rabotnov, I.N., 1969. Creep problems in structural members, illustrated ed. North-Holland Pub. Co., Amesterdam, Netherlands.

Rajagopal, K.R., Srinivasa, A.R., 1998. Mechanics of the inelastic behavior of materials—part 1, theoretical underpinnings. International Journal of Plasticity 14, 945-967.

Rajagopal, K.R., Srinivasa, A.R., 2000. A thermodynamic frame work for rate type fluid models. Journal of Non-Newtonian Fluid Mechanics 88, 207-227.

Reese, S., 2003. A micromechanically motivated material model for the thermo-viscoelastic material behaviour of rubber-like polymers. International Journal of Plasticity 19, 909-940.

Rhee, M., Hirth, J.P., Zbib, H.M., 1994. A superdislocation model for the strengthening of metal matrix composites and the initiation and propagation of shear bands. Acta Metallurgica et Materialia 42, 2645-2655.

Rice, J.R., 1971. Inelastic constitutive relations for solids: an internal-variable theory and its application to metal plasticity. Journal of the Mechanics and Physics of Solids 19, 433-455.

Rolph, W., 1983. On large deformation and large strain elastic-plastic analysis of continua. Massachusetts Institute of Technology.

Rooijackers, H.F.L., 1988. A numerical implementation of the Schapery model for nonlinear visco-elasticity. Eindhoven University of Technology, Eindhoven, Netherlands.

Rosati, L., 2000. A novel approach to the solution of the tensor equation AX+ XA= H. International Journal of Solids and Structures 37, 3457-3477.

Ruoff, R.S., Lorents, D.C., 1995. Mechanical and thermal properties of carbon nanotubes. Carbon 33, 925-930.

Sadkin, Y., Aboudi, J., 1989. Viscoelastic behavior of thermo-rheologically complex resin matrix composites. Composites Science and Technology 36, 351-365.

Salvetat, J.P., Bonard, J.M., Thomson, N.H., Kulik, A.J., Forro, L., Benoit, W., Zuppiroli, L., 1999a. Mechanical properties of carbon nanotubes. Applied Physics A: Materials Science & Processing 69, 255-260.

Salvetat, J.P., Briggs, G.A.D., Bonard, J.M., Bacsa, R.R., Kulik, A.J., Stöckli, T., Burnham, N.A., Forró, L., 1999b. Elastic and shear moduli of single-walled carbon nanotube ropes. Physical Review Letters 82, 944-947.

Sanchez-Palencia, E., Zaoui, A., 1987. Homogenization techniques for composite media, CISM International Center for Mechanical Sciences, Udine, Italy.

Schadler, L.S., Giannaris, S.C., Ajayan, P.M., 1998. Load transfer in carbon nanotube epoxy composites. Applied Physics Letters 73, 3842-3844.

Schapery, R.A., 1964. Application of thermodynamics to thermomechanical, fracture, and birefringent phenomena in viscoelastic media. Journal of Applied Physics 35, 1451-1465.

Schapery, R.A., 1966. An engineering theory of nonlinear viscoelasticity with applications. International Journal of Solids and Structures 2, 407-425.

Schapery, R.A., 1969a. Further development of a thermodynamic constitutive theory: stress formulation. Purdue University, Purdue Resarch Foundation, Lafayette, IN.

Schapery, R.A., 1969b. On the characterization of nonlinear viscoelastic materials. Polymer Engineering and Science 9, 295-310.

Schapery, R.A., 1974. Viscoelastic behavior and analysis of composite materials. Mechanics and Materials Research Center, Texas Engineering Experiment Station, Texas A&M University, College Station, TX.

Schapery, R.A., 1975. A theory of crack initiation and growth in viscoelastic media. International Journal of Fracture 11, 141-159.

Schapery, R.A., 1990. Simplifications in the behavior of viscoelastic composites with growing damage. Springer New York, NY.

Schapery, R.A., 1997. Nonlinear viscoelastic and viscoplastic constitutive equations based on thermodynamics. Mechanics of Time-Dependent Materials 1, 209-240.

Schapery, R.A., 2000. Nonlinear viscoelastic solids. International Journal of Solids and Structures 37, 359-366.

Scheidler, M., 1994. The tensor equation AX+ XA= Φ (A, H), with applications to kinematics of continua. Journal of Elasticity 36, 117-153.

Ségard, E., Benmedakhene, S., Laksimi, A., La, D., 2002. Influence of the fibre-matrix interface on the behaviour of polypropylene reinforced by short glass fibres above glass transition temperature. Composites Science and Technology 62, 2029-2036.

Seidel, G.D., Allen, D.H., Helms, K.L.E., Groves, S.E., 2005. A model for predicting the evolution of damage in viscoelastic particle-reinforced composites. Mechanics of Materials 37, 163-178.

Shenderova, O.A., Zhirnov, V.V., Brenner, D.W., 2002. Carbon nanostructures. Critical Reviews in Solid State and Material Sciences 27, 227-356.

Sheng, N., Boyce, M.C., Parks, D.M., Rutledge, G., Abes, J., Cohen, R., 2004a. Multiscale micromechanical modeling of polymer/clay nanocomposites and the effective clay particle. Polymer 45, 487-506.

Sidoroff, F., 1974. Un mode`le viscoe´lastique non line´aire avec configuration interme´diaire. Journal de Me´chanique 13.4 , 679-713

Sidoroff, F., 1978. Sur l'equation tensorielle AX+ XA= H. CR Acad. Sci. Paris Ser. A 286, 71-73.

Simo, J., Ortiz, M., 1985. A unified approach to finite deformation elastoplastic analysis based on the use of hyperelastic constitutive equations. Computer Methods in Applied Mechanics and Engineering 49, 221-245.

Simo, J.C., 1988. A framework for finite strain elastoplasticity based on maximum plastic dissipation and the multiplicative decomposition: Part I. Continuum formulation. Computer Methods in Applied Mechanics and Engineering 66, 199-219.

Simo, J.C., Hughes, T.J.R., 1998. Computational inelasticity. Springer, New York, NY.

Simo, J.C., Taylor, R.L., Pister, K.S., 1985. Variational and projection methods for the volume constraint in finite deformation elasto-plasticity. Computer Methods in Applied Mechanics and Engineering 51, 177-208.

Smalley, R.E., Colbert, D.T., 1996. Self-assembly of fullerene tubes and balls. ChemInform 27, no. doi: 10.1002/chin. 199650279.

Sohlberg, K., Sumpter, B.G., Tuzun, R.E., Noid, D.W., 1999. Continuum methods of mechanics as a simplified approach to structural engineering of nanostructures. Nanotechnology 9, 30.

Song, Y.S., Youn, J.R., 2006. Modeling of effective elastic properties for polymer based carbon nanotube composites. Polymer 47, 1741-1748.

Sultan, J.N., McGarry, F.J., 1973. Effect of rubber particle size on deformation mechanisms in glassy epoxy. Polymer Engineering & Science 13, 29-34.

Tehrani, A.H., Abu Al-Rub, R.K., 2011. Mesomechanical modeling of polymer/clay nanocomposites using a viscoelastic-viscoplastic-viscodamage constitutive model. ASME Journal of Engineering Materials and Technology 133, 011-017.

Thostenson, E.T., Ren, Z., Chou, T.W., 2001. Advances in the science and technology of carbon nanotubes and their composites: a review. Composites science and technology 61, 1899-1912.

Tjong, S.C., 2006. Structural and mechanical properties of polymer nanocomposites. Material Science and Engineering: Reports 53, 73–197.

Torquato, S., 1991. Random heterogeneous media: microstructure and improved bounds on effective properties. Applied Mechanics Reviews 44, 37.

Torquato, S., Lado, F., 1986. Effective properties of two-phase disordered composite media: II. Evaluation of bounds on the conductivity and bulk modulus of dispersions of impenetrable spheres. Physical Review B 33, 6428.

Torquato, S., Stell, G., 1982. Microstructure of two-phase random media. I. The n-point probability functions. The Journal of Chemical Physics 77, 2071.

Tu, S.T., Cai, W.Z., Yin, Y., Ling, X., 2005. Numerical simulation of saturation behavior of physical properties in composites with randomly distributed second-phase. Journal of Composite Materials 39, 617-631.

Tuttle, M.E., Brinson, H.F., 1986. Prediction of the long-term creep compliance of general composite laminates. Experimental Mechanics 26, 89-102.

Usuki, A., Kojima, Y., Kawasumi, M., Okada, A., Fukushima, Y., Kurauchi, T., Kamigaito, O., 1993. Synthesis of nylon 6-clay hybrid. Journal of Materials Research(USA) 8, 1179-1184.

Van Melick, H., Govaert, L.E., 2009. A representative volume element simulation of a thermo plastic elastomer. Eindhoven University of Technology, Eindhoven, Netherlands.

Vollenberg, P.H.T., Heikens, D., 1989. Particle size dependence of the Young's modulus of filled polymers: 1. Preliminary experiments. Polymer 30, 1656-1662.

Voyiadjis, G.Z., Abu Al-Rub, R.K., Palazotto, A.N., 2003. Non-local coupling of viscoplasticity and anisotropic viscodamage for impact problems using the gradient theory. Archives of Mechanics 55, 39-89.

Voyiadjis, G.Z., Abu Al-Rub, R.K., Palazotto, A.N., 2004. Thermodynamic framework for coupling of non-local viscoplasticity and non-local anisotropic viscodamage for dynamic localization problems using gradient theory. International Journal of Plasticity 20, 981-1038.

Voyiadjis, G.Z., Al-Rub, R.K.A., Palazotto, A.N., 2006. On the small and finite deformation thermo-elasto-viscoplasticity theory for strain localization problems: algorithmic and computational aspects. European Journal of Computational Mechanics. Volume 15.

Wagner, H.D., Lourie, O., Feldman, Y., Tenne, R., 1998. Stress-induced fragmentation of multiwall carbon nanotubes in a polymer matrix. Applied Physics Letters 72, 188-190.

Wagner, M.H., 1978. A constitutive analysis of uniaxial elongational flow data of low-density polyethylene melt. Journal of Non-Newtonian Fluid Mechanics 4, 39-55.

Wang, H.W., Zhou, H.W., Peng, R.D., Mishnaevsky, L., 2011. Nanoreinforced polymer composites: 3D FEM modeling with effective interface concept. Composites Science and Technology 71, 980-988.

Wang, W.M., Sluys, L.J., De Borst, R., 1997. Viscoplasticity for instabilities due to strain softening and strain-rate softening. International Journal for Numerical Methods in Engineering 40, 3839-3864.

Watt, D.F., Xu, X.Q., Lloyd, D.J., 1996. Effects of particle morphology and spacing on the strain fields in a plastically deforming matrix. Acta Materialia 44, 789-799.

Weber, G., Anand, L., 1990. Finite deformation constitutive equations and a time integration procedure for isotropic, hyperelastic-viscoplastic solids. Computer Methods in Applied Mechanics and Engineering 79, 173-202.

Wineman, A.S., 1972. Large axially symmetric stretching of a nonlinear viscoelastic membrane. International Journal of Solids and Structures 8, 775-790.

Xiao, H., Bruhns, O.T., Meyers, A., 1997. Logarithmic strain, logarithmic spin and logarithmic rate. Acta Mechanica 124, 89-105.

Xiao, H., Bruhns, O.T., Meyers, A., 1998. Objective corotational rates and unified work-conjugacy relation between Eulerian and Lagrangean strain and stress measures. Archives of Mechanics 50, 1015-1046.

Xiao, H., Bruhns, O.T., Meyers, A., 2006. Elastoplasticity beyond small deformations. Acta Mechanica 182, 31-111.

Xiao, K.Q., Zhang, L.C., 2004. The stress transfer efficiency of a single-walled carbon nanotube in epoxy matrix. Journal of Materials Science 39, 4481-4486.

Xie, X.L., Zhou, X.P., Mai , Y.W., 2005. Dispersion and alignment of carbon nanotubes in polymer matrix: a review. Material Science Engineering 49, 89-112.

Xu, X., Liao, K., 2001. Molecular and continuum mechanics modeling of graphene deformation. Materials Physics and Mechanics 4, 148-151.

Yano, K., 1957. The theory of Lie derivatives and its applications. North-Holland Pub. Co., Amesterdam, Netherlands.

Yasmin, A., Abot, J.L., Daniel, I.M., 2003. Processing of clay/epoxy nanocomposites by shear mixing. Scripta Materialia 49, 81-86.

Yoon, C., Allen, D.H., 1999. Damage dependent constitutive behavior and energy release rate for a cohesive zone in a thermo-viscoelastic solid. International Journal of Fracture 96, 55-74.

Yuan, Q., Misra, R.D.K., 2006. Impact fracture behavior of clay–reinforced polypropylene nanocomposites. Polymer 47, 4421-4433.

Yung, K.C., Wang, J., Yue, T.M., 2006. Modeling young's modulus of polymer-layered silicate nanocomposites using a modified halpin-tsai micromechanical model. Journal of Reinforced Plastics and Composites 25, 847.

Zaiser, M., Moretti, P., Konstantinidis, A., Aifantis, E.C., 2009. Roughening and pinning of interface cracks in shear delamination of thin films. Journal of Statistical Mechanics: Theory and Experiment 2009, P11009.

Zapas, L.J., Crissman, J.M., 1984. Creep and recovery behavior of UHMW polyethylene in the region of small uniaxial deformations. Polymer 25, 57-62.

Zhang, Y., Xia, Z., Ellyin, F., 2004. Evolution and influence of residual stresses/strains of fiber reinforced laminates. Composites Science and Technology 64, 1613-1621.

Zhong-Heng, G., 1984. Rates of stretch tensors. Journal of Elasticity 14, 263-267.

Zhou, L., Shi, S., 2002. Molecular dynamic simulations on tensile mechanical properties of single-walled carbon nanotubes with and without hydrogen storage. Computational Materials Science 23, 166-174.

Zhou, X., Tamma, K.K., 2003. On the applicability and stress update formulations for corotational stress rate hypoelasticity constitutive models. Finite Elements in Analysis and Design 39, 783-816.

Zhu, J., Peng, H., Rodriguez-Macias, F., Margrave, J.L., Khabashesku, V.N., Imam, A.M., Lozano, K., Barrera, E.V., 2004. Reinforcing epoxy polymer composites through covalent integration of functionalized nanotubes. Advanced Functional Materials 14, 643-648.

APPENDIX A

1. Direct Solution For Stretch Rate Equations

Some problems in solid mechanics that deal with large deformation concept need a solution for a tensorial equation as

$$AX + XA = B \tag{A.1}$$

where A and B are known, and X is unknown and all are second order tensors. A broad review of applications of the recent equation in continuum mechanics and other branches of engineering can be found in Scheidler (1994). For example, denoting by U and V (the right and left stretch tensors (Gurtin, 1981)), their material time derivatives $\dot{U}$ and $\dot{V}$ can be achieved in turn by solving the following tensor equations

$$U\dot{U} + \dot{U}U = \dot{C} = \text{known} \qquad \text{or} \qquad V\dot{V} + \dot{V}V = \dot{B} = \text{known} \tag{A.2}$$

The direct solution for Eq. (A.1) through a systematic approach has been explained by Rosati (2000), through converting Eq. (A.1) to

$$AX + XA = B \quad \Rightarrow \quad \mathbb{A}X = B \quad , \quad \text{where: } \mathbb{A} = A \otimes I + I \otimes A \tag{A.3}$$

Then based on the inverse of the forth rank tensor $\mathbb{A}$, tensor X can be computed as

$$X = \frac{1}{2III_A(I_A II_A - III_A)}\Big[\Big[(I_A II_A - III_A)II_A + I_A^2 III_A\Big]B - I_A^2 II_A(AB + BA) + (I_A^3 + III_A)(ABA) + (I_A II_A - III_A)(A^2B + BA^2) - I_A^2(A^2BA + ABA^2) + I_A(A^2BA^2)\Big]$$

or

$$X = \frac{1}{2III_A(I_A II_A - III_A)}\Big[\Big((I_A II_A - III_A)II_A + I_A^2 III_A\Big)B - I_A^2 II_A(AB + BA) + (I_A II_A - III_A)(A^2B + BA^2) + A\Big((I_A^3 + III_A)B - I_A^2(AB + BA) + I_A(ABA)\Big)A\Big] \tag{A.4}$$

Here I_A, II_A, and III_A are the coefficients of the characteristic equation of the second order tensor A, which can be calculated as

$$I_A = \mathrm{tr}(A) \quad , \quad II_A = \frac{1}{2}\left[(\mathrm{tr}(A))^2 - \mathrm{tr}(A^2)\right] \quad , \quad III_A = \det(A) \tag{A.5}$$

In addition the term $I_A II_A - III_A$ can be written as

$$I_A II_A - III_A = (\lambda_1 + \lambda_2)(\lambda_2 + \lambda_3)(\lambda_3 + \lambda_1) \tag{A.6}$$

where λ_i $(i = 1,2,3)$ are the eigenvalues of tensor A. Therefore, one of the simplest check point criteria for non-singularity of Eq. (A.1) is

$$III_A \neq 0 \quad \text{and} \quad I_A II_A - III_A \neq 0 \tag{A.7}$$

For more detail, the reader is referred to Rosati (2000). Simpler results were obtained by Sidoroff (1978) who was the pioneer to find a direct solution that was just expressed based on terms of A and B. Further expressions of the solution of Eq. (A.1) were later found by Dienes (1979) and Guo (1984) for a skew tensor B, and by Hoger and Carlson (1984) for a generic B, and by Mehrabadi and Nemat-Nasser (1987) who addressed the case of a skew-symmetric right-hand side of Eq. (A.1) having a slightly different form.

APPENDIX B

1. Consistent Tangent Modulus

It can be proved in different ways that the Lagrangian equation of motion is similar to the one in current configuration (Eulerian concept), and can be written as

$$P_{iJ,J} + \rho_0 b_i = \rho_0 a_i \tag{B.1}$$

In which a_i is acceleration vector, b_i is body force, ρ_0 is the density of the domain in undeformed configuration, and P_{iJ} is the first Piola-Kirchhoff stress. Now with the purpose of writing the virtual work; so, through multiplying both sides of Eq. (B.1) by virtual displacement vector, ∇u_i, and integrating over the reference volume, V_o, along with utilizing divergence theorem, and assuming that the acceleration vanishes, virtual work can be found (Lubliner, 1990) as

$$\int_{V_o} P_{iJ} \nabla u_{i,J} \, \mathrm{d}v_o = \int_{V_o} \rho_o b_i \nabla u_i \, \mathrm{d}v_o + \int_{\partial V_{o t}} T_i \, \nabla u_i \, \mathrm{d}s_o \tag{B.2}$$

Here, ∇ and T are the gradient operator and the traction per unit area in the material (reference) configuration. Also, by revisiting the definition of the Green-Lagrange (GL) strain, one can say

$$E = \frac{1}{2}\left(F^T F - I\right) \;\; , \;\; F = I + \nabla u \qquad \Rightarrow \qquad \nabla E = \frac{1}{2}\left(F^T \nabla u + \nabla u^T F\right) \tag{B.3}$$

where ∇E is the virtual Lagrangian strain field. It can be simply shown that

$$P_{iJ} \, \nabla u_{i,J} = S_{IJ} \, \nabla E_{IJ} \tag{B.4}$$

Substituting Eq. (B.4) into Eq. (B.2), makes facilitation to express the principle of virtual work based on second Piola-Kirchhoff (II-PK) stress and GL strain in the next form

$$\int_{V_o} S_{IJ} \nabla E_{IJ} \, \mathrm{d}v_o = \int_{V_o} \rho_o b_i \nabla u_i \, \mathrm{d}v_o + \int_{\partial V_{ot}} T_i \, \nabla u_i \, \mathrm{d}s_o \tag{B.5}$$

Here, S is the II-PK stress field at the current analysis time ($t+\Delta t$), T is the boundary tractions, and u is an acceptable virtual displacement, also Δ denotes the material gradient. Now, if a desired constitutive model for determining the stress field has the following general form

$$S_{t+\Delta t} = \hat{S}\left(F_{t+\Delta t}\right) \tag{B.6}$$

where $F_{t+\Delta t}$ is the current deformation gradient tensor. Considering $T_{t+\Delta t}$ and $f_{t+\Delta t}$ as the traction and the body force vectors at the current time, respectively; Eq. (B.5) can be rewritten as

$$\int_{V_o} \hat{S}\left(F_{t+\Delta t}\right) : E \;\, \mathrm{d}v_o - \int_{V_o} f_{t+\Delta t} \cdot \Delta u \;\, \mathrm{d}v_o - \int_{\partial V_{ot}} T_{t+\Delta t} \cdot \Delta u \;\, \mathrm{d}s_o = 0 \tag{B.7}$$

Eq. (B.7) introduces a set of non-linear equations that can be solved for updating the deformation mapping. Now, for solving this equation by utilizing Newton-Raphson iterative technique, the linearized form for each incremental displacement has the succeeding form

$$\int_{V_o} K_{t+\Delta t} : \nabla u : \nabla E \;\, \mathrm{d}v_o = \text{Applied Forces} \tag{B.8}$$

Here $K_{t+\Delta t}$ is the consistent tangent modulus and can be linearized to upgrade stress by

$$K_{t+\Delta t} \equiv \left.\frac{\partial \Delta S}{\partial \Delta E}\right|_{t+\Delta t} \tag{B.9}$$

Here, it worth to be noted that, if Eqs. (B.2) to (B.8) are written in spatial configuration the consistent tangent in Eq. (B.9) should be mapped to the current configuration.

$$\underset{\approx}{k} = \underset{\sim}{F}\underset{\approx}{K}\,\underset{\sim}{F}^{\mathrm{T}} \qquad \text{or} \qquad k_{ijkl} = F_{jJ}F_{lL}\,K_{iJkL} \qquad \text{(for I-PK configuration)} \qquad \text{(B.10)}$$

$$\underset{\approx}{k} = \frac{1}{J}\underset{\sim}{F}\underset{\approx}{K}\underset{\sim}{F}^{\mathrm{T}}\underset{\sim}{F}\underset{\sim}{F}^{\mathrm{T}} \quad \text{or} \quad k_{ijkl} = \frac{1}{J}F_{iI}F_{jJ}F_{kK}F_{lL}\,K_{IJKL} \quad \text{(for II-PK configuration)} \quad \text{(B.11)}$$

APPENDIX C

1. Derivation of Tangent Compliance of Modified Viscoelastic Model

Here, a consistent tangent modulus for compliance is defined by taking the partial derivative of incremental residual strain with respect to the increment of stress at the end of each time analysis. As mentioned in Appendix B, the consistent tangent compliance matrix can be written as following, at the converged state

$$C_{ijkl}^{t} = \frac{\partial R_{ij}^{t}}{\partial \Delta S_{kl}^{t}} \tag{C.1}$$

There are two ways to find the increment of Lagrangian strain. Based on each method, different residual strain, and consequently different consistent tangent tensor formula will be achieved. The first approach for computing the residual strain tensor may be built on additively decomposition of volumetric and deviatoric portions of strain increments. It can be employed just when the time increment is very small, or when the volumetric portion of the strain measure is small enough in comparison to the distortional part or the deformation gradient tensor changes very slightly; then it has the following form

$$R_{ij}^{t} = \Delta E_{ij}^{t,\mathrm{dev}} + \Delta E_{ij}^{t,\mathrm{vol}} - \Delta E_{ij}^{t} \tag{C.2}$$

In this point of view, similar to Eq. (3.79), both total and incremental volumetric and deviatoric strains are

$$E_{ij}^{t,\mathrm{dev}} = J^{t} S_{ij}^{t,\mathrm{dev}} - d_{ij}^{t} \qquad , \qquad E_{ij}^{t,\mathrm{vol}} = B^{t} S_{ij}^{t,\mathrm{vol}} - V_{ij}^{t} \tag{C.3}$$

$$\begin{aligned} \Delta E_{ij}^{t,\mathrm{dev}} &= \left(F_{ir}^{t-\Delta t}\right)^{-\mathrm{T}} \left[J^{t} S_{rs}^{t,\mathrm{dev}} - J^{t-\Delta t} S_{rs}^{t-\Delta t,\mathrm{dev}} - d_{rs}^{t} + d_{rs}^{t-\Delta t} \right] \left(F_{sj}^{t-\Delta t}\right)^{-1} \\ \Delta E_{ij}^{t,\mathrm{vol}} &= \left(F_{ir}^{t-\Delta t}\right)^{-\mathrm{T}} \left[B^{t} S_{rs}^{t,\mathrm{vol}} - B^{t-\Delta t} S_{rs}^{t-\Delta t,\mathrm{vol}} - V_{rs}^{t} + V_{rs}^{t-\Delta t} \right] \left(F_{sj}^{t-\Delta t}\right)^{-1} \end{aligned} \tag{C.4}$$

By replacing the required relations for J^t, B^t, d_{ij}^t, and V_{ij}^t into $\Delta E_{ij}^{\text{dev}}$ and $\Delta E_{ij}^{\text{vol}}$, Eq. (C.2) can be expanded, similar to Eq. (4.68), as

$$R_{ij}^t = -\Delta E_{ij}^t + \left(F_{ir}^{t-\Delta t}\right)^{-\mathrm{T}} \left[\mathrm{H}_{rs}^t\right] \left(F_{sj}^{t-\Delta t}\right)^{-1} \tag{C.5}$$

where:

$$\begin{aligned}
\mathrm{H}_{rs}^t &= J^t S_{rs}^{t,\text{dev}} - J^{t-\Delta t} S_{rs}^{t-\Delta t,\text{dev}} - \frac{1}{2}\sum_{n=1}^{\mathrm{NP}} J_n \left(g_1^t \exp(-\lambda_n \Delta\psi^t) - g_1^{t-\Delta t}\right) q_{rs,n}^{t-\Delta t,\text{dev}} \\
&\quad - \frac{1}{2} g_2^{t-\Delta t} \sum_{n=1}^{\mathrm{NP}} J_n \left(g_1^{t-\Delta t} \frac{1-\exp(-\lambda_n \Delta\psi^{t-\Delta t})}{\lambda_n \Delta\psi^{t-\Delta t}} - g_1^t \frac{1-\exp(-\lambda_n \Delta\psi^t)}{\lambda_n \Delta\psi^t} \right) S_{rs}^{t-\Delta t,\text{dev}} \\
&\quad + B^t S_{rs}^{t,\text{vol}} - B^{t-\Delta t} S_{rs}^{t-\Delta t,\text{vol}} - \frac{1}{3}\sum_{n=1}^{\mathrm{NP}} B_n \left(g_1^t \exp(-\lambda_n \Delta\psi^t) - g_1^{t-\Delta t}\right) q_{rs,n}^{t-\Delta t,\text{vol}} \\
&\quad - \frac{1}{3} g_2^{t-\Delta t} \sum_{n=1}^{\mathrm{NP}} B_n \left(g_1^{t-\Delta t} \frac{1-\exp(-\lambda_n \Delta\psi^{t-\Delta t})}{\lambda_n \Delta\psi^{t-\Delta t}} - g_1^t \frac{1-\exp(-\lambda_n \Delta\psi^t)}{\lambda_n \Delta\psi^t} \right) S_{rs}^{t-\Delta t,\text{vol}}
\end{aligned}$$

By substituting $S_{rs}^{t,\text{dev}} = S_{rs}^t - S_{rs}^{t,\text{vol}}$ into the above equation, the terms containing J^t and B^t can be modified into a desired form as shown in this expression

$$\begin{aligned}
&J^t S_{rs}^{t,\text{dev}} - J^{t-\Delta t} S_{rs}^{t-\Delta t,\text{dev}} + \\
&B^t S_{rs}^{t,\text{vol}} - B^{t-\Delta t} S_{rs}^{t-\Delta t,\text{vol}} = \left(J^t S_{rs}^t - J^{t-\Delta t} S_{rs}^{t-\Delta t}\right) + \left(B^t - J^t\right) S_{rs}^{t,\text{vol}} - \left(B^{t-\Delta t} - J^{t-\Delta t}\right) S_{rs}^{t-\Delta t,\text{vol}}
\end{aligned} \tag{C.6}$$

Exchanging the achievement of Eq. (C.6) with the related terms in Eq. (C.5), and differentiating the proper terms, and recalling that the derivation of the terms in the previous time increment with respect to the current stress state should be vanished; then, the consistent tangent tensor will be expressed

$$\frac{\partial R_{ij}^t}{\partial S_{kl}^t} = \left(F_{ir}^{t-\Delta t}\right)^{-\mathrm{T}} \left[\frac{\partial \mathrm{H}_{rs}}{\partial S_{kl}^t}\right] \left(F_{sj}^{t-\Delta t}\right)^{-1} \tag{C.7}$$

where

$$\frac{\partial \mathrm{H}_{rs}}{\partial S_{kl}^{t}} = \underbrace{\frac{\partial}{\partial S_{kl}^{t}}\left(J^{t} S_{rs}^{t} + (B^{t} - J^{t}) S_{rs}^{t,\mathrm{vol}}\right)}_{\mathrm{Term}(1)} + \underbrace{\frac{\partial}{\partial S_{kl}^{t}}\left(-\frac{1}{2}\sum_{n=1}^{\mathrm{NP}} J_{n} g_{1}^{t} \exp(-\lambda_{n}\Delta\psi^{t}) q_{\mathrm{rs},n}^{t-\Delta t,\mathrm{dev}}\right)}_{\mathrm{Term}(2)}$$
$$+ \underbrace{\frac{\partial}{\partial S_{kl}^{t}}\left(\frac{1}{2} g_{2}^{t-\Delta t} g_{1}^{t} \sum_{n=1}^{\mathrm{NP}} J_{n}\left(\frac{1-\exp(-\lambda_{n}\Delta\psi^{t})}{\lambda_{n}\Delta\psi^{t}}\right) S_{\mathrm{rs}}^{t-\Delta t,\mathrm{dev}}\right)}_{\mathrm{Term}(3)}$$
$$+ \underbrace{\frac{\partial}{\partial S_{kl}^{t}}\left(-\frac{1}{3}\sum_{n=1}^{\mathrm{NP}} B_{n} g_{1}^{t} \exp(-\lambda_{n}\Delta\psi^{t}) q_{\mathrm{rs},n}^{t-\Delta t,\mathrm{vol}}\right)}_{\mathrm{Term}(4)}$$
$$+ \underbrace{\frac{\partial}{\partial S_{kl}^{t}}\left(\frac{1}{3} g_{2}^{t-\Delta t} g_{1}^{t} \sum_{n=1}^{\mathrm{NP}} B_{n}\left(\frac{1-\exp(-\lambda_{n}\Delta\psi^{t})}{\lambda_{n}\Delta\psi^{t}}\right) S_{\mathrm{rs}}^{t-\Delta t,\mathrm{vol}}\right)}_{\mathrm{Term}(5)}$$

The derivation of the first term of Eq. (C.7) can be written as

$$\mathrm{Term}(1) = \frac{\partial J^{t}}{\partial S_{kl}^{t}} S_{rs}^{t} + J^{t}\frac{\partial S_{rs}^{t}}{\partial S_{kl}^{t}} + \left(\frac{\partial B^{t}}{\partial S_{kl}^{t}} - \frac{\partial J^{t}}{\partial S_{kl}^{t}}\right) S_{rs}^{t,\mathrm{vol}} + \left(B^{t} - J^{t}\right)\frac{\partial S_{rs}^{t,\mathrm{vol}}}{\partial S_{kl}^{t}} \tag{C.8}$$

The volumetric portion of the second Piola-Kirchhoff (II-PK) stress [see Eq. (3.145)] is

$$S_{rs}^{\mathrm{vol}} = \frac{1}{3}(S_{mn} C_{mn}) C_{rs}^{-1} \tag{C.9}$$

Thus, its derivation with respect to the total II-PK stress is a fourth-order tensor as

$$\frac{\partial S_{rs}^{\mathrm{vol}}}{\partial S_{kl}^{t}} = \frac{1}{3}\frac{\partial S_{mn}}{\partial S_{kl}} C_{mn} C_{rs}^{-1} = \frac{1}{3}\delta_{mk}\delta_{nl} C_{mn} C_{rs}^{-1} = \frac{1}{3} C_{kl} C_{rs}^{-1} \tag{C.10}$$

Hence, by substituting $\frac{\partial S_{rs}^{t}}{\partial S_{kl}^{t}} = \delta_{ir}\delta_{js}$ and also Eq. (C.10) into the first term of Eq. (C.7), this term will be modified as

$$\mathrm{Term}(1) = J^{t}\delta_{rk}\delta_{sl} + \frac{1}{3}\left(B^{t} - J^{t}\right) C_{kl} C_{rs}^{-1} + \left(\frac{\partial B^{t}}{\partial S_{kl}^{t}} - \frac{\partial J^{t}}{\partial S_{kl}^{t}}\right) S_{rs}^{t,\mathrm{vol}} + \frac{\partial J^{t}}{\partial S_{kl}^{t}} S_{rs}^{t} \tag{C.11}$$

Now, recalling $S_{rs}^{t} = S_{rs}^{t,\mathrm{dev}} + S_{rs}^{t,\mathrm{vol}}$, one can find Term (1) as

$$\text{Term}(1) = J^t \delta_{rk} \delta_{sl} + \frac{1}{3}\left(B^t - J^t\right) C_{kl} C_{rs}^{-1} + \frac{\partial B^t}{\partial S_{kl}^t} S_{rs}^{t,\text{vol}} + \frac{\partial J^t}{\partial S_{kl}^t} S_{rs}^{t,\text{dev}} \tag{C.12}$$

From now on, the derivation of the reduced time with respect to the incremental stress is required; therefore, one can find it as

$$\psi^t = \frac{t}{a_S} \quad \Rightarrow \quad \Delta\psi^t = \frac{\Delta t}{a_S} \quad \Rightarrow \quad \frac{\partial\left(-\lambda_n \Delta\psi^t\right)}{\partial S_{rs}} = \frac{\lambda_n \Delta t}{\left(a_S\right)^2} \frac{\partial a_S}{\partial S_{rs}} = \frac{\lambda_n \Delta\psi^t}{a_S} \frac{\partial a_S}{\partial S_{rs}} \tag{C.13}$$

In addition, the next derivation is also required and useful for expanding Eq. (C.7).

$$\begin{aligned} \frac{\partial}{\partial S_{kl}}\left(\frac{1-\exp(-\lambda_n \Delta\psi^t)}{\lambda_n \Delta\psi^t}\right) &= \frac{1}{\lambda_n \Delta t} \frac{\partial a_S}{\partial S_{kl}}\left(1-(1+\lambda_n \Delta\psi^t)\exp(-\lambda_n \Delta\psi^t)\right) \\ \text{or} \qquad &= \frac{1}{a_S} \frac{\partial a_S}{\partial S_{kl}}\left(\frac{1-\exp(-\lambda_n \Delta\psi^t)}{\lambda_n \Delta\psi^t} - \exp(-\lambda_n \Delta\psi^t)\right) \end{aligned} \tag{C.14}$$

From now on, for the rest of expressing the mathematical forms, the next relations will be used to simplify the final derivation

$$\mathbb{A}_{kl,n}^1 = \frac{\partial g_1^t}{\partial S_{kl}^t} + \lambda_n \Delta\psi^t \frac{g_1^t}{a_S^t} \frac{\partial a_S^t}{\partial S_{kl}^t} \quad , \quad \mathbb{A}_{kl}^2 = \frac{\partial g_1^t}{\partial S_{kl}^t} + \frac{g_1^t}{a_S^t} \frac{\partial a_S^t}{\partial S_{kl}^t} \quad , \quad \mathbb{A}_{kl}^3 = \frac{g_1^t}{a_S^t} \frac{\partial a_S^t}{\partial S_{kl}^t} \tag{C.15}$$

By considering Eqs. (C.13) to (C.15), one can derive and simplify the second and third terms of Eq. (C.7), as

$$\begin{aligned} \text{Term}(2) &= \frac{-1}{2} \sum_{n=1}^{\text{NP}} \left[J_n \frac{\partial g_1^t}{\partial S_{kl}^t} \exp(-\lambda_n \Delta\psi^t) q_{rs,n}^{t-\Delta t,\text{dev}} + J_n g_1^t \frac{\partial(-\lambda_n \Delta\psi^t)}{\partial S_{kl}^t} \exp(-\lambda_n \Delta\psi^t) q_{rs,n}^{t-\Delta t,\text{dev}} \right] \\ &= -\frac{1}{2} \sum_{n=1}^{\text{NP}} \left[J_n \mathbb{A}_{kl,n}^1 \exp(-\lambda_n \Delta\psi^t) q_{rs,n}^{t-\Delta t,\text{dev}} \right] \end{aligned} \tag{C.16}$$

$$\text{Term}(3)=\frac{1}{2}g_2^{t-\Delta t}\sum_{n=1}^{\text{NP}}\left[J_n\frac{\partial g_1^t}{\partial S_{kl}^t}\left(\frac{1-\exp(-\lambda_n\Delta\psi^t)}{\lambda_n\Delta\psi^t}\right)+J_n g_1^t\frac{\partial}{\partial S_{kl}^t}\left(\frac{1-\exp(-\lambda_n\Delta\psi^t)}{\lambda_n\Delta\psi^t}\right)\right]S_{rs}^{t-\Delta t,\text{dev}}$$

$$=\frac{1}{2}g_2^{t-\Delta t}\sum_{n=1}^{\text{NP}}\left[J_n\left(\mathbb{A}_{kl}^2\left(\frac{1-\exp(-\lambda_n\Delta\psi^t)}{\lambda_n\Delta\psi^t}\right)-\mathbb{A}_{kl}^3\exp(-\lambda_n\Delta\psi^t)\right)\right]S_{rs}^{t-\Delta t,\text{dev}} \quad \text{(C.17)}$$

Again, considering Eqs. (C.13) to (C.15), one can also derive and simplify the fourth and fifth terms of Eq. (C.7), as

$$\text{Term}(4)=-\frac{1}{3}\sum_{n=1}^{\text{NP}}\left[B_n\mathbb{A}_{kl,n}^1\exp(-\lambda_n\Delta\psi^t)q_{rs,n}^{t-\Delta t,\text{vol}}\right] \quad \text{(C.18)}$$

$$\text{Term}(5)=\frac{1}{3}g_2^{t-\Delta t}\sum_{n=1}^{\text{NP}}\left[B_n\left(\mathbb{A}_{kl}^2\left(\frac{1-\exp(-\lambda_n\Delta\psi^t)}{\lambda_n\Delta\psi^t}\right)-\mathbb{A}_{kl}^3\exp(-\lambda_n\Delta\psi^t)\right)\right]S_{rs}^{t-\Delta t,\text{vol}} \quad \text{(C.19)}$$

Because of similarity in mathematical formulation, summation of the second and fourth terms, and also the third and fifth terms of Eq. (C.7) can be combined and written as

$$\text{Terms}(2)+(4)=-\sum_{n=1}^{\text{NP}}\left[\mathbb{A}_{kl,n}^1\exp(-\lambda_n\Delta\psi^t)\left(\frac{1}{2}J_n q_{rs,n}^{t-\Delta t,\text{dev}}+\frac{1}{3}B_n q_{rs,n}^{t-\Delta t,\text{vol}}\right)\right] \quad \text{(C.20)}$$

$$\text{Terms}(3)+(5)=g_2^{t-\Delta t}\sum_{n=1}^{\text{NP}}\left[\left(\frac{1}{2}J_n S_{rs}^{t-\Delta t,\text{dev}}+\frac{1}{3}B_n S_{rs}^{t-\Delta t,\text{vol}}\right)\right.$$
$$\left.\left(\mathbb{A}_{kl}^2\left(\frac{1-\exp(-\lambda_n\Delta\psi^t)}{\lambda_n\Delta\psi^t}\right)-\mathbb{A}_{kl}^3\exp(-\lambda_n\Delta\psi^t)\right)\right] \quad \text{(C.21)}$$

Finally, the viscoelastic consistent tangent compliance tensor of the single convolutional integral, that is modified based on GL strain and II-PK stress, will be expressed

$$\frac{\partial R_{ij}^{t}}{\partial S_{kl}^{t}}=\left(F_{ir}^{t-\Delta t}\right)^{-\mathrm{T}}\Bigg[J^{t}\delta_{rk}\delta_{sl}+\frac{1}{3}\left(B^{t}-J^{t}\right)C_{kl}C_{rs}^{-1}+\frac{\partial B^{t}}{\partial S_{kl}^{t}}S_{rs}^{t,\mathrm{vol}}+\frac{\partial J^{t}}{\partial S_{kl}^{t}}S_{rs}^{t,\mathrm{dev}}$$
$$-\sum_{n=1}^{NP}\mathbb{A}_{kl,n}^{1}\exp(-\lambda_{n}\Delta\psi^{t})\left(\frac{1}{2}J_{n}\,q_{rs,n}^{t-\Delta t,\mathrm{dev}}+\frac{1}{3}B_{n}\,q_{rs,n}^{t-\Delta t,\mathrm{vol}}\right)$$
$$+g_{2}^{t-\Delta t}\sum_{n=1}^{NP}\left(\frac{1}{2}J_{n}S_{rs}^{t-\Delta t,\mathrm{dev}}+\frac{1}{3}B_{n}S_{rs}^{t-\Delta t,\mathrm{vol}}\right) \tag{C.22}$$
$$\left(\mathbb{A}_{kl}^{2}\left(\frac{1-\exp(-\lambda_{n}\Delta\psi^{t})}{\lambda_{n}\Delta\psi^{t}}\right)-\mathbb{A}_{kl}^{3}\exp(-\lambda_{n}\Delta\psi^{t})\right)\Bigg]\left(F_{sj}^{t-\Delta t}\right)^{-1}$$

As mentioned in Chapter 4, since in incremental solution the derivation of non-linear material parameters regarding to the effective stress are achievable; therefore, the derivation of the effective stress, $\Delta\overline{S}$, with respect to the total stress is introduced. This derivation is presented here, in which the $\Delta\overline{S}$ is introduced as the effective stress.

$$\Delta\overline{S}=\sqrt{\frac{3}{2}S_{mn}^{\mathrm{dev}}S_{mn}^{\mathrm{dev}}}\qquad\Rightarrow\qquad\frac{\partial\Delta\overline{S}}{\partial S_{ij}}=\sqrt{\frac{3}{2}}\left(S_{mn}^{\mathrm{dev}}S_{mn}^{\mathrm{dev}}\right)^{-\frac{1}{2}}\left(\frac{\partial S_{mn}^{\mathrm{dev}}}{\partial S_{ij}}S_{mn}\right) \tag{C.23}$$

Substituting the deviatoric portion of the II-PK [see Eq. (3.145)] into Eq. (C.23) gives

$$\frac{\partial\Delta\overline{S}}{\partial S_{ij}}=\frac{3}{2}\frac{1}{\sqrt{\frac{3}{2}S_{mn}S_{mn}}}\left(\frac{\partial}{\partial S_{ij}}\left(S_{mn}-\frac{1}{3}(S_{pq}C_{pq})C_{mn}^{-1}\right)S_{mn}\right) \tag{C.24}$$

The derivation of deviatoric stress with respect to the total II-PK stress may be expressed and simplified as

$$\frac{\partial}{\partial S_{ij}}\left(S_{mn}-\frac{1}{3}(S_{pq}C_{pq})C_{mn}^{-1}\right)S_{mn}=\left(\delta_{mi}\delta_{nj}-\frac{1}{3}\delta_{pi}\delta_{qj}C_{pq}C_{mn}^{-1}\right)S_{mn}=S_{ij}-\frac{1}{3}(C_{ij}C_{mn}^{-1})S_{mn} \tag{C.25}$$

Therefore, replacing Eq. (C.25) into Eq. (C.24), the final mathematical formulation of $\frac{\partial\Delta\overline{S}}{\partial S_{ij}}$ is written as following

$$\frac{\partial \Delta \bar{S}}{\partial S_{ij}} = \frac{3}{2}\frac{1}{\Delta \bar{S}}\left(S_{ij} - \frac{1}{3}(C_{ij}C^{-1}_{mn})S_{mn} \right) \tag{C.26}$$

Now, since factorizing $\frac{\partial \Delta \bar{S}}{\partial S_{ij}}$ from Eq. (C.22) is needed; therefore, such factorization also should be applied to Eq. (C.15) which are embedded inside Eq. (C.22). Thus, similar to Eq. (C.15), the following terms can be defined and used.

$$\mathbb{B}^1_n = \frac{\partial g^t_1}{\partial \Delta \bar{S}} + \lambda_n \Delta \psi^t \frac{g^t_1}{a^t_S}\frac{\partial a^t_S}{\partial \Delta \bar{S}} \quad , \quad \mathbb{B}^2 = \frac{\partial g^t_1}{\partial \Delta \bar{S}} + \frac{g^t_1}{a^t_S}\frac{\partial a^t_S}{\partial \Delta \bar{S}} \quad , \quad \mathbb{B}^3 = \frac{g^t_1}{a^t_S}\frac{\partial a^t_S}{\partial \Delta \bar{S}} \tag{C.27}$$

At this point, through factorizing $\frac{\partial \Delta \bar{S}}{\partial S_{ij}}$ from Eq. (C.22), and employing the result of its derivation in Eq. (C.26), then Eq. (C.22) can be rewritten and shown as the next formula.

$$\begin{aligned}
\frac{\partial R^t_{ij}}{\partial S^t_{kl}} = \left(F^{t-\Delta t}_{ir}\right)^{-\mathrm{T}} \Bigg[& J^t \delta_{rk}\delta_{sl} + \frac{1}{3}\left(B^t - J^t\right)C_{kl}C^{-1}_{rs} + \frac{\partial \Delta \bar{S}}{\partial S^t_{kl}} \Bigg\{ \left(\frac{\partial B^t}{\partial \Delta \bar{S}} - \frac{\partial J^t}{\partial \Delta \bar{S}} \right) S^{t,\mathrm{vol}}_{rs} + \frac{\partial J^t}{\partial \Delta \bar{S}} S^t_{rs} \\
& - \sum_{n=1}^{\mathrm{NP}} \mathbb{B}^1_n \exp(-\lambda_n \Delta \psi^t) \left(\frac{1}{2} J_n \, q^{t-\Delta t,\mathrm{dev}}_{rs,n} + \frac{1}{3} B_n \, q^{t-\Delta t,\mathrm{vol}}_{rs,n} \right) \\
& + g^{t-\Delta t}_2 \sum_{n=1}^{\mathrm{NP}} \left(\frac{1}{2} J_n S^{t-\Delta t,\mathrm{dev}}_{rs} + \frac{1}{3} B_n S^{t-\Delta t,\mathrm{vol}}_{rs} \right) \\
& \left(\mathbb{B}^2 \left(\frac{1-\exp(-\lambda_n \Delta \psi^t)}{\lambda_n \Delta \psi^t} \right) - \mathbb{B}^3 \exp(-\lambda_n \Delta \psi^t) \right) \Bigg\} \Bigg] \left(F^{t-\Delta t}_{sj}\right)^{-1}
\end{aligned} \tag{C.28}$$

The second approach relates to the cases when the time increments become larger, or the quantity of the volumetric strain is not small comparing to the distortional counterpart. Therefore, the additive decomposition of the volumetric and deviatoric strains is not acceptable any more. Thus, the mathematical form for the residual strain should be revised. As introduced in Eq. (4.74), one can express the residual strain tensor as

$$R_{ij}^{t} = \delta E_{ij}^{t} = \frac{1}{2}\left(\Delta F_{ik}^{\mathrm{T}} \Delta F_{kj} - I\right) \qquad , \qquad \text{where: } \Delta F = F^{\mathrm{FEM}} F^{-1} \tag{C.29}$$

where F^{FEM} is the deformation gradient that is provided by FEM software, and F is the one computed through constitutive models.

$$\frac{\partial R_{ij}^{t}}{\partial \Delta S_{kl}^{t}} = \frac{1}{2}\left(\left(\frac{\partial \Delta F_{im}}{\partial \Delta S_{kl}^{t}}\right)^{\mathrm{T}} \Delta F_{mj} + \Delta F_{im}^{\mathrm{T}}\left(\frac{\partial \Delta F_{mj}}{\partial \Delta S_{kl}^{t}}\right)\right) \tag{C.30}$$

Henceforth, one should find the mathematical relation of $\frac{\partial \Delta F_{im}}{\partial \Delta S_{kl}^{t}}$, which is presented in the following. Substituting $\Delta F = F^{\mathrm{FEM}} F^{-1}$ and $F = RU$, one can derive

$$\frac{\partial \Delta F_{ij}}{\partial \Delta S_{kl}^{t}} = F_{ip}^{\mathrm{FEM}} \frac{\partial F_{pj}^{-1}}{\partial \Delta S_{kl}^{t}} = F_{ip}^{\mathrm{FEM}} \frac{\partial U_{pq}^{-1}}{\partial \Delta S_{kl}^{t}} R_{qj}^{\mathrm{T}} \qquad , \qquad \text{Note: } R^{\mathrm{T}} = R^{-1} \tag{C.31}$$

Now, in order to expand the recent equation, the decomposition of total stretch tensor to volumetric and deviatoric as $U = U^{\mathrm{dev}} U^{\mathrm{vol}}$ should be taken into account.

$$\frac{\partial U_{pq}^{-1}}{\partial \Delta S_{kl}^{t}} = \frac{\partial U_{pr}^{\mathrm{vol}\,-1}}{\partial \Delta S_{kl}^{t}} U_{rq}^{\mathrm{dev}\,-1} + U_{pr}^{\mathrm{vol}\,-1} \frac{\partial U_{rq}^{\mathrm{dev}\,-1}}{\partial \Delta S_{kl}^{t}} \tag{C.32}$$

Now, the derivation of U^{vol} and U^{dev} with respect to incremental stress is required. At first, $\partial U^{\mathrm{vol}} / \partial \Delta S$ is derived. For this purpose, the following relations between total volumetric stretch and strain should be recalled.

$$U^{\mathrm{vol}} = \left(I + 2E^{\mathrm{vol}}\right)^{1/2} \qquad , \qquad E_{t+\Delta t}^{\mathrm{vol}} = E_{t}^{\mathrm{vol}} + U_{t}^{\mathrm{vol}}\left(\Delta E_{t+\Delta t}^{\mathrm{vol}}\right) U_{t}^{\mathrm{vol}} \tag{C.33}$$

By utilizing the recent relations, the derivation of volumetric stretch with respect to incremental II-PK stress can be written as

$$\frac{\partial U_{pr}^{t,\mathrm{vol}\,-1}}{\partial \Delta S_{kl}^{t}} = \frac{\partial}{\partial \Delta S_{kl}^{t}} \left(I + 2E^{t,\mathrm{vol}} \right)_{pr}^{-1/2} = -\frac{\partial E_{ps}^{t,\mathrm{vol}}}{\partial \Delta S_{kl}^{t}} \left(I + 2E^{t,\mathrm{vol}} \right)_{sr}^{-3/2} \tag{C.34}$$

Also, according to Eq. (C.33)

$$\frac{\partial E_{ps}^{t,\mathrm{vol}}}{\partial \Delta S_{kl}^{t}} = U_{pm}^{t-\Delta t,\mathrm{vol}} \frac{\partial \Delta E_{mn}^{t,\mathrm{vol}}}{\partial \Delta S_{kl}^{t}} U_{ns}^{t-\Delta t,\mathrm{vol}} \tag{C.35}$$

where:

$$\frac{\partial \Delta E_{mn}^{t,\mathrm{vol}}}{\partial \Delta S_{kl}^{t}} = \left(U_{ma}^{t-\Delta t,\mathrm{vol}} \right)^{-1} \left(\frac{\partial}{\partial \Delta S_{kl}^{t}} \left(B^{t} S_{ab}^{t,\mathrm{vol}} - B^{t-\Delta t} S_{ab}^{t-\Delta t,\mathrm{vol}} \right) - \frac{\partial}{\partial \Delta S_{kl}^{t}} \left(V_{ab}^{t} - V_{ab}^{t-\Delta t} \right) \right) \left(U_{bn}^{t-\Delta t,\mathrm{vol}} \right)^{-1}$$

Substituting this equation into Eq. (C.34), and since the derivations of the quantities in the previous time increment with respect to the current time increment is zero, it delivers

$$\frac{\partial E_{ps}^{t,\mathrm{vol}}}{\partial \Delta S_{kl}^{t}} = \frac{\partial}{\partial \Delta S_{kl}^{t}} \left(B^{t} S_{ps}^{t,\mathrm{vol}} - V_{ps}^{t} \right) = \frac{\partial B^{t}}{\partial \Delta S_{kl}^{t}} S_{ps}^{t,\mathrm{vol}} + B^{t} \frac{\partial S_{ps}^{t,\mathrm{vol}}}{\partial \Delta S_{kl}^{t}} - \frac{\partial V_{ps}^{t}}{\partial \Delta S_{kl}^{t}} \tag{C.36}$$

Then, one can expand Eq. (C.35) as

$$\begin{aligned} \frac{\partial E_{ps}^{t,\mathrm{vol}}}{\partial \Delta S_{kl}^{t}} = {} & \frac{\partial B^{t}}{\partial \Delta S_{kl}^{t}} S_{ps}^{t,\mathrm{vol}} + \frac{1}{3} \left(C_{kl} C_{ps}^{-1} \right) B^{t} - \frac{1}{3} \sum_{n=1}^{\mathrm{NP}} \left[B_n \exp(-\lambda_n \Delta \psi^{t}) q_{ps,r}^{t-\Delta t,\mathrm{vol}} \mathbb{A}_{kl,n}^{1} \right] \\ & + \frac{1}{3} g_2^{t-\Delta t} \sum_{n=1}^{\mathrm{NP}} \left[B_n \left(\mathbb{A}_{kl}^{2} \left(\frac{1-\exp(-\lambda_n \Delta \psi^{t})}{\lambda_n \Delta \psi^{t}} \right) - \mathbb{A}_{kl}^{3} \exp(-\lambda_n \Delta \psi^{t}) \right) \right] S_{ps}^{t-\Delta t,\mathrm{vol}} \end{aligned} \tag{C.37}$$

Finally, the derivation of the inverse of volumetric stretch with respect to the current incremental II-PK stress can be written as

$$\begin{aligned} \frac{\partial U_{pr}^{t,\mathrm{vol}\,-1}}{\partial \Delta S_{kl}^{t}} = {} & -\left[\frac{\partial B^{t}}{\partial \Delta S_{kl}^{t}} S_{ps}^{t,\mathrm{vol}} + \frac{1}{3} \left(C_{kl} C_{ps}^{-1} \right) B^{t} - \frac{1}{3} \sum_{n=1}^{\mathrm{NP}} \left[B_n \exp(-\lambda_n \Delta \psi^{t}) q_{ps,n}^{t-\Delta t,\mathrm{vol}} \mathbb{A}_{kl,n}^{1} \right] \right. \\ & \left. + \frac{1}{3} g_2^{t-\Delta t} \sum_{n=1}^{\mathrm{NP}} \left[B_n \left(\mathbb{A}_{kl}^{2} \left(\frac{1-\exp(-\lambda_n \Delta \psi^{t})}{\lambda_n \Delta \psi^{t}} \right) - \mathbb{A}_{kl}^{3} \exp(-\lambda_n \Delta \psi^{t}) \right) \right] S_{ps}^{t-\Delta t,\mathrm{vol}} \right] \left(I + 2E^{t,\mathrm{vol}} \right)_{sr}^{-3/2} \end{aligned} \tag{C.38}$$

Similarly, one could find the derivation of the inverse of deviatoric stretch with respect to the current incremental II-PK stress as

$$\frac{\partial U_{rq}^{t,\mathrm{dev}\,-1}}{\partial \Delta S_{kl}^{t}} = -\left[\frac{\partial J^{t}}{\partial \Delta S_{kl}^{t}} S_{rs}^{t,\mathrm{dev}} + J^{t}\left(\delta_{rk}\delta_{sl} - \frac{1}{3}C_{kl}C_{rs}^{-1}\right) - \frac{1}{2}\sum_{n=1}^{\mathrm{NP}}\left[J_n \exp(-\lambda_n \Delta\psi^{t}) q_{rs,n}^{t-\Delta t,\mathrm{dev}}\, \mathbb{A}_{kl,n}^{1}\right]\right.$$
$$\left. + \frac{1}{2} g_2^{t-\Delta t} \sum_{n=1}^{\mathrm{NP}}\left[J_n\left(\mathbb{A}_{kl}^{2}\left(\frac{1-\exp(-\lambda_n \Delta\psi^{t})}{\lambda_n \Delta\psi^{t}}\right) - \mathbb{A}_{kl}^{3}\exp(-\lambda_n \Delta\psi^{t})\right)\right] S_{rs}^{t-\Delta t,\mathrm{dev}}\right]\left(I + 2E^{t,\mathrm{dev}}\right)_{sq}^{-3/2} \tag{C.39}$$

Now, to find the final form of Eq. (C.31), one has to recall that $U_{rq}^{t,\mathrm{dev}}$ is symmetric, and the indices r and q can be interchanged. Hence, the next two equations can be achieved

$$\begin{aligned}
\left(I + 2E^{t,\mathrm{vol}}\right)_{sr}^{-3/2} U_{rq}^{\mathrm{dev}\,-1} &= \left(I + 2E^{t,\mathrm{vol}}\right)_{sx}^{-1} U_{xr}^{\mathrm{vol}\,-1} U_{rq}^{\mathrm{dev}\,-1} = \left(I + 2E^{t,\mathrm{vol}}\right)_{sx}^{-1} U_{xq}^{-1} \\
\left(I + 2E^{t,\mathrm{dev}}\right)_{sr}^{-3/2} U_{rp}^{\mathrm{vol}\,-1} &= \left(I + 2E^{t,\mathrm{dev}}\right)_{sx}^{-1} U_{xr}^{\mathrm{dev}\,-1} U_{rp}^{\mathrm{vol}\,-1} = \left(I + 2E^{t,\mathrm{dev}}\right)_{sx}^{-1} U_{xp}^{-1}
\end{aligned} \tag{C.40}$$

So, Eq. (C.32) can be written as

$$\frac{\partial U_{pq}^{-1}}{\partial \Delta S_{kl}^{t}} = -\left[K_{pskl}\left(I + 2E^{t,\mathrm{vol}}\right)_{sx}^{-1} + G_{pskl}\left(I + 2E^{t,\mathrm{dev}}\right)_{sx}^{-1}\right] U_{xq}^{-1} \tag{C.41}$$

where:

$$K_{pskl} = \frac{\partial B^{t}}{\partial \Delta S_{kl}^{t}} S_{ps}^{t,\mathrm{vol}} + \frac{1}{3}\left(C_{kl}C_{ps}^{-1}\right)B^{t} - \frac{1}{3}\sum_{n=1}^{\mathrm{NP}}\left[B_n \exp(-\lambda_n \Delta\psi^{t}) q_{ps,n}^{t-\Delta t,\mathrm{vol}}\, \mathbb{A}_{kl,n}^{1}\right]$$
$$+ \frac{1}{3} g_2^{t-\Delta t} \sum_{n=1}^{\mathrm{NP}}\left[B_n\left(\mathbb{A}_{kl}^{2}\left(\frac{1-\exp(-\lambda_n \Delta\psi^{t})}{\lambda_n \Delta\psi^{t}}\right) - \mathbb{A}_{kl}^{3}\exp(-\lambda_n \Delta\psi^{t})\right)\right] S_{ps}^{t-\Delta t,\mathrm{vol}}$$

$$G_{pskl} = \frac{\partial J^{t}}{\partial \Delta S_{kl}^{t}} S_{ps}^{t,\mathrm{dev}} + J^{t}\left(\delta_{pk}\delta_{sl} - \frac{1}{3}C_{kl}C_{ps}^{-1}\right) - \frac{1}{2}\sum_{n=1}^{\mathrm{NP}}\left[J_n \exp(-\lambda_n \Delta\psi^{t}) q_{ps,n}^{t-\Delta t,\mathrm{dev}}\, \mathbb{A}_{kl,n}^{1}\right]$$
$$+ \frac{1}{2} g_2^{t-\Delta t} \sum_{n=1}^{\mathrm{NP}}\left[J_n\left(\mathbb{A}_{kl}^{2}\left(\frac{1-\exp(-\lambda_n \Delta\psi^{t})}{\lambda_n \Delta\psi^{t}}\right) - \mathbb{A}_{kl}^{3}\exp(-\lambda_n \Delta\psi^{t})\right)\right] S_{ps}^{t-\Delta t,\mathrm{dev}}\Bigg]$$

According to Eqs. (C.23) to (C.27) the forth order tensors in Eq. (C.41) are rewritten as

$$K_{pskl} = \frac{1}{3}\left(C_{kl}C_{ps}^{-1}\right)B^{t} + \frac{\partial \Delta\bar{S}}{\partial S_{kl}^{t}}\left[\frac{\partial B^{t}}{\partial \Delta\bar{S}}S_{ps}^{t,\mathrm{vol}} - \frac{1}{3}\sum_{n=1}^{\mathrm{NP}}\left[B_n \exp(-\lambda_n \Delta\psi^{t}) q_{ps,n}^{t-\Delta t,\mathrm{vol}}\, \mathbb{B}_{kl,n}^{1}\right]\right.$$
$$\left. + \frac{1}{3} g_2^{t-\Delta t}\sum_{n=1}^{\mathrm{NP}}\left[B_n\left(\mathbb{B}_{kl}^{2}\left(\frac{1-\exp(-\lambda_n \Delta\psi^{t})}{\lambda_n \Delta\psi^{t}}\right) - \mathbb{B}_{kl}^{3}\exp(-\lambda_n \Delta\psi^{t})\right)\right] S_{ps}^{t-\Delta t,\mathrm{vol}}\right]$$

$$G_{pskl} = J^{t}\left(\delta_{pk}\delta_{sl} - \frac{1}{3}C_{kl}C_{ps}^{-1}\right) + \frac{\partial \Delta\bar{S}}{\partial S_{kl}^{t}}\left[\frac{\partial J^{t}}{\partial \Delta\bar{S}}S_{ps}^{t,\mathrm{dev}} - \frac{1}{2}\sum_{n=1}^{\mathrm{NP}}\left[J_n \exp(-\lambda_n \Delta\psi^{t}) q_{ps,n}^{t-\Delta t,\mathrm{dev}}\, \mathbb{B}_{kl,n}^{1}\right]\right.$$
$$\left.\left. + \frac{1}{2} g_2^{t-\Delta t}\sum_{n=1}^{\mathrm{NP}}\left[J_n\left(\mathbb{B}_{kl}^{2}\left(\frac{1-\exp(-\lambda_n \Delta\psi^{t})}{\lambda_n \Delta\psi^{t}}\right) - \mathbb{B}_{kl}^{3}\exp(-\lambda_n \Delta\psi^{t})\right)\right] S_{ps}^{t-\Delta t,\mathrm{dev}}\right]\right] \tag{C.42}$$

Hence, according to $U_{xq}^{-1}R_{qj}^{\mathrm{T}} = \left(U_{xq}R_{qj}\right)^{-1} = F_{xj}^{\mathrm{ve}\,-1}$, one may expand Eq. (C.31) as

$$\frac{\partial \Delta F_{ij}}{\partial \Delta S_{kl}^{t}} = -F_{ip}^{\mathrm{FEM}}\left[K_{pskl}\left(I + 2E^{t,\mathrm{vol}}\right)_{sx}^{-1} + G_{pskl}\left(I + 2E^{t,\mathrm{dev}}\right)_{sx}^{-1}\right]F_{xj}^{\mathrm{ve}\,-1} \tag{C.43}$$

Also

$$\Delta F_{im}^{\mathrm{T}} = \left(F_{my}^{\mathrm{FEM}}F_{yi}^{-1}\right)^{\mathrm{T}} = F_{iy}^{-\mathrm{T}}F_{ym}^{\mathrm{FEM}\,\mathrm{T}} \tag{C.44}$$

Therefore, the forth order compliance tensor, Eq. (C.30) will be written finally as

$$\frac{\partial R_{ij}^{t}}{\partial \Delta S_{kl}^{t}} = -\mathrm{symm}\left(F_{iy}^{-\mathrm{T}}C_{yp}^{\mathrm{FEM}}\left[K_{pskl}\left(I + 2E^{t,\mathrm{vol}}\right)_{sx}^{-1} + G_{pskl}\left(I + 2E^{t,\mathrm{dev}}\right)_{sx}^{-1}\right]F_{xj}^{\mathrm{ve}\,-1}\right) \tag{C.45}$$

APPENDIX D

1. Derivation of Consistent Tangent Compliance of Modified Viscoelastic and Viscoplastic Models

Similar to Appendix C, here a consistent tangent modulus for compliance is defined by taking the partial derivative of incremental residual strain with respect to the increment of stress at the end of each time analysis. As explained in Appendix C, the consistent tangent compliance matrix can be written as following, at the converged state

$$C^t_{ijkl} = \frac{\partial R^t_{ij}}{\partial \Delta S^t_{kl}} \tag{D.1}$$

Here, the same approach as mentioned in Appendix C is used for the cases when the time increments become larger or the quantity of the volumetric strain is not small comparing to the distortional counterpart. Thus, the same mathematical form for the residual strain introduced in Eq. (4.74) or (C.29), is recalled and used for this purpose

$$R^t_{ij} = \delta E^t_{ij} = \frac{1}{2}\left(\Delta F^{\mathrm{T}}_{ik}\Delta F_{kj} - I\right) \quad , \quad \text{where: } \Delta F = F^{\mathrm{FEM}} F^{-1} \tag{D.2}$$

where F^{FEM} is the deformation gradient that is provided by FEM software, and F is the one computed through constitutive models.

$$\frac{\partial R^t_{ij}}{\partial \Delta S^t_{kl}} = \frac{1}{2}\left(\left(\frac{\partial \Delta F_{im}}{\partial \Delta S^t_{kl}}\right)^{\mathrm{T}} \Delta F_{mj} + \Delta F^{\mathrm{T}}_{im}\left(\frac{\partial \Delta F_{mj}}{\partial \Delta S^t_{kl}}\right)\right) \tag{D.3}$$

Henceforth, one should find the mathematical relation of $\frac{\partial \Delta F_{im}}{\partial \Delta S^t_{kl}}$, which is presented in the following. Substituting $\Delta F = F^{\mathrm{FEM}} F^{-1}$ and $F = F^{\mathrm{ve}} F^{\mathrm{vp}} = R U^{\mathrm{ve}} U^{\mathrm{vp}}$, one can derive

$$\frac{\partial \Delta F_{ij}}{\partial \Delta S^{t}_{kl}} = F^{\mathrm{FEM}}_{ip}\left[\frac{\partial U^{\mathrm{vp}\,-1}_{pr}}{\partial \Delta S^{t}_{kl}} U^{\mathrm{ve}\,-1}_{rq} + U^{\mathrm{vp}\,-1}_{pr}\frac{\partial U^{\mathrm{ve}\,-1}_{rq}}{\partial \Delta S^{t}_{kl}}\right] R^{\mathrm{T}}_{qj} \tag{D.4}$$

In this equation, the derivation of the inverse of viscoelastic stretch with respect to the incremental II-PK stress is expressed in Eq. (C.41). However, in order to derive the inverse of viscoplastic stretch with respect to the incremental II-PK stress, the definition of viscoplastic stretch should be revisited [see Eq. (3.89) and (3.94)].

$$U^{\mathrm{vp}}_{t} = \exp(\mathbb{X}_{t}\,\Delta t)\, U^{\mathrm{vp}}_{t-\Delta t} \qquad , \qquad \mathbb{X}_{t} = \left(R_{t}\right)^{\mathrm{T}} D^{\mathrm{vp}}_{t}\left(R_{t}\right) \tag{D.5}$$

Therefore, the inverse of viscoplastic stretch in Eq. (D.5) is

$$\left(U^{\mathrm{vp}}_{t}\right)^{-1} = \left(U^{\mathrm{vp}}_{t-\Delta t}\right)^{-1} \exp(-\mathbb{X}_{t}\,\Delta t) \tag{D.6}$$

One can find the derivation of this equation with respect to the incremental II-PK stress

$$\frac{\partial U^{t,\mathrm{vp}\,-1}_{pr}}{\partial \Delta S^{t}_{kl}} = U^{t-\Delta t,\mathrm{vp}\,-1}_{px}(-\Delta t)\,\frac{\partial \mathbb{X}^{t}_{xy}}{\partial \Delta S^{t}_{kl}}\,\exp(-\Delta t\,\mathbb{X}^{t}_{yr}) \tag{D.7}$$

According to the commutability of stretch and incremental stretch tensors, one can write

$$\frac{\partial U^{t,\mathrm{vp}\,-1}_{pr}}{\partial \Delta S^{t}_{kl}} = (-\Delta t) U^{t-\Delta t,\mathrm{vp}\,-1}_{px}\,\exp(-\Delta t\,\mathbb{X}_{xy})\,\frac{\partial \mathbb{X}^{t}_{yr}}{\partial \Delta S^{t}_{kl}} \tag{D.8}$$

which delivers

$$\frac{\partial U^{t,\mathrm{vp}\,-1}_{pr}}{\partial \Delta S^{t}_{kl}} = (-\Delta t) U^{t,\mathrm{vp}\,-1}_{py}\,\frac{\partial \mathbb{X}^{t}_{yr}}{\partial \Delta S^{t}_{kl}} \tag{D.9}$$

According to the definition of the viscoplastic stretch, $D^{\mathrm{t,vp}}$ (see Chapters 3 and 5), the derivation of the rotated viscoplastic stretch regarding to the incremental II-Pk stress, $\frac{\partial \mathbb{X}^t}{\partial \Delta S^t}$, can be written as

$$\frac{\partial \mathbb{X}^t_{yr}}{\partial \Delta S^t_{kl}} = \frac{\partial}{\partial \Delta S^t_{kl}} \left(R^{t\ \mathrm{T}}_{ya} D^{\mathrm{t,vp}}_{ab} R^t_{br} \right) = R^{t\ \mathrm{T}}_{ya} \frac{\partial}{\partial \Delta S^t_{kl}} \left(\Delta \gamma^{\mathrm{vp}} \frac{\partial g}{\partial \Delta \bar{S}_{ab}} \right) R^t_{br} \tag{D.10}$$

Here, one should recall that R_t is constant through each time increment, or if R_t is lumped to the viscoelastic part, then it must be removed from the above and consequently from the following derivations. However, by substituting the relation for $\Delta \gamma^{\mathrm{vp}}$ and the viscoplastic potential function, g; one can get

$$\frac{\partial \mathbb{X}^t_{yr}}{\partial \Delta S^t_{kl}} = \Delta t\ \Gamma^{\mathrm{vp}} R^{t\ \mathrm{T}}_{ya} \frac{\partial}{\partial \Delta S^t_{kl}} \left(\left\langle \frac{f\ (\bar{S}, E^{\mathrm{vp}}_{\mathrm{eff}})}{S^0_{\mathrm{yield}}} \right\rangle^N \frac{\partial g}{\partial \Delta \bar{S}_{ab}} \right) R^t_{br} \tag{D.11}$$

Expanding the recent equation, delivers

$$\frac{\partial \mathbb{X}^t_{yr}}{\partial \Delta S^t_{kl}} = \Delta t\ \Gamma^{\mathrm{vp}} \left(\frac{f}{S^0_{\mathrm{yield}}} \right)^N R^{t\ \mathrm{T}}_{ya} \left[\frac{N}{f} \frac{\partial g}{\partial \Delta \bar{S}_{ab}} \frac{\partial f}{\partial \Delta \bar{S}_{kl}} + \frac{\partial^2 g}{\partial \Delta \bar{S}_{ab} \partial \Delta \bar{S}_{kl}} \right] R^t_{br} \tag{D.12}$$

The definition of the functions f and g are presented in Chapter 5. Now, regarding the definition of the stress invariants, one can simply obtain

$$\frac{\partial \bar{J}_2}{\partial \bar{S}_{ij}} = 3 \bar{S}^{\mathrm{dev}}_{ij} \qquad , \qquad \frac{\partial \bar{J}_3}{\partial \bar{S}_{ij}} = \frac{27}{2} \bar{S}^{\mathrm{dev}}_{ik} \bar{S}^{\mathrm{dev}}_{kj} - 3 \bar{J}_2 \delta_{ij} \tag{D.13}$$

Moreover, the derivation of the yield function, f in Eq. (5.17), regarding to stress is presented here

$$\frac{\partial f}{\partial \bar{S}_{ij}} = \frac{1}{2}\left[\left(1+\frac{1}{d}\right)\left(\frac{\partial \bar{J}_2}{\partial \bar{S}_{ij}}\right)\frac{1}{2\sqrt{\bar{J}_2}} + \left(1-\frac{1}{d}\right)\left(\frac{\partial \bar{J}_3}{\partial \bar{S}_{ij}}\bar{J}_2 - \frac{\partial \bar{J}_2}{\partial \bar{S}_{ij}}\bar{J}_3\right)\frac{1}{\bar{J}_2^2}\right] - \frac{1}{3}\alpha\,\delta_{ij} \tag{D.14}$$

Also, the first and second derivations of the viscoplastic potential function, g in Eq. (5.20), with respect to the stress state are expressed as

$$\frac{\partial g}{\partial \bar{S}_{ij}} = \frac{1}{2}\left[\left(1+\frac{1}{d}\right)\left(\frac{\partial \bar{J}_2}{\partial \bar{S}_{ij}}\right)\frac{1}{2\sqrt{\bar{J}_2}} + \left(1-\frac{1}{d}\right)\left(\frac{\partial \bar{J}_3}{\partial \bar{S}_{ij}}\bar{J}_2 - \frac{\partial \bar{J}_2}{\partial \bar{S}_{ij}}\bar{J}_3\right)\frac{1}{\bar{J}_2^2}\right] - \frac{1}{3}\beta\,\delta_{ij} \tag{D.15}$$

$$\begin{aligned}\frac{\partial^2 g}{\partial \bar{S}_{ij}\partial \bar{S}_{kl}} = 1.5\Bigg[&(\delta_{ik}\delta_{jl} - \frac{1}{3}\delta_{ij}\delta_{kl})\left[\frac{1}{2\sqrt{J_2}}\left(1+\frac{1}{d}\right) - \frac{J_3}{J_2^2}\left(1-\frac{1}{d}\right)\right] \\ &+ \frac{\bar{S}_{kl}}{J_2^2}\left[-\left(1+\frac{1}{d}\right)\frac{\partial \bar{J}_2}{\partial \bar{S}_{ij}}\frac{\sqrt{J_2}}{4} + \left(1-\frac{1}{d}\right)\left(2\frac{\bar{J}_3}{\bar{J}_2}\frac{\partial \bar{J}_2}{\partial \bar{S}_{ij}} - \frac{\partial \bar{J}_3}{\partial \bar{S}_{ij}}\right)\right] \\ &+ \frac{3}{\bar{J}_2^2}\left(1-\frac{1}{d}\right)\left[\frac{3}{2}\left(\delta_{ik}\bar{S}_{lj} + \delta_{jl}\bar{S}_{ik}\right) - \left(\delta_{kl}\bar{S}_{ij} + \delta_{ij}\bar{S}_{kl}\right)\right] \\ &- \left(\frac{9}{2}\bar{S}_{km}\bar{S}_{ml} - J_2\bar{S}_{kl}\right)\left(\left(1-\frac{1}{d}\right)\frac{1}{\bar{J}_2^2}\frac{\partial \bar{J}_2}{\partial \bar{S}_{ij}}\right)\Bigg]\end{aligned} \tag{D.16}$$

Up to now, all the required tensors are determined. Henceforth, the second term of Eq. (C.30) can be found by substituting ΔF into it as

$$\Delta F_{im}^{\mathrm{T}}\frac{\partial \Delta F_{mj}}{\partial \Delta S_{kl}^{t}} = \left(F_{mx}^{\mathrm{FEM}}F_{xi}^{-1}\right)^{\mathrm{T}}F_{mp}^{\mathrm{FEM}}\left[\frac{\partial U_{pr}^{\mathrm{vp}\,-1}}{\partial \Delta S_{kl}^{t}}U_{rq}^{\mathrm{ve}\,-1} + U_{pr}^{\mathrm{vp}\,-1}\frac{\partial U_{rq}^{\mathrm{ve}\,-1}}{\partial \Delta S_{kl}^{t}}\right]R_{qj}^{\mathrm{T}} \tag{D.17}$$

Now, one should recall $F^{\mathrm{ve}\,-1} = U^{\mathrm{ve}\,-1}R^{\mathrm{T}}$, and $C^{\mathrm{FEM}} = F^{\mathrm{FEM}\,\mathrm{T}}F^{\mathrm{FEM}}$. Then, through utilizing Eqs. (C.43) to (C.45), Eq. (D.17) can be expanded as

$$\begin{aligned}\Delta F_{im}^{\mathrm{T}}\frac{\partial \Delta F_{mj}}{\partial \Delta S_{kl}^{t}} = F_{ix}^{-\mathrm{T}}C_{xp}^{\mathrm{FEM}}\Bigg[&(-\Delta t)U_{py}^{t,\mathrm{vp}\,-1}\frac{\partial \mathbb{X}_{yr}^{t}}{\partial \Delta S_{kl}^{t}}U_{rq}^{\mathrm{ve}\,-1} \\ &-U_{pr}^{\mathrm{vp}\,-1}\left[K_{rskl}\left(I+2E^{t,\mathrm{vol}}\right)_{sx}^{-1} + G_{rskl}\left(I+2E^{t,\mathrm{dev}}\right)_{sx}^{-1}\right]U_{xq}^{\mathrm{ve}\,-1}\Bigg]R_{qj}^{\mathrm{T}}\end{aligned} \tag{D.18}$$

After factorizing the inverse of the viscoplastic stretch from left side and viscoelastic one from right side, one can obtain the final form of the compliance tensor as

$$\frac{\partial R_{ij}^{t}}{\partial \Delta S_{kl}^{t}} = -\text{symm}\Bigg(F_{iy}^{-\text{T}} C_{yp}^{\text{FEM}} U_{py}^{t,\text{vp}\,-1} \Bigg[\Delta t \; \frac{\partial \mathbb{X}_{yr}^{t}}{\partial \Delta S_{kl}^{t}} + K_{pskl} \left(I + 2E^{t,\text{vol}} \right)_{sx}^{-1} + G_{pskl} \left(I + 2E^{t,\text{dev}} \right)_{sx}^{-1} \Bigg] F_{xj}^{\text{ve}\,-1} \Bigg) \tag{D.19}$$

The forth order tensors K_{pskl} and G_{pskl} are expressed in Appendix C [see Eq. (C.42)].

APPENDIX E

1. Thermodynamic Based Formulation for Modeling Coupled Viscoelastic, Viscoplastic, Viscodamage Constitutive Material Laws

This appendix briefly presents a general thermodynamic framework for coupling viscoelastic, viscoplastic, and viscodamage models in the isothermal conditions. This framework will then be applied to derive Schapery's (1969a) non-linear viscoelastic model, Perzyna's (1971) viscoplastic model, and the viscodamage model of Darabi et al. (2011). Readers are referred to Abu Al-Rub and Darabi (2012) for detailed information on the general thermodynamic framework for derivation of coupled viscoelastic, viscoplastic, and viscodamage models for time- and rate-dependent materials. For simplicity, the following thermodynamic formulations are presented assuming large deformation concept.

One can start with the principle of virtual power which states that the external outflow of the power, P_{int}, due to a virtual motion should be balanced by the internal expenditure of the power, P_{ext}, associated with the same virtual motion, such that

$$P_{\text{int}} = P_{\text{ext}} \tag{E.1}$$

where P_{int} is assumed to be characterized by the Cauchy stress tensor σ, the drag-stress R associated with the isotropic hardening, the damage force Y conjugate to the damage density variable ϕ, and $N_{\text{int}}^{\text{ve}}$-thermodynamic forces χ_n conjugate to the phenomenological internal state variables associated with viscoelastic process, ξ_n ($n = 1,...,N_{\text{int}}^{\text{ve}};\ N_{\text{int}}^{\text{ve}} \geq 1$). On the other hand, P_{ext} is defined in terms of the macroscopic

body force vector $\boldsymbol{b}$, the macroscopic surface traction $\boldsymbol{t}$, and inertial forces. Hence, P_{int} and P_{ext} can be written, respectively, as

$$P_{\text{int}} = \int_{\Gamma_o} \left(S_{ij} \dot{E}_{ij}^{\text{ve}} + \sum_{n=1}^{N_{\text{int}}^{\text{ve}}} \chi_n \dot{\xi}_n + R \dot{E}_e^{\text{vp}} + Y \dot{\phi} \right) \text{dv} \tag{E.2}$$

$$P_{\text{ext}} = \int_{\Gamma_o} b_i \dot{u}_i \, \text{dv} + \int_{\partial\Gamma_o} t_i \dot{u}_i \, \text{dA} + \int_{\Gamma_o} \rho \ddot{u}_i \dot{u}_i \, \text{dv} \tag{E.3}$$

where $\dot{E}_e^{\text{vp}}$, $\boldsymbol{u}$, Γ_o, and $\partial\Gamma_o$ are the rate of the equivalent viscoplastic strain, the displacement vector, an arbitrary sub-body in the initial configuration, and the boundary of the selected sub-body, respectively. From now on, E_{ij} is the GL strain and S_{ij} is the II-PK stress. It is noteworthy that the internal state variables associated with the viscoelastic process (i.e. ξ_n) are considered as hidden state variables. These hidden state variables are associated with the microstructure of the materials or the chain mobility in polymers and cause the evolution of the viscoelastic strain E^{ve} which is an observable variable that can be measured experimentally. Substituting Eqs. (E.2) and (E.3) into the principle of virtual power (i.e. Eq. (E.1)), and applying the divergence theorem yield

$$S_{IJ,J} + b_I = \rho_o \ddot{u} \quad \text{in} \quad \Gamma_o \qquad , \qquad T_I = S_{IJ} n_J \quad \text{on} \quad \partial\Gamma_o \tag{E.4}$$

$$S_{ij} N_{ij} - R = 0 \qquad \text{in} \quad \Gamma_o \tag{E.5}$$

$$Y = 0 \quad \text{and} \quad \chi_n = 0 \qquad \text{in} \quad \Gamma_o \tag{E.6}$$

where ρ_o is the density in the material configuration, $\boldsymbol{n}$ denotes the outward unit vector normal on the boundary $\partial\Gamma_o$ and $\boldsymbol{N}$ denotes a second-order tensor representing the unit direction of the viscoplastic rate of deformation tensor, D^{vp}, that can be defined using

the non-associative normality flow rule, such that

$$N_{ij} = \frac{\partial g}{\partial S_{ij}} \tag{E.7}$$

where g is the viscoplastic potential function in Eq. (5.20). Eq. (E.4) is the local static or dynamic equilibrium and the boundary traction, respectively. Eq. (E.5) is the viscoplastic micro-force balance (according to notion of Gurtin (2003)) which can be used for deriving the dynamic viscoplasticity yield surface. Similarly in Eq. (E.6), Y and χ_n define the damage micro-force balance (Fremond and Nedjar, 1996) and the viscoelastic micro-force balance (Abu Al-Rub et al., 2010), respectively.

In continuum damage mechanics, in order to transform equations from the nominal (damaged) configuration to the effective (undamaged) configuration, a transformation hypothesis is required. Recently, Darabi et al. (2011) revisited the commonly assumed strain equivalence and strain energy equivalence hypotheses (Abu Al-Rub and Voyiadjis, 2003) and proposed a more physically sound transformation hypothesis for time-dependent materials according to the power equivalence hypothesis. The power equivalence hypothesis states that any type of power (e.g. elastic, viscoelastic, plastic) in the nominal configuration is equal to its identity power in the effective configuration. Therefore, one can rewrite Eq. (E.2) as

$$P_{\text{int}} = \int_{\Gamma_o} (\bar{S}_{ij} \dot{\bar{E}}_{ij}^{\text{ve}} + \sum_{n=1}^{N_{\text{int}}^{\text{ve}}} \bar{\chi}_n \dot{\bar{\xi}}_n + \bar{R} \dot{\bar{E}}_e^{\text{vp}}) \, \text{dv} \tag{E.8}$$

The superimposed dash indicates a quantity in the effective state. For developing the thermodynamic-based constitutive equations, it is assumed that the state of the materials

can be characterized by the suitable internal state variables which implicitly describe important micro-structural mechanisms that affect the macroscopic behavior of the material. The Helmholtz free energy (per unit mass), Ψ, is considered as the thermodynamic state potential depending on the internal state variables. Here, Ψ is assumed to depend on the following internal state variables in the undamaged configuration

$$\Psi = \Psi\left(\bar{E}_{ij}^{ve},\, \bar{E}_{e}^{vp},\, \phi,\, \bar{\xi}_n\right) \tag{E.9}$$

The Clausius-Duhem inequality for isothermal conditions (Gurtin, 2003) can be written as next

$$\int_{\Gamma_o} \rho\, \dot{\Psi}\, \mathrm{dv} \leq P_{\mathrm{ext}} = P_{\mathrm{int}} \tag{E.10}$$

Employing Eqs. (E.2) and (E.9) into Eq. (E.10) and also making use of the power equivalence hypothesis to relate variables in the effective and nominal configurations, Eq. (E.8), deliver the following inequality for the rate of energy dissipation (Π)

$$\begin{aligned} \Pi = &\left(\bar{S}_{ij} - \rho_o \frac{\partial \Psi}{\partial \bar{E}_{ij}^{\mathrm{ve}}}\right)\dot{\bar{E}}_{ij}^{\mathrm{ve}} + \sum_{n=1}^{N_{\mathrm{int}}^{\mathrm{ve}}}\left(\bar{\chi}_n - \rho_o \frac{\partial \Psi}{\partial \bar{\xi}_n}\right)\dot{\bar{\xi}}_n \\ &+ \left(\bar{R} - \rho \frac{\partial \Psi}{\partial \bar{E}_{e}^{\mathrm{vp}}}\right)\dot{\bar{E}}_{e}^{\mathrm{vp}} + \left(Y - \rho_o \frac{\partial \Psi}{\partial \phi}\right)\dot{\phi} \;\geq\; 0 \end{aligned} \tag{E.11}$$

However, to obtain a non-zero dissipation resulting from the viscoelasticity, viscoplasticity, and viscodamage dissipative processes, the following energetic thermodynamic conjugate forces that depend on the Helmholtz free energy are defined from Eq. (E.11), such that

$$\bar{S}_{ij}^{\text{ene}} \equiv \rho_o \frac{\partial \Psi}{\partial \bar{E}_{ij}^{\text{ve}}} \quad , \quad \bar{\chi}_n^{\text{ene}} \equiv \rho_o \frac{\partial \Psi}{\partial \bar{\xi}_n} \quad , \quad \bar{R}^{\text{ene}} \equiv \rho_o \frac{\partial \Psi}{\partial \bar{E}_e^{vp}} \quad , \quad Y^{\text{ene}} \equiv \rho_o \frac{\partial \Psi}{\partial \phi} \tag{E.12}$$

The superscript "ene" means the energetic portion of the thermodynamic conjugate force. Besides, since any thermodynamic force is made ofa dissipative and an energetic component; thus by substituting Eqs. (E.12) into Eq. (E.11), one can get

$$\Pi = \bar{S}_{ij}^{\text{dis}} \dot{\bar{E}}_{ij}^{\text{ve}} + \sum_{n=1}^{N_{\text{int}}^{\text{ve}}} \bar{\chi}_n^{\text{dis}} \dot{\bar{\xi}} + \bar{R}^{\text{dis}} \dot{\bar{E}}_e^{\text{vp}} + Y^{\text{dis}} \dot{\phi} \;\geq\; 0 \tag{E.13}$$

The energetic and dissipative thermodynamic conjugate forces are related to the Helmholtz free energy function, Ψ, and the rate of dissipation potential, Π, respectively. Therefore, in order to formulate constitutive equations for the energetic and dissipative conjugate forces, one needs to know: (1) how the material stores energy, and (2) how the material dissipates energy; which helps in assuming mathematical forms for both Ψ and Π. The dissipative component of the thermodynamic conjugate forces can be determined using the maximum dissipation principle along with the calculus of several variables (Abu Al-Rub and Darabi, 2012), such that

$$\bar{\sigma}_{ij}^{\text{dis}} = \Lambda^{\text{ve}} \frac{\partial \Pi^{\text{ve}}}{\partial \dot{\bar{\varepsilon}}_{ij}^{\text{ve}}} \quad , \quad \bar{\chi}_n^{\text{dis}} = \Lambda^{\text{ve}} \frac{\partial \Pi^{\text{ve}}}{\partial \dot{\bar{\xi}}_n}; \qquad \Lambda^{\text{ve}} = \frac{\Pi^{\text{ve}}}{\frac{\partial \Pi^{\text{ve}}}{\partial \dot{\bar{\varepsilon}}_{ij}^{\text{ve}}} \dot{\bar{\varepsilon}}_{ij}^{\text{ve}} + \frac{\partial \Pi^{\text{ve}}}{\partial \dot{\bar{\xi}}_n} \dot{\bar{\xi}}_n} \tag{E.14}$$

$$\bar{R}^{\text{dis}} = \Lambda^{\text{vp}} \frac{\partial \Pi^{\text{vp}}}{\partial \dot{\bar{\varepsilon}}_e^{\text{vp}}} \quad , \quad \Lambda^{\text{vp}} = \frac{\Pi^{\text{vp}}}{\frac{\partial \Pi^{\text{vp}}}{\partial \dot{\bar{\varepsilon}}_e^{\text{vp}}} \dot{\bar{\varepsilon}}_e^{\text{vp}}} ; \qquad Y^{\text{dis}} = \Lambda^{\text{vp}} \frac{\partial \Pi^{\text{vp}}}{\partial \dot{\phi}}, \; \Lambda^{\text{vp}} = \frac{\Pi^{\text{vp}}}{\frac{\partial \Pi^{\text{vp}}}{\partial \dot{\phi}} \dot{\phi}} \tag{E.15}$$

The energetic and dissipative components of the thermodynamic conjugate forces can now be determined using Eqs. (E.12), (E.14), and (E.15) provided that Ψ and Π are known. Therefore, one needs to assume mathematical forms for Ψ and Π to derive the

specific constitutive equations. The next mathematical assumed forms lead to derive Schapery's non-linear viscoelastic model (stress state as a function of strain history)

$$\begin{aligned} \rho_o \Psi^{\text{ve}} &= \frac{1}{2} L^{(1)}_{ijkl} \bar{E}^{\text{ve}}_{ij} \bar{E}^{\text{ve}}_{kl} + \frac{1}{2} L^{(2)}_{mn} \bar{\xi}_m \bar{\xi}_n + L^{(3)}_{ijn} \bar{E}^{\text{ve}}_{ij} \bar{\xi}_n \\ \Pi^{\text{ve}} &= \mu_{ijkl} \dot{\bar{E}}^{\text{ve}}_{ij} \dot{\bar{E}}^{\text{ve}}_{kl} + P_{mn} \dot{\bar{\xi}}_m \dot{\bar{\xi}}_n \end{aligned} \tag{E.16}$$

The energetic and dissipative components of the viscoelastic conjugate forces can be determined using Eqs. (E.12), (E.14), and (E.16), such that

$$\bar{\chi}^{\text{ene}}_n = L^{(2)}_{mn} \bar{\xi}_m + a_1 \left(\bar{E}^{ve} \right) L^{(3)}_{ijn} \bar{E}^{ve}_{ij} \qquad , \qquad \bar{\chi}^{\text{dis}}_n = P_{mn} \dot{\bar{\xi}}_m \tag{E.17}$$

Replacing Eqs. (E.17) into the viscoelastic internal micro force balance (i.e. $\chi_n = \chi^{\text{ene}}_n + \chi^{\text{dis}}_n = 0$) yields the following partial differential equation that governs the viscoelastic process

$$P_{mn} \dot{\bar{\xi}}_m + L^{(2)}_{mn} \bar{\xi}_m + L^{(3)}_{ijn} \bar{E}^{\text{ve}}_{ij} = 0 \tag{E.18}$$

Solving Eq. (E.18) and using the Laplace transform delivers

$$\bar{\xi}_m(\psi) = -\frac{L^{(3)}_{ijm}}{L^{(2)}_{mm}} \int_0^t \left(1 - \exp[-\omega_m (t-\tau)]\right) \frac{\mathrm{d}\bar{\mathrm{E}}^{\text{ve}}_{ij}}{\mathrm{d}\tau} \mathrm{d}\tau \qquad , \qquad (\text{No sum on } m) \tag{E.19}$$

where $\omega_m = L^{(2)}_{mm} / P_{mm}$. Similarly, the energetic and dissipative components of the stress can be determined using Eqs. (E.12), (E.14), and (E.16), as

$$\bar{S}^{\text{ene}}_{ij} = L^{(1)}_{tukl} \bar{E}^{\text{ve}}_{kl} + L^{(3)}_{tun} \bar{\xi} \qquad , \qquad \bar{S}^{\text{dis}}_{ij} = \mu_{ijkl} \dot{\bar{E}}^{\text{ve}}_{kl} \tag{E.20}$$

The II-PK stress as a function of the viscoelastic GL strain can now be obtained using Eqs. (E.19) and (E.20)

$$\bar{S}_{ij} = \mu_{ijkl} \dot{\bar{E}}^{\text{ve}}_{kl} + C^{(0)}_{pqkl} \bar{E}^{\text{ve}}_{kl} + \int_0^t \left[\sum_{m=1}^{M} C^{(m)}_{pqkl} \left(1 - \exp[-\omega_m (t-\tau)]\right) \right] \frac{\mathrm{d}\left(\bar{E}^{\text{ve}}_{kl}\right)}{\mathrm{d}\tau} \mathrm{d}\tau \tag{E.21}$$

where $C_{ijkl}^{(0)} = L_{ijkl}^{(1)} - \left(L_{ijm}^{(3)} L_{klm}^{(3)}\right) / L_{mm}^{(2)}$ and $C_{ijkl}^{(m)} = L_{ijm}^{(3)} L_{klm}^{(3)} / L_{mm}^{(2)}$. Eq. (E.21) represents a more comprehensive formulation relating the total stress to the viscoelastic strain comparing to classical Schapery's viscoelasticity model. Viscoelastic strain as a function of stress (i.e. Eq. (5.8)) can simply be derived by applying the inverse Laplace transform to Eq. (E.21). Now, in order to derive the Perzyna-type viscoplasticity model used in this work (see Section 2.3), the following mathematical forms are assumed for the viscoplastic components of the Helmholtz free energy and the rate of energy dissipation, such that

$$\rho \Psi^{\text{vp}} = \left(\kappa_0 + \kappa_1\right) \bar{\varepsilon}_e^{\text{vp}} + \frac{\kappa_1}{\kappa_2} \exp\left(-\kappa_2 \bar{\varepsilon}_e^{\text{vp}}\right) \qquad , \qquad \Pi^{\text{vp}} = \sigma_y^0 \Gamma^{\text{vp}} \left(\frac{\dot{\bar{\varepsilon}}_e^{\text{vp}}}{\Gamma^{\text{vp}}}\right)^{1+\frac{1}{N}} \tag{E.22}$$

Substituting Eq. (E.22) into Eqs. (E.12) and (E.15) yields

$$R = \kappa_0 + \kappa_1 \left[1 - \exp\left(-\kappa_2 \bar{\varepsilon}_{\text{eff}}^{\text{vp}}\right)\right] + \sigma_y^0 \left(\frac{\bar{\varepsilon}_{\text{eff}}^{\text{vp}}}{\Gamma^{\text{vp}}}\right)^{\frac{1}{N}} \tag{E.23}$$

Substituting Eqs. (E.7) and (E.23) into the micro-force balance in Eq. (E.5) leads to the viscoplastic model used in this work, such that:

$$\chi = \bar{\tau} - \alpha \bar{I}_1 - \kappa_0 - \kappa_1 \left[1 - \exp\left(-\kappa_2 \bar{\varepsilon}_{\text{eff}}^{\text{vp}}\right)\right] - \sigma_y^0 \left(\frac{\dot{\gamma}^{\text{vp}}}{\Gamma^{\text{vp}}}\right)^{1/N} \leq 0 \tag{E.24}$$

The above expression can be rearranged to obtain Perzyna-type viscoplastic model in Eqs. (5.14) to (5.19). Similarly, the following forms are assumed for the viscodamage components of the Helmholtz free energy and rate of the energy dissipation in order to derive the viscodamage model used in this work

$$\rho \Psi^{\text{vd}} = \frac{(1-\phi)^3}{3Y_0}\left\langle \bar{\tau} - \alpha \bar{I}_1 \right\rangle \exp\left(\frac{k}{q}\bar{E}_{\text{eff}}\right) \qquad , \qquad \Pi^{\text{vd}} = \Gamma_0^{\text{vd}}\left(\frac{\dot{\phi}}{\Gamma_0^{\text{vd}}}\right)^{1+\frac{1}{q}} \tag{E.25}$$

Substituting Eq. (E.25) into Eqs. (E.12) and (E.15) yields

$$Y^{\text{ene}} = -\frac{(1-\phi)^2}{Y_0}\left\langle \bar{\tau} - \alpha \bar{I}_1 \right\rangle \exp\left(\frac{k}{q}\bar{E}_{\text{eff}}\right) \qquad , \qquad Y^{\text{dis}} = \left(\frac{\dot{\phi}}{\Gamma^{\text{vd}}}\right)^{\frac{1}{q}} \tag{E.26}$$

The viscodamage model used in this work is obtained by substituting the energetic and dissipative components of the damage conjugate force into the damage micro-force balance in Eq. (E.6) (i.e. $Y = Y^{\text{ene}} + Y^{\text{dis}} = 0$), such that

$$\dot{\phi} = \Gamma_0^{\text{vd}}\left[\frac{\bar{Y}(1-\phi)^2}{Y_0}\right]^q \exp(k\,\bar{E}_{\text{eff}}) \tag{E.27}$$

It is noteworthy to mention that the presented thermodynamic framework is general and can be used for derivation of different constitutive models for different types of materials depending on the assumed expression for Ψ (Helmholtz free energy function), and Π (rate of dissipation potential).